DEVELOPMENT OF DIRECT-INVERSE 3-D METHODS FOR APPLIED TRANSONIC AERODYNAMIC WING DESIGN AND ANALYSIS

AEROSPACE ENGINEERING DEPARTMENT

Final Report

October 1985 - August 1989

TEXAS A&M UNIVERSITY

TAMRF Report No. 5373-8903

October 1989

NASA Grant No. NAG-1-619

TAMRF Project RF 5373

Leland A. Carlson
Professor of Aerospace Engineering
Texas A&M University
College Station

TEXAS ENGINEERING EXPERIMENT STATION

DEVELOPMENT OF DIRECT-INVERSE 3-D METHODS FOR APPLIED TRANSONIC AERODYNAMIC WING DESIGN AND ANALYSIS

Final Report

October 1985 -- August 1989

TAMRF Report No. 5373 - 89 - 03

October 1989

NASA Grant No. NAG-1-619
TAMRF Project RF 5373

Leland A. Carlson
Professor of Aerospace Engineering
Texas A&M University
College Station, Texas 77843-3141

TABLE OF CONTENTS

DEVELOPMENT OF DIRECT-INVERSE 3-D METHODS FOR APPLIED TRANSONIC AERODYNAMIC WING DESIGN AND ANALYSIS

I. Introduction

This report summarizes the activities and accomplishments associated with Texas A&M Research Foundation Project 5373 which was funded as NASA Grant NAG-1-619 from the NASA Langley Research Center. The project was awarded October 15, 1985 and actively continued until August 31, 1989. The primary objective of this effort was the development of a three dimensional direct-inverse transonic wing design and analysis code based upon the TAWFIVE analysis code (Ref. 1).

Because of its complex nature and the desire to establish proof of concept prior to final code development, the project was divided into two phases. The first phase developed an inviscid design code, established the validity of the method, and demonstrated the versatility of the approach by designing entire wings and discontinuous sections of wings. The second phase extended the method to include viscous interaction and investigated the limits and utility of the method. In addition, it indicated that it is feasible to successfully design a region of a wing which begins aft of the leading edge and which terminates prior to the trailing edge.

II. Personnel

While the project was officially awarded in October 1985, the fiscal paperwork was not completed for several months and the actual work was not permitted to start until January 1986. At that time Mr. Thomas A. Gally was assigned to the project as a graduate research assistant (GRA). Mr. Gally remained with the project on a GRA basis thru August 1987, and since then he has assisted the project whenever needed. In June 1987 Mr. Robert R. Ratcliff joined the project as a GRA to conduct the second phase of research. Mr. Ratcliff remained with the project thru August 1989. Both Mr. Gally and Mr. Ratcliff used their research work on the project as the basis for their master's theses. Mr. Gally recevied his M.Sc. degree in May 1987, while Mr. Ratcliff received his M. Sc. degree in August 1989.

The principal investigator for this project has been Dr. Leland A. Carlson, Professor of Aerospace Engineering. Originally, this entire project was to last two to three years, with each phase requiring about half of the total time. However, due to the discovery of a spanwise oscillation problem during the second phase of the project, the latter portion has taken considerably longer than anticipated. The principal investigator apologizes to NASA for this delay.

III. Accomplishments

The accomplishments and achievements of this project are contained in the following seven publications:

Gally, T. A., "Inverse Transonic Wing Design Using Finite-Volume Methods in Curvilinear Coordinates," M. Sc. Thesis, Texas A&M University, College Station, Texas, May 1987.

Gally, T. A. and Carlson, L. A., "Inverse Transonic Wing Design Using Inverse Methods in Curvilinear Coordinates," AIAA Paper No. 87-2551, Proceedings of the 5th Applied Aerodynamics Conference, AIAA, New York, August 1987, pp. 516-526.

Gally, T. A. and Carlson, L. A., "Transonic Wing Design Using Inverse Methods in Curvilinear Coordinates," Journal of Aircraft, Vol. 25, No. 11, November 1988, pp. 1009-1017.

Carlson, L. A., Ratcliff, R. R., Gally, T. A., and Campbell, R. L., "Inverse Wing Design in Transonic Flow Including Viscous Interaction," Transonic Symposium: Theory, Application, and Experiment, April 19-21, 1988, NASA CP 3020, Vol. 1, Part 2, 1989, pp. 497-519.

Ratcliff, R. R. and Carlson, L. A., "A Direct-Inverse Transonic Wing-Design Method in Curvilinear Coordinates Including Viscous Interaction," AIAA Paper No. 89-2204, Proceedings of the AIAA 7th Applied Aerodynamics Conference, August 1989, pp. 362-379.

Ratcliff, R. R., "Verification, Optimization and Refinement of a Direct-Inverse Transonic Wing Design Method Including Weak Viscous Interaction," M. Sc. Thesis, Texas A&M University, College Station, Texas, August 1989.

Ratcliff, R. R., Gally, T. A., Carlson, L. A., Melson, N. D., and Strett, C. L., "TAW5D: A Users Manual for Analysis and Inverse Design of Wings in Transonic Flow," TAMRF Report No. 5373 - 89 - 04, October 1989.

In the first phase of the project, an inviscid direct-inverse wing design method was developed and demonstrated (Ref 2 - 4). This method was based upon the analysis code TAWFIVE, which in turn was based upon the three dimensional transonic potential flow solver, FL030, developed by Caughey and Jameson (Ref. 5). This approach used a finite volume formulation, an SLOR solution scheme and a wing and fuselage fitted curvilinear grid mesh. In addition to developing the direct inverse design techniques, methods for properly handling trailing edge closure problems were develped and included in the design code.

The research established that:

(1) The method could obtain invsicid wing designs in both subscritical and supercritical flow.
(2) The method could be used to design entire wings or noncontiguous regions of the wing on both the upper and lower surfaces.

In addition, it was shown that the method could handle twist, could be used to change a wing from supercritical to subcritical, and could be used to make large surface changes to the original wing.

In the second phase of the project, viscous interaction was added to the design method. In addition, extensive studies of the method and comparisons with other codes were conducted in order to verify the method. These other codes contained a mixture of similar and different coordinate systems, flow solvers, and design methods. Based upon these studies, (Ref. 6), it was concluded that the present method and code was reliable and accurate. It addition, it was determined that inverse methods using similar coordinate systems and flow solvers will yield the same wing designs, and that inverse methods having different coordinate systems and fuselage representations but similar design procedures will yield different section profiles. However, the pressure distribtuions and lift coefficients in the latter case will be in reasonable agreement.

In addition, extensive studies were conducted to determine the approximate limits on wing aspect ratio and leading edge sweep angle required for a successful design. Also, studies showing the effects on the final design of spanwise grid skewness, grid refinement, viscous interaction, the initial airfoil section , and Mach nubmer pressure distribution compatibility were conducted. It was determined that:

(1) Designing at every other spanwise station is the most efficient approach.
(2) A smoothly varying grid is needed at the wing tip for accurate design.
(3) The final designed airfoil sections are independent of the initial sections if the direct-inverse junction is moved close to the leading edge.
(4) Boundary layer displacement thicknesses must be included in the design process. Otherwise, the designed wing will have less lift and different pressure distributions than desired.
(5) For the conditions considered, wake curvature and displacement effects have very little effect on the designed airfoil shapes or on the wing pressure distributions.
(6) Presently, the design of only high and medium aspect ratio wings is possible with this code, although preliminary approximate results can be obtained for highly swept low aspect ratio wings.

(7) A partial wing design beginning aft of the leading edge and terminating prior to the trailing edge is possible with the present method.

(8) From an accuracy standpoint, detailed wing designs should be performed on the fine grid, although preliminary results can be obtained using medium grids.

For details see the appendices of this report and Ref. 6 - 8.

IV. Conclusion

As indicated above and specifically in the appendices of this report, considerable progress in the development of a direct-inverse transonic wing design method in curvilinear coordinates which includes the effects of viscous interaction has been made. The resulting computer program (Ref. 9), called TAW5D, should be of value in the area of applied aerodynamics. However, the additional development of methods to improve the design scheme at the wing root and wing tip, to more easily permit the design of an entire airfoil section from leading edge to trailing edge, and to incorporate the more rapid multi-grid solver techniques (Ref. 10) would be desirable.

References

1. Melson, N. D. and Streett, C. L., "TAWFIVE: A User's Guide," NASA TM 84619, Sept. 1983.

2. Gally, T. A., "Inverse Transonic Wing Design Using Finite-Volume Methods in Curvilinear Coordinates," M. Sc. Thesis, Texas A&M University, College Station, Texas, May 1987.

3. Gally, T. A. and Carlson, L. A., "Inverse Transonic Wing Design Using Inverse Methods in Curvilinear Coordinates," AIAA Paper No. 87-2551, Proceedings of the 5th Applied Aerodynamics Conference, AIAA, New York, August 1987, pp. 516-526.

4. Gally, T. A. and Carlson, L. A., "Transonic Wing Design Using Inverse Methods in Curvilinear Coordinates," Journal of Aircraft, Vol. 25, No. 11, November 1988, pp. 1009-1017.

5. Caughey, D. A. and Jameson, A., "Progress in Finite Volume Calculation for Wing Fuselage Combinations," AIAA Paper No. 79-1513, July 1979.

6. Carlson, L. A., R. R. Ratcliff, T. A. Gally, and R. L. Campbell, "Inverse Wing Design in Transonic Flow Including Viscous Interaction," Transonic Symposium: Theory, Application, and Experiment, April 19-21, 1988, NASA CP 3020, Vol. 1, Part 2, 1989, pp. 497-519.

7. Ratcliff, R. R. and Carlson, L. A., "A Direct-Inverse Transonic Wing-Design Method in Curvilinear Coordinates Including Viscous Interaction," AIAA Paper No. 89-2204, Proceedings of the AIAA 7th Applied Aerodynamics Conference, August 1989, pp. 362-379.

8. Ratcliff, R. R., "Verification, Optimization and Refinement of a Direct-Inverse Transonic Wing Design Method Including Weak Viscous Interaction," M. Sc. Thesis, Texas A&M University, College Station, Texas, August 1989.

9. Ratcliff, R. R., T. A. Gally, Carlson, L. A., N. D. Melson, and Strett, C. L., "TAW5D: A Users Manual for Analysis and Inverse Design of Wings in Transonic Flow," TAMRF Report No. 5373 - 89 - 04, October 1989.

10. Melson, N. D. and Streett, C. L., "Updated User's Guide for TAWFIVE with Multigrid," NASA TM 4109, May 1989.

Appendix I

AIAA Publications

INVISCID TRANSONIC WING DESIGN USING INVERSE METHODS IN CURVILINEAR COORDINATES

Thomas A. Gally*
Texas A&M University
College Station, Texas

Leland A. Carlson**
Texas A&M University
College Station, Texas

ABSTRACT

An inverse wing design method has been developed around an existing transonic wing analysis code. The original analysis code, TAWFIVE, has as its core the numerical potential flow solver, FLO30, developed by Jameson and Caughey. Features of the analysis code include a finite-volume formulation; wing and fuselage fitted, curvilinear grid mesh; and a viscous boundary layer correction that also accounts for viscous wake thickness and curvature. The development of the inverse methods as an extension of previous methods existing for design in Cartesian coordinates is presented. Results are shown for inviscid wing design cases in super-critical flow regimes. The test cases selected also demonstrate the versatility of the design method in designing an entire wing or discontinuous sections of a wing.

NOMENCLATURE

C_p	- Coefficient of pressure
h	- Jacobian of coordinate transformation
H	- Jacobian matrix
J	- Transpose of inverse Jacobian matrix
M_∞	- Freestream Mach number
q_∞	- Magnitude of freestream velocity
Q	- Magnitude of local velocity
u,v,w	- Components of physical velocity vector
U,V,W	- Components of contravariant velocity vector
α	- Angle of attack
γ	- Ratio of specific heats
δ	- Differential operator
$\delta(x)$	- Displacement thickness
$\delta_T(x)$	- Displacement thickness due to relofting
Δ	- Trailing edge thickness
Δ_t	- User specified trailing edge thickness
μ	- Averaging operator
ρ	- Density
ϕ	- Reduced/perturbation potential function ($\Phi = \phi + x\cos(\alpha) + y\sin(\alpha)$)
Φ	- Potential function

INTRODUCTION

In recent years the importance of transonic flight to both military and commercial aircraft and the development of specialized transonic wings for several flight research experiments have prompted significant efforts to develop accurate and reliable computational methods for the analysis and design of transonic wings. Many methods of solution have been developed, but among those which have shown promise due to their computational efficiency and engineering accuracy have been those based upon the full potential flow equations in either their conservative or non-conservative form[1-3]. The TAWFIVE[4] FORTRAN code in particular has proven to be an excellent and reliable analysis tool. This analysis code is based upon the FLO30 finite volume potential flow method that was developed by Jameson and Caughey[3]. Among the features of FLO30 are its fully conservative formulation and its three-dimensional curvilinear grid. The latter can be fit around any general combination of fuselage shape and wing planform.

The purpose of the research described in this paper has been to develop a wing design method that is based on the existing TAWFIVE analysis code and is compatible with the existing computational methods and program structure of that code. Of the many wing and airfoil design methods available[5-8], the inverse method as developed by Carlson[9-12] was selected for use. The current work extends the previously developed design methods developed for orthogonal grids to the more generalized curvilinear grid system of TAWFIVE, while also providing greater design flexibility and versatility for engineering applications. These last goals were achieved by the inclusion of user options for designing either the entire wing or only discontinuous wing segments as shown in Figure 1. The availability of this option is useful to engineers who are typically faced with designing around regions where the wing geometry may be fixed by constraints other than aerodynamic considerations.

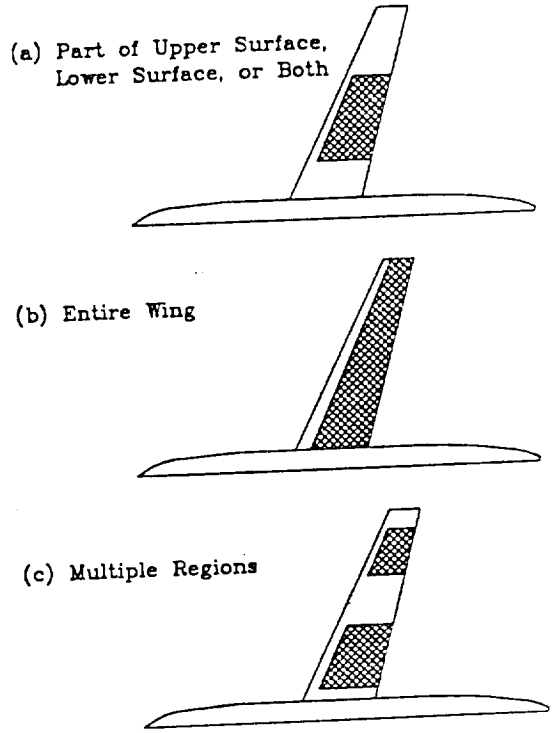

Figure 1. Possible Wing Design Situations

* Graduate research assistant.
** Professor of Aerospace Engineering, Associate Fellow of AIAA

WING ANALYSIS METHODS

Potential Flow Solver

The inviscid potential analysis of TAWFIVE is performed by the program FLO30 developed by Caughey and Jameson[3,13]. For a complete description of the FLO30 code and its theoretical basis the reader is referred to Caughey and Jameson's papers and some earlier developmental work by Jameson[14-15]. A brief description is presented here to provide for completeness and to provide a background for the inverse design developments which will be discussed in detail.

FLO30 solves the full potential equation in conservative form which when transformed from Cartesian coordinates to generalized curvilinear coordinates is:

$$(\rho hU)_\xi + (\rho hV)_\eta + (\rho hW)_\zeta = 0 \qquad (1)$$

where the subscripts denote differentiation with respect to the curvilinear coordinates ξ, η, and ζ. The contravariant velocities are related to the physical velocities and the derivatives of the potential function by:

$$\begin{Bmatrix} U \\ V \\ W \end{Bmatrix} = H^{-1} \begin{Bmatrix} u \\ v \\ w \end{Bmatrix} = (H^T H)^{-1} \begin{Bmatrix} \Phi_\xi \\ \Phi_\eta \\ \Phi_\zeta \end{Bmatrix} \qquad (2)$$

and H is the transformation matrix defined by:

$$H = \begin{bmatrix} x_\xi & x_\eta & x_\zeta \\ y_\xi & y_\eta & y_\zeta \\ z_\xi & z_\eta & z_\zeta \end{bmatrix} \quad \text{with} \quad h = |H| \qquad (3)$$

The local density can be obtained from isentropic relations as:

$$\rho = [1 + \tfrac{\gamma-1}{2} M_\infty^2 (1 - u^2 - v^2 - w^2)]^{\frac{1}{\gamma-1}} \qquad (4)$$

The numerical approach used in FLO30 is a finite volume technique. To understand this approach, consider the simple two dimensional case represented by the grid system shown in Figure 2.

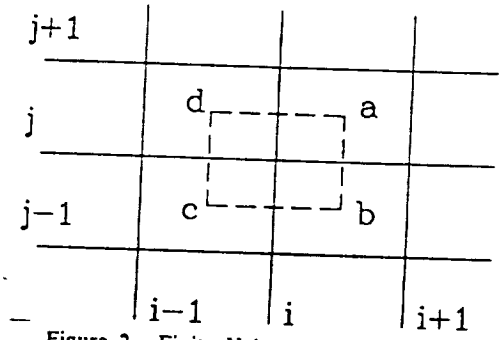

Figure 2. Finite-Volume Cell Location

The dashed cube shown in the figure indicates the area element under consideration. The flux of fluid through side a-b can be approximated by the average of the fluxes at point a and b with similar results for the side c-d. The net flux in the x direction for the elemental area centered at grid point i,j is then:

$$(\rho hU)_\xi = [(\rho hU_a + \rho hU_b) - (\rho hU_c + \rho hU_d)] / 2\Delta\xi$$

or in the notation of Caughey and Jameson,

$$(\rho hU)_\xi = \mu_\eta \delta_\xi (\rho U)$$

where μ indicates averaging and δ indicates differentiation in the indicated directions which are defined as follows (allowing $\Delta\xi=\Delta\eta=\Delta\zeta=1$):

$$(\delta_\xi U)_{i,j,k} = (U_{i+\frac{1}{2},j,k} - U_{i-\frac{1}{2},j,k})$$
$$(\mu_\xi U)_{i,j,k} = (U_{i+\frac{1}{2},j,k} + U_{i-\frac{1}{2},j,k})/2$$
$$(\mu_{\xi\eta} U)_{i,j,k} = (U_{i+\frac{1}{2},j+\frac{1}{2},k} + U_{i+\frac{1}{2},j-\frac{1}{2},k} + U_{j-\frac{1}{2},j+\frac{1}{2},k} + U_{i-\frac{1}{2},j-\frac{1}{2},k})/4$$
$$\ldots \text{ etc.}$$

When extended to the other flux components and to averaging over cube surfaces in three dimensions, the numerical potential equation is of the form:

$$\mu_{\eta\zeta}\delta_\xi(\rho hU) + \mu_{\zeta\xi}\delta_\eta(\rho hV) + \mu_{\xi\eta}\delta_\zeta(\rho hW) = 0$$

To find the flux quantities ρhU, ρhV, and ρhW at the finite volume cell vertices (i.e. points a, b, c, and d for the two dimensional case), it is necessary to evaluate Equations (2) through (4). The derivatives in these expressions can be expanded by the same volume averaging approach used above, thus:

$$\Phi_\xi = \mu_{\eta\zeta}\delta_\xi(\Phi) \qquad x_\xi = \mu_{\eta\zeta}\delta_\xi(x)$$
$$\Phi_\eta = \mu_{\zeta\xi}\delta_\eta(\Phi) \qquad y_\xi = \mu_{\eta\zeta}\delta_\xi(y)$$
$$\Phi_\zeta = \mu_{\xi\eta}\delta_\zeta(\Phi) \qquad z_\xi = \mu_{\eta\zeta}\delta_\xi(z)$$

with similar terms for the other transformation metrics. The above expressions, being centered at grid midpoints, will involve the values of the potential and grid position at grid points which are known from the previous potential solution and the grid geometry, respectively.

When solving transonic flows it is necessary to include in the solution algorithm some form of supersonic upstream dependence in order to account for both the physical nature of the flow and the viscous nature of shock waves, respectively. Caughey and Jameson introduced upwinding by the addition of terms into their potential numerical equation which are only non-zero when the flow is supersonic. Also, the finite volume technique exhibits a tendency for uncoupling of the flow field solution between alternating grid points. As a result, additional terms are included in the numerical potential equation. The final numerical equation which is solved by FLO30 when these terms have been included has the form:

$$\mu_{\eta\zeta}\delta_\xi(\rho hU+P) + \mu_{\zeta\xi}\delta_\eta(\rho hV+Q) + \mu_{\xi\eta}\delta_\zeta(\rho hW+R) - \epsilon(\mu_\zeta\delta_{\xi\eta}Q_{\xi\eta} + \mu_\xi\delta_{\eta\zeta}Q_{\eta\zeta} + \mu_\eta\delta_{\zeta\xi}Q_{\zeta\xi} - \delta_{\xi\eta\zeta}Q_{\xi\eta\zeta}/2) = 0$$

where P, Q, and R are the upwinding terms and $Q_{\xi\eta}$, $Q_{\eta\zeta}$, $Q_{\zeta\xi}$, and $Q_{\xi\eta\zeta}$ are the decoupling terms.

Computational Grid Geometry

The computational grid used by FLO30 is a body fitted, non-orthogonal, curvilinear mesh constructed about a wing fuselage combination. The number of grid points composing the computational domain is typically 40 x 6 x 8, 80 x 12 x 16, or 160 x 24 x 32 for the number of ξ, η, and ζ points in the coarse, medium, and fine grids, respectively. The grid is conformally mapped to the wing and fuselage surfaces as can be seen from the plot of surface grid lines shown in Figure 3.

The grid is formed around spanwise airfoil sections in a similar manner in which "C" grids are mapped to airfoils in two-dimensional analysis. In addition, each spanwise computational plane is also conformally wrapped about the fuselage surface and a line extending forward from the fuselage nose.

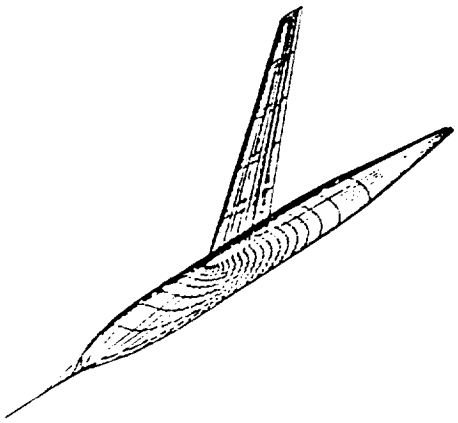

Figure 3. Surface Grid Point Geometry

A final set of grid surfaces are generated beneath the wing and fuselage surfaces and beyond the symmetric plane in order to aid in the formulation of both the finite-volume numerical flow equations and the flow tangency boundary conditions upon these boundaries. The grid points composing the "ghost" surfaces are calculated from linear extrapolations of the computation grid lines from inside the physical domain.

Boundary Conditions

Since the governing potential equations are written in terms of perturbations from free-stream conditions, the subsonic, far-field requirement that the flow return to the free-stream velocity and direction is satisfied by setting the perturbation potential equal to zero on the side and upstream boundaries. The downstream boundary condition is a "zero" order extrapolation of the potential (constant potential assumption) to the outflow boundaries.

A flow tangency condition is applied along both the wing and fuselage solid surfaces by setting the normal contravariant component of the velocity vector to zero on the surfaces. This condition provides an equation which when approximated by a finite-difference expansion about the surface grid points can be used to set a value for the perturbation potential on the "ghost" grid points below each surface. Note that this *finite-difference* boundary condition differs in formulation from the *finite-volume* solution algorithm of the governing equations. As a result, it is possible to impose flow tangency using the finite-difference technique yet still have a slight normal surface velocity when performing the finite-volume calculations. Since it is essential to have accurate boundary conditions at the wing surface in order to generate accurate solutions, a second condition is imposed upon the wing surface. This additional condition involves reflecting the flux quantities calculated by the flow solver for the cell centers directly above the wing surface to the "ghost" cell centers beneath. The reflected normal fluxes then cancel each other out in the residual expression and a net zero flow is obtained through the surface. Similarly, a zero flux condition is applied at the half -body symmetric plane, limiting solutions to symmetric, non-sideslip cases.

The trailing edge slit boundary is not an actual limit to the physical domain as the other boundaries are, but is simply an artificial boundary created by unwrapping the physical plane into the computational domain. The only conditions which need to be imposed at the slit is that the flow velocities, and thus pressure, be continuous across the cut. The flow potential, however, will have a discontinuous jump across the wake which is proportional to the sectional wing lift coefficient.

INVERSE WING DESIGN METHODS

As stated previously, a direct-inverse approach to wing design was selected for incorporation into the TAWFIVE code. The direct-inverse method derives its name from the division of the design wing surface into a fixed geometry leading edge region, where flow tangency boundary conditions are imposed, and an aft, variable geometry section where pressure boundary conditions are enforced. The pressure boundary where the user specified pressure distributions are imposed does not extend forward to the leading edge due to difficulties of enforcing this type boundary condition near the beginning of an airfoil section. This restriction on the size of the pressure specification region does not seriously reduce the versatility of the design method since the leading edge regions for most airfoils are similar, and it is relatively easy to select a leading edge geometry which will produce the desired Mach number or pressure values at the beginning of the inverse region. In addition, specific leading edge shapes may be required due to other design constraints such as the necessity to house a leading edge flap or slot system.

Pressure Boundary Condition

In the inverse design regions on the wing, a pressure boundary condition will be specified rather than the flow tangency condition used in analysis zones. In formulating this boundary condition it is necessary to relate the user specified pressure coefficient, C_p, to the current perturbation potentials at inverse design grid points. Consider the full potential equation for the pressure coefficient:

$$C_p = \frac{2}{\gamma M_\infty^2}\left\{\left[1 + \frac{\gamma-1}{2} M_\infty^2\left(1 - \frac{Q^2}{q_\infty^2}\right)\right]^{\frac{\gamma}{\gamma-1}} - 1\right\}$$

where: $Q^2 = u^2 + v^2 + w^2$.

If it is assumed that the pressure coefficient is primarily a function of the chordwise component of the velocity, u, and only slightly affected by the vertical and spanwise components of velocity, v and w, then a stable approximation is made by time lagging the latter two velocities in the boundary condition expression. This assumption is true everywhere except near the leading edge; but since the inverse design boundaries have already been restricted to regions well behind the leading edge, the simplification is justified. The value of the local velocity, u, can then be calculated from the above expression in terms of the desired pressure coefficient and the current values for the vertical and spanwise velocities. In addition, the velocity u can also be calculated from the perturbation potentials using the relations of Eq. (2). Defining J_{ij} to be the elements of the inverse transpose of the Jacobian matrix, H, the two equations for u yield:

$$J_{11}\phi_\xi + J_{12}\phi_\eta + J_{13}\phi_\zeta = \frac{1 - \frac{2}{(\gamma-1)M_\infty^2}\left[\left(1 + \frac{\gamma M_\infty^2 C_p}{2}\right)^{\frac{\gamma-1}{\gamma}} - 1\right]}{1 + \left(\frac{v}{u}\right)^2 + \left(\frac{w}{u}\right)^2} - \cos(\alpha) \quad (5)$$

Since the spanwise and vertical flow velocities have already been assumed to be constant in the boundary condition relation, it is consistent to make the same approximation in the above expression with respect to the spanwise and vertical derivative terms, ϕ_η and ϕ_ζ. This assumption is similar to the previous one, and leads to an explicit expression for the potential at one point.

The finite difference approximation used involves expanding the derivatives of the potential about the mid-point i-½,j,k. The ξ derivative is determined by a central difference involving the preceding and following grid point values. The η and ζ derivatives are found at the mid-point by averaging the derivatives from the preceding and following grid points found by a three point backwards and central difference approximations, respectively. Figure 4 shows the point dependence and pressure specification point for this method. The resulting numerical expression obtained with these finite approximations is:

$$J_{11}(\phi^{n+1}_{i,j,k} - \phi^{n}_{i-1,j,k}) + J_{12}\left[3(\phi^{n+1}_{i,j,k} + \phi^{n}_{i-1,j,k}) - 4(\phi^{n}_{i,j-1,k} + \phi^{n}_{i-1,j-1,k}) + \phi^{n}_{i,j-2,k} + \phi^{n}_{i-1,j-2,k}\right]/4 + J_{13}(\phi^{n}_{i,j,k+1} + \phi^{n}_{i-1,j,k+1} - \phi^{n}_{i,j,k-1} - \phi^{n}_{i-1,j,k-1})/4 = F(Cp_{i-\frac{1}{2},k})$$

Here, the superscripts n and n+1 refer to current values of the potential and the new values of the potential being imposed by the boundary condition, respectively. Also, the term $F(Cp_{i-\frac{1}{2},k})$ is the right hand side of Eq. (5) evaluated using the pressure coefficient specified at point i-½,k. Solving the above expression for the potential at point i,j,k yields:

$$\phi^{n+1}_{i,j,k} = \frac{1}{J_{11} + 3J_{12}/4}\left\{ J_{11}\phi^{n}_{i-1,j,k} - J_{12}\left[3\phi^{n}_{i-1,j,k} - 4(\phi^{n}_{i,j-1,k} + \phi^{n}_{i-1,j-1,k}) + \phi^{n}_{i,j-2,k} + \phi^{n}_{i-1,j-2,k}\right]/4 - J_{13}(\phi^{n}_{i,j,k+1} + \phi^{n}_{i-1,j,k+1} - \phi^{n}_{i,j,k-1} - \phi^{n}_{i-1,j,k-1})/4 + F(Cp_{i-\frac{1}{2},k})\right\}$$

The potential values at n+1 in the direct region are known initially since they do not change when the inverse boundary condition is applied; i.e. $\phi^{n+1} = \phi^{n}$. All the potentials on the inverse boundary can then be calculated and, since the spanwise and vertical derivatives are small, will primarily be functions of the pressure coefficient at grid point i-½ and the value of the potential at grid point i-1.

The only concern with using this mid-point specification scheme is that the current method of calculating the pressure data output from FLO30 uses a grid point centered difference scheme for the streamwise derivative. This difference could potentially allow a pressure to be specified correctly but still have a significantly different value output from FLO30 due to the inconsistent calculation methods. However, as shown on Figure 5, where the pressures calculated for a typical flow solution are compared for the two different calculation techniques, this possible error has not been significant in practice.

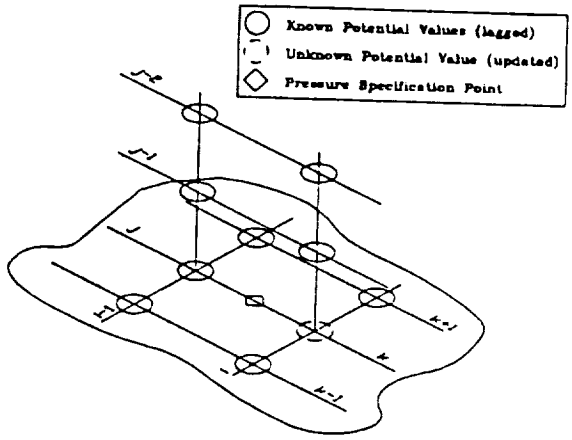

Figure 4. Point Dependance and Location

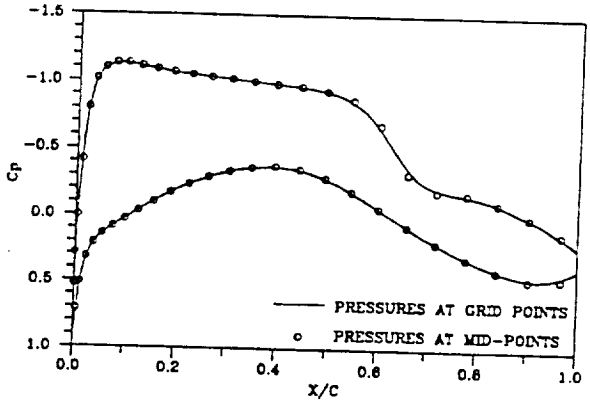

Figure 5. Comparison of Pressure Calculation Methods

Surface Calculations

As the inverse boundary conditions drive the flow field to a converged solution, it is necessary to periodically calculate the location of the new displacement surface and to regenerate the computational grid about this new geometry so that the pressure boundary surface will correspond to the physical boundary surface. Each new surface can be found relative to the previous surface from an integration of the wing surface slopes. However, the surface slopes must first be calculated from the current flow field solution using the flow tangency boundary condition which in curvilinear coordinates is:

$$V^T \times \nabla F = 0$$

where V is the contravariant velocity vector and ∇F is the gradient of the surface function with respect to the curvilinear coordinates. Note this condition is a direct analog to the same condition expressed in physical space.

A more useful expression can be obtained by expanding the above equation to:

$$\left(\frac{\partial \eta}{\partial \xi}\right)_{wing} = \frac{V}{U} - \frac{W}{U}\left(\frac{\partial \eta}{\partial \zeta}\right)_{wing}$$

This expression can be solved for the new chordwise

airfoil slopes, $\partial\eta/\partial\xi$, if the current values of the spanwise slope, $\partial\eta/\partial\zeta$, are used. Since the wing surface is represented in the computational grid as a plane of constant η, the current slopes on the wing surface equal zero and a simplified flow tangency condition results:

$$\left(\frac{\partial\eta}{\partial\xi}\right)_{\text{wing}} = \frac{V}{U}$$

The above expression has been applied to the computational surface plane in order to find the relative location of the new physical surface. This approach is an approximation since the above equation is only exactly true when applied to the new surface itself. Using this method, however, provides for a stable iterative surface updating procedure which quickly converge to the target surface.

To calculate the relative surface slopes, it is first necessary to accurately determine the values of the contravariant velocities, U and V. As was also determined by the work of Weed, et al.[12], a simple finite difference calculation of these velocities is not sufficiently accurate. Borrowing from Weed, et al., a more accurate method was implemented which uses the residual expression to calculate the velocity ratio, V/U, under the assumption that the residual is zero at the surface points. The residual expression from FLO30 can be written in finite volume form as:

$$\mu_{\eta\zeta}\delta_\xi(\rho hU) + \mu_{\zeta\xi}\delta_\eta(\rho hV) + \mu_{\xi\eta}\delta_\zeta(\rho hW) + (\text{other terms}) = 0$$

The "other terms" in the above expression involve the grid point coupling and upwind dependence terms of the formulation and are assumed to be constants in the following development.

The desired velocities can also be written in this finite volume form as:

$$V = \rho hV = \mu_{\xi\eta\zeta}(\rho hV) \quad \text{and} \quad U = \rho hU = \mu_{\xi\eta\zeta}(\rho hU)$$

By simple manipulations, the normal velocity can be obtained from the residual expression as:

$$2\mu_{\xi\eta\zeta}(\rho hV) = 2\mu_{\zeta\xi}(\rho hV)_{\eta-1} - \mu_{\eta\zeta}\delta_\xi(\rho hU) - \mu_{\xi\eta}\delta_\zeta(\rho hW) - (\text{other terms}) \qquad (6)$$

where the subscript η-1 refers to the values at grid cell centers above the wing surface.

In order to use Eq. (6) to find the desired surface velocity ratio, it is necessary to know the U and W velocity components at the "ghost" cell centers below the wing surface. These values can be obtained in a manner consistent with FLO30 by specifying the "ghost" cell values to equal the values at corresponding points immediately above the wing surface. A comparison of the accuracy of both the finite difference approach and residual approach is shown in Figure 6. The calculated displacements are for a converged analysis solution for which the calculated slopes should of course be zero.

With the contravariant velocities known, an integration of Eq. (6) through the inverse design region from the leading edge to the trailing edge yields a set of surface displacements, $\delta(x)$, for the new wing surface relative to the previous one. These displacements are expressed as changes in the computational coordinate η, and are converted to surface displacements in the physical plane via the local grid transformation. The physical plane displacements are coincident with the

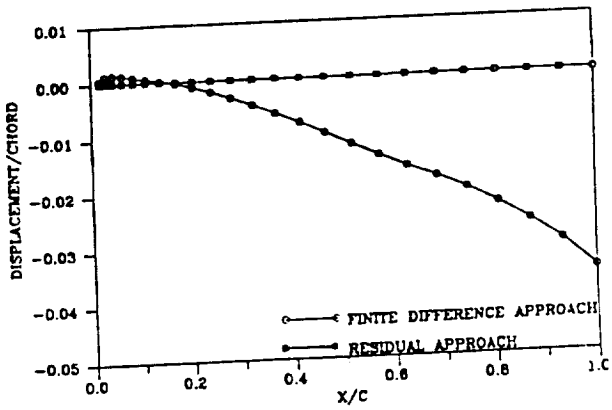

Figure 6. Comparison of Slope Calculation Methods

computational grid points in the inverse regions. To obtain the corresponding displacements at the original geometrical locations specified in the program input data, a linear interpolation of the above data is performed. Finding the displacements at the original geometry stations permits the calculation of the new wing airfoil sections at the same semispan locations.

Trailing Edge Closure

The procedures outlined above will compute a wing surface corresponding to a given, fixed, leading edge geometry and to a desired set of pressure distributions in the inverse regions. The above procedures do not, however, guarantee that this wing geometry will be practical. In particular, past experience[9] has shown that inverse surface calculations may yield airfoil sections which have either excessively blunt trailing edges or which, at least numerically, have the upper and lower surfaces crossed at the trailing edge ("fish tailed"). The former case is undesirable due to aerodynamic considerations, while the latter is physically impossible and may produce unpredictable problems in the grid generation or flow calculation portions of FLO30.

Since for any specified pressure distribution the corresponding wing surface will be controlled by the leading edge geometry, which serves as an initial spatial boundary condition for the inverse region, the problem of assuring trailing edge closure can be viewed as the proper selection of a leading edge shape. A procedure for systematically modifying the leading edge region in order to achieve some desired trailing edge thickness is called relofting. Such a relofting procedure has been incorporated into the present design process in order to both prevent the problems of trailing edge crossover and to allow the user the option of specifying a trailing edge thickness as an additional design variable. This design feature should be very useful in practical applications since it automates the iterative selection of a leading edge shape which would otherwise have to be performed by the user.

Two methods of relofting can presently be selected. The first method is a simple linear rotation scheme. This method can be visualized with the help of Figure 7. The dashed line indicates the original leading edge geometry and a hypothetical new surface shape which has been calculated for the inverse design regions. Without modification, this new surface has a trailing edge thickness of Δ. If a thickness of Δ_t were specified by the user, then the surface would have to be relofted or changed. In the present scheme, in order to obtain the

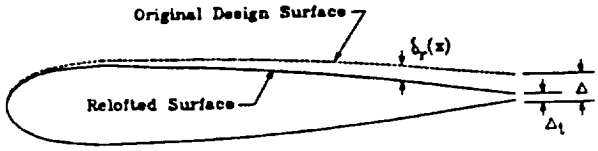

Figure 7. Relofting to Force Trailing Edge Closure

desired thickness, a displacement thickness, δ_r, is added to the current design surface. This thickness has a distribution from the leading to the trailing edge and is determined by the formula:

$$\delta_r(x) = (\Delta_t - \Delta)\,(x/c)$$

where c is the chord length of the local airfoil section. The total displacement for a surface update is then the sum of the two displacements, $\delta(x)$ and $\delta_r(x)$. When both the upper and lower surfaces are designed simultaneously, the displacement magnitudes determined by relofting are divided between the two surfaces so that half is added to the lower surface and half to the upper surface.

The second relofting method uses the same approach as the first for the aft inverse regions, but modifies the leading edge region by a proportional thining or thickening of the surface ordinates. This approach can be expressed by:

$$y^{n+1}(x) = y_j^{n+1}\, y^n(x) \,/\, y_j^n$$

where the j subscript refers to the ordinate at the direct-inverse junction determined from the linear relofting of the aft regions. Note that this method will produce leading edges in the same family of shapes and, for example, allow the design from a NACA 0012 airfoil to a NACA 0006 airfoil (see Test Case F).

RESULTS

A variety of different test cases were run as verification of the current design method. These cases involved both subcritical design and supercritical design over section geometries selected to test the versatility of the input and design control logic. In this section results from three of the more significant test cases will be presented. The results shown were obtained on a medium grid having 81 streamwise, 13 vertical, and 19 spanwise points with 11 spanwise stations and 53 points on the wing at each station; and in all cases the maximum change in the reduced potential was reduced at least three orders of magnitude. Thus, the results do not represent ultimate convergence but should be representative of "engineering accuracy".

The planform selected for the test cases was the Lockheed Wing A wing-body. The wing for this configuration has a quarter chord sweep of 25 deg., a linear twist distribution ranging from 2.28 deg. at the wing body junction to -2.04 deg. at the wing tip, an aspect ratio of eight, and a taper ratio of 0.4. The last two values are based upon the wing without fuselage. However, instead of the supercritical sections normally associated with Wing A, the initial airfoil sections at each span station were assumed to be composed of symmetric NACA four digit airfoil sections.

The target pressure distributions used in the design regions for the first two test cases were selected to yield airfoil shapes thicker in the aft portions of each section; and, at supercritical conditions, to yield on the upper surface weaker and more forward shock waves than those which would normally occur on a NACA 0012 section. On the lower surface, the target pressure distributions were selected to have either a favorable pressure gradient or fairly constant pressure plateau over much of the lower surface.

For the last test case, the pressure distribution was obtained from analysis solutions of an assumed wing geometry. The intent of this cases is to verify the relofting procedures and show the ability of the current method to make large surface changes in going from a thick wing to a thin wing (approximately 12 percent to 6 percent thick respectively).

All cases were for a freestream Mach number of 0.8 and an angle of attack of two degrees. In each case, the pressure distribution was specified in the design regions from the 15% local chord location to the trailing edge and used as the boundary condition in these inverse regions starting with the first iteration. Normally, three hundred SLOR iterations were executed prior to the first design surface update calculation; and subsequently, surface updates were computed every fifty cycles. Usually, the solution was considered converged and terminated after 550 total iterations for the first two cases and, due to the large amount of relofting required, after 950 iterations for the last case.

Test Case C

The inverse design regions for Case C, which was an attempt to design both upper and lower surfaces on two noncontiguous regions of the wing at supercritical conditions, are shown on Figure 8; and a comparison between the initial pressure distribution associated with NACA 0012 sections and the target pressures for two sections is portrayed on Figure 9. As can be seen, the target pressure distribution essentially eliminates at inboard stations the upper surface shock wave present on the original wing; and at outboard stations it weakens the shock and moves it forward. In addition, significant changes in the lower surface pressure gradients are evident. Also shown on Figure 9 are the pressures computed by the program at the end of the inverse design procedure (denoted as "design pressures"). These pressures are in excellent agreement with the target pressures, which indicates that the method is satisfying properly the desired inverse boundary conditions.

The corresponding designed airfoil sections for this case are shown on Figure 10. Even on the expanded scale, the agreement between the designed and target surfaces is excellent at all design stations. However, trailing edge closure was not enforced for this case; and there is at the boundary stations some departure between the designed surfaces and the target surfaces near the trailing edge. It is believed that this slight difference is a ramification of the change in spanwise slopes near the trailing edge between the direct and inverse regions.

In any event, the pressure distributions resulting from an analysis of the designed surfaces shown in Figure 10 are in excellent agreement with the target pressures, as can be seen on Figure 11. In addition, the section lift coefficients at the various design stations are in very good agreement with the target coefficients. Based upon these results it is believed that the present method can adequately design/modify nonadjacent regions of a wing in transonic flow.

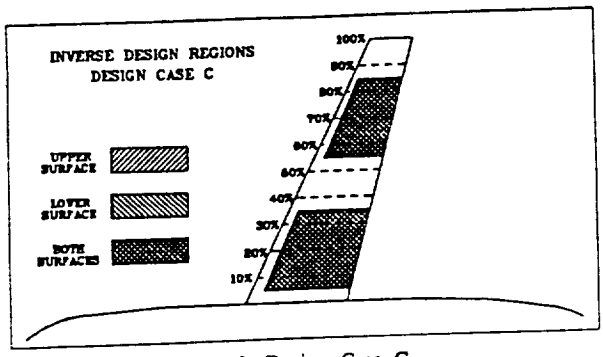

Figure 8. Design Case C

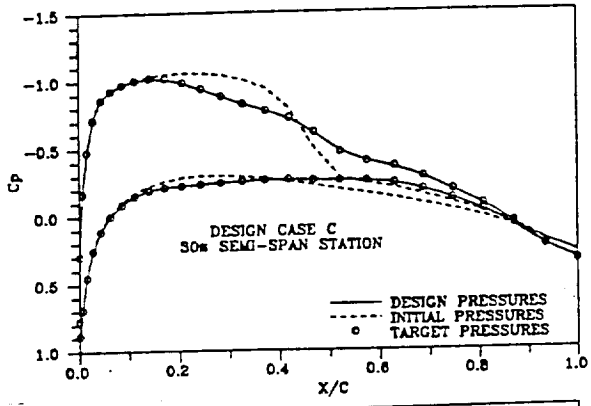

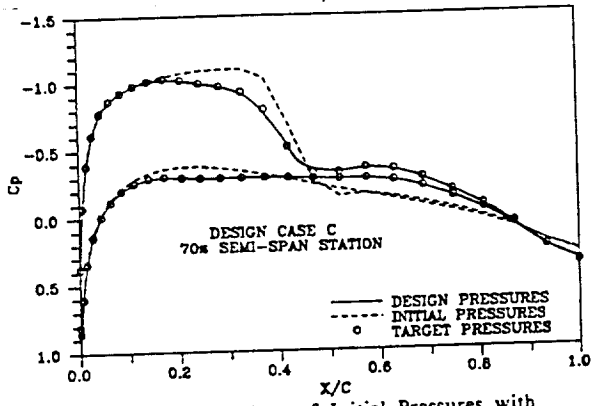

Figure 9. Comparison of Initial Pressures with Target Values (Case C)

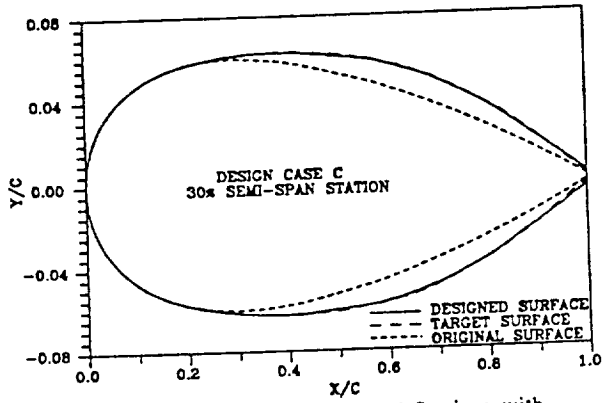

Figure 10. Comparison of Designed Sections with Original and Target Sections (Case C)

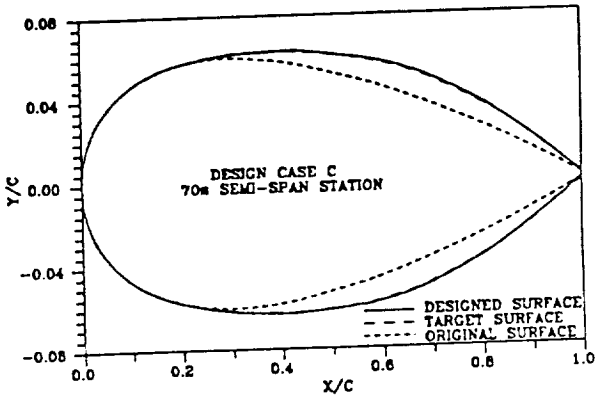

Figure 10. Continued

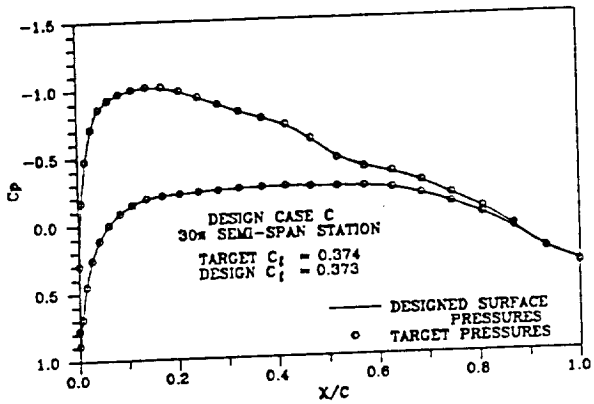

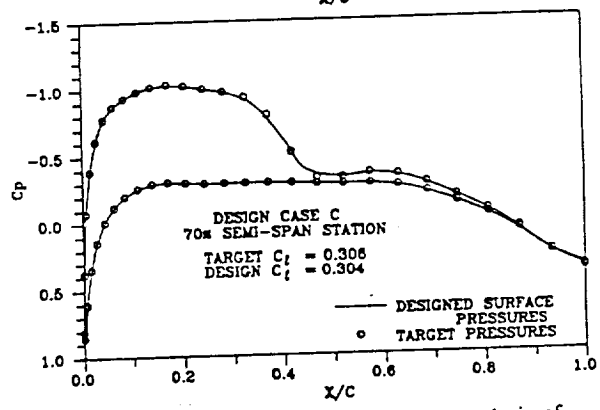

Figure 11. Comparison of Pressures from Analysis of Designed Wing Pressure Distributions (Case C)

Test Case E

For this test case, it was decided to design two non-adjacent upper surface regions simultaneously with a lower surface region which overlapped the upper zones. The location of these inverse design regions is shown on Figure 12. Likewise, Figure 13 compares the pressures associated with the initial wing sections shapes to the target pressures and to the pressures computed at the end of the design calculation for three design stations. It should be noted that this case is for supercritical condition and trailing edge closure is not enforced. As can be seen, at stations where only one surface is being designed (e.g. 50%, and 70%) the pressure distribution on the fixed surface also changes due to three dimensional effects from adjacent station which have been redesigned.

However, as depicted on Figure 14, only the design surfaces change form the original shape; and these surfaces are in reasonable agreement with the target profiles.

Finally, Figure 15 compares analysis results obtained for the designed wing with the target pressures. Even for this complicated case, the agreement between the two distributions and between the actual and target lift coefficients is excellent.

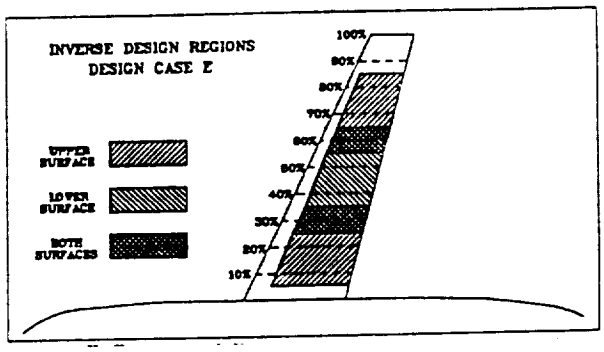

Figure 12. Design Case E

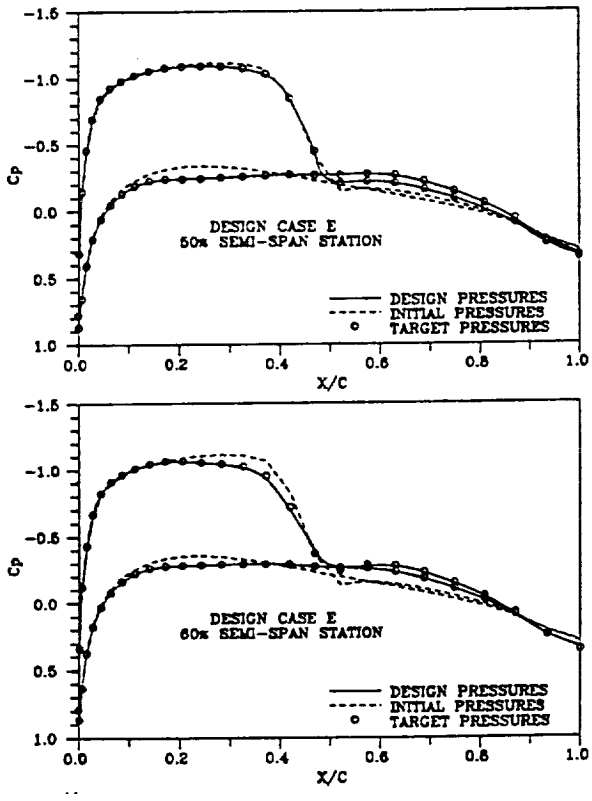

Figure 13. Comparison of Initial Pressures with Target Values (Case E)

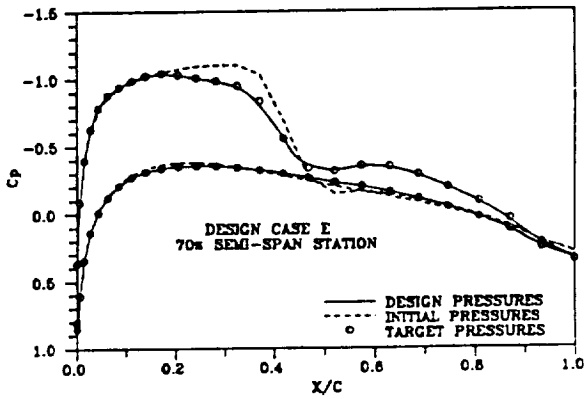

Figure 13. Continued

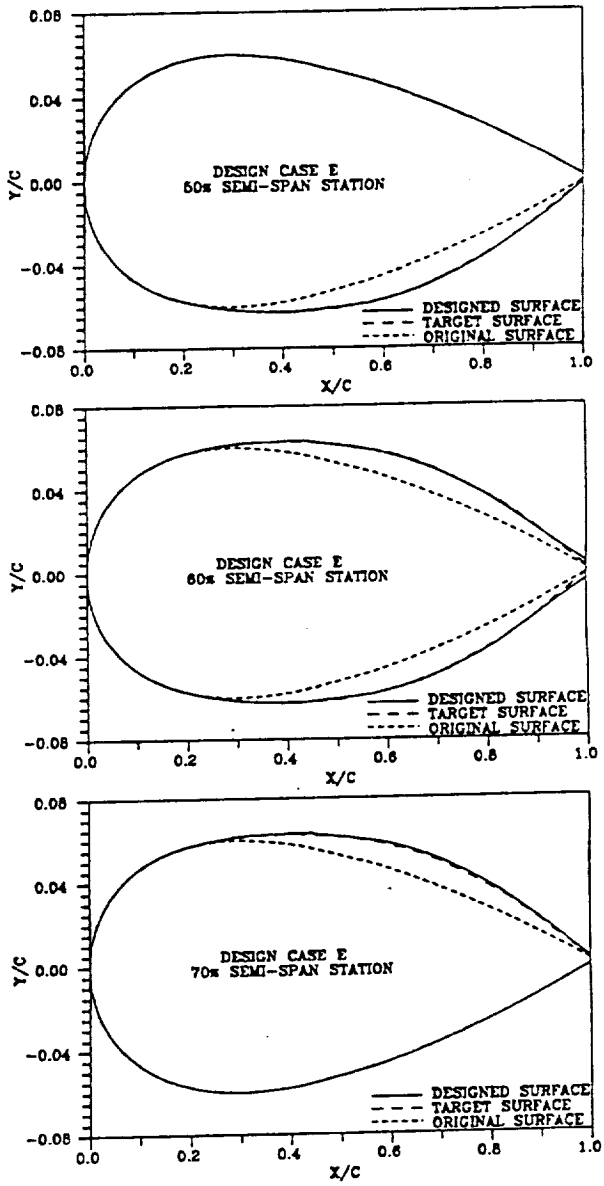

Figure 14. Comparison of Designed Sections with Original and Target Sections (Case E)

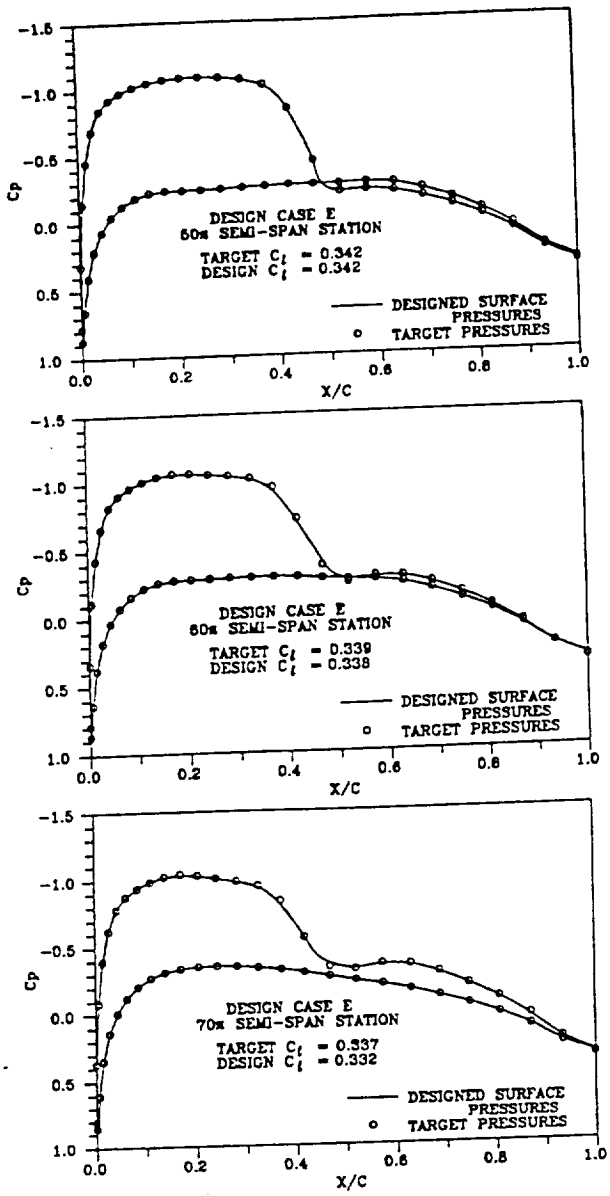

Figure 15. Comparison of Pressures from Analysis of Designed Wing Target Distributions (Case E)

TEST CASE F

The final test case was selected to demonstrate the ability of the design methodology to handle two difficult design tasks. The first task was to change a wing from super-critical to sub-critical. Due to the upstream dependance of the supersonic flow, this required making large changes in the leading edge region through the relofting procedures. The second task was to make large surface changes to the original airfoil without generating large surface distortions from the accumulation of geometry calculation errors. The design regions for this case are shown in Figure 16 where the wing thickness varied from 12% to 6% between the wing root and 80% span location and was constant going outward to the tip. The input design pressures were for a constant 6% thick wing.

The first attempts at this design used the linear leading edge relofting procedure and from a practical standpoint were unsuccessful. The final design surfaces were still supersonic in the leading edge regions while satisfying the subsonic aft surface conditions by producing strong shocks at the direct-inverse junction location. In addition, the surfaces themselves had sharp surface slope discontinuities at the same location.

When the thining approach was used to reloft the leading edge, much better solutions were obtained. Figures 17 through 19 show the changes in pressure distribution and surface shapes with a comparison of target to designed surface pressures for a few span sections as in the previous cases. As can be seen, excellent agreement between target and final pressures and surface were again attained for this extreme case. The only noticeable surface irregularities are a small wiggle at the direct-inverse junction which can also be seen as a small pressure jump in Figures 17 and 19.

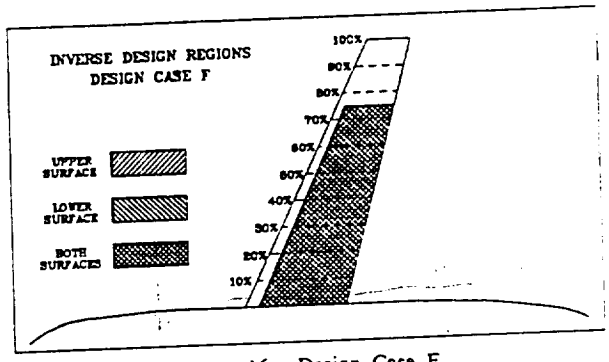

Figure 16. Design Case F

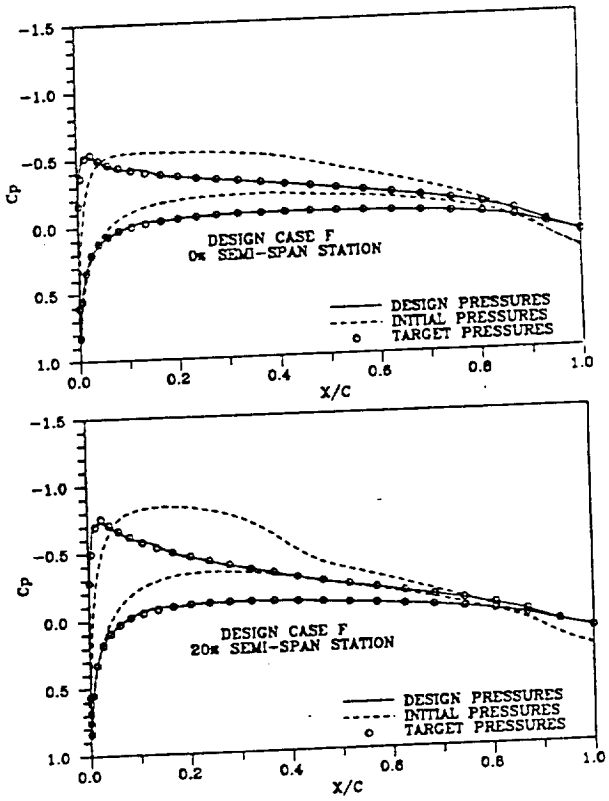

Figure 17. Comparison of Initial Pressures with Target Values (Case F)

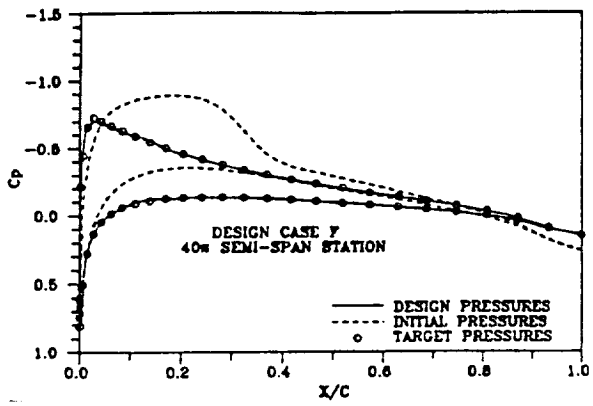

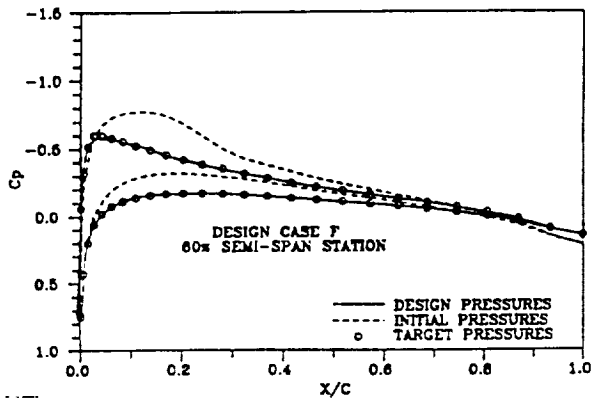

Figure 17. Continued

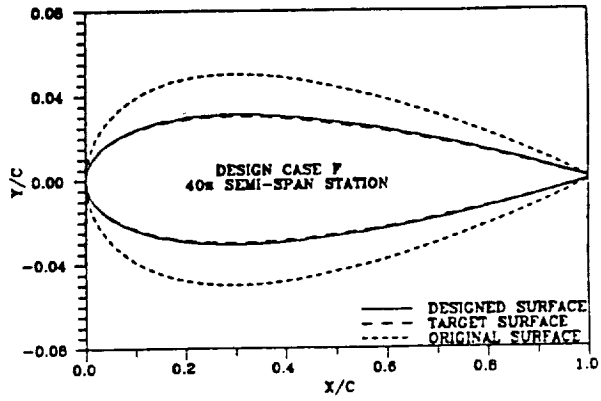

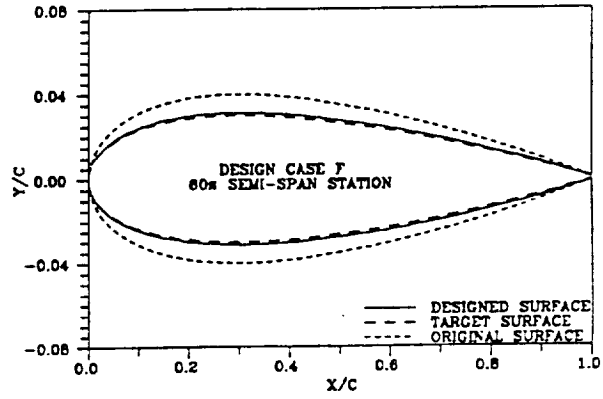

Figure 18. Continued

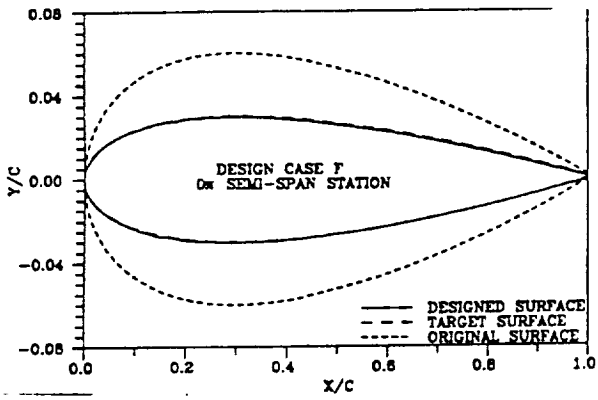

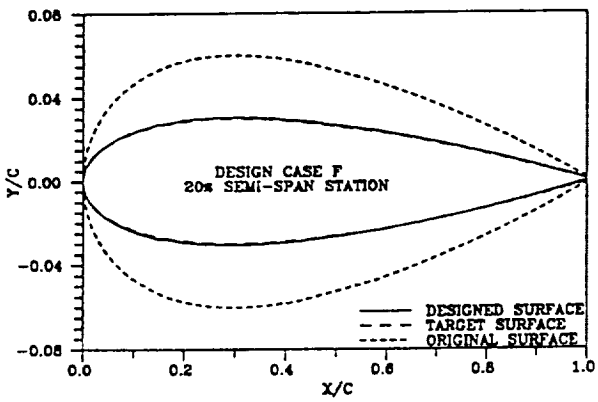

Figure 18. Comparison of Designed Sections with Original and Target Sections (Case F)

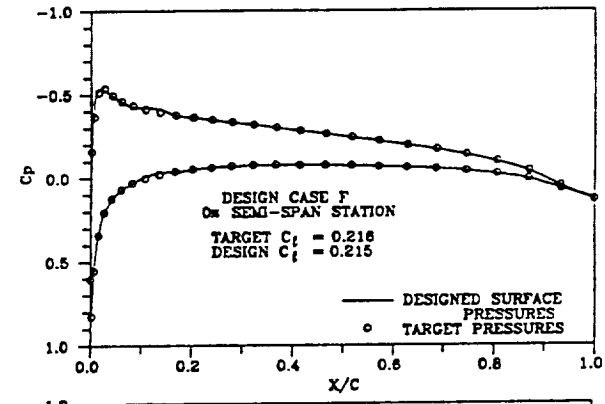

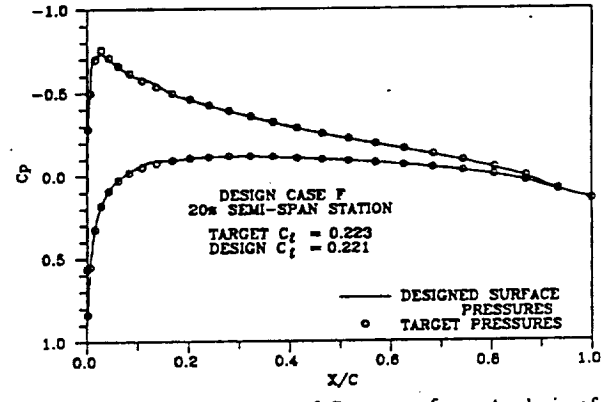

Figure 19. Comparison of Pressures from Analysis of Designed Wing Target Distributions (Case F)

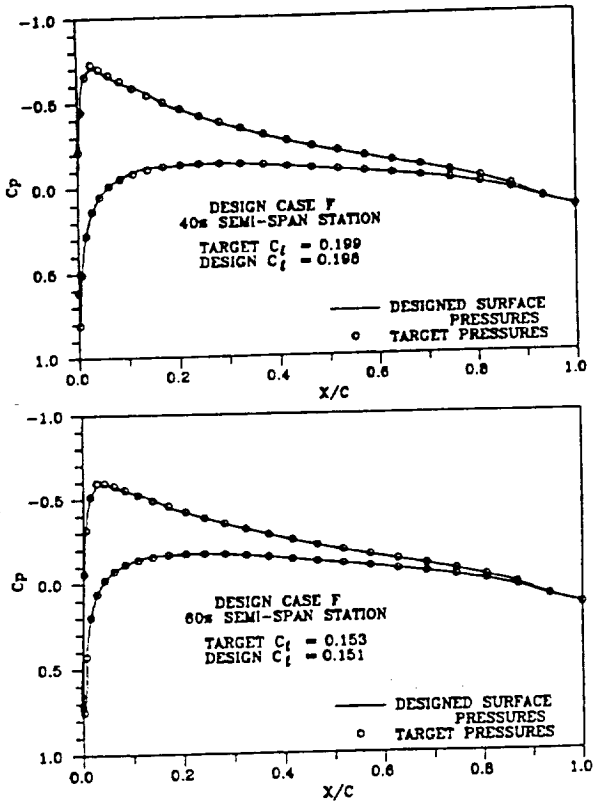

Figure 19. Continued

CONCLUSIONS AND SUGGESTIONS FOR FUTURE WORK

A direct-inverse wing design method has been successfully incorporated into the TAWFIVE transonic wing-body analysis computer code. The resultant code is capable of designing or modifying wings at both transonic and subsonic conditions and includes the effects of wing-body interactions. A series of test cases have been presented which demonstrate the accuracy and versatility of this inverse method.

Inclusion of viscous effects via the addition of the wing surface displacement thickness and wake thickness when performing wing design has been accomplished but not completely verified. Additional work will be required to run a sufficient sampling of test cases for evaluation of this design mode. The unique problems associated with viscous design and the effects of the various viscous correction models available in TAWFIVE would be the subject of a continuing research effort.

The development and evaluation of alternate methods of surface relofting are also topics for which continued research is suggested. The current method of relofting restricts the user to a family of leading edge geometries which can be constructed by the linear rotation of the initial shape. The option of using other relofting methods would extend the family of available shapes and add versatility to the design method.

ACKNOWLEDGMENTS

The work presented in this paper was primarily supported by the National Aeronautics and Space Administration under Grant NAG-1-619 with Richard L. Campbell of the Langley Research Center as technical monitor. The authors express their appreciation to Richard L. Campbell and Edgar Waggoner of NASA Langley for their assistance and helpful suggestions.

REFERENCES

1. Boppe, C. W., "Transonic Flow Field Analysis for Wing-Fuselage Configurations," NASA CR-3243, 1980.

2. Holst, Terry L. and Ballhaus, William F., "Fast, Conservative Schemes for the Full Potential Equation Applied to Transonic Flow," AIAA Journal, Vol. 17, No. 2, Febuary 1979.

3. Caughey, D. A. and Jameson, Anthony, "Progress in Finite-Volume Calculation for Wing-Fuselage Combinations," AIAA Paper 79-1513R, 1979.

4. Melson, N. D. and Streett, C. L., "TAWFIVE: A User's Guide," NASA TM84619, September 1983.

5. Cosentino, G. B. and Holst, T. L., "Numerical Optimization Design of Advanced Transonic Wing Configurations," AIAA Paper 85-0424, January 1985.

6. Davis, W., "TRO-2D: A Code for Rational Transonic Aero Optimization," AIAA Paper 85-0425, January 1985.

7. Bauer, F., Garabedian, P., and McFadden, G., "The NYU Inverse Swept Wing Code," NASA CR-3662, January 1983.

8. Tatsumi, S. and Takanashi, S., "Experimental Verification of Three-Dimensional Transonic Inverse Method," AIAA Paper 85-4077, October 1985.

9. Carlson, L. A., "Transonic Airfoil Design Using Cartesian Coordinates," NASA CR-2578, April 1976.

10. Carlson, L. A., "TRANDES: A Fortran Program for Transonic Airfoil Analysis or Design," NASA CR-2821, June 1977.

11. Anderson, W. K., and Carlson, L. A., "Inverse Transonic Wing Design on a Vector Processor," Texas A&M Research Foundation Report TAMRF-4535-8212, December 1982.

12. Weed, R. A., Anderson, W. K., and Carlson, L. A., "A Direct-Inverse Three-Dimensional Transonic Wing Design Method for Vector Computers," AIAA Paper 84-2156, August 1984.

13. Jameson, Anthony and Caughey, D. A., "A Finite Volume Method for Transonic Potential Flow Calculations," Proceedings of AIAA 3rd Computational Fluid Dynamics Conference, Albuquerque, N. M., June 1977, pp. 35-54.

14. Jameson, Anthony, "Iterative Solution of Transonic Flows over Airfoils and Wings, Including Flows at Mach 1," Comm. Pure Appl. Math., Vol. 27, 1974, pp. 283-309.

15. Jameson, Anthony, "Transonic Potential Flow Calculations Using Conservative Form," Proceedings of AIAA 2nd Computational Fluid Dynamics Conference, Hartfort, Conn., June 1975, pp.148-161.

Transonic Wing Design Using Inverse Methods in Curvilinear Coordinates

T. A. Gally and L. A. Carlson

Reprinted from

Journal of Aircraft

Volume 25, Number 11, November 1988, Pages 1009-1017

AMERICAN INSTITUTE OF AERONAUTICS AND ASTRONAUTICS, INC.

370 L'ENFANT PROMENADE, SW • WASHINGTON, DC 20024

Transonic Wing Design Using Inverse Methods in Curvilinear Coordinates

Thomas A. Gally* and Leland A. Carlson†
Texas A&M University, College Station, Texas

An inverse wing design method has been developed around an existing transonic wing analysis code. The original analysis code, TAWFIVE, has as its core the numerical potential flow solver FLO30, developed by Caughey and Jameson. Features of the analysis code include a finite-volume formulation, an SLOR solution scheme, and a wing and fuselage fitted, curvilinear grid mesh. The development of the inverse method as an extension of previous methods existing for design in Cartesian coordinates is presented. Results are shown for inviscid wing design cases in supercritical flow regimes. The test case selected also demonstrates the versatility of the design method in designing an entire wing or discontinuous sections of a wing.

Nomenclature

c	= chord length
C_p	= coefficient of pressure
h	= Jacobian of coordinate transformation
$\mathbf{H}$	= Jacobian matrix
J	= transpose of inverse Jacobian matrix
M_∞	= freestream Mach number
P,Q,R	= upwinding terms
$Q_{ij}, Q_{i,j,k}$	= decoupling terms
q	= magnitude of local velocity vector
q_∞	= magnitude of freestream velocity vector
S	= wing surface function
u,v,w	= components of physical velocity vector
U,V,W	= components of contravariant velocity vector
V	= contravariant velocity vector
x,y,z	= Cartesian coordinate directions
α	= angle of attack
γ	= ratio of specific heats
δ	= differential operator
$\delta(x)$	= displacement thickness
$\delta_r(x)$	= displacement thickness due to relofting
Δ	= trailing-edge thickness
Δ_t	= user-specified trailing-edge thickness
ϵ	= decoupling factor
μ	= averaging operator
ξ,η,ζ	= curvilinear coordinate directions
ρ	= density
ϕ	= reduced/perturbation potential function
Φ	= potential function ($\Phi=\phi+x\cos\alpha+y\sin\alpha$)

Introduction

IN recent years, the importance of transonic flight to both military and commercial aircraft and the development of specialized transonic wings for several flight research experiments have prompted significant efforts to develop accurate and reliable computational methods for the analysis and design of transonic wings. Many methods of solution have been developed, but among those that have shown promise due to their computational efficiency and engineering accuracy have been those based upon the full potential flow equations in either their conservative or nonconservative form.[1-3] The TAWFIVE[4] code in particular has proven to be an excellent and reliable analysis tool. This code is based upon the FLO30 finite-volume potential flow method that was developed by Caughey and Jameson.[3] Among the features of FLO30 are its fully conservative formulation and its three-dimensional curvilinear grid. The latter can be fit around any general combination of fuselage shape and wing planform.

The purpose of the research described in this paper has been to develop a wing design method that is based on the existing TAWFIVE analysis code and is compatible with the existing computational methods and program structure of that code. Of the many wing and airfoil design methods available,[5-8] the inverse method as developed by Carlson,[9,10] Anderson and Carlson,[11] and Weed et al.[12] was selected for use. The current work extends the previously developed design methods developed for orthogonal grids to the more generalized curvilinear grid system of TAWFIVE, while also providing greater design flexibility and versatility for engineering applications. These last goals were achieved by the inclusion of user options for designing either the entire wing or only discontinuous wing segments as shown in Fig. 1. The availability of this option is useful to engineers who are typically faced with designing around regions where the wing geometry may be fixed by constraints other than aerodynamic considerations.

Wing Analysis Methods

Potential Flow Solver

The inviscid potential analysis of TAWFIVE is performed by the program FLO30 developed by Caughey and Jameson.[3,13] For a complete description of the FLO30 code and its theoretical basis, the reader is referred to Caughey and Jameson's papers and some earlier developmental work by Jameson.[14,15] A brief description is presented here to provide for completeness and a background for the inverse design developments that will be discussed in detail.

FLO30 solves the full potential equation in conservative form that when transformed from Cartesian coordinates to generalized curvilinear coordinates is

$$(\rho hU)_\xi + (\rho hV)_\eta + (\rho hW)_\zeta = 0 \tag{1}$$

where the subscripts denote differentiation with respect to the curvilinear coordinates ξ,η, and ζ. The contravariant velocities are related to the physical velocities and the derivatives of the potential function by

$$\begin{bmatrix} U \\ V \\ W \end{bmatrix} = \mathbf{H}^{-1} \begin{bmatrix} u \\ v \\ w \end{bmatrix} = [\mathbf{H}^T\mathbf{H}]^{-1} \begin{bmatrix} \Phi_\xi \\ \Phi_\eta \\ \Phi_\zeta \end{bmatrix} \tag{2}$$

Presented as Paper 87-2551 at the AIAA 5th Applied Aerodynamics Conference, Monterey, CA, Aug. 17-19, 1987; received Sept. 11, 1987; revision received Oct. 27, 1987.

*Graduate Research Assistant.
†Professor of Aerospace Engineering. Associate Fellow AIAA.

where H is the transformation matrix defined by

$$H = \begin{bmatrix} x_\xi & x_\eta & x_\zeta \\ y_\xi & y_\eta & y_\zeta \\ z_\xi & z_\eta & z_\zeta \end{bmatrix} \tag{3}$$

with $n = |H|$. An equation for the local density can be obtained from isentropic relations as

$$\rho = \left[1 + \frac{\gamma - 1}{2} M_\infty^2 (1 - u^2 - v^2 - w^2)\right]^{1/(\gamma-1)} \tag{4}$$

The numerical approach used in FLO30 is a finite-volume technique. To understand this approach, consider the simple two-dimensional case represented by the grid system shown in Fig. 2. The dashed cube shown in the figure indicates the area element under consideration. The flux of fluid through side a-b can be approximated by the average of the fluxes at point a and b with similar results for the side c-d. The net flux in the x direction for the elemental area centered at grid point i,j is then

$$(\rho hU)_\xi = \frac{[(\rho hU_a + \rho hU_b) - (\rho hU_c + \rho hU_d)]}{2\Delta\xi} \tag{5}$$

or, in the notation of Caughey and Jameson,

$$(\rho hU)_\xi = \mu_\eta \delta_\xi (\rho hU) \tag{6}$$

where δ and μ are differentiating and averaging operators in the indicated directions that are defined as follows (allowing $\Delta\xi = \Delta\eta = \Delta\zeta = 1$):

$$(\delta_\xi u)_{i,j,k} = (U_{i+\frac{1}{2},j,k} - U_{i-\frac{1}{2},j,k}) \tag{7a}$$

$$(\mu_\xi U)_{i,j,k} = (U_{i+\frac{1}{2},j,k} + U_{i-\frac{1}{2},j,k})/2 \tag{7b}$$

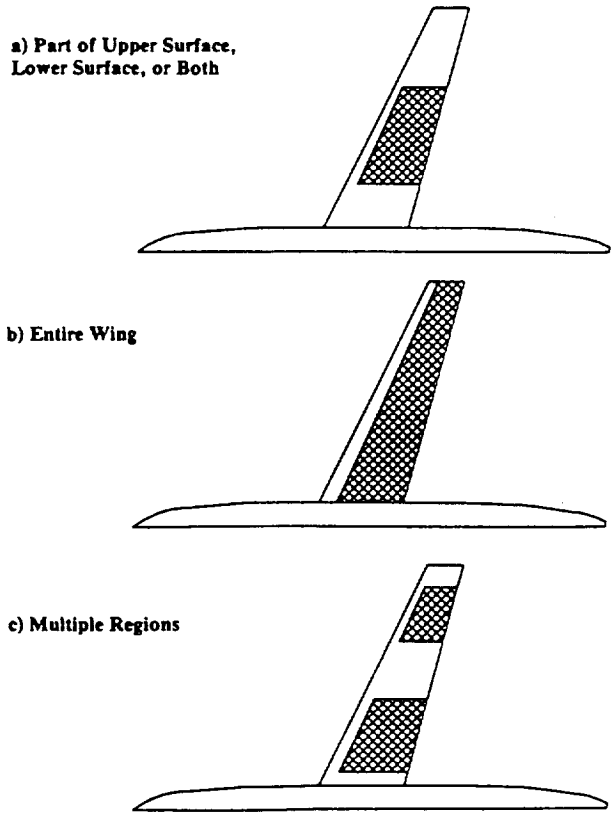

Fig. 1 Possible wing design situations.

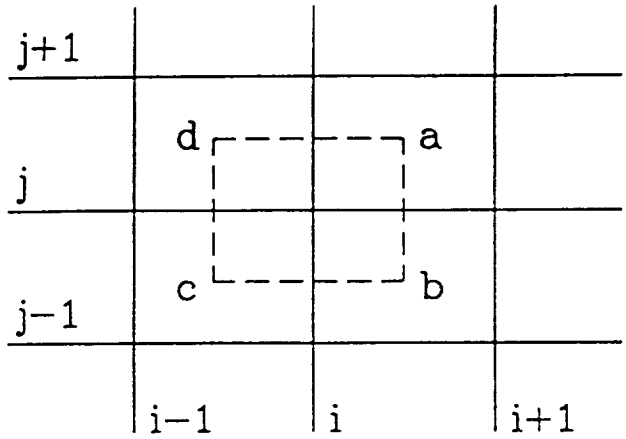

Fig. 2 Finite-volume cell location.

$$(\mu_{\xi\eta} U)_{i,j,k} = (U_{i+\frac{1}{2},j+\frac{1}{2},k} + U_{i+\frac{1}{2},j-\frac{1}{2},k} + U_{i-\frac{1}{2},j+\frac{1}{2},k} + U_{i-\frac{1}{2},j-\frac{1}{2},k})/4 \tag{7c}$$

When extended to the other flux components and to averaging over cube surfaces in three dimensions, the numerical potential equation is of the form

$$\mu_{\eta\zeta}\delta_\xi(\rho hU) + \mu_{\xi\zeta}\delta_\eta(\rho hV) + \mu_{\xi\eta}\delta_\zeta(\rho hW) = 0 \tag{8}$$

To find the flux quantities ρhU, ρhV, and ρhW at the finite-volume cell vortices (i.e., points a, b, c, and d for the two-dimensional case), it is necessary to evaluate Eqs. (2–4). The derivatives in these expressions can be expanded by the same volume averaging approach used above, thus

$$\Phi_\xi = \mu_{\eta\zeta}\delta_\xi(\Phi) \qquad x_\xi = \mu_{\eta\zeta}\delta_\xi(x) \tag{9a}$$

$$\Phi_\eta = \mu_{\xi\zeta}\delta_\eta(\Phi) \qquad y_\xi = \mu_{\eta\zeta}\delta_\xi(y) \tag{9b}$$

$$\Phi_\zeta = \mu_{\xi\eta}\delta_\zeta(\Phi) \qquad z_\xi = \mu_{\eta\zeta}\delta_\xi(z) \tag{9c}$$

with similar terms for the other transformation metrics. The above expressions, being centered at grid midpoints, will involve the values at grid points of the potential and grid position, which are known from the previous potential solution and the grid geometry, respectively.

When solving transonic flows, it is necessary to include some form of supersonic upstream dependence and artificial viscosity in the solution algorithm in order to account for the physical nature of the flow and the viscous nature of shock waves, respectively. Caughey and Jameson introduced upwinding by the addition of terms into their potential numerical equations that are only nonzero when the flow is supersonic. These terms also introduce a numerical error that has the form of a viscous term. Additional terms are also included to correct a tendency of the flowfield solution to uncouple between alternating grid points. The final numerical equation, which is solved by FLO30 when these terms have been included, has the form

$$\mu_{\eta\zeta}\delta_\xi(\rho hU + P) + \mu_{\xi\zeta}\delta_\eta(\rho hV + Q) + \mu_{\xi\eta}\delta_\zeta(\rho hW + R) - \epsilon(\mu_\zeta\delta_{\xi\eta}Q_{\xi\eta} + \mu_\xi\delta_{\eta\zeta}Q_{\eta\zeta} + \mu_\eta\delta_{\xi\zeta}Q_{\xi\zeta} - \delta_{\xi\eta\zeta}Q_{\xi\eta\zeta}/2) = 0 \tag{10}$$

where P, Q, and R are the upwinding terms; $Q_{\xi\eta}$, $Q_{\eta\zeta}$, $Q_{\xi\zeta}$, and $Q_{\xi\eta\zeta}$ are the terms reducing odd-even decoupling; and ϵ is a factor determining the amount of decoupling (typically $\epsilon = 0.25$).

Computational Grid Geometry

The computational grid used by FLO30 is a body-fitted, nonorthogonal, curvilinear mesh constructed about a wing/fuselage combination. The number of grid points composing the computational domain is typically $40\times6\times8$, $80\times12\times16$, or $160\times24\times32$ for the number of ξ, η, and ζ points in the coarse, medium, and fine grids, respectively. The grid is conformally mapped to the wing and fuselage surfaces as can be seen from the plot of surface grid lines shown in Fig. 3.

The grid is formed around spanwise airfoil sections in a similar manner in which "C" grids are mapped to airfoils in two-dimensional analysis. In addition, each spanwise computational plane is also conformally wrapped about the fuselage surface and a line extending forward from the fuselage nose. The reader is referred to Refs. 3 and 13 for additional details on the method of grid generation.

An additional set of grid surfaces are generated beneath the wing and fuselage surfaces and beyond the symmetric plane in order to aid in the formulation of both the finite-volume numerical flow equations and the flow tangency boundary conditions on these boundaries. The grid points composing the "ghost" surfaces are calculated from linear extrapolations of the computation grid lines from inside the physical domain.

Boundary Conditions

Since the governing potential equations are written in terms of perturbations from freestream conditions, the subsonic, far-field requirement that the flow return to the freestream velocity and direction is satisfied by setting the perturbation potential equal to zero on the side and upstream boundaries. The downstream boundary condition is a "zero"-order extrapolation of the potential (constant potential assumption) to the outflow boundaries.

A flow tangency condition is applied along both the wing and fuselage solid surfaces by setting the normal contravariant component of the velocity vector to zero on the surfaces. This condition provides an equation that, when approximated by a finite-difference expansion about the surface grid points, can be used to set a value for the perturbation potential on the "ghost" grid points below each surface. Note that this finite-difference boundary condition differs in formulation from the finite-volume solution algorithm of the governing equations. As a result, it would be possible to impose flow tangency using the finite-difference technique yet still have a slight normal surface velocity when performing the finite-volume calculations. Since it is essential to have accurate boundary conditions at the wing surface in order to generate accurate solutions, a second condition is imposed on the wing surface. This additional condition involves reflecting the flux quantities calculated by the flow solver for the cell centers directly above the wing surface to the "ghost" cell centers beneath. The reflected normal fluxes then cancel each other out in the residual expression and a net zero flow is obtained through the surface. Similarly, a zero flux condition is applied at the half-body symmetric plane, limiting solutions to symmetric, nonsideslip cases.

The trailing-edge slit boundary separating the upper and lower half planes is not an actual limit to the physical domain as the other boundaries are, but is simply an artificial boundary created by unwrapping the physical plane into the computational domain. The only conditions that need to be imposed at the slit are that the flow velocities, and thus pressure, be continuous across the cut. The flow potential, however, will have a discontinuous jump across the wake that is proportional to the sectional wing lift coefficient.

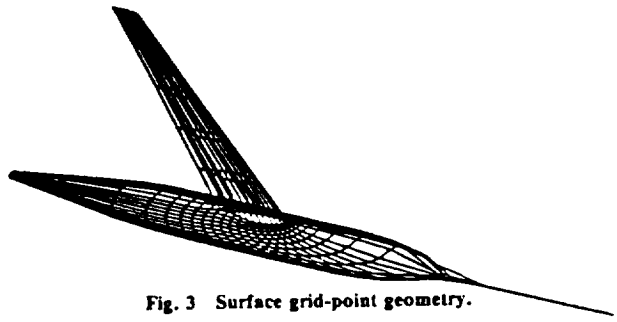

Fig. 3 Surface grid-point geometry.

Inverse Wing Design Methods

As stated previously, a direct-inverse approach to wing design was selected for incorporation into the TAWFIVE code. The direct-inverse method derives its name from the division of the design wing surface into a fixed geometry leading-edge region, where flow tangency boundary conditions are imposed, and an aft, variable geometry section where pressure boundary conditions are enforced. The pressure boundary where the user-specified pressure distributions are imposed does not extend forward to the leading edge due to difficulties of enforcing this type of boundary condition near the beginning of an airfoil section. This restriction on the size of the pressure specification region does not seriously reduce the versatility of the design method since the direct region can be fairly small (as little as 3% chord), the leading-edge regions for most airfoils are geometrically similar, and it is relatively easy to select a leading-edge geometry that will produce the desired Mach number or pressure values at the beginning of the inverse region. In addition, specific leading-edge shapes may be required due to other design constraints such as the necessity to house a leading-edge flap or slat system.

Pressure Boundary Condition

In the inverse design regions on the wing, a pressure boundary condition will be specified rather than the flow tangency condition used in analysis zones. In formulating this boundary condition, it is necessary to relate the user-specified pressure coefficient C_p, to the current perturbation potentials at inverse design grid points. Consider the full potential equation for the pressure coefficient:

$$C_p=\frac{2}{\gamma M_\infty^2}\left\{\left[1+\frac{\gamma-1}{2}M_\infty^2\left(1-\frac{q^2}{q_\infty^2}\right)\right]^{\gamma/(\gamma-1)}-1\right\} \tag{11}$$

where $q^2=u^2+v^2+w^2$.

If it is assumed that the pressure coefficient is primarily a function of the chordwise component of the velocity u and only slightly affected by the vertical and spanwise components of velocity v and w, then a stable approximation is made by time lagging the latter two velocities in the boundary condition expression. This assumption is true everywhere except near the leading edge; but since the inverse design boundaries have already been restricted to regions behind the leading edge, the simplification is justified. The value of the local velocity u can then be calculated from the above expession in terms of the desired pressure coefficient and the current values for the vertical and spanwise velocities. In addition, the velocity u can also be calculated from the perturbtion potentials using the relations of Eq. (2). Defining J_{ij} to be the elements of the inverse transpose of the Jacobian matrix H, the two equations for u yield:

$$J_{11}\phi_\xi+J_{12}\phi_\eta+J_{13}\phi_\zeta=\left[\frac{1-\dfrac{2}{(\gamma-1)M_\infty^2}\left[\left(1+\dfrac{\gamma M_\infty^2 C_p}{2}\right)^{\frac{\gamma-1}{\gamma}}-1\right]}{1+\left(\dfrac{v}{u}\right)^2+\left(\dfrac{w}{u}\right)^2}\right]^{1/2}-\cos\alpha \tag{12}$$

Since the spanwise and vertical flow velocities have already been assumed to be constant in the boundary condition relation, it is consistent to make the same approximation in the above expression with respect to the spanwise and vertical derivative terms ϕ_η and ϕ_ζ. This assumption is similar to the previous one, and leads to an explicit expression for the potential at one point.

The finite-difference approximation used involves expanding the derivatives of the potential about the midpoint $i-\frac{1}{2}, j, k$. The ξ derivative is determined by a central difference involving the preceding and following grid point values. The η and ζ derivatives are found at the midpoint by averaging the derivatives from the preceding and following grid points found by three-point-backwards and central-difference approximations, respectively. Figure 4 shows the point dependence and pressure specification point for this method. The resulting numerical expression obtained with these finite approximations is:

$$J_{11}(\phi^{n+1}_{i,j,k}-\phi^{n}_{i-1,j,k}) + J_{12}[3(\phi^{n+1}_{i,j,k}+\phi^{n}_{i-1,j,k})-4(\phi^{n}_{i,j-1,k}+\phi^{n}_{i-1,j-1,k}) + \phi^{n}_{i,j-2,k}+\phi^{n}_{i,1,j-2,k}]/4 + J_{13}(\phi^{n}_{i,j,k+1}+\phi^{n}_{i-1,j,k+1}-\phi^{n}_{i,j,k-1}-\phi^{n}_{i-1,j,k-1})/4 = F(C_{p,i-\frac{1}{2},k}) \quad (13)$$

Here, the superscripts n and $n+1$ refer to current values of the potential and the new values of the potential being imposed by the boundary condition, respectively. Also, the term $F(C_{p,i-\frac{1}{2},k})$ is the right-hand side of Eq. (12) evaluated using the pressure coefficient specified at point $i-\frac{1}{2}, k$. Solving the above expression for the potential at point i,j,k yields

$$\phi^{n+1}_{i,j,k} = \frac{1}{J_{11}+\frac{3}{4}J_{12}}\{J_{11}\phi^{n}_{i-1,j,k} - J_{12}[3\phi^{n}_{i-1,j,k}-4(\phi^{n}_{i,j-1,k}+\phi^{n}_{i-1,j-1,k}) + \phi^{n}_{i,j-2,k}+\phi^{n}_{i-1,j-2,k}]/4 - J_{13}(\phi^{n}_{i,j,k+1}+\phi^{n}_{i-1,j,k+1}-\phi^{n}_{i,j,k-1} - \phi^{n}_{i-1,j,k-1})/4 + F(C_{p,i-\frac{1}{2},k})\} \quad (14)$$

The potential values at $n+1$ in the direct region are known initially since they do not change when the inverse boundary condition is applied; i.e., $\phi^{n+1}=\phi^{n}$. All the potentials on the inverse boundary can then be calculated and, since the spanwise and vertical derivatives are small, will primarily be functions of the pressure coefficient at grid point $i-\frac{1}{2}$ and the value of the potential at grid point $i-1$.

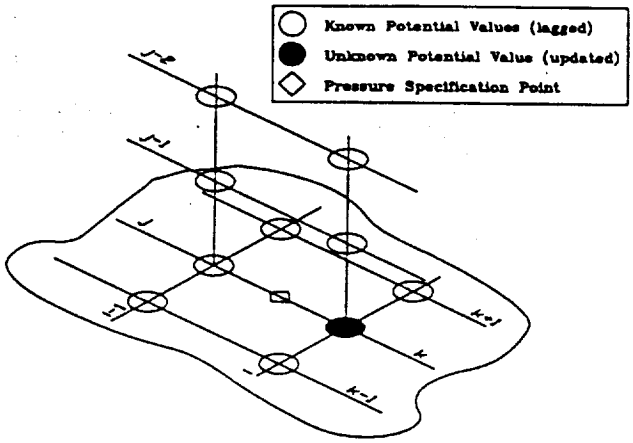

Fig. 4 Point dependence and location.

Surface Calculations

As the inverse boundary conditions drive the flowfield to a converged solution, it is necessary to calculate periodically the location of the new displacement surface and to regenerate the computational grid about this new geometry so that the pressure boundary surface will correspond to the physical boundary surface being designed. Each new surface is found relative to the previous surface from an integration of the wing surface slopes. The surface slopes are calculated from the current flowfield solution using the flow tangency boundary condition, which in curvilinear coordinates is

$$V^T \times \nabla S = 0 \quad (15)$$

Note this condition, with the gradient in the curvilinear plane, is a direct analog to the same condition expressed in the physical plane.

A more useful expression can be obtained by expanding the above equation to:

$$\left(\frac{\partial \eta}{\partial \xi}\right)_{\text{wing}} = -\frac{V}{U} - \frac{W}{U}\left(\frac{\partial \eta}{\partial \zeta}\right)_{\text{wing}} \quad (16)$$

This expression can be solved for the new chordwise airfoil slope $\partial\eta/\partial\xi$ if the current values of the spanwise slope $\partial\eta/\partial\zeta$ are used. Since the wing surface is represented in the computational grid as a plane of constant η, the current slopes on the wing surface equal zero and a simplified flow tangency condition results:

$$(\partial\eta/\partial\xi)_{\text{wing}} = V/U \quad (17)$$

The above expession has been applied to the computational surface plane in order to find the relative location of the new physical surface. This approach is an approximation, since the above equation is only exactly true when applied to the new surface itself. Using this method, however, provides for a stable iterative surface updating procedure that quickly converges[6] to the target surface.

To calculate the relative surface slopes, it is first necessary to determine accurately the values of the contravariant velocities, U and V. As was also determined by the work of Weed et al.,[12] a simple finite-difference calculation of these velocities is not sufficiently accurate. Borrowing from Ref. 12, a more accurate method was implemented that uses the residual expression to calculate the velocity ratio V/U, under the assumption that the residual is zero at the surface points. The residual expression from FLO30 can be written in finite-volume form as

$$\mu_{\eta\zeta}\delta_\xi(\rho hU) + \mu_{\xi\zeta}\delta_\eta(\rho hV) + \mu_{\xi\eta}\delta_\zeta(\rho hW) + (\text{other terms}) = 0 \quad (18)$$

The "other terms" in Eq. (18) involve the grid point coupling and upwind dependence terms of the formulation and are assumed to be constants in the following development.

The desired velocities can also be written in this finite volume form as:

$$\frac{V}{U} = \frac{\rho hV}{\rho hU} = \frac{\mu_{\xi\eta\zeta}(\rho hV)}{\mu_{\xi\eta\zeta}(\rho hU)} \quad (19)$$

By simple manipulations, the normal velocity can be obtained from the residual expression as

$$2\mu_{\xi\eta\zeta}(\rho hV) = 2\mu_{\xi\zeta}(\rho hV)_{\eta-1} - \mu_{\eta\zeta}\delta_\xi(\rho hU) - \mu_{\xi\eta}\delta_\zeta(\rho hW) - (\text{other terms}) \quad (20)$$

where the subscript $\eta-1$ refers to the values at grid cell centers above the wing surface.

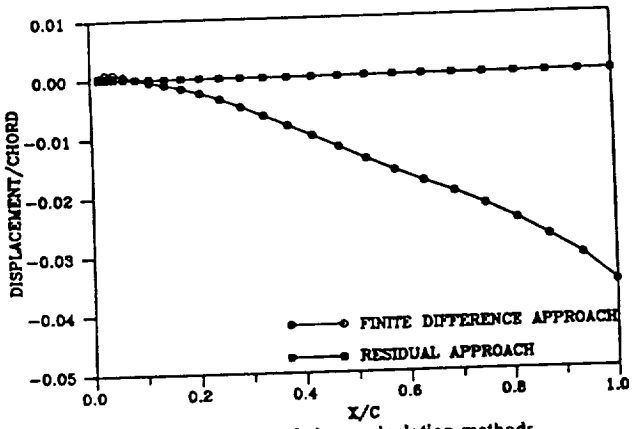

Fig. 5 Comparison of slope calculation methods.

In order to use Eq. (20) to find the desired surface velocity ratio, it is necessary to know the U and W velocity components at the "ghost" cell centers below the wing surface. These values can be obtained in a manner consistent with FLO30 by specifying the "ghost" cell values to equal the values at corresponding points immediately above the wing surface. A comparison of the accuracy of both the finite-difference approach and residual approach is shown in Fig. 5. The calculated displacements are for a converged analysis solution for which the calculated slopes should, of course, be zero.

With the contravariant velocities known, an integration of Eq. (17) in the chordwise direction ξ from the start of the inverse region to the trailing edge yields a set of surface displacements for the new wing surface relative to the previous one. These displacements are expressed as changes in the computational coordinate η and are converted to surface displacements in the physical plane $\delta(x)$ via the local grid transformation. The physical plane displacements are coincident with the computational grid points in the inverse regions. To obtain the corresponding displacements at the original geometrical locations specified in the program input data, a linear interpolation of the above data is performed. Finding the displacements at the original geometry stations permits the calculation of the new wing airfoil sections at the same semispan locations.

Trailing-Edge Closure

The procedures outlined above will compute a wing surface corresponding to a given, fixed, leading-edge geometry and to a desired set of pressure distributions in the inverse regions. The above procedures do not, however, guarantee that this wing geometry will be practical. In particular, past experience[9] has shown that inverse surface calculations may yield airfoil sections that have either excessively blunt trailing edges or which, at least numerically, have the upper and lower surface crossed at the trailing edge ("fish tailed"). The former case is undesirable due to aerodynamic considerations, while the latter is physically impossible and may produce unpredictable problems in the grid generation or flow calculation portions of FLO30.

Since for any specified pressure distribution the corresponding wing surface will be controlled by the leading-edge geometry, which serves as an initial spatial boundary condition for the inverse region, the problem of assuring trailing-edge closure can be viewed as the proper selection of a leading-edge shape. A procedure for systematically modifying the leading-edge region in order to achieve some desired trailing-edge thickness is called relofting. Such a relofting procedure has been incorporated into the present design process in order both to prevent the problems of trailing-edge crossover and to allow the user the option of specifying a trailing-edge thickness as an additional design variable. This design feature should be very useful in practical applications since it automates the iterative selection of a leading-edge shape that would otherwise have to be performed by the user.

Two methods of relofting can presently be selected. The first method is a simple linear rotation scheme. This method can be visualized with the help of Fig. 6. The dashed line indicates the original leading-edge geometry and a hypothetical new surface shape that has been calculated for the inverse design regions. Without modification, this new surface has a trailing-edge thickness of Δ. If a thickness of Δ_t were specified by the user, then the surface would have to be relofted or changed. In the present scheme, in order to obtain the desired thickness, a displacement thickness δ_t is added to the current design surface. This thickness has a distribution from the leading to the trailing-edge and is determined by the formula

$$\delta_t(x) = (\Delta_t - \Delta)(x/c) \tag{21}$$

where c is the chord length of the local airfoil section. The total displacement for a surface update is then the sum of the two displacements $\delta(x)$ and $\delta_t(x)$. When both the upper and lower surfaces are designed simultaneously, the displacement magnitudes determined by relofting are divided between the two surfaces so that half is added to the lower surface and half to the upper surface.

The second relofting method uses the same approach as the first for the aft inverse regions, but modifies the leading-edge region by a proportional thining or thickening of the surface ordinates. This approach can be expressed by:

$$y^{n+1}(x) = y_y^{n+1}[y^n(x)/y_j^n] \tag{22}$$

here the j subscript refers to the ordinate at the direct-inverse junction determined from the linear relofting of the aft regions. Note that this method will produce leading edges in the same family of shapes and, for example, allow the design of an NACA 0006 airfoil when starting from an NACA 0012 airfoil (see test case II).

Results

A variety of different test cases were run as verification of the current design method. These cases involved both subcritical design and supercritical design over section geometries selected to test the versatility of the input and design control logic. In this section, results from two of the more significant test cases will be presented. The results shown were obtained on a medium grid having 81 streamwise, 13 vertical, and 19 spanwise points with 11 spanwise stations and 53 points on the wing at each station; and, in all cases, the maximum change in the reduced potential was reduced at least three orders of magnitude. Thus, the results do not represent ultimate convergence but should be representative of "engineering accuracy."

The use of the medium grid for the design cases shown in the following was dictated by computational cost and time. Fine grid solutions for these type geometries have been obtained but are not significantly different from the medium grid results except for a generally smoother shape. Use of the fine grid in design is necessary, however, when the airfoil sections involved are aft cambered, since a higher grid-point resolution is needed in the trailing-edge regions.

The planform selected for the test cases was the Lockheed wing A wing-body. The wing for this configuration has a quarterchord sweep of 25 deg, a linear twist distribution ranging from 2.28 deg at the wing body junction to −2.04 deg at

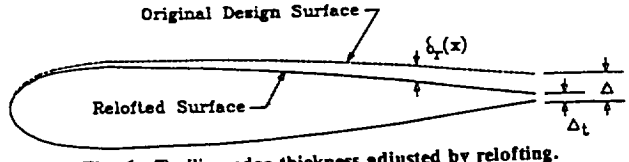

Fig. 6 Trailing-edge thickness adjusted by relofting.

the wing tip, an aspect ratio of 8, and a taper ratio of 0.4. The last two values are based on the wing without fuselage. However, instead of the supercritical sections normally associated with wing A, the initial airfoil sections at each span station were assumed to be composed of symmetric NACA four-digit airfoil sections.

The target pressure distributions used in the design regions for the first test case were selected to yield airfoil shapes thicker in the aft portions of each section and, at supercritical conditions, to yield on the upper surface weaker and more forward shock waves than those that would normally occur on an NACA 0012 section. On the lower surface, the target pressure distributions were selected to have either a favorable pressure gradient or fairly constant pressure plateau over much of the lower surface.

For the second test case, the pressure distribution was obtained from analysis solutions of an assumed wing geometry. The intent of this case is to verify the relofting procedures and show the ability of the current method to make large surface changes in going from a thick wing to a thin wing (approximately 12% to 6% thick, respectively).

Both cases were for a freestream Mach number of 0.8 and an angle of attack of 2 deg. In each case, the pressure distribution was specified in the design regions from the 15% local chord location to the trailing edge and used as the boundary condition in these inverse regions starting with the first iteration. Prior to the first design surface update calculation, 300 SLOR iterations were executed and, subsequently, surface updates were computed every 50 cycles. The solution was considered converged and terminated after 550 total iterations for the first case and, due to the large amount of relofting required, after 950 iterations for the second case.

Test Case I

The inverse design regions for case I, which was an attempt to design both upper and lower surfaces on two noncontiguous regions of the wing at supercritical conditions, are shown in Fig. 7. A comparison between the initial pressure distribution associated with NACA 0012 sections and the target pressures for two of the designed sections is portrayed in Figs. 8 and 9. As can be seen, the target pressure distribution essentially eliminates the upper-surface shock wave present at inboard stations of the original wing; at outboard stations, it weakens the shock and moves it forward. In addition, significant changes in the lower-surface pressure gradients are evident. Also shown in Figs. 10 and 11 are the pressures computed by the program at the end of the inverse design procedure (denoted as "design pressures"). These pressures are in excellent agreement with the target pressures, which indicates that the method is satisfying properly the desired inverse boundary conditions.

The corresponding designed airfoil sections for this case are shown in Figs. 10 and 11. Even on the expanded scale, the agreement between the designed and target surfaces is excellent at all design stations. However, trailing-edge closure

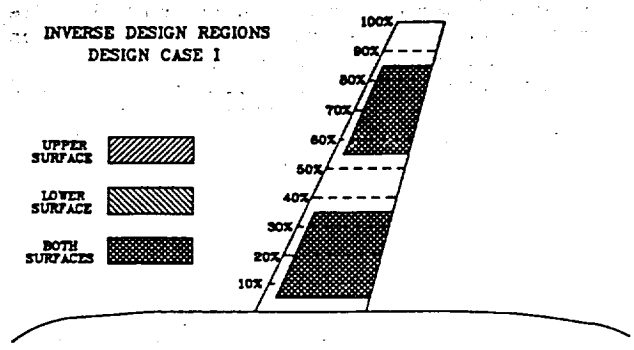

Fig. 7 Design case I.

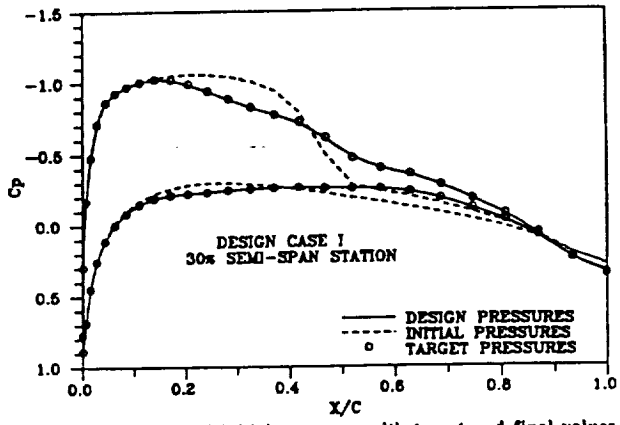

Fig. 8 Comparison of initial pressures with target and final values (case I, 30% station).

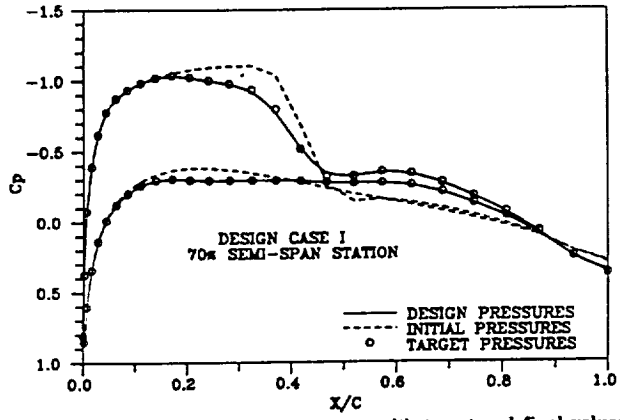

Fig. 9 Comparison of initial pressures with target and final values (case I, 70% station).

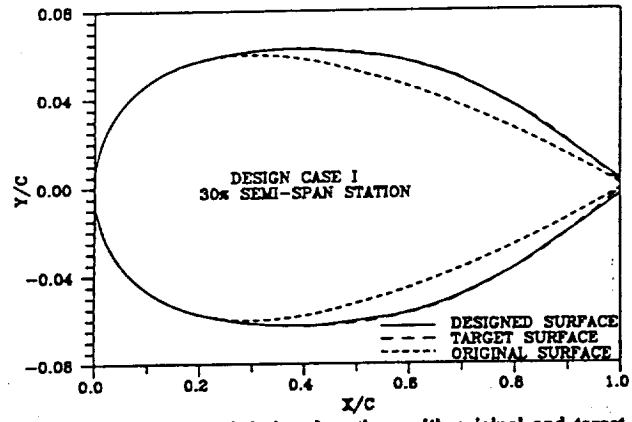

Fig. 10 Comparison of designed sections with original and target sections (case I, 30% station).

was not enforced for this case, and at the boundary stations there is some departure between the designed surfaces and the target surfaces near the trailing edge. It is believed that this slight difference is a ramification of the change in spanwise regions.

In any event, the pressure distributions resulting from an analysis of the designed surface shown in Figs. 10 and 11 are in excellent agreement with the target pressures, as can be seen in Figs. 12 and 13. In addition, the section lift coefficients at the various design stations are in very good agreement with the target coefficients. Based on these results, it is believed that the present method can adequately design/modify nonadjacent regions of a wing in transonic flow.

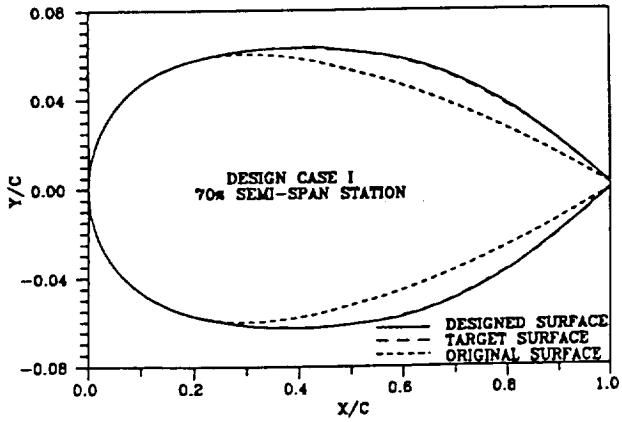

Fig. 11 Comparison of designed sections with original and target sections (case I, 70% station).

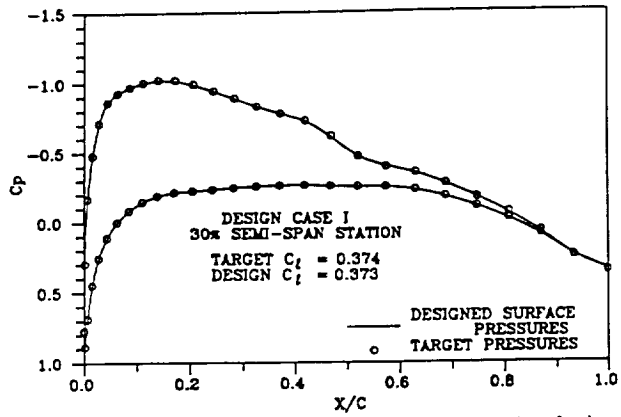

Fig. 12 Comparison of pressures from analysis of designed wing with target pressures (case I, 30% station).

Test Case II

This test case was selected to demonstrate the ability of the design methodology to handle two difficult design tasks. The first task was to change a wing from supercritical to subcritical, which is both a typical engineering task and a significant problem for wing design algorithms. The second task was to make large surface changes to the original airfoil without generating large surface distortions from the accumulation of geometry calculation errors. Due to the upstream dependence of the supersonic flow, this required making large changes in the leading-edge region through the relofting procedures. The design regions for this case are shown in Fig. 14, where the wing thickness varied from 12 to 6% between the wing root and 80% span location, and was constant going outward to the tip. The input design pressures were for a constant 6% thick wing.

The first attempts at this design used the linear leading-edge relofting procedure and from a practical standpoint were unsuccessful. The final design surfaces were still supersonic in the leading-edge regions while satisfying the subsonic aft surface conditions by producing strong shocks at the direct-inverse junction location. In addition, the surfaces themselves had sharp surface slope discontinuities at the same location.

When the thinning approach was used to reloft the leading edge, much better solutions were obtained. Figures 15-26 show the changes in pressure distribution and surface shapes with a comparison of target to designed surface pressures for a few span sections as in the previous case. As can be seen, excellent agreement between target and final pressures and surface were again attained for this extreme case. The only noticeable surface irregularity are a small wiggle at the direct-inverse junction that can be seen as a small pressure wiggle in the pressure plots.

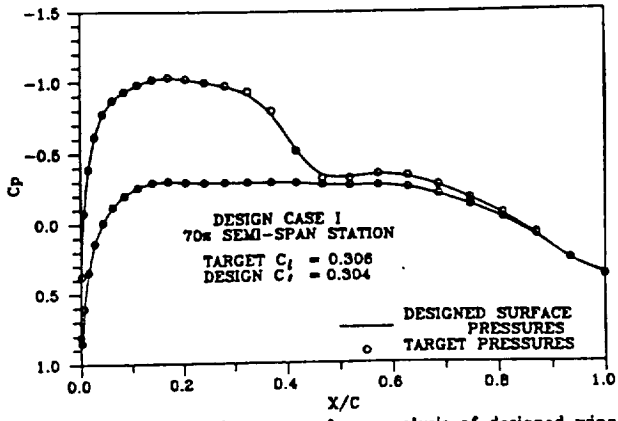

Fig. 13 Comparison of pressures from analysis of designed wing with target pressures (case I, 70% station).

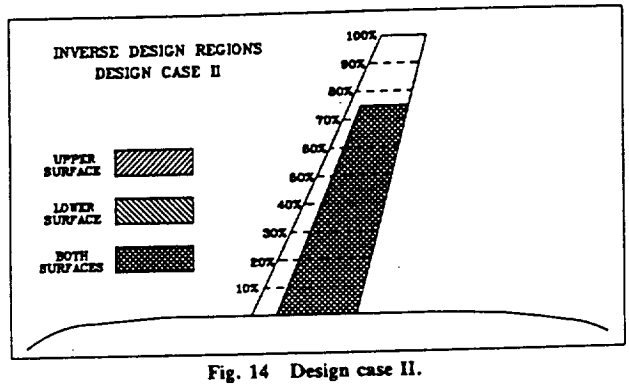

Fig. 14 Design case II.

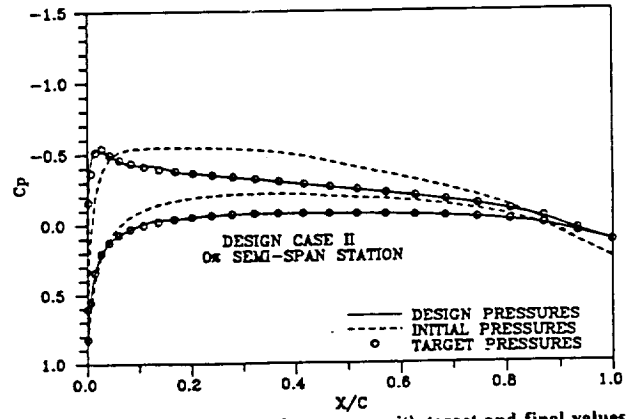

Fig. 15 Comparison of initial pressures with target and final values (case II, 0% station).

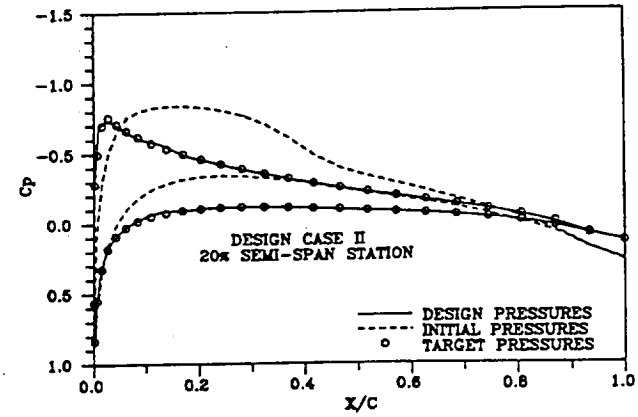

Fig. 16 Comparison of initial pressures with target and final values (case II, 20% station).

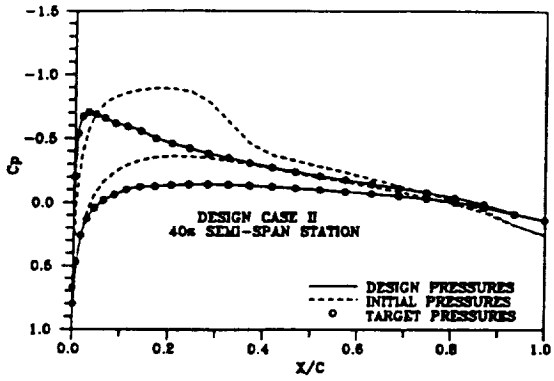

Fig. 17 Comparison of initial pressures with target and final values (case II, 40% station).

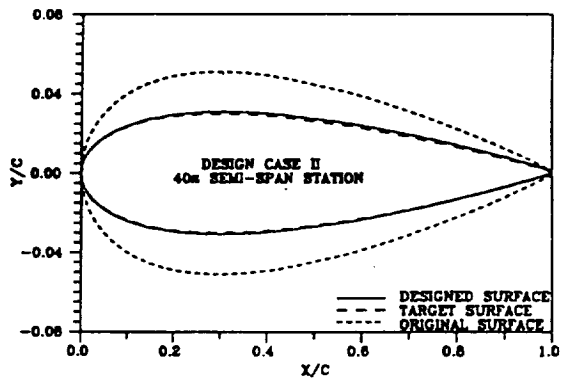

Fig. 21 Comparison of designed sections with original and target sections (case II, 40% station).

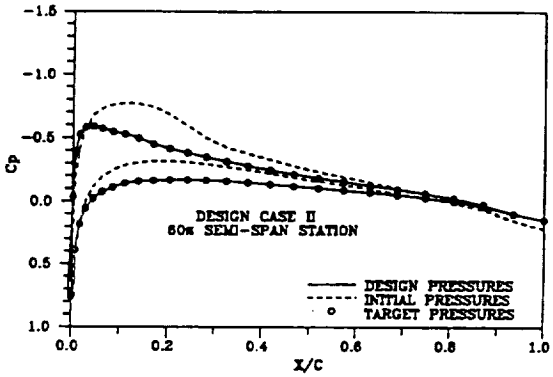

Fig. 18 Comparison of initial pressures with target and final values (case II, 60% station).

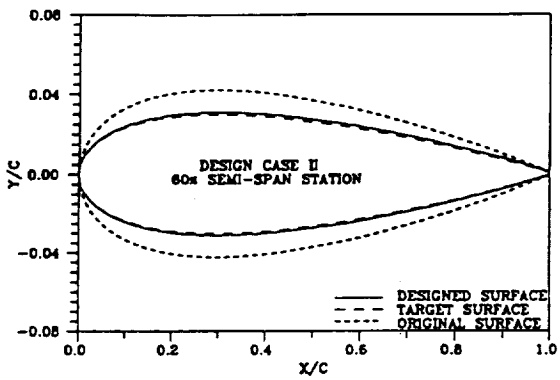

Fig. 22 Comparison of designed sections with original and target sections (case II, 60% station).

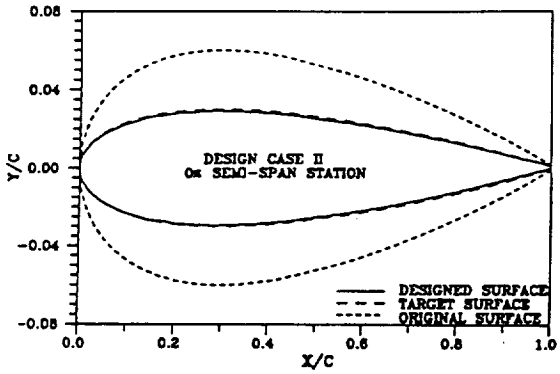

Fig. 19 Comparison of designed sections with original and target sections (case II, 0% station).

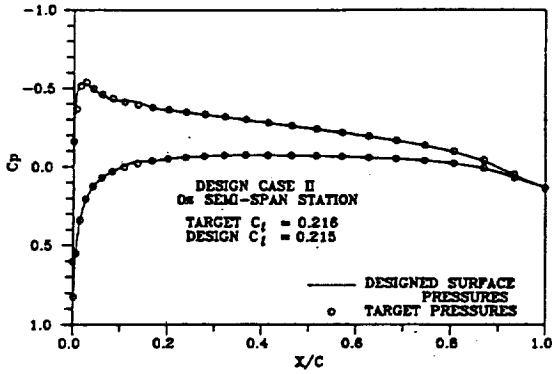

Fig. 23 Comparison of pressures from analysis of designed wing with target pressures (case II, 0% station).

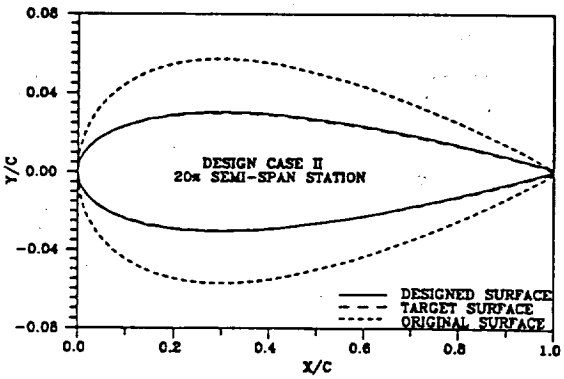

Fig. 20 Comparison of designed sections with original and target sections (case II, 20% station).

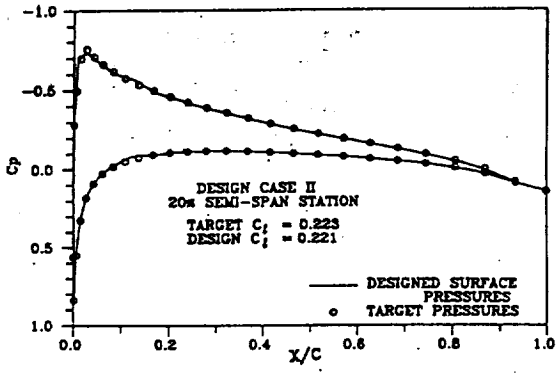

Fig. 24 Comparison of pressures from analysis of designed wing with target pressures (case II, 20% station).

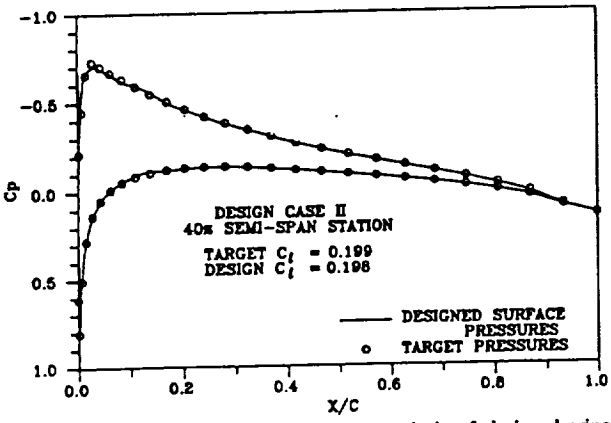

Fig. 25 Comparison of pressures from analysis of designed wing with target pressures (case II, 40% station).

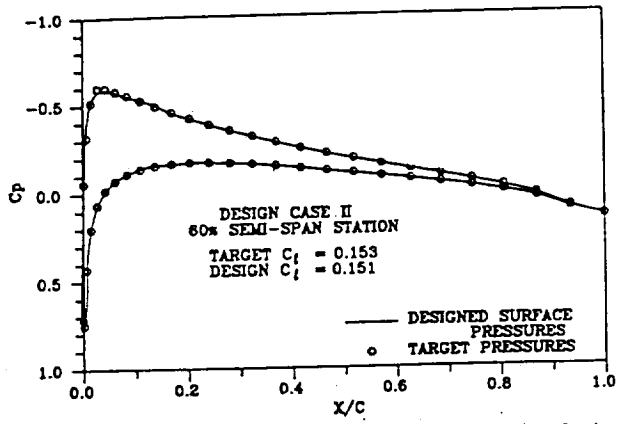

Fig. 26 Comparison of pressures from analysis of designed wing with target pressures (case II, 60% station).

Conclusions

A direct-inverse wing design method has been successfully incorporated into the TAWFIVE transonic wing-body analysis computer code. The resultant code is capable of designing or modifying wings at both transonic and subsonic conditions and includes the effects of wing-body interactions. A series of test cases have been presented that demonstrate the accuracy and versatility of this inverse method. Additional test cases and results are also presented in Refs. 16 and 17.

Acknowledgments

The work presented in this paper was primarily supported by NASA under Grant NAG-1-619 with Richard L. Campbell of the Langley Research Center as technical monitor. The authors express their appreciation to Mr. Campbell and Edgar Waggoner of NASA Langley for their assistance and helpful suggestions.

References

[1]Boppe, C.W., "Transonic Flow Field Analysis for Wing-Fuselage Configurations," NASA CR-3243, May 1980.

[2]Holst, T.L. and Ballhaus, W.F., "Fast, Conservative Schemes for the Full Potential Equation Applied to Transonic Flow," *AIAA Journal*, Vol. 17, Feb. 1979, pp. 145–152.

[3]Caughey, D.A. and Jameson, A., "Progress in Finite-Volume Calculation for Wing-Fuselage Combinations," AIAA Paper 79-1513, July 1979.

[4]Melson, N.D. and Streett, C.L., "TAWFIVE: A User's Guide," NASA TM 84619, Sept. 1983.

[5]Cosentino, G.B. and Holst, T.L., "Numerical Optimization Design of Advanced Transonic Wing Configurations," AIAA Paper 85-0424, Jan. 1985.

[6]Davis, W., "TRO-2D: A Code for Rational Transonic Aero Optimization," AIAA Paper 85-0425, Jan. 1985.

[7]Bauer, F., Garabedian, P., and McFadden, G., "The NYU Inverse Swept Wing Code," NASA CR-3662, Jan. 1983.

[8]Tatsumi, S. and Takanashi, S., "Experimental Verification of Three-Dimensional Transonic Inverse Method," AIAA Paper 85-4077, Oct. 1985.

[9]Carlson, L.A., "Transonic Airfoil Design Using Cartesian Coordinates," NASA CR-2578, April 1976.

[10]Carlson, L.A., "TRANDES: A Fortran Program for Transonic Airfoil Analysis or Design," NASA CR-2821, June 1977.

[11]Anderson, W.K. and Carlson, L.A., "Inverse Transonic Wing Design on a Vector Processor," Texas A&M Research Foundation, TAMRF-4535-8212, Dec. 1982.

[12]Weed, R.A., Anderson, W.K., and Carlson, L.A., "A Direct-Inverse Three-Dimensional Transonic Wing Design Method for Vector Computers," AIAA Paper 84-2156, Aug. 1984.

[13]Jameson, A. and Caughey, D.A., "A Finite Volume Method for Transonic Potential Flow Calculations," *Proceedings of AIAA 3rd Computational Fluid Dynamics Conference*, AIAA, New York, June 1977, pp. 35–54.

[14]Jameson, A., "Iterative Solution of Transonic Flows over Airfoils and Wings, Including Flows at Mach 1," *Communication on Pure and Applied Mathematics*, Vol. 27, 1974, pp. 283–309.

[15]Jameson, A., "Transonic Potential Flow Calculations Using Conservative Form," *Proceedings of AIAA 2nd Computational Fluid Dynamics Conference*, AIAA, New York, June 1975, pp. 148–161.

[16]Gally, T.A. and Carlson, L.A., "Inverse Transonic Wing Design Using Inverse Methods in Curvilinear Coordinates," *5th Applied Aerodynamic Conference*, AIAA, New York, Aug. 1987, pp. 516–526.

[17]Gally, T.A., "Inverse Transonic Wing Design Using Finite-Volume Methods in Curvilinear Coordinates," M.A. Thesis, Texas A&M Univ., College Station, TX, May 1987.

AIAA 89-2204

A Direct-Inverse Transonic Wing-Design Method in Curvilinear Coordinates Including Viscous-Interaction

Robert R. Ratcliff † and Leland A. Carlson‡
Texas A&M University, College Station, Texas

Abstract

Progress in the direct-inverse wing design method in curvilinear coordinates has been made. A spanwise oscillation problem and proposed remedies are discussed. Test cases are presented which reveal the approximate limits on the wing's aspect ratio and leading edge wing sweep angle for a successful design, and which show the significance of spanwise grid skewness, grid refinement, viscous interaction, the initial airfoil section and Mach number - pressure distribution compatibility on the final design. Furthermore, preliminary results are shown which indicate that it is feasible to successfully design a region of the wing which begins aft of the leading edge and terminates prior to the trailing edge.

Introduction

With the advent of efficient numerical schemes that accurately model the irrotational transonic flow about complex configurations such as wing-bodies and the appearance of computers with memory capacities and computational speeds necessary to execute these schemes in a reasonable amount of time, the efficient design of wings for transonic flight is quickly becoming a reality. Although transonic potential schemes combined with integral boundary layer solvers may not model the real flowfield as accurately as Euler or Navier Stokes Schemes, their use can significantly reduce the costs and time expenditures associated with transonic wing design.

Many methods ranging from optimization techniques[1-2] to various inverse methods have been formulated using potential solvers to design wings in transonic flight[3-12]. One such method, which has been under development at Texas A&M University for the last several years, is the direct-inverse transonic wing design method. In this method the airfoil sections making up the wing are created by specifying desired pressure distributions over all or part of the wing aft of the leading edge, solving via finite-difference or finite-volume techniques the mixed Neumann and Dirichlet boundary value problem associated with the full potential equation for compressible flow, and then integrating the flow boundary condition at each spanwise station in the design region. The design pressure distributions can be selected by an experienced user to have such desirable characteristics as mild or nonexistent shocks, a slowly increasing adverse pressure gradient, a center of pressure giving a desirable pitching moment, or an efficient spanwise loading. The designer may also use wind tunnel tests of successful airfoils as an aid in picking a desirable pressure distribution.

The direct-inverse technique has been successfully used in a stretched and sheared cartesian system[6-8] and more recently in a curvilinear system.[9-11] This paper presents progress in the latter. It will include a brief description of the analysis and design methods, techniques used to suppress a spanwise oscillation problem resulting from the interaction of the design method with the potential solver, and a series of test cases. The latter will reveal the lack of dependency of the wing design on the initial airfoil section, the importance of including viscous effects in wing design, and constraints due to aspect ratio, wing sweep and spanwise grid skewness.

Background

FLO30

The original computer program, which was modified intially by Gully[9-11] for inverse wing design, is TAWFIVE[12,13]. This program not only has the capability of computing the potential flowfield about a fairly general wing and fuselage combination, but also contains a three dimensional integral boundary layer scheme which provides the necessary viscous effects in the form of the boundary layer displacement thickness, wake curvature and wake thickness[13].

† Graduate research assistant
‡ Professor of Aerospace Engineering, Associate Fellow AIAA

The inviscid numerical scheme is based upon Jameson and Caughey's conservative, finite-volume, full potential flow solver, FLO30, in which computations are performed on a body-fitted, sheared, parabolic, wind-tunnel type coordinate system. The theory behind this code will only be briefly discussed here, but further details can be found in Refs. (14-18).

FLO30 solves the compressible potential flow equation in conservative form written in curvilinear coordinates

$$(\rho h U)_\xi + (\rho h V)_\eta + (\rho h W)_\zeta = 0 \tag{1}$$

where the nondimensionalized physical velocities, u, v, w are related to the gradient of the reduced potential function, ϕ, by

$$\begin{pmatrix} u \\ v \\ w \end{pmatrix} = \left[\mathrm{H}^T\right]^{-1} \begin{pmatrix} \phi_\xi \\ \phi_\eta \\ \phi_\zeta \end{pmatrix} + \begin{pmatrix} \cos\alpha \\ \sin\alpha \\ 0 \end{pmatrix} \tag{2}$$

and the nondimensionalized contravariant velocities U, V, W are related to the physical velocities by

$$\begin{pmatrix} U \\ V \\ W \end{pmatrix} = \mathrm{H}^{-1} \begin{pmatrix} u \\ v \\ w \end{pmatrix} \tag{3}$$

Here H is the transformation matrix defined as

$$\mathrm{H} = \begin{pmatrix} x_\xi & x_\eta & x_\zeta \\ y_\xi & y_\eta & y_\zeta \\ z_\xi & z_\eta & z_\zeta \end{pmatrix} \qquad \text{with} \qquad h = |\mathrm{H}| \tag{4}$$

The local air density normalized by the freestream density can be obtained in terms of the local speed of sound from the energy equation and isentropic relations as

$$\rho = (aM_\infty)^{\frac{2}{\gamma-1}} \tag{5}$$

and the local speed of sound normalized by the freestream speed, q_∞, can be calculated in terms of the nondimensionalized speed of sound at stagnation, a_o, using

$$a^2 = a_o^2 - \left(\frac{q}{q_\infty}\right)^2 \left(\frac{\gamma-1}{2}\right) \tag{6}$$

Flo30 uses a finite-volume type scheme which makes use of a staggered box approach. Its formulation is directly analagous to the control volume approach used to derive the original PDE in Eq. (1), except in the finite-volume scheme, the discrete nature of the finite difference model is considered from the onset by using a finite control volume in the neighborhood of a grid point in the finite-difference mesh[19]. This method is best explained by using it to discretize the following two-dimensional, incompressible version of Eq. (1) written in cartesian coordinates:

$$u_x + v_y = 0 \tag{7}$$

with the aid of the two-dimensional box shown in Fig. 1. As can be seen from the figure, the staggered box scheme derives its name from the way in which the primary and secondary boxes interlock. The values of the potentials at the four grid points which make up the corners of each primary box are used to calculate the velocities, u, v, in the following manner:

$$\begin{aligned} u &= \phi_x = \mu_y \delta_x \phi \\ v &= \phi_y = \mu_x \delta_y \phi \end{aligned} \tag{8}$$

where μ and δ are averaging and differentiating operators respectively and are defined by Jameson as:

$$\mu_x f = \frac{1}{2}\left(f_{i+\frac{1}{2},j} + f_{i-\frac{1}{2},j}\right) \qquad (9)$$
$$\delta_x f = f_{i+\frac{1}{2},j} - f_{i-\frac{1}{2},j}$$

where it is assumed that $\Delta x = 1$. Therefore, the velocity, u, for instance, at the primary box center located at $(i+\frac{1}{2}, j+\frac{1}{2})$ is found by

$$u_{i+\frac{1}{2},j+\frac{1}{2}} = (\mu_y \delta_x \phi)_{i+\frac{1}{2},j+\frac{1}{2}} = \frac{(\phi_{i+1,j} - \phi_{i,j}) + (\phi_{i+1,j+1} - \phi_{i,j+1})}{2} \qquad (10)$$

The flux at the midpoint of each secondary box is determined by averaging the velocities, u and v, at the corners of that box in the y and x direction respectively; and the net flux into the secondary box at (i,j) is obtained, giving the discretized version of Eq. (7) :

$$\mu_y \delta_x (u) + \mu_x \delta_y (v) = 0 \qquad (11)$$

where for example

$$(\mu_y \delta_x u)_{i,j} = \frac{\left(u_{i+\frac{1}{2},j-\frac{1}{2}} - u_{i-\frac{1}{2},j-\frac{1}{2}} + u_{i+\frac{1}{2},j+\frac{1}{2}} - u_{i-\frac{1}{2},j+\frac{1}{2}}\right)}{2} \qquad (12)$$

In the previous discussion, the implicit assumption was made that the velocity varied in a linear fashion between primary cell centers so that the flux into the top of the seconday cell face would be, for instance:

$$\int_{x_{i-\frac{1}{2},j+\frac{1}{2}}}^{x_{i+\frac{1}{2},j+\frac{1}{2}}} v(\bar{x}, y) d\bar{x} \approx \int_{x_{i-\frac{1}{2},j+\frac{1}{2}}}^{x_{i+\frac{1}{2},j+\frac{1}{2}}} \frac{v_{i-\frac{1}{2},j+\frac{1}{2}} - v_{i+\frac{1}{2},j+\frac{1}{2}}}{\Delta x} \bar{x} + v_{i-\frac{1}{2},j+\frac{1}{2}} d\bar{x} = \left(\frac{v_{i-\frac{1}{2},j+\frac{1}{2}} + v_{i+\frac{1}{2},j+\frac{1}{2}}}{2}\right) \qquad (13)$$

Jameson and Caughey[15] found that lumping the fluxes at the primary cell centers led to an uncoupling of the solution between adjacent grid points. Therefore, he added some compensation terms which basically extrapolate the fluxes from the corners of the secondary cell to a distance, ϵ, towards the midpoint of each secondary cell face. For example, given an $\epsilon = .25$ the flux, u, at the corresponding grid location $(i+\frac{1}{2}, j+\frac{1}{4})$ would be

$$u_{i+\frac{1}{2},j+\frac{1}{4}} = u_{i+\frac{1}{2},j+\frac{1}{2}} - .25\left(\frac{\partial u}{\partial y}\right)_{i+\frac{1}{2},j+\frac{1}{2}} \qquad (14)$$

where

$$\left(\frac{\partial u}{\partial y}_{i+\frac{1}{2},j+\frac{1}{2}}\right) = \delta_{xy}(\phi)_{i+\frac{1}{2},j+\frac{1}{2}} \qquad (15)$$

When all the fluxes are extrapolated in this manner and included in Eq. (11), the result is

$$\mu_{yy}\delta_{xx}\phi + \mu_{xx}\delta_{yy}\phi - .25\delta_{xxyy}\phi = 0 \qquad (16)$$

If the same procedure is applied to a three dimensional flowfield in curvilinear coordinates, the discretized full potential flow equation becomes

$$\mu_{\eta\zeta}\delta_\xi(\rho h U + P) + \mu_{\zeta\xi}\delta_\eta(\rho h V + Q) + \mu_{\xi\eta}\delta_\zeta(\rho h W + R) - \epsilon\left(\mu_\zeta \delta_{\xi\eta} Q_{\xi\eta} + \mu_\xi \delta_{\eta\zeta} Q_{\eta\zeta} + \mu_\eta \delta_{\zeta\xi} Q_{\zeta\xi} - \frac{\delta_{\xi\eta\zeta} Q_{\xi\eta\zeta}}{2}\right) = 0 \qquad (17)$$

where the Q's are the compensation terms defined as

$$\begin{aligned} Q_{\xi\eta} &= (A_\xi + A_\eta)\mu_\zeta \delta_{\xi\eta}\phi \\ Q_{\eta\zeta} &= (A_\eta + A_\zeta)\mu_\xi \delta_{\eta\zeta}\phi \\ Q_{\zeta\xi} &= (A_\zeta + A_\xi)\mu_\eta \delta_{\zeta\xi}\phi \\ Q_{\xi\eta\zeta} &= (A_\xi + A_\eta + A_\zeta)\delta_{\xi\eta\zeta}\phi \end{aligned} \qquad (18)$$

A_ξ, A_η, A_ζ are influence coefficients which compensate for the dependence of ρ on ϕ_ξ, ϕ_η, and ϕ_ζ.[15,16] P, Q, and R are upwinding terms which desymmetrize the scheme in supersonic zones and exclude unreal, discontinous expansions from the solution by providing an artificial viscosity. This equation, solved via SLOR, is of course a direct statement of the conversation of mass and should tend to zero as the solution converges.

As mentioned earlier, a body-fitted, wind tunnel-type grid is used in FLO30. The grid shown in Fig. 2 is the coarsest mesh and has 40 x 6 x 8 points in the ξ, η, and ζ directions respectively. With this grid, the wing becomes a constant η surface, and each cylindrical looking shell is a constant ζ surface. Constant ξ lines can be seen running spanwise on the wing at constant chord fractions from the leading edge. Notice also, due to the conformal transformation used[17], that constant ξ lines are packed close to the leading edge of the wing. This clustering is an attractive feature when designing airfoil sections using the direct-inverse approach. Moreover, constant ζ lines are spaced evenly on the wing and, on the finest mesh, give the designer up to 21 spanwise stations where the pressure distributions can be specified.

The flow tangency boundary conditions are enforced by reflecting the fluxes above the surface to ghost points below the wing, fuselage, or symmetry plane such that the net out of plane component of the flux is zero at the surface.

Inverse Design Method

In the direct-inverse method a pressure boundary condition is enforced in the design region rather than flow tangency. As shown by Gally[9,10], the input pressure coefficient can be written in terms of the freestream Mach number, M_∞, and the local velocity , q, as

$$C_p = \frac{2}{\gamma M^2_\infty}\left[\left[1 + \frac{\gamma-1}{2} M_\infty{}^2\left(1 - \frac{q^2}{q^2_\infty}\right)\right]^{\frac{\gamma}{\gamma-1}} - 1\right] \qquad (19)$$

where $q^2 = (u^2 + v^2 + w^2)\, q^2_\infty$.

Solving for u in Eq. (2) and Eq. (19) and then equating the two results gives

$$J_{11}\phi_\xi + J_{12}\phi_\eta + J_{13}\phi_\zeta = \left[\frac{1 - \frac{2}{(\gamma-1)M^2_\infty}\left[\left(1 + \frac{\gamma M^2_\infty C_p}{2}\right)^{\frac{\gamma-1}{\gamma}} - 1\right]}{1 + \left(\frac{v}{u}\right)^2 + \left(\frac{w}{u}\right)^2}\right]^{\frac{1}{2}} - \cos\alpha \qquad (20)$$

where $J_{i,j}$ are the elements of $\left(\mathrm{H}^T\right)^{-1}$

A potential, $\phi_{i,j,k}$, can be found in terms of the pressure coefficient by applying Eq. (20) at the grid point location $(i-\frac{1}{2}, j, k)$, and then using central differences in the ξ and ζ direction and second order backward differences in the normal direction, η, yielding

$$\begin{aligned} \phi^{n+1}_{i,ky,k} = \frac{1}{J_{11} + \frac{3}{4}J_{12}}\Big\{ & J_{11}\phi^n_{i-1,ky,k} \\ & - \frac{J_{12}}{4}\left[3\phi^n_{i-1,ky,k} - 4\left(\phi^n_{i,ky-1,k} + \phi^n_{i-1,ky-1,k}\right)\right. \\ & \left. + \phi^n_{i,ky-2,k} + \phi^n_{i-1,ky-2,k}\right] \\ & - \frac{J_{13}}{4}\left(\phi^n_{i,ky,k+1} + \phi^n_{i-1,ky,k+1} - \phi^n_{i,ky,k-1} - \phi^n_{i-1,ky,k-1}\right) \\ & + F\left(C_{p\ i-\frac{1}{2},k}\right)\Big\} \end{aligned} \qquad (21)$$

where $F\left(C_{p\ i-\frac{1}{2},k}\right)$ is the right hand side of Eq. (20) and $j = ky$ on the wing's surface.

Since the grid is boundary conforming, the wing sections in the design region must be updated every so often by integrating the flow tangency condition written in curvilinear coordinates

$$\left(\frac{\partial \eta}{\partial \xi}\right)_{i,ky,k} = \frac{V}{U} - \frac{W}{U}\left(\frac{\partial \eta}{\partial \zeta}\right)_{i,ky,k} \qquad (22)$$

The integration of this equation can be handled in two different ways. If the spanwise term, $\frac{\partial \eta}{\partial \zeta}$, is lagged one global iteration, it will always be zero since upon the creation of a new grid, all derivatives of η with respect to the ξ or ζ direction vanish on the wing's surface; and, Eq. (22) reduces to

$$\left(\frac{\partial \eta}{\partial \xi}\right)_{i,ky,k} = \left(\frac{V}{U}\right)_{i,ky,k} \qquad (23)$$

The other approach would be to integrate Eq. (22) iteratively. If the contravariant velocities are frozen at their current values, and the spanwise terms are initially assumed to be zero, Eq. (23) can be integrated to find the approximate inverse changes $\Delta\eta$. These can then be used to find approximations to the spatial spanwise derivative, $\frac{\delta\eta}{\delta\zeta}$. These can then be included in Eq. (22) to provide a better approximation to the flow tangency equation, and the process can be repeated using Eq. (22) until the spatial derivatives are converged. Numerical experiments reveal that the spanwise terms are at least two orders of magnitude smaller than the chordwise terms prior to the creation of the new grid. Hence, the spanwise terms can be normally neglected.

The contravariant velocity, V, can be obtained most accurately from the residual expression[9,10]. Combining the previously defined averaging and differencing operators

$$\mu_\eta (\rho hV)_{i,k_y,k} = \frac{1}{2}\left((\rho hV)_{i,k_y+\frac{1}{2},k} + (\rho hV)_{i,k_y-\frac{1}{2},k}\right) \tag{24}$$

$$\delta_\eta (\rho hV)_{i,k_y,k} = \left((\rho hV)_{i,k_y-\frac{1}{2},k} - (\rho hV)_{i,k_y+\frac{1}{2},k}\right) \tag{25}$$

yields

$$\delta_\eta (\rho hV)_{i,k_y,k} = 2(\rho hV)_{i,k_y-\frac{1}{2},k} - 2\mu_\eta (\rho hV)_{i,k_y,k} \tag{26}$$

Substituting this into the residual expression, Eq. (17), and solving for the out of plane flux, ρhV, on the wing surface yields

$$\begin{aligned} 2\mu_{\xi\eta\zeta}(\rho hV)_{i,k_y,k} = {} & \mu_{\eta\zeta}\delta_\xi (\rho hU)_{i,k_y,k} + 2\mu_{\xi\xi}\left(\rho hV_{i,k_y-\frac{1}{2},k}\right) \\ & + \mu_{\xi\eta}\delta_\zeta (\rho hW_{i,k_y,k}) \\ & + \text{compensation and upwinding terms} \end{aligned} \tag{27}$$

Since at convergence the flow should be tangent to the designed surface, the tangency condition is enforced in the residual expression, Eq. (17), by setting

$$(\rho hV)_{i,k_y+\frac{1}{2},k} = -(\rho hV)_{i,k_y-\frac{1}{2},k} \tag{28}$$

Since the resulting expression is identical to the RHS of Eq. (27), the expression for the normal flux becomes

$$\mu_{\xi\eta\zeta}(\rho hV)_{i,k_y,k} = \frac{Residual}{2.0} \tag{29}$$

Note that since the residual obtained in the iterative process is not initially zero in the design region due to the application of the inverse boundary condition, Eq. (29) reveals that there will be an ejection of fluid from the wing boundary.[3,4,23] No attempt was made in the present iterative scheme to account for this temporary addition of mass into the flowfield, since at convergence it would be negligible. Upon substitution of Eq. (29) into Eq. (23) and using the cell averaged flux ρhU on the surface, the equation for the required slope change becomes

$$\frac{\partial\eta}{\partial\xi} = \frac{V}{U} \approx \frac{\mu_{\xi\eta\zeta}(\rho hV)}{\mu_{\xi\eta\zeta}(\rho hU)} = \frac{Residual}{2\mu_{\xi\eta\zeta}(\rho hU)} \tag{30}$$

The changes normal to the surface at each spanwise station are obtained by integrating from the beginning of the inverse region to the trailing edge using the trapesoidal rule. (Higher order integration schemes were tried but had little effect on the final answers, except for coarse grids in regions of high curvature such as the cove region of a supercritical airfoil.) Assuming that the grid line leaving the wing in the η direction is normal to the wing, these changes, $\Delta\eta$, are then converted from computational to physical units by scaling them by the transformation metrics such that

$$\Delta l = \Delta\eta\sqrt{\frac{\partial x}{\partial\xi}^2 + \frac{\partial y}{\partial\eta}^2} \tag{31}$$

After subtracting the boundary layer displacement thicknesses from the inverse corrections, Δl, which have been linearly interpolated to the user defined input stations, the resulting changes are added to the initial airfoil sections yielding the new wing surface for the current time level.

Many times, the trailing edge thickness may be too large if the leading edge curvature is too small or may be 'fish-tailed' if the leading edge curvature is too large. These undesirable situations are remedied by a procedure called relofting where the designed surface is rotated about the leading edge to meet a specified trailing edge ordinate.[3,4,20,21] This relofting procedure[9-11] is usually carried out for every surface update. To illustrate the previous procedures, the first global iteration of a typical design before and after relofting is shown in Fig. 3.

Spanwise Oscillations

An annoying divergent spanwise oscillation problem sometimes occurred when designing a wing which required extensive relofting, especially when the initial section was thinner than the target. This oscillation led to sections which were too thick or too thin at adjacent constant ζ grid stations. An example of this phenomenon is shown in Fig. 4. This problem was more pronounced when the sweep was increased or the aspect ratio was decreased. After many failed attempts at remedying this problem by reformulating the inverse boundary condition, attention was directed towards the residual and the terms composing it. The residual was broken into its components and plotted after each surface update. Sample plots for a divergent case are shown at four different time levels in Fig 5. As can be seen, the compensation terms that include spanwise derivatives of ϕ are at first very small compared to the rest of the terms, but later tend to dominate and amplify the oscillation. This oscillation starts at the direct-inverse interface or, in other words, at the first spanwise station from the root in the design region and propagates spanwise as a damped oscillation with a period of two grid spacings. Presently, it is believed that the initial mismatch in the potentials at the direct-inverse interface in the spanwise direction is amplified by those compensation terms which include spanwise derivatives of the potential function. The residual is then undershot and overshot on alternating spanwise stations. This oscillation is further magnified by relofting, which creates a section that is too thin when the slopes defined in Eq. (30), which of course are directly proportional to the residual, are too large and vice-versa. Since more or less fluid has to be ejected from the section that is too thin or thick respectively to give the streamline approximately corresponding to the correct target section, the potential field at each design station is taken further away from the adjacent fields by the inverse boundary condition which forces an even further undershoot or overshoot of the residual. It should be noted that this problem is not soley due to the implementation of the direct-inverse technique since this oscillation has not been observed with the ZEBRA design code[24], but seems to be unique to the coupling of the method with the analysis code, FLO30.

After exploring many alternatives to counter this problem, four methods have been developed to damp out the spanwise oscillation:

A) Specify the inverse boundary condition at at least every other spanwise station and linearly interpolate the inverse displacements to the stations lying in between. This has been named the type II-2 method.

B) Specify the inverse boundary condition at every station, but again only calculate inverse changes at every other station and linearly interpolate the inverse changes to the stations in between. This will be referred to as the type II method.

C) Immediately prior to every surface update, calculate all spanwise derivatives of the potential used in the residual based upon a potential function smoothed in the spanwise direction. This is accomplished by first defining the smoothing operator σ_ζ as

$$\sigma_\zeta f = \frac{\epsilon}{4}f_{k-1} + \left(1-\frac{\epsilon}{2}\right)f_k + \frac{\epsilon}{4}f_{k+1}, \qquad 0 \le \epsilon \le 1 \tag{32}$$

where ϵ determines the amount of smoothing. Then using σ in the spanwise differentiation of ϕ with the maximum amount of smoothing (i.e., $\epsilon = 1$)

$$\left(\frac{\partial\phi}{\partial\zeta}\right)_{i,j,k+\frac{1}{2}} = \sigma_\zeta\delta_\zeta\phi \tag{33}$$

the smoothed spanwise derivative of ϕ becomes

$$(\phi_\zeta)_{i,j,k+\frac{1}{2}} = \frac{(\phi_{i,j,k+2} - \phi_{i,j,k} + \phi_{i,j,k+1} - \phi_{i,j,k-1})}{4.0} \tag{34}$$

D) Smooth the slopes, $\frac{\rho h V}{\rho h L^2}$, in the spanwise direction in the design region in the same manner as method C. (Note: Smoothing the integrated slopes, i.e the inverse corrections, did not suppress the oscillation but only slowed the rate of divergence.)

Results are shown in Fig. 6 for the four different approaches. The wing wrs designed inviscidly on a medium grid (80x12x16) using as a target, Lockheed Wing-A, at an angle of attack of two degrees and a Mach number of .8. A NACA 0012 section was used as the initial section in the entire design region, which stretched from 30-70% semispan and began 5% aft of the leading edge and extended to the trailing edge. Although all four approaches worked well for this case, by using the RMS of the errors, shown in Fig. 7, between the target and the designed sections as a measure of goodness, method A and C produced the best results in the interior as well as at the edges of the design region. On the other hand, for the same number of flowfield iterations, method D produced the most unsatisfactory results when compared to the target sections. The effect of each approach on the residual at the trailing edge after 10 surface updates can be seen in Fig. 8. The discontinuities in the residual for method A is due to the fact that the inverse boundary condition is applied only at the 30, 50 and 70% semispan locations. All four approaches have a characteristic jump in the residual at the first spanwise design station at 30% semispan. This is probably due to the previously discussed spanwise mismatch problem with the potentials at the direct-inverse interface, which manifests itself in the compensation terms.

An entire wing was also designed with the four methods (not shown); and, it was discovered that the smoothing approaches (methods C and D) work well when designing in the interior of the wing, but did not give satisfactory results at the root or at the tip of the wing where smoothing the quickly varying potential functions leads to large errors in the residual. In contrast, the type II and type II-2 methods work well on the entire wing surface.

In summary, each method may have certain advantages in different design situations. For instance, methods C and D give the designer the most flexibility; the desired pressure distributions can be imposed at every spanwise grid station, and the section shapes corresponding to each grid station can be calculated relatively independently of the adjacent stations. On the other hand, because of the interpolation required in the first two methods, the section shapes at 'odd' stations are directly dependent upon the shapes at 'even' stations; so although the designer loses a little flexibility, he gains a smoother spanwise distribution of section thicknesses in the spanwise direction. From a designer's standpoint of course, method A is the most restrictive of the four, but it yields the smoothest designs in the spanwise direction, and converges the quickest.

Results

Since the versatility of the method in designing multiple, overlapping regions of the wing has already been well demonstrated by Gally[9,10], most of the test cases presented, herein, were chosen, instead, to exhibit some of the constraints and limitations of the current inverse design procedure. The cases were chosen to reveal the approximate limits imposed on the aspect ratio and sweep of the wing; and the significance of grid skewness, viscous interaction, grid refinement, and the initial airfoil on the final airfoil section design. Some questions about the compatibility of Mach number and pressure distribution will be answered by designing a wing at one Mach number using pressures obtained from a wing analysis at a different Mach number. Preliminary results will be revealed for a partial wing design beginning aft of the leading edge and terminating forward of the trailing edge.

Spanwise Grid Skewness

Recently it was discovered that the skewness of the constant ξ grid lines leaving the tip of the wing (Fig. 9) can have a dramatic effect on the design of the sections near the wing tip. As can be seen in Fig. 10, if the design grid was significantly skewed and the input pressures were obtained from an analysis on an unskewed grid, the converged design yielded incorrect airfoil shapes in the tip region. This difficulty is due to the large errors near the wing tip associated with a skewed grid which are revealed in the pressure distributions (Fig. 11). The grid skewness has caused the shock location to move further aft. Although the skewness of the grid was quite extreme in this case, these results affirm the need for smoothly varying grids in wing design, at least in the spanwise direction. It should be noted though, that if the input pressures were obtained on a skewed grid and used in the design process with a skewed grid that the tip sections were well resolved. In summary then, if the pressures calculated on an unskewed grid are correct or are closer to real pressures encountered in transonic flight, then it would be wise to ensure that the grid is as smoothly varying as possible.

Boundary Layer and Wake Effects

One of the objectives of this study was to determine the significance of various viscous effects in the design of transonic wings[16]. To study these effects, an input pressure distribution was obtained by analyzing Lockheed wing-A using full viscous effects, which included boundary layer displacement thickness, wake thickness and wake curvature. The flight Mach number of .8, angle of attack of two degrees and Reynolds number, Re, of 25 million used in the analysis were thought to be representative of true flight conditions for a typical, average-sized transport. This distribution was considered to be typical of a pressure distribution which would be available to and desired by a designer. All computations were performed on a fine (160x24x32) grid.

This pressure distribution was then used in three cases. In the first case, the wing was designed inviscidly. In the second case, the wing was designed without the wake options but included the boundary displacement thickness effects. And in the third case, all viscous effect were used in the design of the wing. The design region for all three cases extended from 30-70% semispan and began 10% aft of the leading edge of the airfoil. However, the inverse pressure design boundary condition was only enforced at the 30, 50 and 70% semispan stations; and, the displacements were linearly interpolated to the design stations in between. The initial airfoil section at 50% semispan was formed by thinning the supercritical target section by 6% and removing the cove region. The initial sections at the edges of the design region were the same as the target sections, while the remaining initial design sections were obtained through linear interpolation.

The results for these cases are presented in Fig. 12. Neglecting wake effects seems to only have a small effect on the resulting airfoils, in that the sections are only a little thicker than the sections designed with full viscous effects. In order to better understand the reason for this, the target wing was analyzed with and without wake effects. The resulting pressure distributions shown in Fig. 13, reveal that at the Re chosen, wake curvature and wake thickness have a very small effect on the Wing's lift and the shape of the pressure distributions, except near the trailing edge and the shock. But when the boundary layer displacement thicknesses were investigated, it was discovered that neglecting wake effects in the analysis produced boundary layer displacement thicknesses that were on the average 3.5% thicker at the trailing edge than those obtained from a full viscous analysis. Since the boundary layer displacement thicknesses are subtracted from the initial inverse changes to yield the hard airfoil, these larger displacement thicknesses would produce a section that was thinner than the target; but, after relofting the airfoil section would actually be thicker than the target.

The wing sections designed inviscidly are profoundly different at 30 and 70% semispan, but only slightly different at 50% semispan. The thinning of the top surface in complement with the thickening of the lower surface has significantly decambered these sections. The large differences at the inboard and outboard design stations are due to the influence of the inviscid pressures outside the design region; and, the remarkable agreement in the middle of the design region, except in the cove region where the boundary layer is thick, is due to the influence of the viscous boundary condition at the edges of the design region. These observations were verified by designing the entire wing inviscidly using the same viscous pressure distributions used in the previous case. This case, shown in Fig. 14, led to airfoil sections which varied smoothly in the spanwise direction at all stations. In Fig. 14, the boundary layer displacement thicknesses obtained from a viscous analysis of the target were added to the target sections for comparison with the inviscidly designed sections.

After the wings were designed, all three were then analyzed with full viscous effects to assess the significance of the changes made to the wing on the pressure distributions and to see how well these pressures matched the target pressures. Knowing that the wing designed with full viscous effects is correct, it is quite obvious from Fig. 15 and Table 1 that the wing designed inviscidly is quite unsatisfactory. The shock

is not far enough aft and the lift produced is sometimes 20% smaller than that desired.

Based on the results of this study, it can be concluded that for the Re and Mach number chosen, wake curvature and wake thickness have a very small effect on the airfoil sections designed. However, the boundary layer displacement effect has a profound effect on the section shapes and hence must be included in the design process to yield a wing which will produce the desired lift in a viscous environment.

Wing Planform Effects

Three cases were attempted to roughly delimit the applicable range of aspect ratios and leading edge sweep angles. These included Lockheed Wing A, B and C. These wings have aspect ratios of 8, 3.8, and 2.6, leading edge sweep angles of 27, 35, and 45 degrees and taper ratios of .4, .4, and .3 respectively. The target pressure distributions were obtained by a direct analysis of the target wings in an inviscid environment. The initial section for Wing-A was a NACA 0012, while a NACA 0006 was used for Wing-B. The original section was used with Wing-C due to the difficulty of the case. Also for Wing-C, as opposed to the circular cross-section, an elliptical cross section of the fuselage was used to provide a flatter surface for the grid generation package. The circular cross-section combined with the large relative thickness of the root section compared with the width of the fuselage played havoc on the grid at the root, as can be seen in Fig. 16.

In order to better understand flow about each wing, the corresponding velocity vectors on the surface of each wing were plotted, as shown in Figs. 17-18. As to be expected, the spanwise component of the flow increases as the aspect ratio decreases and sweep increases. It is also interesting that there seems to be an inboard flow for all three cases on the upper surfaces aft of the leading edge. If this is correct, this inboard flow may be attributed to the effect of the fuselage and the wing tip vortex.

The design region for Wing-A and Wing-B extended from 10-100% semispan and began 5% and 2.5% aft of the leading edge, respectively. Computations were performed on a fine grid. Results for Wing-A are shown in Fig. 19, while results for Wing-B are shown in Fig. 20. As can be seen the designed and target sections for both wings are in excellent agreement in the interior of the design region and closely match at the edges of the design region.

In the case of Wing-C, the section shapes should not have changed with the application of the inverse boundary condition. But, because of the large amount of spanwise flow and the associated spanwise gradients for Wing-C, the spanwise oscillation effect could not be overcome with any of the present remedies. Further information about this case was obtained by using the Type II method and not relofting the section shapes. The results for such a converging fine grid case are shown in Fig. 21. The first design station at 18% semispan is too thick on the upper surface as compared to the target. This discrepancy is again due to the over prediction of the residual at the first station due to the initial mismatch in the potentials in the spanwise direction, and, hence, to large spanwise gradients of the potential. The errors diminish as the tip is approached, but are always relatively large in the trailing edge region due to the difficulty in accurately imposing the inverse boundary condition near the trailing edge for this case. If an attempt were made to converge this case further by continuously relofting the shapes to meet the trailing edge ordinate, the same spanwise oscillation problem would again occur.

Initial Profile Effects

One of the disadvantages of the direct-inverse method is that a-priori knowledge about the shape of the leading edge must be known to achieve suitable airfoil shapes and desired trailing edge thicknesses. Relofting does alleviate this to a large degree; but it will not, in general, happen to produce a leading edge that will yield the desired pressure distribution in the leading edge region if the inverse boundary condition is by necessity applied too far aft. It was thought that because FLO30's grid package clusters grid lines close to the leading edge of the airfoil, that the design could be started quite close to the leading edge, thus relieving the designer of the difficulty of choosing a correct nose shape. Two test cases were conducted to investigate the dependence of the final design on the initial airfoil section. Both used Lockheed Wing-A at the same conditions mentioned earlier for the viscous study. For the first case, the initial airfoils were the same as those in the viscous study. These airfoils all had leading edges which were in the same family as the target section. The design was started 10% aft of the leading edge. In the second case, NACA 0012 sections were used at all design stations; the leading edge of these sections were not in the same family as the target airfoil sections. For this case, the pressure boundary condition began 4% aft of the leading edge. Referring to Fig. 22, it can be said that although slightly better results were obtained near the leading edge for the first case, that the airfoils designed were fairly insensitive to the initial section.

The Effect of the Direct-Inverse Junction Proximity to the Leading Edge

Since experience with the method has shown that the closer the inverse boundary condition is applied to the leading edge, the longer it takes for the solution to converge, it was of interest to learn how the location of the direct-inverse interface affected the final design and the resulting pressure distributions. This study was accomplished with the aid of the previously discussed Wing-B case, which began at 2.5% chord, and an inviscid design of Wing-B also with NACA 0006 sections as the initial geometry. With the second case, the design was begun at 5% chord from the leading edge, and the input pressures were obtained from an inviscid analysis of Wing-B. Since the pressure distributions were consistent in both of these cases, the fact that one was a viscous design and the other an inviscid design is not important.

Some representative samples of the resulting section shapes for the second case are shown in Fig. 23. The resulting wings were analyzed under the same conditions that the original input pressure distributions were obtained. Representative samples of the resulting pressure distributions are compared to their respective target distributions in Figs. 24-25. As can be seen, the wing whose design began 2.5% aft captured the suction peek at the leading edge, while the other case, which began at 5% aft of the leading edge, did not.

When designing close (less than 5%) to the leading edge, the solution sometimes began to slightly diverge or ceased converging. Usually the design could be converged to the point where there was only a maximum change in the surface of .1-.2% chord. This was more a problem on the fine grid than on the medium. If it was necessary to converge it further, the beginning of the design region was moved aft. This is an important observation, for if it is necessary to begin the design close to the leading edge to properly determine the shape of the nose, a successful design may be accomplished by beginning the design as close to the leading edge as desired or is possible, then moving the beginning of the design region aft as the solution approaches the last stages of convergence. This method not only frees the designer from the task of choosing the correct leading edge shape, but it should also accelerate the convergence of the design considerably.

Fixed Trailing Edge Design

This case was investigated to verify that a fixed trailing edge design could be accomplished with the present version of the code. The case chosen utilized Lockheed Wing-A at a Mach number of .8 and an angle of attack of 2°. A NACA 0012 section was used as the initial geometry from 30% to 70% semispan, while the remaining part of the wing used the original supercritical sections. The inverse boundary condition was enforced from 5% to 80% chord. The airfoil aft of 80% chord was fixed so that it maintained the NACA 0012 trailing edge shape. The input pressures were obtained through a medium grid inviscid analysis of the wing with the original supercritical sections used throughout. Furthermore, to provide for a smooth transition at the aft direct-inverse junction, the displacements were smoothed in the chordwise direction. The type II-2 design method was used in this case.

The resulting section shapes are revealed in Fig. 26 . The target airfoil section would actually be the first 80% of the supercritical section and the last 20% of the NACA 0012 section. Surprisingly, even with the aft portion of the wing fixed, the designed sections came quite close to matching the original Wing-A profiles at the 30% and 50% semispan locations. At the 70% semispan location, the designed section as compared to the original Wing-A section is much thicker on top and thinner on the bottom leading to more cambered profile. This shape is probably due to the interaction of the geometric constraints and the required design pressures. The shock strength of the input C_p distribution does become quite large at this location and it appears that the section may have had to become more cambered to account for this. Or, the increased camber may have been needed to provide the necessary lift required by the inverse boundary condition. The pressure distributions obained from an inviscid anlaysis of the resulting shapes

are compared with those produced by the original wing-A sections and the NACA 0012 sections in Fig. 27. The figure reveals that the design pressure distributions are a combination of the Wing-A and NACA 0012 pressure distributions. It is also interesting that it seems a secondary shock near the aft limit of the design region was necessary to meet the constraints of this problem. This very impractical case, of course, was only meant to demonstrate that it is feasible to fix the aft region of the wing. If a more realistic trailing edge was used, better results would surely follow.

Pressure Distribution Compatibility

Since it was thought that a designer might not readily have available an input pressure distribution compatible with the design freestream Mach number, it was of interest to discover the effect of designing a wing at one Mach number using a pressure distribution obtained from an analyisis of the wing at a different Mach number. The Wing-A planform was used throughout this portion of the study. NACA 0012 sections were used as the targets and NACA 0006 sections were used as the initial sections in the design. The entire wing was designed on a medium grid from root to tip, and the design region was begun at 10% aft of the leading edge of the wing.

Two separate tests were performed. The first involved a fine design at a nearly incompressible Mach number of .2 using a pressure distribution obtained from an analysis of the target at a Mach number of .1. As can be seen from Fig. 28, thinner section shapes were obtained at the higher Mach number. This is in agreement with the 2-D Prandtl-Glauert similarity rule[25]

$$\frac{\tau_1}{\tau_2} = \frac{\sqrt{1-M_1^2}}{\sqrt{1-M_2^2}} \tag{35}$$

which states that the C_p will be invariant with Mach number if the thickness, τ, is reduced as the Mach number is increased for linearized flow. For this case, Eq. (35) would predict that a 1.54% decrease in thickness would be necessary to have the same pressure distribution at the higher Mach number. The design code for this 3-D case produced a section which was on the average 1.6% thinner than the NACA 0012 section.

The second case involved a medium grid design at a Mach number of .85 using a pressure distribution obtained at a Mach number of .80. Referring to Fig. 29, the section shapes produced are again thinner than the initial section. The top surface, though, required a sudden thinning of the surface at the shock location. Surprisingly, upon analyzing this wing, the pressure distibutions shown in Fig. 30 match quite well with the target everywhere except in the tip region of the wing. So given the constraints of the problems, it appears that the only way the boundary conditions could be met was to have these dips in the airfoil surface. Since these dips might lead to boundary layer difficulties, it would probably behoove the designer to vary the Mach number or alter the pressure distribution to eliminate the necessity of these dips.

Grid Refinement Effects

Since the computational time required for a design on the medium grid is about an eighth of that required on a fine grid, it may be tempting to try to design on the medium grid using fine grid or real pressures. In order to assess the practicality of this, a transonic design on a medium grid using fine grid pressures was executed. The case was performed using a Mach number of .8, and an angle of attack of two degrees. The original supercritical sections for Wing-A were used as the initial, as well as, the target sections. The results are shown in Fig. 31. The only place where the designs came close to the target was near the middle of the wing. A slight wave appears in the upper surfaces of the designed sections near the shock location. This is due to the smearing of the shock on the medium grid. The section designed at the wing tip deviated well away from the target. The fact that the fine grid C_l is lower than the medium grid C_l at the wing tip most probably necessitated the decambering of the sections at the wing tip.

No attempt was made to match the C_L's of the fine grid and medium grid analyses by varying the Mach number or angle of attack, but a comparison of the medium grid pressures at various Mach numbers and angles of attack with the target fine grid pressures for the supercritical wing shown in Fig. 32 reveal that it would probably be necessary to alter the twist of the wing to closely match the C_l's at all of the design stations. It also shows that increasing the angle of attack to 2.1° would have produced closer matching C_l's and hence perhaps better designs. In retrospect though, given that the fine grid pressures are correct or more realistic, it will be necessary, unless appropriate corrections can be found, to use the fine grid to properly resolve the correct airfoil sections.

Conclusions

Progress in the direct-inverse wing design method in curvilinear coordinates has been made. This included the remedying of a spanwise oscillation problem and the assessment of grid skewness, viscous interaction, grid refinement and the initial airfoil section on the final design. It was found that: 1) In response to the spanwise oscillation problem, designing at every other spanwise station produced the smoothest results for the cases presented. 2) A smoothly varying grid is especially needed for the accurate design at the wing tip. 3) The final airfoil section designed is independent of the initial section if the direct-inverse junction is moved close to the leading edge; 4) Boundary layer displacement thicknesses must be included in the successful design of a wing in a viscous environment. 5) Presently the design of only high and medium aspect ratio wings is possible with this code. 6) A partial wing design beginning aft of the leading edge and terminating prior to the trailing edge is possible with the present method 7) Designs must be performed on a fine grid.

Acknowledgements

The work presented in this paper was primarily supported by the National Aeronautics and Space Administration under Grant NAG-1-619 with Richard L. Campbell of the Langley Research Center as technical monitor. The authors express their appreciation to Richard L. Campbell and Edgar Waggoner of NASA Langley and to Thomas Gally for their assistance and helpful suggestions. Much thanks also goes to the Computer Service Center at Texas A&M University for their very generous computer support.

References

[1] Davis, W., "TRO-2D: A Code for Rational Transonic Aero Optimization," AIAA Paper 85-0425, January 1985.

[2] Hicks. R., "Wing Design by Numerical Optimization," AIAA Paper 77-1247, August 1985.

[3] Shankar, V., Malmuth, N.D, "Computational Transonic Design Procedure for Three-Dimensional Wings and Wing-Body Combinations," presented at the 17th Aerospace Sciences Meeting, New Orleans, La., January 15-17, 1979, AIAA paper 79-0344.

[4] Shankar, V. and Malmuth, N.D.,, "Computational Transonic Inverse Procedure for Wing Design," AIAA Paper 80-1390R, 1980.

[5] Campbell, R.C., and Smith, L.A., "A Hybrid Algorithm for Transonic Airfoil and Wing Design," presented at the AIAA 5th Applied Aerodynamics Conference, Monterey, California, August 17-19, AIAA paper 88-0009.

[6] Anderson, W. K., and Carlson, L. A., "Inverse Transonic Wing Design on a Vector Processor," Texas A&M Research Foundation Report TAMRF-4535-8212, December 1982.

[7] Weed, R.A, Carlson, L.A., "A Direct-Inverse Three-Dimensional Transonic Wing Design Method for Vector Computers," *AIAA 2nd Applied Aerodynamics Conference*, Seattle, Wa., AIAA paper 84-2156, pp. August, 21-23, 1984.

[8] Carlson, L.A. and Weed, R.A, "A Direct-Inverse Transonic Wing Analysis-Design Method with Viscous Interaction," *Journal of Aircraft*, vol. 23, September, 1986, pp. 711-718.

[9] Gally, T. A. and Carlson, L. A., "Transonic Wing Design Using Inverse Methods in Curvilinear Coordinates," *Journal of Aircraft*, vol. 25, November, 1988, pp. 1009-1017.

[10] Gally, T. A. and Carlson, L. A., "Inverse Transonic Wing Design Using Finite Volume Methods in Curvilinear Coordinates," *5th Applied Aerodynamics Conference*, Monterey, California, August 17-19, 1987, pp. 516-526.

[11] Gally, T. A., "Inverse Transonic Wing Design Using Finite-Volume Methods in Curvilinear Coordinates," M.S. Thesis, Texas A&M Univ., College Station, TX, May, 1987.

[12] Melson, N. D. and Streett, C. L., "TAWFIVE: A User's Guide," NASA TM84619, September 1983.

[13] Street, C.L, "Viscous-Inviscid Interaction For Transonic Wing-Body Configurations Including Wake Effects," *AIAA Journal*, vol. 20, July,1982, pp. 915.

[14] Jameson, Anthony, "Transonic Potential Flow Calculations Using Conservative Form," *Proceedings of AIAA 2nd Computational Fluid Dynamics Conference*, Hartfort, Conn., June 1975, pp. 148-161.

[15] Jameson, Anthony and Caughey, D. A., "A Finite Volume Method for Transonic Potential Flow Calculations," *Proceedings of AIAA 3rd Computational Fluid Dynamics Conference*, Albuquerque, N. M., June 1977, pp. 35-54.

[16] Jameson, Anthony, "Iterative Solution of Transonic Flows over Airfoils and Wings, Including Flows at Mach 1," *Comm. Pure Appl. Math.*, vol. 27, 1974, pp. 283-309.

[17] Caughey, D. A. and Jameson, Anthony, "Progress in Finite-Volume Calculation for Wing-Fuselage Combinations," AIAA Paper 79-1513R, 1979.

[18] Caughey, D.A., "Multi-Grid Calculation of Three Dimensional Transonic Potential Flows," *AIAA 21st Aerospace Sciences Meeting*, Reno, Nevada, AIAA paper 83-0374, pp. January 10-13, 1983.

[19] Anderson, D.A., Tannehill, J.C., and Pletcher, R.H., *Computational Fluid Mechanics and Heat Transfer*, First Edition, Hemisphere Publishing Co., Washington, New York, London, 1984, pp. 50–53,63–66.

[20] Carlson, L. A., "Transonic Airfoil Design Using Cartesian Coordinates," NASA CR-2578, April 1976.

[21] Carlson, L. A., "TRANDES: A Fortran Program for Transonic Airfoil Analysis or Design," NASA CR-2821, June 1977.

[22] Bristow, D. R., and Hawk, J.D., "Subsonic Panel Method for Designing Wing Surfaces From Pressure Distribution," NASA CR-3713, 1983.

[23] Volpe, G., and Melnik, R.E., "The Role of Constraints in the Inverse Design Problem for Transonic Airfoils," presented at the AIAA 14th Fluid and Plasma Dynamics Conference, Palo Alto, California, June 23-25, 1981, AIAA paper 81-1233.

[24] Carlson, L.A., Ratcliff, R.R., Gally, T. A. , "Inverse Wing Design In Transonic Flow Including Viscous Interaction," *Transonic Symposium*, Hampton, Virginia , April 19-21, 1988, NASA CP-3020, pp. 497-519.

[25] Liepmann, H.W., and Roshko, A., *Elements of Gasdynamics*, 1st Edition, John Wiley & Sons, Inc., New York, New York, 1957.

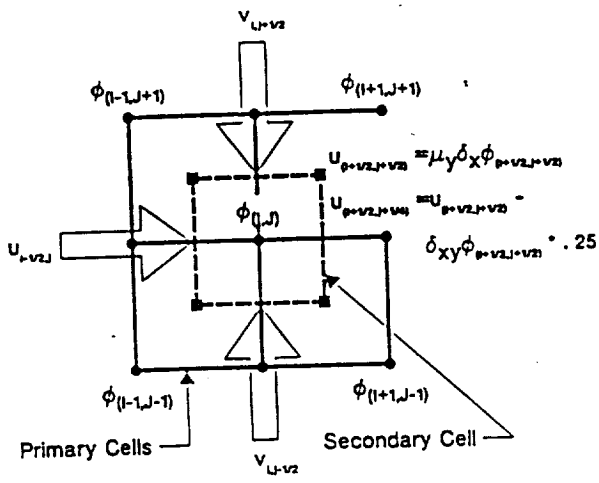

Fig. 1 Staggered box finite-volume cell

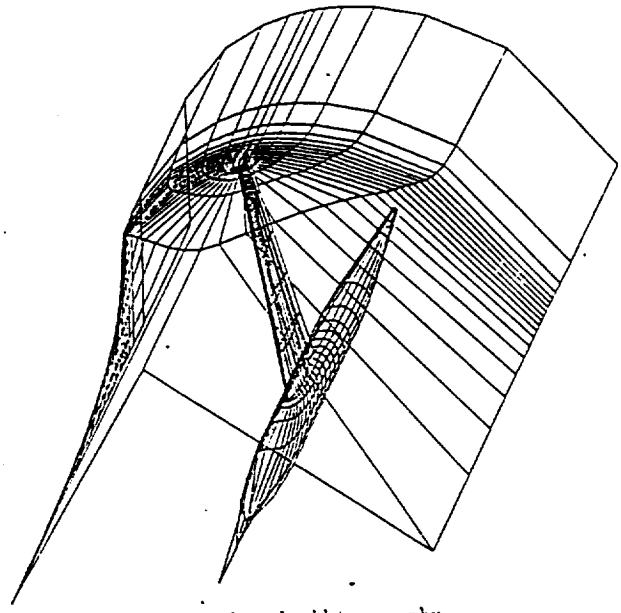

Fig. 2 Conformal grid topography

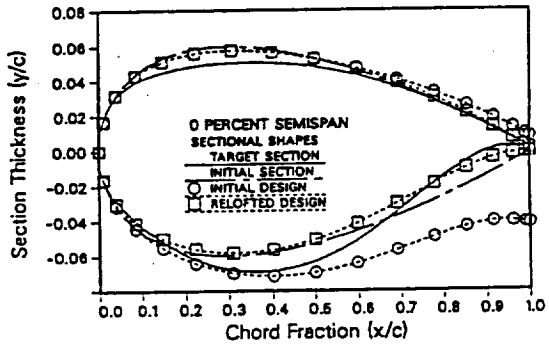

Fig. 3 The effect of relofting on the design in the initial stages of convergence

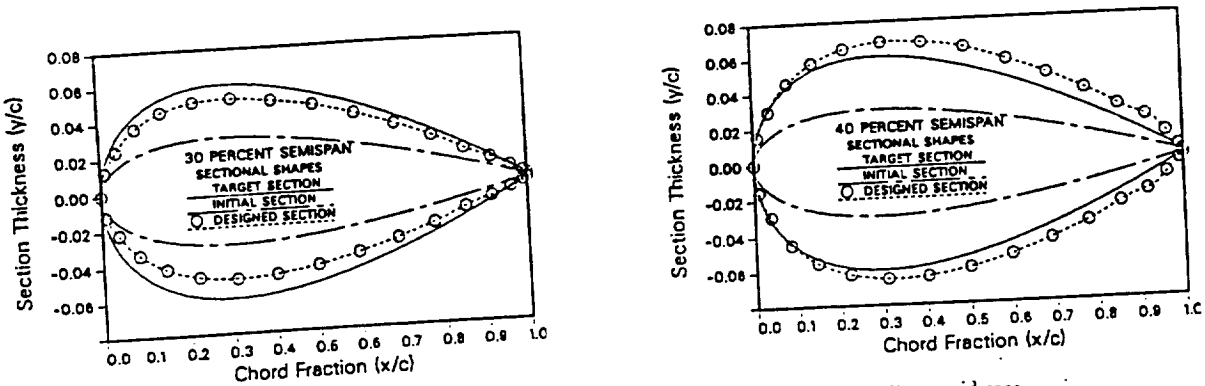

Fig. 4 Alternating thick-thin sections for a divergent medium grid case

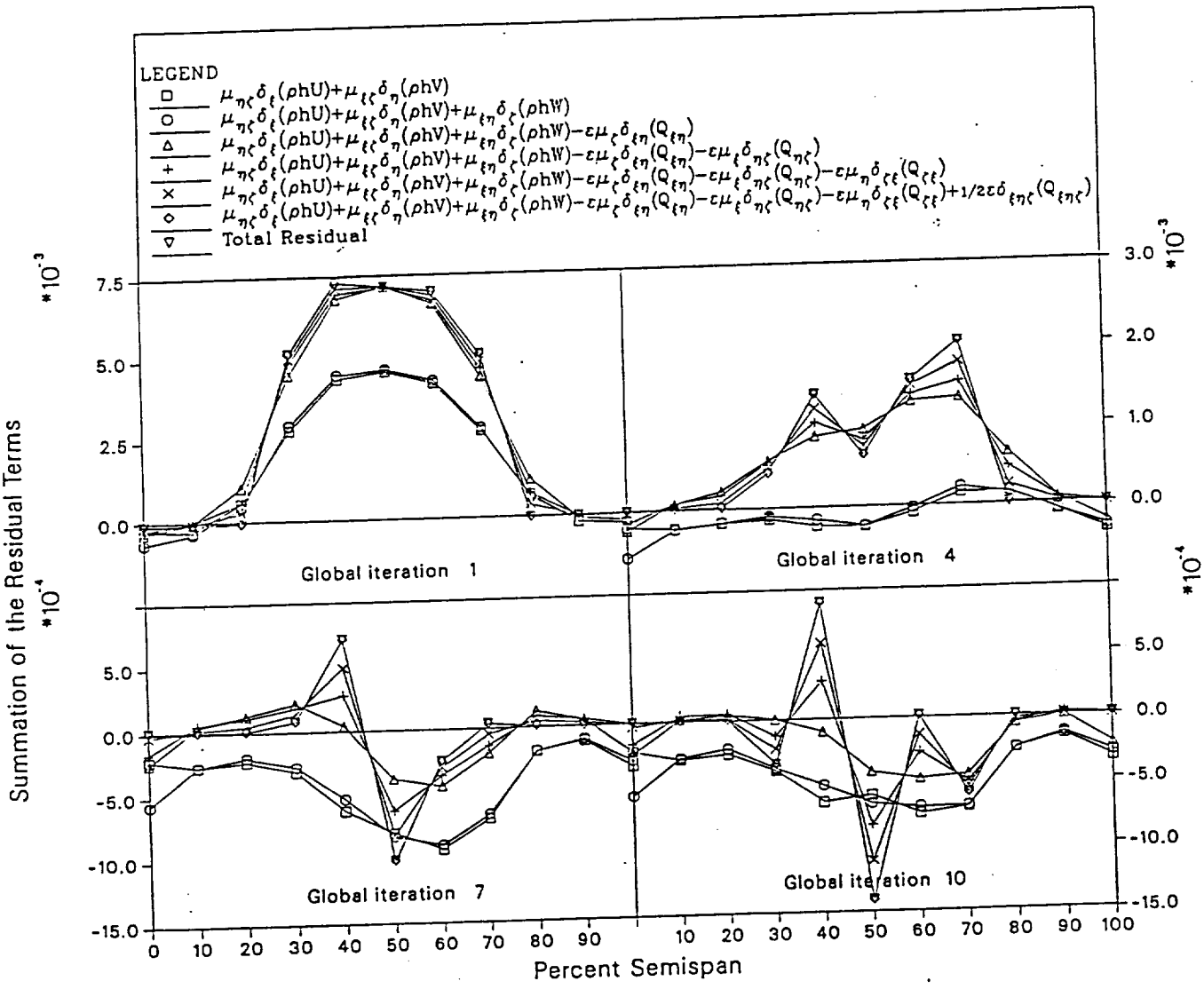

Fig. 5 The time history of the residual and the terms composing it at the uppper trailing edge for a typical divergent solution. (The design region extends from 30-70% semispan)

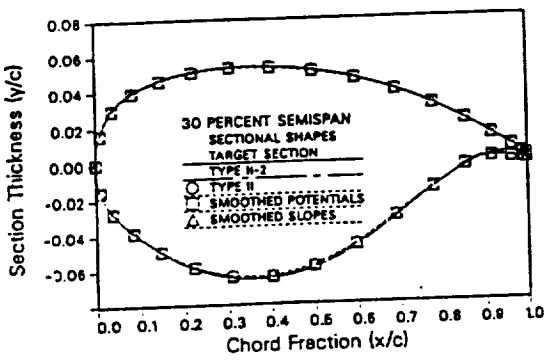

Fig. 6a

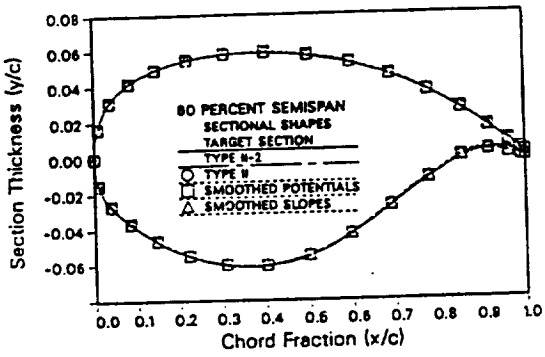

Fig. 6d

Figs. 6a-6e Comparison of airfoil sections designed using the four spanwise oscillation remedies.

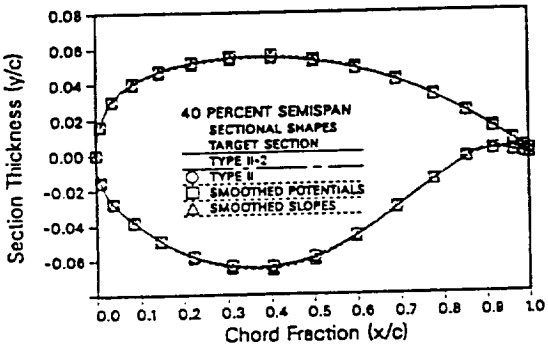

Fig. 6b

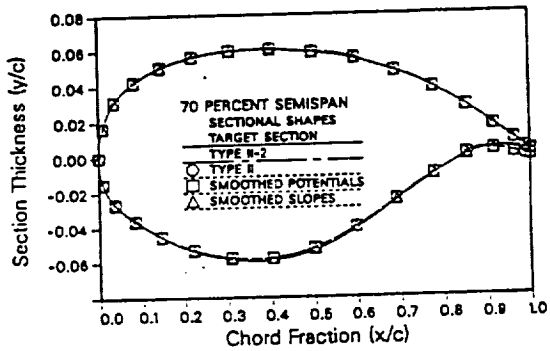

Fig. 6e

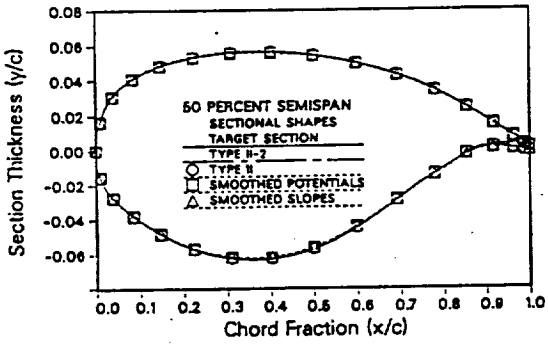

Fig. 6c

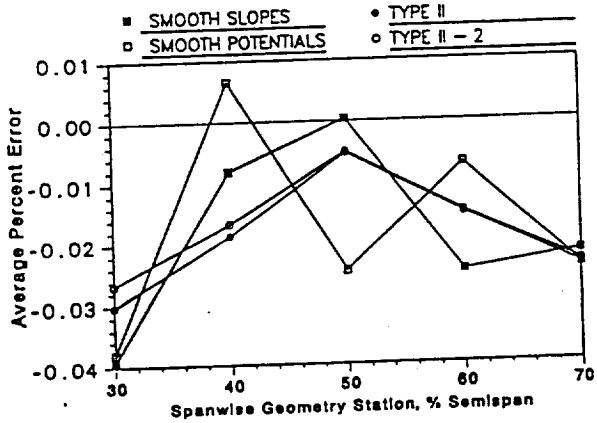

Fig. 7 The effect of the four spanwise oscillation remedies on the average percent error between the target and the design sections

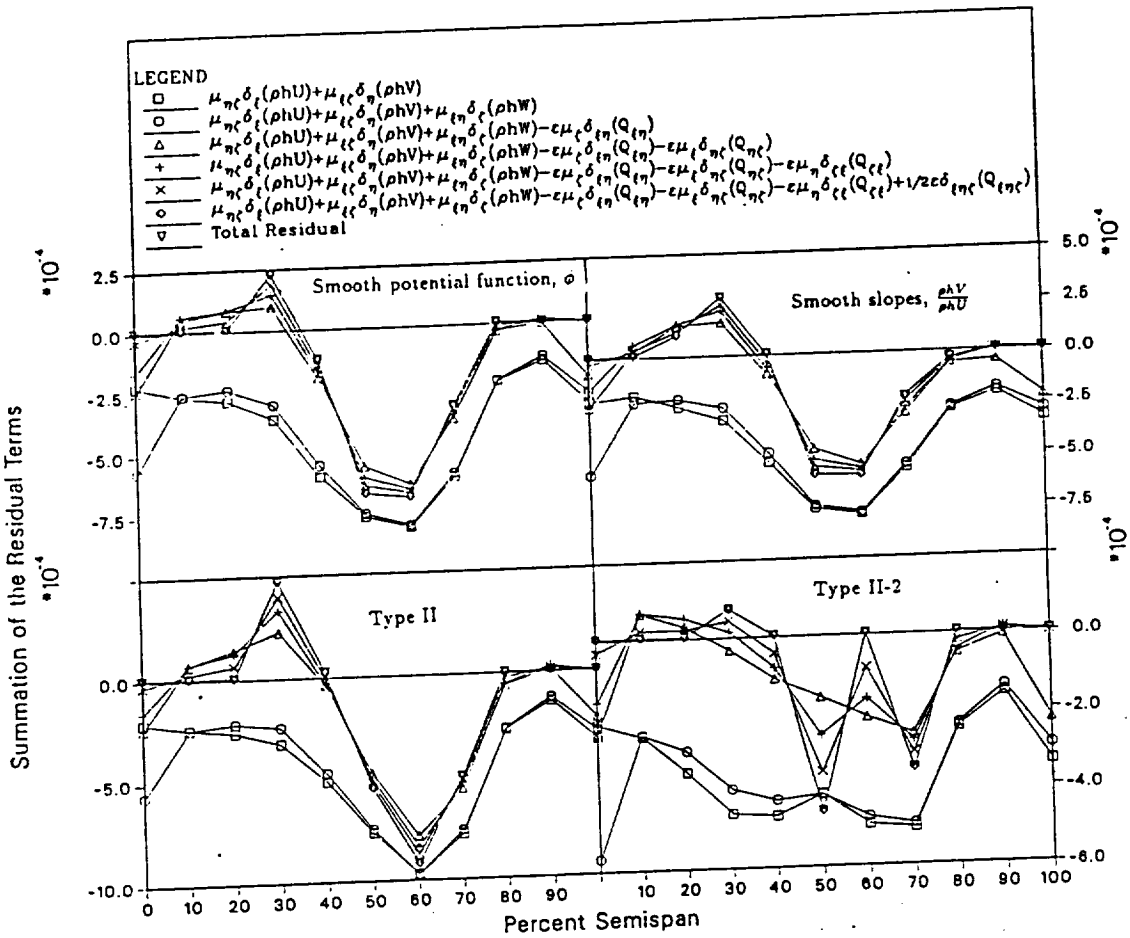

Fig. 8 Breakdown of the Residual at the trailing edge on the upper surface for the four spanwise oscillation remedies after 10 global iterations

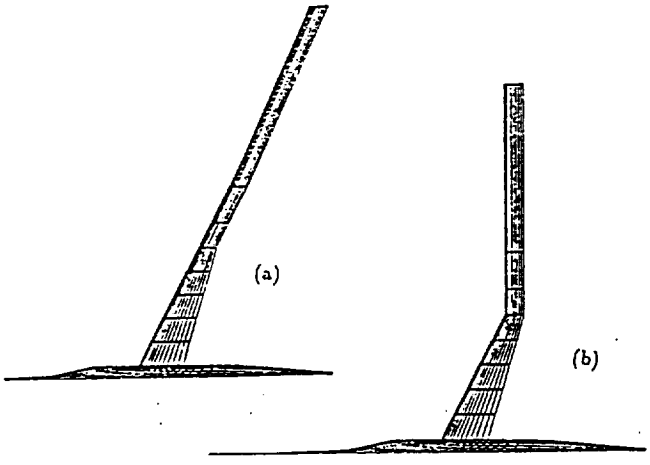

Fig. 9 Comparison between a fairly unskewed (a) and skewed grid (b)

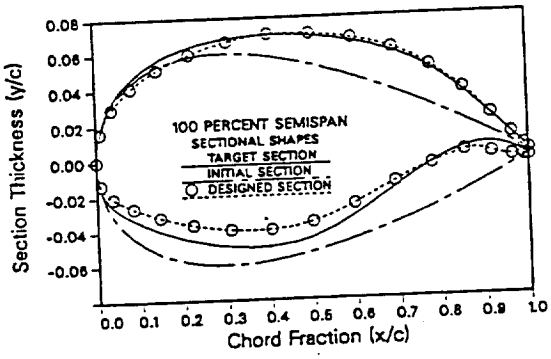

Fig. 10a

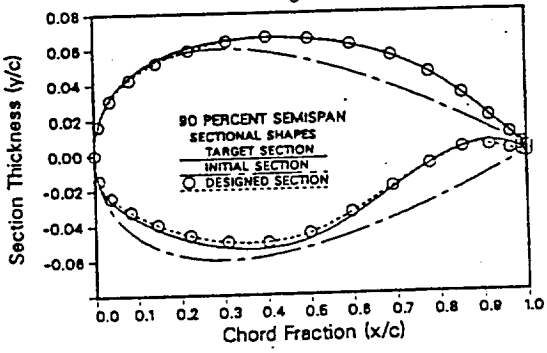

Fig. 10b

Figs. 10a-10b Sections designed with a skewed grid using pressures obtained from an analysis on an unskewed grid

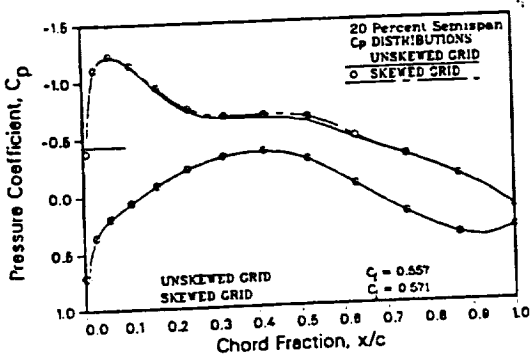

Fig. 11a

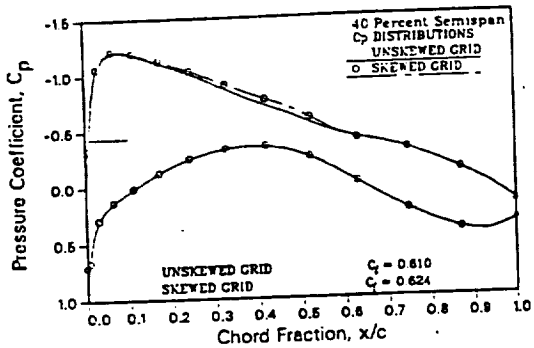

Fig. 11b

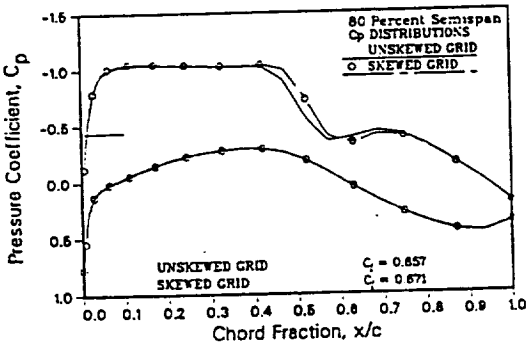

Fig. 11c

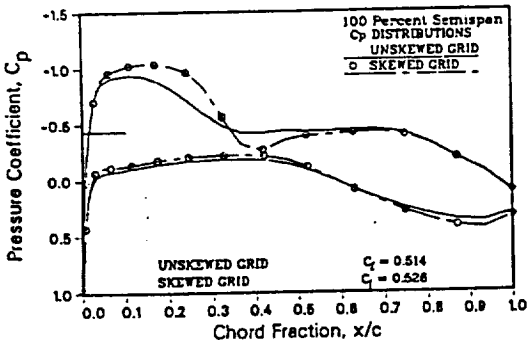

Fig. 11d

Figs. 11a-11d Comparison of a pressure distribution obtained from an analysis of a skewed grid with one obtained from an analysis of an unskewed grid

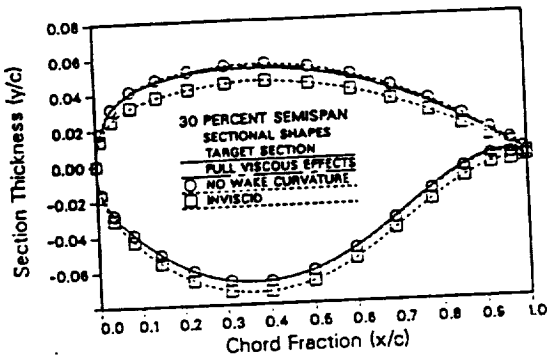

Fig. 12a

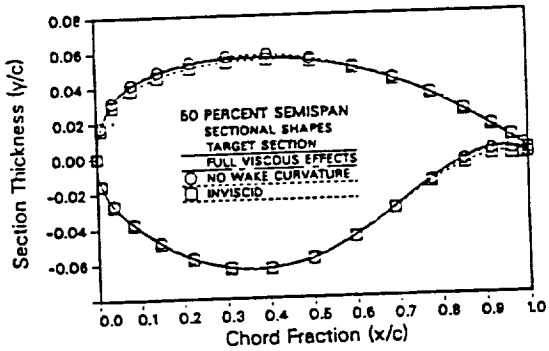

Fig. 12b

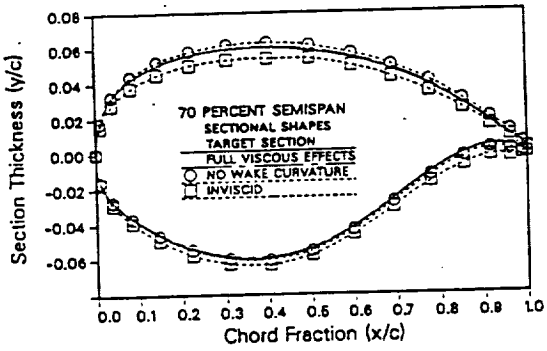

Fig. 12c

Figs. 12a-12c Comparison of the sectional shapes designed using different viscous interaction assumptions with a pressure distibution obtained from a fully viscous analysis of Lockheed Wing-A at a Re = 24×10^6, M = .8, and an $\alpha = 2°$

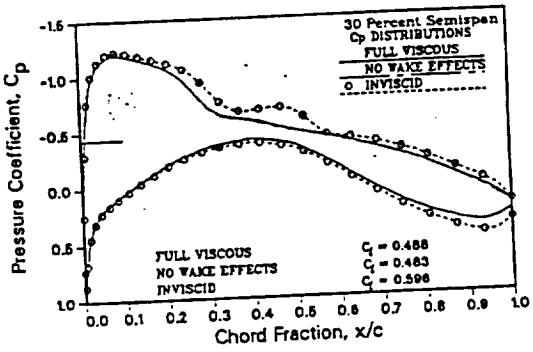

Fig. 13a

Figs. 13a-13c Comparison of pressure distributions obtained from a viscous analysis of the Lockheed Wing-A using three different viscous interaction assumptions with a Mach = .8, $\alpha = 2°$, Re = 24×10^6

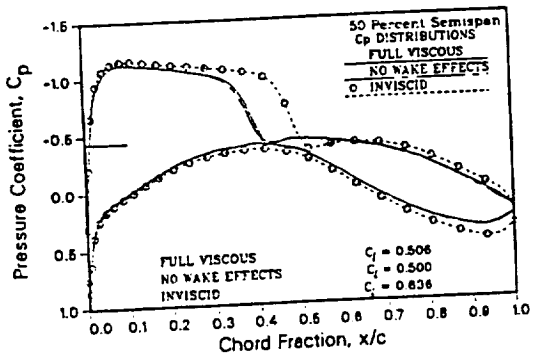

Fig. 13b

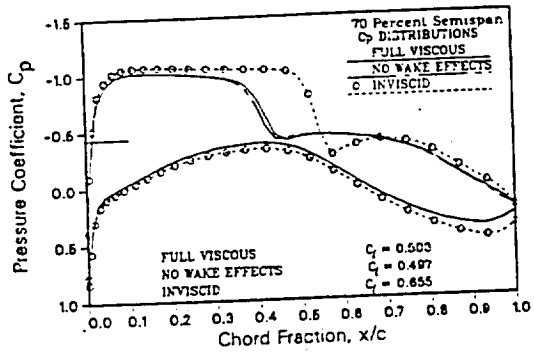

Fig. 13c

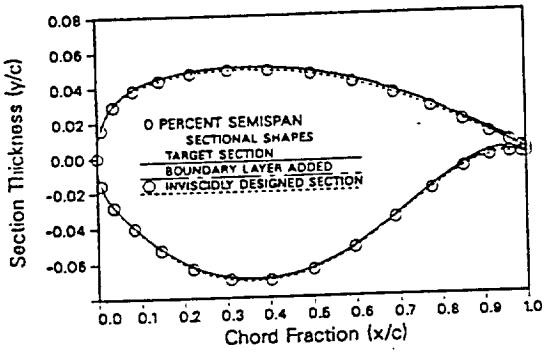

Fig. 14a

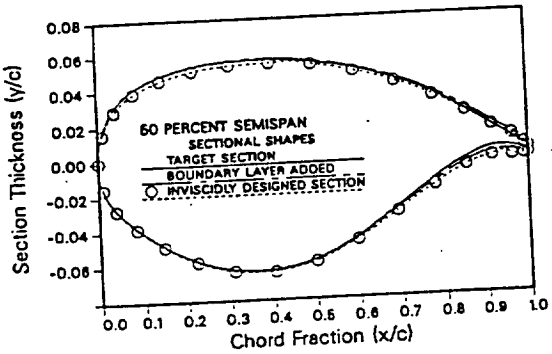

Fig. 14b

Figs. 14a-14c Comparison of an inviscidly designed section using viscous pressures with the target and the target plus the associated boundary layer displacement thicknesses

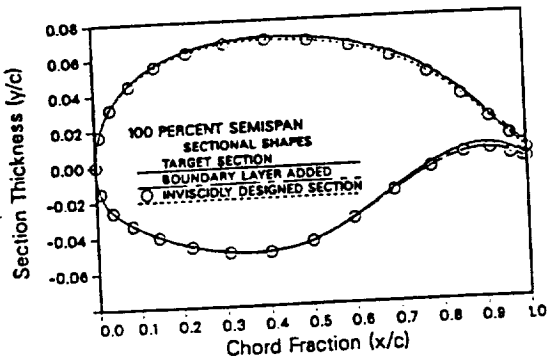

Fig. 14c

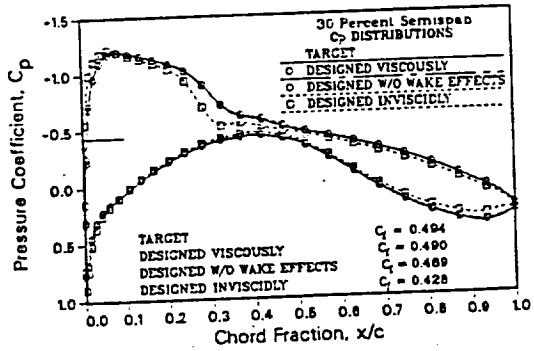

Fig. 15a

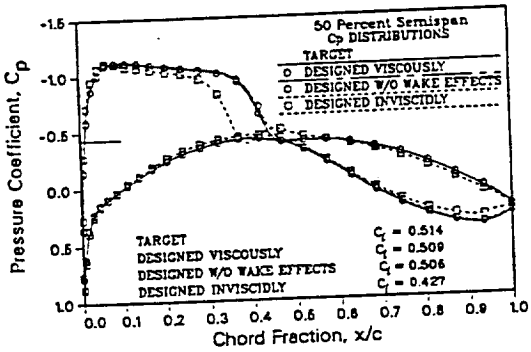

Fig. 15b

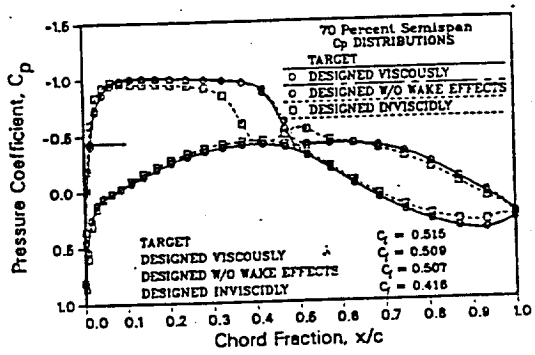

Fig. 15c

Figs. 15a-15c Comparison of pressure distributions obtained by fully viscous analyses of the wings designed using different viscous interaction assumptions for a Mach = .8, $\alpha = 2°$, Re = 24×10^6

Lift Coefficient	Target	Full Viscous Design	No Wake Design	Inviscid Design
C_l	.514	.509	.506	.427
Wing C_L	.483	.478	.477	.419

Table 1 Comparison of the total and wing lift coefficient obtained from a fully viscous anaiysis of the wings designed using different viscous interaction assumptions

Fig. 16 Grid generated about Wing-C with an incompatible root section and fuselage cross section

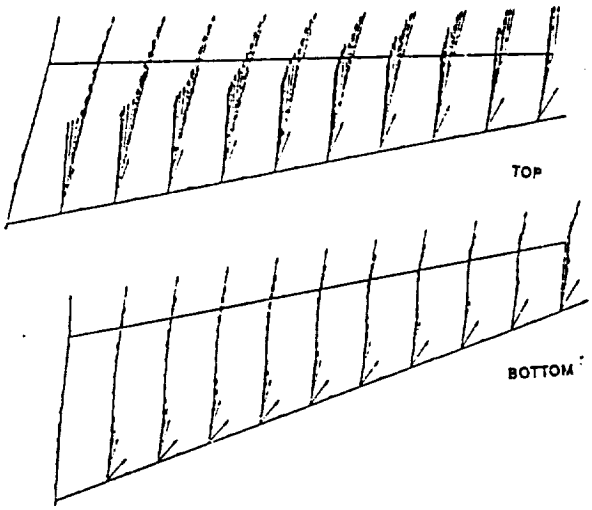

Fig. 17 Surface velocity vectors for Lockheed Wing-A on the upper and lower surface

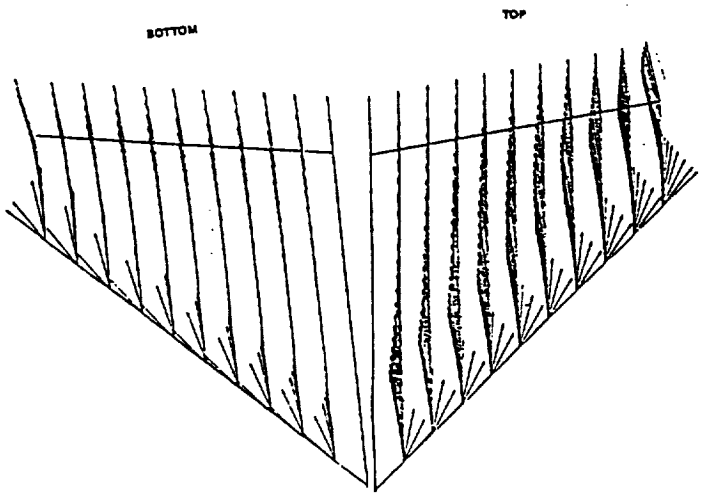

Fig. 18 Surface velocity vectors for Lockheed Wing-C on the upper and lower surface

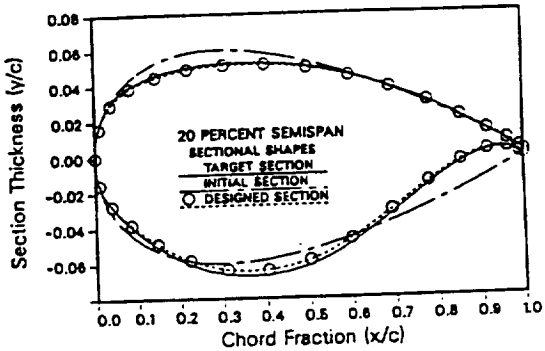

Fig. 19a

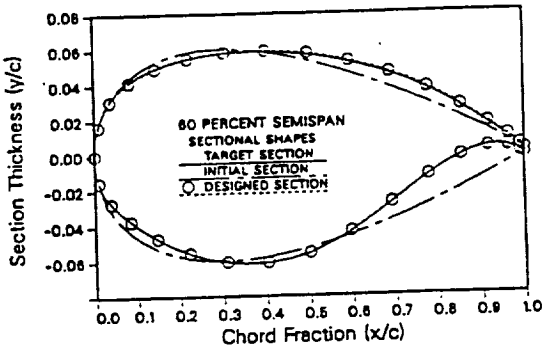

Fig. 19b

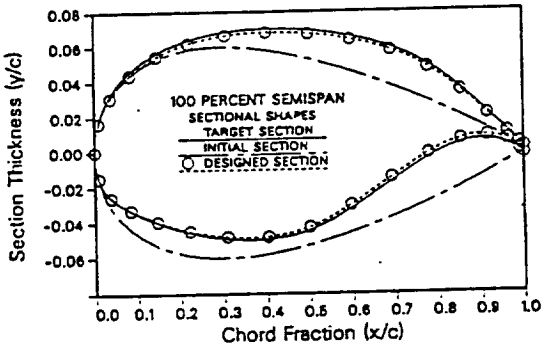

Fig. 19c

Figs. 19a-19c Comparison of the designed sections with the targets and the initial sections for a fine grid case using Lockheed Wing-A

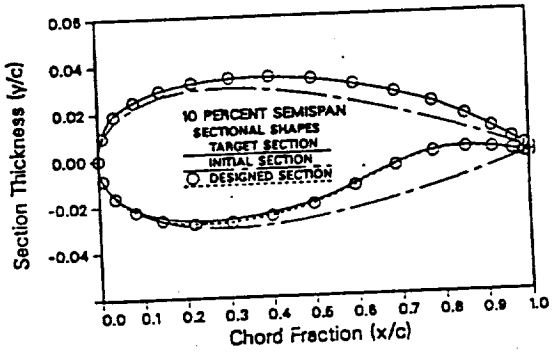

Fig. 20a

Figs. 20a-20c Comparison of the designed sections with the targets and the initial sections for a fine grid case using Lockheed Wing-B and a design region beginning at 2.5% aft of the leading edge.

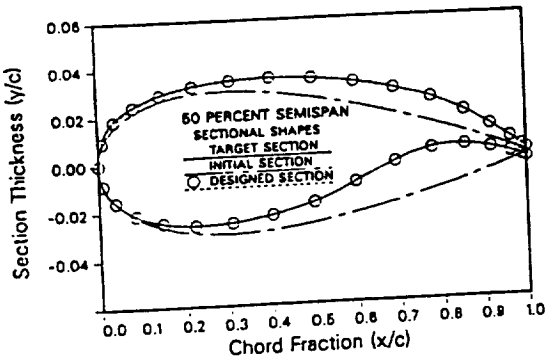

Fig. 20b

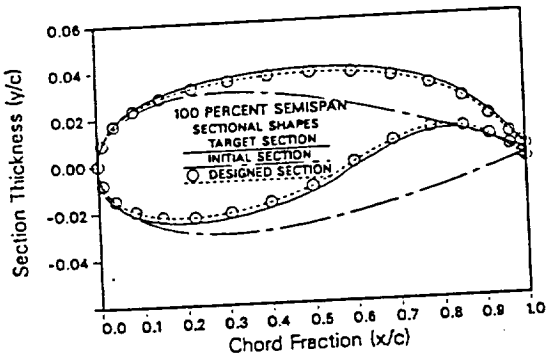

Fig. 20c

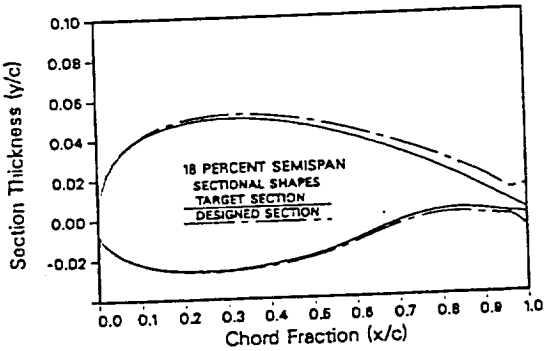

Fig. 21a

Figs. 21a-21c Comparison of the designed section with the target for an unrelofted fine grid case using Lockheed Wing-C

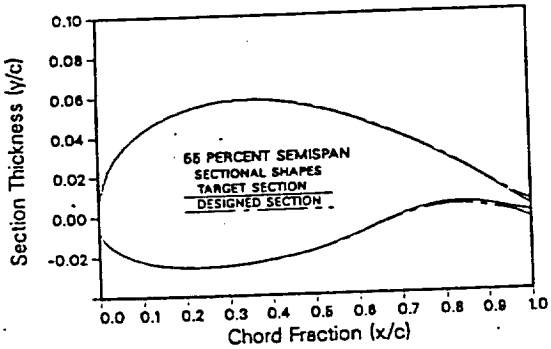

Fig. 21b

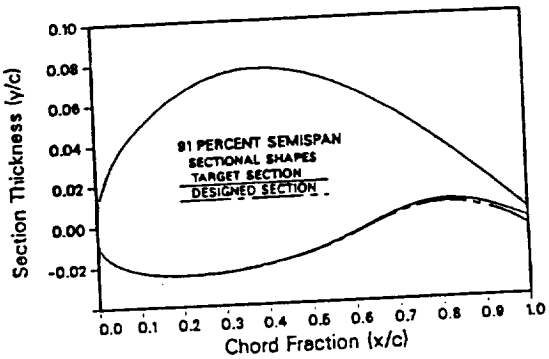

Fig. 21c

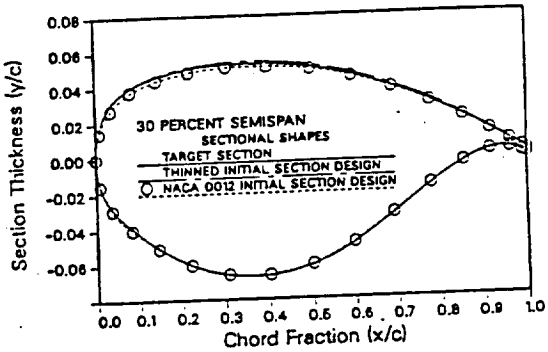

Fig. 22a

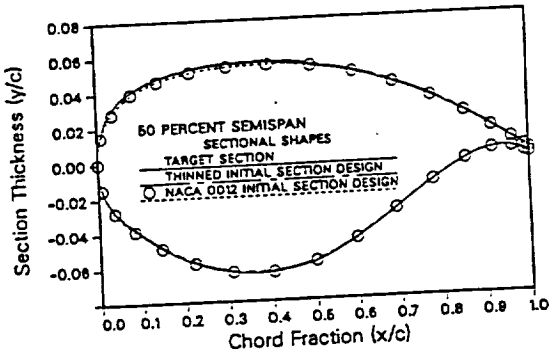

Fig. 22b

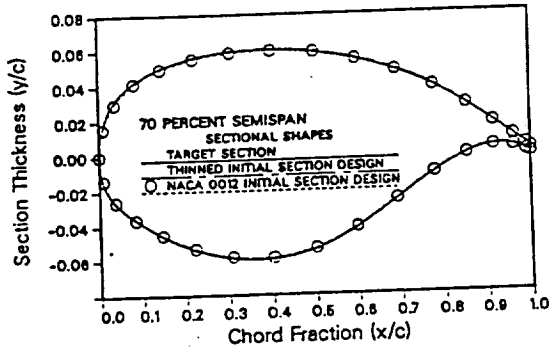

Fig. 22c

Figs. 22a-22c Comparison of sections designed using two different initial sections

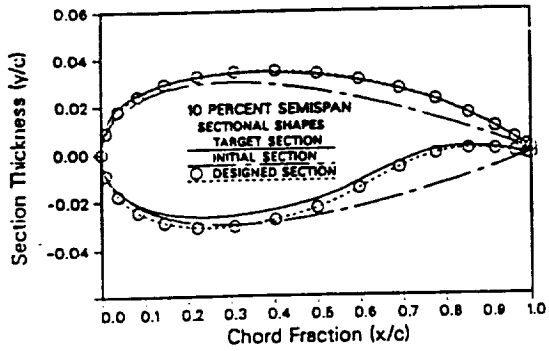

Fig. 23a

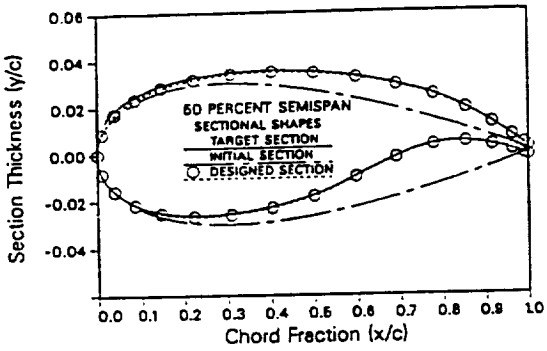

Fig. 23b

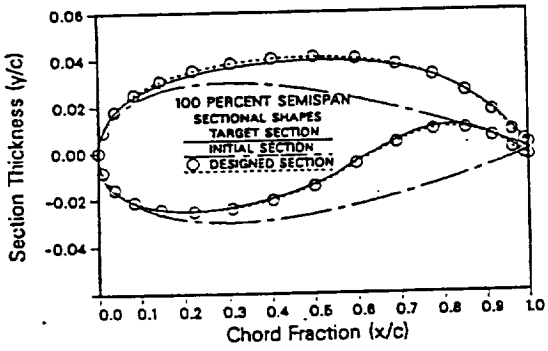

Fig. 23c

Figs. 23a-23c Comparison of the designed sections with the targets and the initial sections for a fine grid case using Lockheed Wing-B and a design region beginning at 5.0% aft of the leading edge.

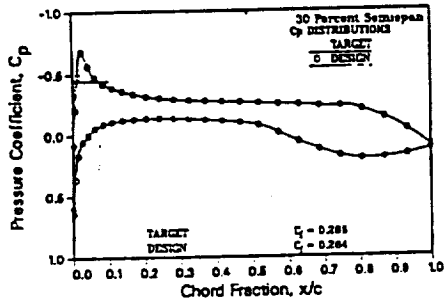

Fig. 24a

Figs. 24a-24c Comparison of the pressure distributions obtained from an analysis of the Wing-B design, which had a design region which began 2.5% aft of the leading edge, with the target pressure distributions

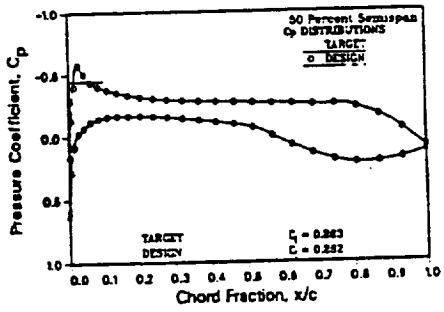

Fig. 24b

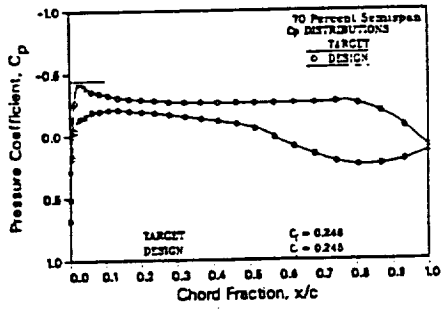

Fig. 24c

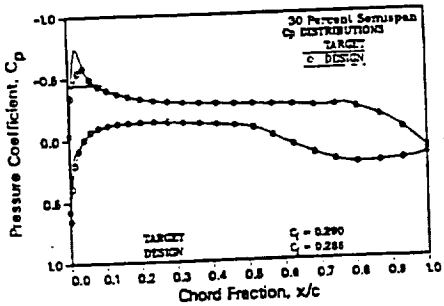

Fig. 25a

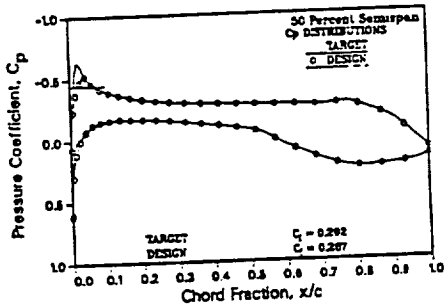

Fig. 25b

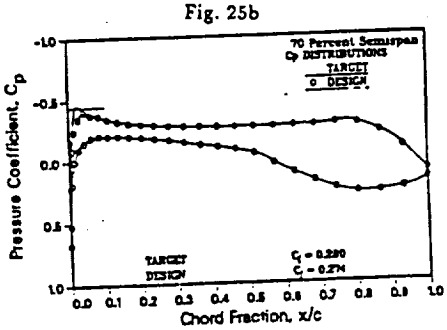

Fig. 25c

Figs. 25a-25c Comparison of the pressure distributions obtained from an analysis of the Wing-B design, which had a design region which began 5.0% aft of the leading edge, with the target pressure distributions

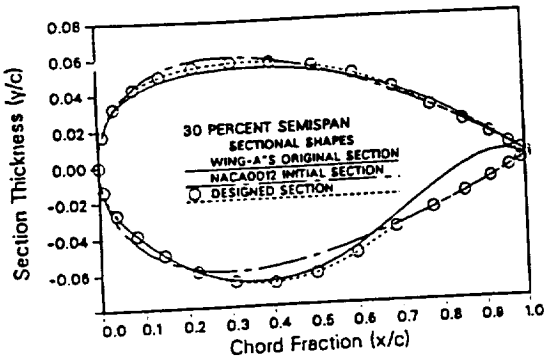

Fig. 26a

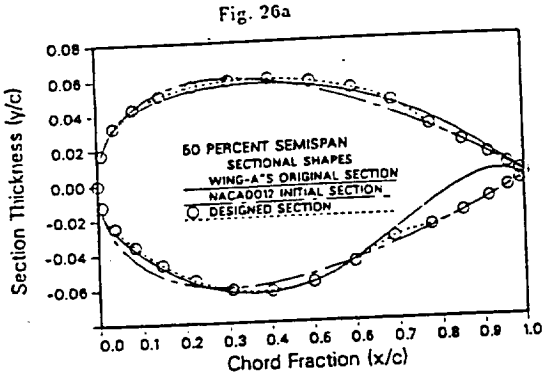

Fig. 26b

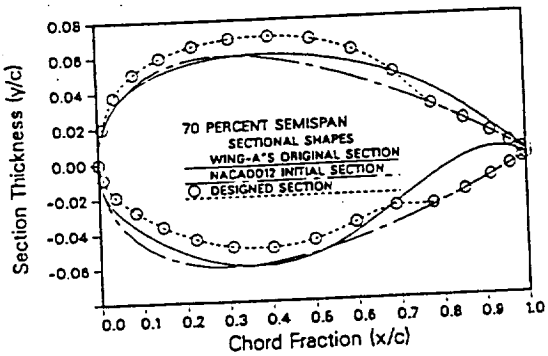

Fig. 26c

Figs. 26a-26c Comparison of the sectional shapes designed with a fixed trailing edge region with a NACA0012 and the original Lockheed Wing-A section

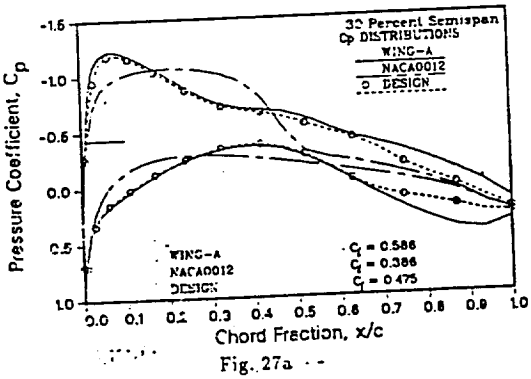

Fig. 27a

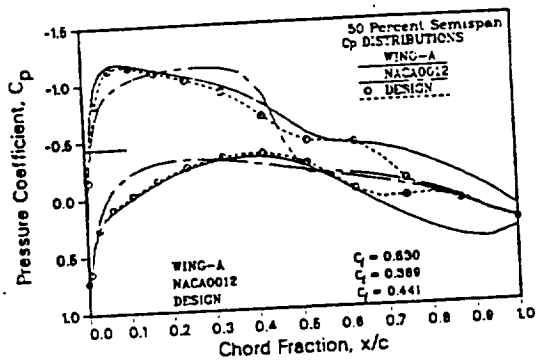

Fig. 27b

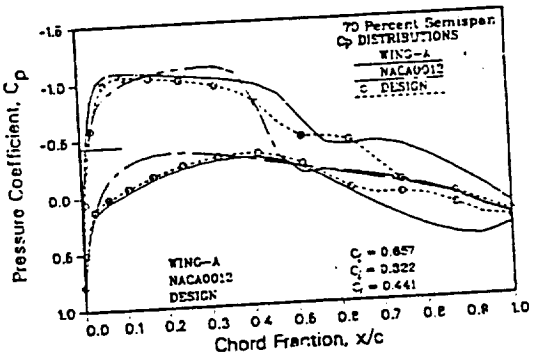

Fig. 27c

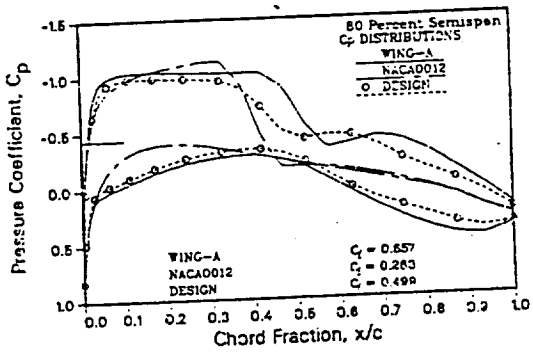

Fig. 27d

Figs. 27a-27d Comparison of the pressure distributions obtained by an inviscid analysis of the sectional shapes designed with a fixed trailing edge region with those for a NACA0012 and the original Lockheed Wing-A section. (M =.8, $\alpha = 2°$)

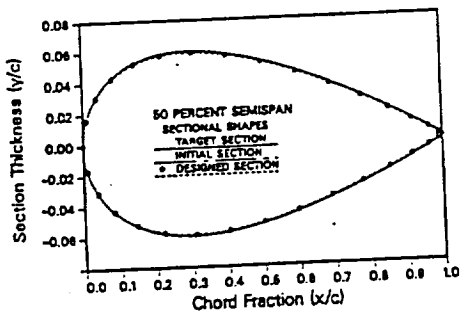

Figs. 28 Comparison of the section designed at a Mach number of .2, using input pressure distributions obtained from an analysis at a Mach number of .1, with the original Naca 0012 sections

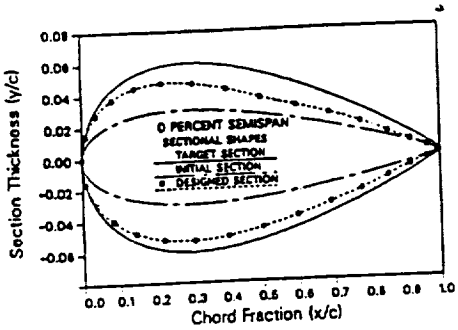

Fig. 29a

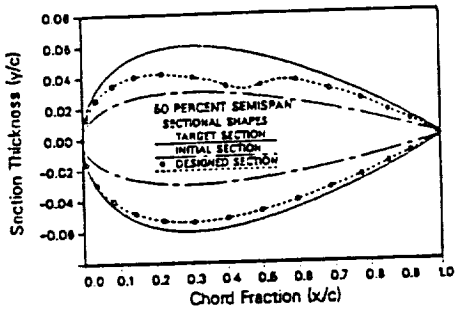

Fig. 29b

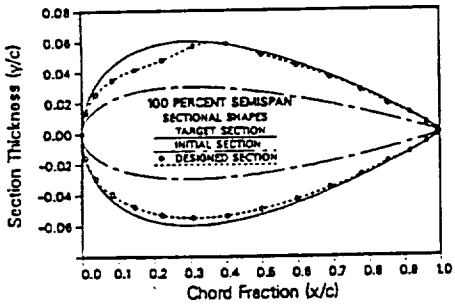

Fig. 29c

Figs. 29a-29c Comparison of the sections designed at a Mach number of .85, using input pressure distributions obtained from an analysis at a Mach number of .8, with the original supercritical sections

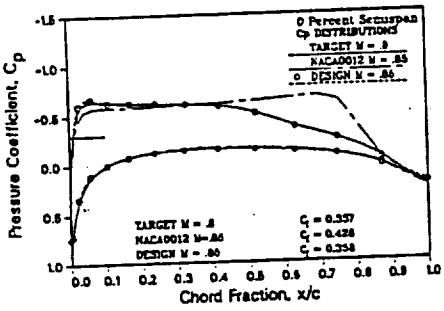

Fig. 30a

Figs. 30a-30c Comparison of the pressure distributions obtained from an analysis at a M=.85 of the Lockheed Wing-A which was designed at a M = .85 using input pressure distributions obtained from an analysis at a Mach number of .8, with the input pressure distributions

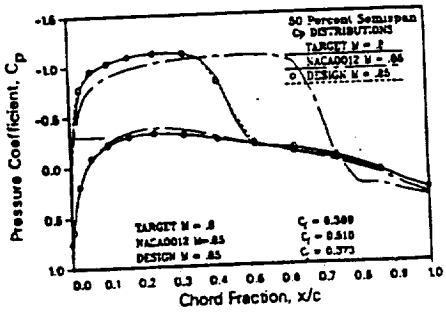

Fig. 30b

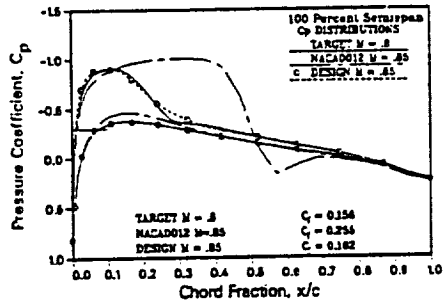

Fig. 30c

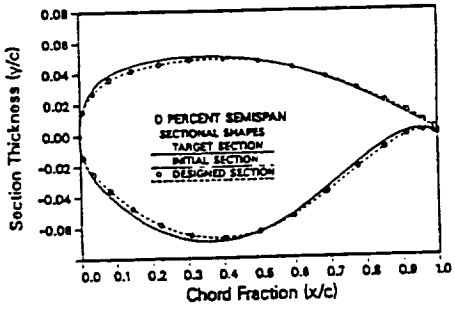

Fig. 31a

Figs. 31a-31d Comparison of the sections obtained from a medium grid design at at M = .8 using input pressure distributions obtained from a fine grid analysis of Lockheed Wing-A with the target sections

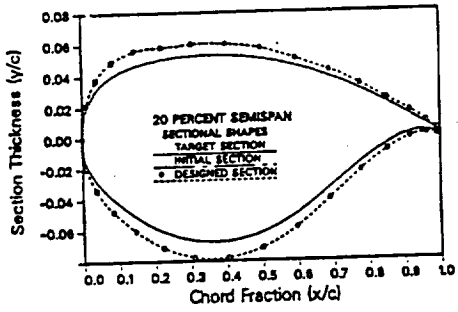

Fig. 31b

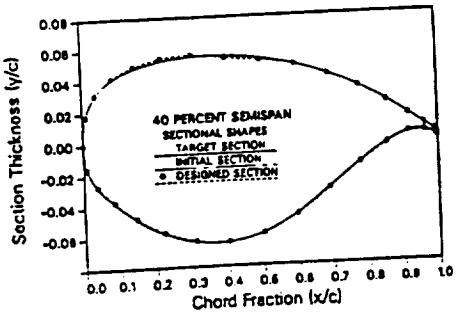

Fig. 31c

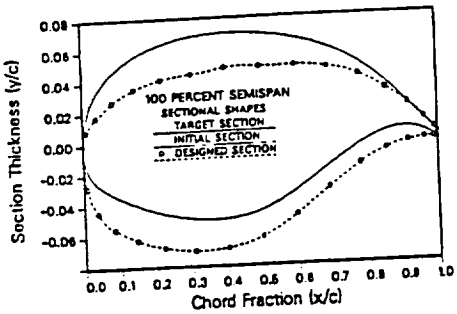

Fig. 31d

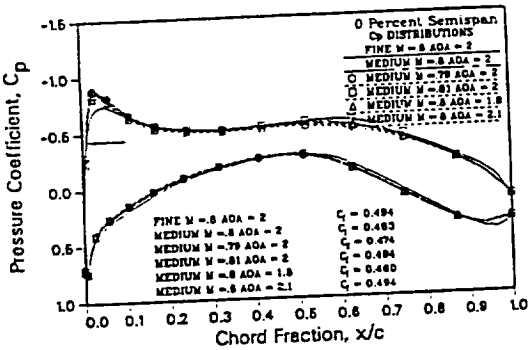

Fig. 32a

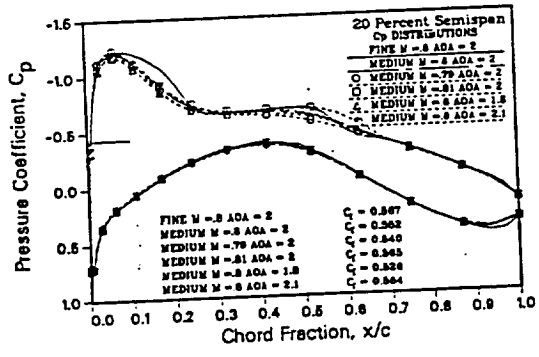

Fig. 32b

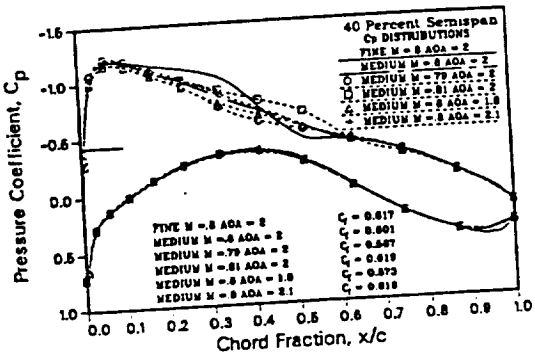

Fig. 32c

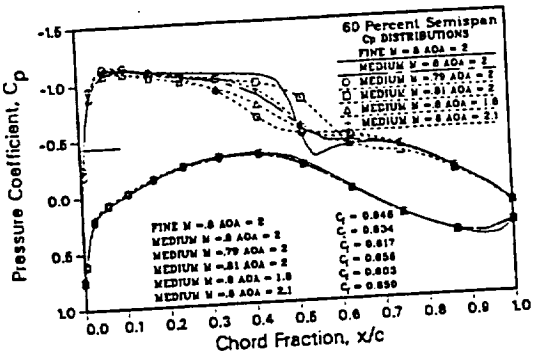

Fig. 32d

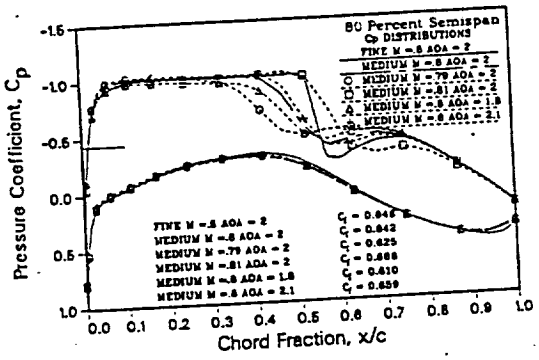

Fig. 32e

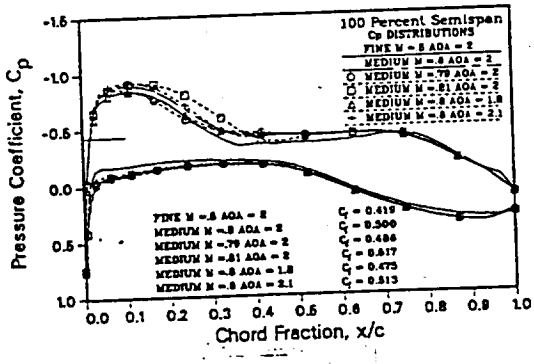

Fig. 32f

Figs. 32a-32f Comparison of fine grid pressure distributions with medium grid pressure distributions obtained from an analysis of Lockheed Wing-A at various angles of attack and Mach numbers

Appendix II

NASA Publications

INVERSE WING DESIGN IN TRANSONIC FLOW INCLUDING VISCOUS INTERACTION*

Leland A. Carlson, Robert R. Ratcliff, and Thomas A. Gally
Texas A&M University
College Station, Texas

and

Richard L. Campbell
NASA Langley Research Center
Hampton, Virginia

SUMMARY

Several inverse methods have been compared and initial results indicate that differences in results are primarily due to coordinate systems and fuselage representations and not to design procedures. Further, results from a direct-inverse method that includes three-dimensional wing boundary-layer effects, wake curvature, and wake displacement are presented. These results show that boundary-layer displacements must be included in the design process for accurate results.

INTRODUCTION

Over the past several years, a variety of transonic wing design methods and computer codes (refs. 1-5) have been developed. In general, these methods solve the full potential flow equation and utilize the inverse approach in that pressure distributions are specified over all or part of the wing surface. Several include some of the effects of viscous interaction via strip boundary-layer calculations (ref. 1) or two-dimensional computations that include a correction for three-dimensional viscous effects (ref. 3). However, none of these methods includes a true three-dimensional boundary-layer calculation or the effects due to wake curvature, etc., which might have important effects on computed wing designs. In addition, they differ in the number and spacing of grid points, the design approach, the treatment of fuselage effects, and the control of trailing-edge thickness. Obviously whether or not these formulation differences significantly affect design results is of interest.

Currently, the design version of TAWFIVE (refs. 6-7), termed TAW5D (ref. 4), is being extended to include three-dimensional boundary-layer and wake viscous interaction effects and is being used to study various leading-edge relofting/trailing-edge control design procedures. As part of this study, it was believed that it would be interesting to investigate the consequences of differences in both numerical and physical formulations on the design process and resultant wing designs. Thus, this paper will present initial results of two ongoing studies. The first part will compare several inverse

*This work was supported by NASA Grant NSG 1-619.

design methods and their results, while the second portion will discuss the influence of viscous interaction on transonic wing design.

INVERSE METHOD COMPARISON STUDIES

The RAE Wing Body 'A' configuration (ref. 8) at a freestream Mach number of 0.8 and angle of attack of 2 degrees was selected as the test case for the comparison studies. The wing for this configuration has an aspect ratio of 5.5, a leading-edge sweep of 36.7 degrees, and a taper ratio of 0.375, is untwisted, and is composed of RAE 101 symmetrical airfoil sections. Three different inverse design methods were selected for the comparison, the direct-inverse curvilinear coordinate system TAW5D code (ref. 4), the stretched Cartesian grid direct-inverse ZEBRA method (ref. 2-3), and the inverse predictor-corrector FLO30DC approach (ref. 5); and their characteristics and features are listed on Table I.

In order to avoid the complexities associated with various viscous interaction schemes, it was decided to limit this comparison study to inviscid flow; and, since it was believed that one of the primary usages of design codes would be to modify only portions of wings, it was decided to design only between 30 and 70 percent span. The target pressure distribution for the design zone was obtained from an inviscid analysis by the TAW5D code (essentially TAWFIVE, ref. 7), which indicated that the flowfield at the selected conditions was slightly supercritical and that the wing lift coefficient was 0.210. In addition, the starting airfoil shapes were the correct 9% thick sections from root to 30% span, linearly thinning down to a 6% thick symmetrical section at 50% span and back to 9% at 70% span, followed by the correct sections on the outboard portions of the wing.

For the design studies, TAW5D was operated in the span lofting mode in which pressures were only specified at 30, 50, and 70% span. Under this procedure, airfoils were only inversely designed at these stations; and after each design update, in between sections were obtained by linear spanwise lofting. In all cases, the flow at these in between stations was computed in the direct-analysis mode. On the other hand, in the ZEBRA method, pressures were specified at each spanwise station from 30 thru 70%; and in the predictor-corrector, FLO30DC the pressure was specified and an airfoil section designed only at the 50% span location, with linear span lofting to 30% and 70% respectively. In all cases, leading-edge relofting options were selected in order to force the designs to have the proper trailing-edge thicknesses.

PROBLEMS

In setting up the test cases, several interesting problems were encountered. First, analysis computations of the RAE 'A' wing/body configuration by the ZEBRA and TAW5D codes yielded slightly different pressure distributions; and, in order to minimize these differences, the angle of attack used in ZEBRA was decreased to 1.8 degrees so as to match

the wing CL predicted by TAW5D. The corresponding pressure distributions are shown on figure 1; and since both methods solve the same equation, the variations must be due to differences in grid, fuselage, and boundary condition treatments. Near the root, ZEBRA predicts a greater fuselage effect in that the flow is more accelerated on the upper surface; while outboard, the leading-edge grid clustering inherent in TAW5D results in better resolution of the leading-edge region and minimum pressure peak. Near the trailing edge, where the ZEBRA coordinate system is actually finer, there are also some variations in the predicted pressures. However, between 30 and 70% span the two methods are in reasonable agreement, and meaningful design studies for this region should be possible.

The second problem was that FLO30DC could only handle for this case an infinite cylinder fuselage; and, thus, TAW5D and ZEBRA were "modified" to have as an option an infinite fuselage as well as a finite one. Figure 2 compares at the 50% span station on the RAE configuration the pressure distributions calculated by TAW5D associated with these two fuselages, and it can be seen that the effect is only a slight shift in the pressure coefficient level. This trend was true at all span stations, and overall wing and section lift coefficients were essentially identical. Nevertheless, as a result of these differences, two sets of target pressures for the design region were generated, one for the finite wing/body configuration and one for the infinite cylinder fuselage; and these were used as input into the appropriate versions of the codes.

RESULTS AND COMPARISONS

Figures 3-5 show results obtained at the design stations using the TAW5D method. In this case, each section was designed from 10% chord to the trailing edge and leading-edge relofting was utilized to force trailing-edge closure. However, the actual ordinate of the trailing edge was not specified. As can be seen, the starting profiles were a linear variation from the correct section at 30% and 70% span down to a thin symmetrical section at mid-span. While the 30 and 70% stations started with the correct shapes, they were design stations and could and did change during the computation. However, as shown on the figures, all three sections converged to the target shapes; and results for the finite fuselage and infinite fuselage cases were indistinguishable.

Results were also obtained with the ZEBRA code for both the infinite and finite body cases and by the FLO30DC code for the infinite cylinder fuselage using the appropriate pressure inputs. Figures 6-8 compare the designed sectional shapes obtained by the three codes for the infinite fuselage. It should be noted that the ZEBRA results were well converged having maximum ordinate changes of less than 1E-6 of chord when computations were terminated. Also, it can be seen that the FLO30DC and TAW5D results (denoted as CAMPBELL and TAWFIVE on the figures) are virtually identical, even though the methods used entirely different design procedures.

At the 30% span station, the lower surface profile predicted by ZEBRA is in agreement with the other methods, but on the upper surface it is considerably different. Examination of the pressure profiles on figure 1 indicate that at 30% TAW5D and ZEBRA analysis results agree on the lower surface but disagree on the upper. Consequently, when the TAW5D pressures are used as design input to ZEBRA, it is not surprising that a slightly different airfoil section resulted. At 50%, figure 7, where analysis results are in better agreement, particularly on the upper surface, the three methods predict virtually identical upper surfaces although the ZEBRA lower surface profile is slightly thicker; and at 70% span the ZEBRA prediction is again slightly thicker. (Similar differences between TAW5D and ZEBRA were obtained for the finite fuselage case.) Since TAW5D and ZEBRA use similar design procedures and TAW5D and FLO30DC have similar grids and body representations, it can be concluded that the differences in profile shapes portrayed in figures 6-8 are primarily due to coordinate system and fuselage representations.

In order to see infinite versus finite fuselage effects, the infinite cylinder fuselage wing pressures were used as input into both the infinite cylinder and wing/body versions of TAW5D; and a typical result is shown on figure 9. Here the infinite cylinder result is the "correct" profile; and as can be seen, the finite fuselage result is thinner and significantly different near the trailing edge. In fact, at the 30 and 70% stations, the upper and lower surfaces criss-crossed before coming together to satisfy trailing-edge closure. It is believed that this result demonstrates an important effect often encountered in inverse design, i.e., when a pressure distribution that is somehow incompatible with either physical reality or the computational model (in this case the fuselage representation) is used as input, the effect is almost always observed as either unrealistic profiles near the trailing edge or in the inability of the design process to satisfy the design input pressures near the trailing edge or both. In many cases, the "problem" can be solved by slight adjustments in the specified pressure distribution.

Now even though figures 6-8 show that the methods predicted different profiles, the significance of these differences can only be determined by an analysis of the designed wings and a comparison of the analysis results with the desired targets. Since TAW5D had previously been shown to be self consistent (ref. 4) and since the wing designed by TAW5D, fig. 3-5, had the correct airfoil sections, no analysis results for the TAW5D design are presented. However, figures 10-14 compare the target pressure distributions with analysis results by both TAW5D and ZEBRA for the wing designed by ZEBRA, which had different profile sections in the design region. First, it should be noted that in the design region, figures 11-13, the ZEBRA analysis agrees with the target pressure values for the inverse design zone, which extends from 0.1 chord to the trailing edge. This agreement indicates that the ZEBRA method did indeed satisfy the desired pressure boundary conditions. Second, due to inherent grid clustering near the leading edge, the TAW5D analysis of the ZEBRA design probably gives better resolution in the leading-edge region; and, finally, if it is assumed that the TAW5D analysis is the "most accurate" of the methods due to its fuselage and

boundary condition representations, then it is apparent from figures 10-14 that the ZEBRA design closely matches the target pressure distributions and lift coefficients. Overall, the TAW5D analysis of the ZEBRA design predicted a wing lift coefficient of 0.203 compared to the target value of 0.210; and similar results were obtained for both the finite and infinite fuselage cases. In many respects these good results are somewhat surprising considering the airfoil section differences on figures 6-8. In any event, the results shown on figures 10-14 are probably indicative of the level of agreement to be expected when using design methods differing in coordinate systems and fuselage treatment.

To conclude this section, it is believed that the results presented demonstrate the following:

(1) Inverse methods using similar coordinate systems and flow solvers will yield the same wing designs, and

(2) Inverse methods having different coordinate systems and fuselage representations but similar design procedures will yield different section profiles, but the pressure distributions and lift coefficients will be in reasonable agreement.

VISCOUS INTERACTION STUDIES

The configuration selected for these studies was the Lockheed Wing A wing-body (ref. 4 and 7) at a freestream Mach number of 0.8, an angle of attack of 2 degrees, and a mean chord Reynolds number of 24 million. The wing for this combination is composed of supercritical aft-cambered sections and has a quarter chord sweep of 25 deg., a linear twist distribution ranging from 2.28 deg. at the wing body junction to -2.04 deg. at the wing tip, an aspect ratio of eight, and a taper ratio of 0.4. Target pressure distributions were generated by an analysis using TAW5D with full boundary-layer and wake viscous interaction effects. As before, wing design was only between 30 and 70% span, target pressures were specified at 30,50 and 70%, and the span lofting technique described above was utilized. However, in order to properly include viscous interaction, after each boundary layer and wake update, displacement thicknesses were added to the airfoil ordinates at each analysis station to provide the correct displacement surface. Likewise, since at the design stations the displacement surface is the surface computed, the displacement thicknesses were subtracted to yield the ordinates of the actual airfoil at those locations. In addition, leading-edge relofting was utilized in order to obtain proper trailing-edge behavior. However, contrary to the situation for inviscid cases, convergence problems were observed when only the trailing-edge thicknesses were specified. Consequently, the actual trailing-edge ordinates desired at the design stations were specified.

STARTING PROFILE EFFECTS

Obviously, the initial airfoil section profiles should not affect the final designed sections; and, consequently, two cases were studied having significantly different starting profiles. The results for the first case

are shown on figures 15-17, and as can be seen the initial sections linearly varied from the correct aft-cambered profile at 20% span to a conventional non-aft cambered section at mid-span back to the correct aft-cambered section at 80% span. Here, the inverse design procedure started at 0.1 chord; and the initial leading edge at each design station was thinner than the target shape. As shown on the figures, the target sections and designed sections are in excellent agreement, particularly considering the extensive curve fits and interpolations involved in the design and viscous interaction procedures.

For the second test, the initial sections consisted of the correct profiles inboard from the root to 20% and outboard from 80% to the wing tip. However, as shown on figures 18-20, from 30% span through 70% span the initial sections were NACA 0012 airfoils; and linear lofting was used between 20 and 30% and 70 and 80%. In this case the inverse design procedure started at 0.04 chord, and the initial leading edge at each design station was thicker than the target section. As can be seen, the final designed sections are in excellent agreement with the target shapes, particularly in the leading-edge and cove regions.

It should be noted that in both of these cases, the section and wing lift coefficients and the section pressure distributions were essentially identical to the target values. Based upon these results, it is believed that the present viscous inverse design procedure can yield correct target profiles independent of initial airfoil section shapes.

BOUNDARY-LAYER AND WAKE EFFECTS

Studies conducted under the present program have indicated that design including full viscous interaction effects is more computationally intensive and that convergence is slower. Consequently, it was decided to compare the full viscous interaction design results with those obtained including viscous boundary-layer interaction but excluding wake effects and with those obtained assuming inviscid flow. For each case, the input pressure distributions were identical and corresponded to those predicted by a full viscous analysis of the Lockheed Wing A wing/body since those should be the closest to reality. The starting section profiles were those shown on figures 15-17, and the design region was from 30 to 70% span. As before, span relofting and leading-edge relofting were both used in all three cases.

The final section profiles resulting from these computations are shown on figures 21-23, and at all design stations the sections obtained by ignoring wake effects are very close but slightly thicker than those corresponding to the full viscous case. Further, while the inviscid case profile is very close to the others at 50% span, they are significantly different from those including viscous effects at 30 and 70% span. The results at 50% are not surprising since at that station the boundary layer is relatively thin over much of the surface and the design is strongly influenced by the viscous pressure boundary conditions at 30 and 70% span. However, the cove region is not well predicted; and, as can be seen on figure 22, the upper surface inviscid profile here is thinner than the full

viscous result, rather than thicker as would normally be expected. In this case, specification of the trailing-edge ordinate and use of relofting has forced a change in the leading-edge shape such that the final inviscid case airfoil upper surface is slightly thinner than expected.

At the 30 and 70% stations, it is believed that the shapes predicted by the inviscid computation are due to the fact that these design locations sense the viscous pressures specified at 50% but are strongly influenced by the inviscid pressures computed inboard and outboard respectively. In other words, as shown in the analysis case in reference 6, three-dimensional viscous effects also appear to be very important in the design case. Based upon these results, it appears that the effect of wake curvature and displacement on the airfoil section designs is relatively small. However, if the flowfield is assumed to be inviscid and only a portion of the wing is designed, the use of realistic pressure distributions as input to design stations may lead to unusual or even erroneous profiles, particularly at the boundaries of the design region.

ANALYSIS AND COMPARISON OF DESIGNS

As in the code comparison studies, the effect of including or excluding viscous effects can only be determined by comparing analysis results for the designed wings. Consequently, each of the wings portrayed on figures 21-23 was analyzed using TAW5D including boundary-layer interaction and wake displacement and curvature effects. Full viscous interaction effects were included because it was believed that such a representation would be the most realistic representation of the actual flow to be expected about the designed wing/body combination. The results of these analyses are shown in Table II and on figures 24-28. On these figures, the viscous pressures are very close to the target pressures; and comparison of the pressure distributions and sectional lift coefficients indicates that from a practical standpoint the differences between full viscous design and design including wing boundary layer but excluding wake effects is negligible.

However, analysis of the inviscidly designed wing indicates that in the design region, figures 25-27, the sections determined by inviscid design have lower than expected lifts and pressure distributions significantly different than the targets. (At this point, it should be noted that the "inviscid" curves on figures 24-28 are from a full viscous analysis of the inviscidly designed wing and are not the result of an inviscid analysis.) In addition, three-dimensional effects lead to lift losses and more forward shock locations on the sections inboard and outboard of the design region, even though these sections have the correct airfoil shapes. As can be seen, the effect is particularly significant on the outboard region. It should be noted that this decrease in lift due to designing inviscidly instead of including viscous effects is consistent with results previously obtained for airfoils (ref. 9).

It is believed that these initial results demonstrate the following:

(1) Section profiles for wings in transonic flow can be designed using the direct-inverse technique including the interaction effects of the three-dimensional wing boundary-layer and wake curvature and displacement. The resulting profiles are independent of the starting shapes.

(2) For the conditions considered, wake effects have very little effect on the designed airfoil shapes or on the wing pressure distributions.

(3) For the conditions considered, at least the wing boundary-layer displacement effect must be included in the design process. Otherwise, the designed wing will have less lift and different pressure distributions than desired.

CONCLUDING REMARKS

In summary, several inverse methods have been compared and initial results indicate that differences in results are primarily due to coordinate systems and fuselage representations and not to design procedures. Also, results from an inverse method that includes three dimensional wing boundary-layer effects, wake curvature, and wake displacement have been presented. These results show that boundary-layer displacements must be included in the design process for accurate results.

REFERENCES

1. Henne, P. A.: Inverse Transonic Wing Design Method. Journal of Aircraft, vol. 18, no. 2, February 1981, pp. 121-127.

2. Weed, R. A., Carlson, L. A., and Anderson, W. K.: A Direct-Inverse Three Dimensional Transonic Wing Design Method for Vector Computers. AIAA Paper No. 84-2156, August 1984.

3. Carlson, L. A. and Weed, R. A.: Direct-Inverse Transonic Wing Analysis-Design Method with Viscous Interaction. Journal of Aircraft, vol. 23, no. 9, September 1986, pp. 711-718.

4. Gally, T. A. and Carlson, L. A.: Inviscid Transonic Wing Design Using Inverse Methods in Curvilinear Coordinates. AIAA Paper No. 87-2551, August 1987.

5. Campbell, R. L. and Smith, L. A.: A Hybrid Algorithm for Transonic Airfoil and Wing Design. AIAA Paper No. 87-2552, August 1987.

6. Streett, C. L.: Viscous-Inviscid Interaction for Transonic Wing-Body Configurations Including Wake Effects. AIAA Journal, vol. 20, no. 7, July 1982, pp. 915-923.

7. Melson, N.D. and Streett, C. L.: TAWFIVE: A Users' Guide. NASA Technical Memorandum 84619, September 1983.

8. Treadgold, D. A., Jones, A. F., and Wilson, K. H.: Pressure Distribution Measured in the RAE 8'x6' Transonic Wind Tunnel on RAE Wing 'A' in Combination with an Axisymmetric Body at Mach Numbers of 0.4, 0.8, and 0.9. Experimental Data Base for Computer Program Assessment, Appendix B1, AGARD-AR-138, May 1979, pp. B4-1 -B4-25.

9. Carlson, L. A.: Inverse Transonic Airfoil Design Including Viscous Interaction. NASA CP-2001, Vol. 4, November 1976, pp. 1387-1395.

TABLE I. -- CHARACTERISTICS OF INVERSE METHODS

Method	TAW5D	ZEBRA	FLO30DC
Coordinate System	Body Fitted	Stretched Cartesian	Body Fitted
Boundary Conditions	On Surface	At Z = 0	On Surface
Fuselage	General Shape	Axisymmetric Body Approx. by Source/Sinks	Infinite Cylinder
Design Method	Direct-Inverse	Direct-Inverse	Predictor-Corrector
Grid	160x24x32	90x30x30	160x24x32
Points on Airfoil Section	105 with LE Clustering	100 almost equally spaced	105 with LE Clustering
Number of Span Stations	21	21	21

TABLE II. -- RESULTS OF ANALYSIS OF DESIGNED WINGS

	Target	Full Viscous Design	No Wake Design	Inviscid Design
cl at 50%	.514	.509	.506	.427
Wing CL	.483	.478	.477	.419

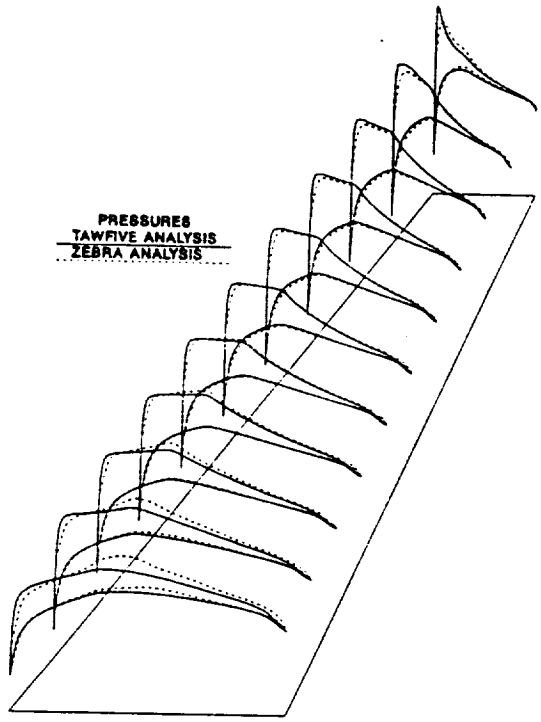

Figure 1. Comparison of analysis results for RAE wing body 'A' at Mach No. = 0.8, AOA = 2 degrees.

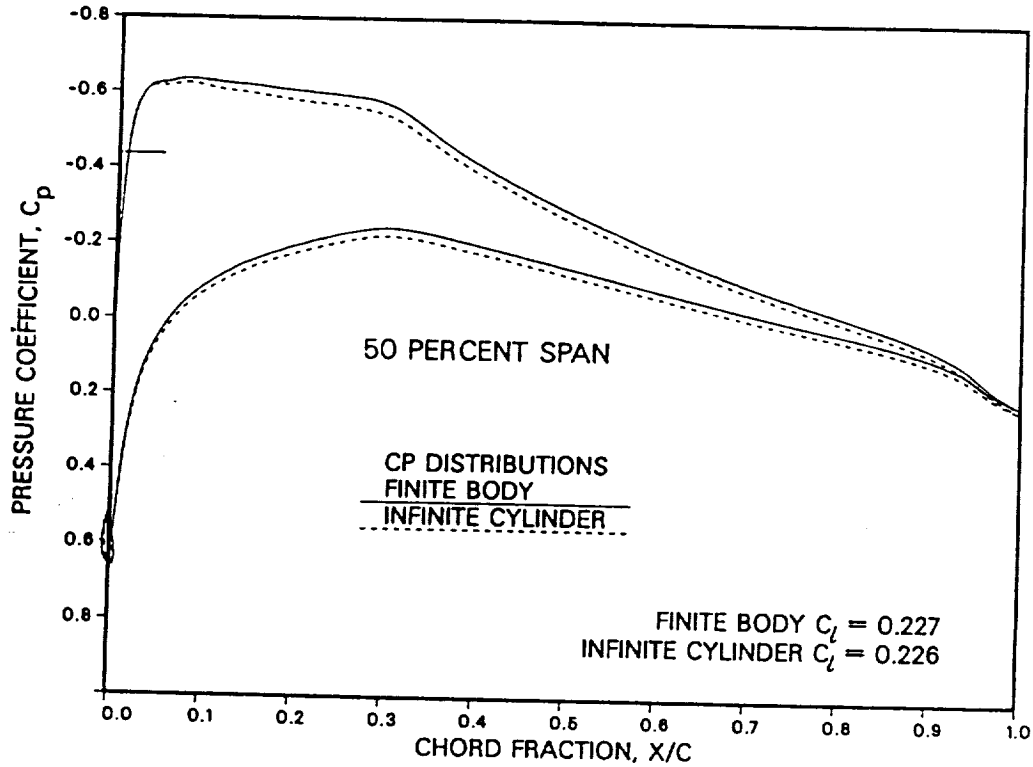

Figure 2. Comparison of finite fuselage midspan pressures with infinite cylinder fuselage results for RAE wing body 'A'.

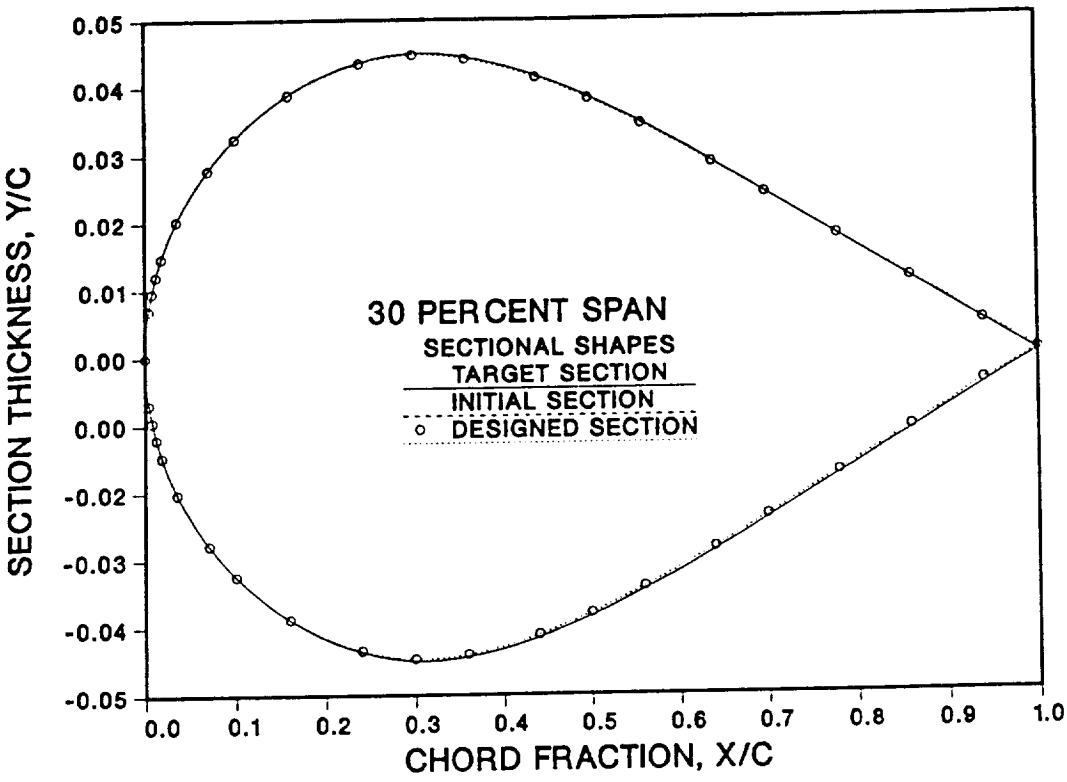

Figure 3. Comparison of section designed by TAW5D at 30 percent span for RAE wing body 'A' with initial and target sections.

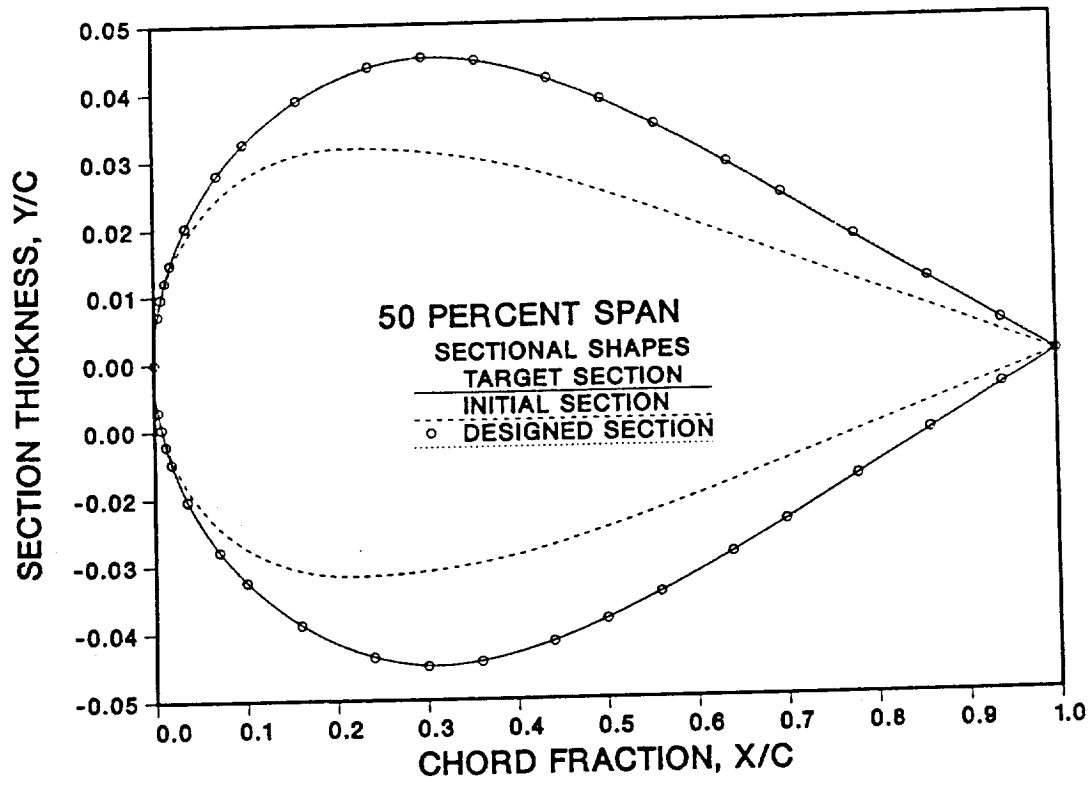

Figure 4. Comparison of section designed by TAW5D at 50 percent span for RAE wing body 'A' with initial and target sections.

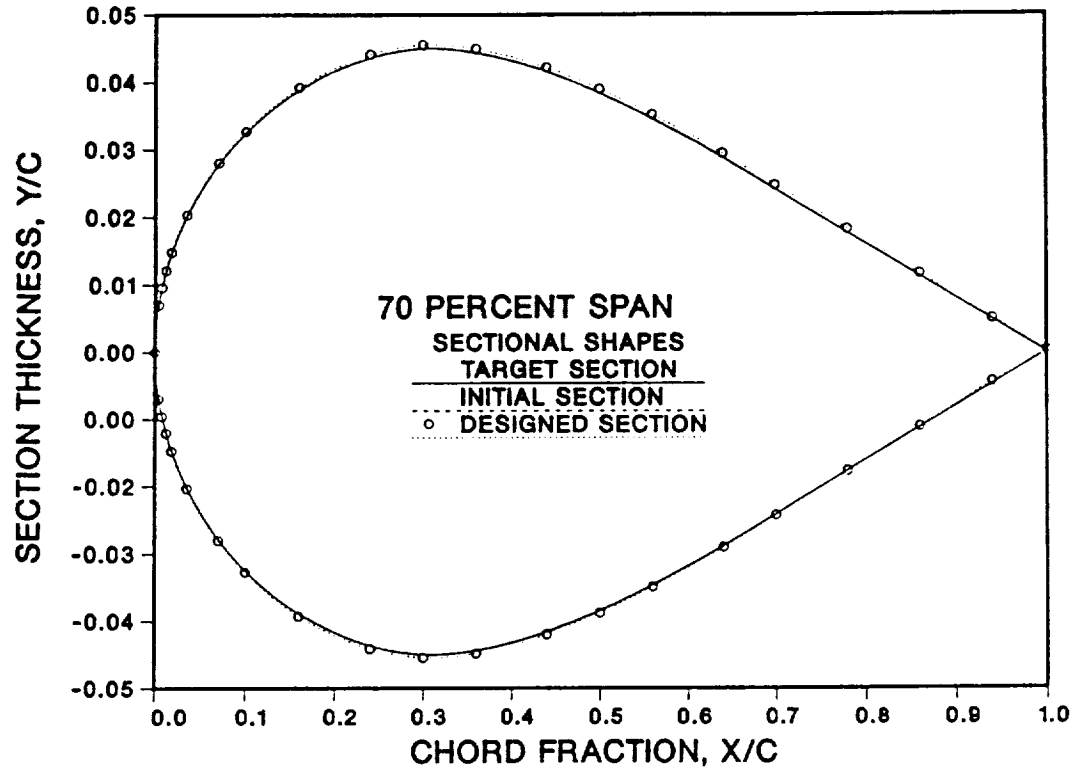

Figure 5. Comparison of section designed by TAW5D at 70 percent span for RAE wing body 'A' with initial and target sections.

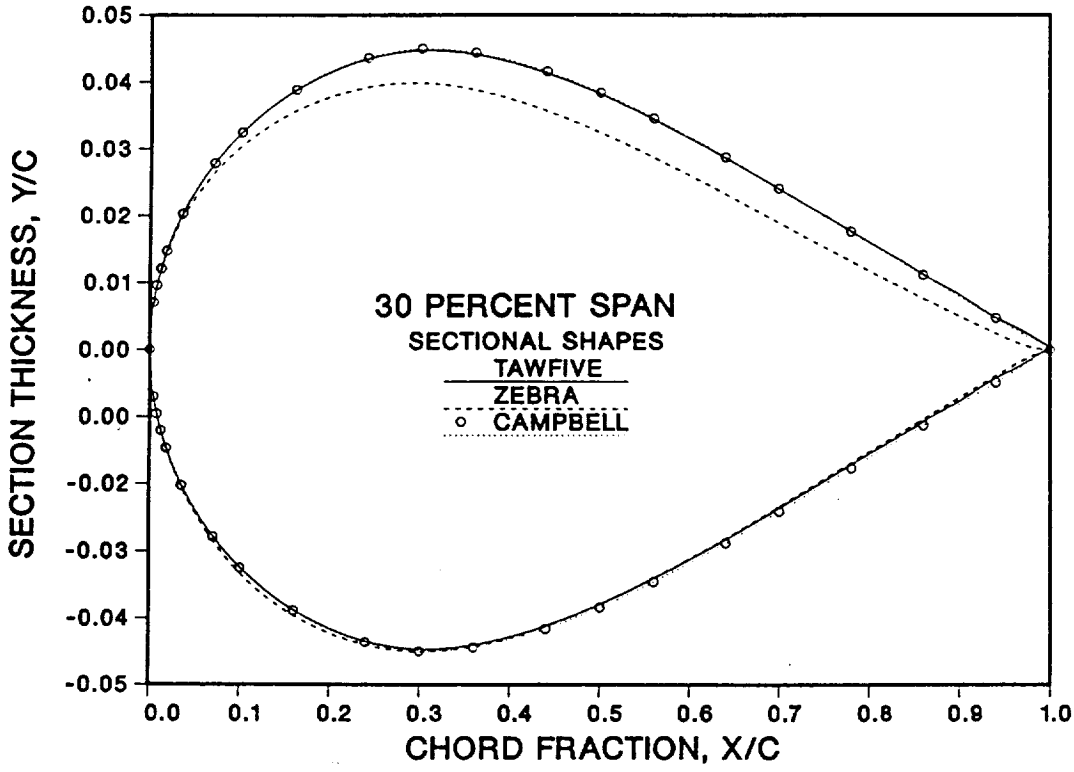

Figure 6. Comparison of sections designed by different methods at 30 percent span for RAE wing 'A' with infinite fuselage.

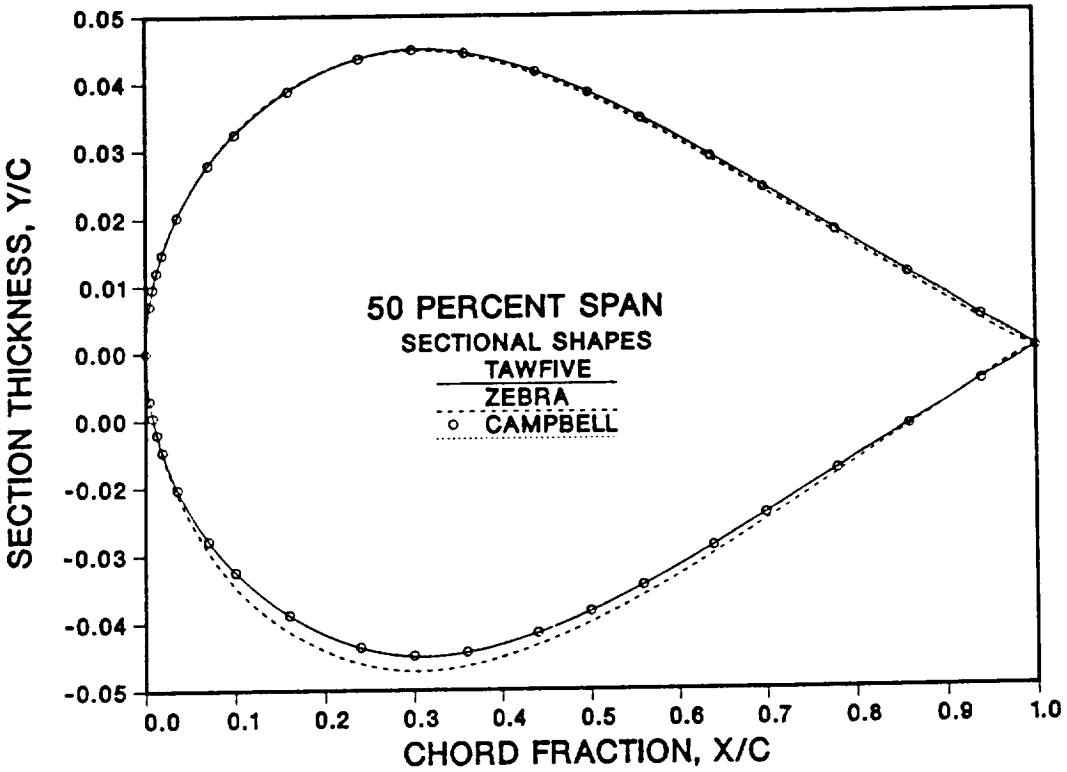

Figure 7. Comparison of sections designed by different methods at 50 percent span for RAE wing 'A' with infinite fuselage.

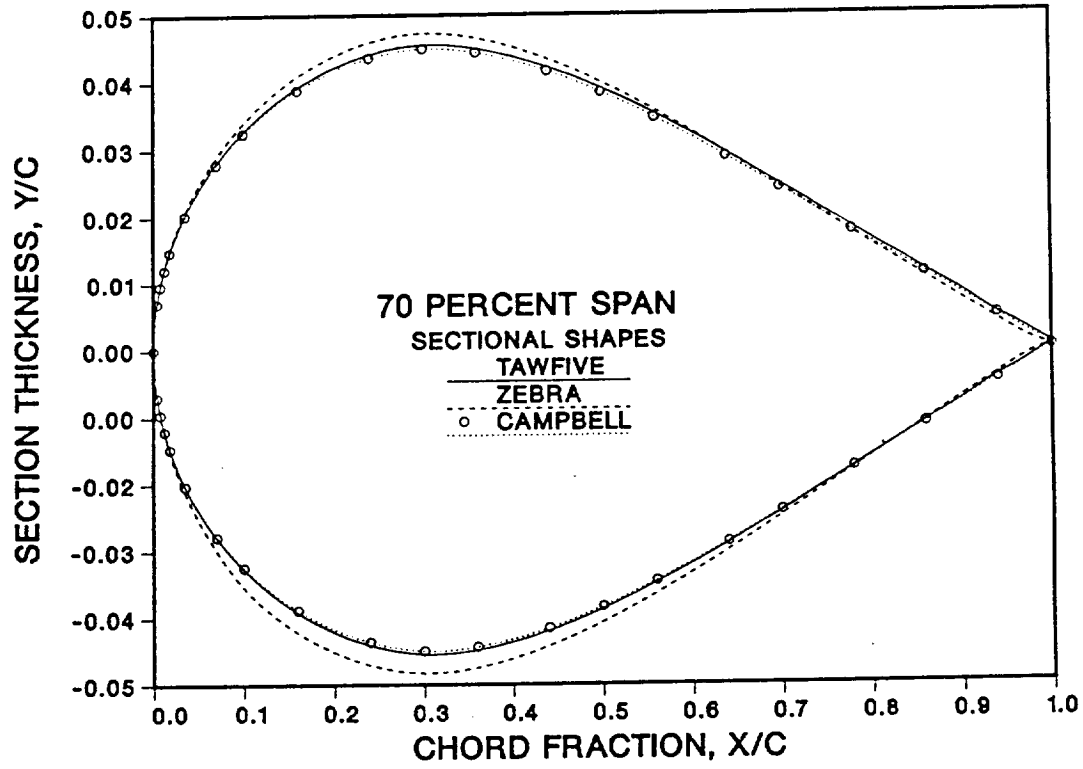

Figure 8. Comparison of sections designed by different methods at 70 percent span for RAE wing 'A' with infinite fuselage.

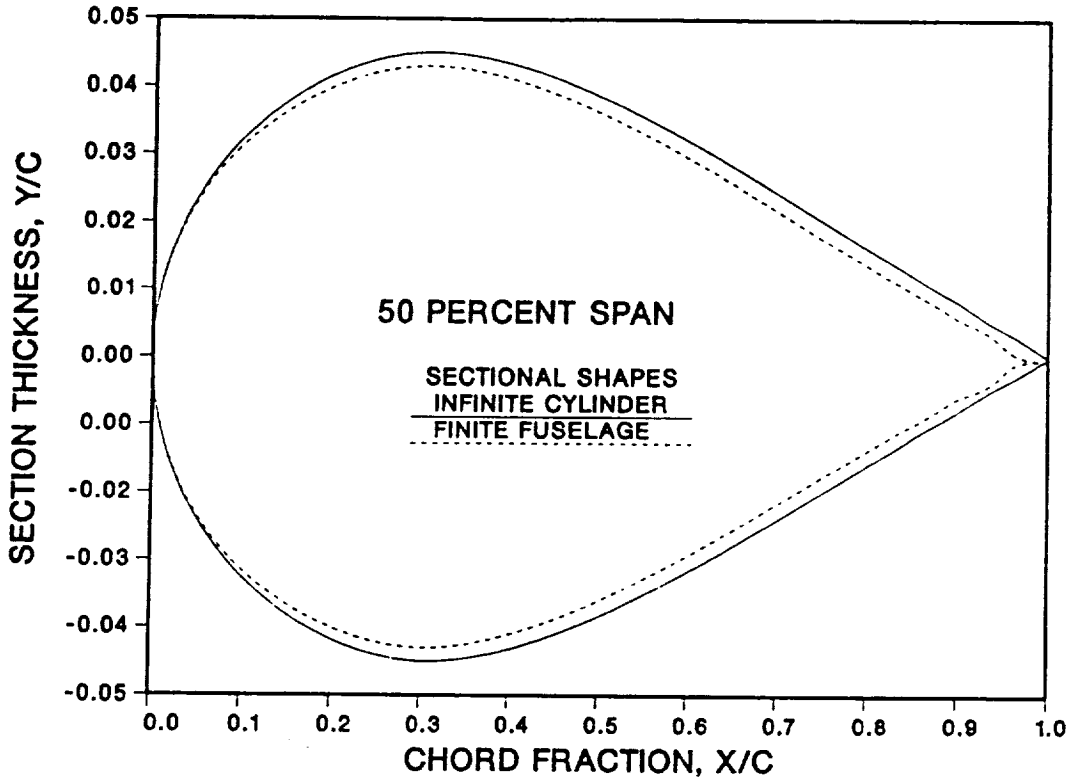

Figure 9. Comparison of sections designed by finite and infinite fuselage versions of TAW5D using infinite fuselage wing pressures as input in both cases (RAE wing 'A').

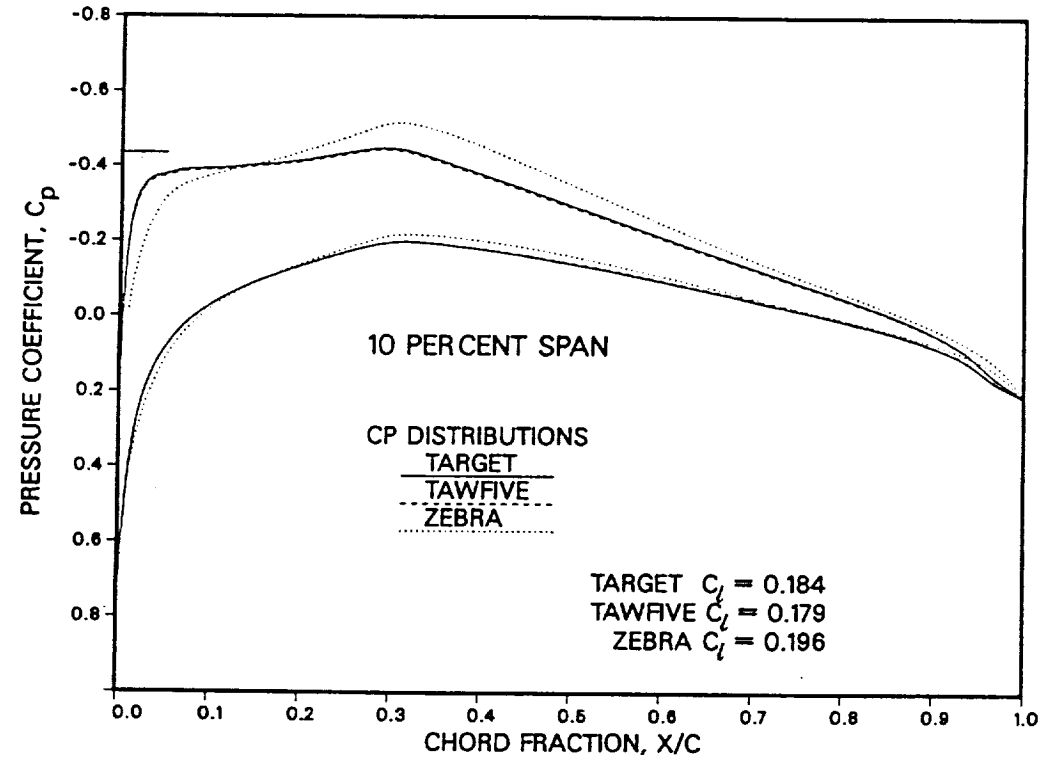

Figure 10. Comparison at 10 percent span of target values with pressures obtained by analyses of the wing designed by ZEBRA (RAE wing body 'A', Mach = 0.8, AOA = 2 degrees).

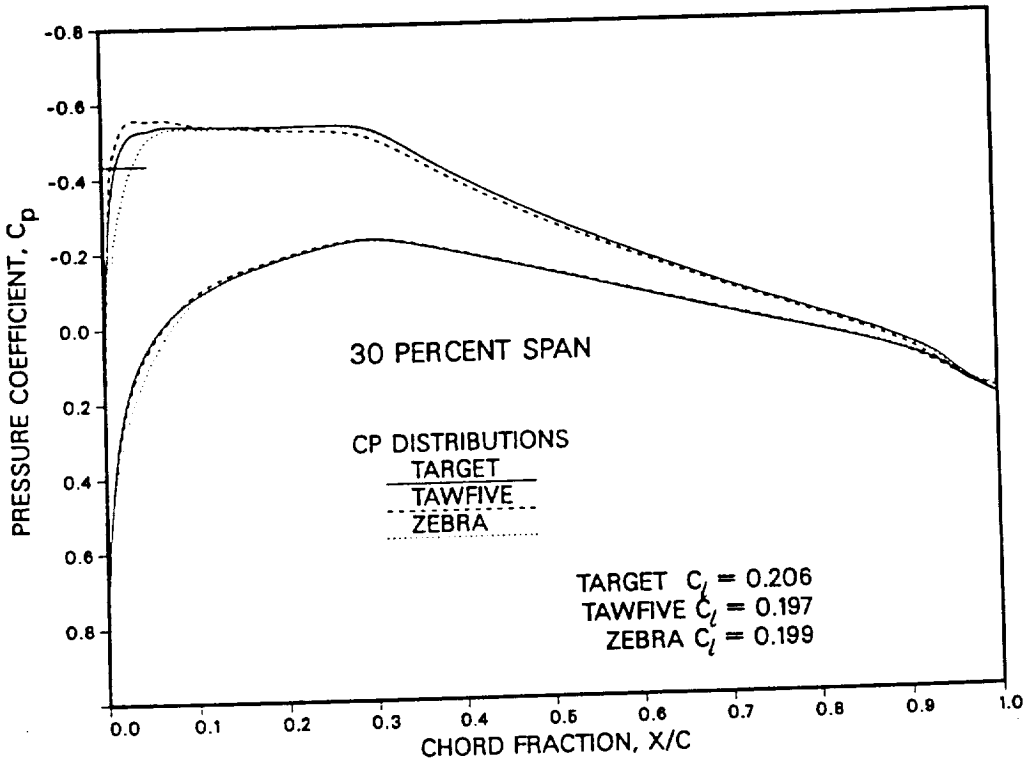

Figure 11. Comparison at 30 percent span of target values with pressures obtained by analyses of the wing designed by ZEBRA (RAE wing body 'A', Mach = 0.8, AOA = 2 degrees).

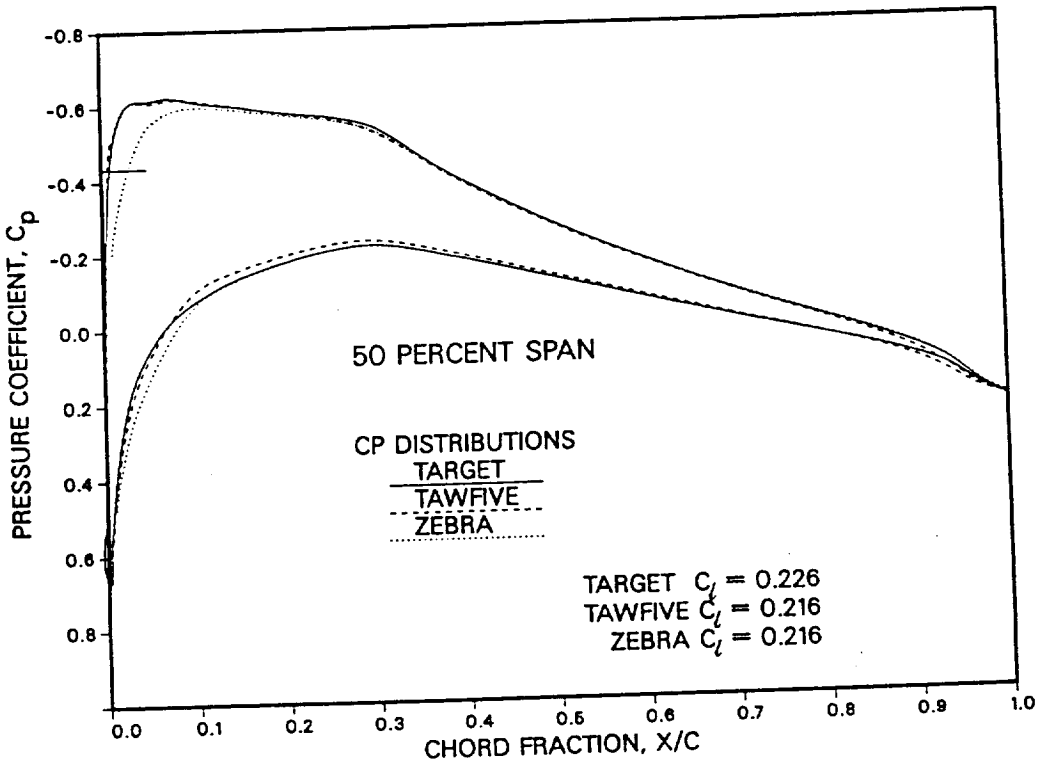

Figure 12. Comparison at 50 percent span of target values with pressures obtained by analyses of the wing designed by ZEBRA (RAE wing body 'A', Mach = 0.8, AOA = 2 degrees).

511

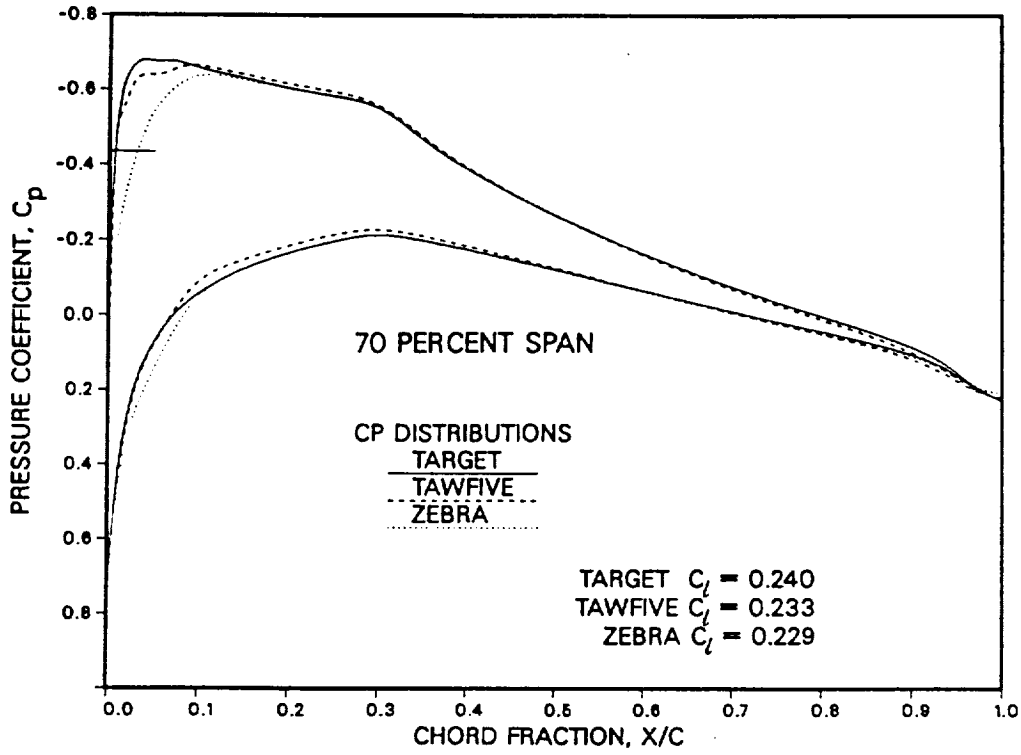

Figure 13. Comparison at 70 percent span of target values with pressures obtained by analyses of the wing designed by ZEBRA (RAE wing body 'A', Mach = 0.8, AOA = 2 degrees).

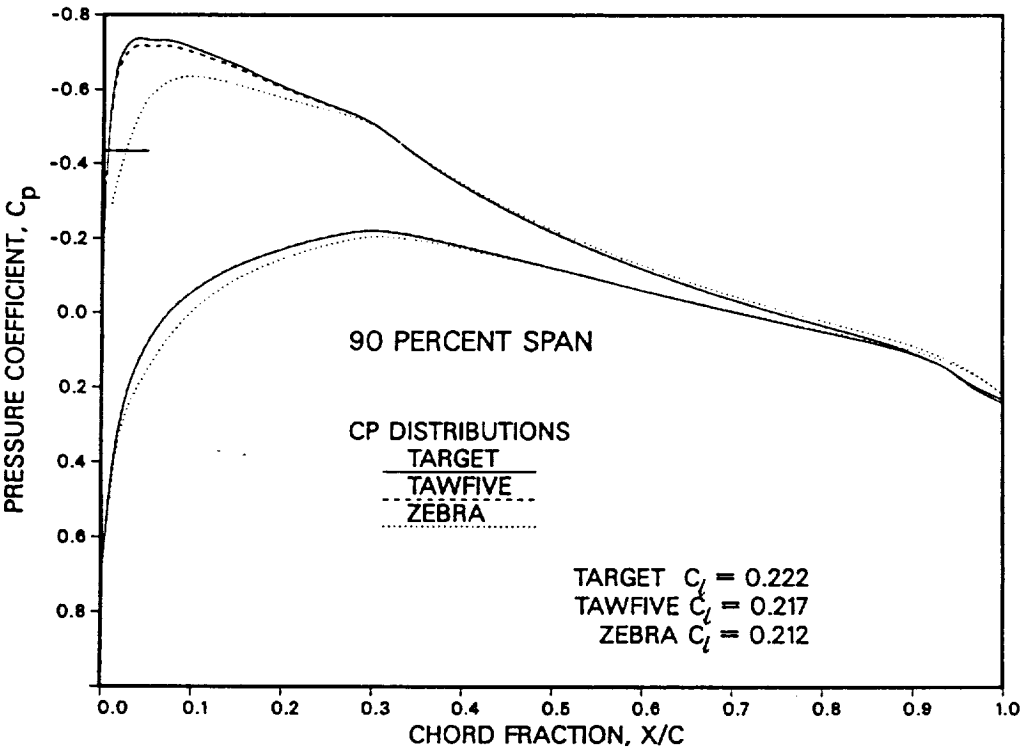

Figure 14. Comparison at 90 percent span of target values with pressures obtained by analyses of the wing designed by ZEBRA (RAE wing body 'A', Mach = 0.8, AOA = 2 degrees).

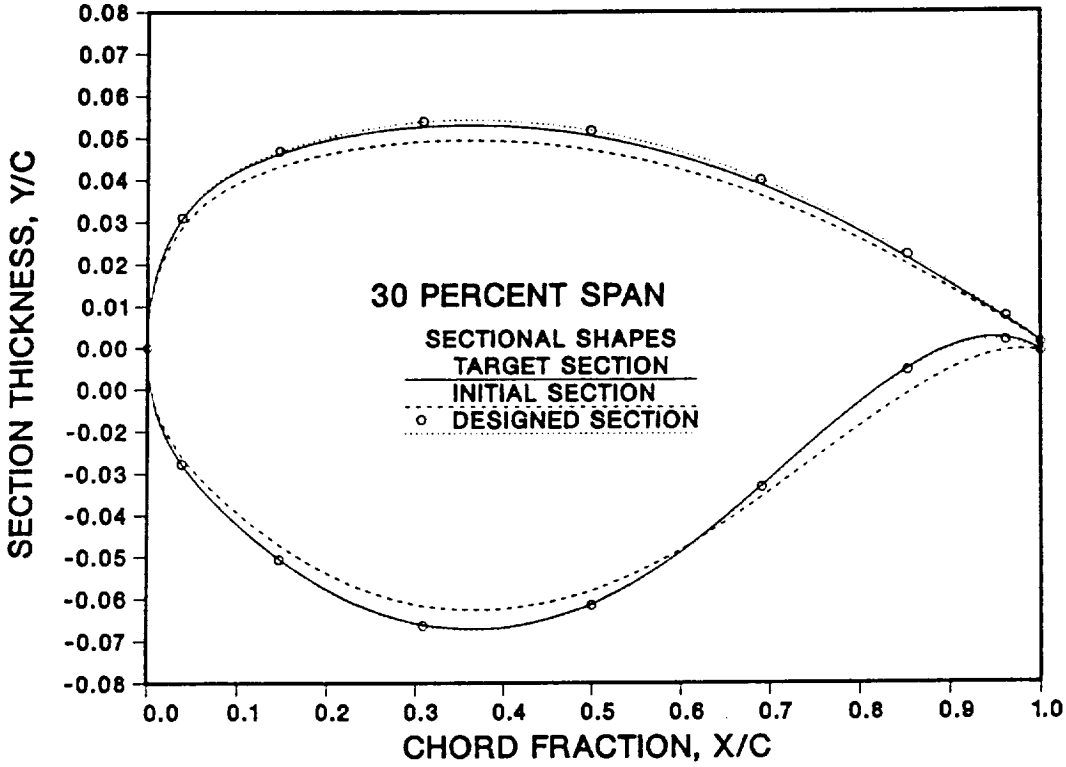

Figure 15. Comparison of section designed by TAW5D at 30 percent span for Lockheed Wing A wing body with target and first type of initial section.

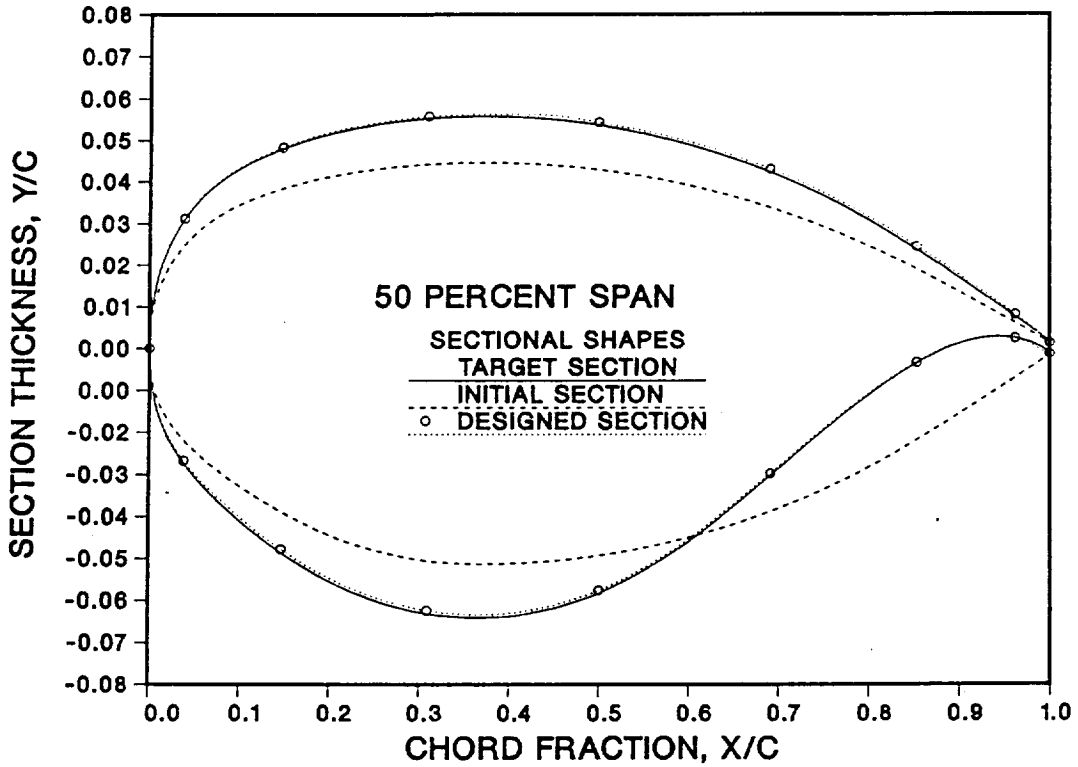

Figure 16. Comparison of section designed by TAW5D at 50 percent span for Lockheed Wing A wing body with target and first type of initial section.

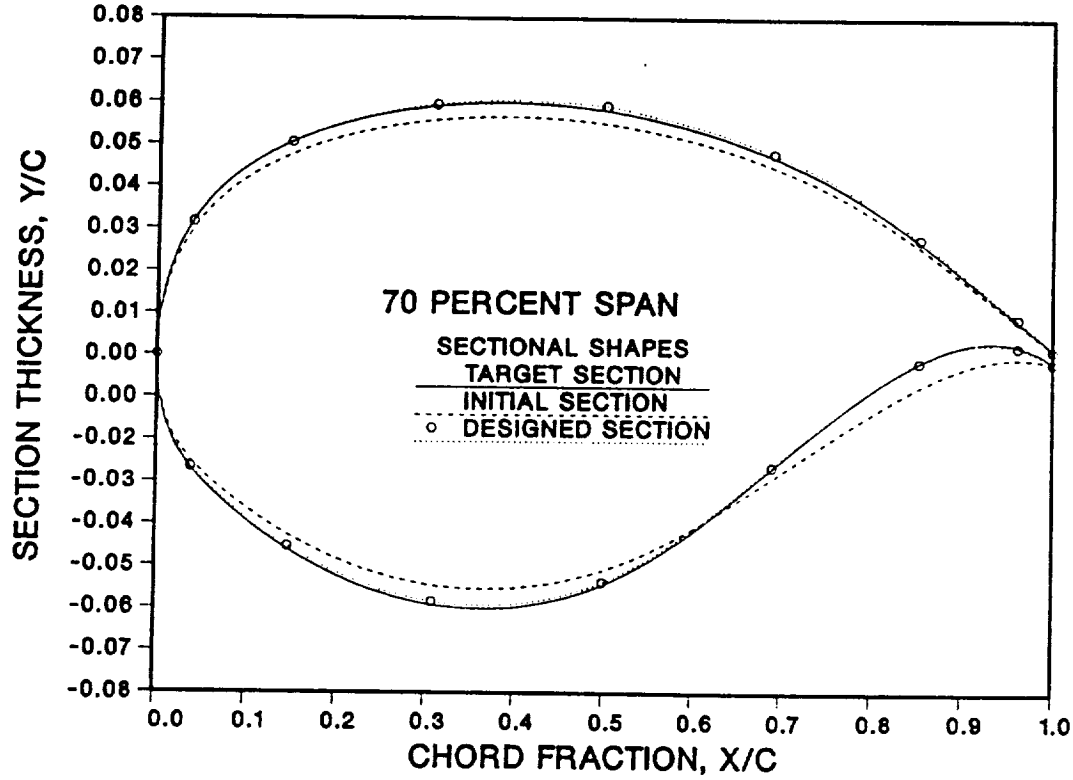

Figure 17. Comparison of section designed by TAW5D at 70 percent span for Lockheed Wing A wing body with target and first type of initial section.

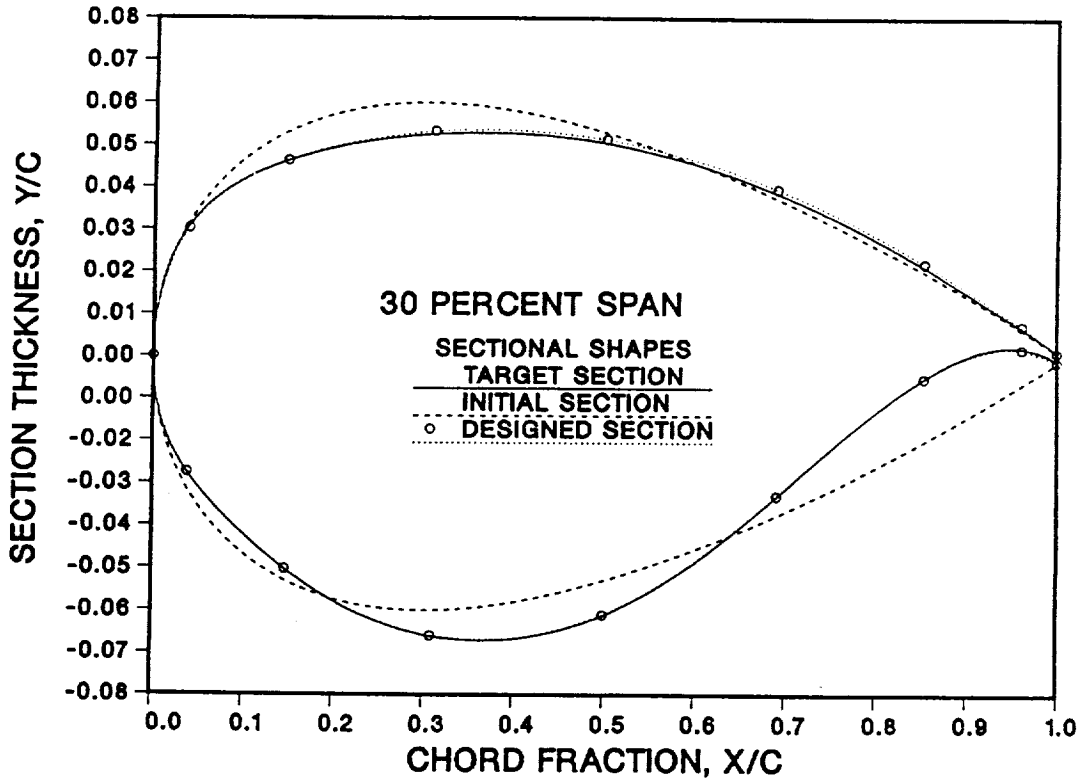

Figure 18. Comparison of section designed by TAW5D at 30 percent span for Lockheed Wing A wing body with target and second type of initial section.

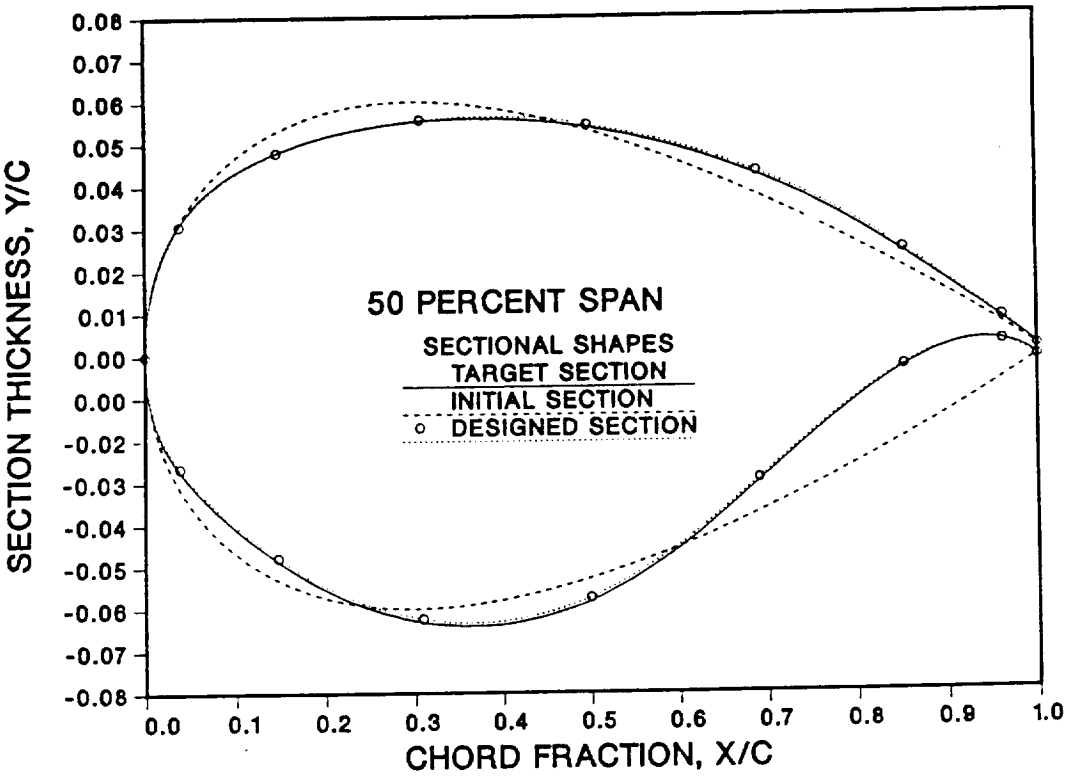

Figure 19. Comparison of section designed by TAW5D at 50 percent span for Lockheed Wing A wing body with target and second type of initial section.

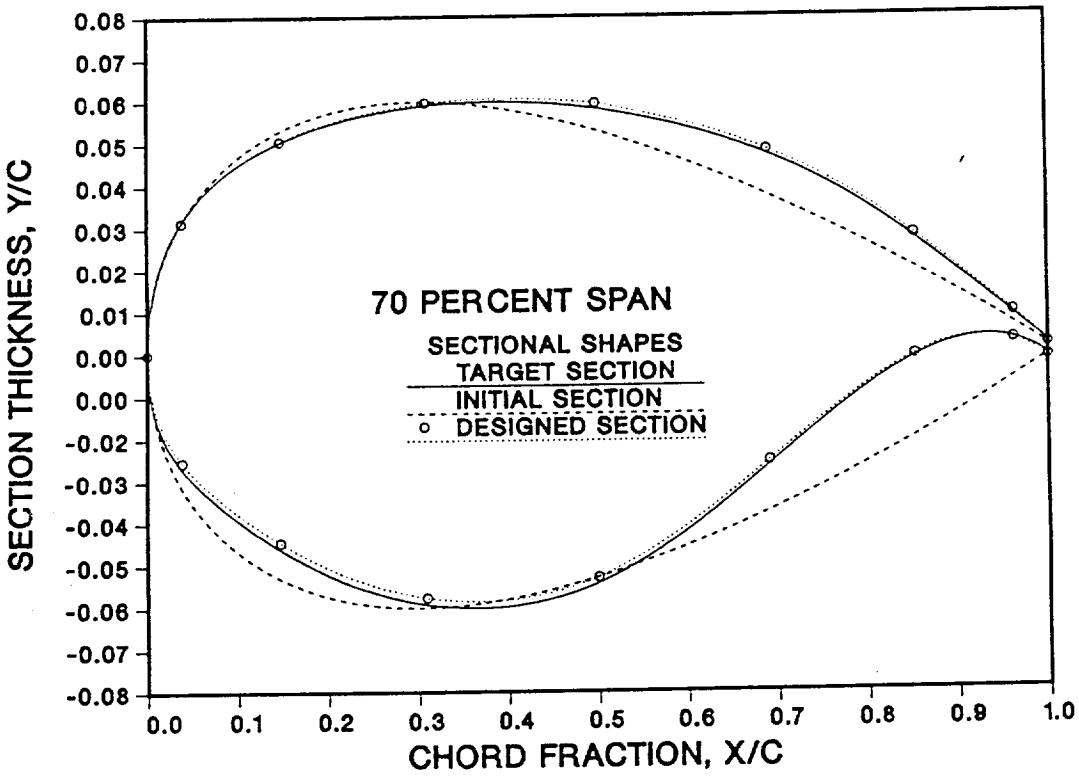

Figure 20. Comparison of section designed by TAW5D at 70 percent span for Lockheed Wing A wing body with target and second type of initial section.

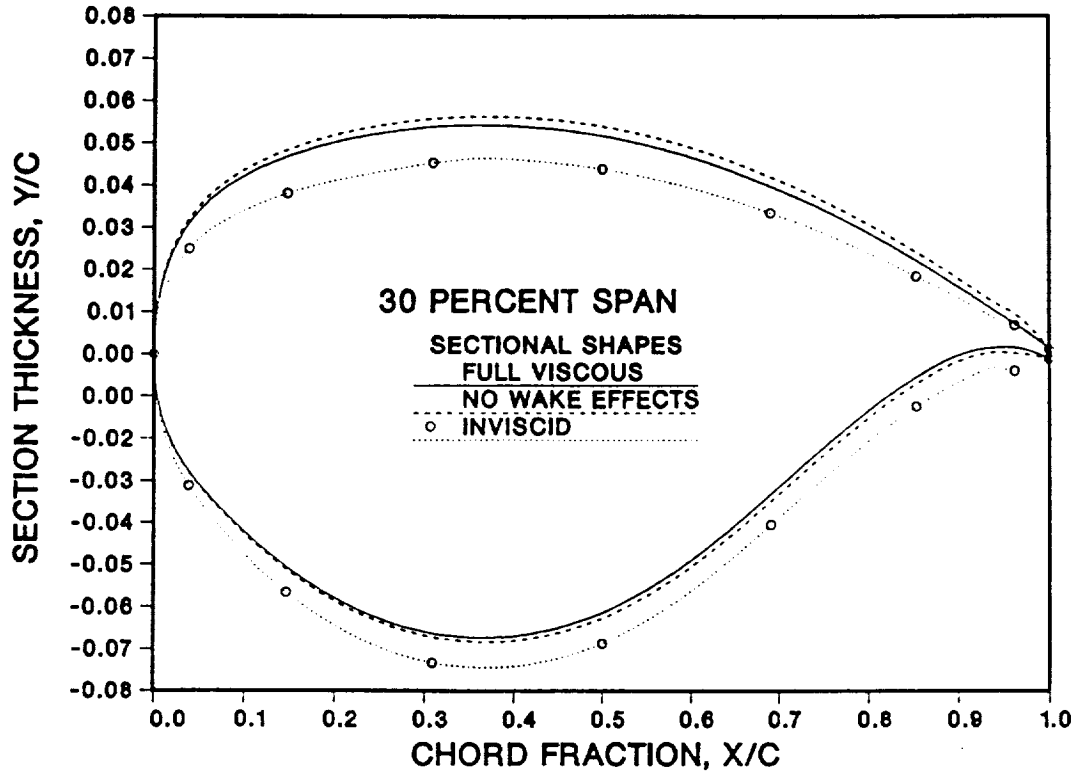

Figure 21. Comparison of sections designed at 30 percent span using different viscous interaction assumptions for Lockheed Wing 'A' wing body.

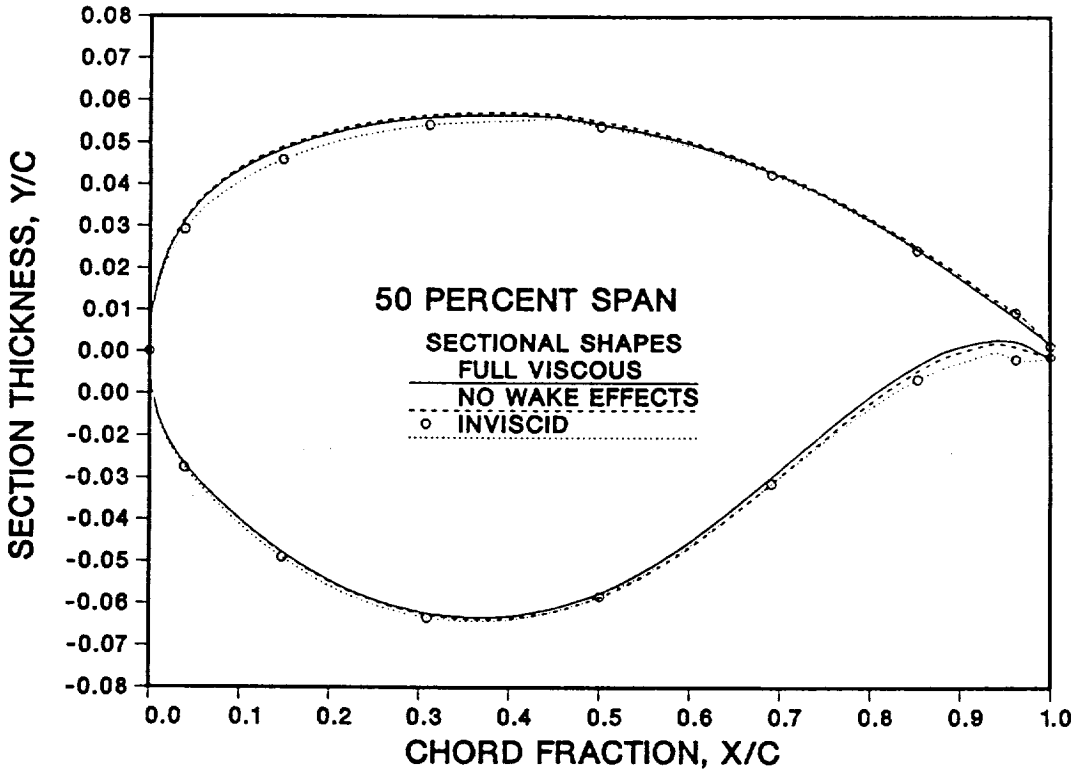

Figure 22. Comparison of sections designed at 50 percent span using different viscous interaction assumptions for Lockheed Wing 'A' wing body.

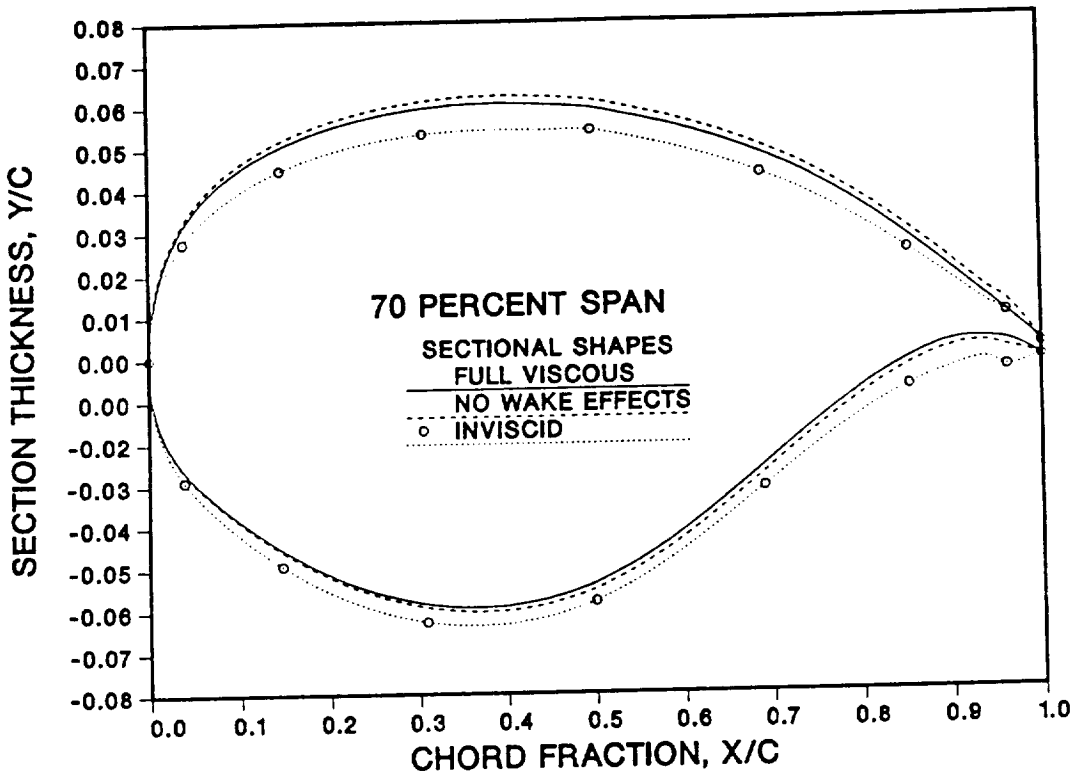

Figure 23. Comparison of sections designed at 70 percent span using different viscous interaction assumptions for Lockheed Wing 'A' wing body.

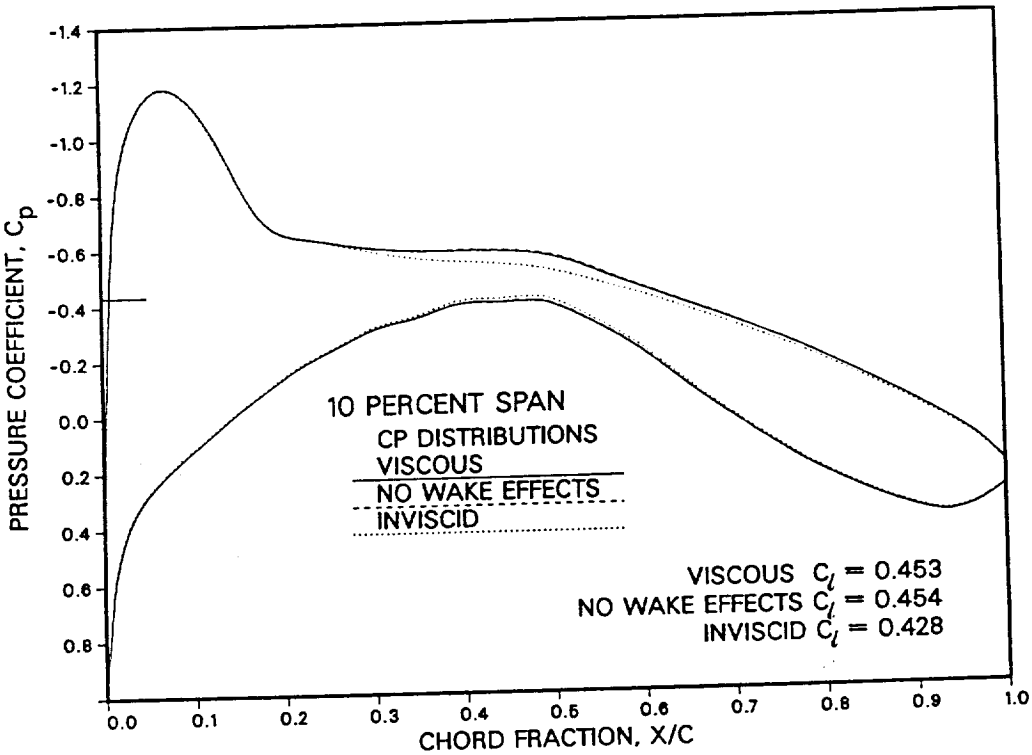

Figure 24. Comparison of pressures at 10 percent span obtained by viscous analyses of the wings designed using different viscous interaction assumptions (Lockheed Wing 'A', Mach = 0.8, AOA = 2 degrees, Reynolds No. = 24 million).

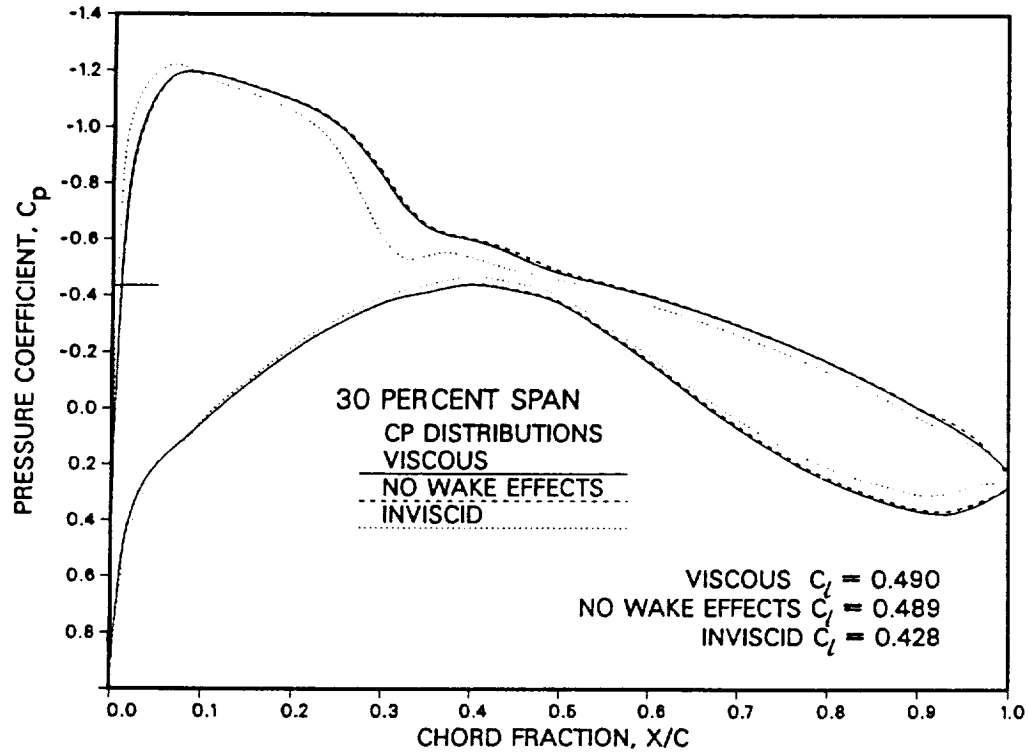

Figure 25. Comparison of pressures at 30 percent span obtained by viscous analyses of the wings designed using different viscous interaction assumptions (Lockheed Wing 'A', Mach = 0.8, AOA = 2 degrees, Reynolds No. = 24 million).

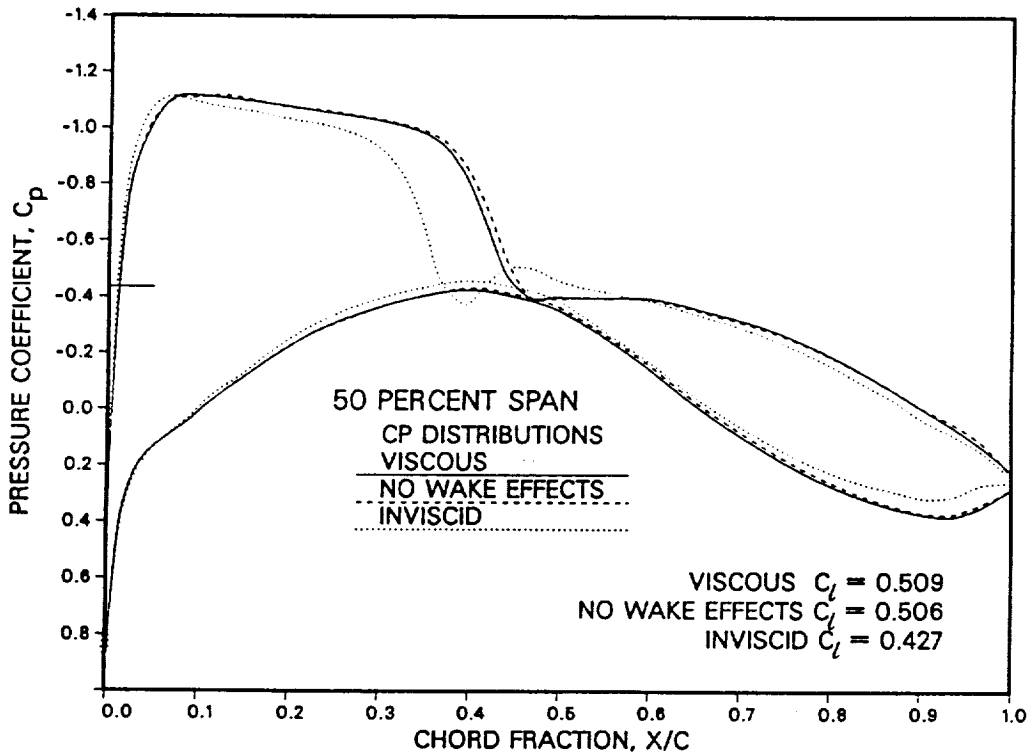

Figure 26. Comparison of pressures at 50 percent span obtained by viscous analyses of the wings designed using different viscous interaction assumptions (Lockheed Wing 'A', Mach = 0.8, AOA = 2 degrees, Reynolds No. = 24 million).

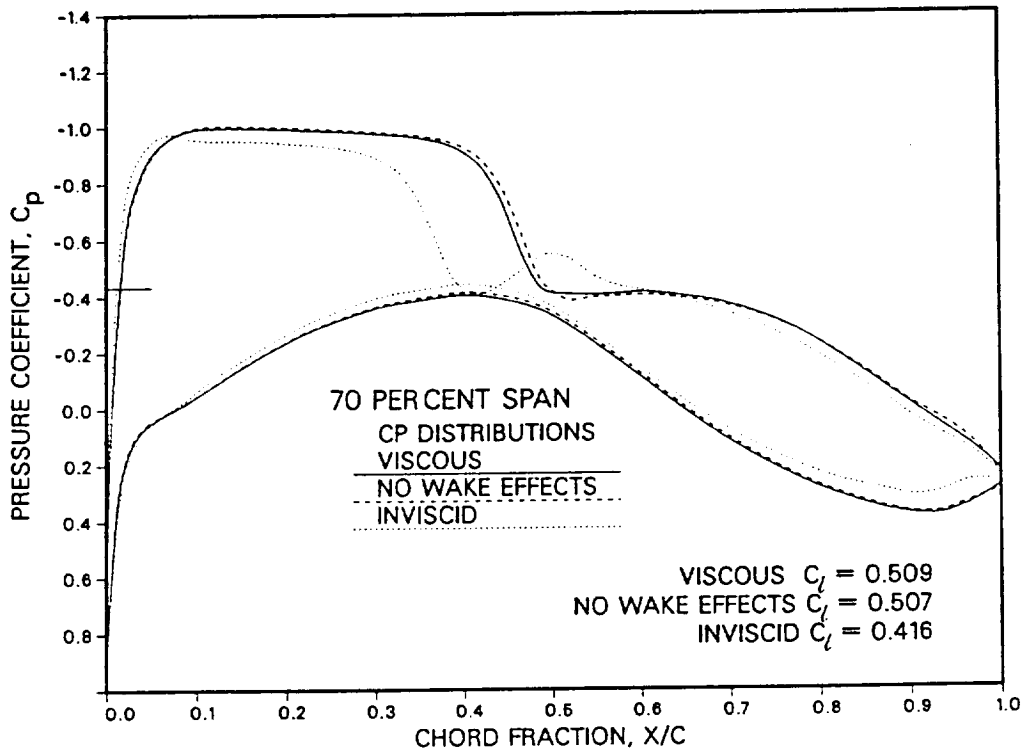

Figure 27. Comparison of pressures at 70 percent span obtained by viscous analyses of the wings designed using different viscous interaction assumptions (Lockheed Wing 'A', Mach = 0.8, AOA = 2 degrees, Reynolds No. = 24 million).

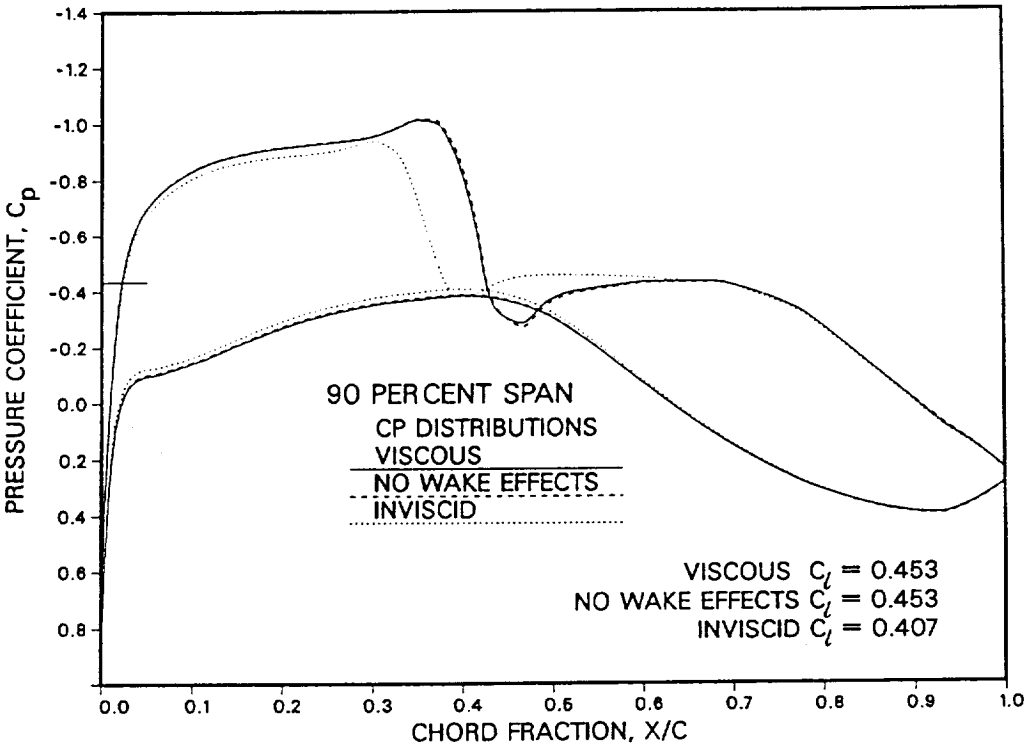

Figure 28. Comparison of pressures at 90 percent span obtained by viscous analyses of the wings designed using different viscous interaction assumptions (Lockheed Wing 'A', Mach = 0.8, AOA = 2 degrees, Reynolds No. = 24 million).

Appendix III

Masters Theses

INVERSE TRANSONIC WING DESIGN USING FINITE-VOLUME METHODS IN CURVILINEAR COORDINATES

A Thesis

by

THOMAS ANTHONY GALLY

Submitted to the Graduate College of
Texas A&M University
in partial fulfillment of the requirements for
the degree of

MASTER OF SCIENCE

May 1987

Major Subject: Aerospace Engineering

INVERSE TRANSONIC WING DESIGN USING FINITE-VOLUME METHODS IN CURVILINEAR COORDINATES

A Thesis

by

THOMAS ANTHONY GALLY

Approved as to style and content by:

Dr. Leland A. Carlson
(Chairman of Committee)

Dr. Cyrus Ostowari
(Member)

Dr. Robert H. Page
(Member)

Dr. Walter E. Haisler
(Head of Department)

May 1987

ABSTRACT

Inverse Transonic Wing Design Using Finite-Volume Methods in Curvilinear Coordinates (May 1987)

Thomas Anthony Gally, B.S., Texas A&M University

Chairman of Advisory Committee: Dr. Leland A. Carlson

An inverse wing design method has been developed around an existing transonic wing analysis code. The original analysis code, TAWFIVE, has as its core the numerical potential flow solver, FLO30, developed by Jameson and Caughey. Features of the analysis code include a finite-volume formulation; wing and fuselage fitted, curvilinear grid mesh; and a viscous boundary layer correction that also accounts for viscous wake thickness and curvature. The development of the inverse methods as an extension of previous methods existing for design in Cartesian coordinates is presented. Demonstrative results are shown for inviscid wing design in both sub-critical and super-critical flow regimes. The test cases selected also demonstrate the versatility of the design method in the designing of an entire wing or any discontinuous sections of a wing.

ACKNOWLEDGEMENTS

The author wishes to thank members of his Advisory Committee for their participation and assistance. Particular thanks go to Dr. Leland Carlson for his much appreciated support and guidance thoughout this project. Funding of this project has been provided by NASA Langley Reseach Center under NASA GRANT NAG-1-619 with Richard L. Campbell as technical monitor.

TABLE OF CONTENTS

LIST OF FIGURES

LIST OF FIGURES (CONTINUED)

NOMENCLATURE

C_p	-	Coefficient of pressure
h	-	Jacobian of coordinate transformation
H	-	Jacobian matrix
J	-	Transpose of inverse Jacobian matrix
M_∞	-	Freestream Mach number
q_∞	-	Magnitude of freestream velocity
Q	-	Magnitude of local velocity
u,v,w	-	Components of physical velocity vector
U,V,W	-	Components of contravariant velocity vector
α	-	Angle of attack
γ	-	Ratio of specific heats
δ	-	Differential operator
$\delta(x)$	-	Displacement thickness
$\delta_r(x)$	-	Displacement thickness due to relofting
Δ	-	Trailing edge thickness
Δ_t	-	User specified trailing edge thickness
μ	-	Averaging operator
ρ	-	Density
ϕ	-	Reduced/perturbation potential function ($\Phi = \phi + x\cos(\alpha) + y\sin(\alpha)$)
Φ	-	Potential function

INTRODUCTION

In recent years the importance of transonic flight to both military and commercial aircraft and the development of specialized transonic wings for several flight research experiments have prompted significant efforts to develop accurate and reliable computational methods for the analysis and design of transonic wings. Many methods of solution have been developed, but those which have shown the most promise due to their computational efficiency and engineering accuracy have been based upon the full potential flow equations in either their conservative or non-conservative form[1-3]. When these potential flow codes have been coupled with accurate viscous boundary layer routines, they have had great success in predicting such complex flow phenomena as wing-body interactions, three-dimensional shock wave formations, and weak viscous interactions.

The TAWFIVE[4] FORTRAN code in particular has proven to be an excellent and reliable analysis tool. This analysis code is based upon the FLO30 finite volume potential flow method that was developed by Jameson and Caughey[3]. Among the features of FLO30 are its fully conservative formulation and its three-dimensional curvilinear grid. The latter can be fit around any general combination of fuselage shape and wing planform. In addition, TAWFIVE gives the user the option of including the viscous effects associated with both a wing surface boundary layer and a

---

Format in accordance with AIAA Journal

viscous wake having both finite thickness and curvature.

The purpose of the research outlined in this thesis has been to develop an inverse wing design method that is based on the existing TAW-FIVE analysis code and is compatible with the existing computational methods and program structure of that code. The particular inverse method used extends previously developed design methods[5-6] developed for orthogonal grids to the more generalized curvilinear grid system of TAW-FIVE, while also providing for greater design flexibility and versatility for engineering applications. These last goals were achieved by the inclusion of user options for designing either the entire wing or only discontinuous wing segments as shown in Figure 1. The availability of this option is useful to engineers who are typically faced with designing around regions where the wing geometry may be fixed by constraints other than aerodynamic considerations.

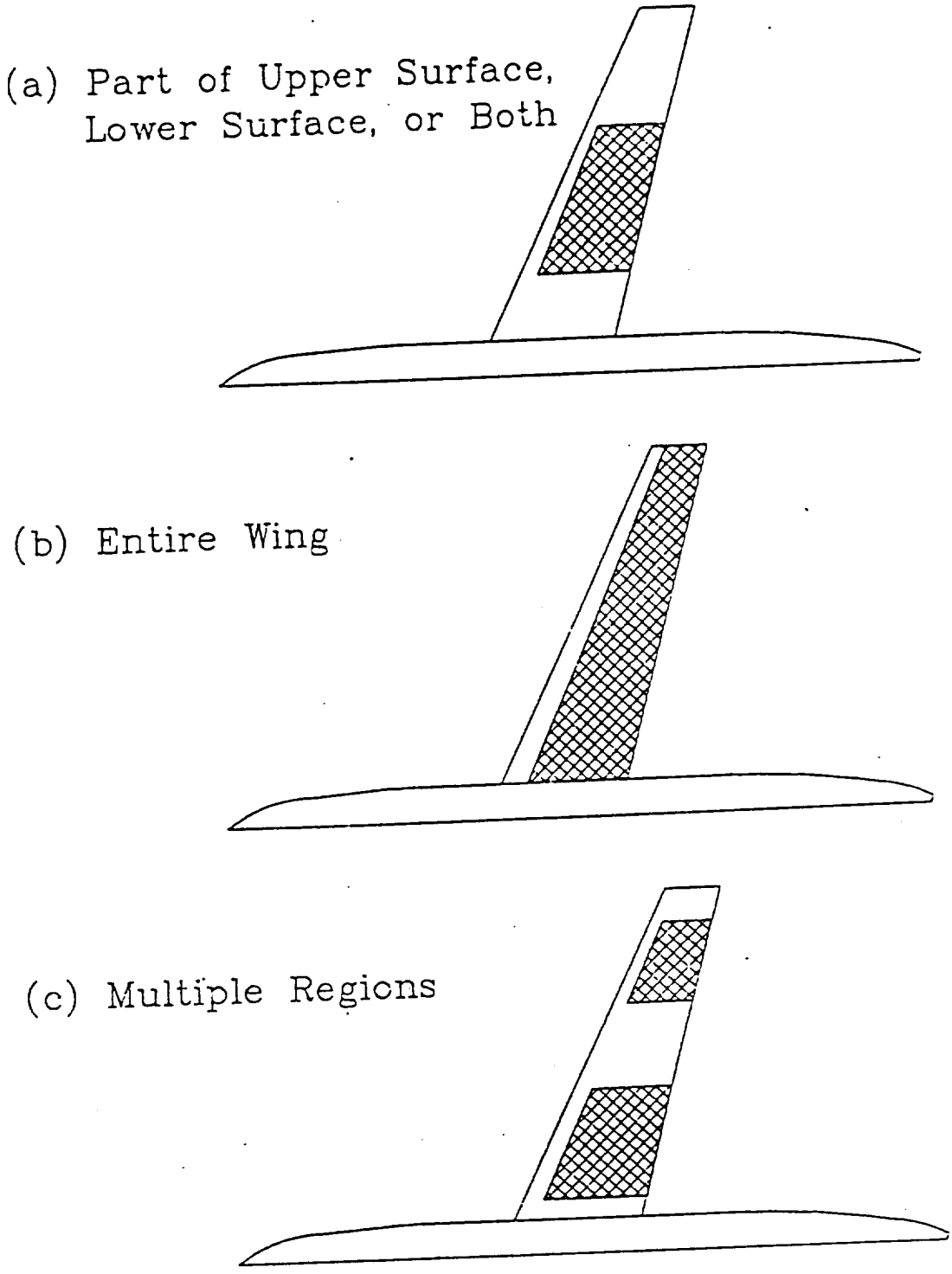

Figure 1. Possible Wing Design Situations

BACKGROUND

There are a number of approaches to the solution of viscous transonic flows over wing-body combinations. The most exact method, if a suitable numerical algorithm is available, would be to solve the complete set of continuity, momentum, and energy equations with viscous effects either included in the governing equations or with a separate boundary layer solver; i.e. the Navier-Stokes or Euler equations with boundary layer. At present, however, solution methods of this type are still under development and are far too demanding of computational speed and memory requirements to be used for practical engineering applications. However, with the great advances being made in both numerical methods and computer capacity, solutions of this type may become common in the future.

As previously mentioned, the solution methods which are primarily used today combine the compressible potential flow equations with a viscous boundary layer solver. The compressible potential flow equations are:

$$(\rho\Phi_x)_x + (\rho\Phi_y)_y + (\rho\Phi_z)_z = 0$$

$$\rho = \left[1 + \frac{\gamma-1}{2} M_\infty^2(1 - \Phi_x^2 - \Phi_y^2 - \Phi_z^2)\right]^{\frac{1}{\gamma-1}} \qquad (1)$$

The derivation of these equations from the continuity and inviscid momentum and energy equations can be found in almost any textbook dealing with compressible subsonic or transonic flow. The use of the inviscid forms of the governing equations as the basis for the potential

equations is necessary due to the fact that the potential function is not defined for fluid flow in the presence of vorticity, the natural by-product of viscous effects. While the potential equations are suitable for most flow regions where viscous effects are negligible, there are two situations where viscous effects cannot be ignored. The first is the boundary layer over a wing, and the second is across shock waves.

The wing viscous interaction problem is usually solved by separating the flow field into two regions: the inviscid region away from the body where the potential flow equations apply and the viscous region on the wing surface where a separate set of boundary layer equations can be solved. The boundary for the potential solution region is usually offset from the physical surface by a distance called the boundary layer displacement thickness. This thickness is calculated within the boundary layer routines based upon the momentum loss and mass flow decrease of the flow within the viscous layer. Since the potential flow and boundary layer equations are usually solved separately but are dependent upon each other, it is necessary to iterate between the two methods in order to obtain a final converged solution.

The second viscous region of concern, shock waves, is accounted for by the approximate numerical solution methods used in transonic potential flows. An examination of the nonlinear partial differential potential flow equations reveals that the nature of the equations changes from elliptic to hyperbolic as the flow accelerates from subsonic to supersonic speeds. In numerically solving these equations of mixed nature, it is necessary to use a numerical approximation which exhibits the proper upstream dependence in the supersonic flow regions. In the

original paper by Murman and Cole[7] suggesting this flow dependent method for solving transonic flows, the authors noted that their numerical solution technique for supersonic flow regions introduced a numerical error term to the inviscid equations which had the effect of an artificial viscosity. The result was the appearance of numerical shock waves in their solutions which were very similar in nature and location to what would be expected of physical shock waves. While this result is somewhat serendipitous, it is of great consequence and has become the foundation of transonic potential methods. Methods newer than those of Murman and Cole do not make use of the same numerical approach but always try to introduce a supersonic artificial viscosity of roughly the same character.

In the area of numerical airfoil/wing design using transonic potential flow solutions, recent efforts can be categorized as being either optimization or inverse methods. The optimization problem can be expressed mathematically as finding the local extrema (maxima or minima) of a function of many variables subject to a given set of constraints. A practical example would be to find the set of airfoil ordinates which would produce the minimum transonic wave drag but which is not undesirable thin.

For a function described by a set of analytic expressions, this optimization problem is straight forward and has distinct solutions. When applied to airfoil/wing design, the problem is complicated by the nonlinear, often discontinuous, and unknown form of the dependent function and also by the numerical accuracy and nature of the flow field solver to which the optimization routine is coupled. With a proper

selection of independent variables and constraints, however, the problem becomes manageable and good results can be obtained.

An excellent example of the optimization approach is the work of Cosentino and Holst[8]. They chose to use a finite number of wing surface ordinates as their independent functions and exercised their program by minimizing the ratio of drag to lift for various wing planforms and flight conditions. However, most airfoils require a large number of surface ordinates, on the order of 30 or more, to smoothly define the airfoil surface. For a typical wing which may be defined by 10 or more spanwise airfoil sections, this approach could possibly involve 300 independent variables. As mentioned earlier, the relationship between a change in a surface ordinate and the resulting change in the property being minimized is not known a priori but must be calculated from the flow solution itself. The relationship can be determined by displacing each of the surface ordinates individually and evaluating the response of the dependent function. If all the relationships were linear in nature, a minimum of N iterations would be necessary to minimize a function of N variables; and more than 300 converged flow field solutions would have to be obtained in order to minimize the proscribed optimization function. Obviously, such a procedure would require an unacceptable amount of computational time. In practice, however, the optimization routine attempts to drive the solution to the minimum before the system has been completely defined; and it is quite probable that the minimum can be reached before N iterations. Nevertheless, a large number of iterations can still be expected for unconstrained problems.

To reduce the size of the task, Cosentino and Holst only varied a

few surface ordinates over a restricted region of the upper surface and depended upon spline fits through these points to provide a smooth surface. Of course, by minimizing the number of surface ordinates, the problem is constrained to only having solutions within the family of spline curves which can be fit through the points.

Another recent work by Davis[9] reduces the airfoil surface to a series of parametric curves that have predetermined functional relationships to certain flow phenomena. It only remains for the optimization routine to determine the functional relationship between the specific flow phenomena and the desired optimization function. For example, if a family of curves for a section of say the upper surface has been found to have a particular effect on the location of shock waves, then if a location for a shock wave can be found which maximizes the lift to drag ratio for the airfoil, the surface which corresponds to this shock location is proscribed by the function relating the two. In essence this approach is another means of constraining the problem to manageable levels as was done by Cosentino and Holst, but it is accomplished in a more elaborate manner and requires and makes use of known surface to flow relationships.

The other set of design techniques are called inverse methods. Their distinguishing feature is that they require the specification of desired velocity or pressure distributions over an airfoil or wing and calculate the corresponding surface shapes. The usefulness of inverse methods lies in the fact that experienced airfoil designers will usually have an idea of what velocity/pressure distributions will produce desirable design properties. An example of such design would be modifying

the pressure distribution on an existing wing section so that an undesirable shock could be moved or even eliminated. Such design cases will typically occur when an airfoil has been optimized for a given flight condition but is also expected to perform adequately in off design conditions.

Within the range of inverse methods, there exist two distinct subgroups. For one group of methods, the transonic flow field solution in used as a "black box" that calculates the velocity/pressure distribution for a given geometry. The inverse procedure then generates a modified geometry based upon the difference between the calculated and desired flow profiles. The NYU code of Bauer, Garabedian, and McFadden[10] and the more recent method of Takanashi[11] are two such inverse techniques. In a sense, these types of inverse methods are related to the optimization methods with the minimized function being the difference between the actual and desired velocity/pressure profile. These inverse methods differ from the optimization techniques because, instead of allowing the functional relationship between shape profile and flow field to be determined numerically from the convergence history, the functional relationship has been determined beforehand based upon the governing flow equations.

The other method of inverse wing design, called the direct-inverse method, uses the desired pressure distribution for an airfoil or wing surface as a boundary condition which must be incorporated into the flow field solution. Thus, rather than satisfying the usual flow tangency condition on the body surface, the flow instead must satisfy the desired pressure distribution in the inverse regions. From the flow direction

on the pressure boundary or from the mass flux through it, the location of a physical surface satisfying the desired pressure profile can be calculated. Since the equations will generally only be exact when the pressure boundary and physical boundary coincide, these methods also involve some iteration on the surface geometry.

As mentioned, the primary task of this research effort has been to modify the existing finite volume transonic potential flow analysis code known as TAWFIVE for use in wing design. In selecting a design method to apply to this existing code, it was decided use the direct-inverse method as developed by Carlson[5,6,11,12]. Carlson's previous inverse design work has been with both airfoil design[5,12] and, more recently, with wing design[6,13]. The reasons for selecting this method include the relative simplicity of the method along with its record for successful use with a variety of different numerical algorithms. In addition, the previous applications of this method have been in Cartesian or sheared Cartesian coordinate systems. Thus, by adapting this method to the curvilinear coordinate system of TAWFIVE, original work and results would be obtained.

WING ANALYSIS METHODS

Potential Flow Solver

The inviscid potential analysis of TAWFIVE is performed by the program FL030 developed by Caughey and Jameson[3,14]. For a complete description of the FL030 code and its theoretical basis the reader is referred to Caughey and Jameson's papers and some earlier developmental work by Jameson[15-16]. A brief description is presented here to provide for completeness and to provide a background for the inverse design developments which will be discussed in detail.

FL030 solves the full potential equation in conservative form which when transformed from Cartesian coordinates, Eq. (1), to generalized curvilinear coordinates is:

$$(\rho hU)_\xi + (\rho hV)_\eta + (\rho hW)_\zeta = 0$$

where ρ is the local density; U, V, and W are the components of the contravariant velocity vector; h is the Jacobian of the transformation from Cartesian coordinates; and subscripts denote differentiation with respect to the curvilinear coordinates ξ, η, and ζ. The contravariant velocities are related to the physical velocities and the derivatives of the potential function by:

$$\begin{Bmatrix} U \\ V \\ W \end{Bmatrix} = H^{-1} \begin{Bmatrix} u \\ v \\ w \end{Bmatrix} = (H^T H)^{-1} \begin{Bmatrix} \Phi_\xi \\ \Phi_\eta \\ \Phi_\zeta \end{Bmatrix} \qquad (2)$$

and H is the transformation matrix defined by:

$$H = \begin{bmatrix} x_\xi & x_\eta & x_\zeta \\ y_\xi & y_\eta & y_\zeta \\ z_\xi & z_\eta & z_\zeta \end{bmatrix} \quad \text{with} \quad h = |H| \qquad (3)$$

The local density can be obtained from isentropic relations as:

$$\rho = \left[1 + \frac{\gamma-1}{2} M_\infty^2 (1 - u^2 - v^2 - w^2)\right]^{\frac{1}{\gamma-1}} \qquad (4)$$

The numerical approach used in FLO30 is a finite volume technique. To understand this approach, consider the simple two dimensional case represented by the grid system shown in Figure 2. The dashed cube shown in the figure indicates the area element under consideration. The flux of fluid through side a-b can be approximated by the average of the fluxes at point a and b with similar results for the side c-d. The net flux in the x direction for the elemental area centered at grid point i,j is then:

$$(\rho hU)_\xi = [(\rho hU_a + \rho hU_b) - (\rho hU_c + \rho hU_d)] \;/\; 2\Delta\xi$$

or in the notation of Caughey and Jameson,

$$(\rho hU)_\xi = \mu_\eta \delta_\xi (\rho U)$$

where μ indicates averaging and δ indicates differentiation in the indicated directions which are defined as follows (allowing $\Delta\xi = \Delta\eta = \Delta\zeta = 1$):

$$(\delta_\xi U)_{i,j,k} = (U_{i+\frac{1}{2},j,k} - U_{i-\frac{1}{2},j,k})$$

$$(\mu_\xi U)_{i,j,k} = (U_{i+\frac{1}{2},j,k} + U_{i-\frac{1}{2},j,k})/2$$

$$(\mu_{\xi\eta} U)_{i,j,k} = (U_{i+\frac{1}{2},j+\frac{1}{2},k} + U_{i+\frac{1}{2},j-\frac{1}{2},k} + U_{i-\frac{1}{2},j+\frac{1}{2},k} + U_{i-\frac{1}{2},j-\frac{1}{2},k})/4$$

. . . etc.

When extended to the other flux components and to averaging over cube surfaces in three dimensions, the numerical potential equation is of the form:

$$\mu_{\eta\zeta}\delta_\xi(\rho hU) + \mu_{\zeta\xi}\delta_\eta(\rho hV) + \mu_{\xi\eta}\delta_\zeta(\rho hW) = 0$$

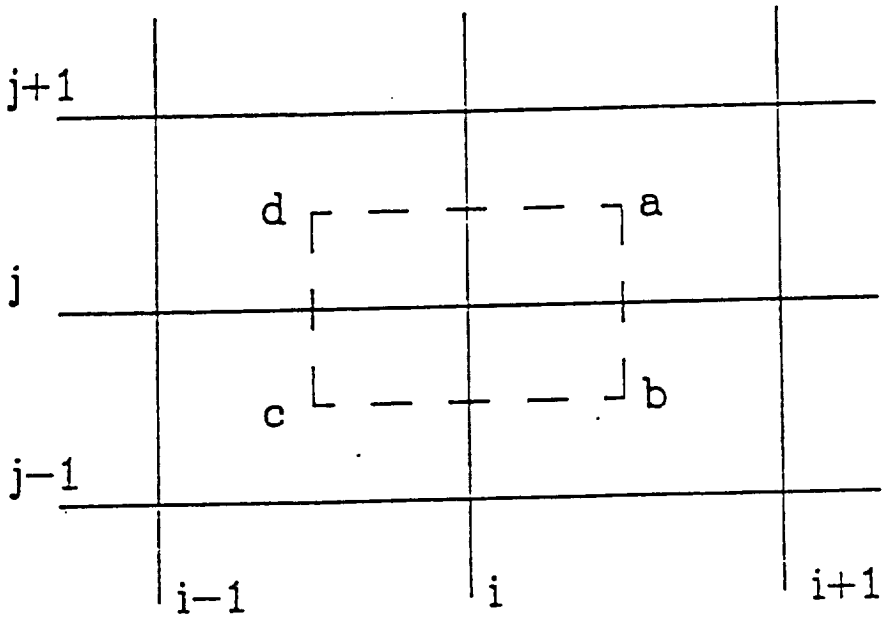

Figure 2. Finite-Volume Cell Location

To find the flux quantities ρhU, ρhV, and ρhW at the finite volume cell vertices (i.e. points a, b, c, and d for the two dimensional case), it is necessary to evaluate Equations (2) through (4). The derivatives in these expressions can be expanded by the same volume averaging approach used above, thus:

$$\Phi_\xi = \mu_{\eta\zeta}\delta_\xi(\Phi) \qquad x_\xi = \mu_{\eta\zeta}\delta_\xi(x)$$
$$\Phi_\eta = \mu_{\zeta\xi}\delta_\eta(\Phi) \qquad y_\xi = \mu_{\eta\zeta}\delta_\xi(y)$$
$$\Phi_\zeta = \mu_{\xi\eta}\delta_\zeta(\Phi) \qquad z_\xi = \mu_{\eta\zeta}\delta_\xi(z)$$

with similar terms for the other transformation metrics. The above expressions, being centered at grid midpoints, will involve the values of the potential and grid position at grid points which are known from the previous potential solution and the grid geometry, respectively.

As mentioned in the Background discussion, when solving transonic flows it is necessary to include in the solution algorithm some form of supersonic upstream dependence in order to account for both the physical nature of the flow and the viscous nature of shock waves, respectively. Caughey and Jameson introduced upwinding by the addition of terms into their potential numerical equation which are only non-zero when the flow is supersonic. Also, the finite volume technique used exhibits a tendency for uncoupling of the flow field solution between alternating grid points. As a result, additional terms are included in the numerical potential equation. The final numerical equation which is solved by FLO30 when these terms have been included has the form:

$$\mu_{\eta\zeta}\delta_\xi(\rho hU+P) + \mu_{\zeta\xi}\delta_\eta(\rho hV+Q) + \mu_{\xi\eta}\delta_\zeta(\rho hW+R)$$
$$- \epsilon(\mu_\zeta\delta_{\xi\eta}Q_{\xi\eta} + \mu_\xi\delta_{\eta\zeta}Q_{\eta\zeta} + \mu_\eta\delta_{\zeta\xi}Q_{\zeta\xi} - \delta_{\xi\eta\zeta}Q_{\xi\eta\zeta}/2) = 0$$

where P, Q, and R are the upwinding terms and $Q_{\xi\eta}$, $Q_{\eta\zeta}$, $Q_{\zeta\xi}$, and $Q_{\xi\eta\zeta}$ are the decoupling terms.

A reader interested in an in depth description of the nature and derivation of the additional terms mentioned above may find this information in Reference 14.

Computational Grid Geometry

As mentioned previously, the computational grid used by FL030 is a body fitted, non-orthogonal, curvilinear mesh constructed about a wing fuselage combination. The number of grid points composing the computational domain is typically 40 x 6 x 8, 80 x 12 x 16, or 160 x 24 x 32 for the number of ξ, η, and ζ points in the coarse, medium, and fine grids, respectively. The grid is conformally mapped to the wing and fuselage surfaces as can be seen from the plot of surface grid lines shown in Figure 3.

The grid is formed around spanwise airfoil sections in a similar manner in which "C" grids are mapped to airfoils in two-dimensional analysis. This mapping for the two-dimensional case unwraps the physical plane from around the airfoil and from along a slit extending from the airfoil trailing edge to the downstream boundary. The wing surface and slit are then a line of constant η as are the upper, lower and upstream boundaries. The upper and lower half outflow boundaries are lines of constant ξ.

The FL030 grid differs from the "C" grids due to the need to map the grid to the fuselage surface in addition to the wing surface. As a result, rather than allowing the constant ζ planes to extend to the

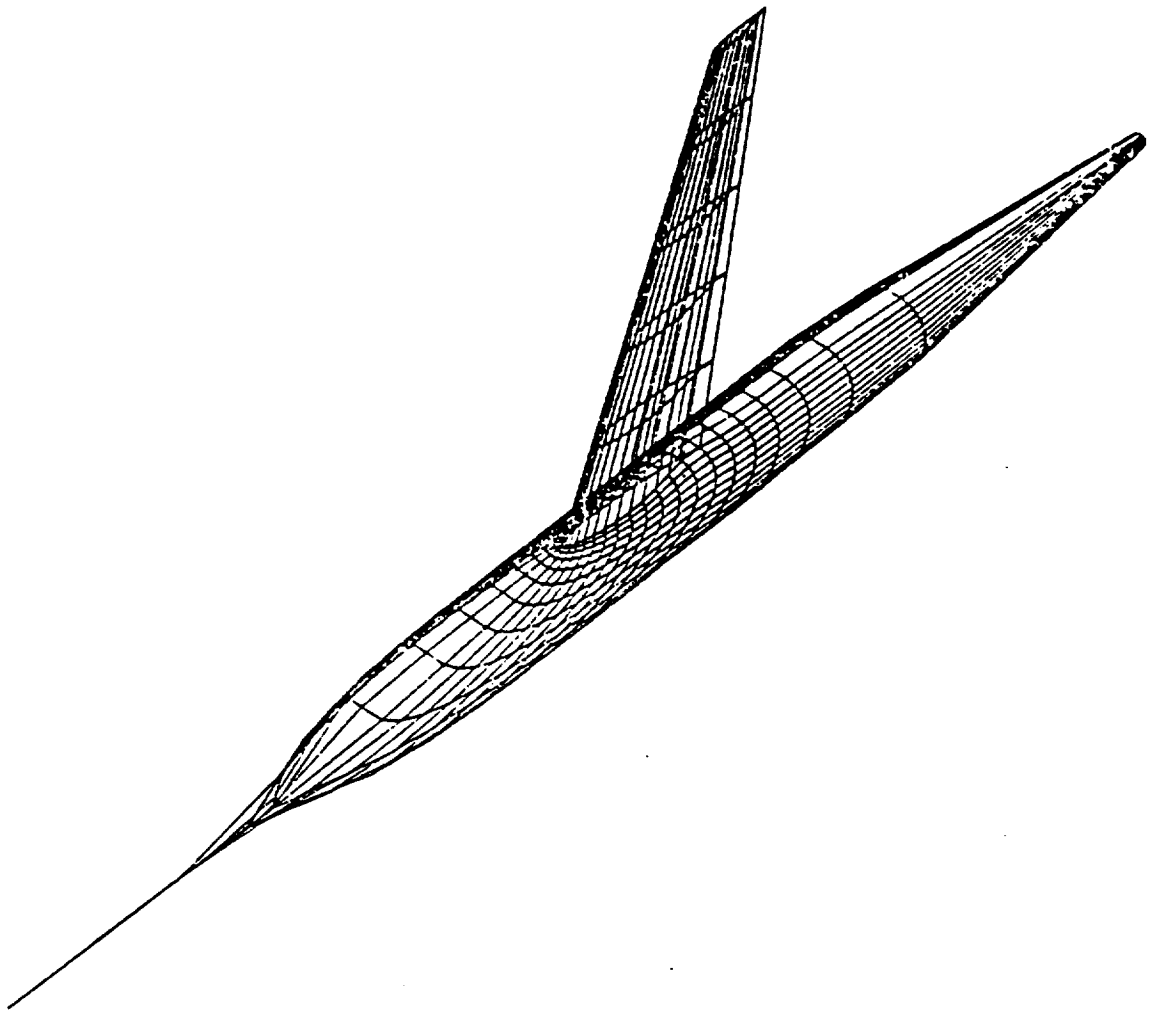

Figure 3. Surface Grid Point Geometry

upper and lower boundaries, these surfaces are wrapped around the fuselage and a line extending forward from the fuselage nose. The line of constant η which forms the upper and lower surface boundaries in two-dimensions now becomes the upper and lower half plane symmetric boundaries for the three-dimensional grid. Figure 4 shows a plot of the constant ζ surface which coincides with the wing tip airfoil section. Note that for this grid geometry, the far field side boundaries are all formed by the maximum η surface; and the upstream and downstream boundaries are the same as for the "C" grid case.

In addition to the grid surfaces which form the physical extents of the computational grid, additional "ghost" coordinate surfaces are automatically generated below the wing and fuselage surfaces and beyond the symmetric boundary. These "ghost" surfaces are necessary for the formulation of both the finite-volume numerical flow equations and the flow tangency boundary conditions upon these boundaries. The grid points composing the "ghost" surfaces are calculated from linear extrapolations of the computation mesh grid points immediately inside the physical domain.

Boundary Conditions

The original FL030 code included the following physical boundaries: solid surfaces, far field boundaries, symmetric plane boundary, and trailing edge slit boundary. Note that when viscous effects are included by adding on to the wing surface a displacement thickness, the new displaced surface acts like a solid surface and has the same boundary condition as for the inviscid wing surface. However, as will be

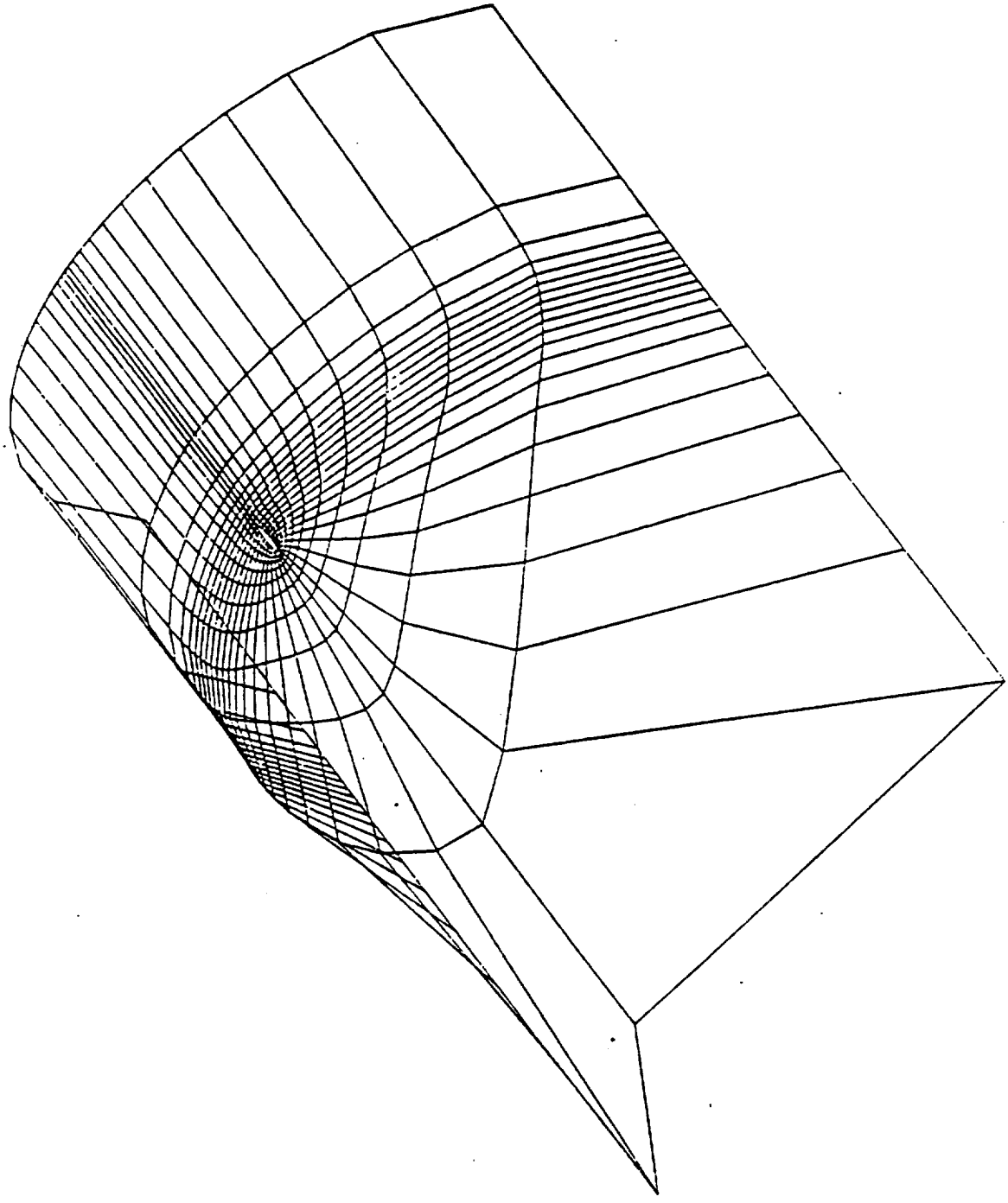

Figure 4. Typical Grid Surface

discussed in the next section, inclusion of viscous wake effects will influence the boundary conditions applied across the trailing edge slit.

Since the governing potential equations are written in terms of perturbations from free-stream conditions, the subsonic, far-field requirement that the flow return to the free-stream velocity and direction are satisfied by setting the perturbation potential equal to zero on the side and upstream boundaries. These boundaries are formed by the maximum ζ grid surface and part of the minimum η surface as mentioned previously in the grid geometry section.

For a purely subsonic and inviscid flow, the zero perturbation potential boundary condition would also exist on the downstream outflow boundary due to the isentropic (reversible) nature of the flow field. When solving transonic flows with shock waves or when viscous effects on the wing surface are being included, the flow field processes are irreversible and a return to free-stream conditions will not be expected. The downstream boundary condition allows for these effects by simply utilizing a "zero" order extrapolation of the potential (constant potential assumption) to the outflow boundaries.

A flow tangency condition is applied along both the wing and fuselage solid surfaces by setting the normal contravariant component of the velocity vector to zero on the surfaces. This condition provides an equation which when approximated by a finite-difference expansion about the surface grid points can be used to set a value for the perturbation potential on the "ghost" grid points below each surface. Note that this finite-difference boundary condition is not exactly similar in form to the finite-volume solution algorithm of the governing equations. As a

result, it is possible to impose flow tangency using the finit-difference technique yet still have some normal surface velocity when performing the finite-volume calculations. Since it is essential to have the most exact boundary condition imposed upon the wing surface in order to generate the most accurate solutions, a second condition exists upon the wing surface. This additional condition involves reflecting the flux quantities calculated by the flow solver for the cell centers directly above the wing surface to the "ghost" cell centers beneath. The reflected normal fluxes then cancel each other out in the residual expression and a net zero flow is obtained through the surface.

Since FL030 only solves the flow field for a half body configuration, only cases of no sideslip can be analyzed. Thus, the symmetric boundary has no flux through it and a flow tangency condition exists on the half plane. This condition is imposed numerically in the same fashion as for the wing surface with both the weak finite-difference and the strong finite-volume methods being used.

For an inviscid calculation, the trailing edge slit boundary is not an actual limit to the physical domain as the other boundaries are, but is simply an artificial boundary created by unwrapping the physical plane into the computational domain. The only conditions which need to be imposed at the slit is that the flow velocities, and thus pressure, be continuous across the cut. The flow potential, however, will have a discontinuous jump across the wake which is proportional to the sectional wing lift coefficient.

Viscous Boundary Layer and Wake Effects

The program routines for the calculation of the viscous boundary layer and wake have been integrated into FL030 as part of an investigation by Streett[17] into more accurate methods of correcting potential flow solutions for viscous effects. These routines model the three dimensional laminar and turbulent surface boundary layer with the transition location specified by the user. The turbulent, viscous wake trailing the wing surface is modeled as having both finite thickness and curvature that vary with downstream location. The procedure for obtaining a converged viscous solution is to alternate between solving the potential flow and boundary layer equations until both solutions are converged.

As mentioned previously, the effect of the surface boundary layer on the potential flow is accounted for by assuming a displacement thickness. These displacements are calculated by the boundary layer routines at the points which are originally input by the user for the wing geometry. When regenerating the computational grid after a viscous calculation, the displacements are added normal to the original surface and the grid formed around this displaced surface. The boundary conditions on the displacement surface is the same as for a physical surface, i.e. flow tangency.

The wake thickness correction is similar to that for the surface displacement thickness and is also included in generating the computational grid in order to produce a trailing edge slit which has a nonzero width. However, the boundary conditions applied across the finite slit are different from the inviscid potential flow case due to the pos-

sibility of a pressure jump across the wake and, thus, some wake curvature in the downstream flow. The presence of wake curvature is imposed on opposing sides of the wake cut, as a difference in potentials, which decays to zero or freestream conditions far enough downstream.

Since, the present investigation deals with the design of the wing surface itself, alternate boundary conditions on the design surface will be required. In the existing analysis code, only the general potential flow solution method, the wing/displacement boundary conditions, and the application of the boundary layer displacement thickness on the surface of the wing are of immediate concern in this thesis.

INVERSE WING DESIGN METHODS

As stated previously, a direct-inverse approach to wing design was selected for incorporation into the TAWFIVE code. The direct-inverse method derives its name from the division of the design wing surface into a fixed geometry leading edge region, where flow tangency boundary conditions are imposed, and an aft, variable geometry section where pressure boundary conditions are enforced. The pressure boundary where the user specified pressure distributions are imposed does not extend forward to the leading edge due to difficulties of enforcing this type boundary condition near the beginning of an airfoil section. This restriction on the size of the pressure specification region does not seriously reduce the versatility of the design method since the leading edge regions for most airfoils are similar, and it is relatively easy to select a leading edge geometry which will produce the desired Mach number or pressure values at the beginning of the inverse region. In addition, specific leading edge shapes may be required due to other design constraints such as the necessity to house a leading edge flap or slot system. Finally, as will be shown later, the application of the inverse approach only to back portions of the wing aft of the leading edge means that it is used in regions where the pressures are primarily dominated by the chordwise flow velocity; and, thus, the direct-inverse approach allows some useful simplifications when formulating the equations.

The following sections will provide details concerning the usage of the pressure distribution as a boundary condition in the inverse wing regions and how a new surface which would produce these pressures can be

calculated. An additional feature which helps to restrict the inversely designed wings to practical geometries by imposing a desired trailing edge thickness is also described. The final section details how the inverse design procedures are integrated into the program as a whole and presents a logical design strategy for use in designing actual wings. Part of this last section also discusses the code's data input structure and design options available.

Pressure Boundary Condition

In the inverse design regions on the wing, a pressure boundary condition will be specified rather than the flow tangency condition used in analysis zones. In formulating this boundary condition it is necessary to relate the user specified pressure coefficient, C_p, to the current perturbation potentials at inverse design grid points. Consider the full potential equation for the pressure coefficient:

$$C_p = \frac{2}{\gamma M_\infty^2}\left\{\left[1 + \frac{\gamma-1}{2} M_\infty^2\left(1 - \frac{Q^2}{q_\infty^2}\right)\right]^{\frac{\gamma}{\gamma-1}} - 1\right\}$$

where $$Q^2 = u^2 + v^2 + w^2$$

If it is assumed that the pressure coefficient is primarily a function of the chordwise component of the velocity, u, and only slightly affected by the vertical and spanwise components of velocity, v and w, then the latter two velocities can be time lagged in the boundary condition without introducing any solution instabilities. This assumption is true everywhere except near the leading edge; but since the inverse design boundaries have already been restricted to regions well behind

the leading edge, the simplification is justified. The value of the local velocity, u, can then be calculated from the above expression in terms of the desired pressure coefficient and the current values for the vertical and spanwise velocities. In addition, the velocity u can also be calculated from the perturbation potentials using the relations of Eq. (2). Defining J_{ij} to be the elements of the inverse transpose of the Jacobian matrix, H, the two equations for u yield:

$$J_{11}\phi_\xi + J_{12}\phi_\eta + J_{13}\phi_\zeta = \frac{1 - \frac{2}{(\gamma-1)M_\infty^2}\left[\left(1 + \frac{\gamma M_\infty^2 C_p}{2}\right)^{\frac{\gamma-1}{\gamma}} - 1\right]}{1 + \left(\frac{v}{u}\right)^2 + \left(\frac{w}{u}\right)^2} - \cos(\alpha) \quad (5)$$

Since the spanwise and vertical flow velocities have already been assumed to be constant in the boundary condition relation, it is consistent to make the same approximation in the above expression with respect to the spanwise and vertical derivative terms, ϕ_η and ϕ_ζ. This assumption is similar to the previous one, and it will lead to an explicit expression for the potential at one point.

Two different finite difference approximations of Eq. (5) have been considered. The first method involves expanding the derivatives of the potential function as central differences about a grid point in the ξ (chordwise) and ζ (spanwise) directions and a three point backwards finite difference in the η (vertical) direction. The reason for the special treatment on the η derivative is due to the value of the potential not being defined at the "ghost" points in the inverse regions. The numerical equation with the above expansions is:

$$J_{11}(\phi^{n+1}_{i,j,k} - \phi^{n}_{i-2,j,k})/2 + J_{12}(3\phi^{n}_{i-1,j,k} - 4\phi^{n}_{i-1,j-1,k} + \phi^{n}_{i-1,j-2,k})/2 + J_{13}(\phi^{n}_{i-1,j,k+1} - \phi^{n}_{i-1,j,k-1})/2 = F(Cp_{i-1,k})$$

Here, the superscripts n and n+1 refer to current values of the potential and the new values of the potential being imposed by the boundary condition, respectively. Also, the term $F(Cp_{i-1,k})$ is the right hand side of Eq. (6) evaluated using the pressure coefficient specified at point i-1,k. Figure 5 shows the points involved in the above expression and the point at which the pressure is being specified. This equation can then be solved for the potential at grid point i+1,j,k which yields the equation:

$$\phi^{n+1}_{i,j,k} = \frac{1}{J_{11}}\left[J_{11}\phi^{n}_{i-2,j,k} - J_{12}(3\phi^{n}_{i-1,j,k} - 4\phi^{n}_{i-1,j-1,k} + \phi^{n}_{i-1,j-2,k}) - J_{13}(\phi^{n}_{i-1,j,k+1} - \phi^{n}_{i-1,j,k-1}) + 2F(Cp_{i-1,k})\right]$$

The potential values at n+1 in the direct region are known initially since they do not change when the inverse boundary condition is applied; i.e. $\phi^{n+1} = \phi^{n}$. All the potentials on the inverse boundary can then be calculated and, since the spanwise and vertical derivatives are small, will primarily be functions of the pressure coefficient at grid point i-1 and the value of the potential at grid point i-2.

This method of approximation has the possibility of producing two independent solutions for the alternating set of even and odd grid points which is a problem commonly seen when using simple central difference approximations. The reason that this solution uncoupling may exist is due to the dependence of each potential on the value two grid

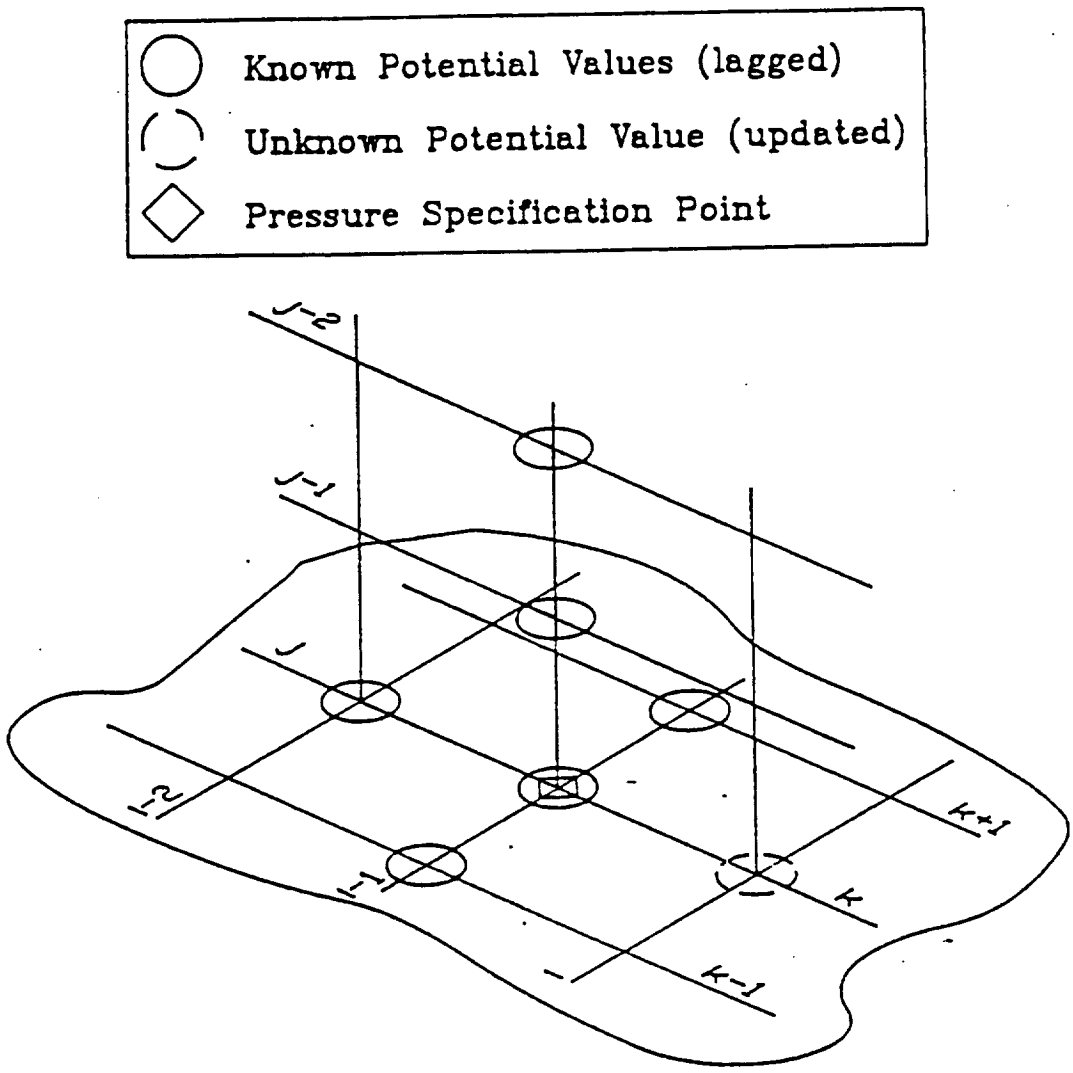

Figure 5. Point Dependance for Grid Point Specification Method

points ahead or behind rather than the one immediately adjacent. To preclude the possibility of this problem occurring, another finite difference method has been considered.

The second finite difference approximation involves expanding the derivatives of the potential about the mid-point $i+\frac{1}{2},j,k$. The ξ derivative for this case is determined by a central difference involving the preceding and following grid point values. The η and ζ derivatives can be found at the mid-point by averaging the derivatives from the preceding and following grid points found be the three point backwards and central difference approximations as in the previous method. Figure 6 shows the point dependence and pressure specification point for this method. The resulting numerical expression obtained with these finite approximations is:

$$J_{11}(\phi^{n+1}_{i,j,k} - \phi^{n}_{i-1,j,k}) + J_{12}\,3(\phi^{n+1}_{i,j,k} + \phi^{n}_{i-1,j,k}) - 4(\phi^{n}_{i,j-1,k} + \phi^{n}_{i-1,j-1,k}) + \phi^{n}_{i,j-2,k} + \phi^{n}_{i-1,j-2,k}\ /4 + J_{13}(\phi^{n}_{i,j,k+1} + \phi^{n}_{i-1,j,k+1} - \phi^{n}_{i,j,k-1} - \phi^{n}_{i-1,j,k-1})/4 = F(Cp_{i-\frac{1}{2},k})$$

from which the potential value at i+1,j,k can be found as:

$$\phi^{n+1}_{i,j,k} = \frac{1}{J_{11} + 3J_{12}/4}\Big[J_{11}\phi^{n}_{i-1,j,k} - J_{12}\,3\phi^{n}_{i-1,j,k} - 4(\phi^{n}_{i,j-1,k} + \phi^{n}_{i-1,j-1,k}) + \phi^{n}_{i,j-2,k} + \phi^{n}_{i-1,j-2,k}\ /4 - J_{13}(\phi^{n}_{i,j,k+1} + \phi^{n}_{i-1,j,k+1} - \phi^{n}_{i,j,k-1} - \phi^{n}_{i-1,j,k-1})/4 + F(Cp_{i-\frac{1}{2},k})\Big]$$

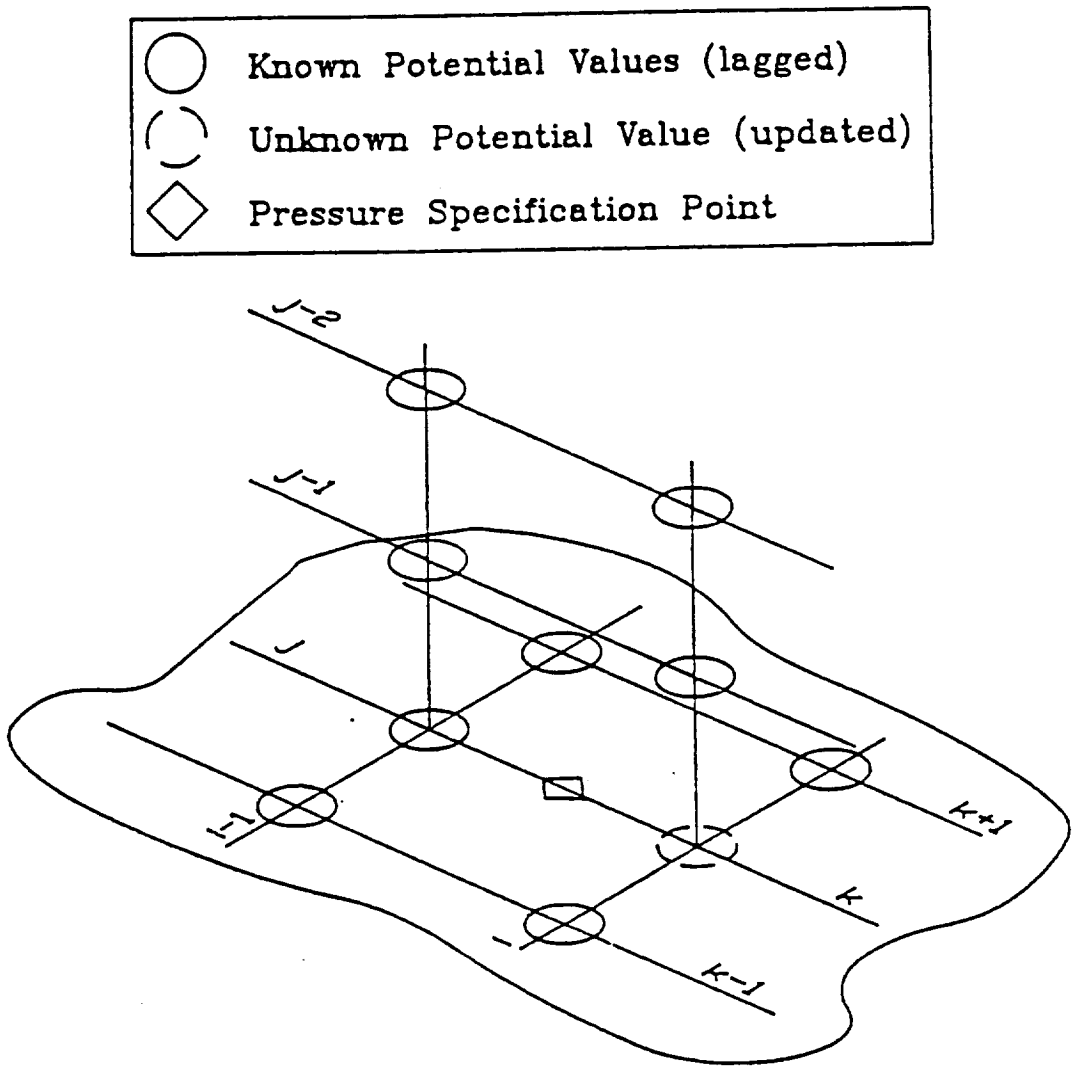

Figure 6. Point Dependance for Mid-point Specification Method

The only concern with using this mid-point specification scheme is that the current method of calculating the pressure data output from FLO30 uses the first difference scheme for the streamwise derivative. This difference could potentially allow a pressure to be specified correctly but still have a significantly different value output from FLO30 due to the inconsistent calculation methods. However, as shown on Figure 7, where the pressures calculated for a typical flow solution are compared for the two different calculation techniques, this possible error has not been significant in practice.

Surface Calculations

As the inverse boundary conditions drive the flow field to a converged solution, it is necessary to periodically calculate the location of the new displacement surface and to regenerate the computational grid about this new geometry so that the pressure boundary surface will correspond to the physical boundary surface. Each new surface can be found relative to the previous surface from an integration of the wing surface slopes. However, the surface slopes must first be calculated from the current flow field solution using the flow tangency boundary condition which in Cartesian coordinates is:

$$U^T \times \nabla F = 0$$

where U is the Cartesian velocity vector and ∇F is the gradient of the surface function F.

Since all of the numerical calculations are performed in the curvil-

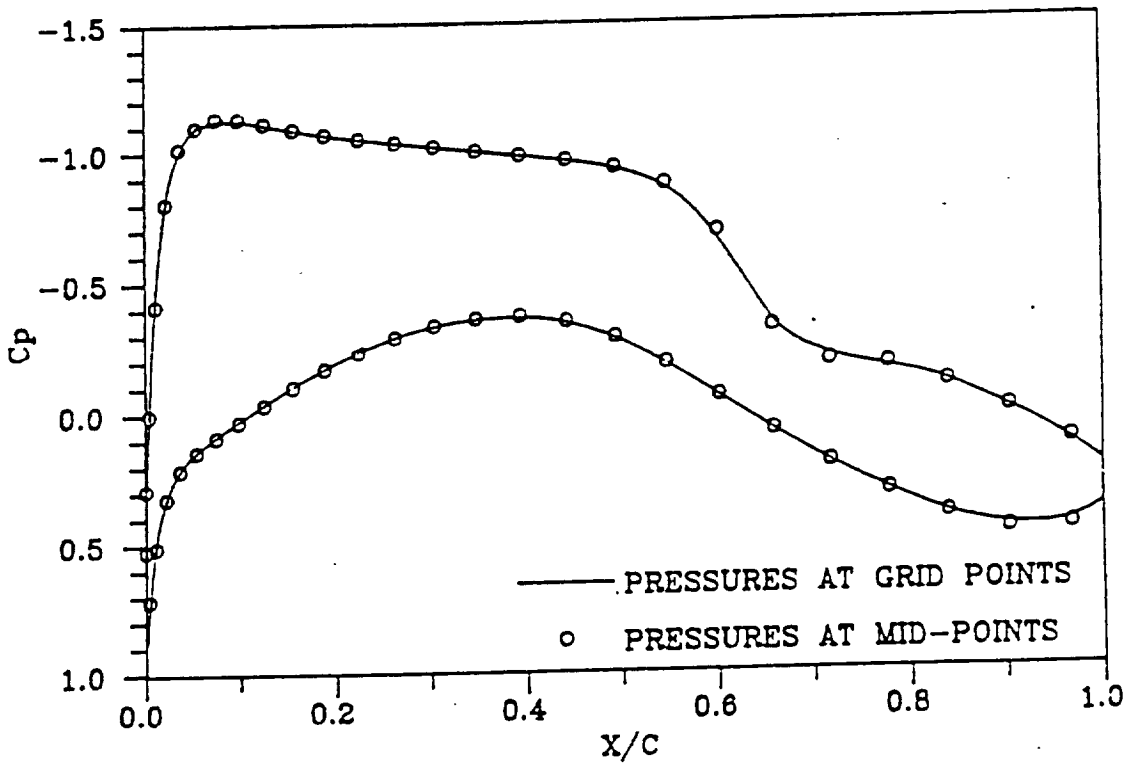

Figure 7. Comparison of Pressures Calculated at Grid Points and Grid Mid-points

inear computational space, it is necessary to express the boundary conditions in the same manner. Defining $\nabla' F$ to equal the gradient of F with respect to the curvilinear coordinates and V to be the contravariant velocity vector, the following relations can be obtained from Equations (2) and (3):

$$U = H \times V \qquad\qquad \nabla F = (H^{-1})^T \times \nabla' F$$

From these the transformed boundary condition can be obtained as:

$$(H \times V)^T \times [(H^{-1})^T \times \nabla' F] = V^T \times [H^{-1} \times H]^T \times \nabla' F = 0$$

or simply

$$V \times \nabla' F = 0$$

As can be seen, the tangency boundary condition written in terms of the curvilinear coordinate system using contravariant velocities is a direct analog to the same condition expressed in physical space.

A more useful expression can be obtained by expanding the above equation to:

$$\left(\frac{\partial \eta}{\partial \xi}\right)_{wing} = \frac{V}{U} - \frac{W}{U}\left(\frac{\partial \eta}{\partial \zeta}\right)_{wing}$$

This expression can be solved for the new chordwise airfoil slopes, $\partial\eta/\partial\xi$, if the current values of the spanwise slope, $\partial\eta/\partial\zeta$, are used. Since the wing surface is represented in the computational grid as a plane of constant η, the current slopes on the wing surface equal zero and a simplified flow tangency condition results:

$$\left(\frac{\partial \eta}{\partial \xi}\right)_{wing} = \frac{V}{U} \qquad (5)$$

This flow tangency condition is only exactly true when the velocities are calculated at the new physical surface boundary. Using these velocities is difficult in practice, however, since the new surface

being calculated will typically lie at locations between grid points, where velocities are difficult to calculate; or even at locations outside the flow field altogether, as when the new surface falls below the old surface. Thus, for simplification, the contravariant velocities used in calculating the surface slopes are the velocities at the inverse pressure boundary; i.e. the current grid boundary which is also the previous physical surface boundary. This approximation is justified by the fact that for the converged surface solution the pressure and physical surface coincide and the equation becomes exact. In addition, no surface convergence problems resulting from this approximation have been observed, even for cases where the pressure and physical boundaries initially differed by a significant amount.

A second factor affecting the slope calculations is the accuracy of the contravariant velocity calculations. A first approach to calculating the U and V velocity components was simply to apply the relations of Eq. (2). The derivatives of the potential function were evaluated by central difference approximations in the ξ and ζ directions and a three point backwards difference in the η direction. The later was required because, as has already been mentioned in the pressure boundary section of this thesis, the potential function was not defined at ghost points in the inverse regions. As was expected from the previous experience of Weed et al.[9], this approach did not yield accurate values for the V velocity component. As can be seen from the data plotted in Figure 8, the surface displacements, labeled "Finite Difference Approach," based upon velocities calculated using the above method for a converged analysis solution of a wing section are significantly different from zero.

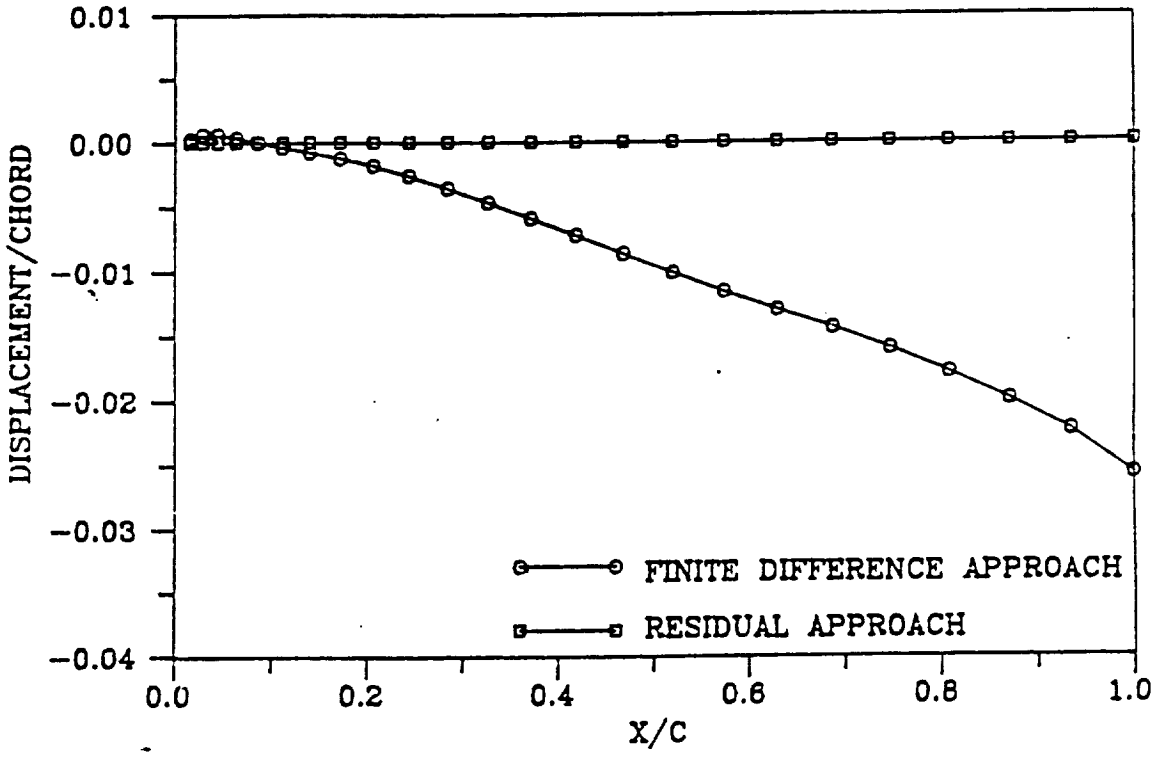

Figure 8. Comparison of Accuracy of Finite-Difference Method and Residual Method

The later is, of course, the proper displacement expected for a converged solution.

The other data plotted on Figure 8, labeled "Residual Approach", are the result of using an alternate approach which is an extension of the formulation of Weed et al.[9]. This second method involves solving the residual expression from the potential flow solver for the surface velocity ratio, V/U, under the assumption that the residual is zero. For this problem, the residual expression from FLO30 can be written in finite volume form as:

$$\mu_{\eta\zeta}\delta_\xi(\rho hU) + \mu_{\zeta\xi}\delta_\eta(\rho hV) + \mu_{\xi\eta}\delta_\zeta(\rho hW) + (\text{other terms}) = 0$$

The "other terms" in the above expression involve the grid point coupling and upwind dependence terms of the formulation and will be assumed to be constants in the following development.

The desired velocity ratio, V/U, can also be written in this finite volume form as:

$$\frac{V}{U} = \frac{\rho hV}{\rho hU} = \frac{\mu_{\xi\eta\zeta}(\rho hV)}{\mu_{\xi\eta\zeta}(\rho hU)}$$

By simple manipulations, this ratio can be obtained from the residual expression as:

$$\frac{\mu_{\xi\eta\zeta}(\rho hV)}{\mu_{\xi\eta\zeta}(\rho hU)} = \frac{2\mu_{\zeta\xi}(\rho hV)_{\eta-1} + \mu_{\eta\zeta}\delta_\xi(\rho hU) + \mu_{\xi\eta}\delta_\zeta(\rho hW) + (\text{other terms})}{2\mu_{\xi\eta\zeta}(\rho hU)} \quad (6)$$

where the subscript η-1 refers to the values at grid cell centers above the wing surface.

In order to use Eq. (6) to find the desired surface velocity ratio,

it is necessary to know the U and W velocity components at the "ghost" cell centers below the wing surface. These values can be obtained in a manner consistent with FLO30 by specifying the "ghost" cell values to equal the values at corresponding points immediately above the wing surface. Eq. (6) then explicitly defines the velocity ratio at the boundary grid points and, as seen from Figure 8, is very accurate.

It should be noted that an interesting program simplification has been achieved in performing this calculation. In the discussion of the analysis surface boundary condition, it was stated that the "ghost" cell velocities were obtained by reflection about the wing surface. This procedure amounts to setting the chordwise and spanwise velocities, U and W, at "ghost" points equal to those above the wing surface and setting the vertical velocity component, V, at the "ghost" point equal in magnitude but in the opposite direction to the V velocity above the wing surface. If the residual were calculated in this manner at the surface grid points in the inverse regions, then the surface slopes can then be found simply by:

$$\left(\frac{\partial \eta}{\partial \xi}\right)_{\text{wing}} = \frac{\mu_{\xi\eta\zeta}(\rho hV)}{\mu_{\xi\eta\zeta}(\rho hU)} - \frac{(\text{Residual})}{2\mu_{\xi\eta\zeta}(\rho hU)} \qquad (7)$$

Thus, a converged surface solution where $\partial\eta/\partial\xi$ tends to zero corresponds to a converged finite-volume solution on the surface where the residual tends to zero.

With the contravariant velocities known, an integration of Eq. (7) through the inverse design region from the leading edge to the trailing edge will yield a set of surface displacements for the new wing surface relative to the previous one. These changes will be expressed as

changes in the computational coordinate η, which can be converted to surface displacements in the physical plane via the transformation:

$$\Delta x = x_\eta \, \Delta\eta \qquad\qquad \Delta y = y_\eta \, \Delta\eta$$

However, since the computational grid lines are orthogonal at the surface, the normal displacement, $\delta(x)$, is:

$$\delta(x) = ((x_\eta \, \Delta\eta)^2 + (y_\eta \, \Delta\eta)^2)^{1/2}$$

These displacements will be defined at the computational grid points in the inverse regions. To obtain the corresponding displacements at the original geometrical locations specified in the program input data, a linear interpolation of the above data is performed. The reasons that the displacement surfaces are needed at the original geometry points is two fold. First, as mentioned previously in the discussion of viscous interaction, the boundary layer displacement thickness, which is numerically analogous to the inverse displacement thickness, is defined at the original input stations; and finding the inverse displacement thickness at the same locations allows the use of the same routines for adding the boundary layer and inverse design displacements to the original geometry. Second, finding the displacements at the original geometry stations permits the calculation of the new wing airfoil sections at the same semispan locations.

Trailing Edge Closure

The procedures outlined above will compute a wing surface corresponding to a given, fixed, leading edge geometry and to a desired set

of pressure distributions in the inverse regions. The above procedures do not, however, guarantee that this wing geometry will be practical. In particular, past experience[9] has shown that inverse surface calculations may yield airfoil sections which have either excessively blunt trailing edges or which, at least numerically, have the upper and lower surfaces crossed at the trailing edge ("fish tailed"). The former case is undesirable due to aerodynamic considerations, while the latter is physically impossible and may produce unpredictable problems in the grid generation or flow calculation portions of FLO30.

Since for any specified pressure distribution the corresponding wing surface will be controlled by the leading edge geometry, which serves as an initial spatial boundary condition for the inverse region, the problem of assuring trailing edge closure can be viewed as the proper selection of a leading edge shape. A procedure for systematically modifying the leading edge region in order to achieve some desired trailing edge thickness is called relofting. Such a relofting procedure has been incorporated into the present design process in order to both prevent the problems of trailing edge crossover and to allow the user the option of specifying a trailing edge thickness as an additional design variable. This design feature should be very useful in practical applications since it automates the iterative selection of a leading edge shape which would otherwise have to be performed by the user.

The present method of surface relofting is a simple linear rotation scheme. This method can be visualized with the help of Figure 9. The dashed line indicates the original leading edge geometry and a hypothetical new surface shape which has been calculated for the inverse design

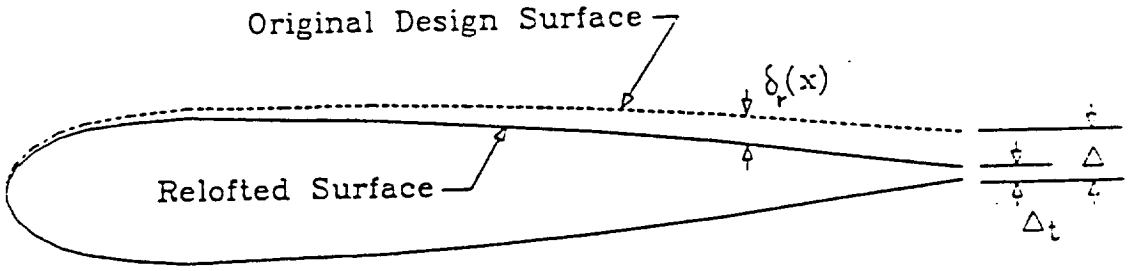

Figure 9. Relofting to Force Trailing Edge Closure

regions. Without modification, this new surface has a trailing edge thickness of Δ. If a thickness of Δ_t was specified by the user, then the surface would have to be relofted or changed. In the present scheme, in order to obtain the desired thickness, a displacement thickness, δ_r, is added to the current design surface. This thickness has a distribution from the leading to the trailing edge and is determined by the formula:

$$\delta_r(x) = (\Delta_t - \Delta)\ (x/c)$$

where c is the chord length of the local airfoil section. The total displacement for a surface update is then the sum of the two displacements, δ and δ_r. When both the upper and lower surfaces are designed simultaneously, the displacement magnitudes determined by relofting are divided between the two surfaces so that half is added to the lower surface and half to the upper surface.

It should be noted that the above procedure for relofting the leading edge region is a practical method, and it is not based upon any known dependance between the leading edge shape and the trailing edge thickness. Experience has shown, however, that this method does indeed produce the appropriate effect at the trailing edge; and with iteration, a converged geometry solution with the desired trailing edge thickness can be obtained.

Design Strategy

All of the above procedures are part of the overall wing design program structure. The addition of the necessary program statements and subroutines to the TAWFIVE code has been made in an unobtrusive manner

so that the original TAWFIVE program logic and input formats are preserved. This section will discuss in detail how these inverse design methods interface with the analysis portions of the code and how the inverse design of a wing would be performed.

Consider first how the TAWFIVE program is used when performing an analysis of a specified wing geometry. The wing and fuselage geometry data are input and the desired computational grid is subsequently generated. Typically, there is a choice of three different computational grids which may be thought of as coarse, medium, and fine. The usual procedure is to start a wing analysis on the coarse grid and then to halve the grid spacing to the medium size after some specified number of iterations of the potential flow solver have been performed. After additional potential flow iterations on the medium grid, the grid spacing is again halved to the fine grid size; and, for purely inviscid analysis, iterations are repeated until a converged potential flow solution is obtained.

For an analysis with viscous interaction, it is sufficient to only partially converge the potential solution on the fine grid so that reasonable wing surface pressures can be calculated; and the boundary layer routines are then called in order to calculate an initial displacement thickness. With the displacement surface known, the procedure generates a new grid around the displaced surface; and the iterative and grid halving procedure is repeated until a converged solution for both the potential flow and the boundary layer is obtained. Note that as the solutions converge, it is usually not necessary to return to the coarse grid after each displacement surface update; but solutions can continue

on the fine grid starting with the most recent potential solution.

As shown from the flowchart in Figure 10, an inverse wing design will proceed in a very similar manner to that of a viscous wing analysis. After the initial wing geometry is input and the computational grid has been generated, the inverse pressure distribution data and design control parameters are inputted and the pressures to be specified at the grid mid-points are calculated. Before each potential flow iteration is performed, a call is now made to the pressure boundary subroutine where the potentials on the wing surface in the inverse regions are specified. The potential flow solver then proceeds as normal except that the changes of the potential values computed on the inverse wing surface are set to zero. After all the desired grid halvings are performed and a semi-converged solution is obtained, the surface update routines are called. These routines compute both a new surface geometry and a set of inverse displacement thicknesses. The new geometry is output to a print file in the same format as the input geometry file and is not saved in memory. The displacement thicknesses, however, are retained and are used in computing a new computational grid in the same manner as the viscous displacement thicknesses are used.

When performing an inverse design with viscous interaction effects included, the procedure is exactly the same as the inviscid design procedure with the viscous and inverse displacement thicknesses being used in the direct and inverse regions of the wing, respectively. It has been observed, however, that it is best to obtain a semi-converged boundary layer solution (at least one iteration) before beginning the inverse design. The reason for needing an initial boundary layer solu-

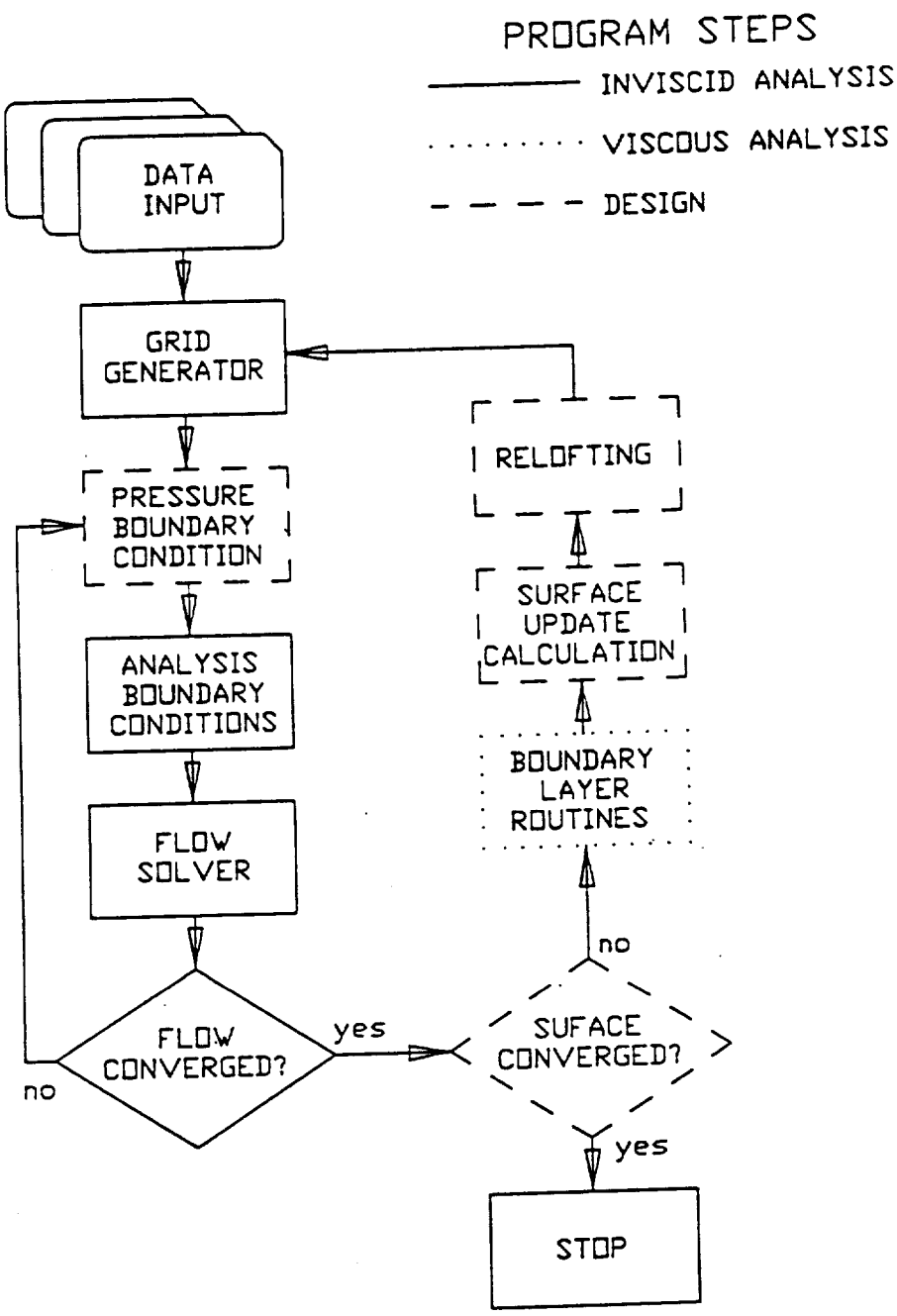

Figure 10. Flowchart of Inverse Design Procedure

tion is due to an occasional over prediction of the boundary layer thickness at the trailing edge by the first boundary layer calculation. These excessive, erroneous thicknesses may cause the physical surface beneath the displacement surface to appear to be fish tailed. If forced trailing edge thickness is being imposed, the result is an unnecessary surface relofting which must be undone by additional surface updates, thus slowing down the solution convergence.

Design Input and Control

The inverse pressure file is oriented around individual span stations in the same manner as the wing geometry input file is organized about sectional airfoil geometries. As such, pressures are input as chordwise distributions of the pressure coefficient for each span station with as many span stations as necessary being specified in order to fully define the desired wing pressure distribution. Every set of two spanwise stations may be thought of as a design panel on the wing surface, with each panel being either an upper surface design, lower surface design, or both. Since input pressure stations and computational grid span stations will not necessarily correspond to one another, once a design panel is specified, the program searches to find which, if any, grid stations are positioned within the inverse region. Pressures and the other design variables are then linearly interpolated from the surrounding pressure stations to obtain the values at the grid station. These other variables are the location of the direct-inverse junction near the leading edge and the trailing edge thickness desired for trailing edge closure. Contiguous design panels which involve design of the

same surfaces (i.e. upper, lower, or both surfaces) can be formed by inputting a single additional pressure station which will define the panel between the last input station and the new. Figure 11 shows the input pressure sections and the resulting computational inverse regions for a design case which involves both a continuous design region defined by multiple pressure input stations and a separate design section near the wing tip. The computational grid lines shown are typical for medium grid spacing. Note that the design region between the first two pressure stations does not contain any computational grid lines and thus will have no affect on the final wing design. This example indicates that the user should be familiar with where the computational grid will be formed before arbitrarily selecting input stations.

Two control parameters have been added to the TAWFIVE iteration control input file. The first controls whether or not the inverse boundary conditions will be imposed for a given set of potential flow iterations and, if the conditions will be imposed, at which iteration count they begin. This latter option has been included because it is foreseen that for geometry cases with a difficult convergence trend, it may be necessary to obtain a semi-converged solution before attempting to enforce the design conditions. All of the design cases which will be discussed in the results section of this thesis have been obtained by enforcing the design boundary conditions starting with the first iteration and no convergence difficulties have been observed.

The second control variable is used by the surface updating routine to determine what type of relofting control is desired. Since relofting will always occur it the current wing surface will result in a computa-

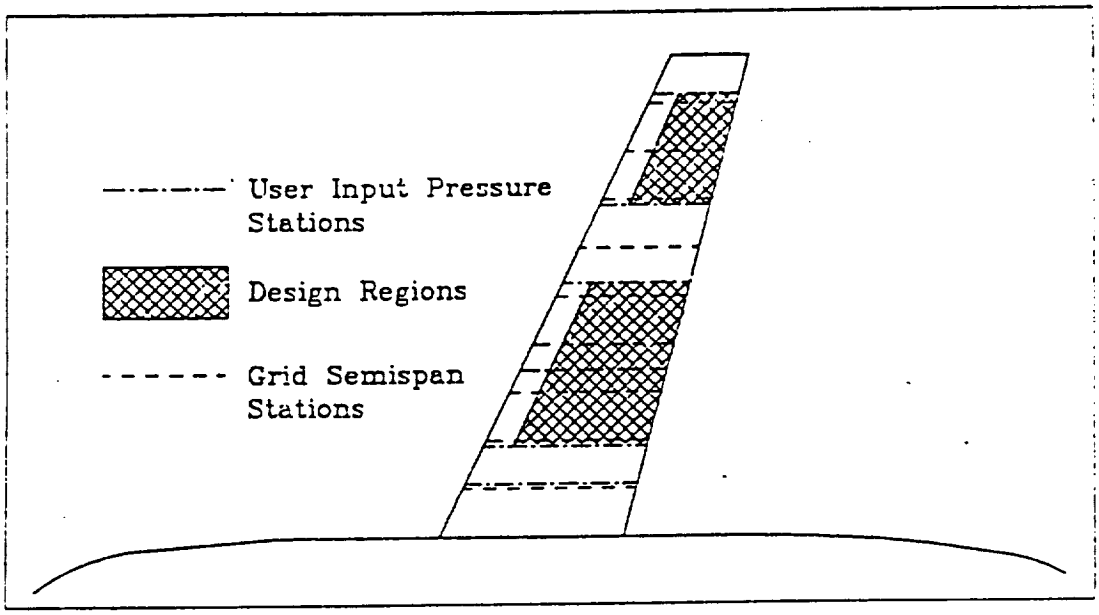

Figure 11. Typical Design Input Geometry

tional grid which crosses itself prior to the trailing edge, this variable is used only to determine if the trailing edge thickness is to be "forced" to a user specified value. Note that relofting will automatically occur if the grid itself crosses, but it will not take place if only the airfoil crosses itself. The distinction is due to the fact that when the viscous boundary layer is added to the problem, it is possible that the airfoil may be fish tailed while the displaced surface is not. In these cases a fish tailed airfoil may actually be designed if the user does not force trailing edge closure.

RESULTS

In this section results from five different test cases for both subcritical and supercritical conditions will be presented. These cases are not intended to be definitive or even representative of practical designs but have been selected as examples of the capabilities of the present inverse design technique. The results shown were obtained on a medium grid having 81 streamwise, 13 vertical, and 19 spanwise points with 11 spanwise stations and 53 points on the wing at each station; and in all cases the maximum change in the reduced potential was reduced at least three orders of magnitude. Thus, the results do not represent ultimate convergence but should be representative of "engineering accuracy".

The planform selected for the test cases was the Lockheed Wing A wing-body. The wing for this configuration has a quarter chord sweep of 25 deg., a linear twist distribution ranging from 2.28 deg. at the wing body junction to -2.04 deg. at the wing tip, an aspect ratio of eight, and a taper ratio of 0.4. The last two values are based upon the wing without fuselage. However, instead of the supercritical sections normally associated with Wing A, the initial airfoil sections at each span station were assumed to be NACA 0012 airfoils.

The target pressure distributions used in the design regions were selected to yield airfoil shapes thicker in the aft portions of each section; and, at supercritical conditions, to yield on the upper surface weaker and more forward shock waves than those which would normally occur on a NACA 0012 section. On the lower surface, the target pressure

distributions were selected to have either a favorable pressure gradient or fairly constant pressure plateau over much of the lower surface.

All subcritical cases were for a freestream Mach number of 0.7 and an angle of attack of two degrees. In each case, the pressure distribution was specified in the design regions from the 15% local chord location to the trailing edge and used as the boundary condition in these inverse regions starting with the first iteration. Normally, two hundred SLOR iterations were executed prior to the first design surface update calculation; and subsequently, surface updates were computed every fifty cycles. Usually, the solution was considered converged and terminated after 450 total iterations.

Supercritical cases followed a similar procedure except that the freestream Mach number was 0.8. Again the angle of attack was two degrees. However, for these cases three hundred iterations were performed prior to the first surface update calculation in order to better resolve the leading edge pressure distribution in design regions. Because of the upstream dependance of the flowfield, particularly for the supercritical cases, it was determined to be essential to obtain a good computational solution in the leading edge region before any surface updates. Otherwise the initial surface changes were so drastic that a large number of additional surface calculations, and accompanying iterations, were necessary in order to achieve convergence.

Finally, for those cases where trailing edge closure was specified by the input, forced relofting was not performed until the second surface update. This approach was used because the first surface update usually involved large changes in the surface shape, and it was believed

that attempting to force closure at the same time might lead to convergence difficulties.

Test Case A

As shown on Figure 12, the objective of Case A was to modify only the upper surface between 45% and 85% semi-span. As indicated above, the input pressure distribution for the design region corresponded to that of a wing composed of airfoil sections which were thicker than a NACA 0012 in the aft portion of each section; and these pressures were previously obtained with a corresponding analysis computation. Thus, since this case also required trailing edge closure, Case A was a test of the ability of the method to reproduce the airfoil sections of a known wing. Both subcritical, designated Case A1, and supercritical, designated Case A2, solutions were obtained.

The resultant designed airfoil sections for the case having a subcritical freestream are shown on Figure 13. As can be seen, the designed sections are considerably different than the original NACA 0012 airfoils; and they are in reasonable agreement, even on the expanded scale, with the target sections. However, there are some slight discrepancies at the boundary stations at 50% and 80% semi-span. It is believed that these are due to a combination of terminating the computation prior to ultimate convergence and to the significant variation in spanwise slope near the trailing edge resulting from the change between the NACA 0012 sections in the analysis zones to the designed airfoils in the inverse regions. Nevertheless, it is believed that the agreement between the designed surfaces and the target surfaces is adequate.

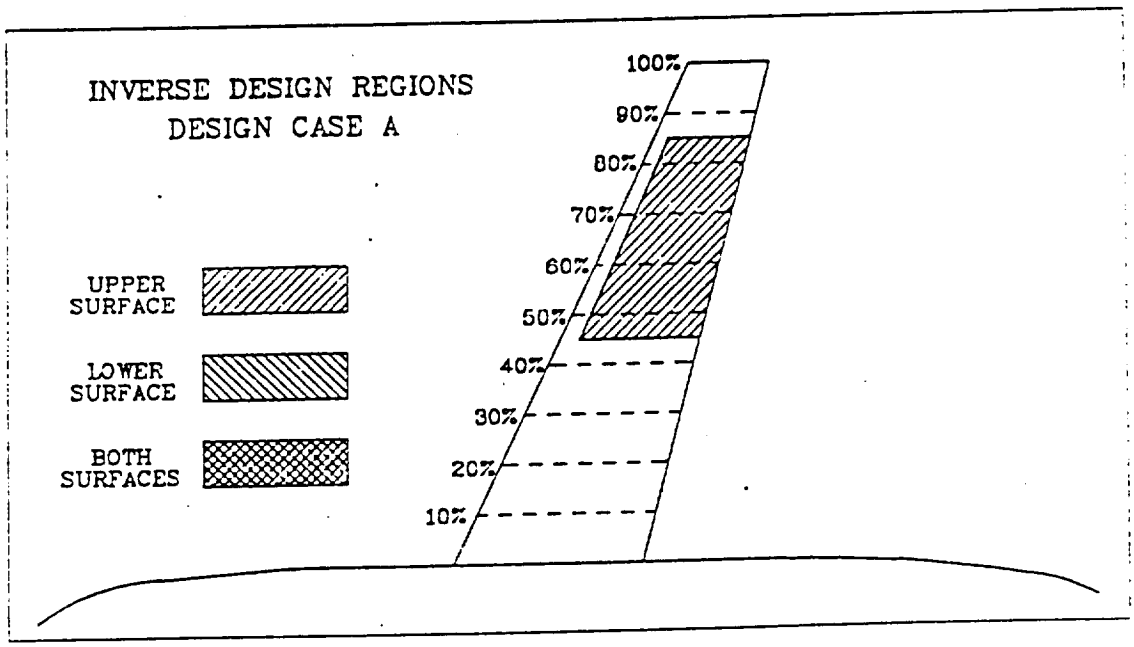

Figure 12. Inverse Design Regions for Case A

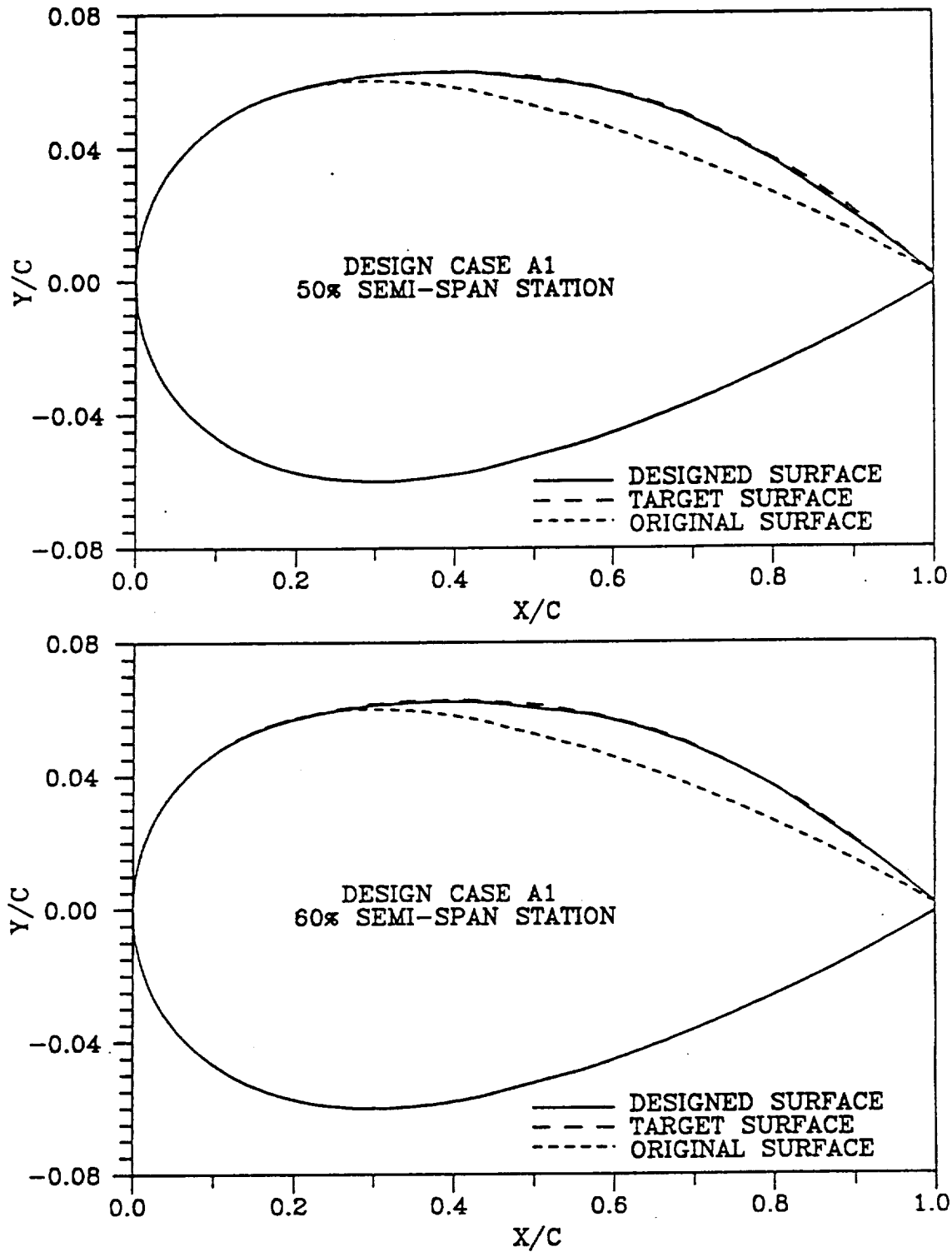

Figure 13. Comparison of Designed Sections with Original and Target Sections (Case A1)

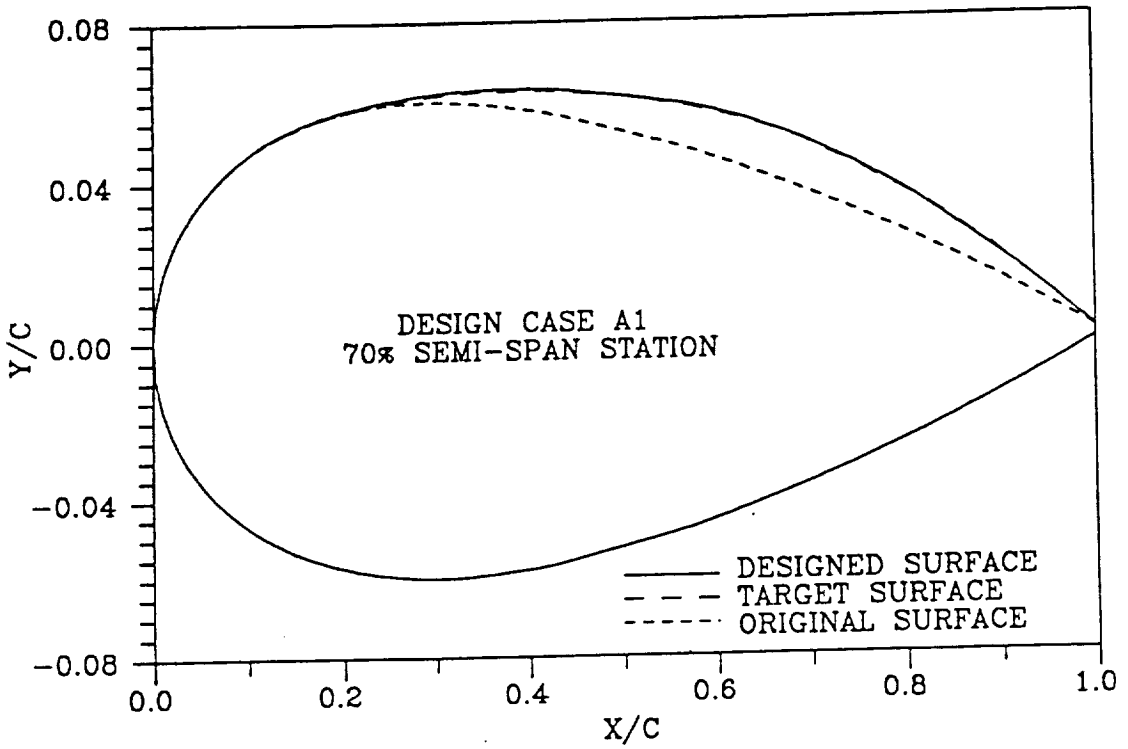

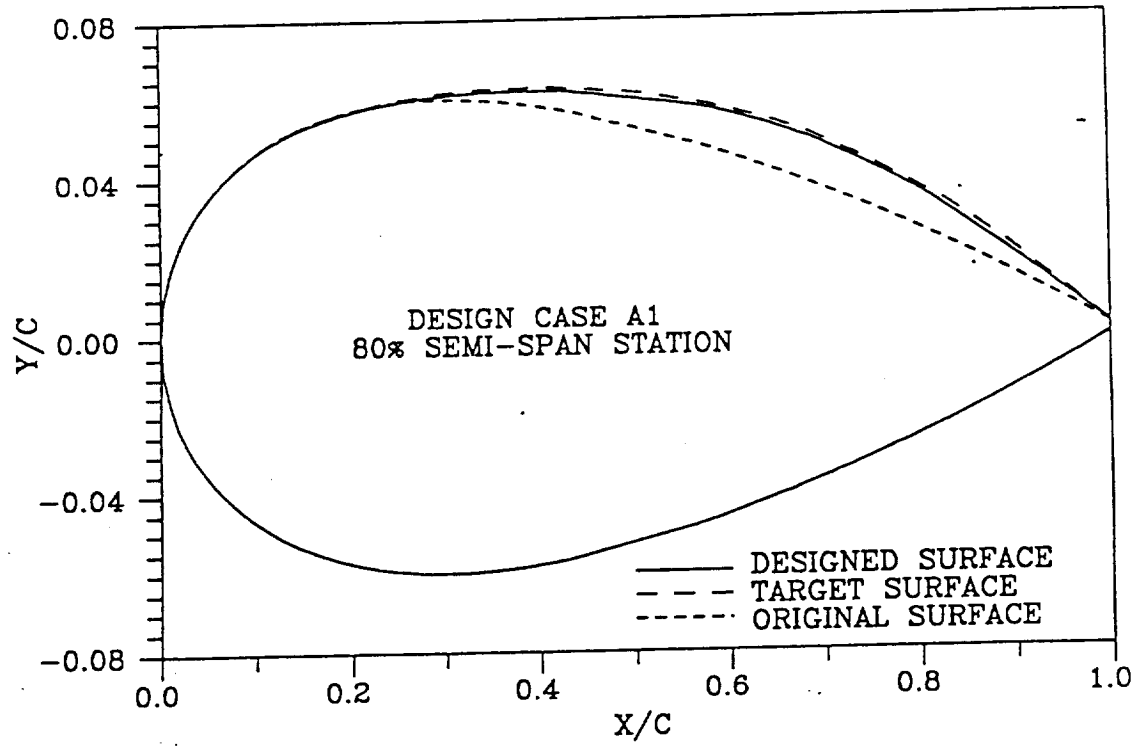

Figure 13. (Continued)

The true test, however, of an inverse wing design method is not its ability to reproduce "known" airfoil sections but rather a comparison between the target pressure distributions used to design the wing and those computed by an analysis of the designed wing. Figure 14 presents such a comparison for subcritical Case A1; and, as can be seen, the analysis results for the designed wing (labeled "designed surface pressures") are in excellent agreement with the target pressures as are the local lift coefficients.

Figure 15 and 16 show similar section profiles and pressure distribution for Case A2 at supercritical conditions. Again the agreement between the designed surfaces and the target surfaces and the pressures from an analysis of the designed wing and the target pressures are excellent. It is believed that Figures 13-16 demonstrate that the current method can be used to modify the design of the upper surface of a wing mounted on a body.

Test Case B

This case, which is depicted on Figure 17, was created to test the ability of the method to design both upper and lower surfaces. Subcritical (Case B1) and supercritical (Case B2) results are shown on Figures 18-21. As in the previous case, trailing edge closure was required; and as a result the designed surface shapes have the same character as those for Case A in that there is good agreement at the inner stations but slight discrepancies between the designed surfaces and the target sections at the boundary stations. However, as shown on Figures 19 and 21, there is still excellent agreement between the pressures computed by an

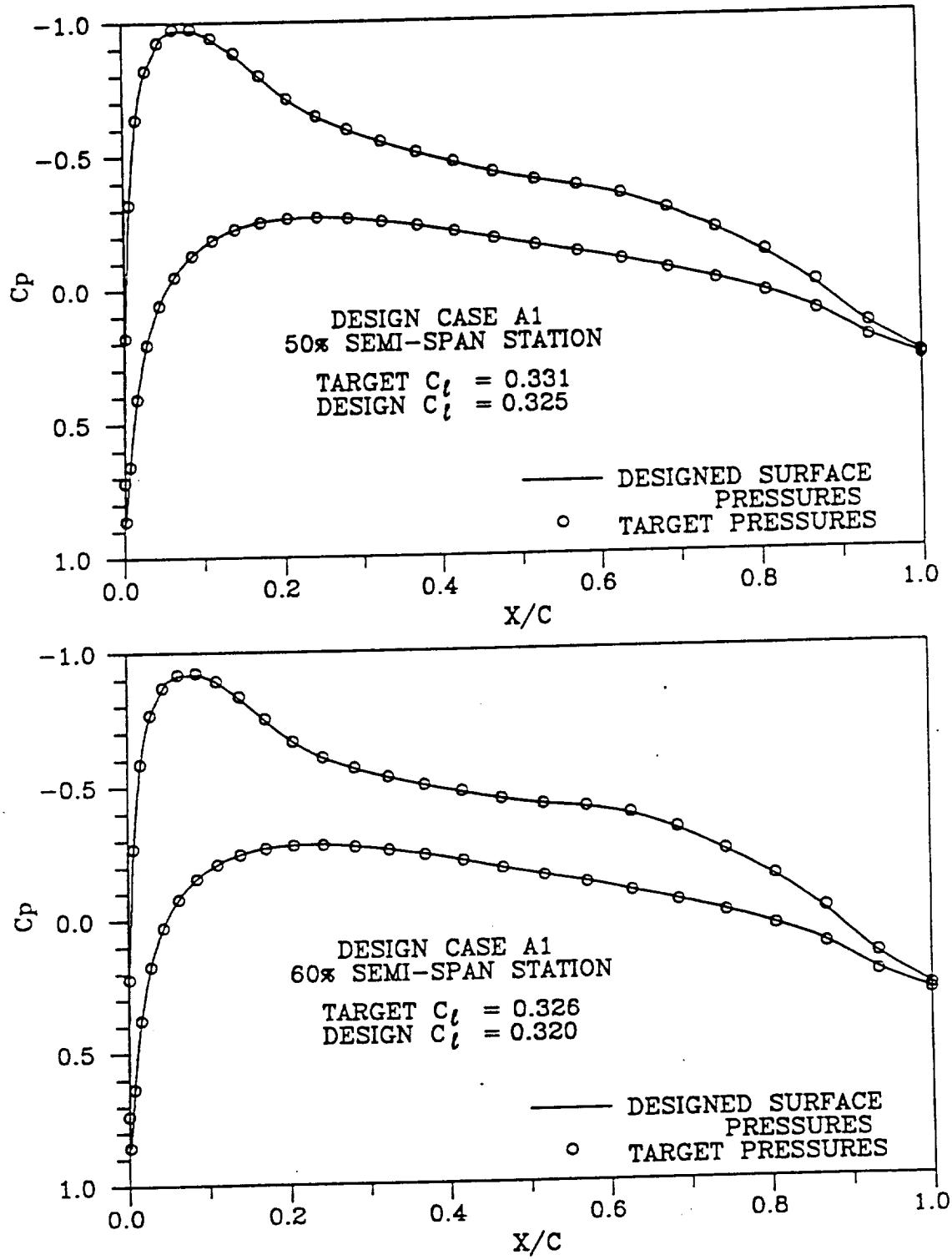

Figure 14. Comparison of Pressures from Analysis of Designed Wing with Target Distributions (Case A1)

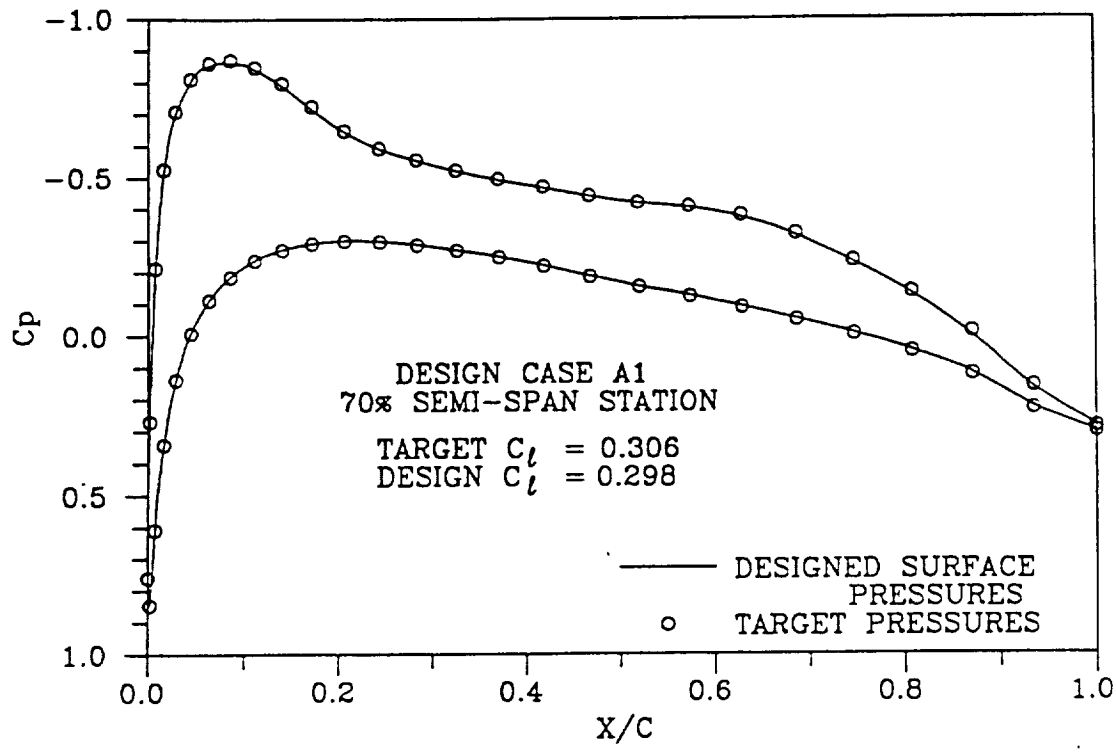

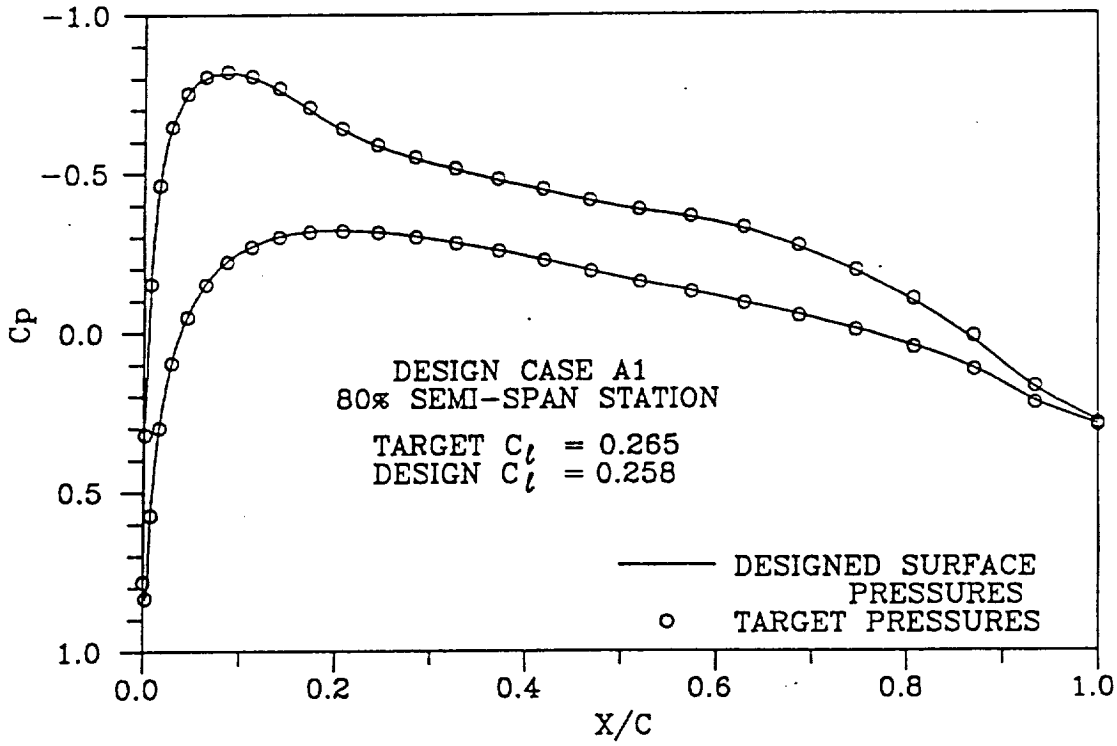

Figure 14. (Continued)

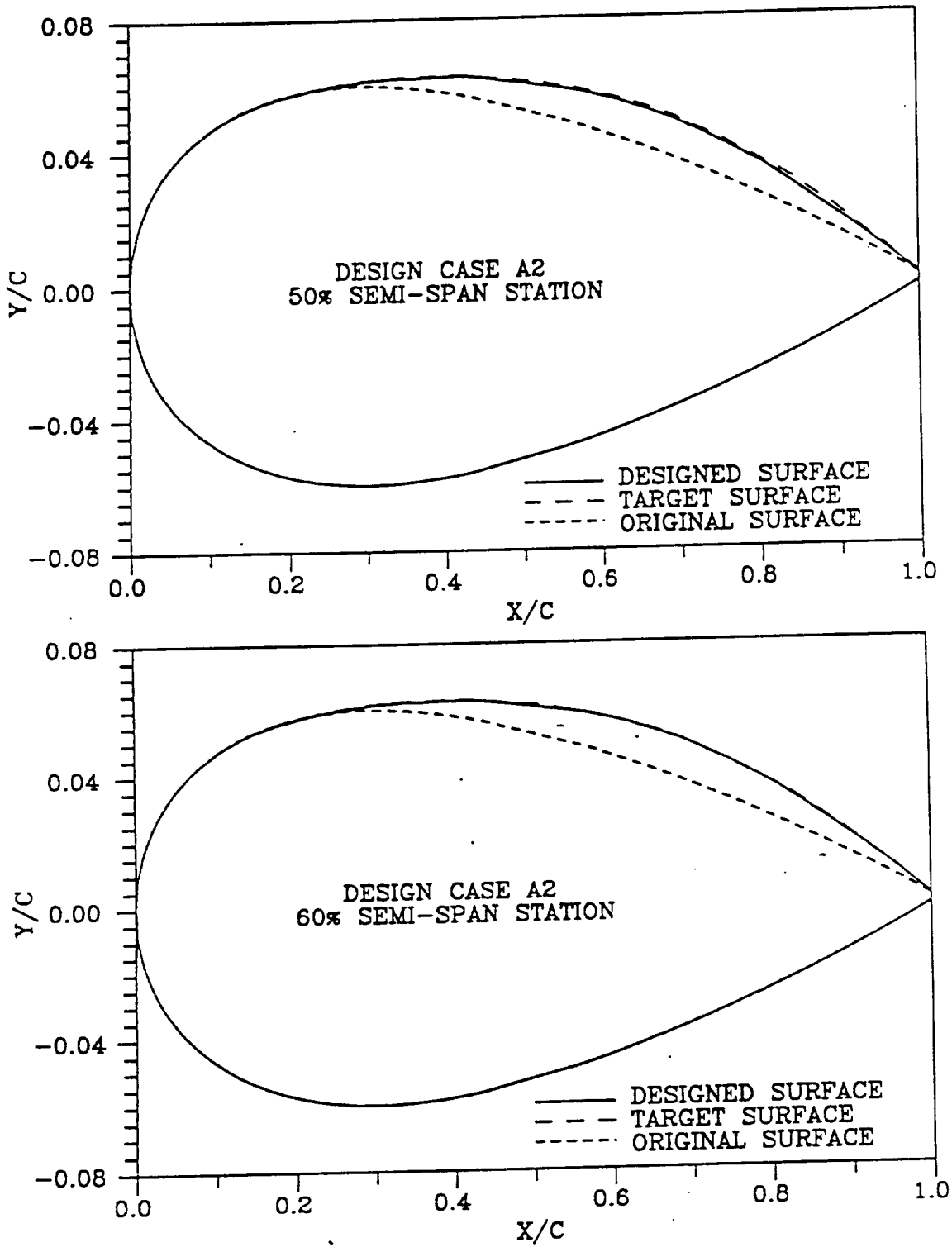

Figure 15. Comparison of Designed Sections with Original and Target Sections (Case A2)

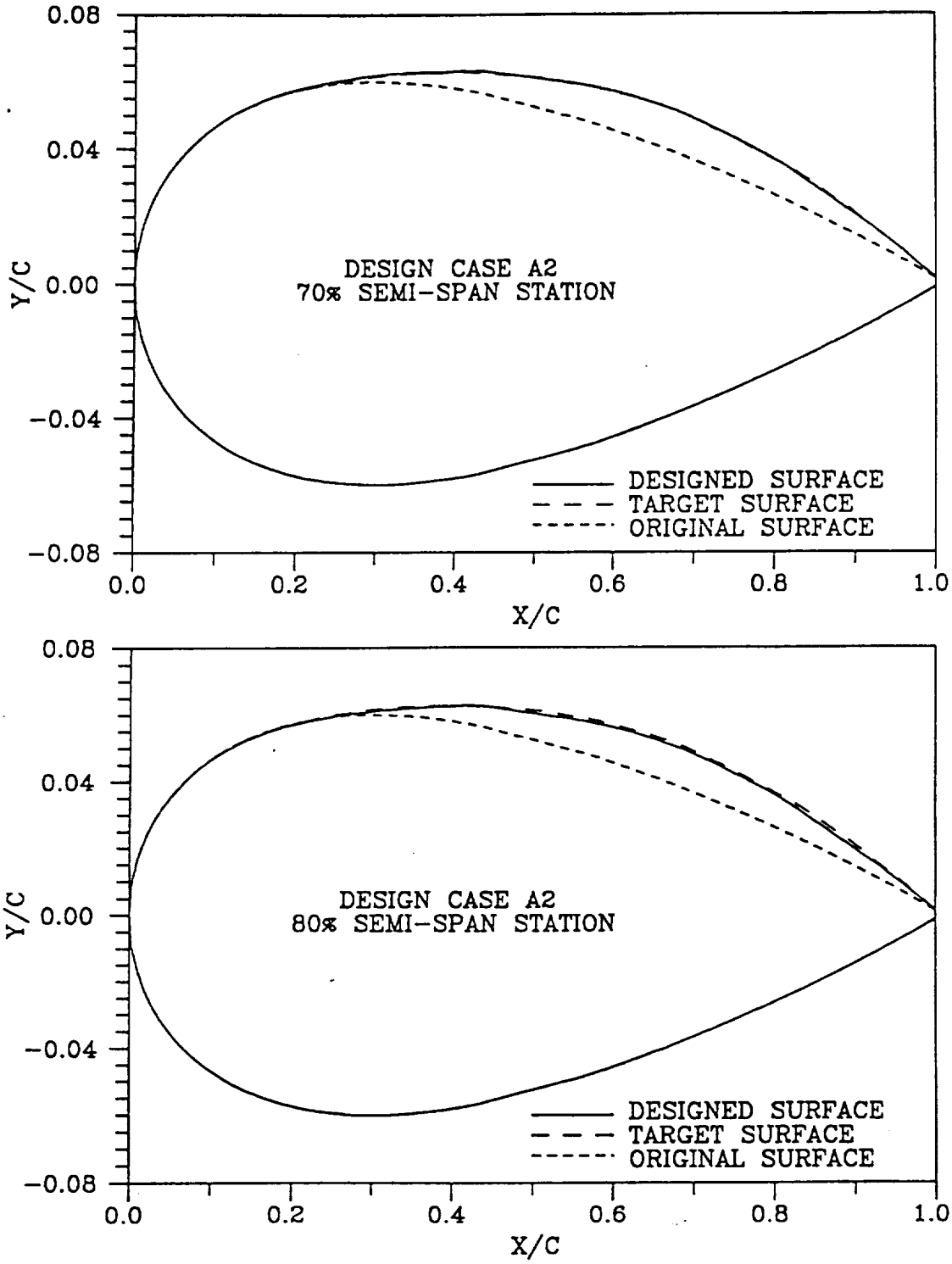

Figure 15. (Continued)

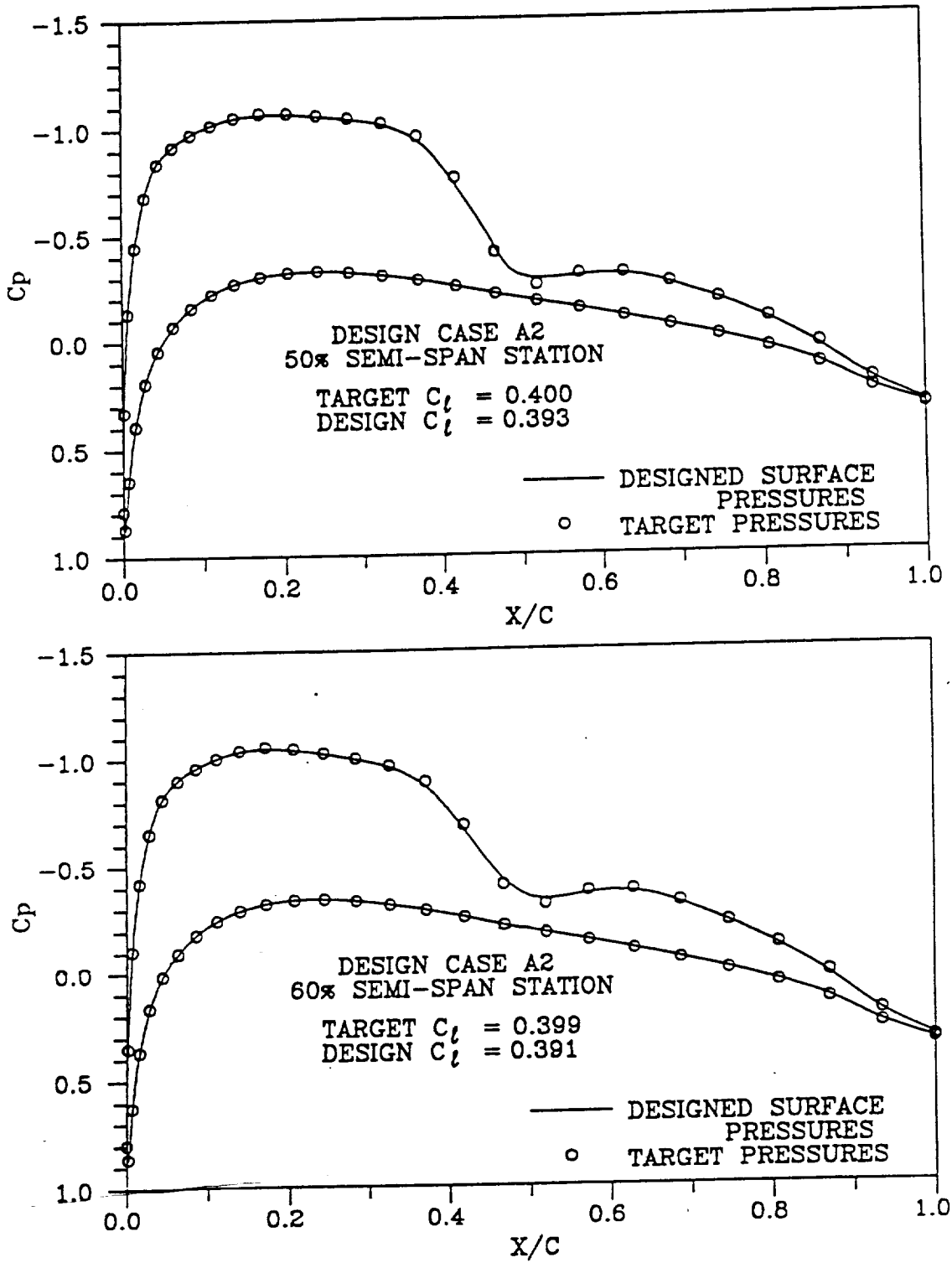

Figure 16. Comparison of Pressures from Analysis of Designed Wing with Target Distributions (Case A2)

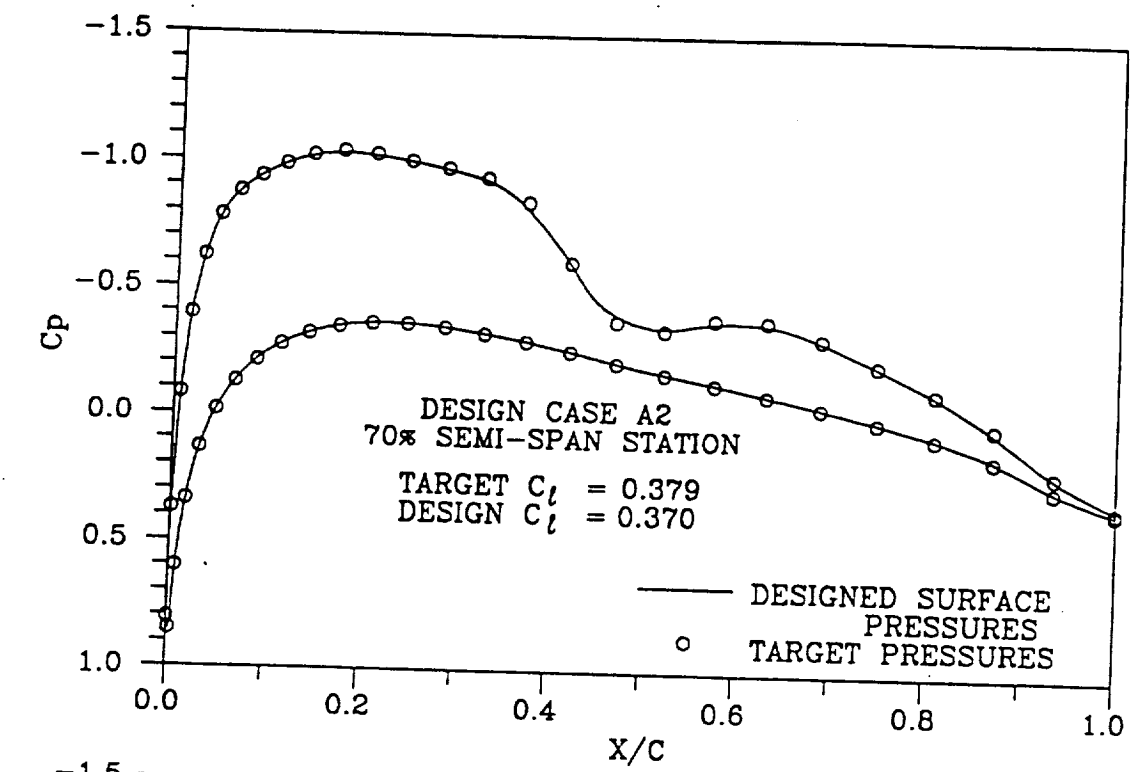

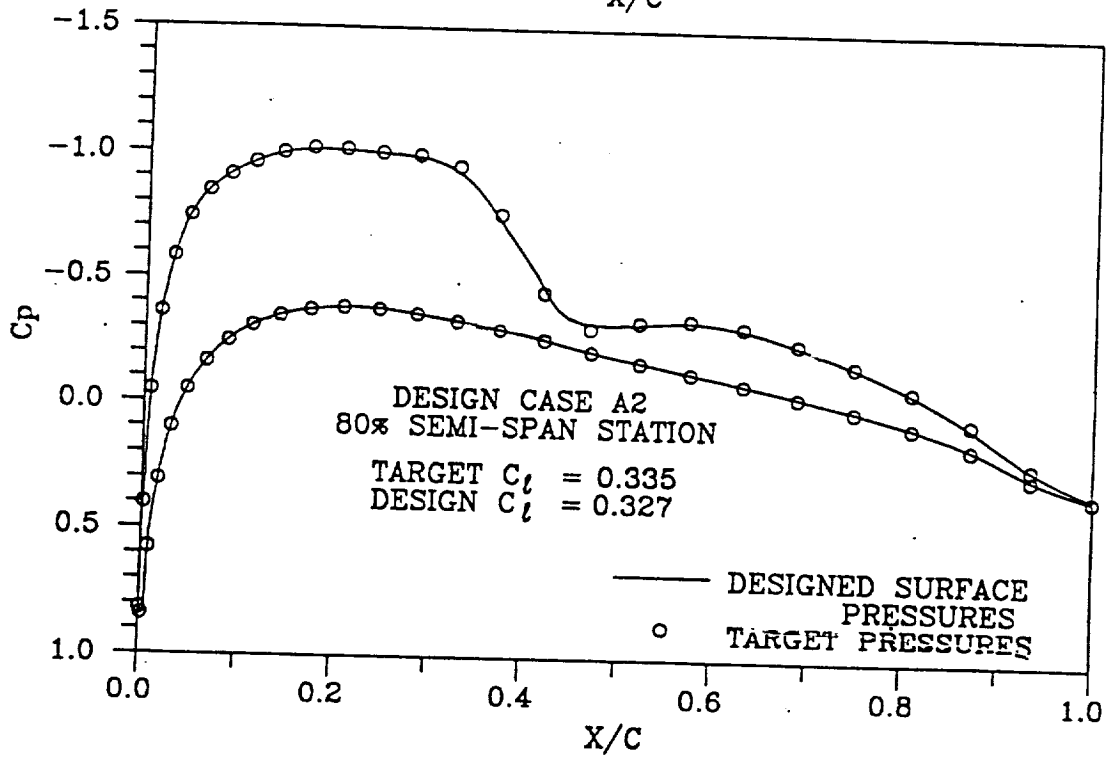

Figure 16. (Continued)

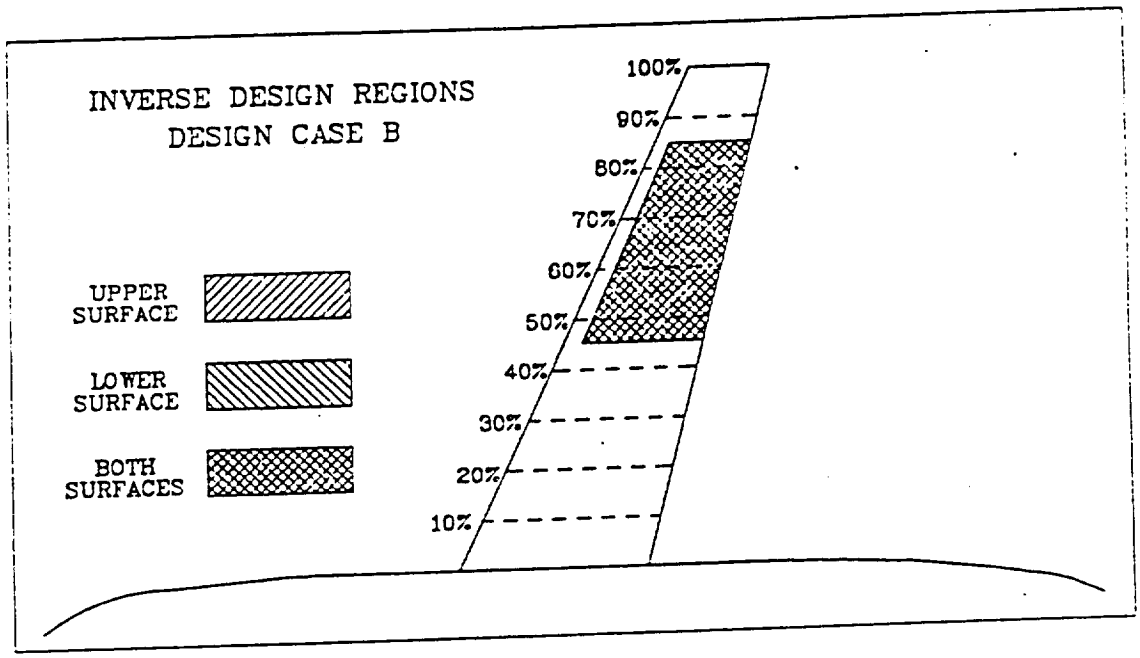

Figure 17. Inverse Design Regions for Case B

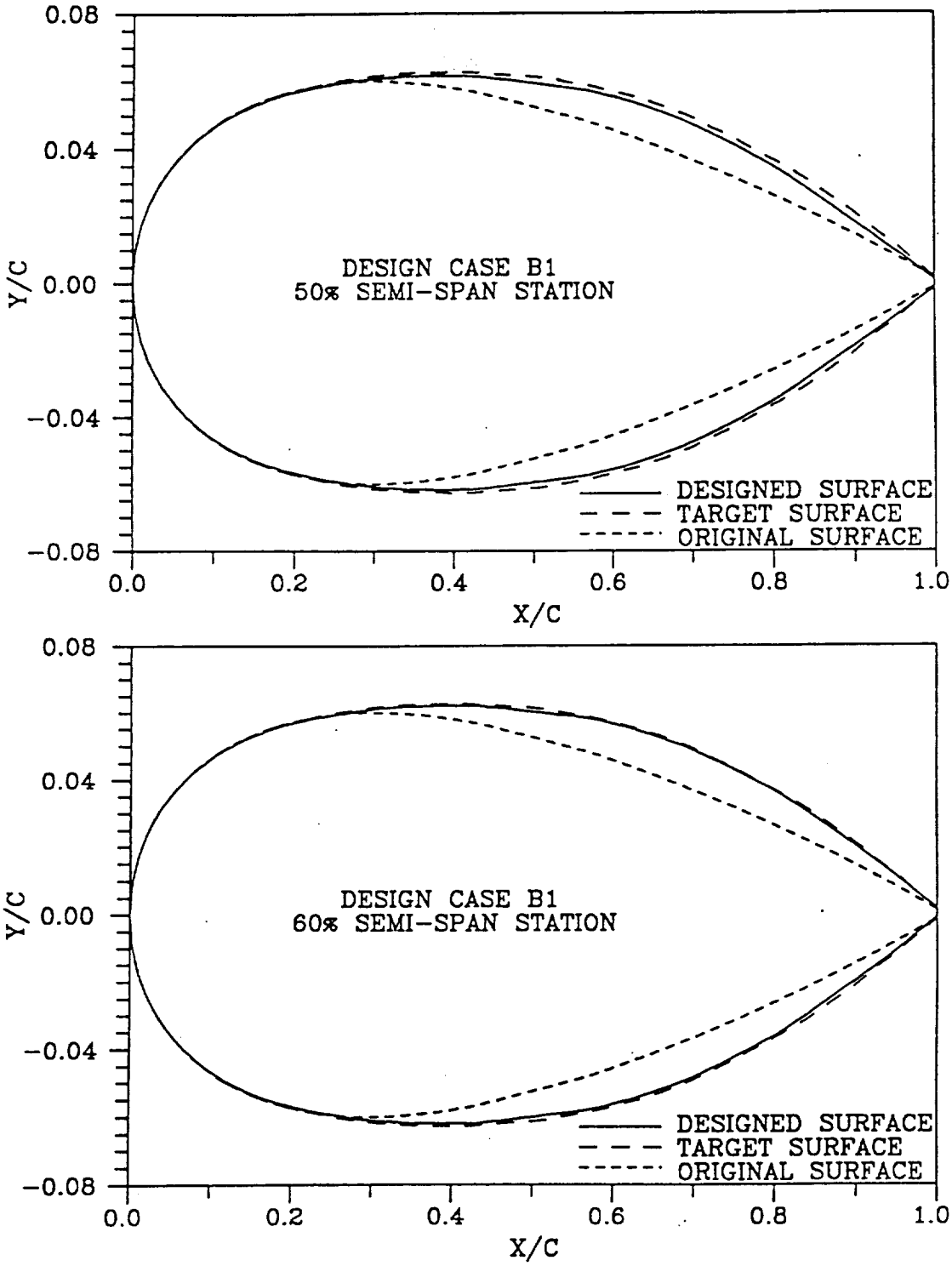

Figure 18. Comparison of Designed Sections with Original and Target Sections (Case B1)

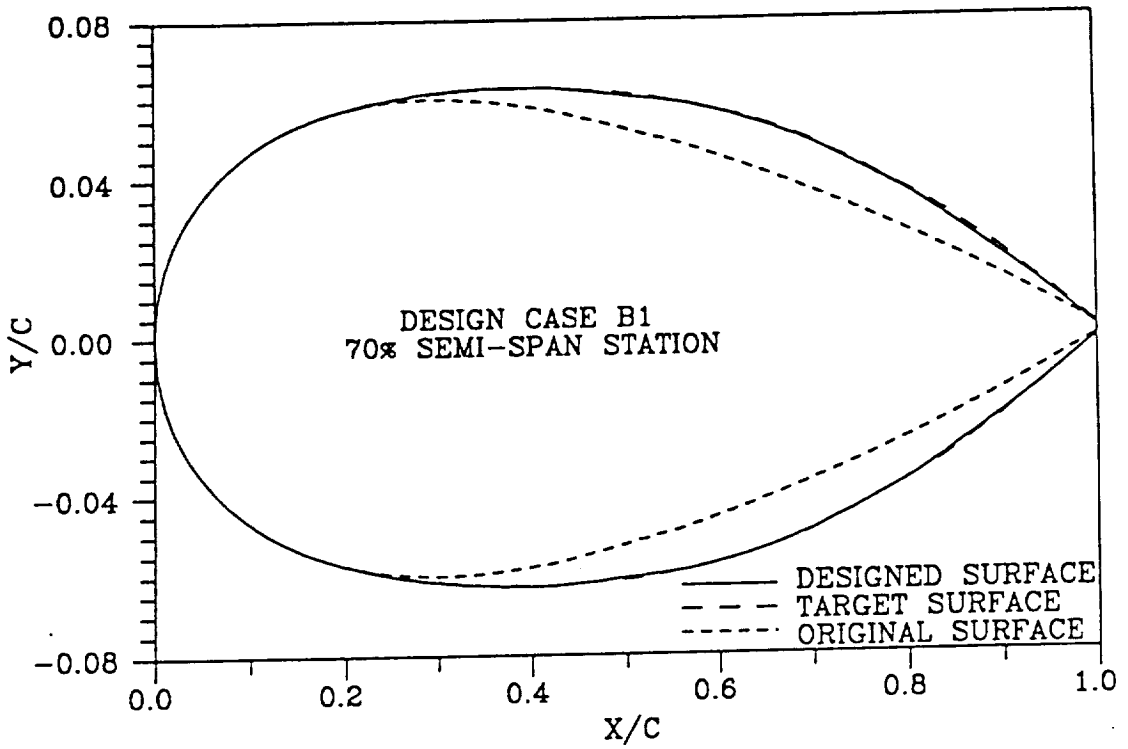

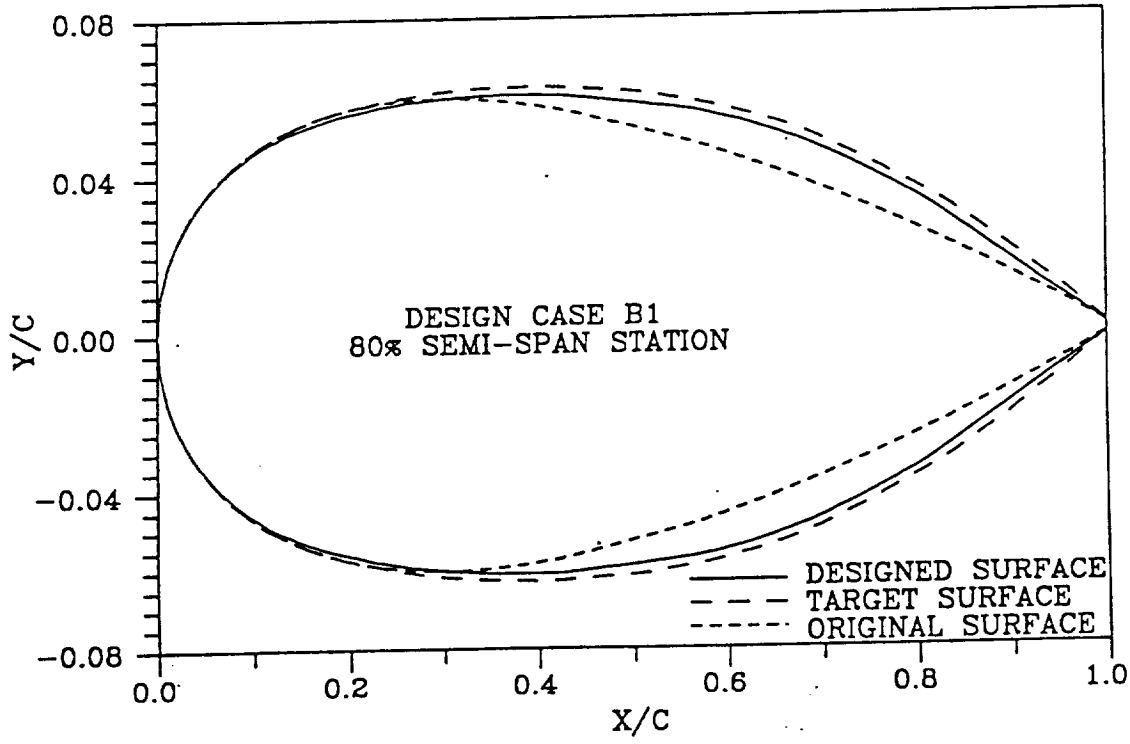

Figure 18. (Continued)

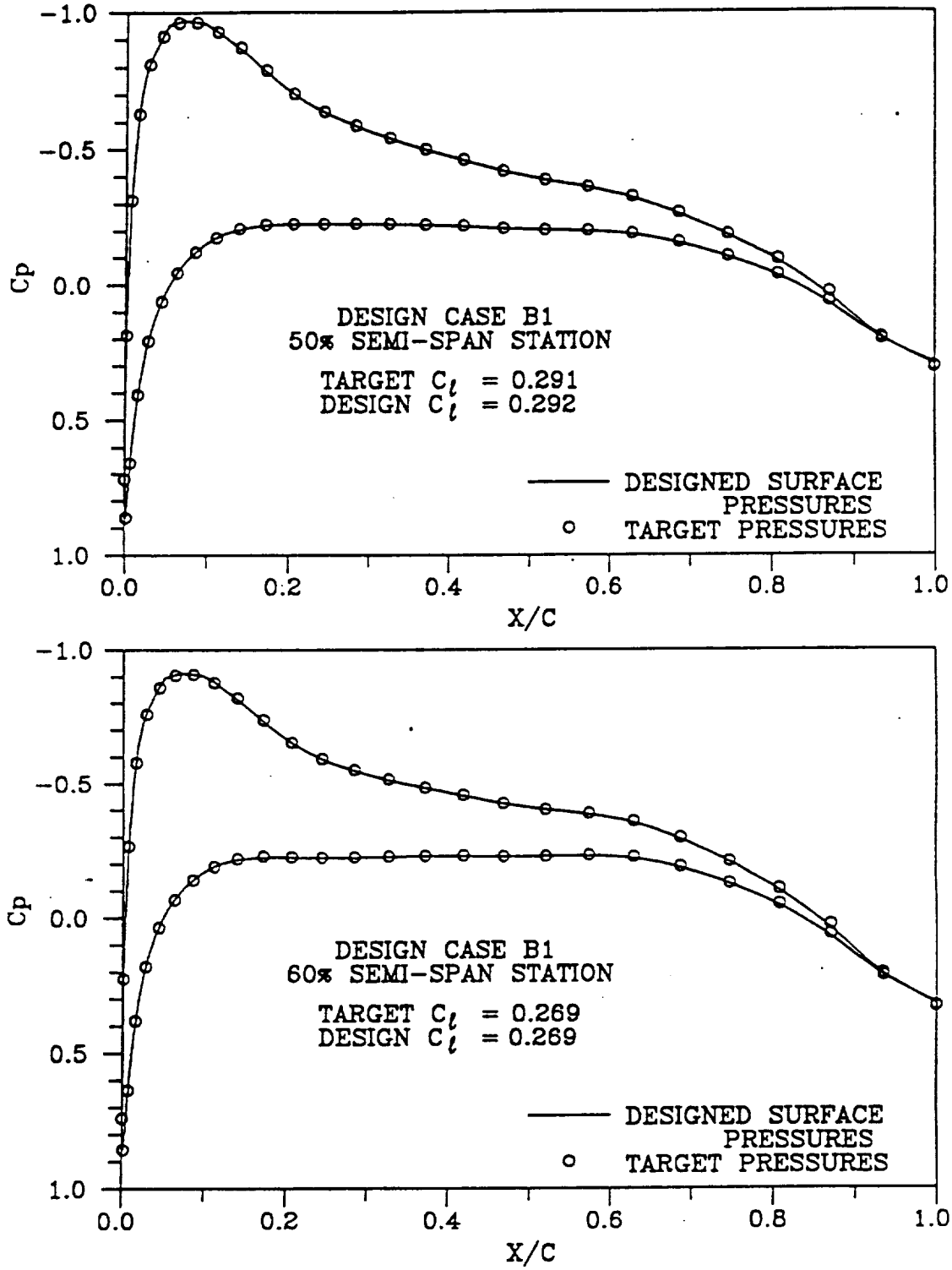

Figure 19. Comparison of Pressures from Analysis of Designed Wing with Target Distributions (Case B1)

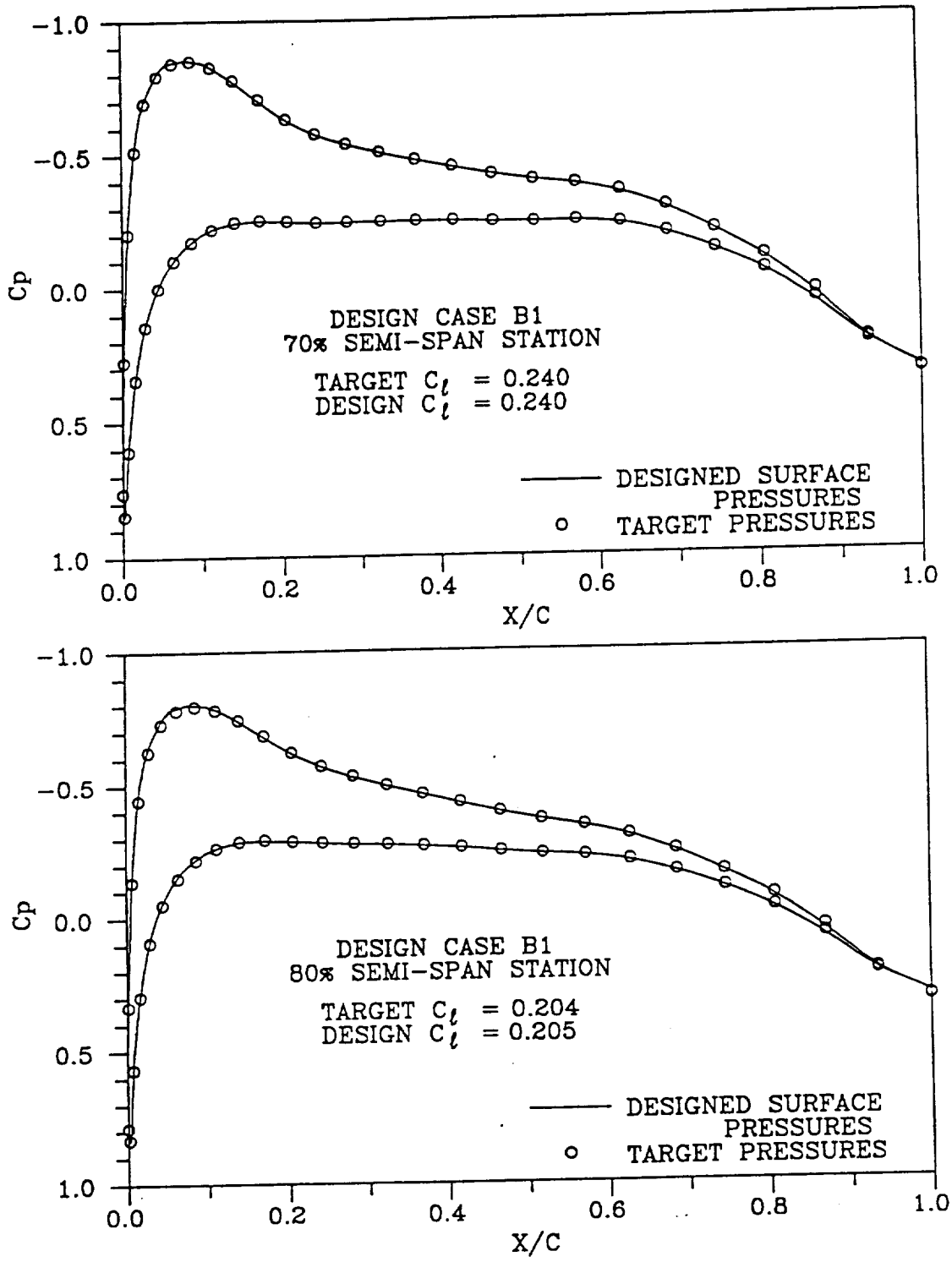

Figure 19. (Continued)

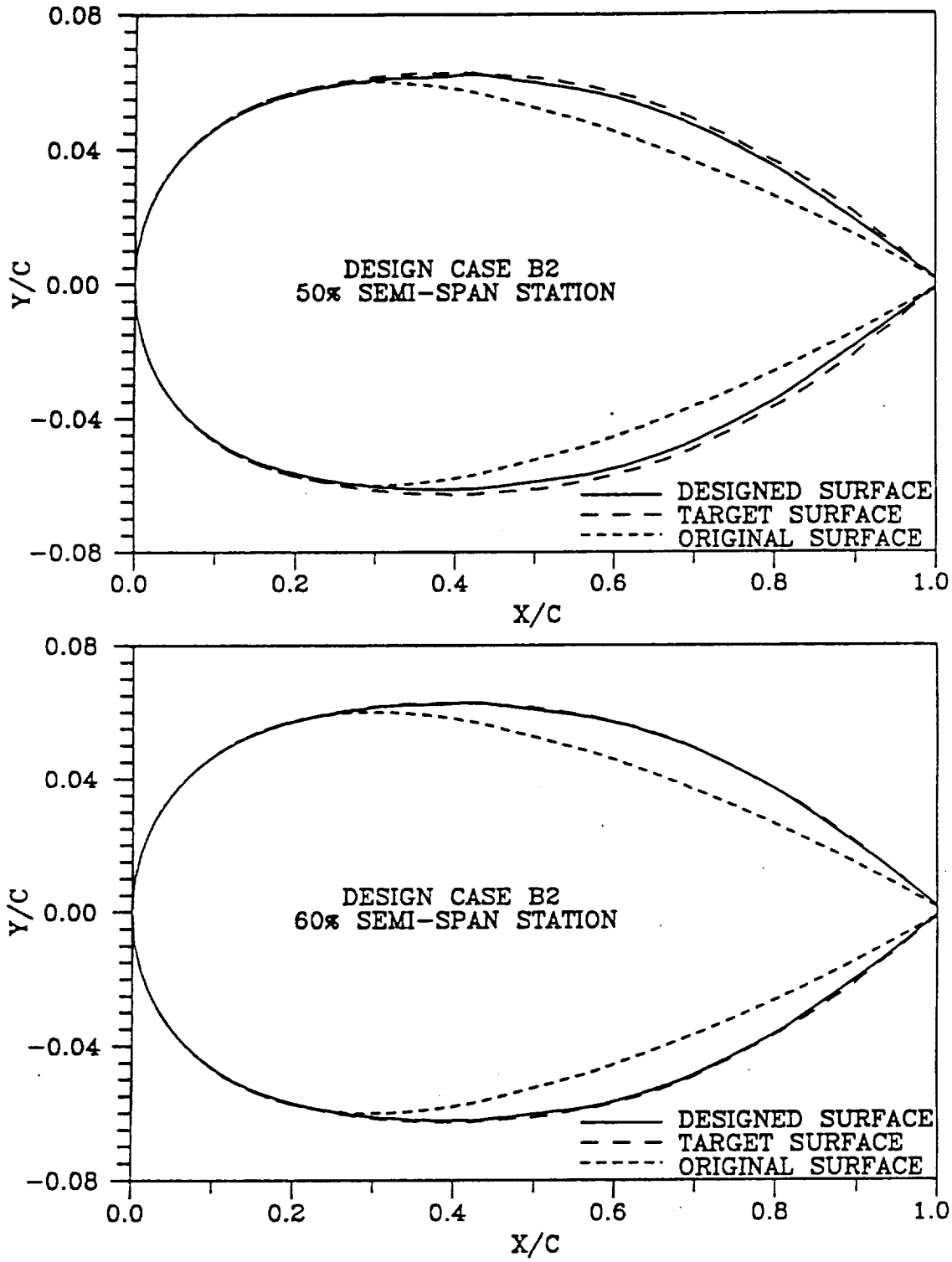

Figure 20. Comparison of Designed Sections with Original and Target Sections (Case B2)

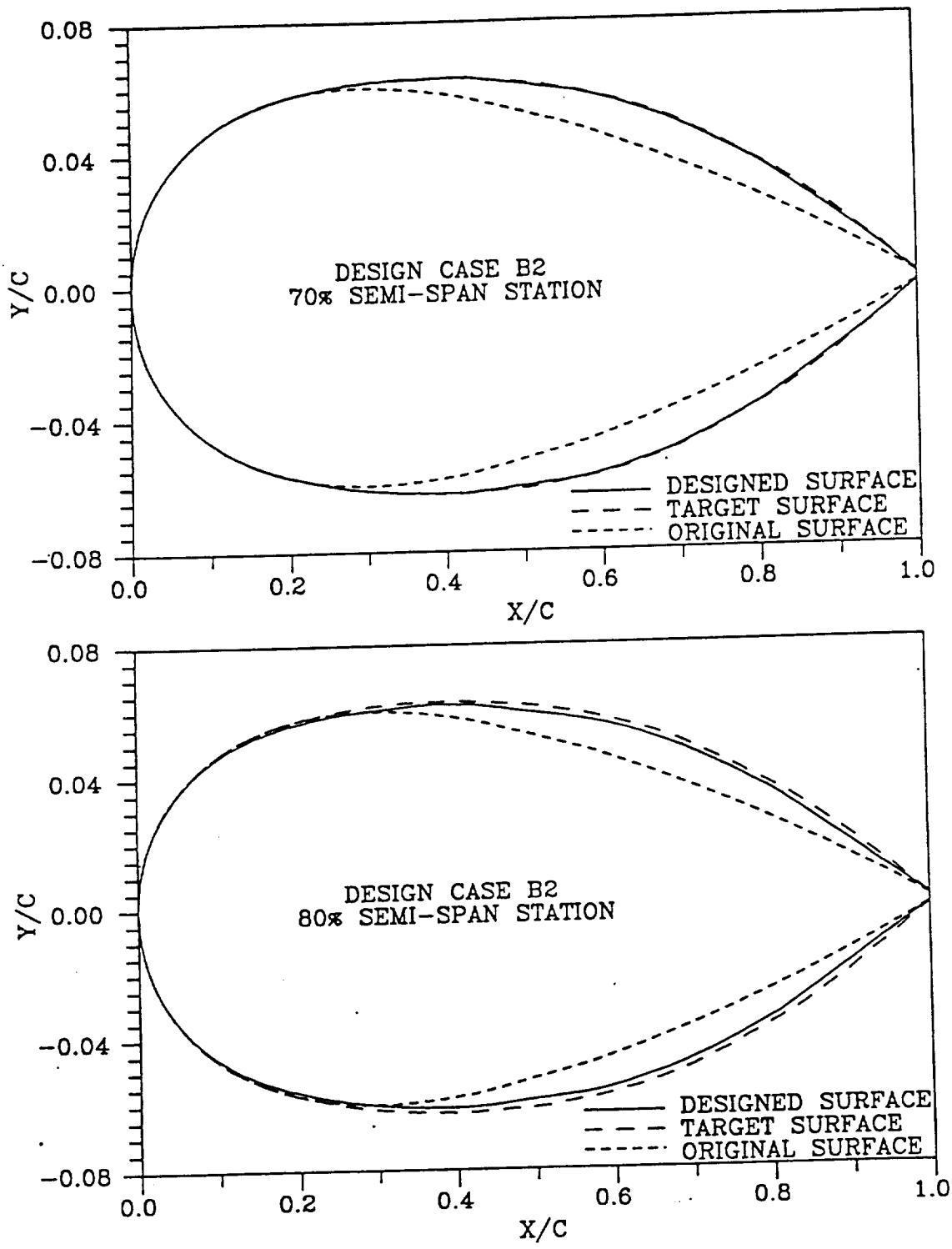

Figure 20. (Continued)

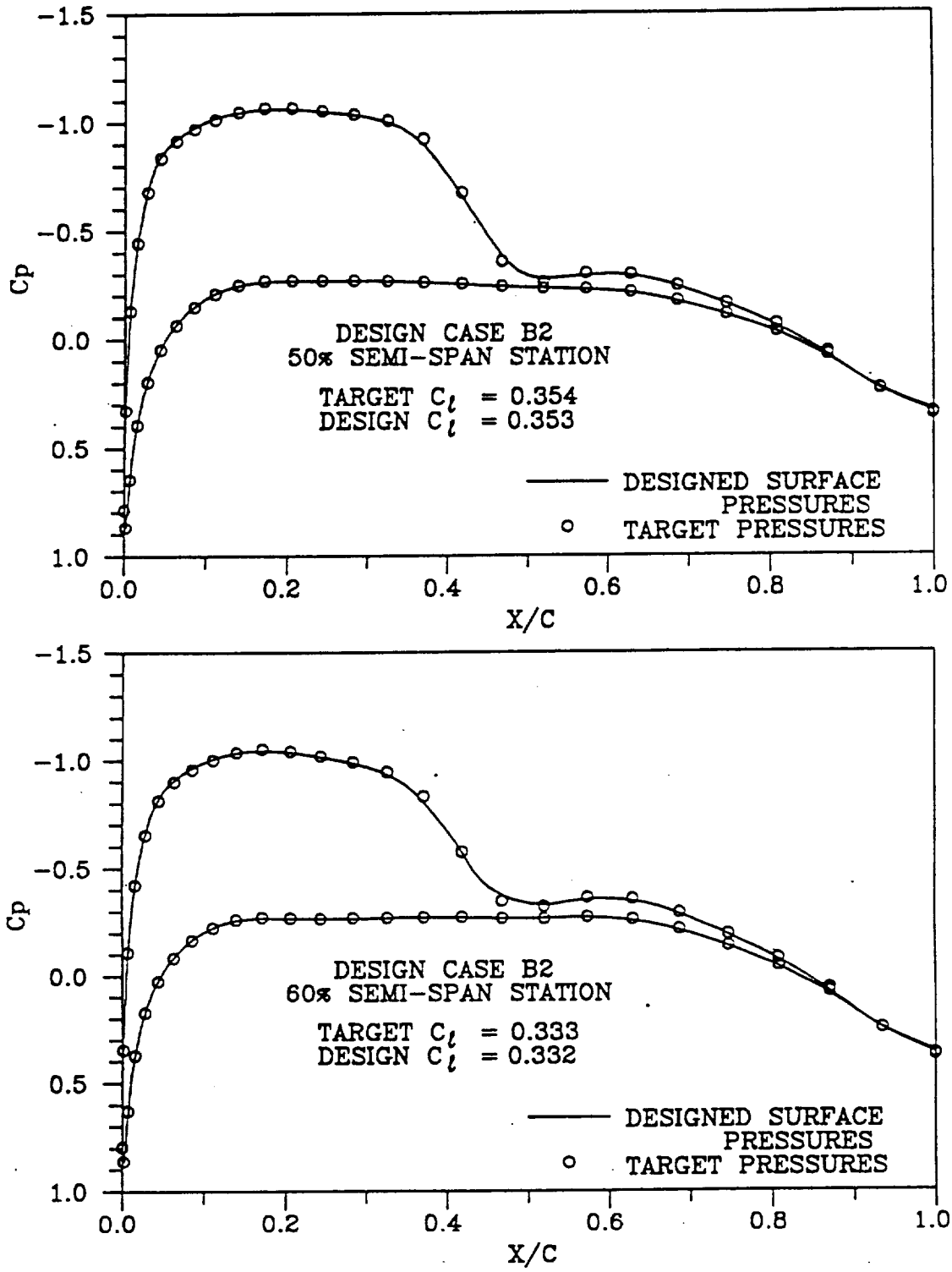

Figure 21. Comparison of Pressures from Analysis of Designed Wing with Target Distributions (Case B2)

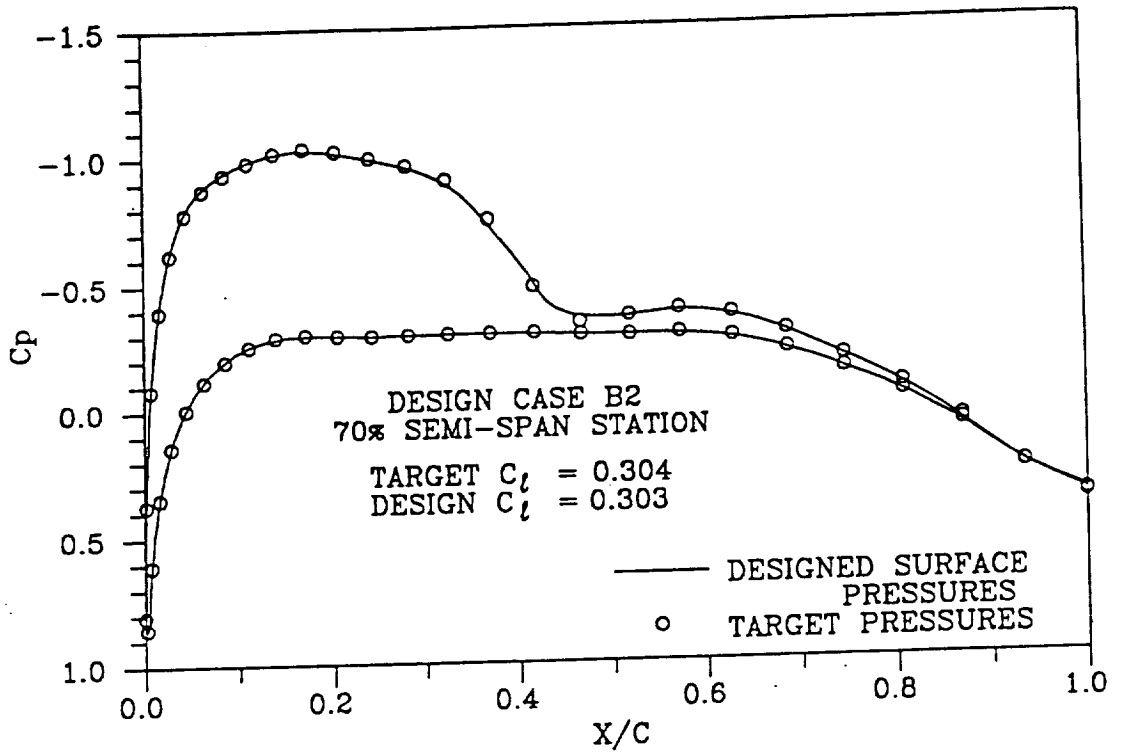

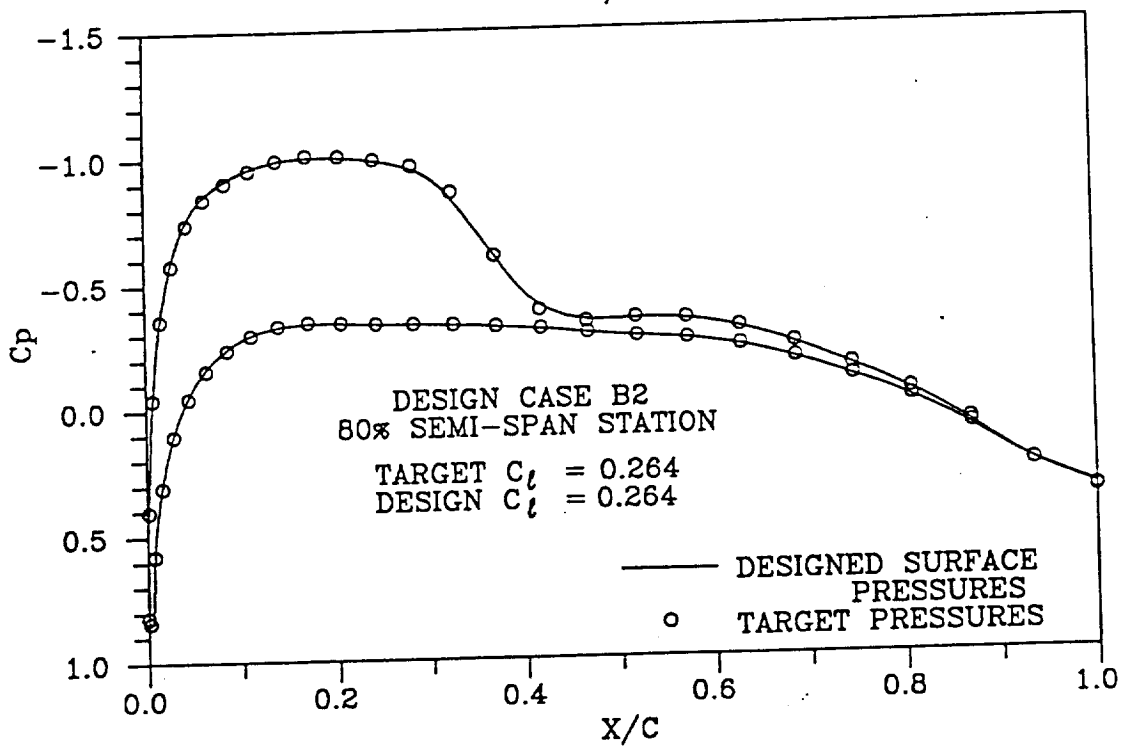

Figure 21. (Continued)

analysis of the designed wings and the desired target pressures used in the inverse design. Thus, it can be concluded that the method can be used to modify the design of the upper and lower surfaces of a wing mounted on a body.

Test Case C

The inverse design regions for Case C, which was an attempt to design both upper and lower surfaces on two noncontiguous regions of the wing at supercritical conditions, are shown on Figure 22; and a comparison between the initial pressure distribution associated with NACA 0012 sections and the target pressures is portrayed on Figure 23. As can be seen, the target pressure distribution essentially eliminates at inboard stations the upper surface shock wave present on the original wing; and at outboard stations it weakens the shock and moves it forward. In addition, significant changes in the lower surface pressure gradients are evident. Also shown on Figure 23 are the pressures computed by the program at the end of the inverse design procedure (denoted as "design pressures"). These pressures are in excellent agreement with the target pressures, which indicates that the method is satisfying properly the desired inverse boundary conditions.

The corresponding designed airfoil sections for this case are shown on Figure 24. Even on the expanded scale, the agreement between the designed and target surfaces is excellent at all design stations. However, trailing edge closure was not enforced for this case; and there is at the boundary stations some departure between the designed surfaces and the target surfaces near the trailing edge. Again it is believed

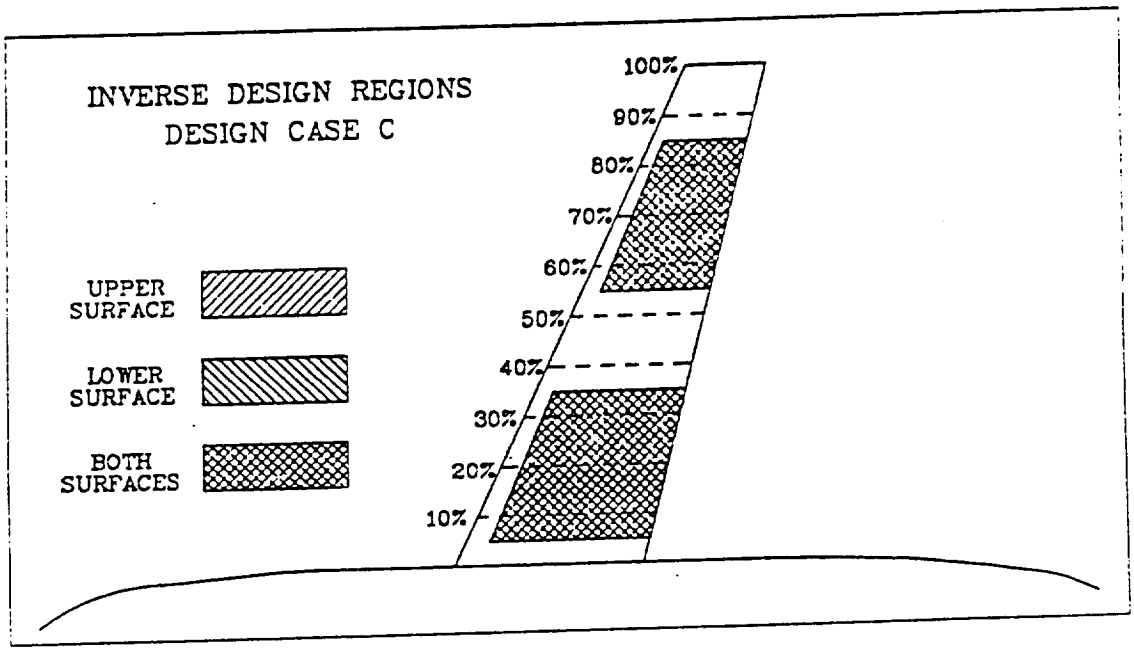

Figure 22. Inverse Design Regions for Case C

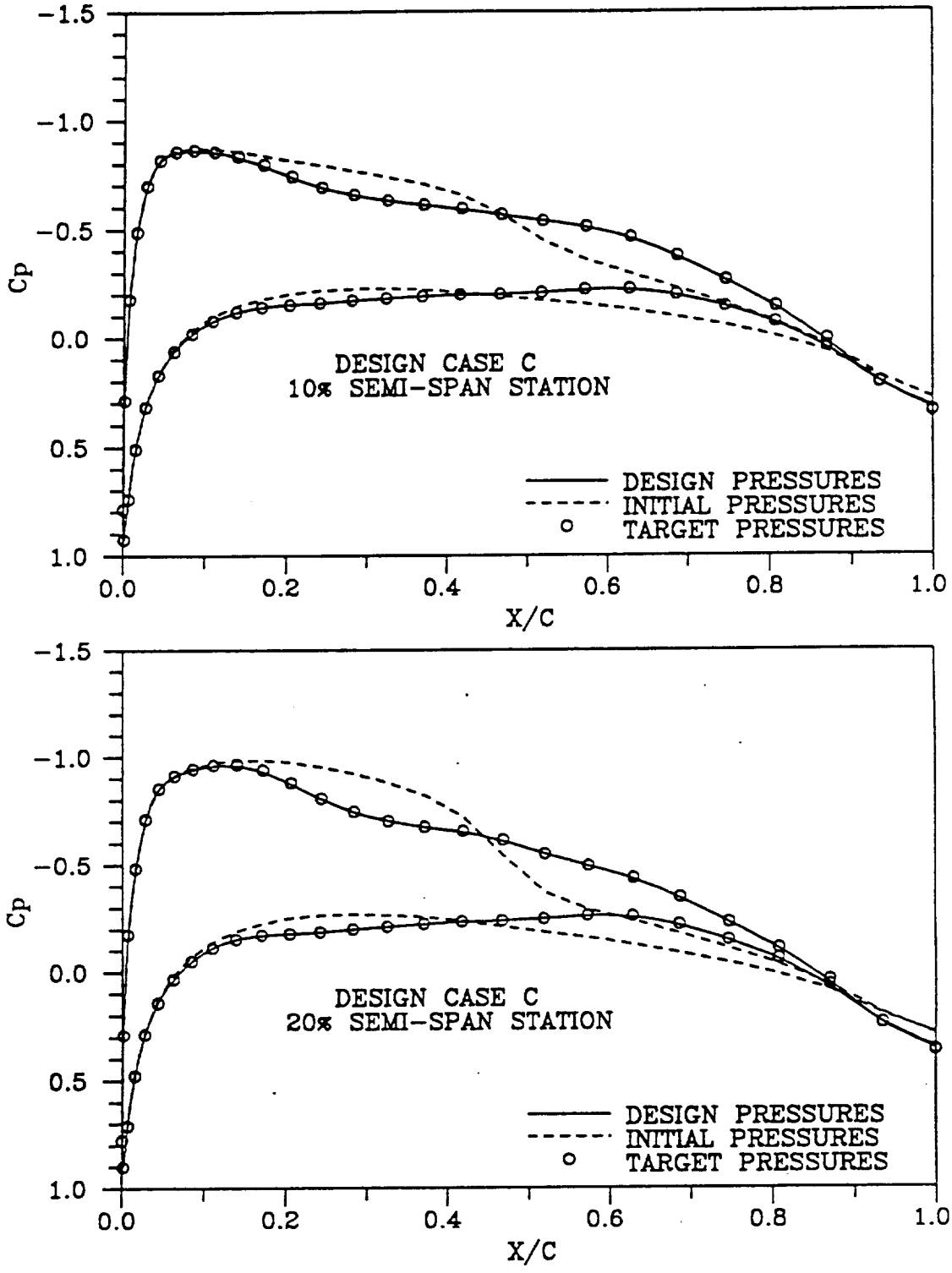

Figure 23. Comparison of Initial Pressures with Target Values (Case C)

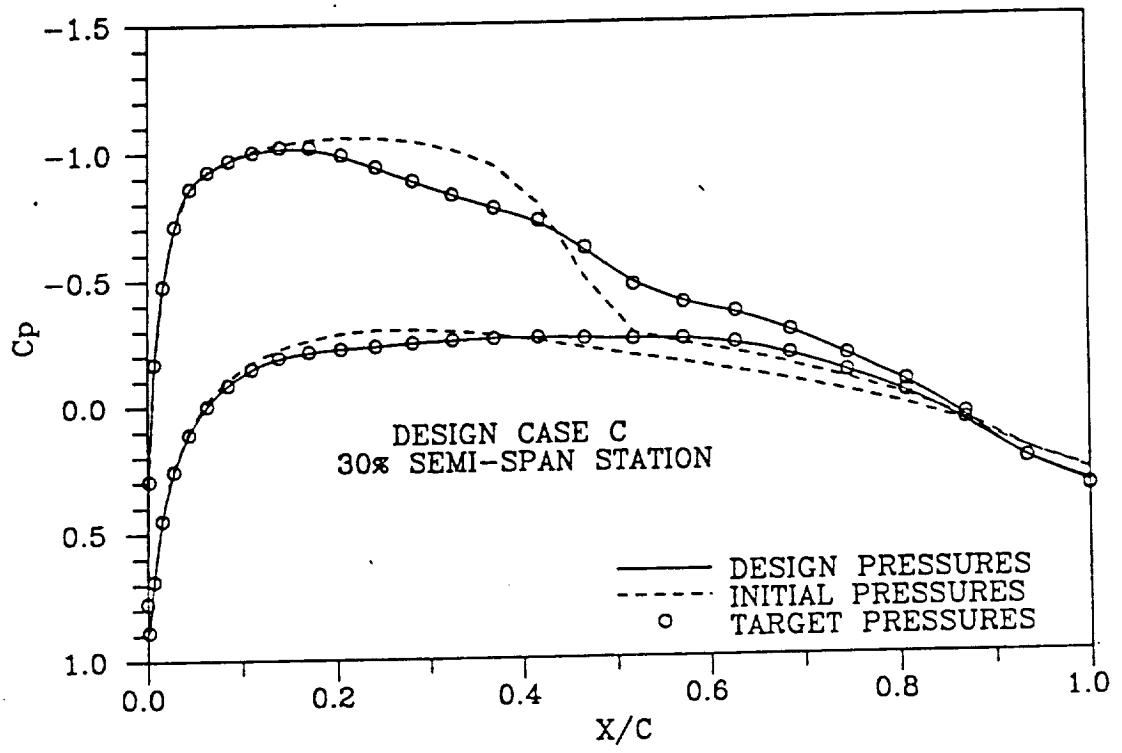

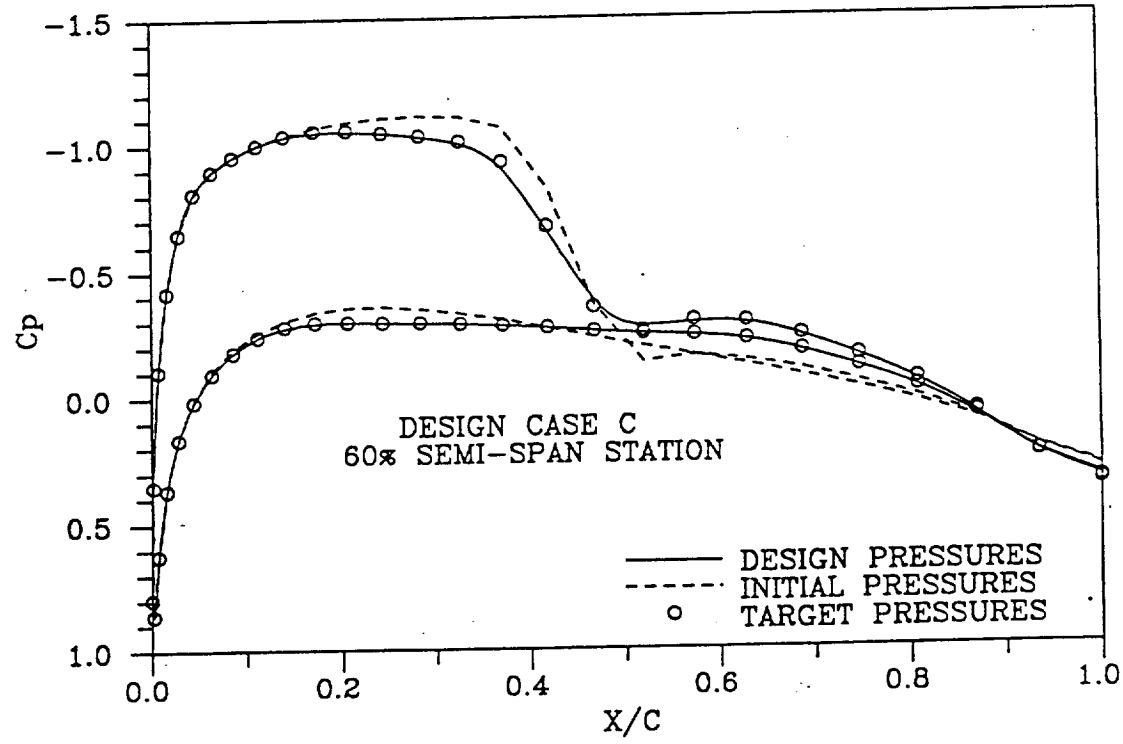

Figure 23. (Continued)

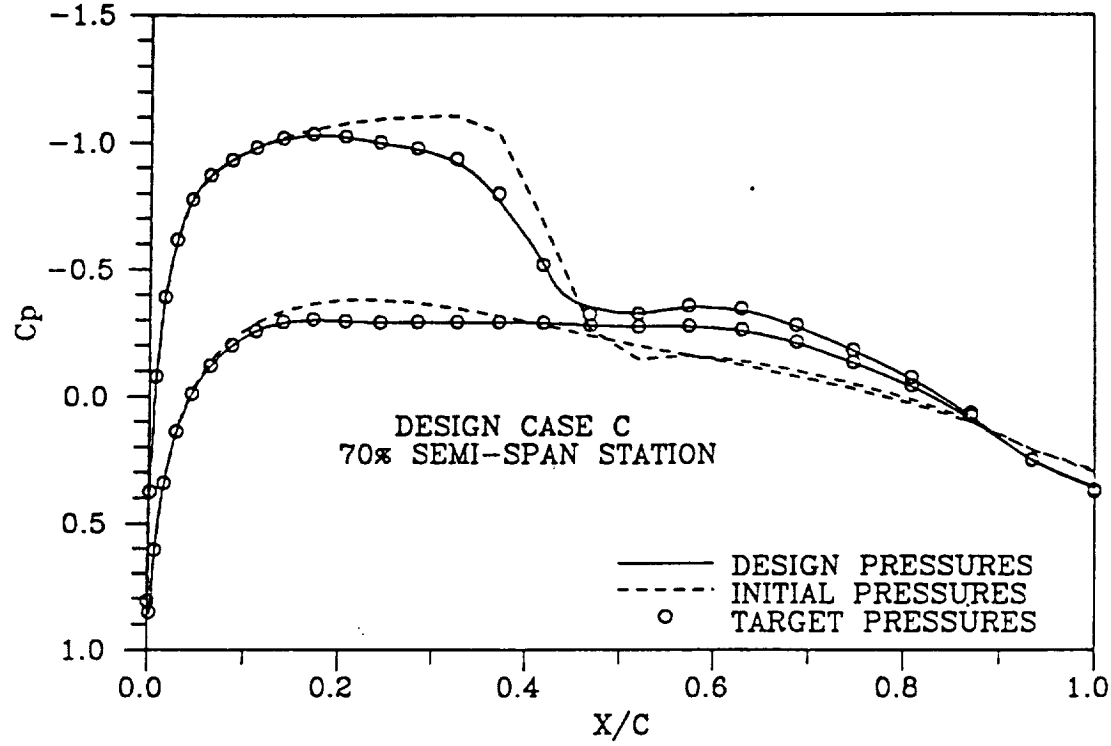

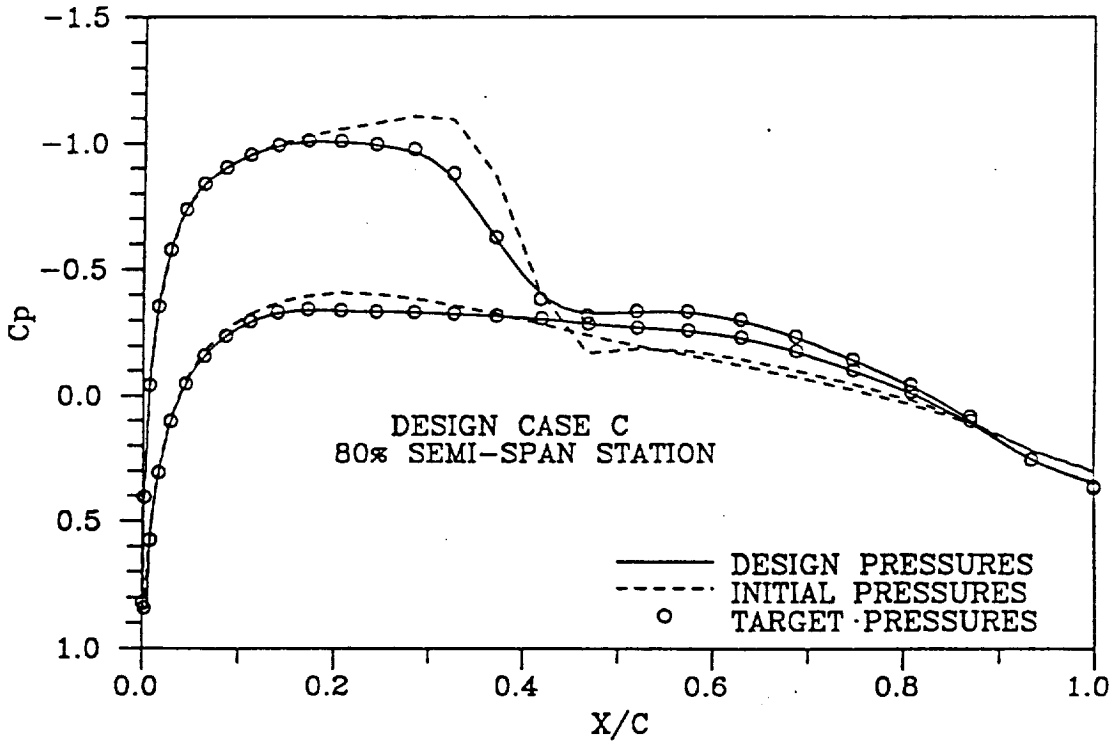

Figure 23. (Continued)

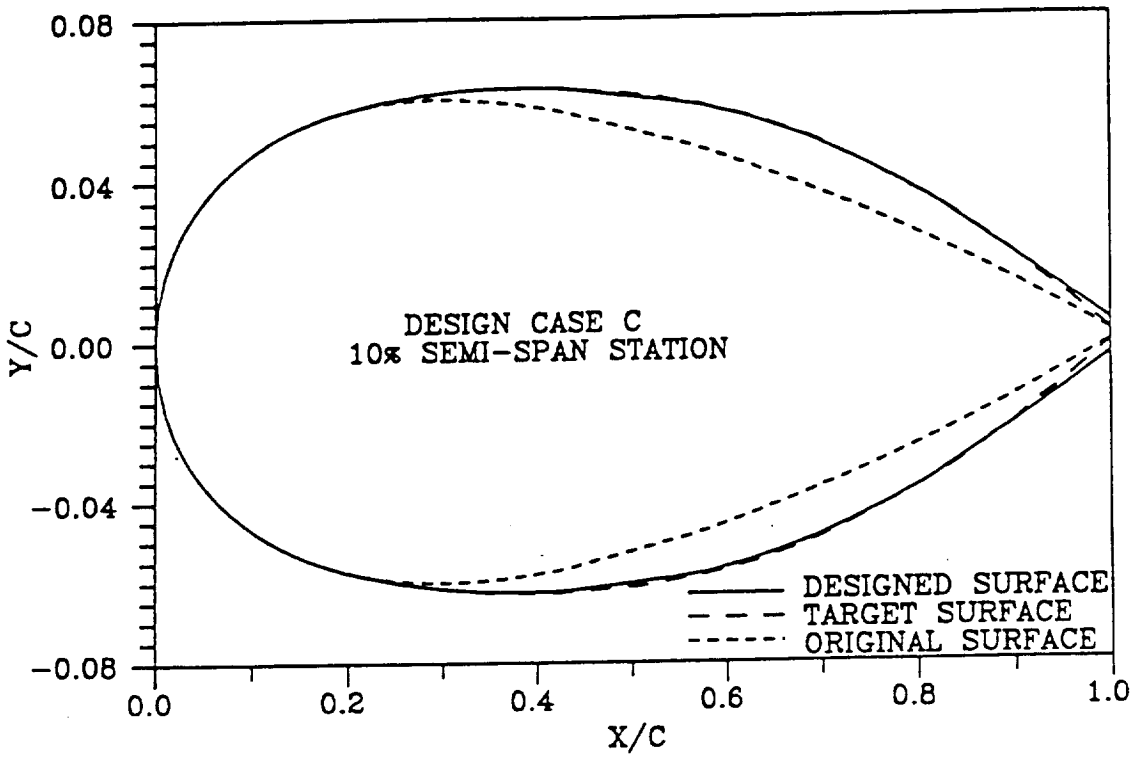

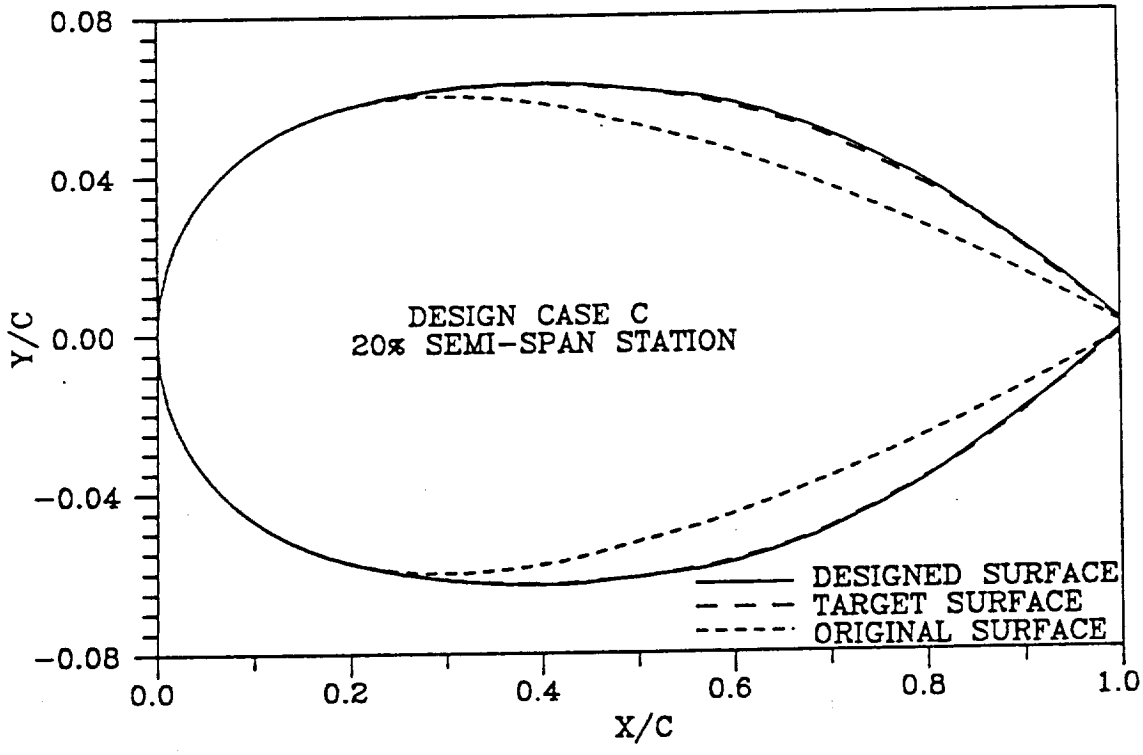

Figure 24. Comparison of Designed Sections with Original and Target Sections (Case C)

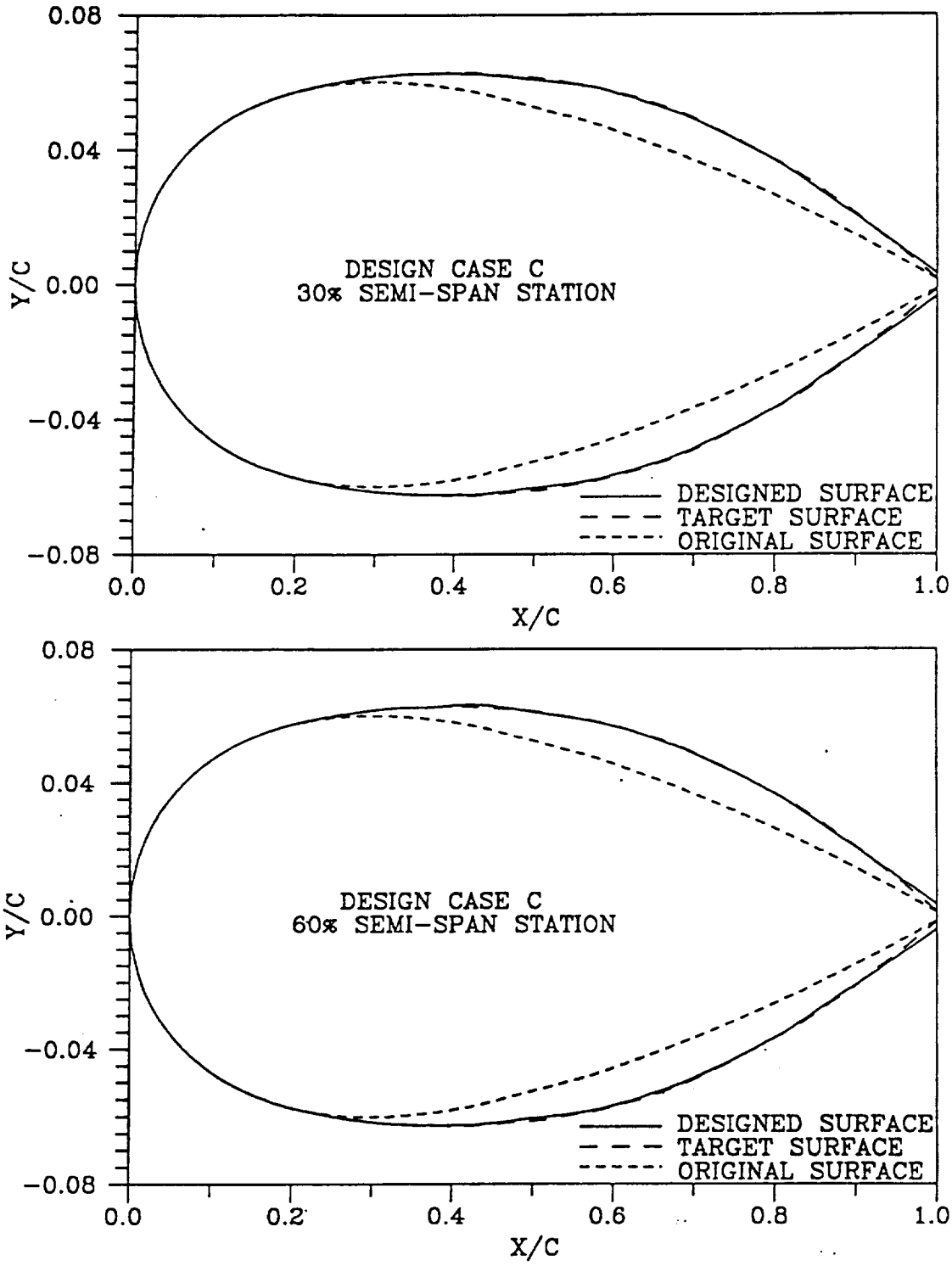

Figure 24. (Continued)

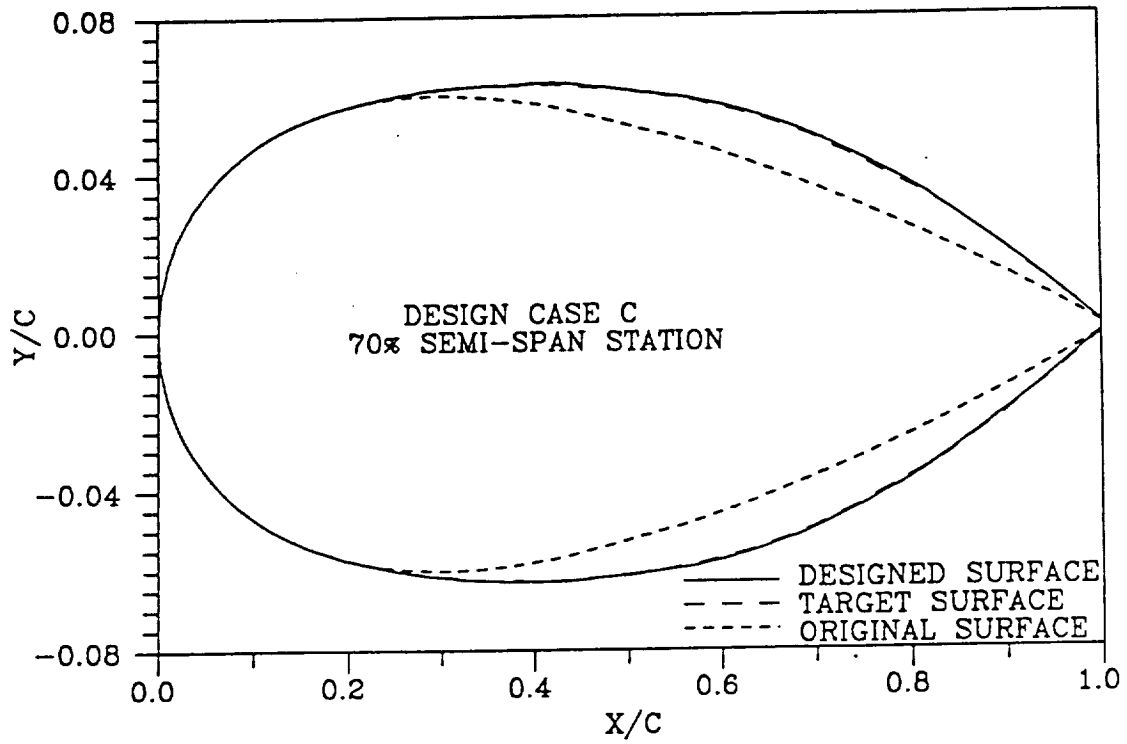

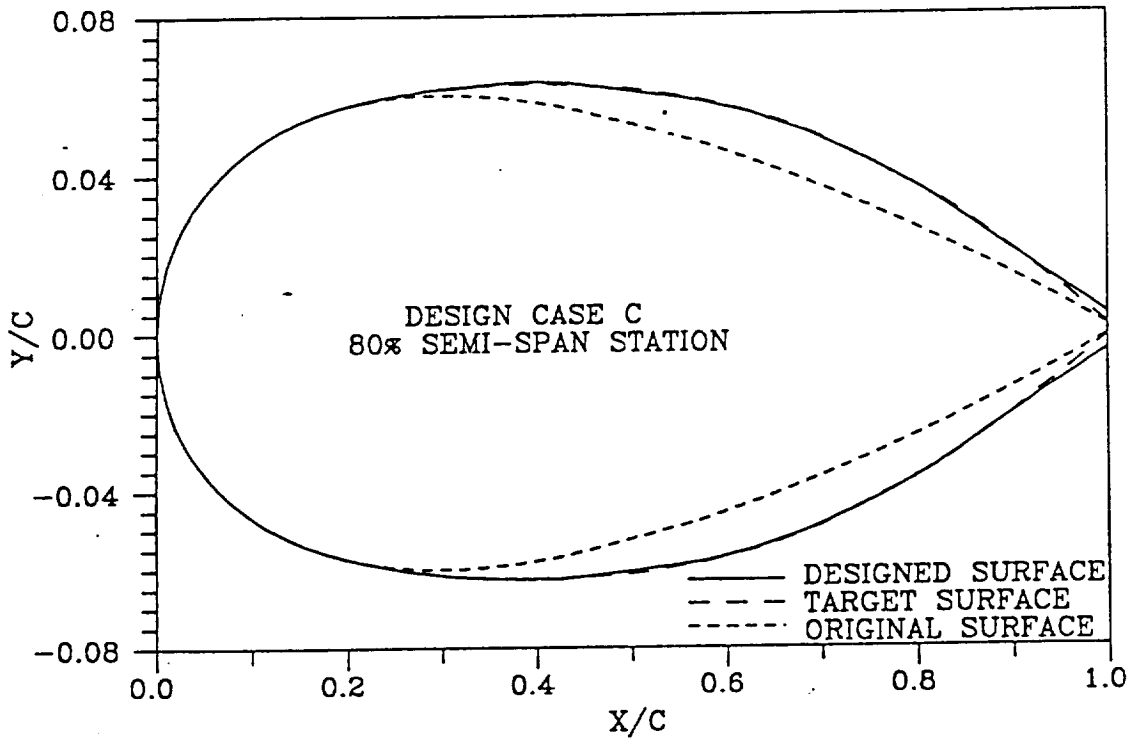

Figure 24..(Continued)

that this slight difference is a ramification of the change in spanwise slopes near the trailing edge between the direct and inverse regions.

In any event, the pressure distributions resulting from an analysis of the designed surfaces shown in Figure 24 are in excellent agreement with the target pressures, as can be seen on Figure 25. In addition, the section lift coefficients at the various design stations are in very good agreement with the target coefficients. Based upon these results it is believed that the present method can adequately design/modify non-adjacent regions of a wing in transonic flow.

Test Case D

As shown on Figure 26, Case D involved the inverse design of the entire wing on both the upper and lower surfaces. In addition, as depicted on Figure 27, the initial twist distribution was constant from root to 40% semi-span followed by a linear distribution between 40% and the wing tip; and the inverse pressure distribution was selected to correspond to an approximately linear twist distribution between the root and the tip. Thus, this case was a test of both the ability of the method to design an entire wing and to modify the twist distribution. Obviously, since the twist had to be permitted to vary, trailing edge closure was not required. Also, the results shown are for supercritical conditions.

As can be seen on Figure 27, the twist distribution resulting from the design calculation, while considerably different than the initial distribution, is slightly different than the target distribution. This difference occurred for several reasons. First, in the current version

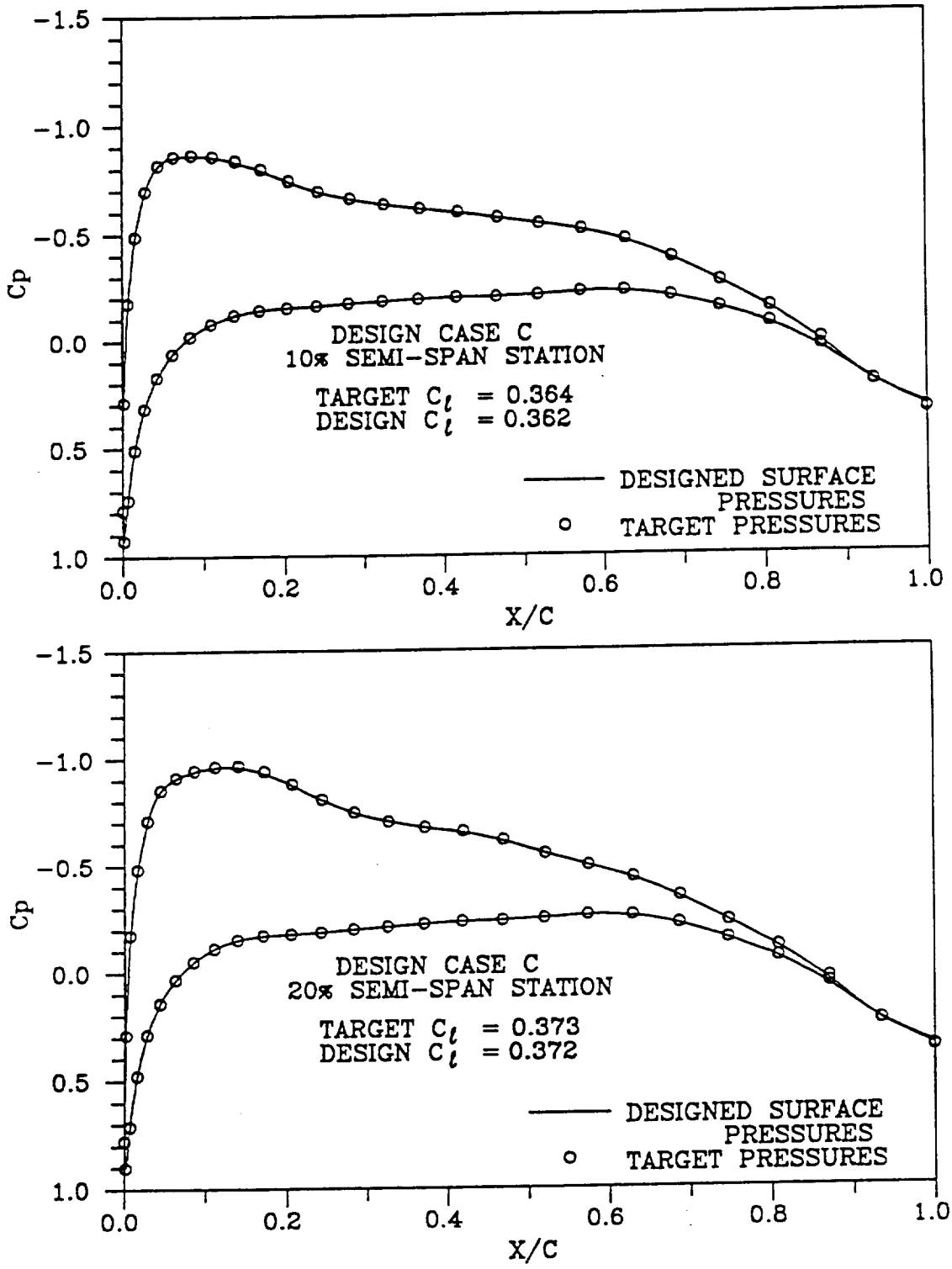

Figure 25. Comparison of Pressures from Analysis of Designed Wing with Target Distributions (Case C)

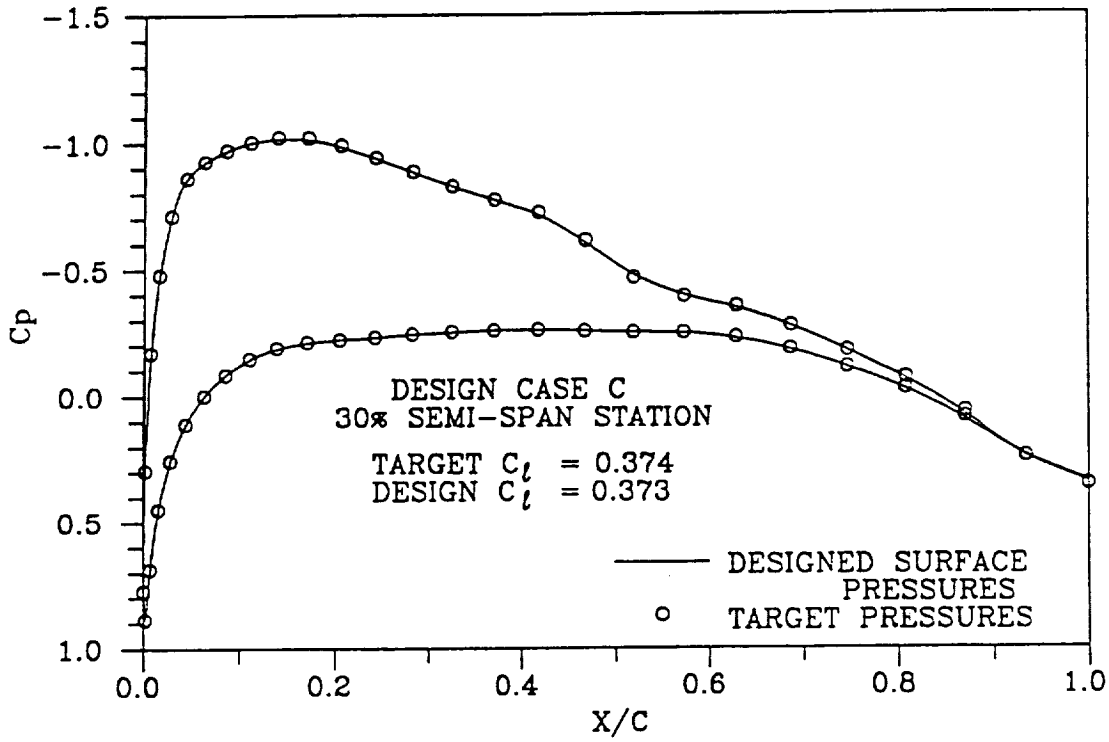

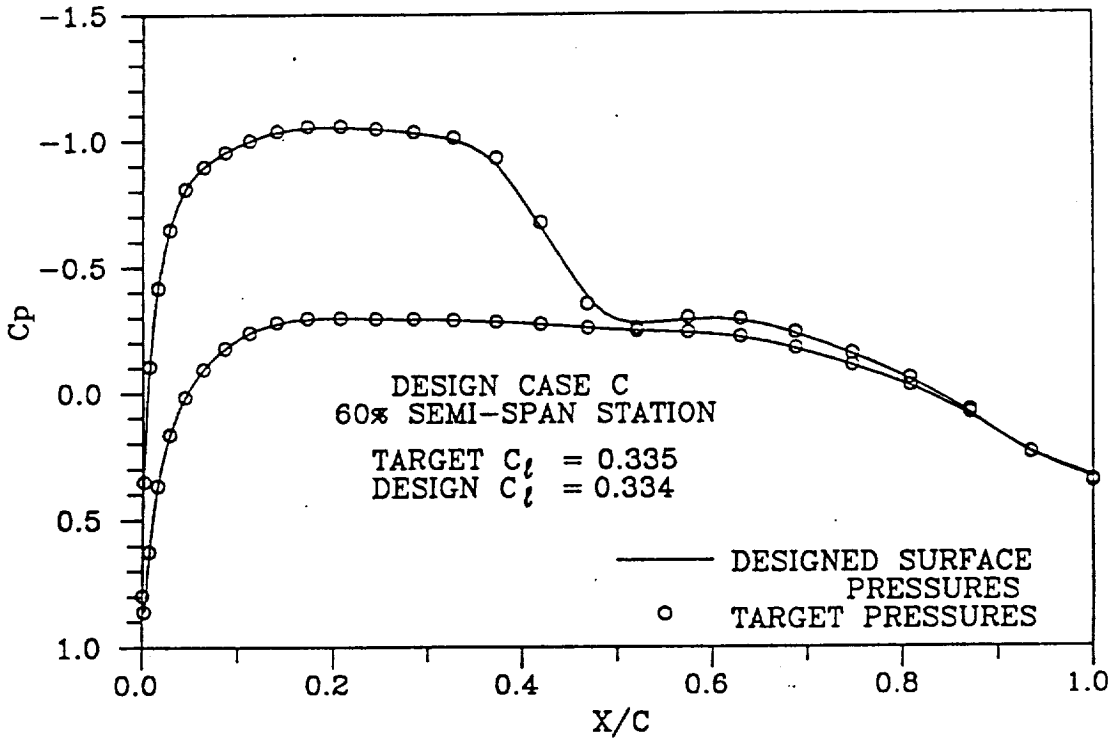

Figure 25. (Continued)

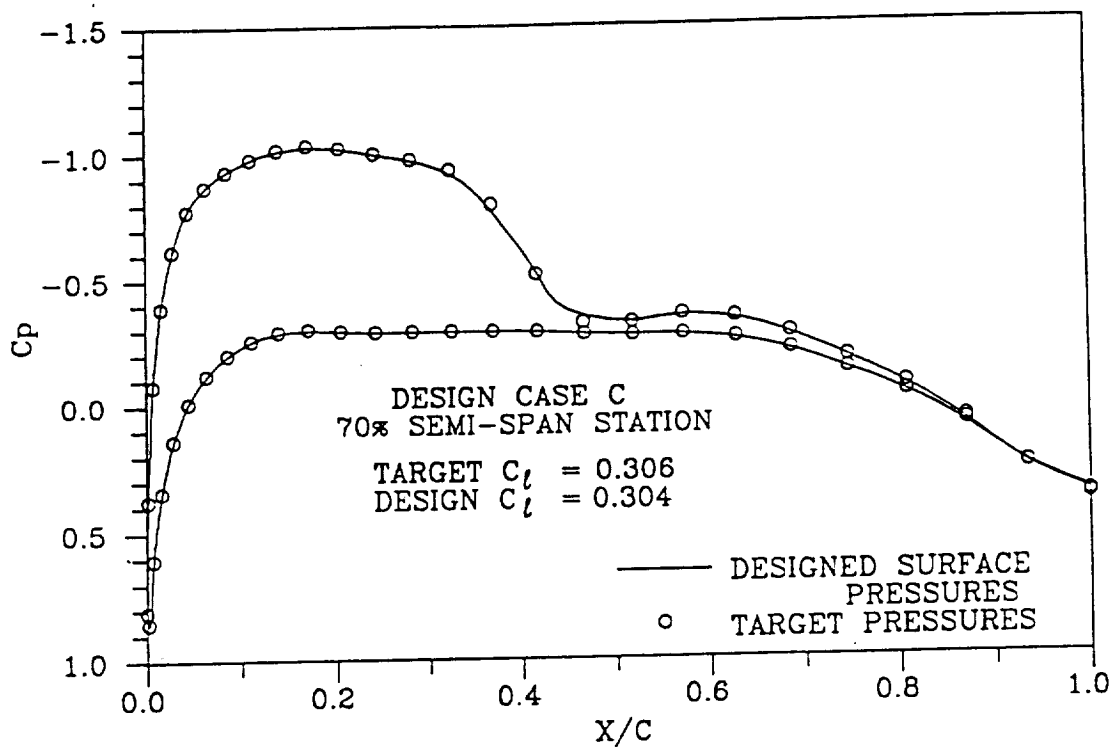

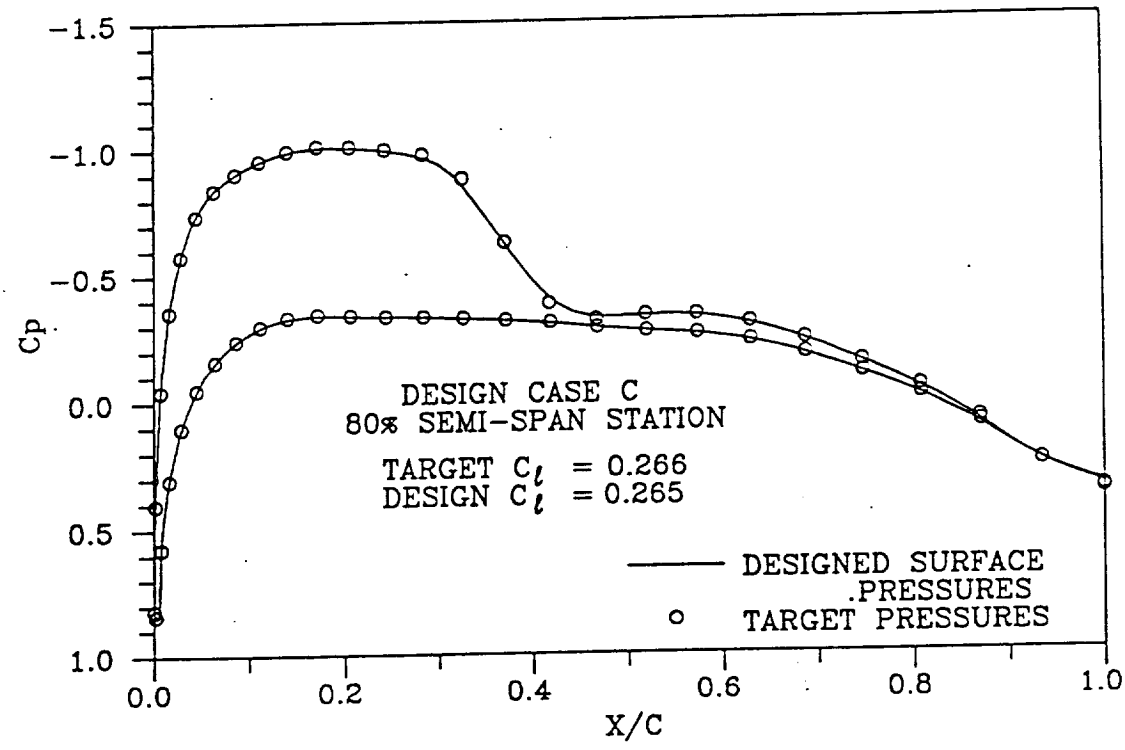

Figure 25. (Continued)

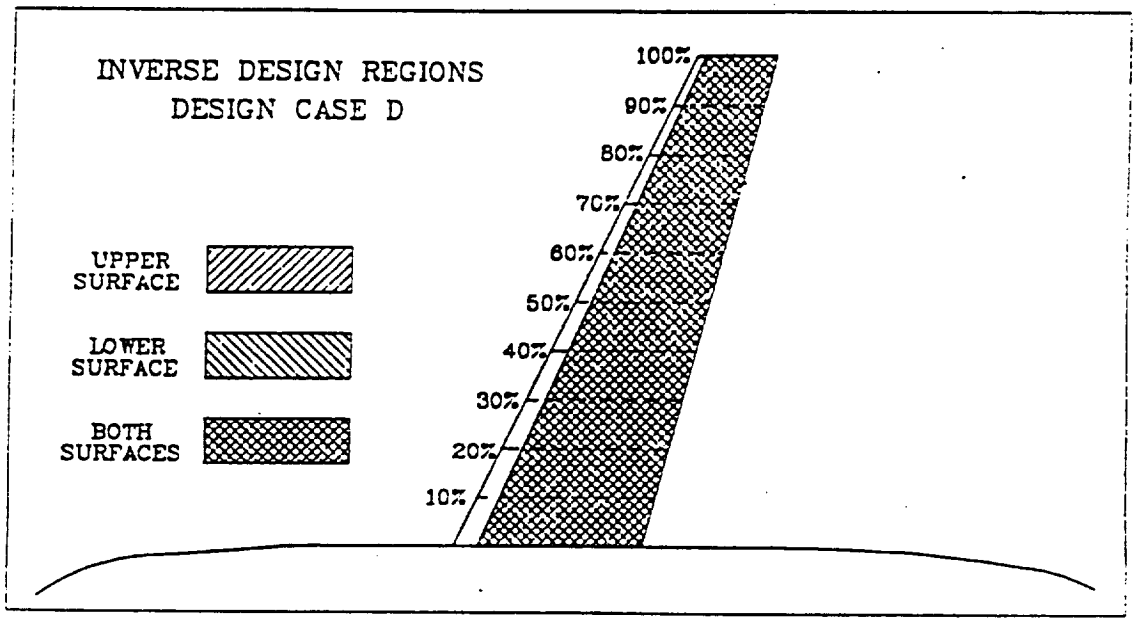

Figure 26. Inverse Design Regions for Case D

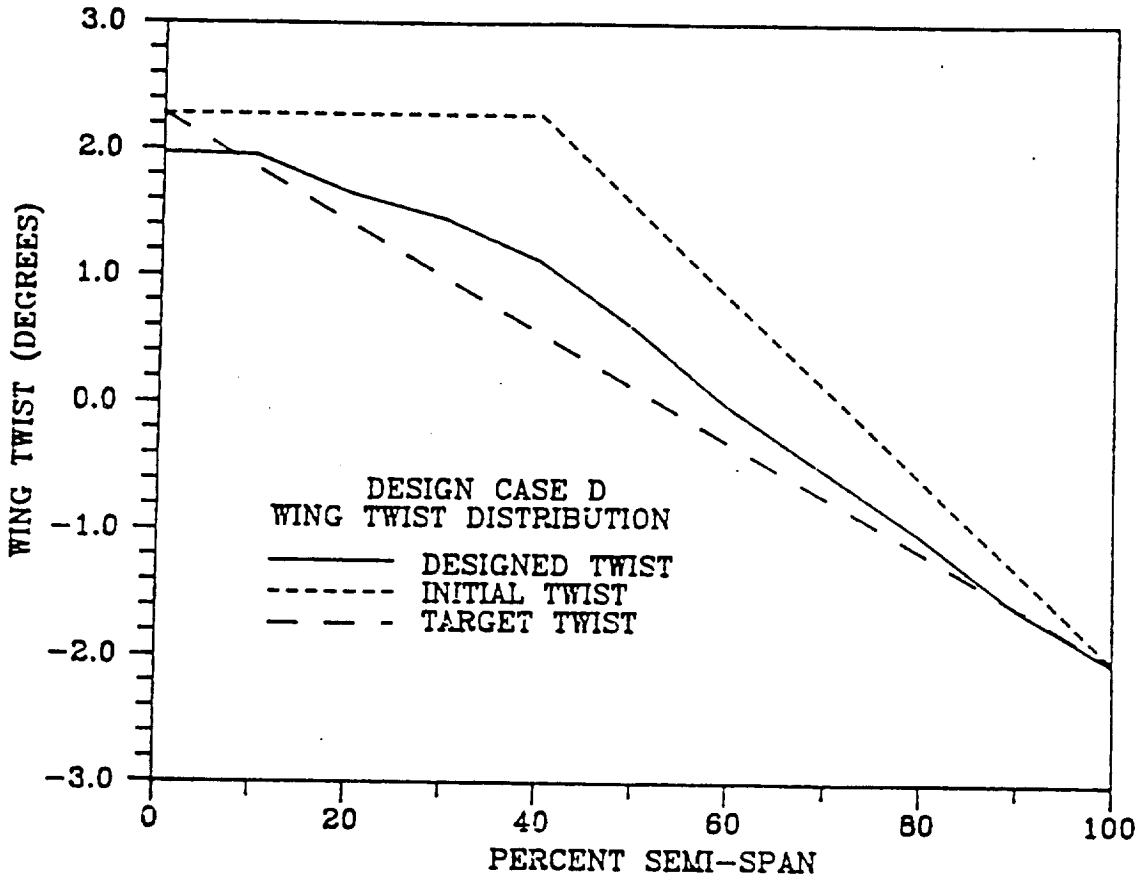

Figure 27. Comparison of Initial Twist with Final Twist Distribution

of the program the wing section at the root-body junction cannot be inversely designed. Thus, when designing the entire wing, the program automatically makes the root section nondimensionally identical to that at the first span station; and the twist at the root and at the 10% semi-span station are identical. Second, the leading edge shapes in the direct region forward of 15% chord correspond to the initial shapes and are oriented by the initial twist distribution. Thus, they do not correspond to those associated with the target twist. Consequently, if the method correctly matches the input pressure distribution in the inverse region from 15% chord aft, it should yield slightly different pressures near the leading edge and a slightly different final twist distribution.

Figure 28 compare the designed airfoil sections with the original surfaces. Due to the manner in which these plots were constructed, if the trailing edge of a designed surface is above that of the corresponding original surface, then that design station has a lower twist angle than the initial twist. As can be seen from Figures 27 and 28, the designed wing is considerably different than the original and has an almost linear twist distribution.

As indicated above, the only way a design can be validated is to analyze the designed wing and compare the resultant pressures in the inverse regions with the target values. Figures 29 present such a comparison for Case D, and it is apparent that the present direct-inverse method did design a wing having the appropriate pressures in the inverse regions aft of 15% chord. However, as should be expected, since the leading edge regions were different then those corresponding to a true linear twist case, the pressure distributions in the leading edge

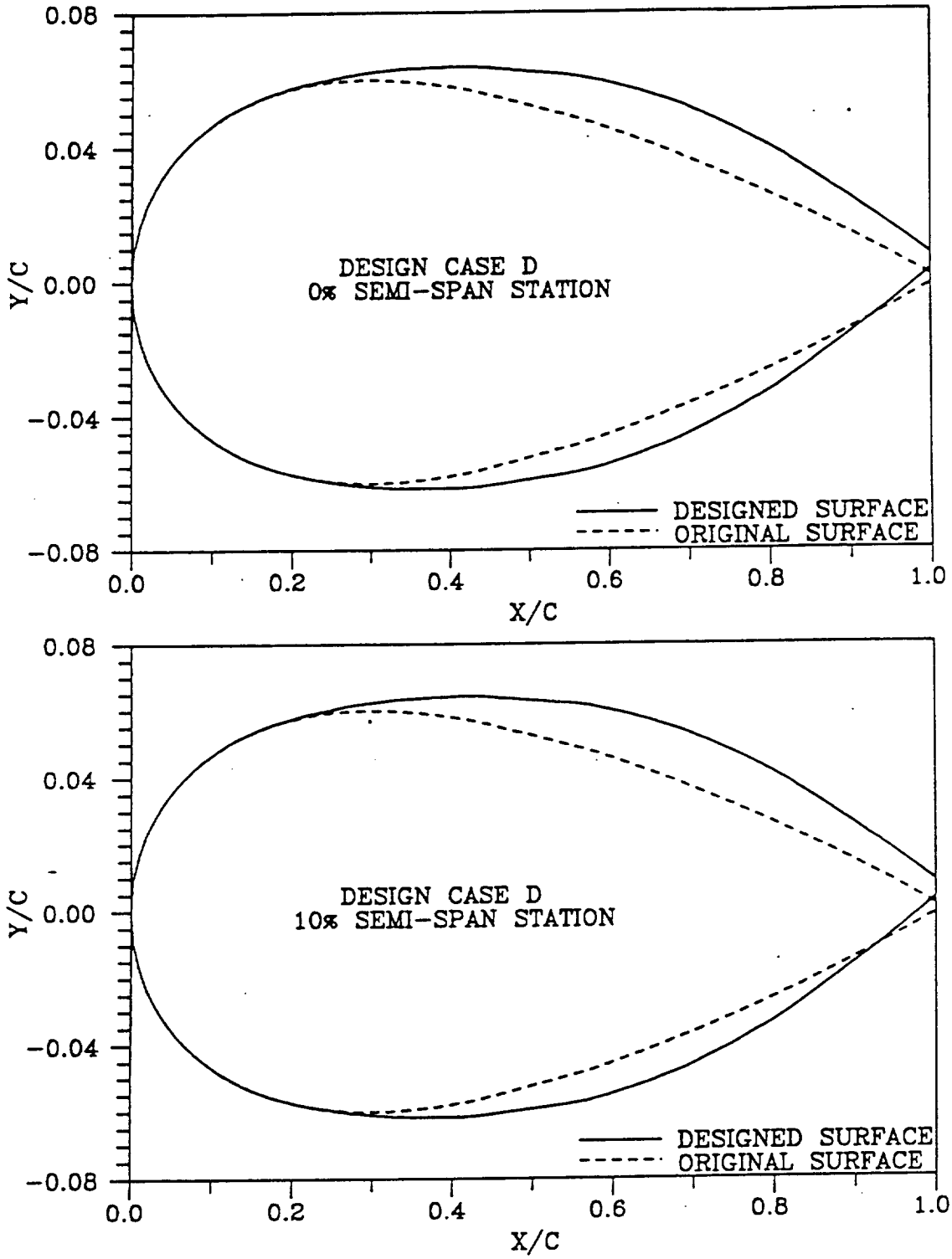

Figure 28. Comparison of Designed Sections with Original and Target Sections (Case D)

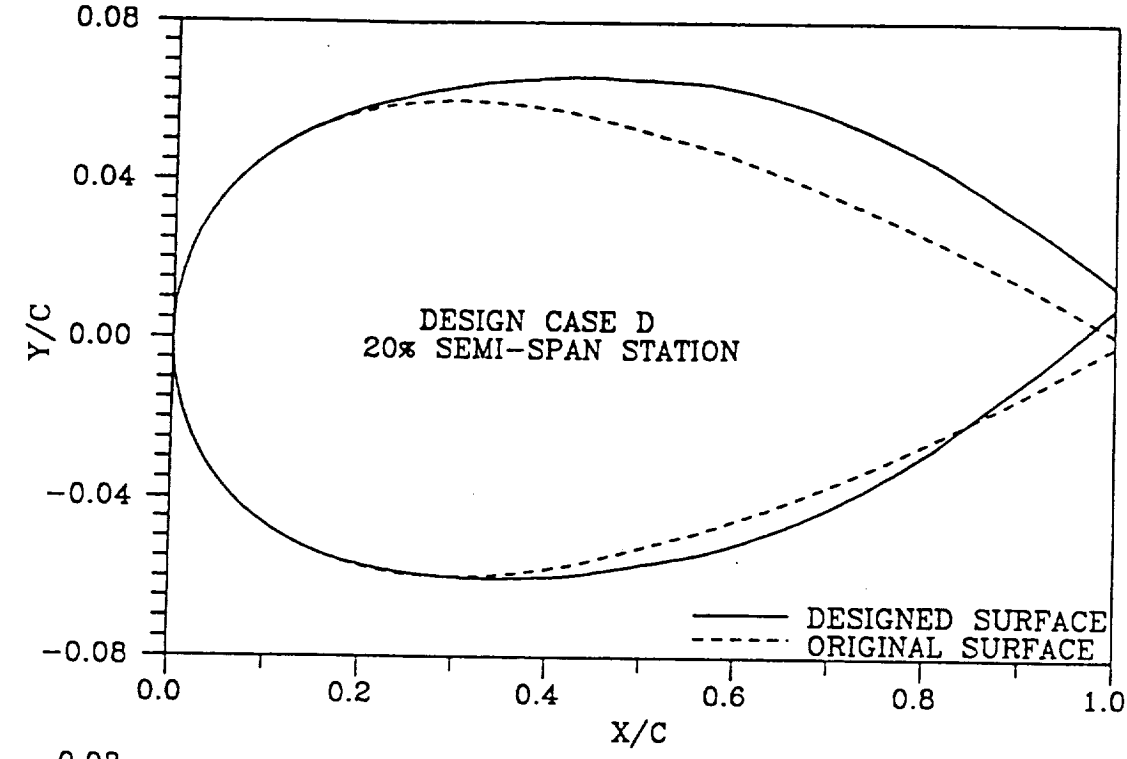

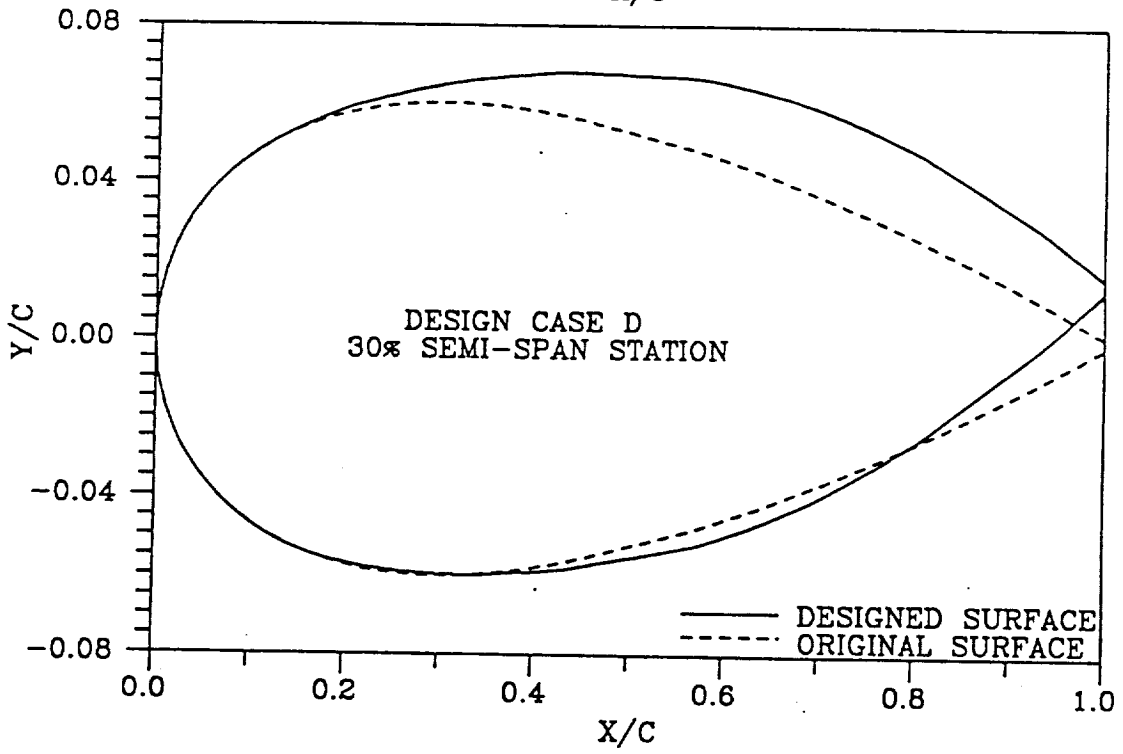

Figure 28. (Continued)

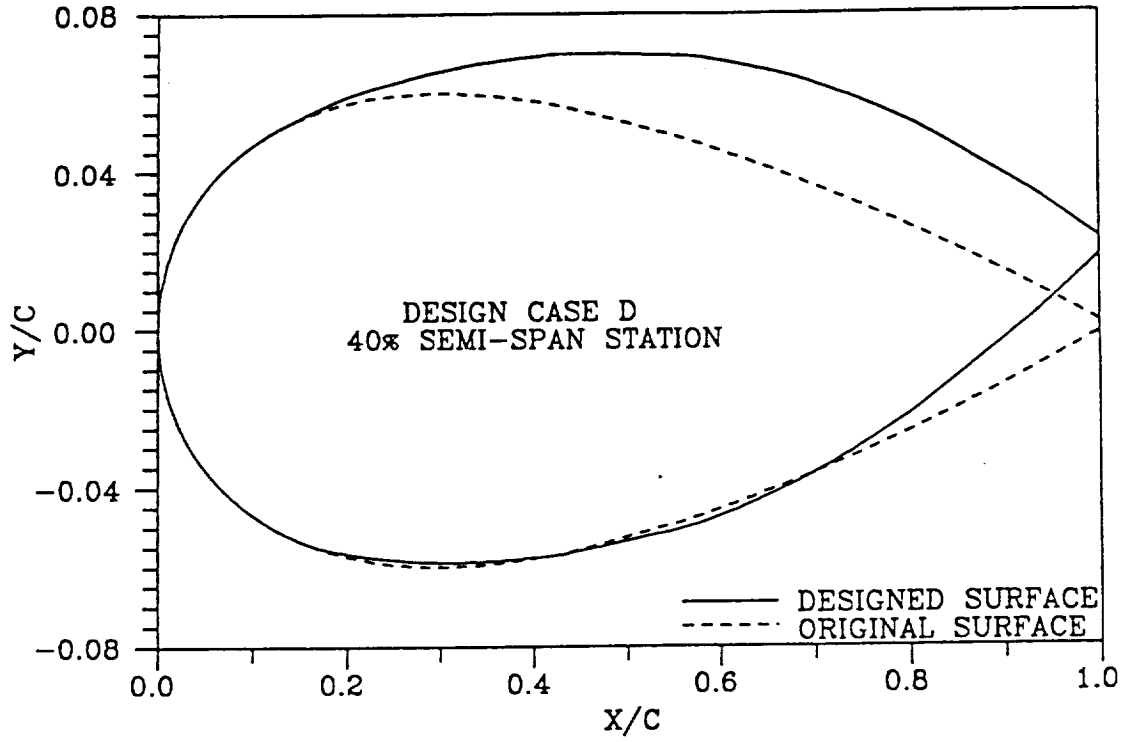

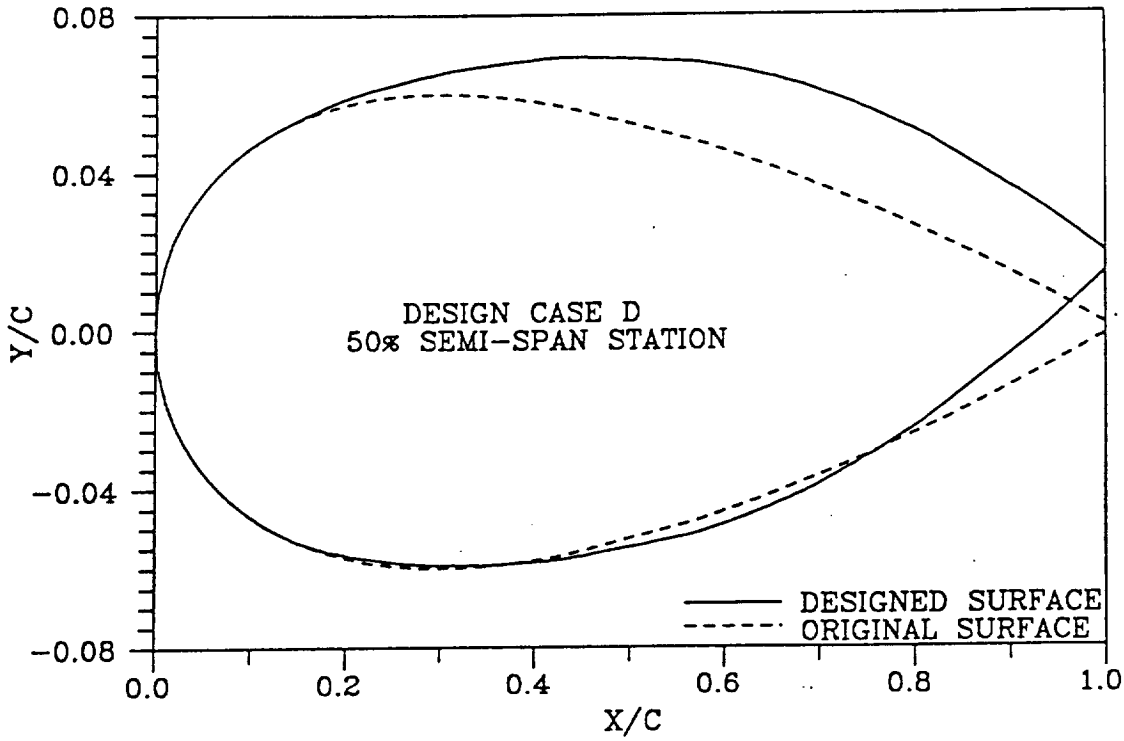

Figure 28. (Continued)

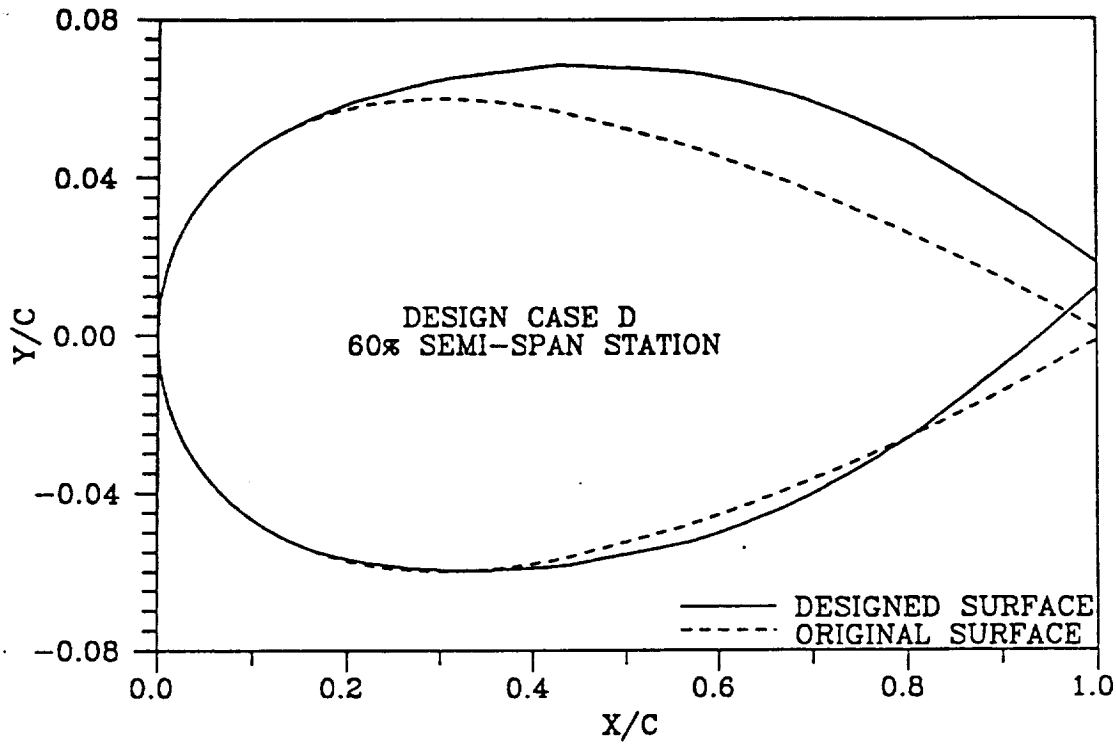

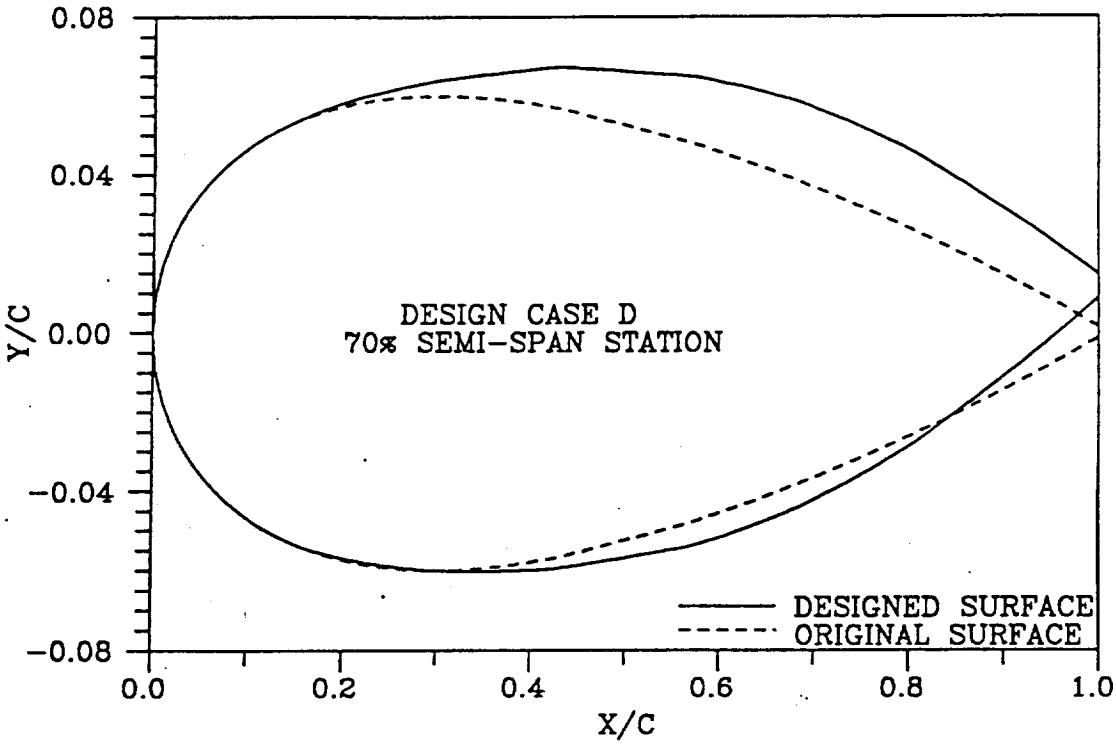

Figure 28. (Continued)

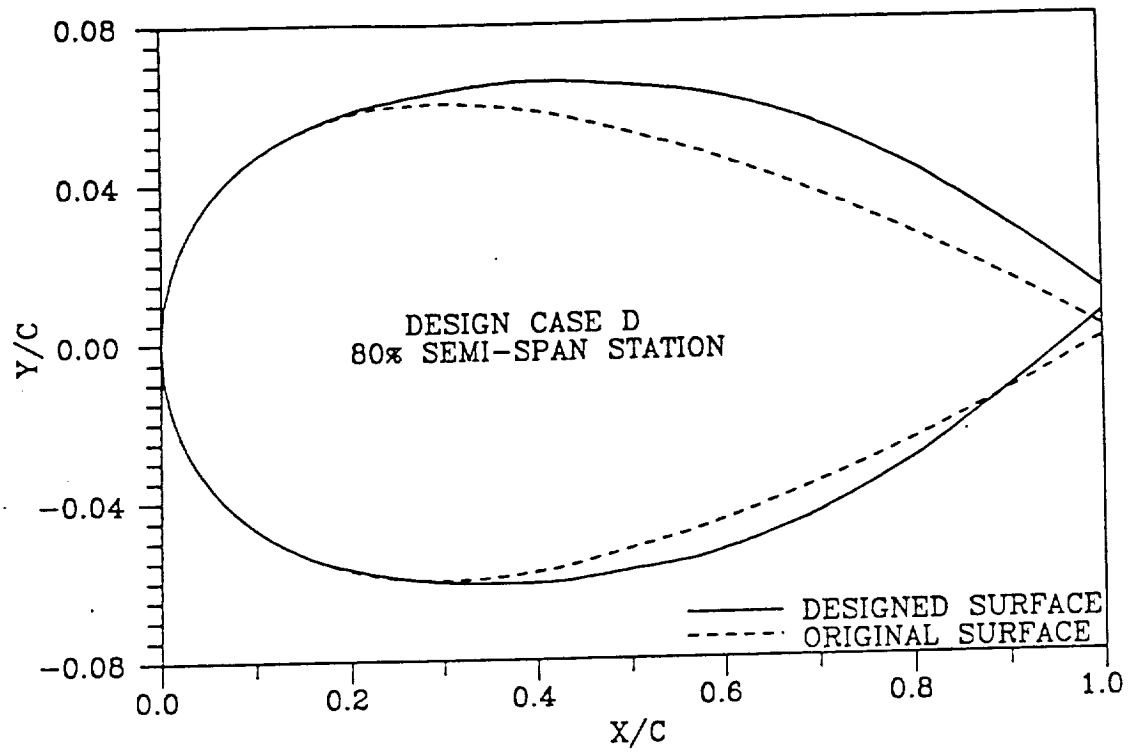

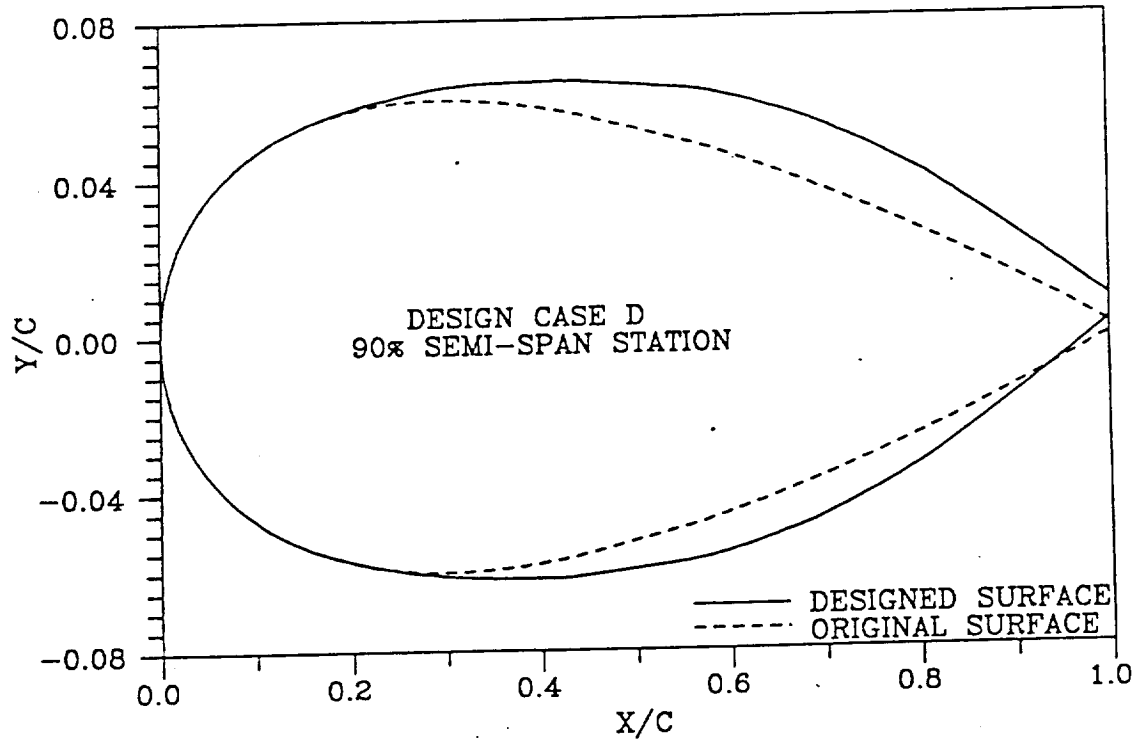

Figure 28. (Continued)

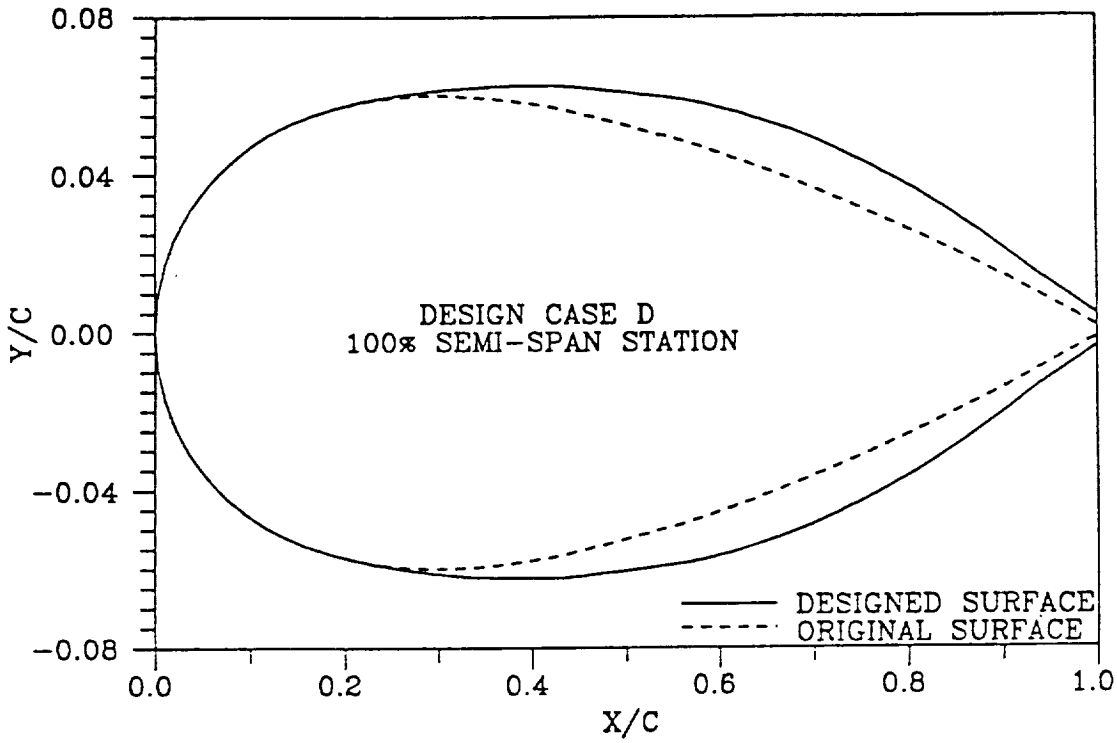

Figure 28. (Continued)

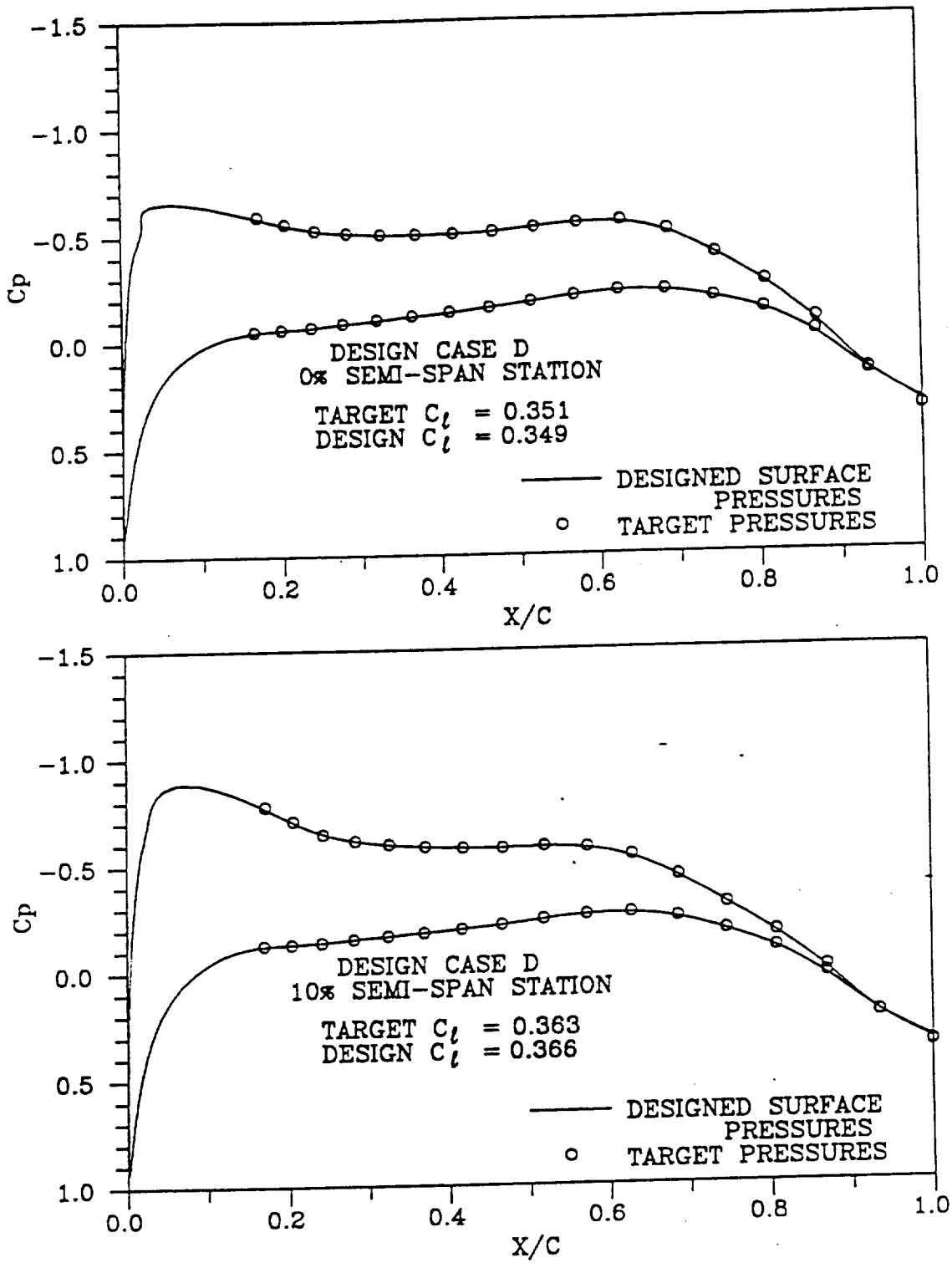

Figure 29. Comparison of Pressures from Analysis of Designed Wing with Target Distributions (Case D)

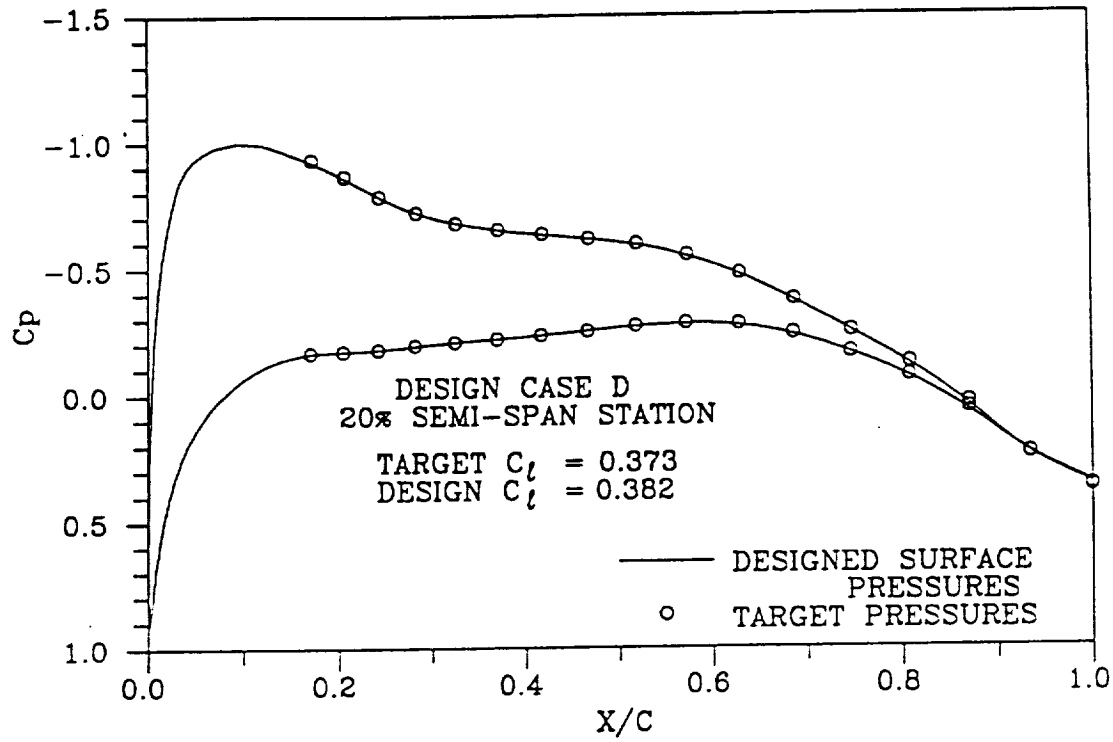

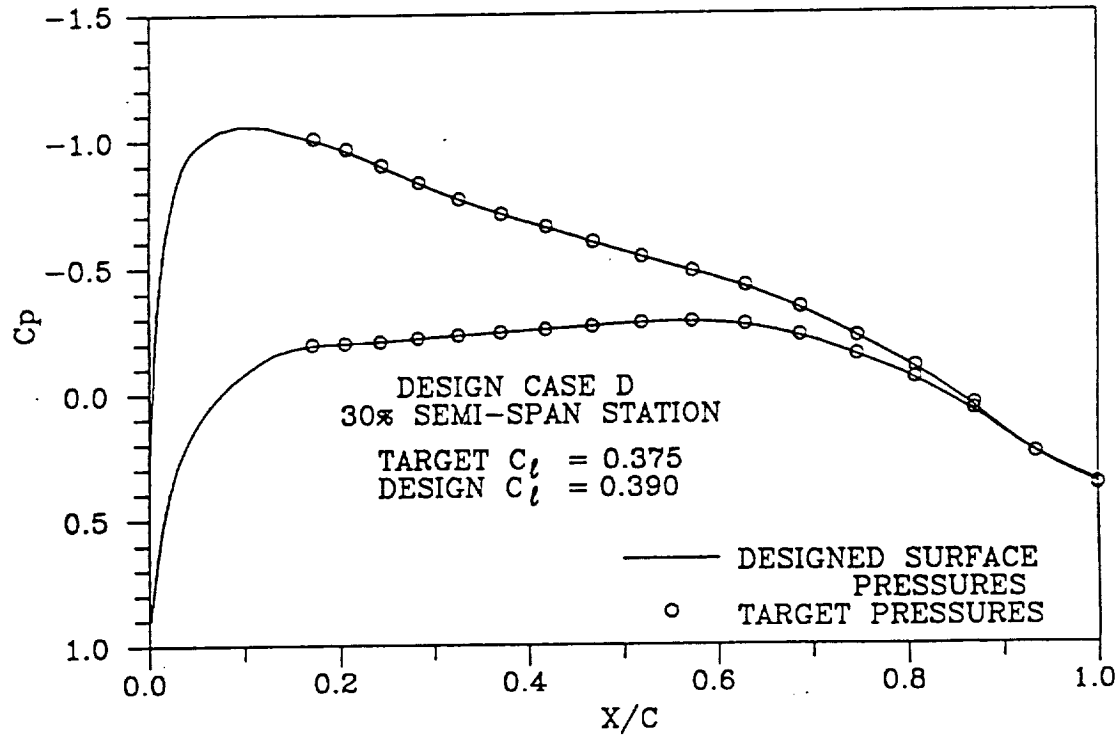

Figure 29. (Continued)

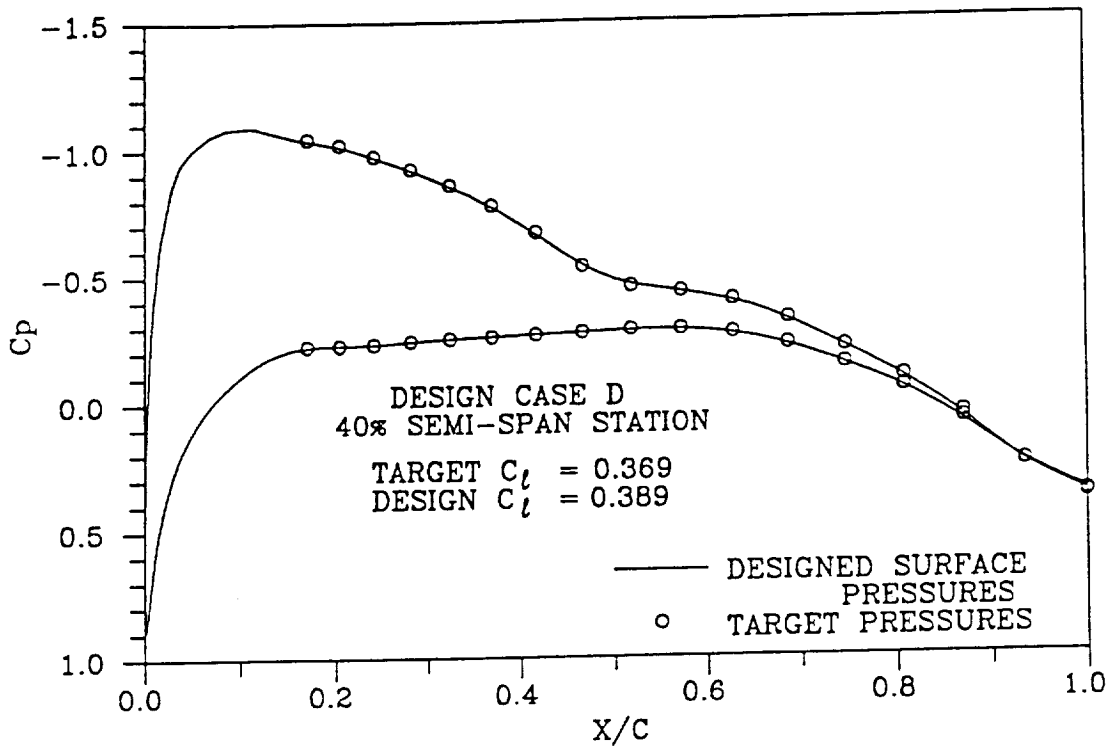

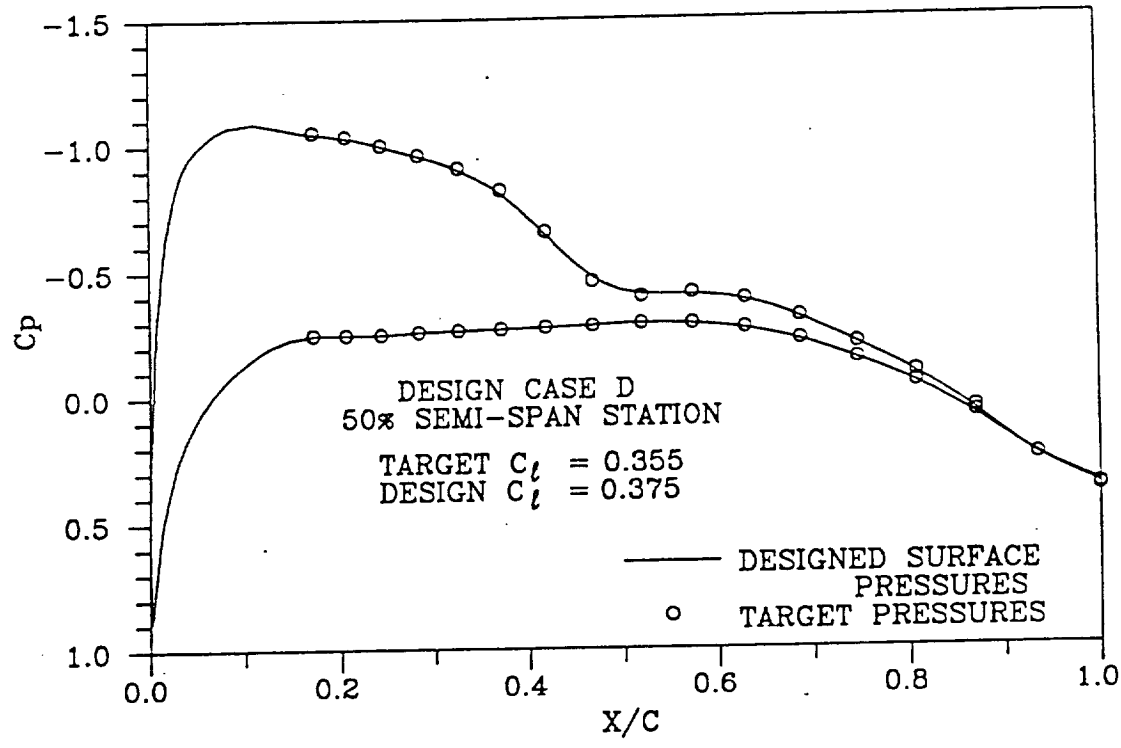

Figure 29. (Continued)

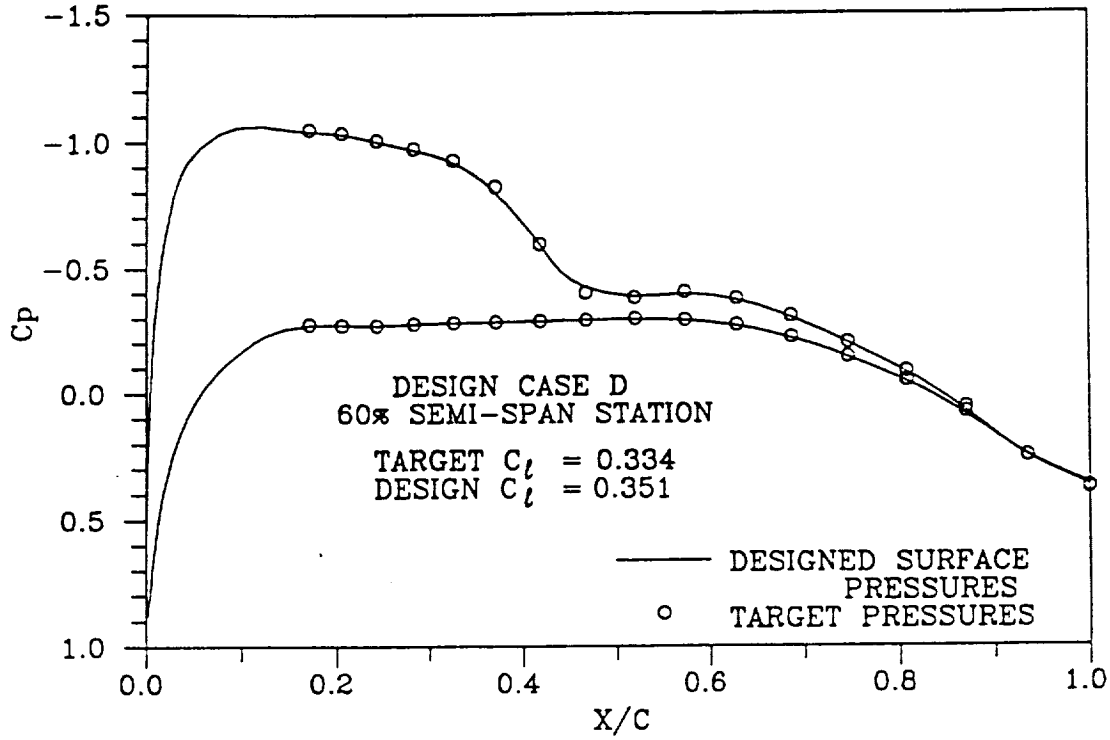

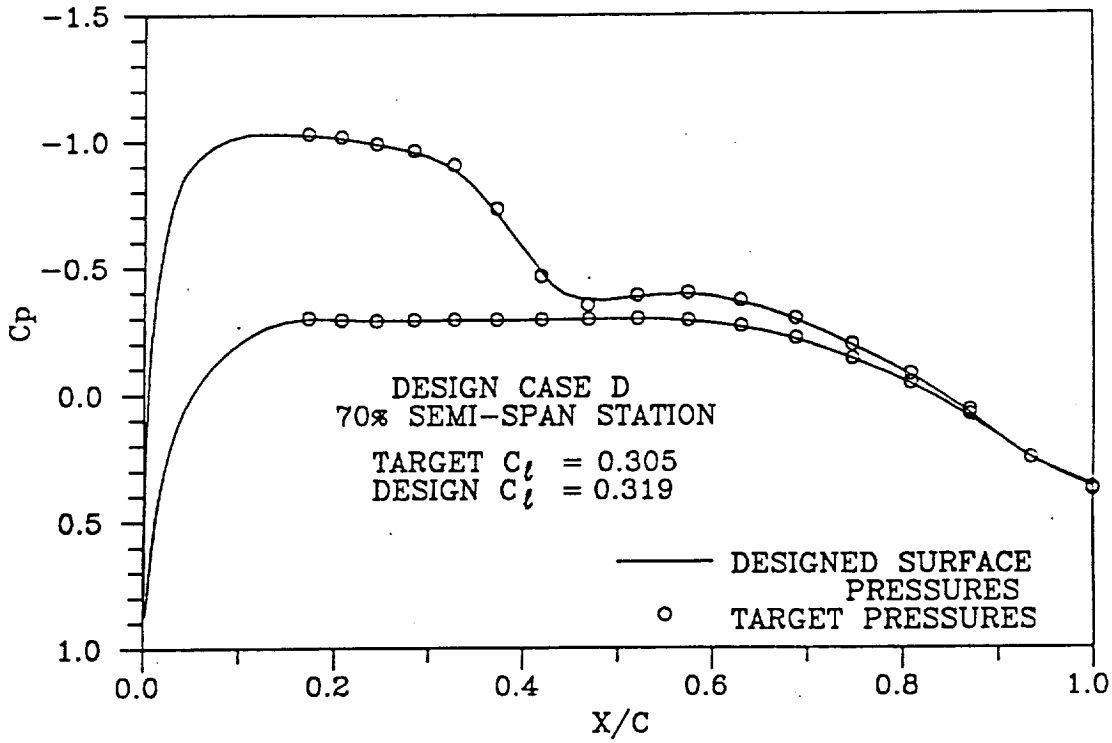

Figure 29. (Continued)

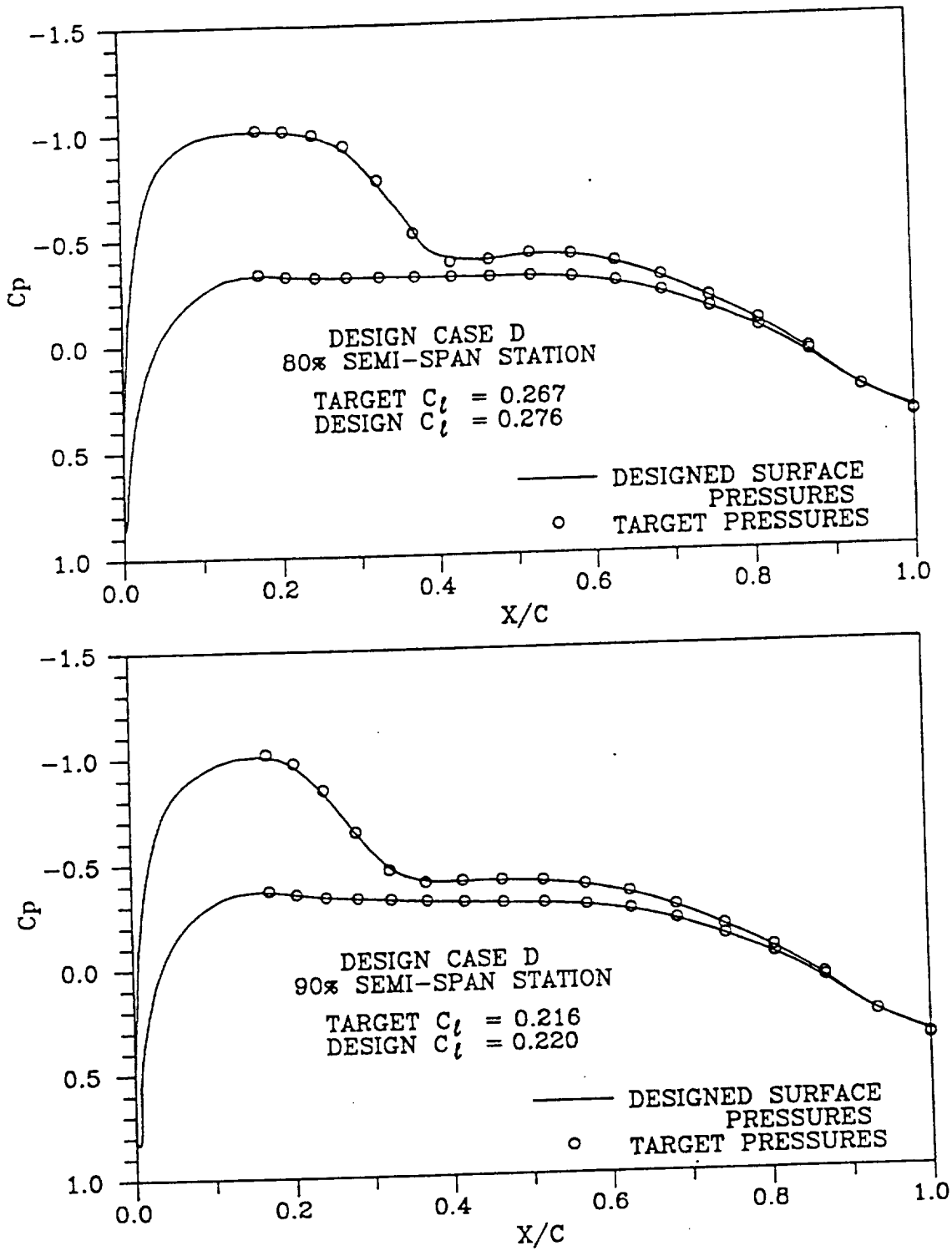

Figure 29. (Continued)

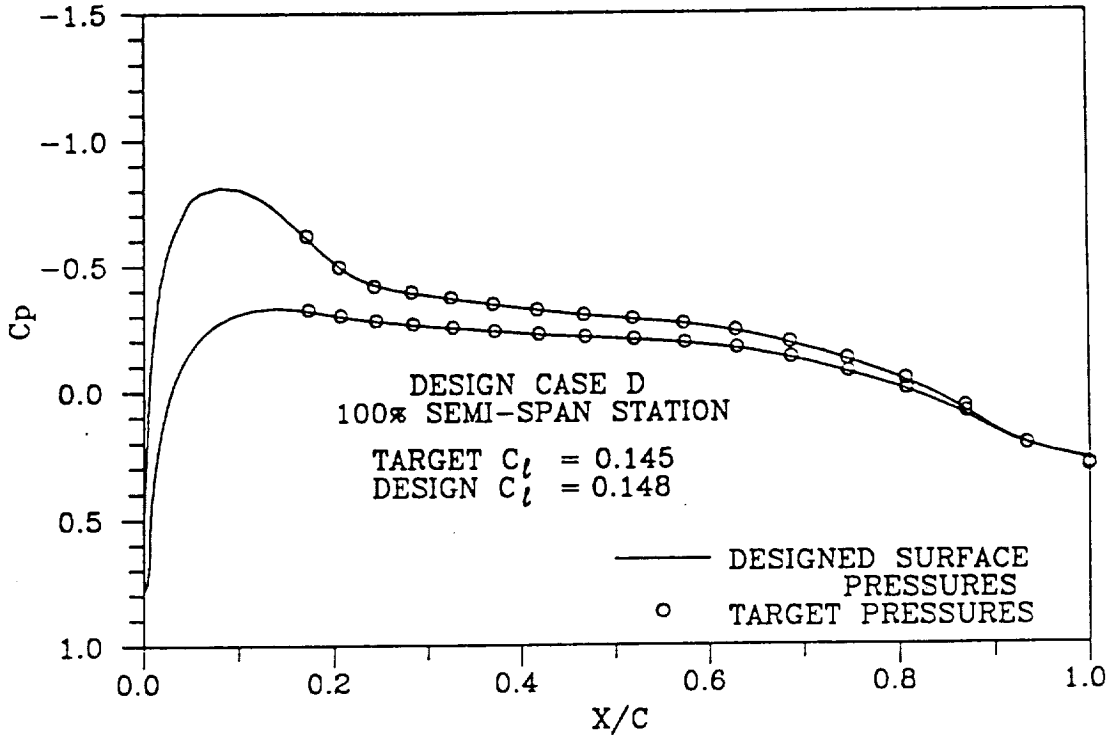

Figure 29. (Continued)

regions and the section lift coefficients were slightly different than those of the target case. (The target lift coefficients were obtained by an analysis of the target section shapes with a linear twist distribution.) It is believed that the results shown on Figure 29 demonstrate that the present method can be used to design an entire wing in supercritical flow.

Test Case E

As a final test case, it was decided to design two non-adjacent upper surface regions simultaneously with a lower surface region which overlapped the upper zones. The location of these inverse design regions is shown on Figure 30. Likewise, Figure 31 compares the pressures associated with the initial wing sections shapes to the target pressures and to the pressures computed at the end of the design calculation. It should be noted that this case is for supercritical condition and trailing edge closure is not enforced. As can be seen, at stations where only one surface is being designed (e.g. 20%, 40%, 50%, and 70%) the pressure distribution on the fixed surface also changes due to three dimensional effects from adjacent station which have been redesigned. However, as depicted on Figure 32, only the design surfaces change form the original shape; and these surfaces are in reasonable agreement with the target profiles.

Finally, Figure 33 compares analysis results obtained for the designed wing with the target pressures. Even for this complicated case, the agreement between the two distributions and between the actual and target lift coefficients is excellent.

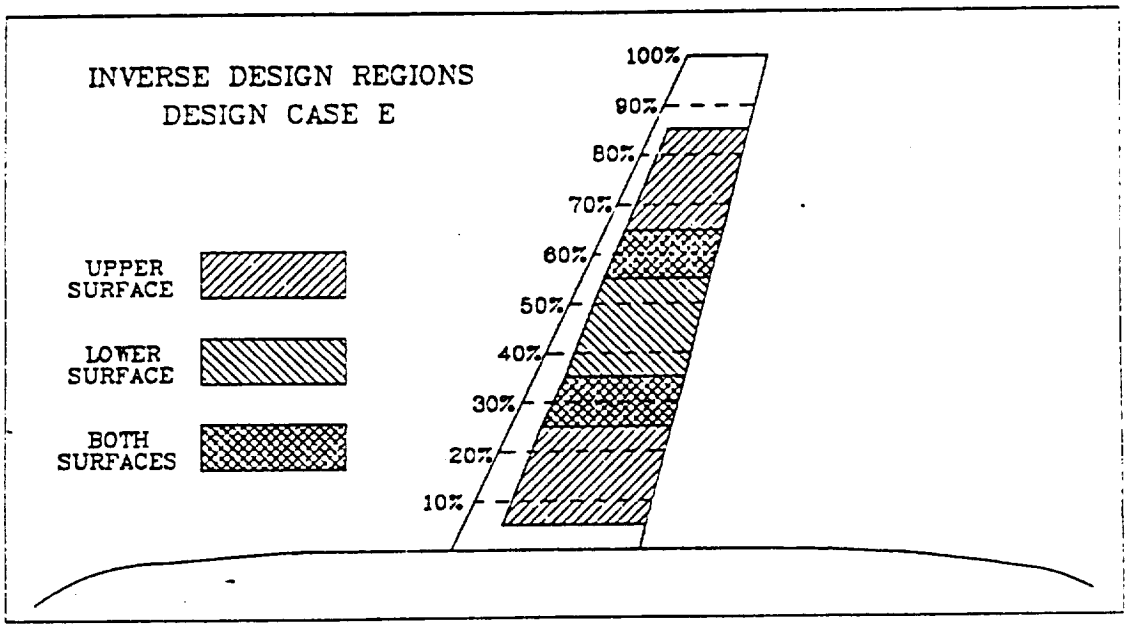

Figure 30. Inverse Design Regions for Case E

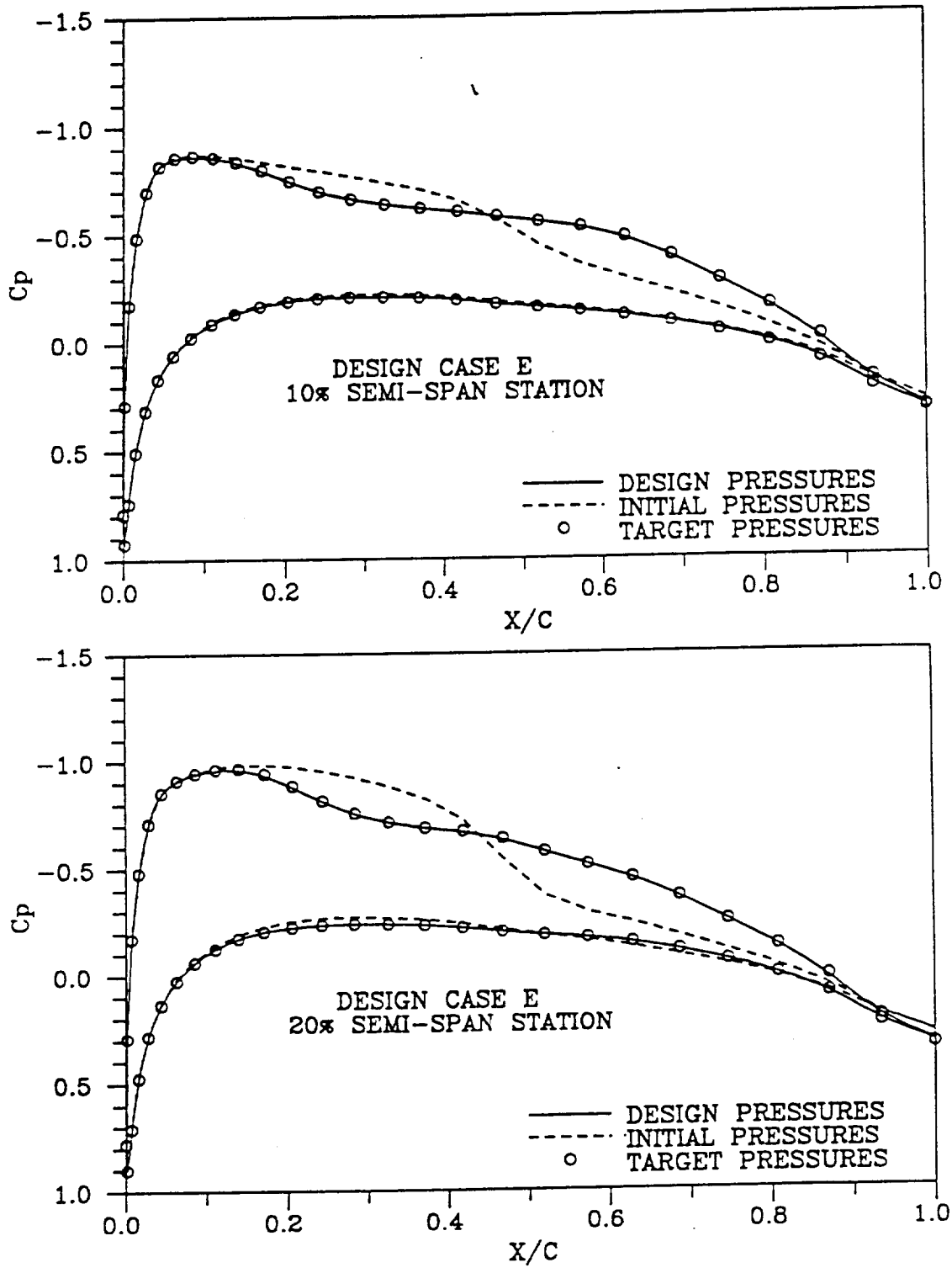

Figure 31. Comparison of Initial Pressures with Target Values (Case E)

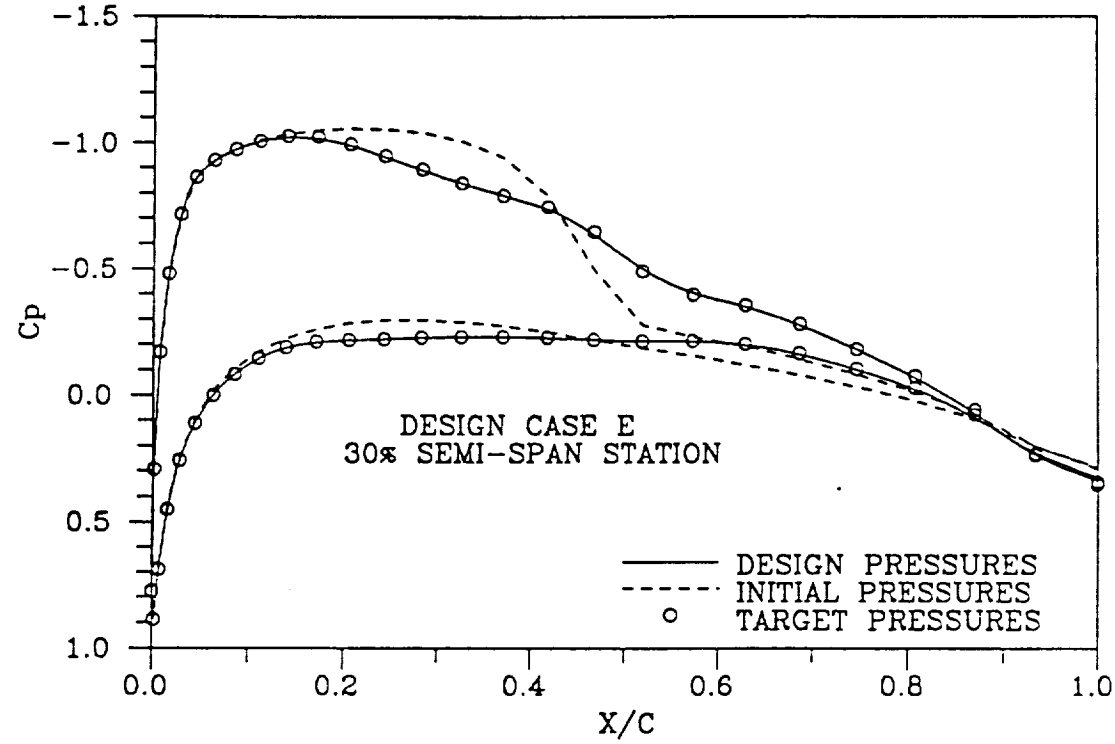

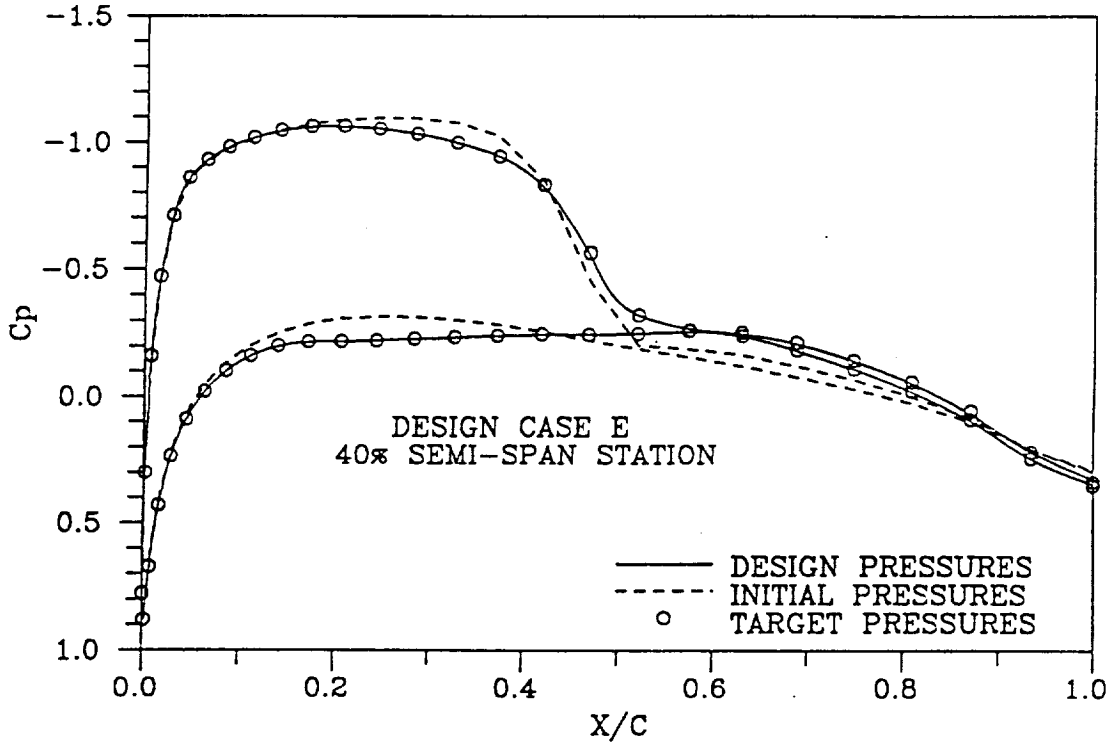

Figure 31. (Continued)

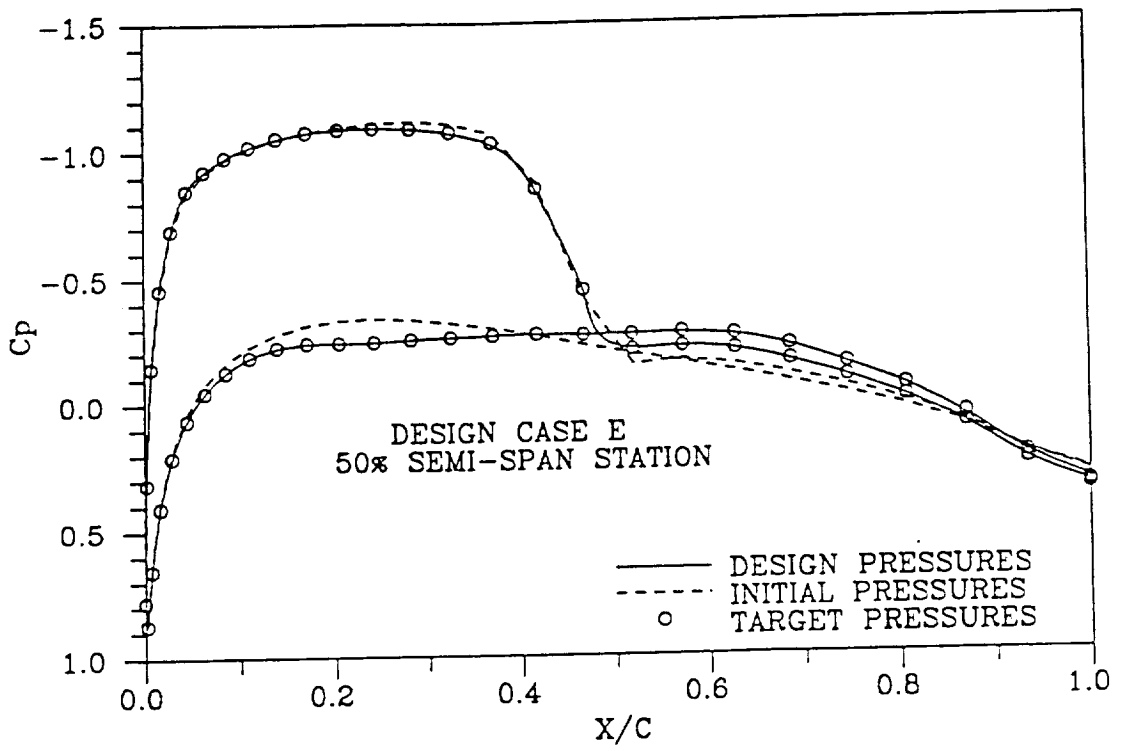

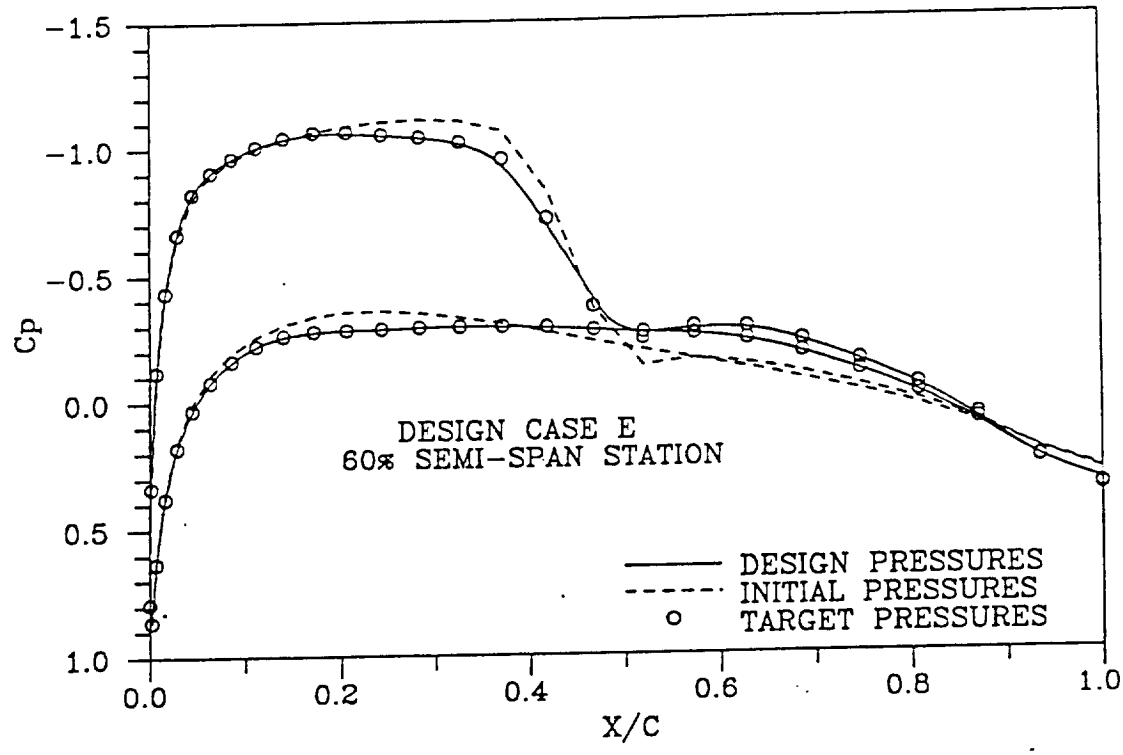

Figure 31. (Continued)

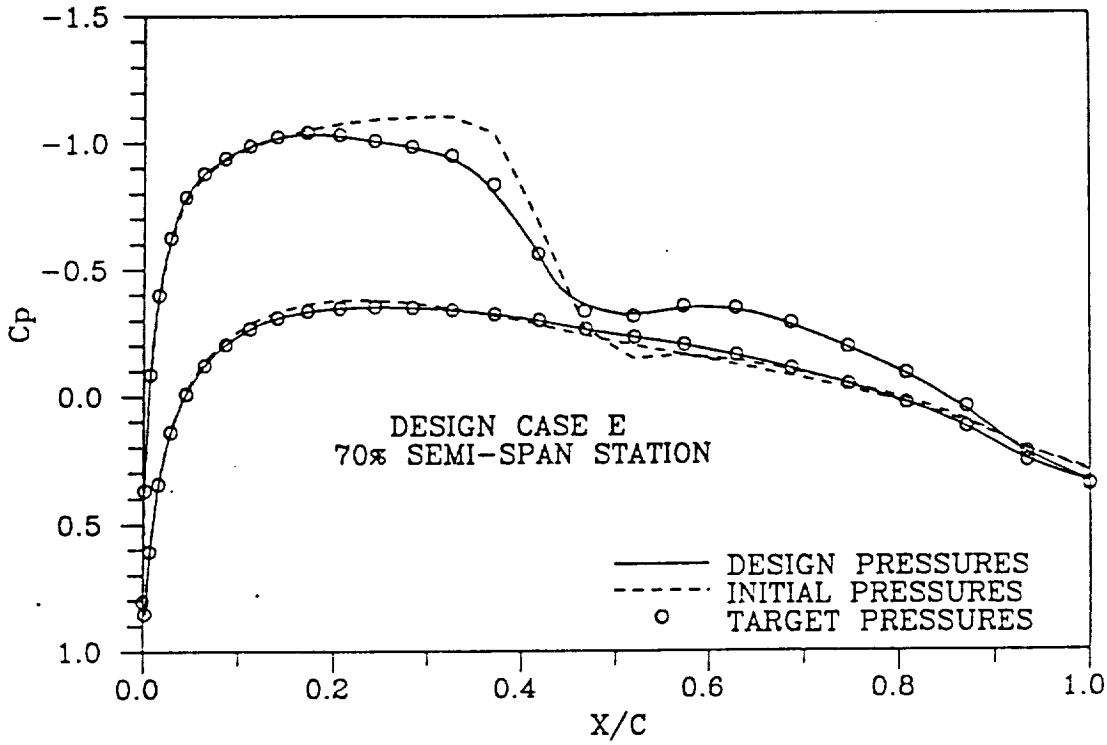

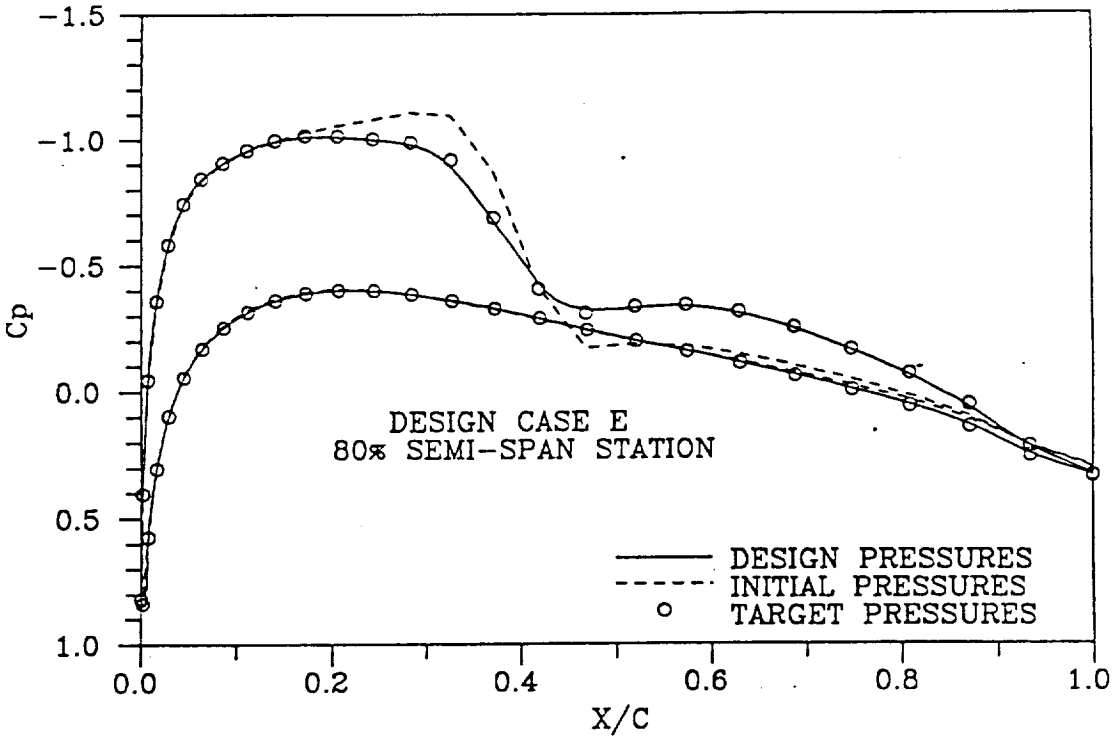

Figure 31. (Continued)

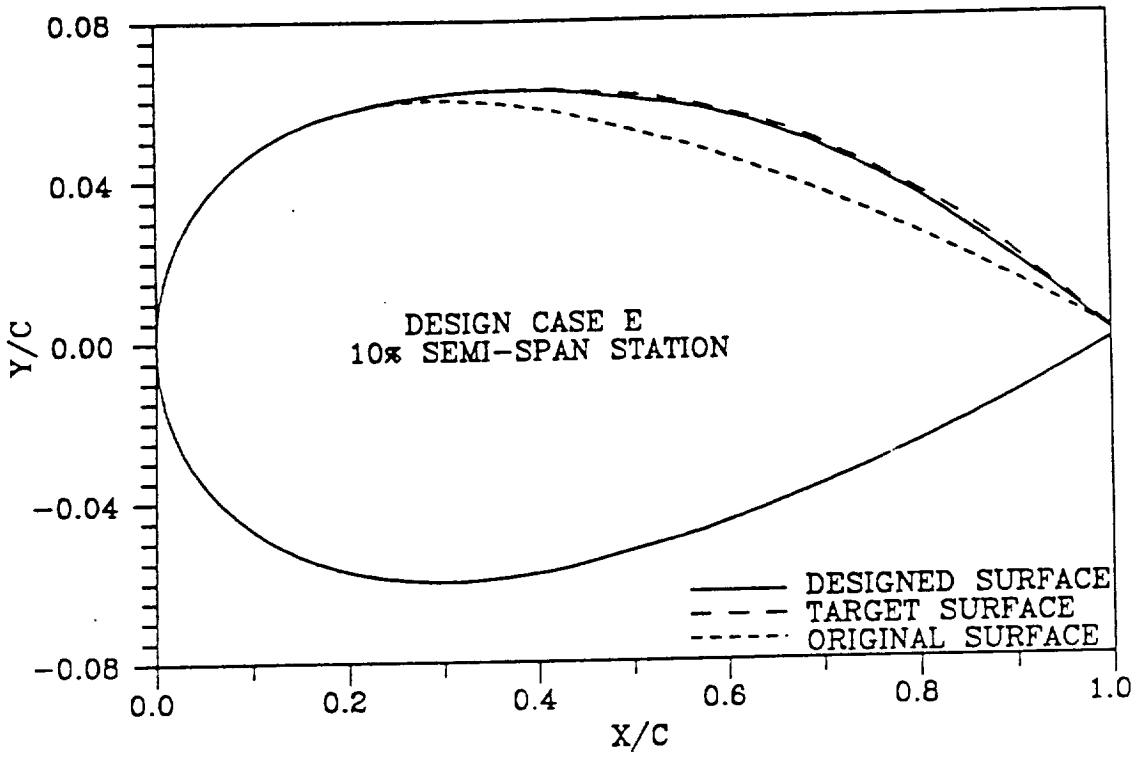

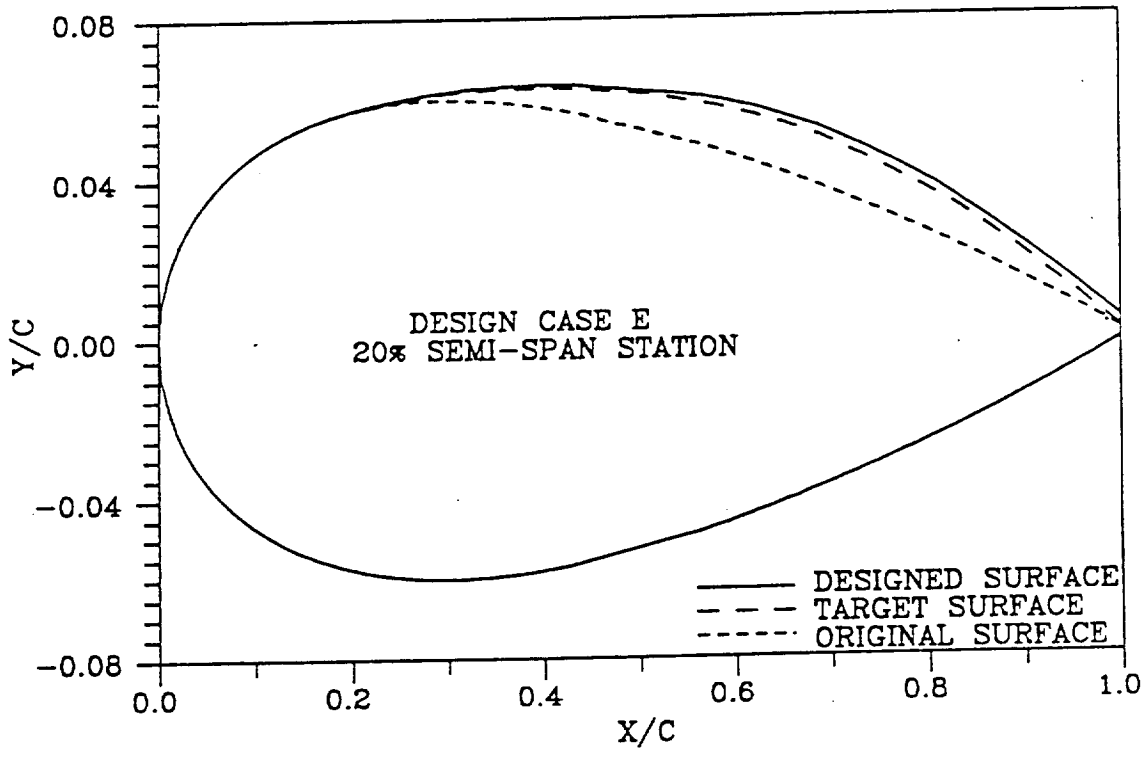

Figure 32. Comparison of Designed Sections with Original and Target Sections (Case E)

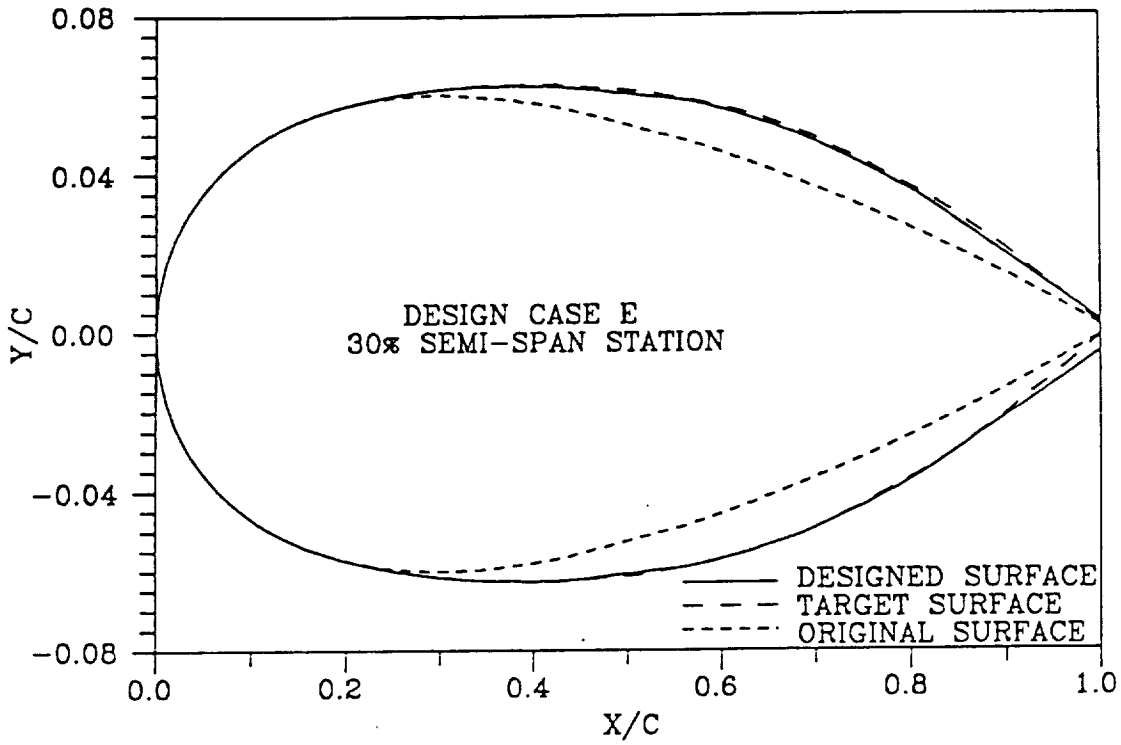

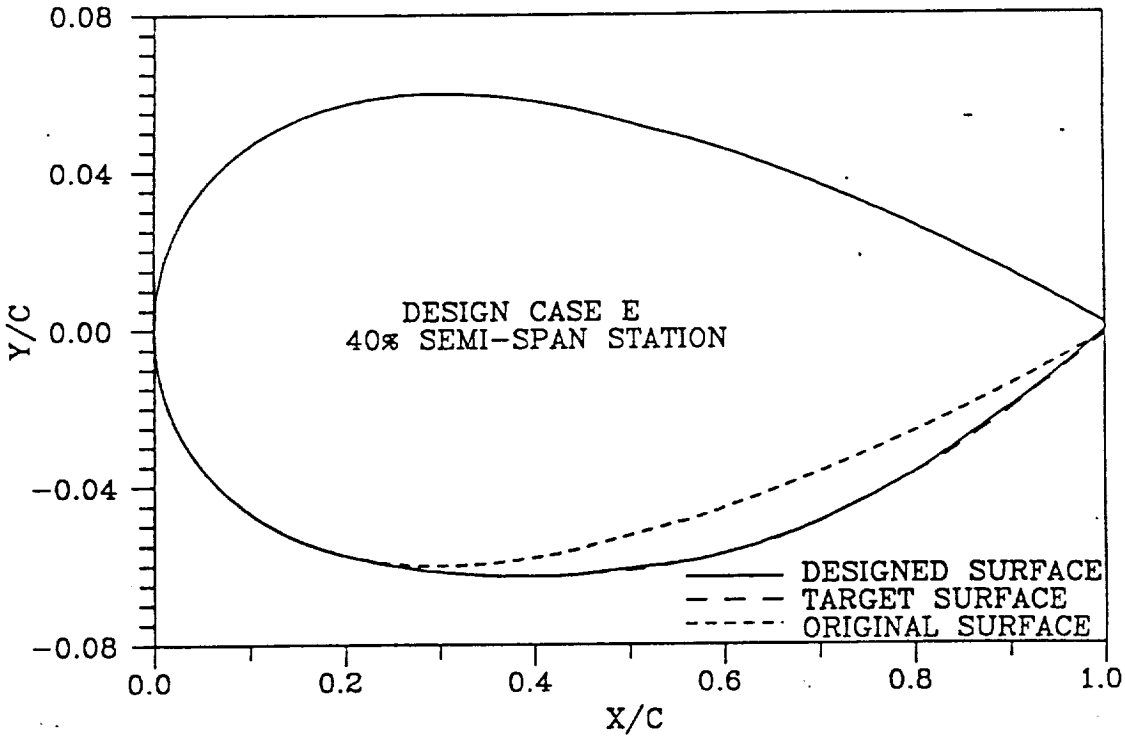

Figure 32. (Continued)

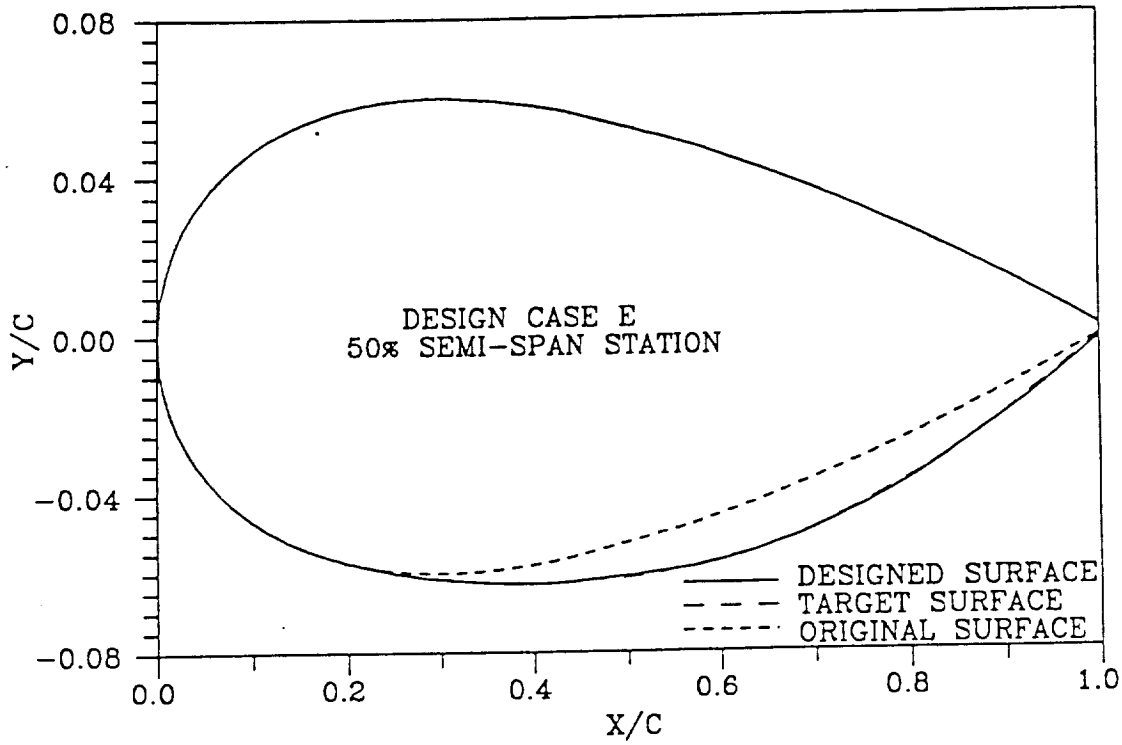

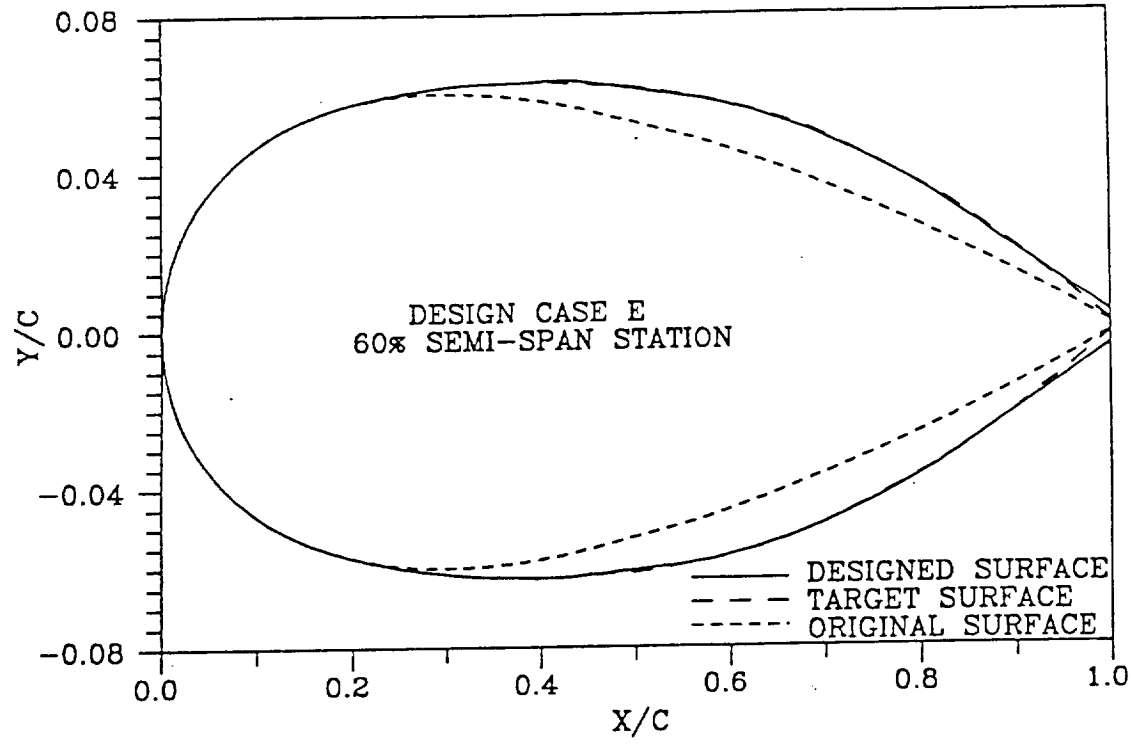

Figure 32. (Continued)

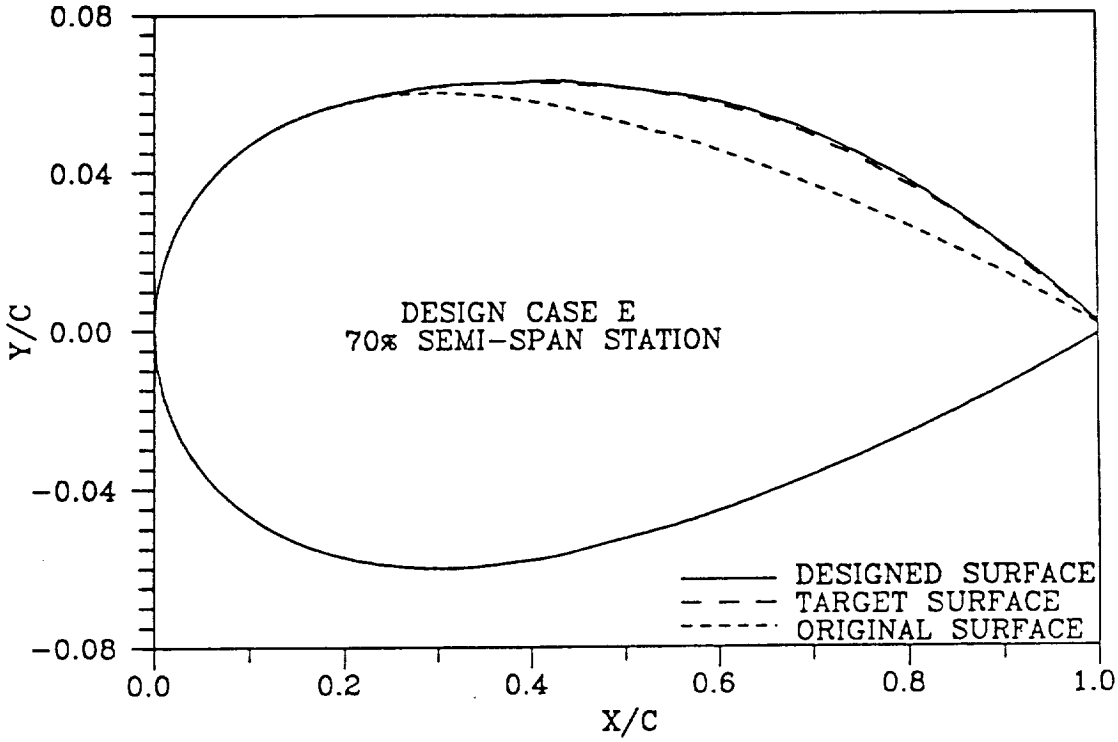

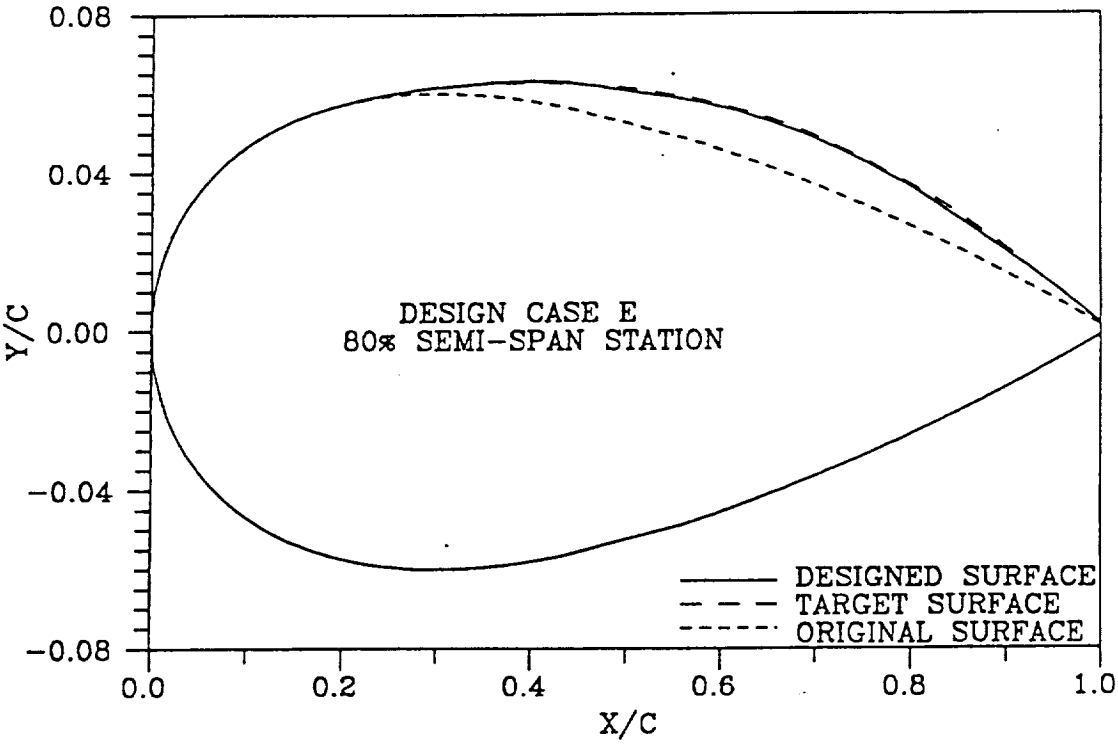

Figure 32. (Continued)

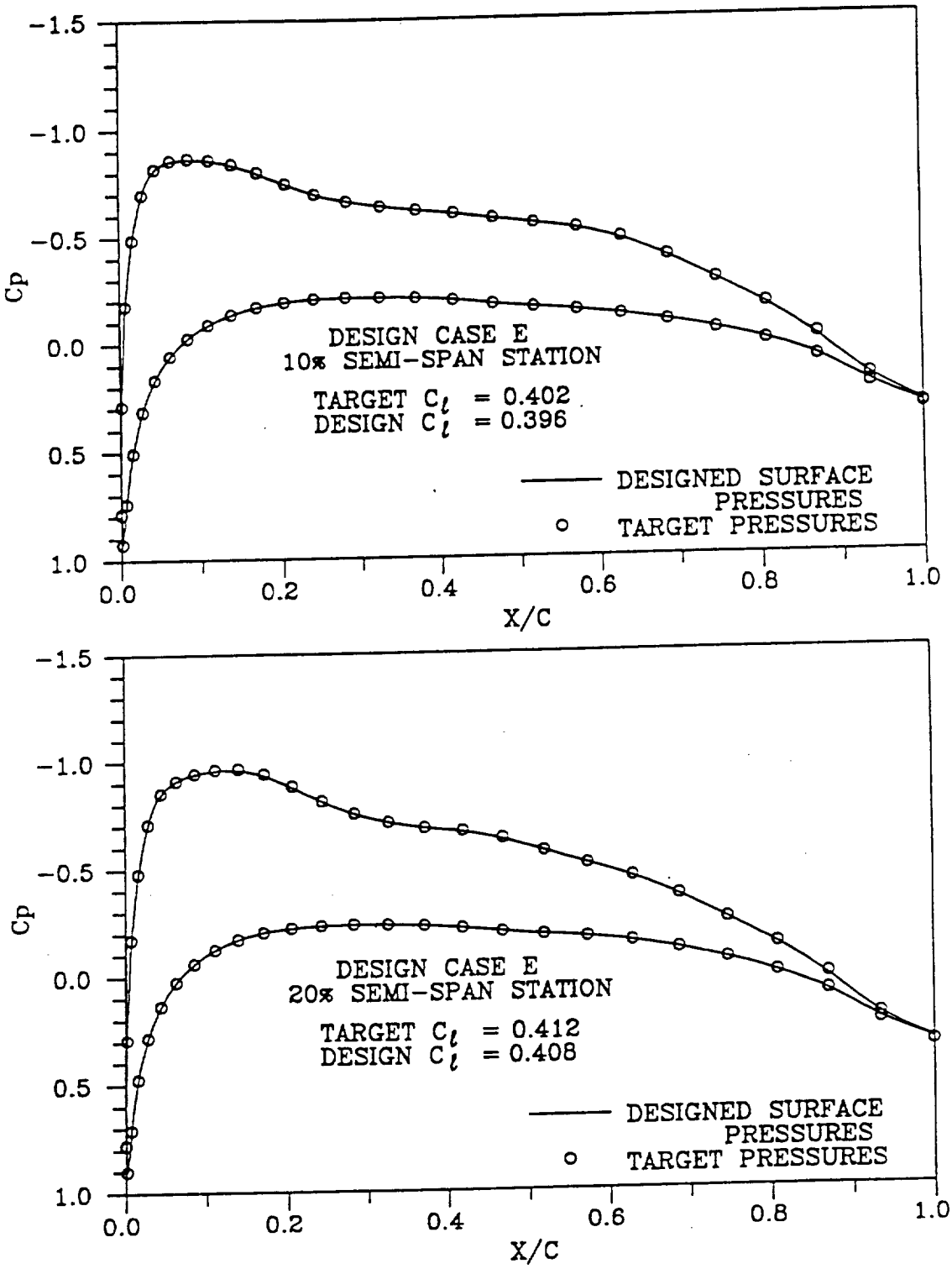

Figure 33. Comparison of Pressures from Analysis of Designed Wing with Target Distributions (Case E)

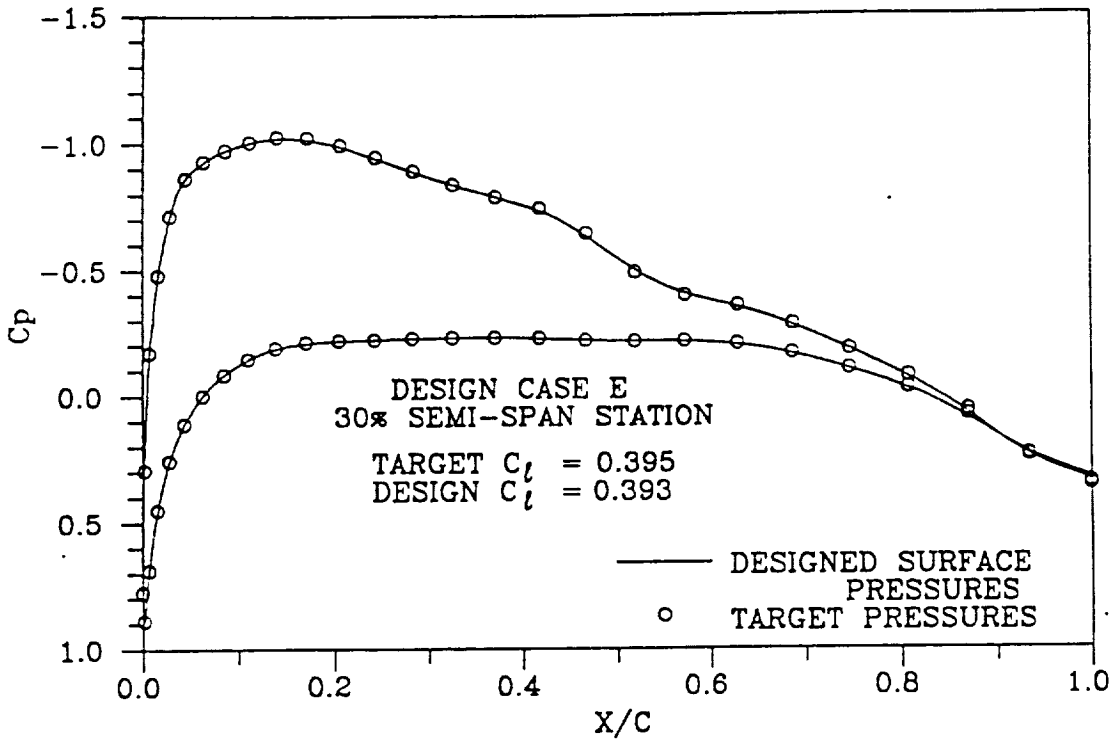

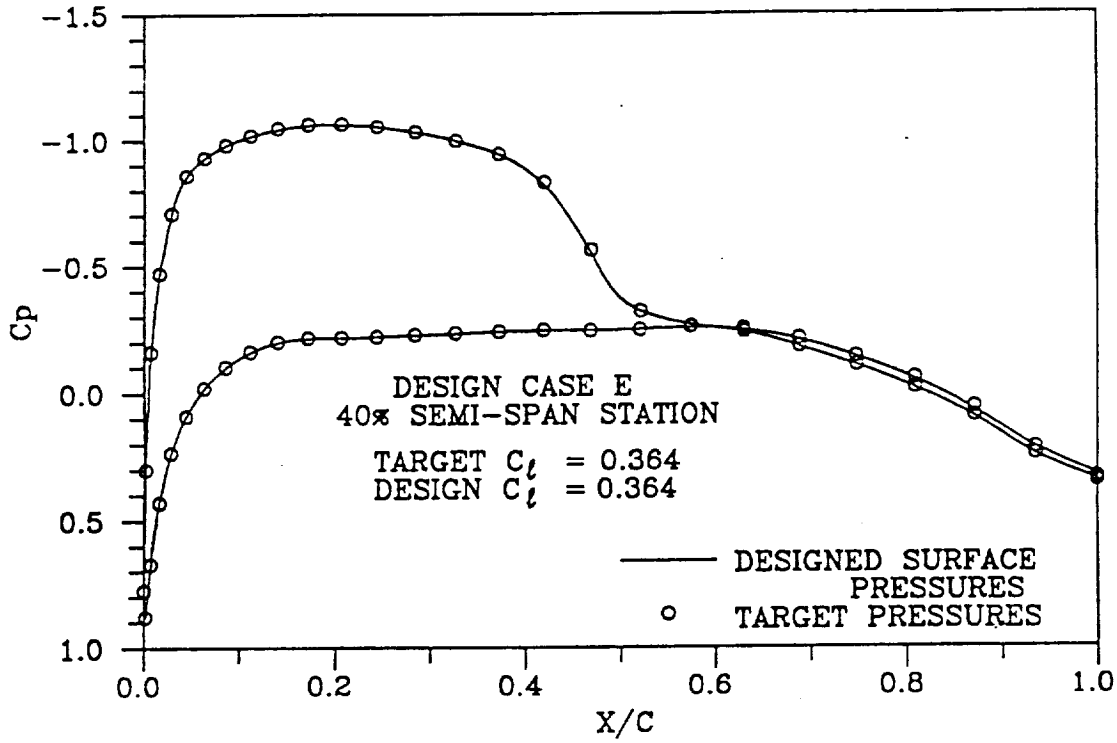

Figure 33. (Continued)

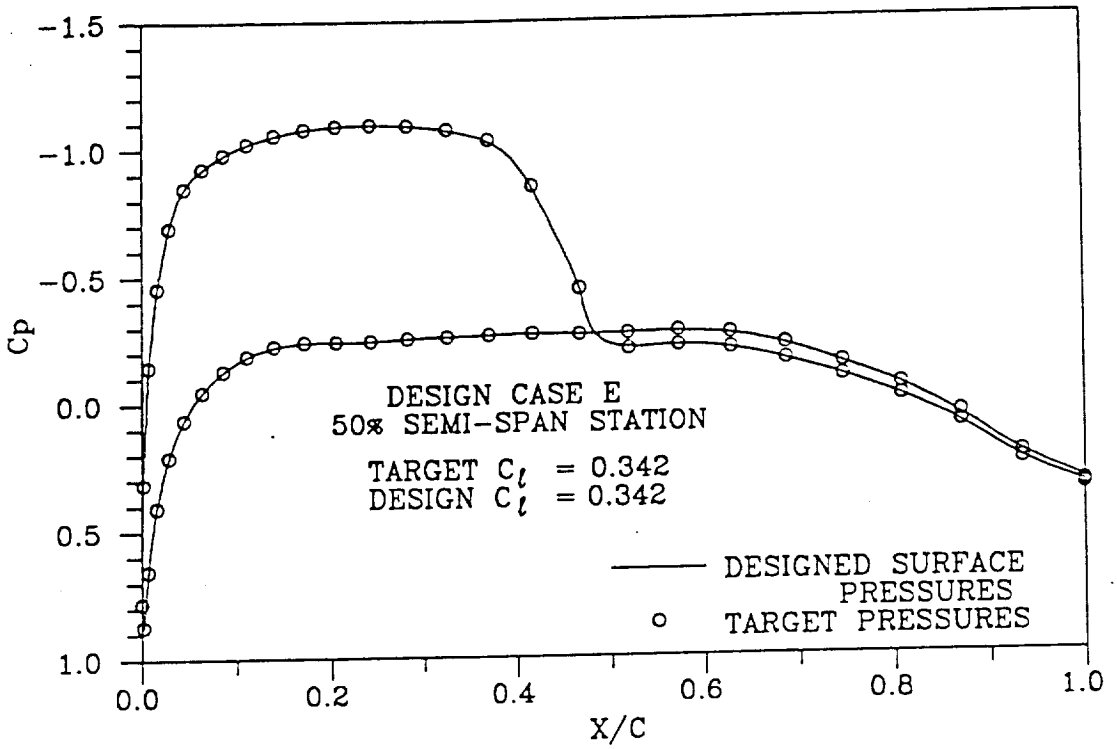

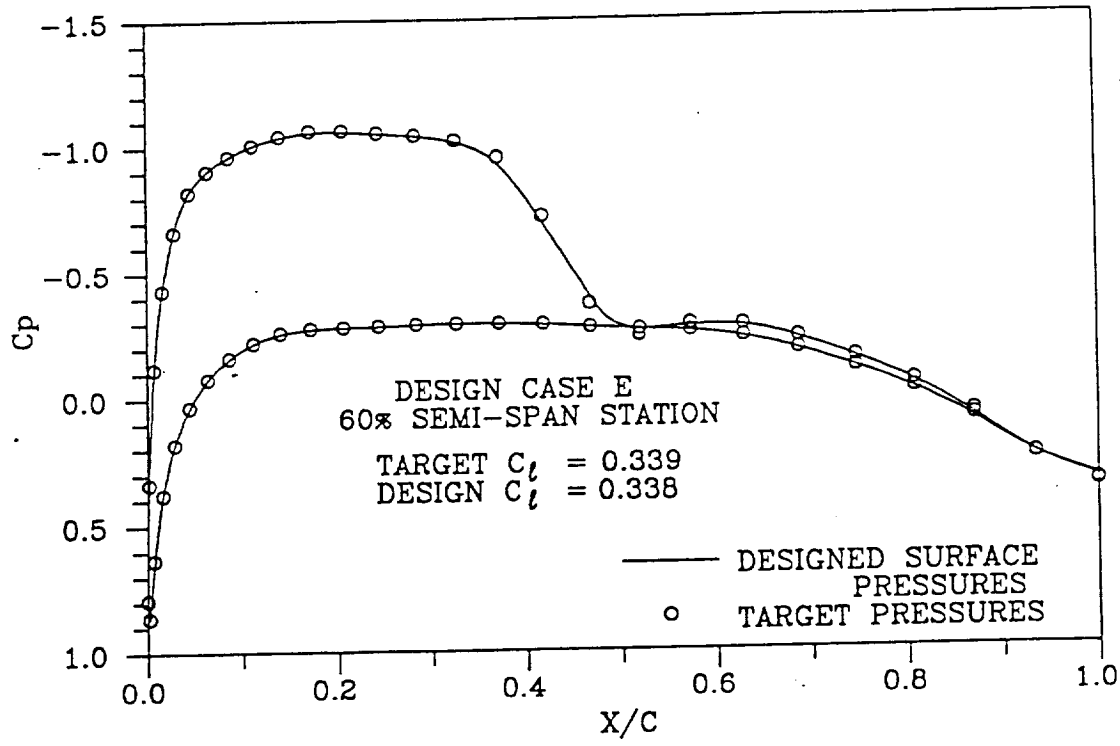

Figure 33. (Continued)

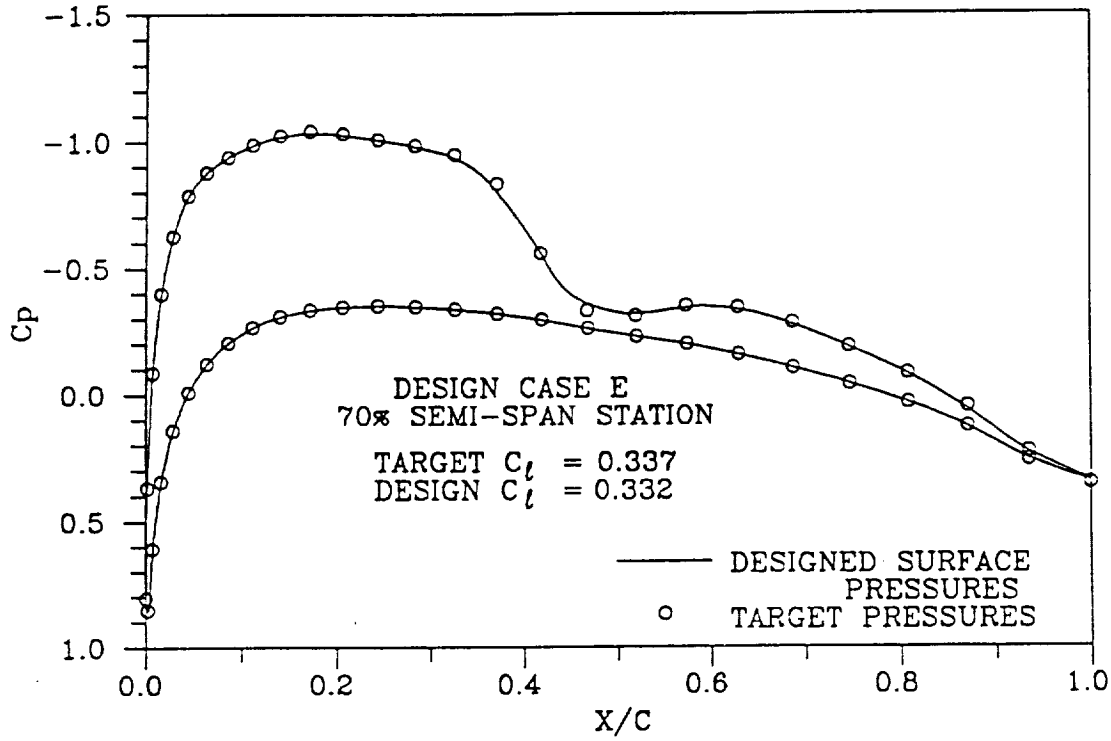

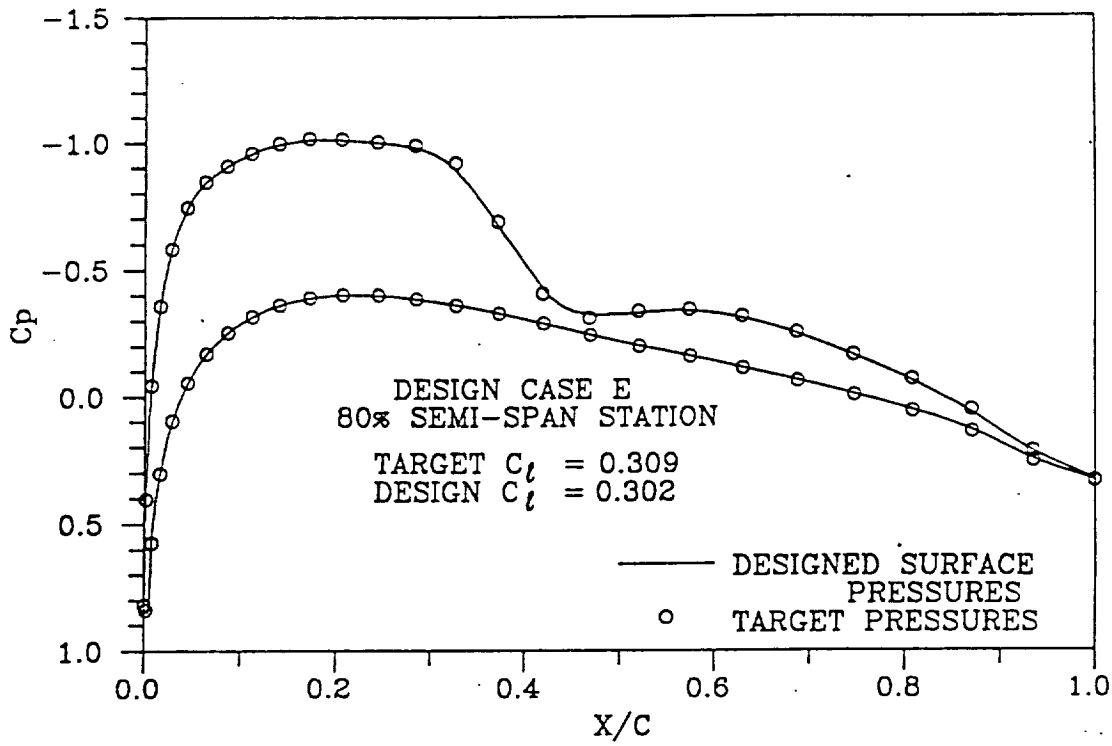

Figure 33. (Continued)

CONCLUSIONS AND SUGGESTIONS FOR FUTURE WORK

A direct-inverse wing design method has been successfully incorporated into the TAWFIVE transonic wing-body analysis computer code. The resultant code is capable of designing or modifying wings at both transonic and subsonic conditions and includes the effects of wing-body interactions. A series of test cases have been presented which demonstrate the accuracy and versatility of this inverse method.

Inclusion of viscous effects via the addition of the wing surface displacement thickness and wake thickness when performing wing design has been accomplished but not completely verified. Additional work will be required to run a sufficient sampling of test cases for evaluation of this design mode. The unique problems associated with viscous design and the effects of the various viscous correction models available in TAWFIVE would be the subject of a continuing research effort.

The development and evaluation of alternate methods of surface relofting are also topics for which continued research is suggested. The current method of relofting restricts the user to a family of leading edge geometries which can be constructed by the linear rotation of the initial shape. The option of using other relofting methods would extend the family of available shapes and add versatility to the design method.

REFERENCES

1. Boppe, C. W., "Transonic Flow Field Analysis for Wing-Fuselage Configurations," NASA CR-3243, 1980.

2. Holst, Terry L. and Ballhaus, William F., "Fast, Conservative Schemes for the Full Potential Equation Applied to Transonic Flow," AIAA Journal, Vol. 17, No. 2, Febuary 1979.

3. Caughey, D. A. and Jameson, Anthony, "Progress in Finite-Volume Calculation for Wing-Fuselage Combinations," AIAA Paper 79-1513R, 1979.

4. Melson, N. D. and Streett, C. L., "TAWFIVE: A User's Guide," NASA TM84619, September 1983.

5. Carlson, L. A., "TRANDES: A Fortran Program for Transonic Airfoil Analysis or Design," NASA CR-2821, June 1977.

6. Weed, R. A., Anderson, W. K., and Carlson, L. A., "A Direct-Inverse Three-Dimensional Transonic Wing Design Method for Vector Computers," AIAA Paper 84-2156, August 1984.

7. Murman, E. M., and Cole, J. D., "Calculation of Plane Steady Transonic Flows," AIAA Journal, Vol. 9, 1971, pp.114-121.

8. Cosentino, G. B. and Holst, T. L., "Numerical Optimization Design of Advanced Transonic Wing Configurations," AIAA Paper 85-0424, January 1985.

9. Davis, W., "TRO-2D: A Code for Rational Transonic Aero Optimization," AIAA Paper 85-0425, January 1985.

10. Bauer, F., Garabedian, P., and McFadden, G., "The NYU Inverse Swept Wing Code," NASA CR-3662, January 1983.

11. Tatsumi, S. and Takanashi, S., "Experimental Verification of Three-Dimensional Transonic Inverse Method," AIAA Paper 85-4077, October 1985.

12. Carlson, L. A., "Transonic Airfoil Design Using Cartesian Coordinates," NASA CR-2578, April 1976. 13. Anderson, W. K., and Carlson, L. A., "Inverse Transonic Wing Design on a Vector Processor," Texas A&M Research Foundation Report TAMRF-4535-8212, December 1982.

14. Jameson, Anthony and Caughey, D. A., "A Finite Volume Method for Transonic Potential Flow Calculations," Proceedings of AIAA 3rd Computational Fluid Dynamics Conference, Albuquerque, N. M., June 1977, pp. 35-54.

15. Jameson, Anthony, "Iterative Solution of Transonic Flows over Airfoils and Wings, Including Flows at Mach 1," Comm. Pure Appl. Math., Vol. 27, 1974, pp. 283-309.

16. Jameson, Anthony, "Transonic Potential Flow Calculations Using Conservative Form," Proceedings of AIAA 2nd Computational Fluid Dynamics Conference, Hartford, Conn., June 1975, pp.148-161.

17. Streett, Craig L., "Viscous-Inviscid Interaction for Transonic Wing-Body Configurations Including Wake Effects," AIAA Journal, Vol. 20, No. 7, July 1982, pp.915-923.

VITA

Thomas Anthony Gally was born in [redacted] on [redacted] After graduating from Eastwood High School, El Paso in 1980 he entered Texas A&M University where he recieved his BS degree in Aerospace Engineering in 1984. After spending one year working with General Dynamics Corporation in Fort Worth, Texas, he returned to Texas A&M to continue his education in the Aerospace department. He will recieve his MS degree in May 1987 and expects to continue working towards his PhD.

Correspondance may be addressed to him care of the Aerospace Engineering Department, Texas A&M University, College Station, Texas 77840.

VERIFICATION, OPTIMIZATION AND REFINEMENT OF A DIRECT-INVERSE TRANSONIC WING DESIGN METHOD INCLUDING WEAK VISCOUS INTERACTION

A Thesis

by

ROBERT R. RATCLIFF

Submitted to the Office of Graduate Studies of
Texas A&M University
in partial fulfillment of the requirements for the degree of

MASTER OF SCIENCE

August 1989

Major Subject: Aerospace Engineering

VERIFICATION, OPTIMIZATION AND REFINEMENT OF A DIRECT-INVERSE TRANSONIC WING DESIGN METHOD INCLUDING WEAK VISCOUS INTERACTION

A Thesis

by

ROBERT R. RATCLIFF

Approved as to style and content by:

Leland A. Carlson
(Chair of Committee)

Cyrus Ostowari
(Member)

E. A. Baskharone
Erian A. Baskharone
(Member)

Walter E. Haisler
Walter E. Haisler
(Head of Department)

August 1989

ABSTRACT

Verification, Optimization and Refinement of a Direct-Inverse Transonic Wing Design Method Including Weak Viscous Interaction. (August 1989)

Robert R. Ratcliff, B.S., Texas A&M University

Chair of Advisory Committee: Dr. Leland A. Carlson

New developments in the direct-inverse wing design method in curvilinear coordinates are presented. A spanwise oscillation problem and proposed remedies are discussed. Test cases are presented which reveal the approximate limits on wing aspect ratio and leading edge sweep angle for a successful design, and which show the significance of spanwise grid skewness, grid refinement, viscous interaction, the initial airfoil section and Mach number - pressure distribution compatibility on the final design. Furthermore, preliminary results are shown which indicate that it is feasible to successfully design a region of the wing which begins aft of the leading edge and terminates prior to the trailing edge.

To Mom

ACKNOWLEDGMENTS

The work presented in this paper was primarily supported by the National Aeronautics and Space Administration under Grant NAG-1-619 with Richard L. Campbell of the Langley Research Center as technical monitor. The author expresses his appreciation to Dr. Carlson for his support, guidance, and patience and to Thomas Gally for his assistance and helpful suggestions. Much thanks also goes to the Computer Service Center at Texas A&M University for their very generous computer support.

NOMENCLATURE

A	influence coefficients used in compensation terms
AR	aspect ratio
cos	cosine
c	local chord
C_l	airfoil section lift coefficient
C_L	wing lift coefficient
C_p	pressure coefficient
c_p	specific heat at constant pressure
cosh	hyperbolic cosine
F	Wing surface function in the physical domain
a	speed of sound
$a_{i,j}$	Fourier coefficients used in grid scheme
d	the relative x distance from the sectional quarter chord point
f	general function
$\|h\|$	determinant of the inverse jacobian matrix
H	inverse Jacobian transformation matrix
h	enthalpy per unit mass
I, J, K	grid locations in ξ, η, ζ directions
J	Jacobian transformation matrix
M	Mach number

P, Q, R	Jameson's upwinding terms
p	pressure
Q	compensation terms
q	magnitude of physical velocity
r	radius, radial distance; coefficient of determination
Re	Reynolds number
R_f	radius of fuselage
R_t	radius of wing tip
S	coordinates of the wing's surface in the auxiliary plane
S	wing surface function in the computational domain
S_w	arc length along approximated wake location
U	velocity at the edge of the boundary layer
U	velocity vector in Cartesian coordinates
u , v , w	velocity components in Cartesian coordinates
U, V, W	contravariant velocity components
V	velocity vector in computational space
x, y, z	Cartesian coordinates
y_{design}	ordinate of the design section
y_{mean}	mean ordinate of the target section
y_t	ordinate of airfoil at trailing edge
z	$\bar{x} + i\bar{\theta}$
α	angle of attack

β	angle between the wall shear line and the external streamline of the boundary layer
Δ	transformed boundary layer displacement thickness
Δl	magnitude of change in the airfoil surface in physical coordinates
Δ_t	user specified trailing edge thickness in units of chord fraction
δ	central-difference operator defined in Eq. (2-20)
δ_τ	relofting correction
δ^*	boundary layer displacement thickness
ϵ	degree of extrapolation coefficient
γ	ratio of specific heats
Γ	circulation
κ_w	flow curvature at the approximate wake location
μ	averaging operator defined in Eq. (2-20)
∇	vector differential operator
ϕ	reduced velocity potential function
Φ	velocity potential function
ρ	density
σ	smoothing operator, standard deviation
sinh	hyperbolic sine
τ	airfoil section thickness
τ_1	original airfoil thickness
τ_2	airfoil thickness at different Mach number
θ	momentum thickness

ϵ	degree of smoothing coefficient
ξ', η'	coordinates in auxiliary plane
ξ, η, ζ	transformed coordinates

Subscripts

avg	average quantity
$idle$	forward direct-inverse interface
$idte$	aft inverse-direct interface
II	index increment
i, j, k	grid locations in the ξ, η, ζ directions
ky	value at the wing's surface
l	lower surface
le	leading edge
o	stagnation conditions
s	singular line location
T	iteration time level
te	trailing edge
u	upper surface
w	wake
x, y, z	components in the x, y, z directions
∞	freestream conditions
ξ, η, ζ	components in the ξ, η, ζ directions

Superscripts

n	iteration time level
o	degrees

TABLE OF CONTENTS

APPENDIX Page

LIST OF TABLES

LIST OF FIGURES

Figure Page

Figure Page

Figure Page

CHAPTER I

INTRODUCTION

With the advent of efficient numerical schemes that accurately model the irrotational transonic flow about complex configurations such as wing-bodies and the appearance of computers with memory capacities and computational speeds necessary to execute these schemes in a reasonable amount of time, the efficient design of wings for transonic flight is quickly becoming a reality. Although transonic potential schemes combined with integral boundary layer solvers may not model the real flowfield as accurately as Euler or Navier Stokes schemes,[1-3] their use can significantly reduce the costs and time expenditures associated with transonic wing design.

There are basically two general types of inverse design methods: inverse solvers and predictor/corrector (P/C) methods. In the P/C type methods, an analysis code is used to calculate the flowfield for an arbitrary initial geometry; and then, this geometry is systematically modified by considering the differences between the calculated and target pressures. The changes to the airfoil sections can be obtained through optimization type procedures; or, as shown by Campbell,[4] the appropriate geometry changes can be systematically determined by using a design algorithm which relates pressure changes to changes in airfoil curvature.

An example of an inverse solver is the direct-inverse transonic wing analysis-design method, which has been under development at Texas A&M University.[5-15] In

Journal model is *AIAA Journal of Aircraft*

this method, the wing geometry is determined by specifying pressure distributions over part of the wing and then solving the mixed Neumann and Dirichlet boundary value problem associated with the full potential equation for compressible flow via finite difference and/or finite-volume techniques. The specified pressure distributions can be selected by the experienced designer to have such desirable characteristics as weak or nonexistent shock waves, a slowly increasing adverse pressure gradient to limit boundary layer separation, a center of pressure location giving a desirable pitching moment, or an efficient spanwise loading. The designer may also use wind-tunnel tests of successful airfoils as an aid in picking a desirable pressure distribution. The direct-inverse technique has been successfully used in stretched and sheared Cartesian coordinate systems[5-12,16,17] and most recently by Gally[13-15] in a curvilinear coordinate system.

It would be convenient if only the inviscid flowfield had to be included in the design process; but, unfortunately, it has been verified through transonic wind tunnel tests at low Reynold's numbers and flight testing at high Reynold's numbers that viscous effects are very significant[18]. For example, as the Reynold's number increases, the shock wave location is further aft on the wing. Thus, the shock wave in a viscous flowfield (finite Re) is located further upstream than that predicted by an inviscid (infinite Re) flowfield calculation. Although the inclusion of the viscous interaction significantly weakens the shock strength compared to inviscid results, the accompanying upstream displacement of the shock wave causes the sum of the differences between the upper and lower surface pressure distributions to be smaller than in the inviscid case; hence, the wing lift coefficient will be smaller in the viscous case.

Furthermore, it has been discovered that a wing using an aft-cambered airfoil section designed inviscidly for transonic conditions might develop 25-50% less lift in a viscous environment[9].

In light of the previous discussion its obvious that viscous effects must be taken into account through some means. One approach that applies in cases where there are no regions of massive separation is referred to as the weak viscous interaction technique. Since the weak primary viscous interaction effect is the formation of a boundary layer on the wing which effectively makes the airfoil thicker, the external streamlines for the wing boundary of the inviscid potential field are shifted outwards by a distance called the displacement thickness. This shifting is due to the decrease in velocity of the fluid in the boundary layer[19]. Thus, to include the effects of weak viscous interaction in an analysis of a wing, one simply needs to determine the potential solution for the surface, find the displacement thickness using the properties associated with the streamline representing the body, add this displacement thickness to the original surface, and repeat the process until the displacement thicknesses and the potential field converge.

Weak viscous interaction can be included in the inverse design process in much the same way. In the inverse regions, where the pressure boundary condition is applied, the new surface which approximately satisfies the boundary condition is calculated periodically by an integration of the flow boundary condition. At that time, the displacement thickness from the boundary layer calculations can be subtracted from this new surface to yield the hard or actual designed airfoil. This process can be carried out iteratively until there is an insignificant change in the displacements

due to boundary layer interaction and the inverse boundary condition, and in the flowfield's potential solution.

Fortunately, there is a computer program called TAWFIVE (for Transonic Analysis of a Wing And Fuselage and Interacted Viscous Effects) which not only has the capability of computing the potential field about a wing and fuselage combination but also contains a robust three dimensional integral boundary layer scheme which provides the necessary viscous effects in the form of boundary layer displacement thickness, wake curvature, and wake thickness. It should be noted that a three dimensional boundary layer code is desirable in order to properly predict the increased decambering of the sections near the tip due to the cross flow in the boundary layer[20]. In TAWFIVE, the inviscid numerical scheme is based upon Jameson and Caughey's FLO-30 conservative, finite-volume, full-potential flow method where computations are performed on a body-fitted, sheared, parabolic, wind-tunnel type coordinate system. The three dimensional boundary layer scheme added by Streett[20] to the originally-inviscid code computes the first order, weak, self-consistent, viscous interactions which include the boundary layer displacement effect on the wing's surface, the displacement in the wake, and the curvature/pressure jump in the wake. The boundary layer on the wing is found using a compressible integral method for laminar and turbulent flow with a fixed transition location. The turbulent method was based on work by Smith[21], while the laminar method was developed by Stock[22]. Small regions of separation are also modeled. This latter feature is an important addition for successful convergence, since small regions of separation often occur in the initial stages of computations behind shockwaves, in the cove region of aft-cambered

airfoils and near the trailing edge on the upper surface of the wing, even though they may not exist in the final converged solution[11]. The parameters in the wake region are computed in streamwise strips using a two dimensional entrainment integral technique. This method has been deemed valid for transport type wings[20].

Gally[13–15] has successfully incorporated the inverse design process into the TAWFIVE program. Since the modifications made were compatible with the existing computational methods and program structure of TAWFIVE, his work resulted in a versatile design code capable of allowing the user to design an entirely new wing or even discontinuous, nonadjacent segments of a wing. The latter option may be invaluable to engineers who are typically faced with the dilemma of designing around regions where the wing geometry may be fixed by constraints other than aerodynamic considerations. As seen in Fig. 1 these segments can even be non-adjacent upper or lower surfaces with overlapping lower or upper surfaces respectively.

On the other hand, as a consequence of the inverse method, previous experience has revealed that specified pressure distributions may not be imposed in regions less than about ten percent behind the leading edge of the wing section. This limitation was due to the difficulties associated with enforcing the pressure boundary condition near the leading edge of the airfoil where the vertical velocities are large. However this feature was not viewed as a real limitation since the leading edge regions of most airfoils are similar, the leading edge shapes may be constrained by non-aerodynamic factors, and since a leading edge geometry can be selected to produce the desired pressure values at the beginning of the design region[13].

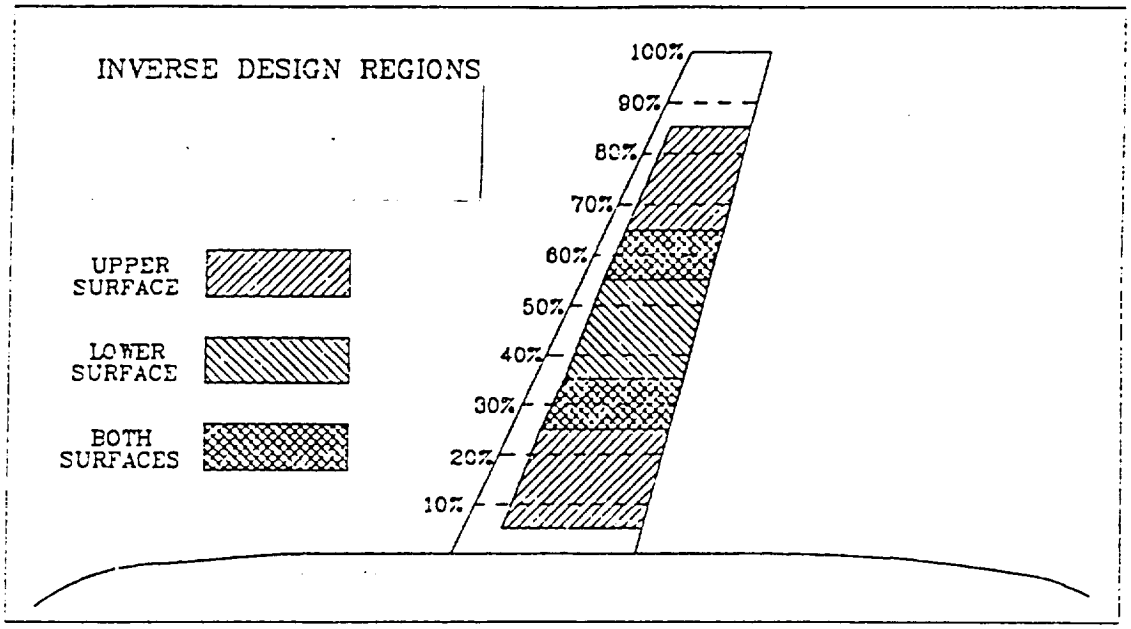

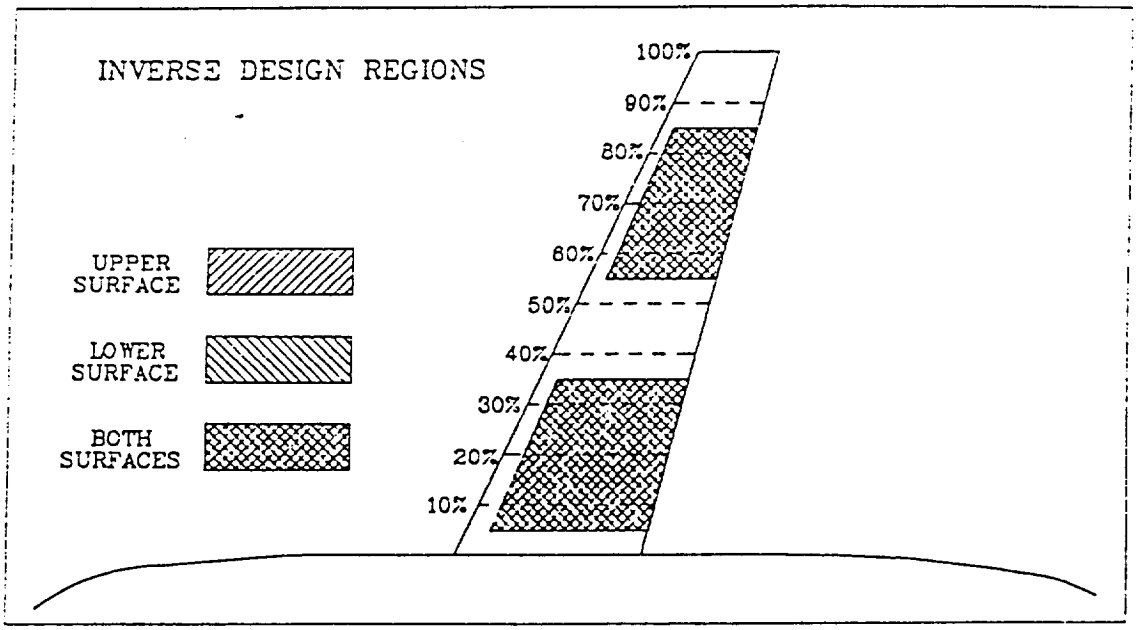

Fig. 1 Typical examples of overlapping and non-adjacent design regions [13]

Moreover, the imposed pressure distributions may often lead to an impractical airfoil that has an excessively blunt trailing edge or one in which the upper or lower surfaces cross prior to the trailing edge resulting in a fish tail shape. An excessively blunt trailing edge might cause a wing to have an excessive amount of drag due to base pressure at the trailing edge, while the fish tail shape would be impossible to construct. Since the nose shape or curvature has been shown to control trailing edge closure,[10,12,23,24] these undesirable shapes can be eliminated with a procedure which systematically modifies the leading edge thickness distribution called relofting. Two types of relofting procedures have already been included in the program by Gally. One is a simple linear rotation scheme where the surface being designed is rotated about the leading edge a proper amount to achieve the desired trailing edge thickness. In the second procedure, the leading edge is proportionally thinned or thickened a proper amount so that the relofted leading edges are in the same family of airfoil shapes.

Gally's original design code has been tested in a variety of ways for a Lockheed Wing-A wing-body. The self-consistency of the approach was tested by designing airfoil sections using certain desired pressure distributions, analyzing the resulting designed airfoils, and then comparing the desired pressure distributions input to those found through analysis. In all of the inviscid cases considered, the code proved itself consistent; the section lift coefficients of the designed and target sections and the respective pressure distributions were in strong agreement. The relofting procedures and the ability of the code to make large surface changes was verified by transforming

a 12% thick airfoil at supercritical conditions to a 6% thick airfoil at subcritical conditions in the same NACA family.

Although the code worked well for the inviscid cases attempted, there were some modifications and test cases which were required to make this code more valuable. For instance, since Streett found that the wake effects (wake displacement and curvature) were relatively important in the calculation of the lift distribution on a three dimensional wing,[20] presumably their includsion in the design process would be important as well. This was investigated by utilizing the wake options in the code and and comparing their effect on the design of a wing. The logic necessary to include the viscous effects in the design process originally added by Gally was tested and modified where necessary.

Recently, a spanwise decoupling in the design regions which led to instabilities in the design solution was observed. The supposed source of this instability and the various methods used to combat this problem will be discussed later in the report.

One modification added to the program, which helps smooth out the rippling spanwise variations in the wing and give the designer added versatility, is an option where the user specifies pressure distributions at the edges of the design region and then the changes in the thicknesses of the airfoil sections calculated by the program for those stations are interpolated and added to the stations delimited by the edges. This approach is different from the original method where the target pressure distributions, not the change in thicknesses, were interpolated to the stations in the design region.

Since the designer is admonished in the TAWFIVE user's manual[25] that the wing is not modeled accurately enough to allow analysis of very low-aspect ratio

wings and that grid problems may be encountered for wings which have high taper ratios or sweep angles, three wings of different aspect ratios and sweep angles will be used in the inverse design process to approximately delimit the range of geometries applicable to the present design code, TAW5D.

Because of the high computer costs associated with executing this program for fine computational grids, results will be shown which will reveal how fine the grid needs to be for satisfactory preliminary designs.

In summary, this thesis presents developments in the inverse design method. It includes a brief description of the analysis and design methods and techniques used to suppress a spanwise oscillation problem resulting from the interaction of the design method with the potential solver. In addition, it presents a series of test cases that reveal the lack of dependency of the design on the initial airfoil section, the importance of including viscous effects in wing design, and constraints due to aspect ratio, wing sweep, spanwise grid skewness. In addition, some questions about the necessary refinement of the grid and about any necessary constraints due to Mach-number-input-pressure-distribution compatibility will be answered.

CHAPTER II

DESCRIPTION OF TAWFIVE

As was stated in the introduction, the inverse-wing-design program, TAW5D, which was originally modified by Gally,[13-15] uses as its core the computer program TAWFIVE, which can be broken into three major sections: the inviscid, transonic, potential flow solver; the cylindrical/wind-tunnel type grid generation scheme; and the three dimensional, laminar and turbulent, integral boundary layer code included by Streett[20] which is based on the works of Smith[21], Stock[22] and Green.[26-28] Since the theory behind the code is spread across numerous references, an attempt will be made to summarize its formulation in a succinct fashion for the reader's convenience.

II.1 FLO-30

The transonic potential flow solver, FLO-30, [29-35] by Jameson and Caughey, is a finite volume method which solves the full potential equation in divergence form

$$(\rho u)_x + (\rho v)_y + (\rho w)_z = 0 \qquad (2-1)$$

transformed from Cartesian to curvilinear coordinates :

$$(\rho h U)_\xi + (\rho h V)_\eta + (\rho h W)_\zeta = 0 \qquad (2-2)$$

The derivation of the transformation of Eq. (2-2) is presented in Appendix A.

An expression for the local density, ρ, and the local speed of sound, a, nondimensionalized by the appropriate freestream quantities can be found by beginning with the energy equation

$$\frac{q_1^2}{2} + h_1 = \frac{q_2^2}{2} + h_2 \qquad (2-3)$$

where $q^2 = \left(u^2 + v^2 + w^2\right) q_\infty^2$

Then assuming the existence of a perfect gas such that

$$h = c_p T = \frac{a^2}{\gamma - 1} \qquad (2-4)$$

the energy equation becomes

$$\frac{\gamma - 1}{2} q_1^2 + a_1^2 = \frac{\gamma - 1}{2} q_2^2 + a_2^2 \qquad (2-5)$$

Next, assuming freestream and stagnation conditions such that

$$\begin{aligned} q_1 &= q_\infty \qquad & a_1 &= a_\infty \\ q_2 &= 0 \qquad & a_2 &= a_o \end{aligned} \qquad (2-6)$$

and upon normalizing all the primitive variables by the appropriate freestream quantities

$$\begin{aligned} \bar{p} &= \frac{p}{\rho_\infty q_\infty^2} \qquad & \bar{\rho} &= \frac{\rho}{\rho_\infty} \\ \bar{a} &= \frac{a}{q_\infty} \qquad & \bar{T} &= \frac{T}{T_\infty} \end{aligned} \qquad (2-7)$$

The bars on the nondimensionalized quantities will hereafter be omitted for convenience.

Eq. (2-5) becomes

$$a_o^2 = \frac{\gamma - 1}{2} + \frac{1}{M_\infty^2} \qquad (2-8)$$

The local speed of sound is obtained using Eqs. (2-5) and (2-8), yielding

$$a^2 = a_o^2 - \left(\frac{q}{q_\infty}\right)^2 \left(\frac{\gamma - 1}{2}\right) \qquad (2-9)$$

Using the isentropic relation

$$\frac{p}{p_\infty} = \rho^\gamma \qquad (2-10)$$

and realizing that

$$p_\infty = \frac{1}{\gamma M_\infty^2} \tag{2-11}$$

the isentropic relation becomes

$$p = \frac{\rho^\gamma}{\gamma M_\infty^2} \tag{2-12}$$

Then making use of the speed of sound relation

$$a^2 = \frac{\gamma p}{\rho} \tag{2-13}$$

a relation for density is found

$$\rho = (aM_\infty)^{\frac{2}{\gamma-1}} \tag{2-14}$$

which for air can be simplified to

$$\rho = \left(\frac{a}{a_\infty}\right)^{\frac{2}{\gamma-1}} = \left(\frac{a}{a_\infty}\right)^5 \tag{2-15}$$

This expansion is the actual form used in FLO-30, but the more familiar formula for density is shown in Eq. (2-16) and can be easily determined by substituting the speed of sound relation of Eq. (2-9) into Eq. (2-14).

$$\rho = \left[1 + \frac{\gamma-1}{2} M_\infty^2 \left(1 - u^2 - v^2 - w^2\right)\right]^{\frac{1}{\gamma-1}} \tag{2-16}$$

The nonconservative form of Eq. (2-1) shown in Eq. (2-17) can be determined by expanding the derivatives of Eq. (2-1); substituting in the appropriate derivatives of the density using the expression in Eq. (2-3); multiplying by $\frac{\rho}{a^2}$; and then implementing the equation of state for a perfect gas, the definition of the speed of sound; and finally defining the velocities in terms of a velocity potential, ϕ.

$$\begin{aligned}\left(a^2 - u^2\right)\phi_{xx} + \left(a^2 - v^2\right)\phi_{yy} + \left(a^2 - w^2\right)\phi_{zz} \\ - 2uv\phi_{xy} - 2vw\phi_{yz} - 2uw\phi_{xz} = 0\end{aligned} \tag{2-17}$$

Both of these forms are valid for isentropic, irrotational flows of Mach numbers ranging from zero to transonic[25]; but, by using the conservative form of the potential equation, a finite difference scheme will result[36] which conserves mass, especially in areas containing large gradients such as with the flow through a shock. Although, nonconservative schemes have been successively implemented due in part to the fact that the effective mass production at the base of the shock wave fortuitously models the shock/boundary layer interactions, the best approach may be to use a conservative scheme with viscous corrections added by a separate boundary layer model[37]. This approach is the method utilized by TAWFIVE to include viscous effects.

FLO-30 uses a finite-volume type scheme which makes use of a staggered box approach. Its formulation is directly analagous to the control volume approach used to derive the original PDE in Eq. (2-1), except in the finite-volume scheme, the discrete nature of the finite difference model is considered from the onset by using a finite control volume in the neighborhood of a grid point in the finite-difference mesh[36]. This method is best illustrated by using it to discretize the following two-dimensional, incompressible version of Eq. (2-1) written in Cartesian coordinates

$$u_x + v_y = 0 \qquad (2-18)$$

With the aid of the two-dimensional box shown in Fig. 2, it can be seen that the staggered box scheme derives its name from the way in which the primary and secondary boxes interlock. The values of the potentials at the four grid points which

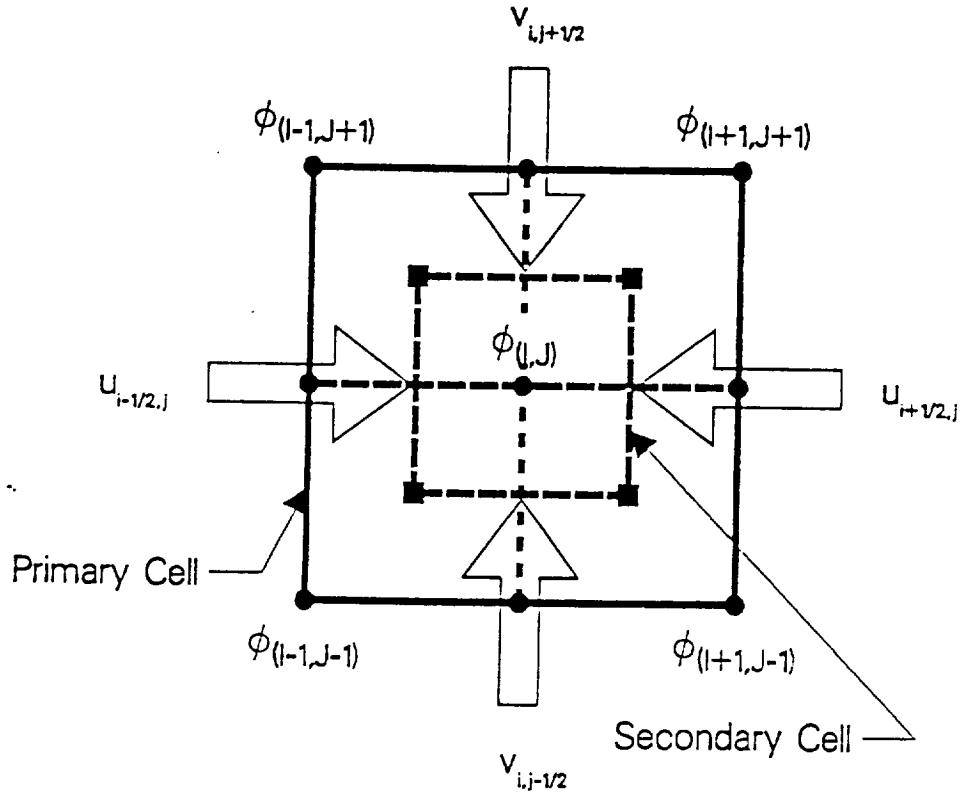

Fig. 2 Staggered box finite-volume cell

make up the corners of each primary box are used to calculate the velocities, u, v, in the following manner:

$$u = \phi_z = \mu_y \delta_z \phi$$
$$v = \phi_y = \mu_x \delta_y \phi \qquad (2-19)$$

where μ and δ are averaging and differentiating operators respectively and are defined by Jameson as

$$\mu_x f = \frac{1}{2}\left(f_{i+\frac{1}{2},j} + f_{i-\frac{1}{2},j}\right)$$
$$\delta_x f = f_{i+\frac{1}{2},j} - f_{i-\frac{1}{2},j} \qquad (2-20)$$

where it is assumed that $\Delta x = 1$. Therefore, the velocity, u, for instance, at the primary box center located at $(i+\frac{1}{2}, j+\frac{1}{2})$ is found by

$$u_{i+\frac{1}{2},j+\frac{1}{2}} = (\mu_y \delta_x \phi)_{i+\frac{1}{2},j+\frac{1}{2}} = \frac{(\phi_{i+1,j} - \phi_{i,j}) + (\phi_{i+1,j+1} - \phi_{i,j+1})}{2} \qquad (2-21)$$

The flux at the midpoint of each secondary box is determined by averaging the velocities u and v at the corners of that box in the y and x direction respectively; and the net flux into the secondary box at (i,j) is obtained, giving the discretized version of Eq. (2-18)

$$\mu_y \delta_x (u) + \mu_x \delta_y (v) = 0 \qquad (2-22)$$

where for example

$$(\mu_y \delta_x u)_{i,j} = \frac{\left(u_{i+\frac{1}{2},j-\frac{1}{2}} - u_{i-\frac{1}{2},j-\frac{1}{2}} + u_{i+\frac{1}{2},j+\frac{1}{2}} - u_{i-\frac{1}{2},j+\frac{1}{2}}\right)}{2} \qquad (2-23)$$

The previous discussion implicitly assumes that the velocity varies in a linear fashion between the primary cell centers so that the flux into the top of the secondary cell face would be, for instance:

$$\begin{aligned}\int_{x_{i-\frac{1}{2},j+\frac{1}{2}}}^{x_{i+\frac{1}{2},j+\frac{1}{2}}} v(x,y)dx &\approx \int_{x_{i-\frac{1}{2},j+\frac{1}{2}}}^{x_{i+\frac{1}{2},j+\frac{1}{2}}} \frac{v_{i+\frac{1}{2},j+\frac{1}{2}} - v_{i-\frac{1}{2},j+\frac{1}{2}}}{\Delta x} x + v_{i-\frac{1}{2},j+\frac{1}{2}} dx \\ &= \left(\frac{v_{i-\frac{1}{2},j+\frac{1}{2}} + v_{i+\frac{1}{2},j+\frac{1}{2}}}{2}\right)\end{aligned} \qquad (2-24)$$

Jameson and Caughey found that this lumping of the fluxes at the primary cell centers reduced to a rotated Laplacian type difference scheme and hence to an uncoupling of the solution between adjacent grid points. Therefore, compensation terms were added which basically extrapolate the fluxes from the corners of the secondary cell to a distance, ϵ, towards the midpoint of each secondary cell face. Considering Fig. 3 and using an $\epsilon = .25$, the flux, u, at the corresponding grid location $\left(i+\frac{1}{2}, j+\frac{1}{4}\right)$ is

$$u_{i+\frac{1}{2},j+\frac{1}{4}} = u_{i+\frac{1}{2},j+\frac{1}{2}} - .25\left(\frac{\partial u}{\partial y}\right)_{i+\frac{1}{2},j+\frac{1}{2}} \qquad (2-25)$$

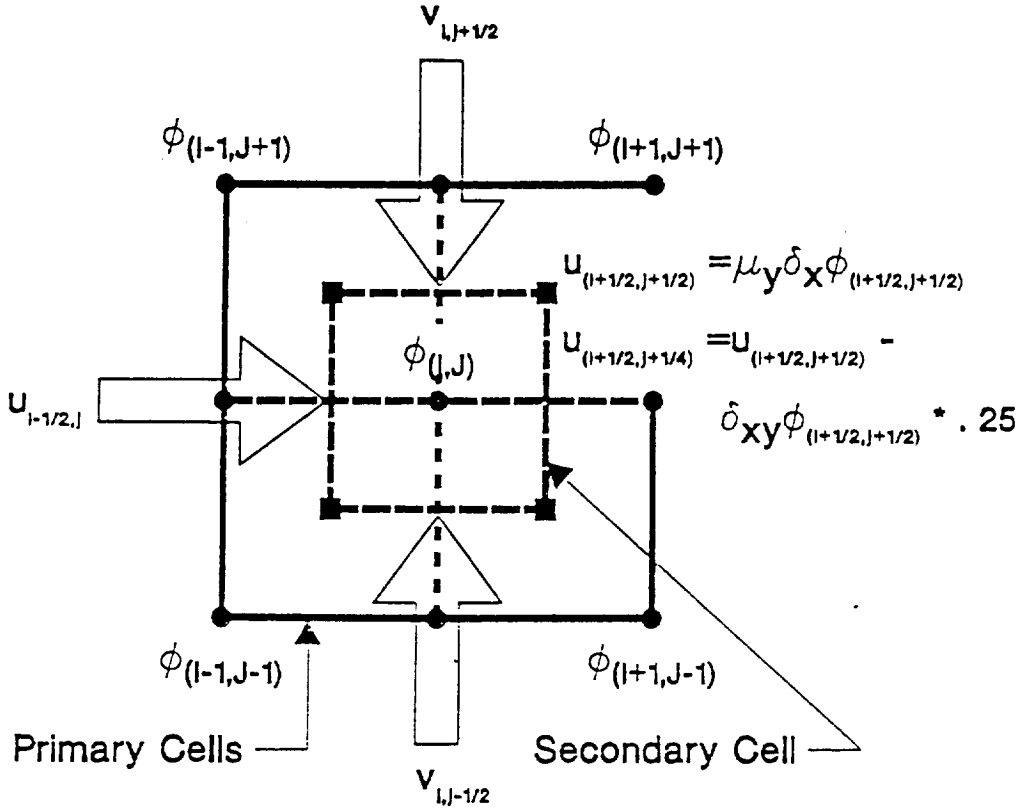

Fig. 3 Staggered box finite-volume cell with compensation terms defined

where

$$\left(\frac{\partial u}{\partial y}\right)_{i+\frac{1}{2},j+\frac{1}{2}} = \delta_{xy}(\phi)_{i+\frac{1}{2},j+\frac{1}{2}} \qquad (2-26)$$

When all the fluxes are extrapolated in this manner, the fluxes at the secondary cell centers become

$$\begin{aligned}
u_{i+\frac{1}{2},j} &= \frac{u_{i+\frac{1}{2},j-\frac{1}{2}} - \epsilon(\phi_{xy})_{i+\frac{1}{2},j+\frac{1}{2}} + u_{i+\frac{1}{2},j-\frac{1}{2}} + \epsilon(\phi_{xy})_{i+\frac{1}{2},j-\frac{1}{2}}}{2} \\
u_{i-\frac{1}{2},j} &= \frac{u_{i-\frac{1}{2},j-\frac{1}{2}} - \epsilon(\phi_{xy})_{i-\frac{1}{2},j+\frac{1}{2}} + u_{i-\frac{1}{2},j-\frac{1}{2}} + \epsilon(\phi_{xy})_{i-\frac{1}{2},j-\frac{1}{2}}}{2} \\
v_{i,j+\frac{1}{2}} &= \frac{v_{i+\frac{1}{2},j-\frac{1}{2}} - \epsilon(\phi_{xy})_{i+\frac{1}{2},j-\frac{1}{2}} + v_{i-\frac{1}{2},j+\frac{1}{2}} + \epsilon(\phi_{xy})_{i-\frac{1}{2},j+\frac{1}{2}}}{2} \\
v_{i,j-\frac{1}{2}} &= \frac{v_{i+\frac{1}{2},j-\frac{1}{2}} - \epsilon(\phi_{xy})_{i+\frac{1}{2},j-\frac{1}{2}} + v_{i-\frac{1}{2},j-\frac{1}{2}} + \epsilon(\phi_{xy})_{i-\frac{1}{2},j-\frac{1}{2}}}{2}
\end{aligned} \qquad (2-27)$$

When the net flux into the secondary box is accounted for, Eq. (2-22) becomes

$$\mu_y \delta_x u + \mu_x \delta_y v - \epsilon \left((\phi_{xy})_{i+\frac{1}{2},j+\frac{1}{2}} - (\phi_{xy})_{i+\frac{1}{2},j-\frac{1}{2}} - (\phi_{xy})_{i-\frac{1}{2},j+\frac{1}{2}} + (\phi_{xy})_{i-\frac{1}{2},j-\frac{1}{2}} \right) = 0 \qquad (2-28)$$

which is equivalent to

$$\mu_{yy}\delta_{xx}\phi + \mu_{xx}\delta_{yy}\phi - \epsilon\delta_{xxyy}\phi = 0 \qquad (2-29)$$

(Typically, ϵ is .25)

Notice that the compensation terms lead to a fourth derivative of the potential; this higher order derivative will become important later in the discussion of a spanwise oscillation problem that occured in the design process.

The previous concepts can be extended to three dimensional compressible flow in curvilinear coordinates by considering eight primary boxes as shown in Fig. 4. The three-dimensional potential equation

$$(\rho h U)_\xi + (\rho h V)_\eta + (\rho h W)_\zeta = 0 \qquad (2-30)$$

is again descretized in the same way as in the two-dimensional case to give

$$\mu_{\eta\zeta}\delta_\xi(\rho h U) + \mu_{\zeta\xi}\delta_\eta(\rho h V) + \mu_{\xi\eta}\delta_\zeta(\rho h W) = 0 \qquad (2-31)$$

The same averaging scheme is used in this case except that the derivatives now have to be averaged in two of the coordinate directions instead of one. For example, $(\rho h W)_\zeta$ becomes:

$$(\mu_{\xi\eta}\delta_\zeta \rho h W)_{i,j,k} = \frac{\left(\rho h W_{i+\frac{1}{2},j+\frac{1}{2},k-\frac{1}{2}} + \rho h W_{i+\frac{1}{2},j-\frac{1}{2},k-\frac{1}{2}} + \rho h W_{i-\frac{1}{2},j+\frac{1}{2},k-\frac{1}{2}} + \rho h W_{i-\frac{1}{2},j-\frac{1}{2},k-\frac{1}{2}}\right)}{4} - \frac{\left(\rho h W_{i+\frac{1}{2},j+\frac{1}{2},k+\frac{1}{2}} + \rho h W_{i+\frac{1}{2},j-\frac{1}{2},k+\frac{1}{2}} + \rho h W_{i-\frac{1}{2},j+\frac{1}{2},k+\frac{1}{2}} + \rho h W_{i-\frac{1}{2},j-\frac{1}{2},k+\frac{1}{2}}\right)}{4} \qquad (2-32)$$

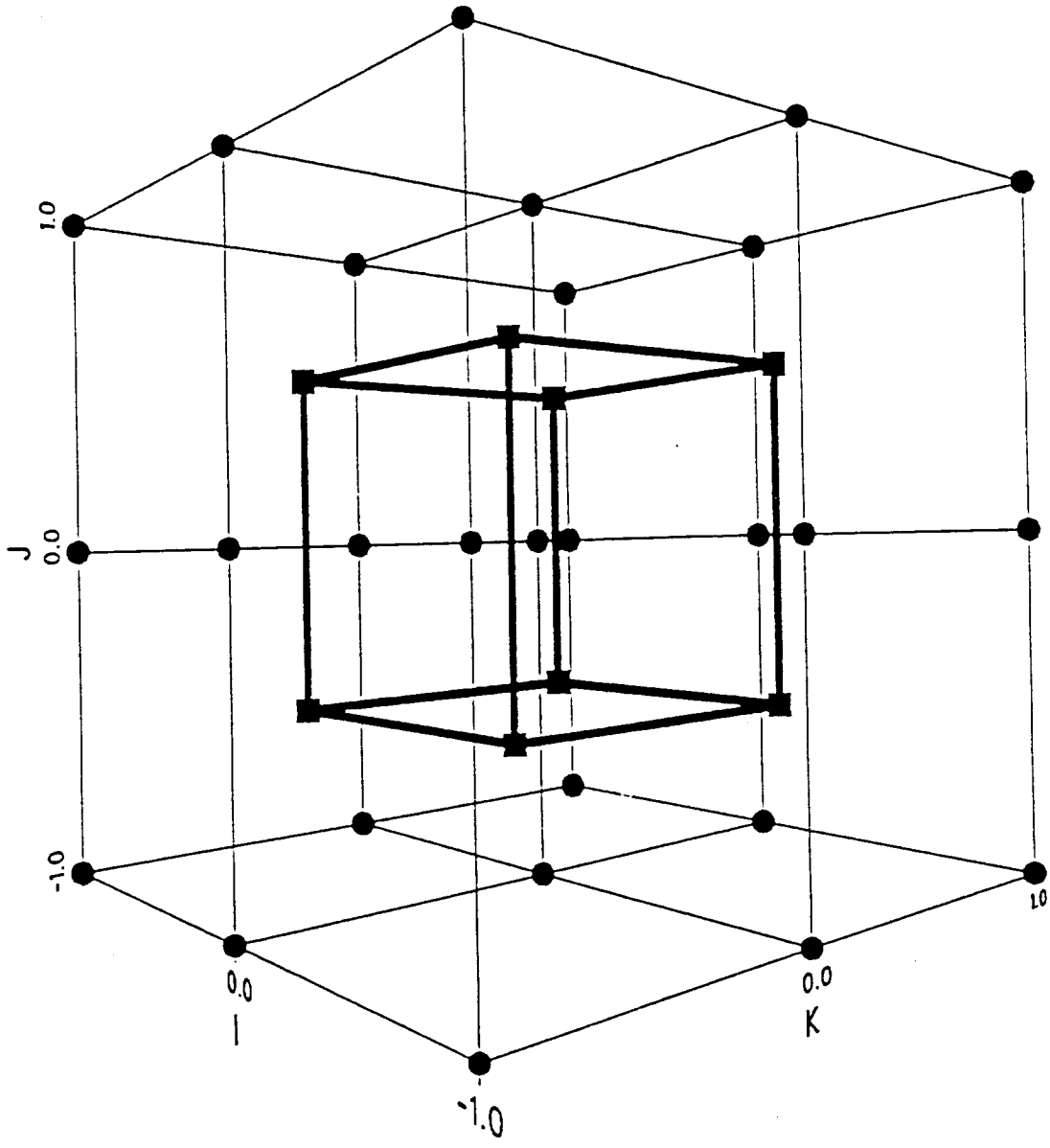

Fig. 4 Three dimensional staggered box finite-volume cell

Since relating the potential, ϕ, to the contravariant velocities, U, V, and, W may be somewhat unclear to the uninitiated, it is explained here for convenience. First, considering the the full potential function, Φ, defined as

$$\Phi = \phi + x\cos(\alpha) + y\sin(\alpha) \qquad (2-33)$$

the standard chain rule can be applied to it to give u, v and, w as follows:

$$\begin{aligned} u &= \frac{\partial\Phi}{\partial x} = \frac{\partial\phi}{\partial\xi}\frac{\partial\xi}{\partial x} + \frac{\partial\phi}{\partial\eta}\frac{\partial\eta}{\partial x} + \frac{\partial\phi}{\partial\zeta}\frac{\partial\zeta}{\partial x} + \cos\alpha \\ v &= \frac{\partial\Phi}{\partial y} = \frac{\partial\phi}{\partial\xi}\frac{\partial\xi}{\partial y} + \frac{\partial\phi}{\partial\eta}\frac{\partial\eta}{\partial y} + \frac{\partial\phi}{\partial\zeta}\frac{\partial\zeta}{\partial y} + \sin\alpha \\ w &= \frac{\partial\Phi}{\partial z} = \frac{\partial\phi}{\partial\xi}\frac{\partial\xi}{\partial z} + \frac{\partial\phi}{\partial\eta}\frac{\partial\eta}{\partial z} + \frac{\partial\phi}{\partial\zeta}\frac{\partial\zeta}{\partial z} \end{aligned} \qquad (2-34)$$

Defining

$$[J] = \begin{pmatrix} \xi_x & \eta_x & \zeta_x \\ \xi_y & \eta_y & \zeta_y \\ \xi_z & \eta_z & \zeta_z \end{pmatrix} \qquad (2-35)$$

and realizing that

$$[J] = \left[\mathrm{H}^T\right]^{-1} \qquad (2-36)$$

where H is the transformation matrix defined by

$$\mathrm{H} = \begin{pmatrix} x_\xi & x_\eta & x_\zeta \\ y_\xi & y_\eta & y_\zeta \\ z_\xi & z_\eta & z_\zeta \end{pmatrix} \qquad \text{with} \qquad h = |\mathrm{H}| \qquad (2-37)$$

the physical velocities, u, v, w normalized by q_∞ can be related to the gradient of the reduced potential function, ϕ, by

$$\begin{pmatrix} u \\ v \\ w \end{pmatrix} = \left[\mathrm{H}^T\right]^{-1} \begin{pmatrix} \phi_\xi \\ \phi_\eta \\ \phi_\zeta \end{pmatrix} + \begin{pmatrix} \cos\alpha \\ \sin\alpha \\ 0 \end{pmatrix} \qquad (2-38)$$

Note that since the grid point coordinate locations in the physical space, $(x,\ y,\ z)$, are generated as functions of $(\xi,\ \eta,\ \zeta)$, it is convenient to use H instead of J explicitly.

The contravariant velocities U, V, W, whose directions lie along the corresponding ξ, η, ζ grid lines are related to the physical velocities by :

$$\begin{pmatrix} U \\ V \\ W \end{pmatrix} = \mathrm{H}^{-1} \begin{pmatrix} u \\ v \\ w \end{pmatrix} \qquad (2-39)$$

and the derivatives of the potentials and the metrics are defined as:

$$\begin{aligned} \phi_\xi &= \mu_{\eta\zeta}\delta_\xi(\phi) & x_\xi &= \mu_{\eta\zeta}\delta_\xi(x) \\ \phi_\eta &= \mu_{\zeta\xi}\delta_\eta(\phi) & y_\xi &= \mu_{\eta\zeta}\delta_\xi(y) \\ \phi_\zeta &= \mu_{\xi\eta}\delta_\zeta(\phi) & z_\xi &= \mu_{\eta\zeta}\delta_\xi(z) \end{aligned} \qquad (2-40)$$

The density, ρ, and Jacobian, h, are evaluated at the centers of the of their respective primary cell centers. Again, by lumping the fluxes at the corners of the secondary cell's corners, the solution is decoupled on odd and even grid points leading to two independent solutions. This problem is remedied with compensation terms which again move the evaluation location of the fluxes to a point somewhere in between the corner and the midpoint of the secondary cell face. When this procedure is performed for all the cell faces, the potential equation takes on the form of

$$\begin{aligned} &\mu_{\eta\zeta}\delta_\xi(\rho h U) + \mu_{\zeta\xi}\delta_\eta(\rho h V) + \mu_{\xi\eta}\delta_\zeta(\rho h W) \\ &\quad - \epsilon\left(\mu_\zeta\delta_{\xi\eta}Q_{\xi\eta} + \mu_\xi\delta_{\eta\zeta}Q_{\eta\zeta} + \mu_\eta\delta_{\zeta\xi}Q_{\zeta\xi} - \frac{1}{2}\delta_{\xi\eta\zeta}Q_{\xi\eta\zeta}\right) = 0 \end{aligned} \qquad (2-41)$$

where the Q's are the compensation terms defined by Jameson as :

$$\begin{aligned} Q_{\xi\eta} &= (A_\xi + A_\eta)\,\mu_\zeta\delta_{\xi\eta}\phi \\ Q_{\eta\zeta} &= (A_\eta + A_\xi)\,\mu_\xi\delta_{\eta\zeta}\phi \\ Q_{\zeta\xi} &= (A_\zeta + A_\xi)\,\mu_\eta\delta_{\zeta\xi}\phi \\ Q_{\xi\eta\zeta} &= (A_\xi + A_\eta + A_\zeta)\,\delta_{\xi\eta\zeta}\phi \end{aligned} \qquad (2-42)$$

Here, A_ξ, A_η, A_ζ are the influence coefficients which compensate for the dependence of ρ on ϕ_ξ, ϕ_η, and ϕ_ζ. These terms end up being the coefficients of of $\phi_{\xi\xi}$, $\phi_{\eta\eta}$ and $\phi_{\zeta\zeta}$ in the expanded form of Eq. (2-30)[35].

Since the formation of entropy through a shock wave has been neglected through the use of the potential function, artificial viscosity must be added to eliminate the physically unrealistic solutions. In general, if central differences are used throughout the flow field, it is possible for the solution to predict discontinuous expansion shocks followed by compression shocks. This situation is a case where entropy decreases which is a physical impossibility, and is remedied by adding Jameson's[30,31] P, Q, and R terms which provide the necessary artificial viscosity by producing an upwind bias in the supersonic zones. The form of these terms can be found by formulating the potential equation in streamline coordinates which reveals the true zone of dependence in the supersonic zones. Then in these supersonic zones, the second derivatives of the potential, $\dot{\phi}$, included in the streamwise term are formulated with upstream or backward differences while the second derivatives included in the crossflow term are differenced centrally[29]. As shown in the final form of the following finite volume equation, the terms are formulated in such a way as to maintain the conservative form of the potential equation.

$$\mu_{\eta\zeta}\delta_\xi(\rho hU+P)+\mu_{\zeta\xi}\delta_\eta(\rho hV+Q)+\mu_{\xi\eta}\delta_\zeta(\rho hW+R) - \epsilon\left(\mu_\zeta\delta_{\xi\eta}Q_{\xi\eta}+\mu_\xi\delta_{\eta\zeta}Q_{\eta\zeta}+\mu_\eta\delta_{\zeta\xi}Q_{\zeta\xi}-\frac{\delta_{\xi\eta\zeta}Q_{\xi\eta\zeta}}{2}\right)=0 \qquad (2-43)$$

This numerical equation is then embedded into an artificial time dependent equation

$$\frac{\partial}{\partial\xi}(\rho hU+P)+\frac{\partial}{\partial\eta}(\rho hV+Q)+\frac{\partial}{\partial\zeta}(\rho hW+R) + \text{compensation terms} = \alpha\dot{\phi}_{\xi T}+\beta\dot{\phi}_{\eta T}+\gamma\dot{\phi}_{\zeta T}+\delta\dot{\phi}_T \qquad (2-44)$$

and solved via a successive line overrelaxation (SLOR) scheme which sweeps in the ξ direction along constant ζ surfaces starting at the root of the wing and implicitly solves for the potentials in the η direction. Equation (2-43) is a direct statement of the conservation of mass and should approach zero as the solution converges.

After obtaining a solution on a coarse grid, grid halving is used so that the finer grid has a better initial approximate solution, thus speeding up the convergence of the solution.

II.2 Grid Geometry

The computational grid used by the potential solver, FLO-30, is a body-fitted, curvilinear mesh which can be wrapped around a generalized wing-fuselage combination that is symmetric about the x-z plane. A body-fitted grid system is desirable in a full-potential scheme when the boundary conditions are applied at the actual surface of the airfoil. With a body-fitted grid, no interpolation is required and the boundary conditions are easily and accurately applied. Because of the shape the grid system resembles, it is called a wind-tunnel type grid. An example of this grid is portrayed in Fig. 5. The grid shown is the coarsest mesh and has 40 x 6 x 8 points in the ξ, η, and ζ directions respectively. With this grid, the wing becomes a constant η surface, and each cylindrical looking shell is a constant ζ surface. Constant ξ lines can be seen running spanwise on the wing at constant chord fractions from the leading edge. Notice also that due to the conformal transformation used[32,34] constant ξ lines are packed close to the leading edge of the wing. This clustering is an attractive feature when designing airfoil sections using the direct-inverse approach. Moreover, constant

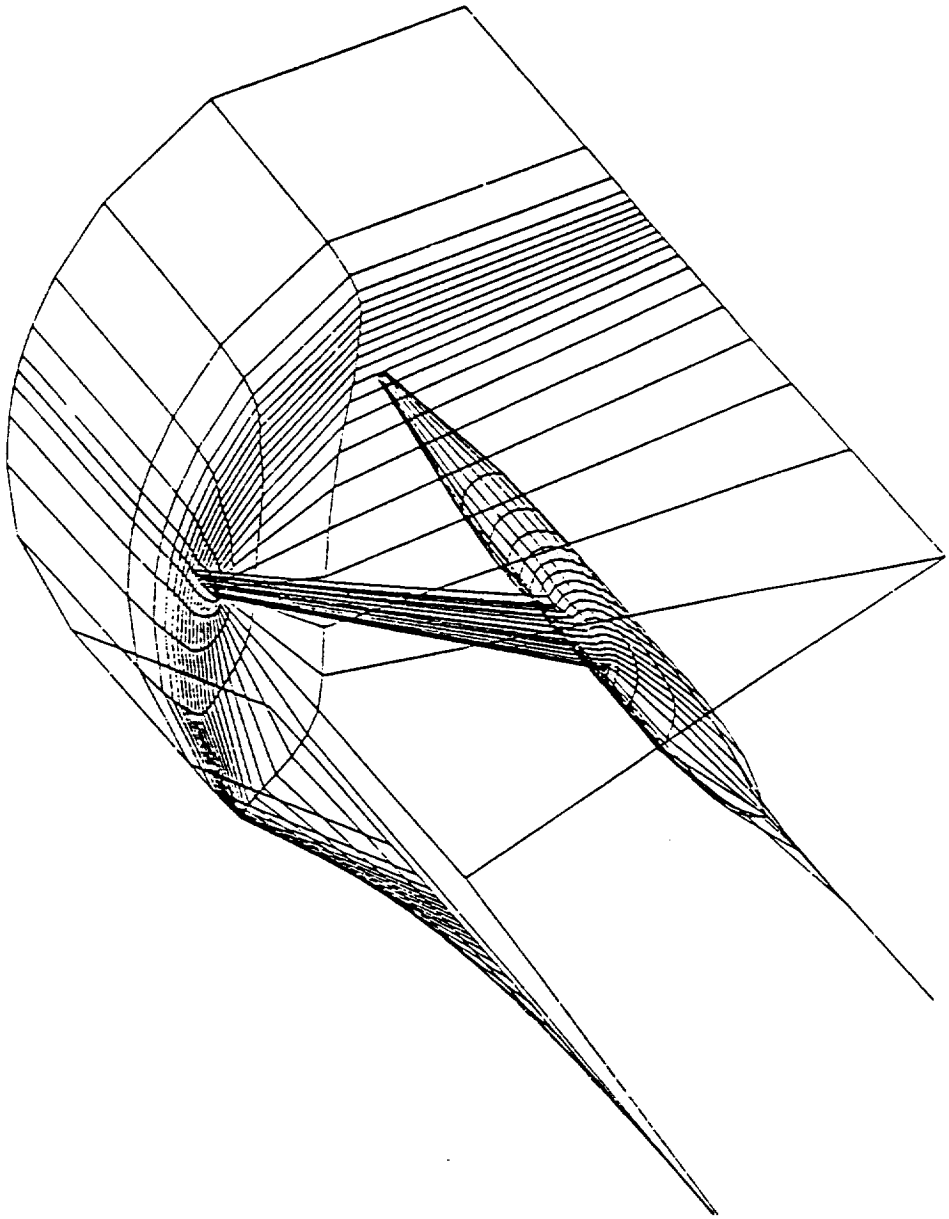

Fig. 5 Conformal grid topography

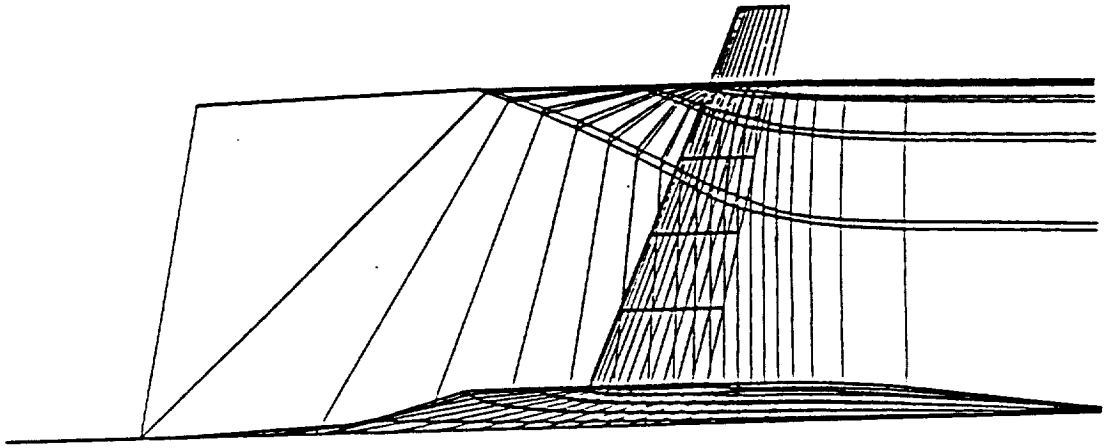

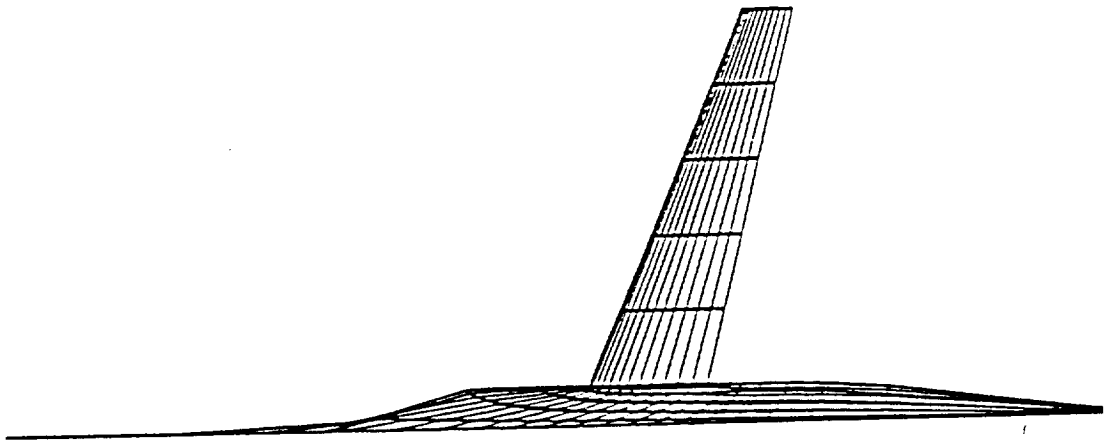

Fig. 5 Continued

ζ lines are spaced evenly on the wing and, on the finest mesh, give the designer up to 21 spanwise stations where the pressure distributions can be specified. As can be also seen from the figure, the lines of constant ξ and η are nearly orthogonal on the constant ζ surface[34] shown at the wing tip of the airplane, while lines of constant ξ and ζ on surfaces of constant η, such as the wing, are not orthogonal except, of course, for cases where the wing has no sweep or taper. The lines of constant ζ leaving the surface of the wing are nearly orthogonal to the surface; this fact will be important later on in the discussion of the wing-design methodology.

The computational grid system is created using a series of analytically-defined algebraic, conformal, and shearing transformations to transform the the wing-fuselage combination and surrounding flowfield in the physical space to a box in the computational space shown in Fig. 6. Following Caughey[34], the polar coordinates r and θ are defined in the crossflow planes as

$$r = \left(y^2 + z^2\right)^{\frac{1}{2}} \qquad (2-45)$$

$$\theta = \tan^{-1}\left(\frac{y}{z}\right) \qquad (2-46)$$

The fuselage surface, which is symmetric about the x-y plane, is defined by $r = R_f(x,\theta)$. All points in the flowfield are then referenced to the surface of the fuselage at the same x and θ location and normalized by the distance between radius, R_t, of the cylindrical surface passing through the wing tip and the radius of the fuselage, R_f at the given x and θ location :

$$\bar{r} = \frac{\left[r - R_f(x,\theta)\right]}{\left[R_t - R_f(x,\theta)\right]} \qquad (2-47)$$

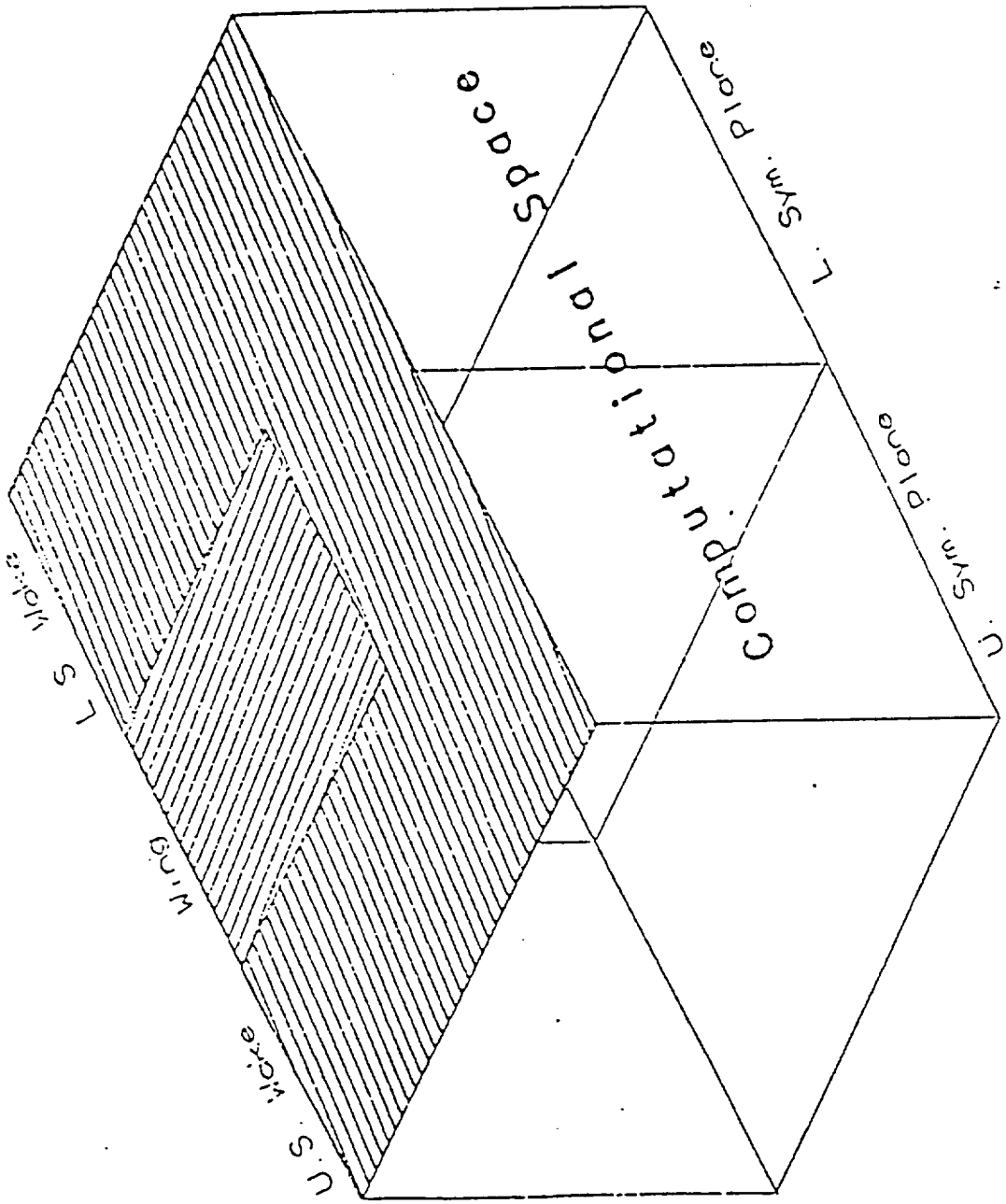

Fig. 6 The computational domain [25]

This normalization causes the lines of constant $\bar{r}$, or equivalently k, on the surface of the wing to be curved in the x-z plane so they will not coincide exactly with the chord line of the airfoil section. This procedure also maps the fuselage to a slit in the computational domain. This type of normalization allows for high, low, and mid-wing configurations.

The function $R_f(x,\theta)$ is found through a Fourier decomposition of the user-defined fuselage cross sections such that

$$R_f(x_i,\theta) = \sum_{j=1}^{m} a_{ij} \cos j(\theta + \frac{\pi}{2}) \qquad (2-48)$$

The coefficients, a_{ij}, which are assumed to be continuous functions of x, are spline fitted in the x direction for each j. The required radius of the fuselage can be found for any point on the wing, or in the flowfield, by interpolating these coefficients to the desired x.

A singular point is located at the focus of a parabola which is fit to the leading edge of each wing section with a least squares curve fit. The wing sweep, taper and dihedral are accounted for by referencing the coordinates in each surface of constant $\bar{r}$ to the location of the singular line, which is the locus of points comprising the singular points, $x_s(\bar{r})$, $\theta_s(\bar{r})$ at the leading edge of the wing.

$$\bar{x} = \frac{(x - x_s(\bar{r}))}{c(\bar{r})} + log(2) \qquad (2-49)$$

$$\bar{\theta} = 2\left(\frac{\theta - \left(1 - 4\frac{\theta^2}{\pi^2}\theta_s(\bar{r})\right)}{\left(1 - 4\frac{\theta_s^2(\bar{r})}{\pi^2}\right)}\right) \qquad (2-50)$$

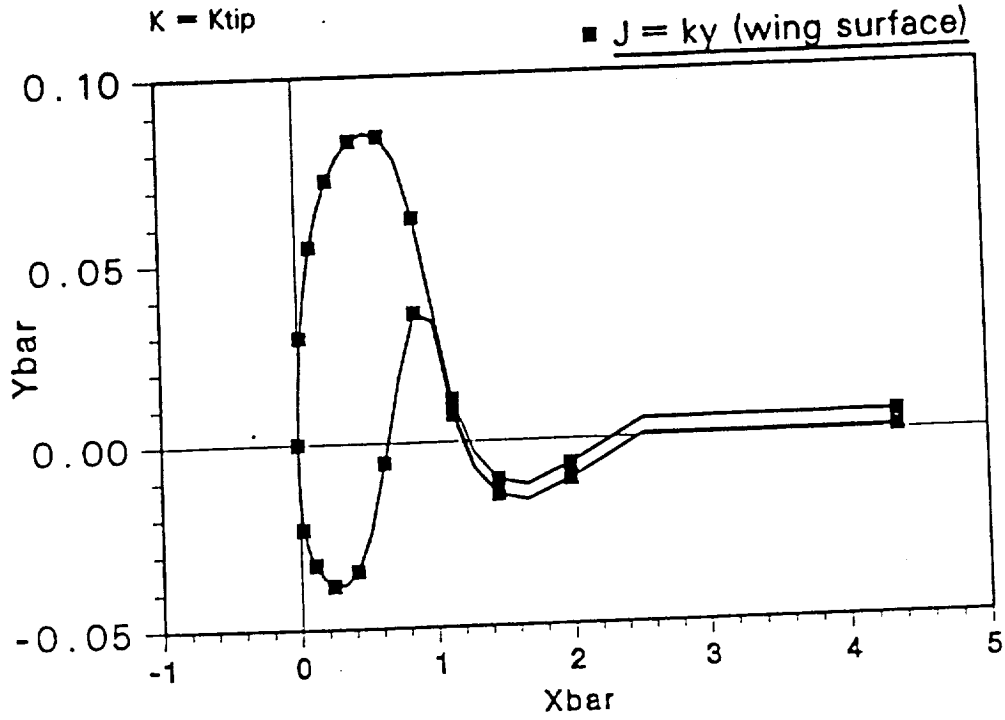

Fig. 7 Section surface and wake representation at a constant $\bar{r}$ station in the normalized plane

This normalization effectively maps the wing's planform to a rectangle in the computational space. The θ coordinates of the wing corresponding to the given $\bar{r}$ and x are found by linearly interpolating the coordinates of the airfoil sections at input stations defining the wing in the spanwise direction. Then at the intersection of a surface of constant $\bar{r}$ with the wing's surface shown in Fig. 7, the wing section and the wake is transformed into a bump in the conformally mapped plane, as shown in Fig. 8, with the inverse of the conformal transformation

$$\bar{x} + i\bar{\theta} = log\left[1 - \cosh\left(\xi' + i\eta'\right)\right] \qquad (2-51)$$

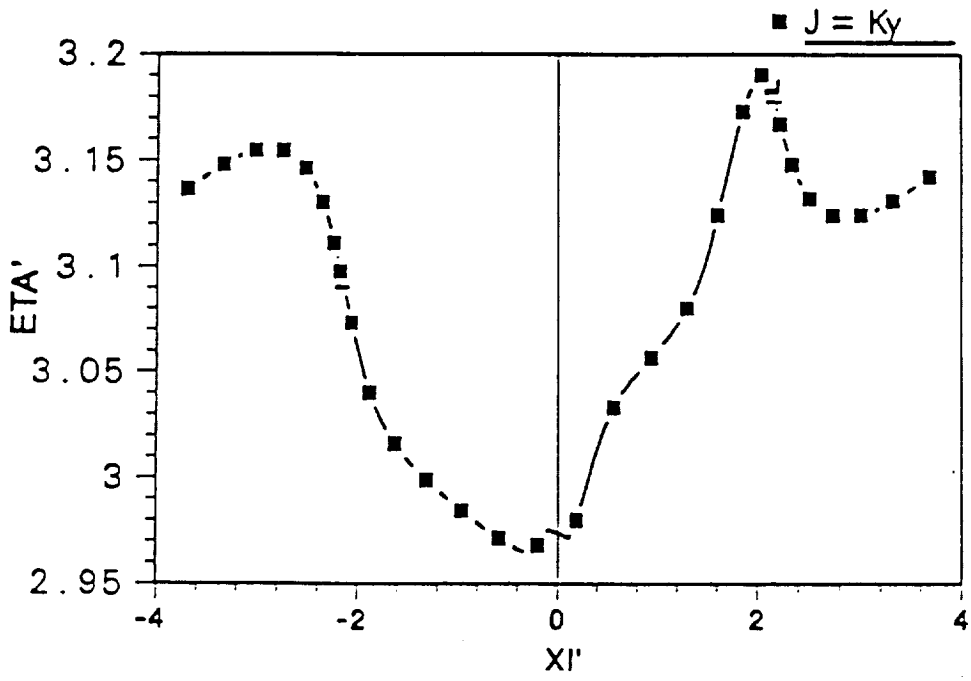

Fig. 8 Section surface and wake representation at a constant $\bar{\tau}$ station in the auxiliary plane

Fig. 9 reveals an entire constant $\bar{\tau}$ surface in the auxiliary plane. A function $S(\xi', \bar{\tau})$ is defined to be the η' coordinate corresponding to the wing's surface defined by the input geometry at a constant $\bar{\tau}$.

The η' coordinate is sheared out with a simple normalization according to

$$\xi = \xi', \quad \eta = \eta'/S(\xi', \bar{\tau}), \quad \zeta = \bar{\tau} \tag{2-52}$$

so that the wing surface lies on a coordinate line in a nearly orthogonal coordinate system of $\zeta = const.$

Next, the spacing of the coordinate points in the physical domain is controlled by introducing a Cartesian grid into the ξ, η, ζ computational domain where

$$-\xi_{lim} \leq \xi \leq \xi_{lim}, \quad 0 \leq \eta \leq 1, \quad 0 \leq \zeta \leq \zeta_{lim} \tag{2-53}$$

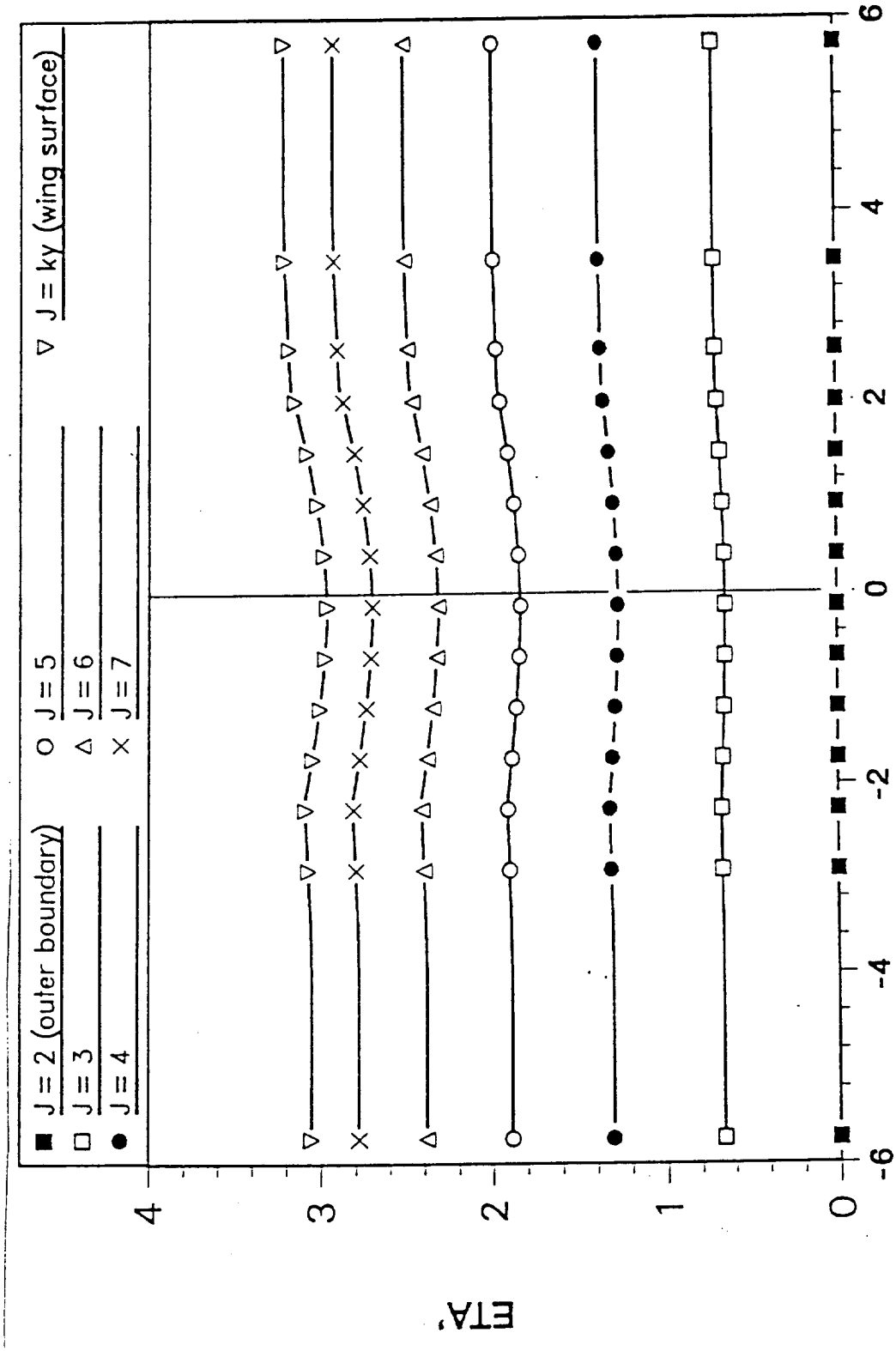

Fig. 9 Constant $\bar{r}$ surface in the auxiliary plane

Since the derivatives of the spatial coordinates needed for the transformation metrics are evaluated numerically, stretching to infinity is impossible; thus the computational domain is truncated a finite distance away from the airplane. The outer limits of ξ and ζ are chosen such that the grid stretches out far enough from the wing-fuselage so that freestream boundary conditions can be safely applied. These constants are not user specified, but rather are hard coded in Subroutine COOR of TAWFIVE, such that the distance of the outer boundary from the fuselage is about 3 wing spans. This distance is probably more than sufficient for most applications; but if a low aspect ratio wing is used, which has a large powerful potential vortex at the wing tip and significant amounts of spanwise flow, the aerodynamicist may want to increase the outer boundary distance.

The ξ, η and, ζ functions for a coarse grid (40x6x8) are shown in Figs. 10-12. Notice that distribution of ξ between grid points 8 and 24, which corresponds to the upper and lower trailing edges respectively, in this domain varies linearly and evenly on the wing and then varies quite quickly into the wake ending at a downstream location where the flowfield is assumed to be nonchanging. The ζ stretching function has the same form, but of course the outer limit at $K = 12$ determines the outer, radial boundary where the freestream conditions are imposed, which in this case, as mentioned earlier, will be about 3 wing spans. The η stretching function varies in a parabolic fashion from the wing's surface at $J = 14$. Although this stretching does seem to pack grid points close to the surface of the wing, since η is basically an angular ordinate, the grid spacing above the wing becomes greater as one proceeds

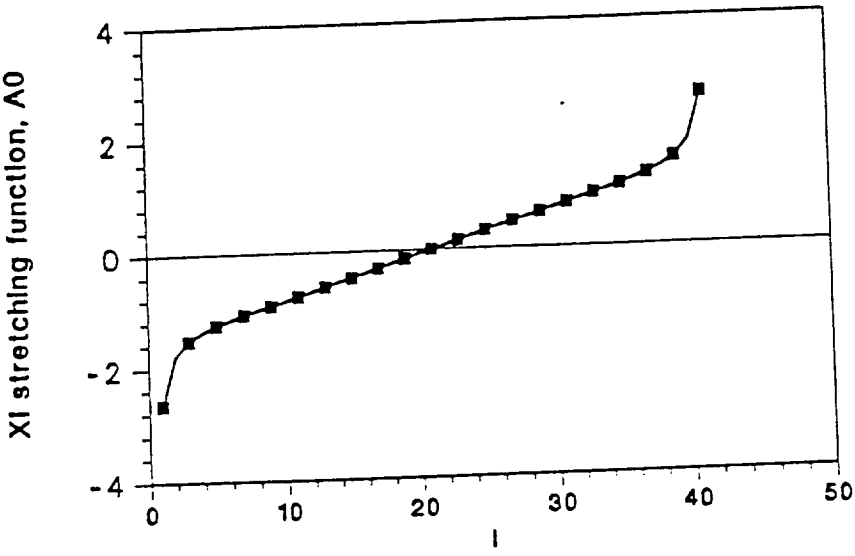

Fig. 10 Stretching function for the ξ (I) direction

towards the tip. This increase means that the resolution at the tip region is much less than that at the root, but this is countered later with a radial correction so that the grid spacing immediately above the wing is essentially constant for every spanwise station.

Once the function $S(\xi', \bar{r})$ has been linearly interpolated to the new ξ coordinates, the physical coordinates of the grid system can be found through the reverse procedure. First, ξ', η', and $\bar{r}$ are found using Eq. (2-52). Then Eq. (2-51) is used to extract $\bar{x}$ and $\bar{\theta}$. But before this operation is performed, $\bar{x}$ and $\bar{\theta}$ have to be

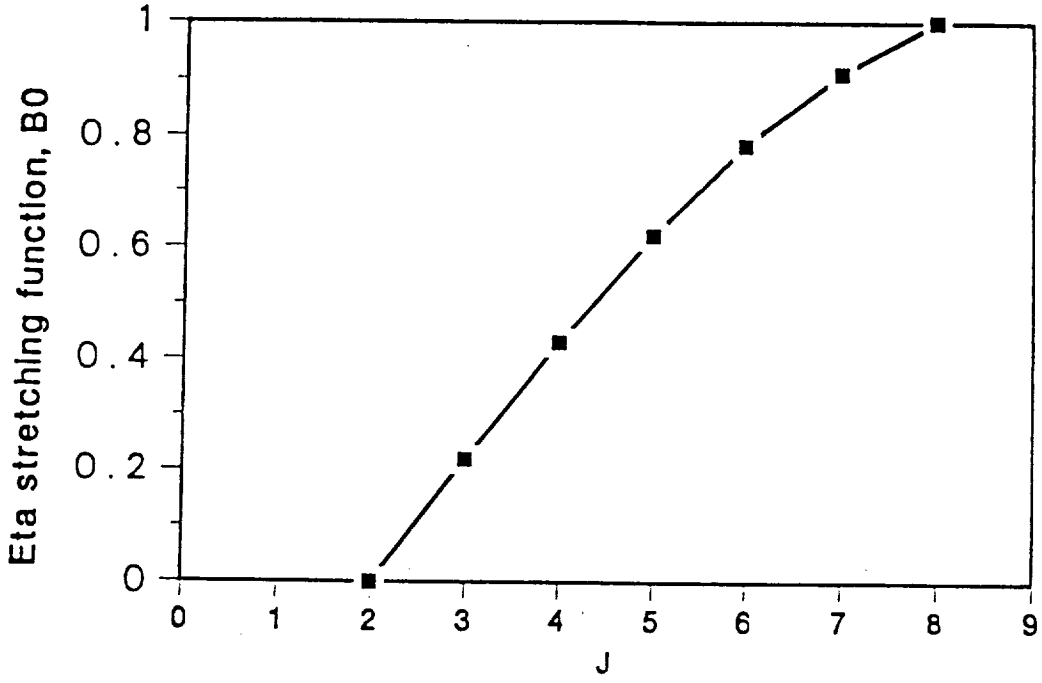

Fig. 11 Stretching function for the η (J) direction

separated in Eq. (2-51). First, both sides are exponentiated and the definition of the hyperbolic cosine is used so that Eq. (2-51) becomes

$$e^{\bar{z}}e^{i\bar{\theta}} = 1 - \frac{1}{2}\left(e^{\xi'}e^{i\eta'} + e^{-\xi'}e^{-i\eta'}\right) \qquad (2-54)$$

Using Euler's identity,

$$e^{iz} = \cos(z) + i\sin(z) \qquad (2-55)$$

rearranging, and separating imaginary and real parts, gives

$$e^{\bar{z}}\cos\bar{\theta} = 1 - \frac{1}{2}\cos\eta'\left(e^{\xi'} + e^{-\xi'}\right) \qquad (2-56)$$

$$e^{\bar{z}}\sin\bar{\theta} = -\frac{1}{2}\sin\eta'\left(e^{\xi'} - e^{-\xi'}\right) \qquad (2-57)$$

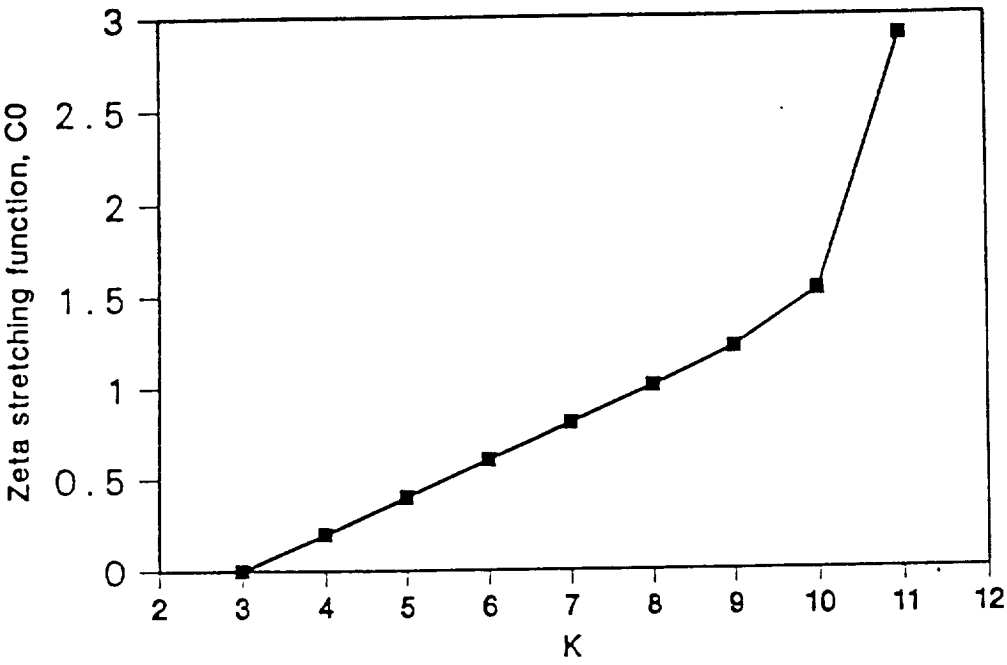

Fig. 12 Stretching function for the ζ (K) direction

Dividing these two equations by each other and solving for $\bar{\theta}$ explicitly yields

$$\bar{\theta} = \tan^{-1}\left[\frac{-\sin\eta' \sinh\xi'}{1-\cos\eta' \cosh\xi'}\right] \qquad (2-58)$$

Next $\bar{x}$ is found explicitly by first using a trigonometric identity and Eq. (2-58) to generate

$$\sin\bar{\theta} = \frac{-\sin\eta' \sinh\xi'}{\sqrt{(1-\cos\eta' \cosh\xi')^2 + \sin\eta' \sinh^2\xi'}} \qquad (2-59)$$

Substituting this into Eq. (2-57) and performing some algebra gives

$$\bar{x} = ln\left(\cosh\xi' - \cos\eta'\right) \qquad (2-60)$$

So given ξ' and η' from the previous steps, the normalized coordinates $\bar{x}$ and $\bar{\theta}$ are obtained for all the grid points in the domain. At this time, two more special stretching functions are introduced. One function is used to further stretch $\bar{x}$ downstream

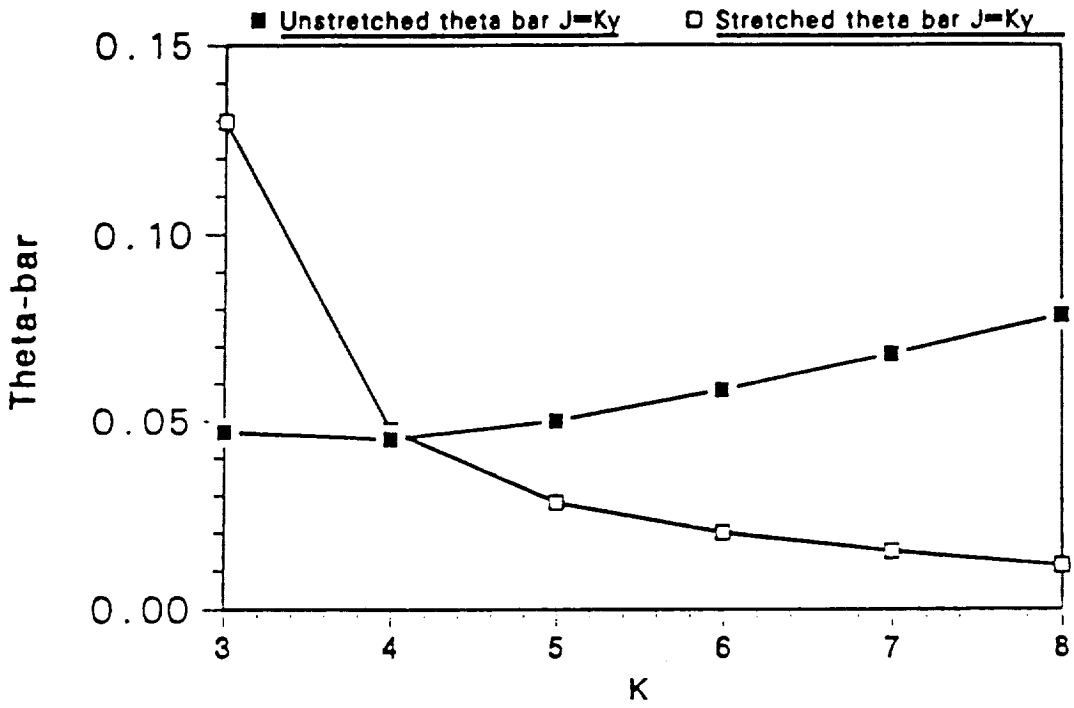

Fig. 13 Comparison between stretched and unstretched $\bar{\theta}$

of the wing and another scales $\bar{\theta}$ such that nearly constant grid spacing is achieved immediately above the wing from the root to the outer boundary. The effects of the stretching functions can be seen in Fig. 13.

Notice that this conformal transformation packs grid lines at the leading edge of the wing where the gradients are large. This clustering is an attractive feature for the inverse design procedure. However, it is paired with the disadvantage that the chordwise grid spacing is large at the trailing edge where high resolution is needed to accurately satisfy the Kutta condition and to resolve trailing edge pressures accurately especially with those generated by aft cambered airfoils.

Equations (2-49) and (2-50) are inverted to give x and θ and then Eq. (2-47) is inverted to yield r for a given x and θ. This last step requires extensive interpolation

to find the radius of the fuselage, $R_f(x,\theta)$, for all of the grid points. Then Eqs. (2-45) and (2-46) are used to find the physical coordinates y and z of the grid. Finally, coordinates of the points located in 'ghost' surfaces are obtained through simple linear extrapolation of the adjacent grid points along the appropriate ξ, η or, ζ grid line.

II.3 Boundary Conditions

There are a number of boundary conditions which must be applied to the mathematical model of the physical flow about the wing-body. These include flow tangency on the wing, fuselage, and the symmetry plane; appropriate far-field boundary conditions at the finite limits of the computational domain; the Kutta condition at the trailing edge of the lifting wing; appropriate treatment of the wake; and the computational slit outboard of the wing tip.

II.3.1 Flow tangency

The flow tangency condition is easily implemented due to the curvilinear system. The fluxes above the surface need only be reflected to the ghost points beneath it so that the net out of plane component of the flux vanishes at the surface. In the case of the wing this becomes

$$\begin{aligned} \rho h U_{i,ky+\frac{1}{2},k} &= \rho h U_{i,ky-\frac{1}{2},k} \\ \rho h V_{i,ky+\frac{1}{2},k} &= -\rho h V_{i,ky-\frac{1}{2},k} \qquad \text{where: } ky = j_{wing} \\ \rho h W_{i,ky+\frac{1}{2},k} &= \rho h W_{i,ky-\frac{1}{2},k} \end{aligned} \qquad (2-61)$$

Similarly for the symmetry plane

$$\begin{aligned} \rho h U_{i,1\frac{1}{2},k} &= \rho h U_{i,2\frac{1}{2},k} \\ \rho h V_{i,1\frac{1}{2},k} &= -\rho h V_{i,2\frac{1}{2},k} \qquad \text{where: } j = 2 \text{ on the symmetry plane} \\ \rho h W_{i,1\frac{1}{2},k} &= \rho h W_{i,2\frac{1}{2},k} \end{aligned} \qquad (2-62)$$

While for the fuselage this becomes

$$\rho h U_{i,j,2\frac{1}{2}} = \rho h U_{i,j,3\frac{1}{2}}$$

$$\rho h V_{i,j,2\frac{1}{2}} = \rho h V_{i,j,3\frac{1}{2}} \qquad \text{where: } k = 3 \text{ on the fuselage} \qquad (2-63)$$

$$\rho h W_{i,j,2\frac{1}{2}} = -\rho h W_{i,j,3\frac{1}{2}}$$

The previously discussed compensation terms and upwinding terms are also similarly reflected in an appropriate manner.

Potentials at the ghost points located at grid points beneath the surfaces are needed for the calculation of surface velocities used in the upwinding terms and the surface pressures. These are found for the wing and fuselage by setting the appropriate contravariant velocity to zero in

$$\begin{pmatrix} U \\ V \\ W \end{pmatrix} = \left[\mathrm{H}^T \mathrm{H}\right]^{-1} \begin{pmatrix} \phi_\xi \\ \phi_\eta \\ \phi_\zeta \end{pmatrix} + \mathrm{H}^{-1} \begin{pmatrix} \cos\alpha \\ \sin\alpha \\ 0 \end{pmatrix} \qquad (2-64)$$

and using the resulting equation to solve for the unknown potential at the ghost point. In the case of the fuselage, this method of defining the ghost points is used solely when they are needed in the calculation of the upwinding terms in the residual expression. When the pressures are calculated, the ghost points are defined by assuming

$$\phi_{\zeta\zeta} = 0 \qquad (2-65)$$

so that the potential at the ghost point is, in effect, linearly extrapolated in the spanwise direction. As seen in Fig. 14, these two methods lead to quite different values. The first leads to a discontinuous spanwise variation in the potential while the second has a much smoother variation. The first approach guarantees that the flow will be tangent at the fuselage, while the second does not. However, the pressures calculated

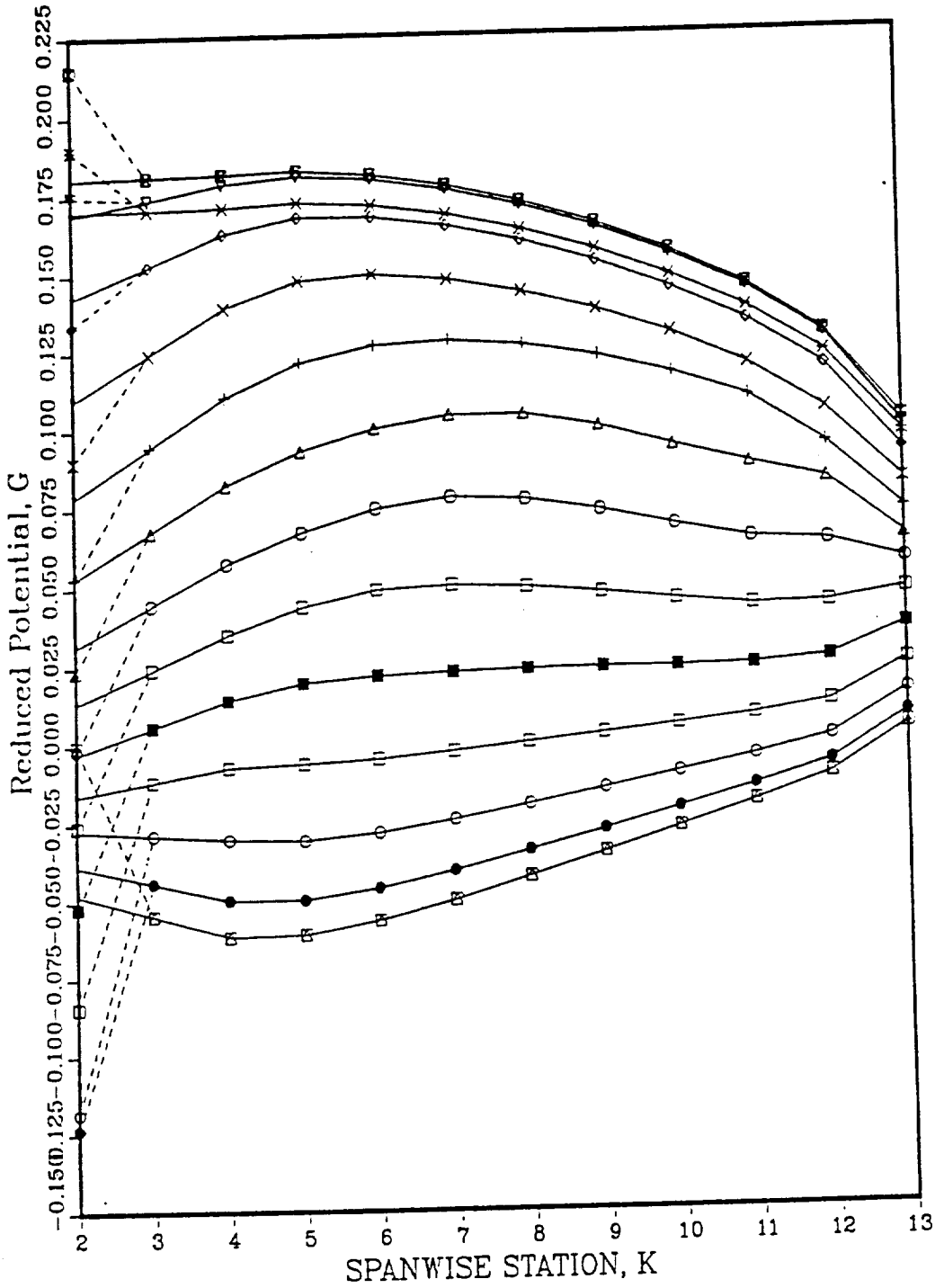

Fig. 14 Comparison between the ghost-point potentials defined with flow tangency (dashed lines) and extrapolation (solid lines)

at the root are fairly independent of the method used to define the potentials at the ghost points in the fuselage.

The potentials at the ghost points of the symmetry plane are similarly calculated by assuming

$$\phi_{\eta\eta} = 0 \qquad (2-66)$$

This process imposes an inflexion point on the pertubation velocity in the η direction at the symmetry plane since only symmetrical cases are treated. It is uncertain why ϕ_η was not set to zero instead to approximate tangency at the plane of symmetry. However, this situation is rather academic since these ghost points are used only for supersonic regions adjacent to the symmetry plane to compute the small spanwise upwinding term.

II.3.2 Far-field boundary conditions

Since the reduced potential used in the formulation of the numerical method represents a pertubation from the freestream value, they are set explicitly to zero on the radial boundary, ζ_{max}, and the upstream boundary represented by part of the minimum η surface.

At the outflow boundary, ($\xi = \xi_{min,max}$), the streamwise pertubation velocity, ϕ_ξ is set to zero. This latter condition implies that the pressure will return to its freestream value, assuming that there is not any crossflow[34].

II.3.3 Wake treatment

In the original method of FLO-30, the wake is treated as a vortex sheet which has a discontinuous jump in the tangential velocity and a continuous normal velocity

through the sheet. The rolling up of the sheet is ignored and the vertical convection of the sheet is approximated by assuming that the wake lies along the constant η grid line that leaves the trailing edge smoothly and returns to the plane of the wing at the outflow boundary. The requirement that the normal velocity be continuous is enforced by setting $V_\eta = 0$ on the wake, which fixes the values of the potentials at the ghost points, and the jump in the tangential velocity is satisfied by forcing a constant jump in potentials on the the surface of the sheet along a constant ζ and η line. This jump in potential is obtained using the circulation determined at the trailing edge of the wing.

II.3.4 Outboard computational slit

Due to the C-grid type formation of the grid, there exists a computational slit outboard of the wing tip on the plane of the wing. Since physically the pressure must be continuous across this cut, the potentials on the surface and at the corresponding ghost points are defined such that the reduced velocities normal and tangential to to the surface are continuous across the slit.

II.4 Boundary Layer Scheme

II.4.1 Integral method

Streett[20] included an integral boundary layer scheme in TAWFIVE to account for the necessary viscous effects in the form of the boundary layer displacement thickness, wake curvature and wake thickness. An integral method was chosen for its computational efficiency and its relative robustness.

In an integral approach the degree of the partial differential equations is reduced by an *a priori* integration in the direction normal to the surface.[21] This reduction can be illustrated by considering the boundary layer equations governing a two dimensional incompressible flow[19]:

$$\frac{\partial u}{\partial x} + \frac{\partial v}{\partial y} = 0 \qquad (2-67)$$

$$u\frac{\partial u}{\partial x} + v\frac{\partial u}{\partial y} = \mathrm{U}\frac{d\mathrm{U}}{dx} + \nu\frac{\partial^2 u}{\partial y^2} \qquad (2-68)$$

If Eq. (2-68) is integrated with respect to y from the wall ($y = 0$) to a distance h outside the boundary layer, it becomes

$$\int_{y=0}^{h} (u\frac{\partial u}{\partial x} + v\frac{\partial u}{\partial y} - \mathrm{U}\frac{d\mathrm{U}}{dx})dy = \frac{\tau_o}{\rho} \qquad (2-69)$$

where τ_o is the shearing stress at the wall.

Using the continuity equation, Eq. (2-67), to obtain the normal velocity component, v, as

$$v = -\int_0^y (\frac{\partial u}{\partial x})dy \qquad (2-70)$$

and substituting this result into Eq. (2-69), the result is

$$\int_{y=0}^{h} (u\frac{\partial u}{\partial x} - \frac{\partial u}{\partial y}\int_0^y \frac{\partial u}{\partial x}dy - \mathrm{U}\frac{d\mathrm{U}}{dx})dy = -\frac{\tau_o}{\rho} \qquad (2-71)$$

After integrating by parts and reducing, Eq. (2-71) becomes

$$\int_0^h \frac{\partial}{\partial x}\left[u\left(\mathrm{U}-u\right)\right]dy + \frac{d\mathrm{U}}{dx}\int_0^h \left(\mathrm{U}-u\right)dy = \frac{\tau_o}{\rho} \qquad (2-72)$$

Now, taking $h \rightarrow \infty$ and defining a displacement thickness, δ_1^*, and a momentum thickness, θ as

$$\begin{aligned} \delta_1^*\mathrm{U} &= \int_{y=0}^{\infty} (\mathrm{U}-u)dy \\ \theta\mathrm{U}^2 &= \int_{y=0}^{\infty} u(\mathrm{U}-u)dy \end{aligned} \qquad (2-73)$$

and substituting them into Eq. 2-72, it becomes

$$\frac{d}{dx}(U^2\theta) + \delta_1^* U \frac{dU}{dx} = \frac{\tau_o}{\rho} \qquad (2-74)$$

In this reduction process, two partial differential equations have been replaced by one ordinary differential equation. Since only the integrated quantities, δ^* and θ, are really the only quantities required of the boundary routine to model the weak viscous interaction, the fact that the solution to this equation does not provide the exact local variation of primitive flow properties across the boundary layer is not of consequence. The required functional form of the variation in u across the boundary layer is assumed *a priori*–by a polynomial for instance.

II.4.2 Laminar scheme

In three-dimensional, compressible, laminar flow the same integration procedure is implemented using two bounday-layer momentum equations and their corresponding moment of momentum relations to yield a system of four coupled partial-differential equations.[20] In the formulation of these equations, it is assumed that the streamwise velocity profile is of the Faulker-Skan (F-S) family of similarity profiles and that the cross flow profile is a linear combination of the F-S family of profiles. These incompressible profiles are extended to compressible flow by the scaling of the normal coordinate with the Stewartson transformation.

II.4.3 Turbulent scheme

The formulation of the turbulent scheme is similar to the laminar, but the streamwise velocity is assumed to have a simple power-law profile which is a function

of the streamwise shape factor and the transformed boundary layer thickness and normal coordinate; and, the cross flow profile has the form of

$$\frac{v}{U} = \frac{u}{U}(1 - \frac{Z}{\Delta})^2 \tan\beta \qquad (2-75)$$

where Z is the transformed normal coordinate, Δ is the transformed boundary layer displacement thickness, and β is the angle between the external streamline of the potential flow and the wall shear direction. In the turbulent scheme, the final three governing equations are two momentum integral equations derived from the continuity and boundary layer momentum equations and one entrainment equation. The latter equation accounts for the addition of mass into the boundary layer from the surrounding flow as the boundary layer grows.

II.4.4 Lag entrainment

Originally, in the work by Smith[21], the relationship between the entrainment coefficient and the shape factor required in the previous scheme was formulated empirically with a simple algebraic equation. Later Green found a relationship for the required quantities through the use of the turbulent kinetic energy equation which explicitly represents the balance between production, advection, diffusion and dissipation of turbulent energy in the boundary layer. He referred to this as the Lag-Entrainment method[27].

Also, in Green's method the desired momentum and displacement thickness of the wake is determined by simply continuing the integration of the three governing equations past the trailing edge on either side of the wake. It is assumed that aft of the trailing edge that the skin friction coefficient is zero and that the dissipation

length scale is twice that on the wing. Once the integration is performed on either side of the wake, the required integral properties are simply the sum of those calculated on both sides.

II.4.5 Solution of the governing equations

The resulting governing equations are solved through an explicit type integration scheme in the x (or chordwise direction) along constant span stations. In this scheme, the domain of dependence is conservatively assumed to lie between the external streamline of the potential flow and the shear angle of the boundary layer. To account for this dependency, the spanwise derivatives found in the governing equations are backward differenced if the external streamline and the wall shear line lie on the outboard side of the chordline and central differenced if the streamline and the shear line lie on opposite sides of the chordline.

Boundary conditions are required at all inflow boundaries. At the root, a plane of symmetry is assumed. Here, the cross flow velocity is set to zero, as are all all spanwise derivatives. At the wing tip, all spanwise derivatives are also set equal to zero. And finally, an attachment line approach[38] is used to determine the initial conditions at the leading edge.

II.4.6 Wake curvature

When the flow leaves the wing at the trailing edge, it initially follows a curved path and then soon aligns itself with the freestream downstream of the wing. This large curvature of the flow near the trailing edge can have a measurable effect on the overall lift of the wing. In fact, Streett found that in one instance the sectional lift coefficient near the tip of the wing was decreased by about four percent when the

curvature of the wake was taken into account. Usually, if only first order effects are considered, the pressures at the trailing edge would be equal on the upper and lower surface. But, if the wake is considered to have an effective thickness of $\delta^* + \theta$ due to viscous effects and curvature, the pressures on either side of the wake will not be equal except at the centerline of the wake. Since the flowfield about the wing and the wake with the displacement thickness added to it is modeled inviscidly, the trick is to calculate a pressure difference across the wake at the trailing edge in the inviscid flow which will yield a zero pressure difference at the centerline of the wake in the real viscous flow[39]. It has been shown that the appropriate pressure jump across the wake with a thickness of δ^* can be written as a function of the curvature, κ_w, of the centerline of the actual wake, the mean tangential velocity, u_w, and the mean density, ρ_w, in the wake as

$$\Delta p = p_{top} - p_{bottom} = \kappa \rho_w u^2{}_w \theta_w \qquad (2-76)$$

Given that the pressure difference is small, this can be related to the circulation, Γ, by

$$\int_{x_{te}}^{x_\infty} d\Gamma_w = -\int_{x_{te}}^{x_\infty} \theta_w \kappa_w dS_w \qquad (2-77)$$

where S_w is the arc distance along the wake. The circulation at the trailing edge is calculated by the difference in the potentials at the trailing edge in the inviscid solution and Eq. (2-77) is numerically integrated from the trailing edge to one grid point upstream of the downstream boundary. The circulation at the downstream boundary is then matched to the circulation obtained from the integration.

Since the wake effects are relatively small,[39] it is only important to know the approximate location of the wake centerline. This simplifies the problem since the actual wake location would have to be found by tracking the streamline of the inviscid solution leaving the trailing edge and then a new grid would have to be created about the new wake so that the boundary conditions on the wake could be applied. Alternatively, the approximate shape of the wake can be found by assuming that the streamline leaves the trailing edge smoothly at the average of the local trailing edge angles and that then the angle between the wake centerline surface and the freestream decays logarithmically, similar to that of a point vortex in a uniform freestream at a given angle of attack[20]. The circulation, Γ, of this point vortex located at the quarter chord point could be determined by forcing flow tangency at the trailing edge of the wing section. The ordinate of the centerline of the wake would then have a form similar to

$$y_{wake} = y_{te} + \tan\alpha(d - \frac{3}{4}c) - \frac{3}{4}c\tan(\alpha)ln\frac{d}{\frac{3}{4}c}/d \qquad (2-78)$$

where d is the x distance from the quarter chord point of the wing section.

The curvature of the flow, κ, can be determined by calculating the rate of change of the flow angle at the approximated wake location.

II.4.7 Wake thickness

The thickness of the wake is accounted for by simply adding the displacement thicknesses obtained from the boundary layer solver to either side of the predefined wake location. The ghost points in the wake are then redefined such that strict flow tangency is enforced along this new surface.

II.5 Comparison to Experiment

TAWFIVE was used to analyze RAE Wing-A wing-body at a Mach number of .8, an angle of attack of 2 degrees, and a Reynolds number of 2.66 million based on the root chord. The pressure obtained from this analysis are compared to some experimental data at two convenient stations in Fig. 15. Even though no attempt was made to try and match lift coefficients by changing Mach number or angle of attack, the comparison between the experimental and predicted pressures is fairly good up to the trailing edge. There TAWFIVE predicts slightly higher pressures. This characteristic behavior has been attributed to the improper modeling of the the strong viscous-interaction region at the trailing edge[20] but may also be due to a combination of the coarseness of the grid at the trailing edge and wind tunnel interference errors.

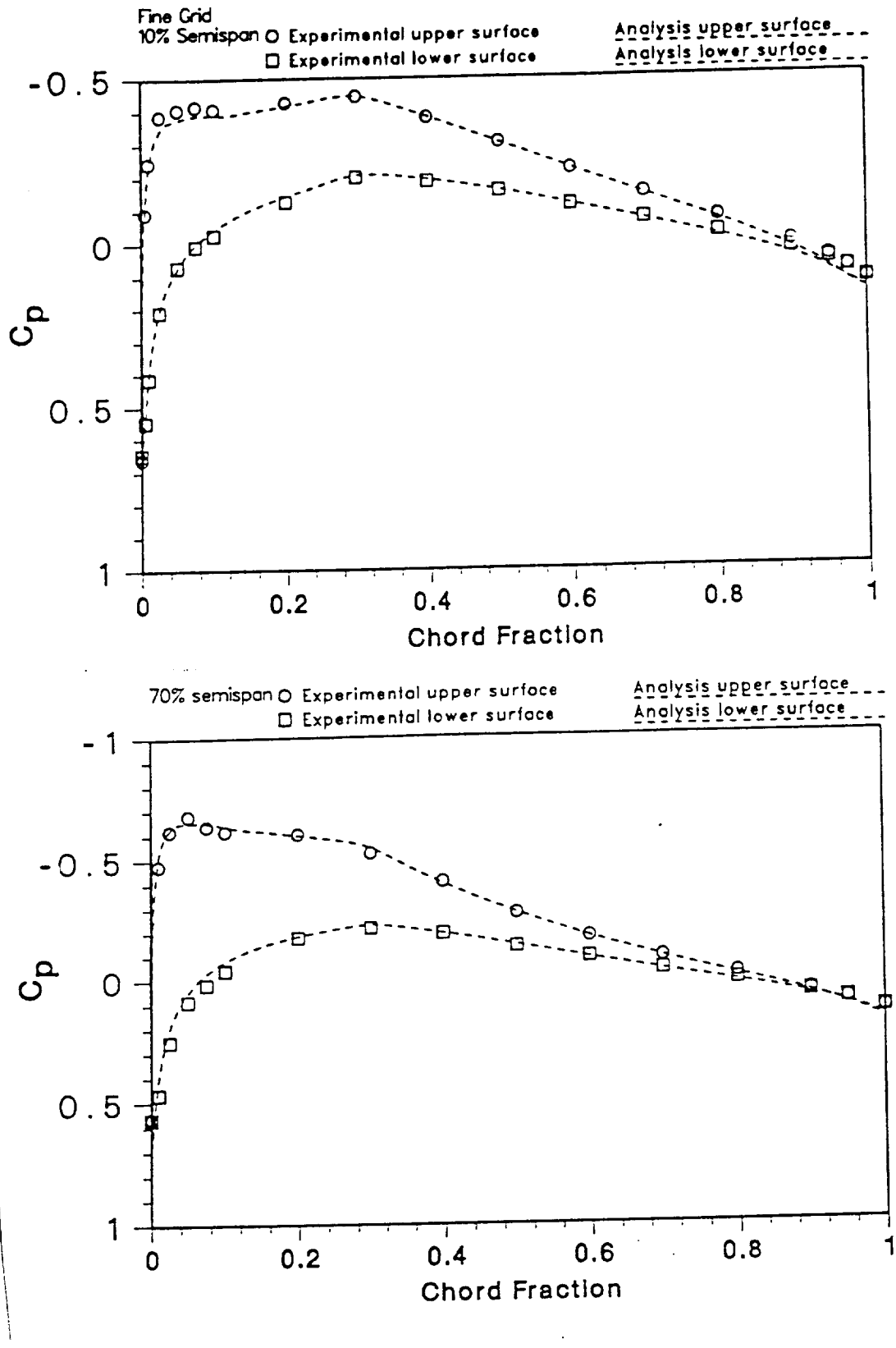

Fig. 15 Comparison of experimental and analytical pressures for RAE Wing-A

CHAPTER III

INVERSE DESIGN METHOD

III.1 Inverse Boundary Condition

As stated earlier, in the direct-inverse method a pressure boundary condition is enforced rather than flow tangency aft of the portions of the wing which are to be designed. Following Gally,[13-15] the input pressure coefficient can be written in terms of the Mach number, M, and the freestream speed, q, as

$$C_p = \frac{2}{\gamma M^2{}_\infty}\left[\left[1 + \frac{\gamma-1}{2}M_\infty{}^2\left(1 - \frac{q^2}{q^2_\infty}\right)\right]^{\frac{\gamma}{\gamma-1}} - 1\right] \qquad (3-1)$$

where $q^2 = \left(u^2 + v^2 + w^2\right) q^2{}_\infty$.

Solving for u in Eq. (3-1) yields

$$u = \left[\frac{1 - \frac{2}{(\gamma-1)M^2{}_\infty}\left[\left(1 + \frac{\gamma M^2{}_\infty C_p}{2}\right)^{\frac{\gamma-1}{\gamma}} - 1\right]}{1 + \left(\frac{v}{u}\right)^2 + \left(\frac{w}{u}\right)^2}\right]^{\frac{1}{2}} \qquad (3-2)$$

This form of the equation seems to have been chosen over the more obvious form of

$$u = \left[1 - \frac{2}{(\gamma-1)M^2_\infty}\left[\left(1 + \frac{\gamma M^2{}_\infty C_p}{2}\right)^{\frac{\gamma-1}{\gamma}} - 1\right] - v^2 - w^2\right]^{\frac{1}{2}} \qquad (3-3)$$

since it is less likely that its radicand would be negative. Equating Eq. (3-2) and the first row of Eq. (2-38) results in

$$J_{11}\phi_\xi + J_{12}\phi_\eta + J_{13}\phi_\zeta = \left[\frac{1 - \frac{2}{(\gamma-1)M^2{}_\infty}\left[\left(1 + \frac{\gamma M^2{}_\infty C_p}{2}\right)^{\frac{\gamma-1}{\gamma}} - 1\right]}{1 + \left(\frac{v}{u}\right)^2 + \left(\frac{w}{u}\right)^2}\right]^{\frac{1}{2}} - \cos\alpha \qquad (3-4)$$

where $J_{i,j}$ are the elements of $\left(\mathbf{H}^T\right)^{-1}$. A potential, $(\phi_{i,j,k})$, can be formulated in terms of the pressure coefficient by expanding about the grid point location $\left(i-\frac{1}{2},j,k\right)$, and then using central differences in the ξ and ζ direction and second order backward differences in the normal direction, η, yielding

$$\begin{aligned} & J_{11}\left(\phi^{n+1}_{i,j,k}-\phi^{n}_{i-1,j,k}\right) \\ & \quad + J_{12}[3\left(\phi^{n-1}_{i,j,k}+\phi^{n}_{i-1,j,k}\right)-4\left(\phi^{n}_{i,j-1,k}+\phi^{n}_{i-1,j-1,k}\right) \\ & \qquad + \phi^{n}_{i,j-2,k}+\phi^{n}_{i-1,j-2,k}]/4 \\ & \quad + J_{13}\left(\phi^{n}_{i,j,k+1}+\phi^{n}_{i-1,j,k+1}-\phi^{n}_{i,j,k-1}-\phi^{n}_{i-1,j,k-1}\right)/4 \\ & \qquad = F\left(C_{p,i-\frac{1}{2},k}\right) \end{aligned} \tag{3-5}$$

where ϕ^n are the potentials at the current time level and ϕ^{n+1} are the updated potentials.

Solving for the ϕ to be specified, Eq. (3-5) becomes

$$\begin{aligned} \phi^{n+1}_{i,ky,k} = \frac{1}{J_{11}+\frac{3}{4}J_{12}}\Big\{ & J_{11}\phi^{n}_{i-1,ky,k} \\ & - J_{12}\Big[3\phi^{n}_{i-1,ky,k}-4\left(\phi^{n}_{i,ky-1,k}+\phi^{n}_{i-1,ky-1,k}\right) \\ & + \phi^{n}_{i,ky-2,k}+\phi^{n}_{i-1,ky-2,k}\Big]/4 \\ & - J_{13}\left(\phi^{n}_{i,ky,k+1}+\phi^{n}_{i-1,ky,k+1}-\phi^{n}_{i,ky,k-1}-\phi^{n}_{i-1,ky,k-1}\right)/4 \\ & + F\left(C_{p\ i-\frac{1}{2},k}\right)\Big\} \end{aligned} \tag{3-6}$$

where $F\left(C_{p\ i-\frac{1}{2},k}\right)$ is the right hand side of Eq. (2-72) and $j = ky$ on the wing surface. Also, the η grid lines are numbered such that $ky-1$ is the location of the grid point immediately above the wing's surface. Pressures are specified at half grid point locations in the ξ direction to eliminate the chance of the solution decoupling

on 'odd' and 'even' grid points. Since the actual sectional shape of the final wing is unknown initially, the potentials are specified on the wing's surface at the present time level.

III.2 Integration of the Flow Tangency Boundary Condition

Since the grid is boundary conforming, the wing sections in the design region must be updated every so often by integrating the flow tangency condition written in curvilinear coordinates. After Gally, the curvilinear form of the equation can be found by first considering the flow tangency condition for Cartesian coordinates

$$\mathrm{U}^T \nabla F = 0 \qquad \text{with } F(x,y,z) = 0 \tag{3-7}$$

where U is the physical velocities and F is the function describing the surface of the wing.

The physical velocities can be related to the contravariant velocities using the aforementioned relations, which are repeated here for convenience.

$$[\mathrm{U}] = \begin{pmatrix} x_\xi & x_\eta & x_\zeta \\ y_\xi & y_\eta & y_\zeta \\ z_\xi & z_\eta & z_\zeta \end{pmatrix} \begin{pmatrix} U \\ V \\ W \end{pmatrix} = [\mathrm{H}][\mathrm{V}] = \mathrm{HV} \tag{3-8}$$

By using the chain rule in the same manner in which the above expression was derived, the gradient, ∇, of the surface function, F, with respect to the physical coordinates, x, y, z can be related to the gradient, ∇', of the surface function $S(\xi, \eta, \zeta)$ by

$$[\nabla F] = \begin{pmatrix} \xi_x & \eta_x & \zeta_x \\ \xi_y & \eta_y & \zeta_y \\ \xi_z & \eta_z & \zeta_z \end{pmatrix} \begin{pmatrix} \frac{\partial S}{\partial \xi} \\ \frac{\partial S}{\partial \eta} \\ \frac{\partial S}{\partial \zeta} \end{pmatrix} = (\mathrm{H}^{-1})^T \nabla' S \tag{3-9}$$

Substituting these two into the tangency equation gives

$$(\mathrm{HV})^T (\mathrm{H}^{-1})^T \nabla' S = 0 \tag{3-10}$$

Using the identity from linear algebra,

$$[\mathbf{A}\ \mathbf{B}]^T = \mathbf{B}^T\mathbf{A}^T \qquad (3-11)$$

Eq. (3-10) becomes

$$\mathbf{V}^T\left[\mathbf{H}^{-1}\mathbf{H}\right]^T\nabla' S = 0 \qquad (3-12)$$

which is reduced to the desired form of the flow tangency condition for curvilinear coordinates :

$$\mathbf{V}^T\cdot\nabla' S = 0 \qquad (3-13)$$

A more convenient form is obtained by expanding this to

$$U\frac{\partial S}{\partial \xi} + V\frac{\partial S}{\partial \eta} + W\frac{\partial S}{\partial \zeta} = 0 \qquad (3-14)$$

Since the wing is a surface of constant η , where

$$\begin{aligned} S(\xi,\eta,\zeta) &= \eta(\xi,\zeta)_{ky} - \eta = 0 \\ \frac{\partial S}{\partial \xi} &= \frac{\partial \eta(\xi,\zeta)_{ky}}{\partial \xi} \\ \frac{\partial S}{\partial \eta} &= -1 \\ \frac{\partial S}{\partial \zeta} &= \frac{\partial \eta(\xi,\zeta)_{ky}}{\partial \zeta} \end{aligned} \qquad (3-15)$$

Eq. (3-14) reduces to

$$\left(\frac{\partial \eta}{\partial \xi}\right)_{i,ky,k} = \frac{V}{U} - \frac{W}{U}\left(\frac{\partial \eta}{\partial \zeta}\right)_{i,ky,k} \qquad (3-16)$$

The integration of this equation can be handled in two different ways. If the spanwise term, $\frac{\partial \eta}{\partial \zeta}$, is lagged one global iteration, it will always be zero since upon the

creation of a new grid, all derivatives of η with respect to the ξ or ζ direction vanish on the wing's surface; and, Eq. (3-16) reduces to

$$\left(\frac{\partial \eta}{\partial \xi}\right)_{i,ky,k} = \left(\frac{V}{U}\right)_{i,ky,k} \qquad (3-17)$$

The other approach would be to integrate Eq. (3-16) iteratively. If the contravariant velocities are frozen at their current values, and the spanwise terms are initially assumed to be zero, Eq. (3-17) can be integrated to find the approximate inverse changes $\Delta\eta$. These can be used to find approximations to the spatial spanwise derivative, $\frac{\partial \eta}{\partial \zeta}$, which can then be included in Eq. (3-16) to provide a better approximation to the flow tangency equation. The process can then be repeated using Eq. (3-16) until the spatial derivatives converge. Numerical experiments reveal that the spanwise terms are at least two orders of magnitude smaller than the chordwise terms prior to the creation of the new grid. Hence, the spanwise terms can normally be neglected. Equation (3-17) was integrated using the trapezoidal rule

$$\eta_{i,k} = \frac{II}{2}\left(\left(\frac{V}{U}\right)_{i,k} + \left(\frac{V}{U}\right)_{i-II,k}\right) + (\eta)_{i-II,k} \qquad (3-18)$$

$II = -1$ upper surface

$II = +1$ lower surface

For comparison purposes the fourth order scheme

$$\eta_{i,k} = \frac{II}{24}\left(9\left(\frac{V}{U}\right)_{i,k} + 19\left(\frac{V}{U}\right)_{i-II,k} - .5\left(\frac{V}{U}\right)_{i-2II,k} + \left(\frac{V}{U}\right)_{i-3II,k}\right) + (\eta)_{i-II,k} \qquad (3-19)$$

was also used. With the fourth order scheme the trapezoidal rule was used for the first two integration steps. This higher order integration scheme had little effect on

the final answers, except for coarse grids in regions of high curvature such as the cove region of a supercritical airfoil.

Since Gally found that calculating V using strictly finite differences was not accurate enough, he instead, using an approach similar to that in Ref. (60), discovered that V was most accurately obtained from the residual expression. First, assume that

$$\frac{V}{U} \approx \frac{\rho h V}{\rho h U} = \frac{\mu_{\xi\eta\zeta}(\rho h V)}{\mu_{\xi\eta\zeta}(\rho h U)} \qquad (3-20)$$

and then combine the previously defined averaging and differencing operators

$$\mu_\eta (\rho h V)_{i,ky,k} = \frac{1}{2}\left((\rho h V)_{i,ky+\frac{1}{2},k} + (\rho h V)_{i,ky-\frac{1}{2},k}\right) \qquad (3-21)$$

$$\delta_\eta (\rho h V)_{i,ky,k} = \left((\rho h V)_{i,ky-\frac{1}{2},k} - (\rho h V)_{i,ky+\frac{1}{2},k}\right) \qquad (3-22)$$

to generate

$$\delta_\eta (\rho h V)_{i,ky,k} = 2(\rho h V)_{i,ky-\frac{1}{2},k} - 2\mu_\eta (\rho h V)_{i,ky,k} \qquad (3-23)$$

Substituting this result into the residual expression, Eq. (2-43), and solving for the out of plane flux, $\rho h V$, on the wing surface gives

$$2\mu_{\xi\eta\zeta}(\rho h V)_{i,ky,k} = \mu_{\eta\zeta}\delta_\xi (\rho h U)_{i,ky,k} + 2\mu_{\xi\zeta}\left(\rho h V_{i,ky-\frac{1}{2},k}\right) + \mu_{\xi\eta}\delta_\zeta (\rho h W_{i,ky,k}) + \textit{compensation and upwinding terms} \qquad (3-24)$$

Since at convergence the flow should also be tangent to the designed surface, the tangency condition is enforced in the residual expression, Eq. (2-43), by setting

$$(\rho h V)_{i,ky+\frac{1}{2},k} = -(\rho h V)_{i,ky-\frac{1}{2},k} \qquad (3-25)$$

The resulting expression is identical the RHS of Eq. (3-24), and the expression for the normal flux becomes

$$\mu_{\xi\eta\zeta}(\rho hV)_{i,ky,k} = \frac{Residual}{2.0} \qquad (3-26)$$

Note that since the residual is not zero in the design region due to the inverse boundary condition, this expression reveals that there will be a mass flux of fluid from the boundary[23-37] during the iterative design process. No attempt was made to account for this transient flux, since at convergence it would be zero.

Upon substitution of Eq. (3-26) into Eq. (3-20) and using the cell averaged flux, ρhU, on the surface the boundary condition becomes

$$\frac{\partial\eta}{\partial\xi} = \frac{V}{U} \approx \frac{\mu_{\xi\eta\zeta}(\rho hV)}{\mu_{\xi\eta\zeta}(\rho hU)} = \frac{Residual}{2\mu_{\xi\eta\zeta}(\rho hU)} \qquad (3-27)$$

The changes normal to the surface at each spanwise station are obtained by integrating from the beginning of the inverse region to the trailing edge using the trapezoidal rule.

Assuming that the grid line leaving the wing in the η direction is normal to the wing, these changes, $\Delta\eta$, are then converted from computational to physical units by scaling by transformation metrics such that

$$\Delta l = \Delta\eta\sqrt{\frac{\partial x}{\partial\xi}^2 + \frac{\partial y}{\partial\eta}^2} \qquad (3-28)$$

After subtracting the boundary layer displacement thickness from the inverse changes, Δl's, which are linearly interpolated to the user defined input stations, the resulting displacements are added to the initial airfoil sections yielding the new wing surface for the current time level.

III.3 Relofting

Many times the trailing edge thickness may be too large if the leading edge curvature is too small or may be 'fish-tailed' if the leading edge curvature is too large. These undesirable situations can be remedied by a procedure called relofting where the designed surface is rotated about the leading edge to meet a specified trailing edge ordinate or trailing edge thickness.[6,24]

This relofting procedure can be accomplished in two separate ways.[13,14] In the first method, assuming both the upper and lower surfaces of the wing are being designed, the user specified trailing edge ordinate,

$$y_{t_{\substack{upper \\ lower}}} = y_{avg} \pm \frac{\Delta_t}{2} \qquad (3-29)$$

is subtracted from the ordinate of the displaced surface,

$$y_{design} = y_{initial_{\substack{upper \\ lower}}} \pm \Delta_{\substack{upper \\ lower}} \qquad (3-30)$$

to yield a correction of

$$\delta_{r_{te}} = y_t - y_{design} \qquad (3-31)$$

where Δ_t is the user specified trailing edge thickness, $\Delta_{\substack{upper \\ lower}}$ is the initial inverse change, $y_{initial}$ is the trailing edge ordinate of the original airfoil section, and y_{avg} is the average of the trailing edge ordinates of the input geometry.

This correction,

$$\delta_r(x) = \delta_{r_{te}} \times \left(\frac{x - x_{le}}{chord} \right) \qquad (3-32)$$

is proportionally added to the initial inverse displacements which amounts to a rotation of the displaced surface about the leading edge to meet the trailing edge ordinate.

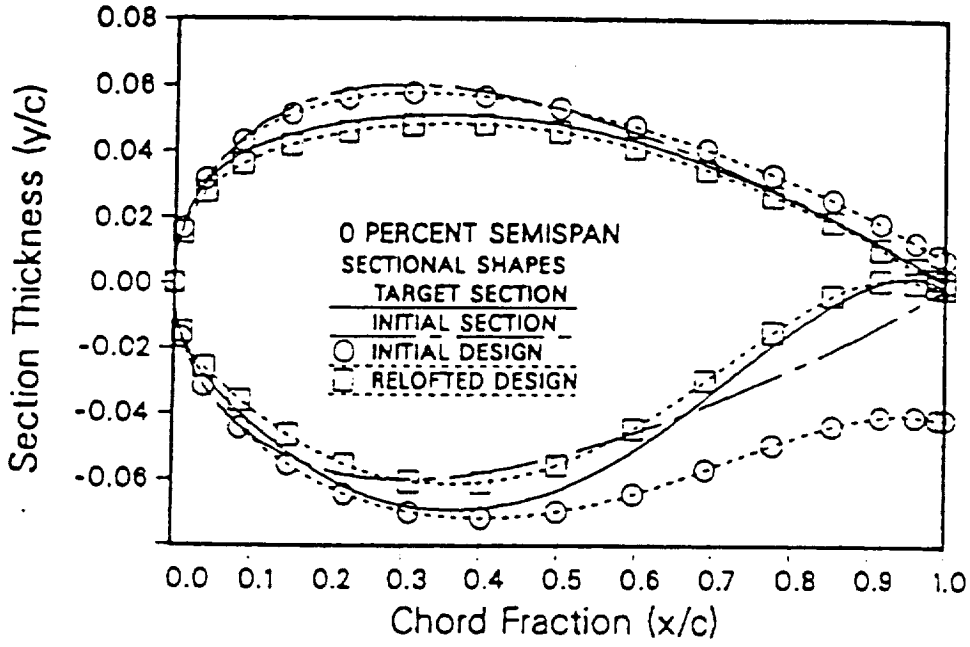

Fig. 16 The effect of relofting on the design in the initial stages of convergence

To illustrate this relofting procedure, the first global iteration of a typical design before and after relofting is revealed in Fig. 16.

If only the trailing edge thickness is specified, allowing the trailing edge ordinate the freedom to vary, the correction instead becomes

$$\delta_{r_{te}} = \left(\frac{\Delta_t}{2} - \frac{\Delta_u + \Delta_l}{2}\right)\left(\frac{x - x_{le}}{chord}\right) \qquad (3-33)$$

where Δ_u and Δ_l are the initial inverse changes on the upper and lower surfaces respectively. It should be noted that the inverse displacements are positive when they cause an increase in thickness.

The second relofting scheme determines the displacements aft of the direct-inverse junction of the design region in the same way, but the leading edge ordinates are thinned to meet the displaced surface at the beginning of the design region. This insures that the leading edge shapes remain in the same family of airfoils.

$$y^{n+1}(x) = y^{n}(x)\left(\frac{{y_{idle}}^{n+1}}{{y_{idle}}^{n}}\right) \qquad (3-34)$$

where y_{idle} is the airfoil thickness at the direct-inverse interface in the chordwise direction.

In order afford the designer extra flexibility, one more relofting scheme was devised where a portion of the trailing edge region is user specified instead of just the trailing edge ordinate. Using the same rational as with the rotation scheme, the correction added to the displaced surface to meet the specified ordinate at the aft direct-inverse junction located at x_{idte}, is

$$\delta_r(x) = \delta_r(x_{idte}) \times \left(\frac{x - x_{le}}{x_{idte} - x_{le}}\right) \qquad (3-35)$$

CHAPTER IV

REMEDYING SPANWISE INSTABILITIES

IV.1 Spanwise Oscillations

In the original work by Gally[13,14], the pressure distributions applied at the computational grid stations of constant ζ lines on the wing in the design region were obtained by spanwise, linear interpolation of the pressures input by the user at design stations to every grid station delimited. This meant that the inverse boundary condition was enforced at every constant ζ grid station in the design region, and that every sectional shape was determined relatively independent of the others. Unfortunately, an annoying divergent spanwise oscillation problem sometimes occurred when designing a wing which required extensive relofting, especially when the initial section was thinner than the target. This oscillation led to sections which were too thick or too thin at adjacent constant ζ grid station. (see Fig. 17). This problem was more pronounced when the sweep was increased or the aspect ratio was decreased and was usually divergent except for very high aspect-ratio wings (AR=10) with no sweep.

Early in the research, it was discovered that the problem could be circumvented by specifying the C_p distribution at at least every other constant ζ grid station and then linearly interpolating the inverse displacements calculated at those grid stations to the other grid stations included in the design region. The regions in the middle of the design region were simply analyzed using the original flow-tangency boundary

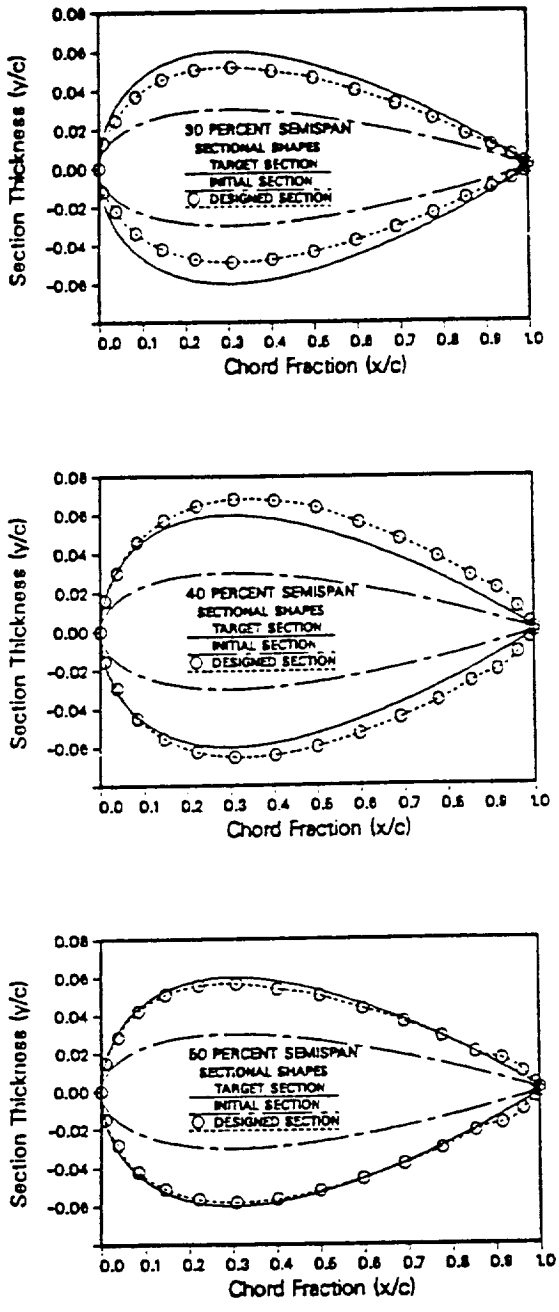

Fig. 17 Alternating thick-thin sections for a divergent medium grid case

condition. The resulting sections, interpolated to the geometry input stations, were all relofted as usual to satisfy the trailing edge ordinate condition. This procedure led to a convergent solution most of the time, except when designing wings with significant sweep or with low aspect ratios, such as Lockheed Wing-B and Wing-C.

It was later discovered that a similar procedure was briefly discussed in Ref. 40 to overcome a decoupling of the solution in the chordwise and spanwise direction leading to a numerical instability when using an inverse panel-method code. In this case, the ordinates of the 'odd' points along the chord were obtained by quadratic interpolation using the ordinates of adjacent 'even' chordwise points while the ordinates of each 'odd' spanwise grid station were generated using linear interpolation between the contiguous 'even' spanwise stations. This procedure effectively eliminated half of the unknowns. The similarities of the decoupling problem in this scheme and our direct-inverse method are quite evident, even though the design schemes are quite different in methodology.

Although this somewhat heuristic cure to the problem seemed to work for the most part, the fundamental cause for this problem was not well understood, hence the oscillation problem was investigated in much greater depth. Initially, it was thought that either the inverse boundary condition or the relofting scheme was solely to blame, which led at first to a series of reformulations; while none of these were successful, they did create great insight into the problem.

Since the oscillation problem seemed to stem from the uncoupling of the solution in the spanwise direction, the original inverse boundary condition in Eq. (3-5) was

rewritten as

$$\phi^{n+1}_{i,ky,k-1} - \frac{4J_{11}+3J_{12}}{J_{13}}\phi^{n+1}_{i,ky,k} - \phi^{n+1}_{i,ky,k+1} =$$
$$\frac{-4}{J_{13}}\Big\{ J_{11}\phi^{n}_{i-1,ky,k}$$
$$- J_{12}\Big[3\phi^{n}_{i-1,ky,k} - 4\left(\phi^{n}_{i,ky-1,k} + \phi^{n}_{i-1,ky-1,k}\right) \qquad (4-1)$$
$$+ \phi^{n}_{i,ky-2,k} + \phi^{n}_{i-1,ky-2,k}\Big]/4 + F\left(C_{p\ i-\frac{1}{2},k}\right)\Big\}$$
$$+ \phi^{n}_{i-1,ky,k+1} - \phi^{n}_{i-1,ky,k-1}$$

such that the $\phi's$ could be obtained implicitly in the spanwise direction. Although this would seem to strongly couple the potential field in the spanwise direction, it did not deter the solution from oscillating in the slightest regard.

One form of Eq. (3-4) was tried using one-sided differences for the spanwise derivatives, and yet another which specified the C_p at $(i+\frac{1}{2}, ky, k+\frac{1}{2})$ grid locations; but they did not cure the problem either.

The idea of devising a conservative formulation of the inverse boundary condition using a control volume approach more in keeping with the spirit of the finite volume scheme used in FLO-30 or the approach used in Ref. (41) was conceived, but the details necessary to implement this approach were never pursued.

Attention was then directed towards the methods used to integrate the flow tangency equation and the relofting of the resulting shapes. Since the problem seemed to stem from the lack of spanwise information, the spanwise terms in Eq. (3-16) were included during the surface update process. The ratio $\frac{W}{U}$ was obtained from Eq. (2-39) and the potentials at the present time level. An approximation of the spanwise derivatives, $\frac{\partial \eta}{\partial \zeta}$, was calculated using central spanwise differences of the

initial displacements which were calculated using Eq. (3-17). Then Eq. (3-16) was solved iteratively until there was no appreciable change in the displacements. In case the relofting adversely affected the results, this process was also tried after the inverse displacements were changed with relofting. However, the inclusion of these terms had very little effect on the displacements calculated since, in both cases, they were at least an order of magnitude smaller and did not help the divergence problem in the slightest regard.

Spanwise smoothing of the displacements was also tried. Although this technique did provide a smoothly varying distribution of sectional thicknesses, the divergence was merely slowed. Sometimes the solution would reach a settling point where it would not converge further, but the resulting section shapes were not satisfactorily accurate.

In the midst of the search for a cure for the oscillation problem, it was discovered that if the potentials obtained from a converged solution of the target section were specified on the wing using a different initial geometry, the design solution would converge without oscillating. This result appeared to condemn the inverse boundary condition and redeem the integration and relofting schemes. On the other hand, if the inverse boundary condition was applied at <u>every</u> grid station, and displacements were calculated only at <u>every other</u> spanwise grid station and were interpolated to the stations in between, the solution also converged, which seemed to indicate that the inverse boundary condition was not the sole origin of the problem. Thus, it appeared that the problem was stemmed from a combination of causes.

IV.2 Success

After the many failed attempts of remedying the oscillation problem by reformulating the inverse boundary condition and the integration and relofting shemes, attention was directed towards the residual and the terms composing it. The residual is directly affected by the inverse boundary condition; moreover, the residual directly influences the section shapes through the integration of the flow tangency boundary condition. Consequently, the residual was broken into its major components and plotted in the spanwise direction after each surface update of a known divergent case. This case happened to be a medium-grid design of Lockheed Wing-A with the initial section being a NACA 0006 section over the entire wing and the target being a NACA 0012 section. The design region extended from 30% to 70% semispan. Sample plots for this divergent case are shown at four different time levels in Fig. 18, where the total residual also includes the upwinding terms. As can be seen, the compensation terms, which include spanwise derivatives of ϕ, at first are very small compared to the rest of the terms but later tend to dominate and amplify the oscillation. This oscillation starts at the direct-inverse interface or, in other words, at the first spanwise station from the root in the design region and propagates spanwise as a damped oscillation with a period of two grid spacings.

The oscillation problem seems to be driven by a combination of events which build upon each other causing a divergence. It is believed that the initial mismatch in the potentials at the direct-inverse interface in the spanwise direction is amplified by the compensation terms which include spanwise derivatives of the potential function.

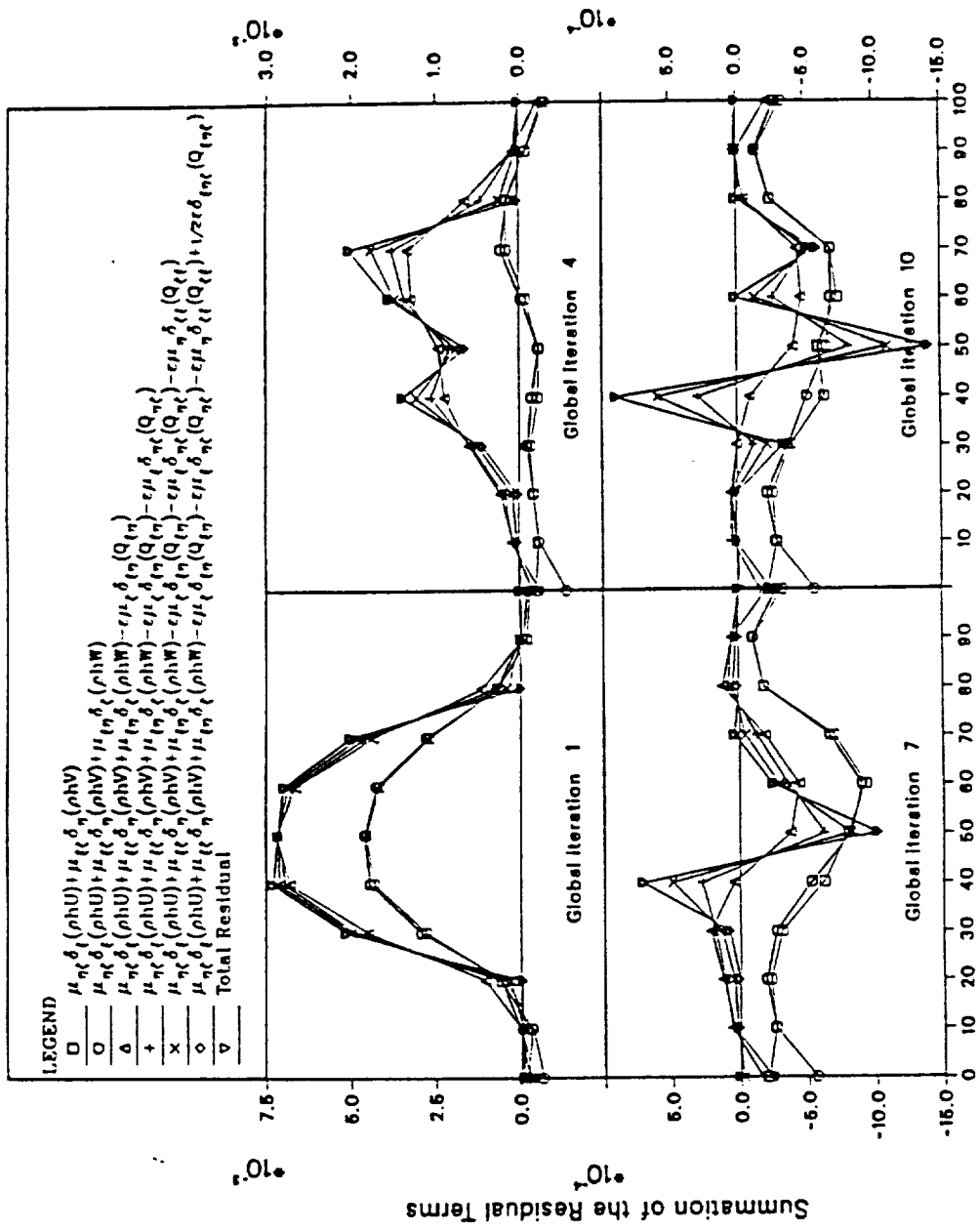

Fig. 18 The time history of the residual and the terms composing it at the upper trailing edge for a typical divergent solution. (The design region extends from 30-70% semispan)

The residual is then undershot and overshot on alternating spanwise stations. This oscillation is further magnified by relofting, which creates a section that is too thin when the slopes defined in Eq. (3-27), which of course are directly proportional to the residual, are too large and vice-versa. Since more or less fluid has to be ejected from the section that is too thin or thick, respectively, to give a streamline approximately corresponding to the correct target section, the potential field shown in Fig. 19 at each design station is forced further away from the adjacent fields by the inverse boundary condition which in turn forces an even further undershoot or overshoot of the residual, resulting in a growing spanwise oscillation. With the aid of other numerical experiments, it has been found that it is only necessary to have two adjacent design stations to drive this oscillation to divergence. It is of interest that when the wavy wing surface resulting from a divergent solution was analyzed with TAWFIVE, the potential field varied more smoothly in the spanwise direction than did the potential field obtained from the design solution. In light of the previous discussion, this result verifies that the inverse boundary condition was, in fact, forcing the adjacent potential fields away from each other.

It should be noted that this problem is not due solely to the implementation of the direct-inverse technique since this oscillation has not been observed with the ZEBRA design code. Rather, it seems to be unique to the coupling of the method with the analysis code, FLO-30. Seemingly, two pertinent differences between the two codes exit. Firstly, the ZEBRA code, which uses a sheared Cartesian coordinate system aligned with the wing, applies the boundary conditions at the mean plane of

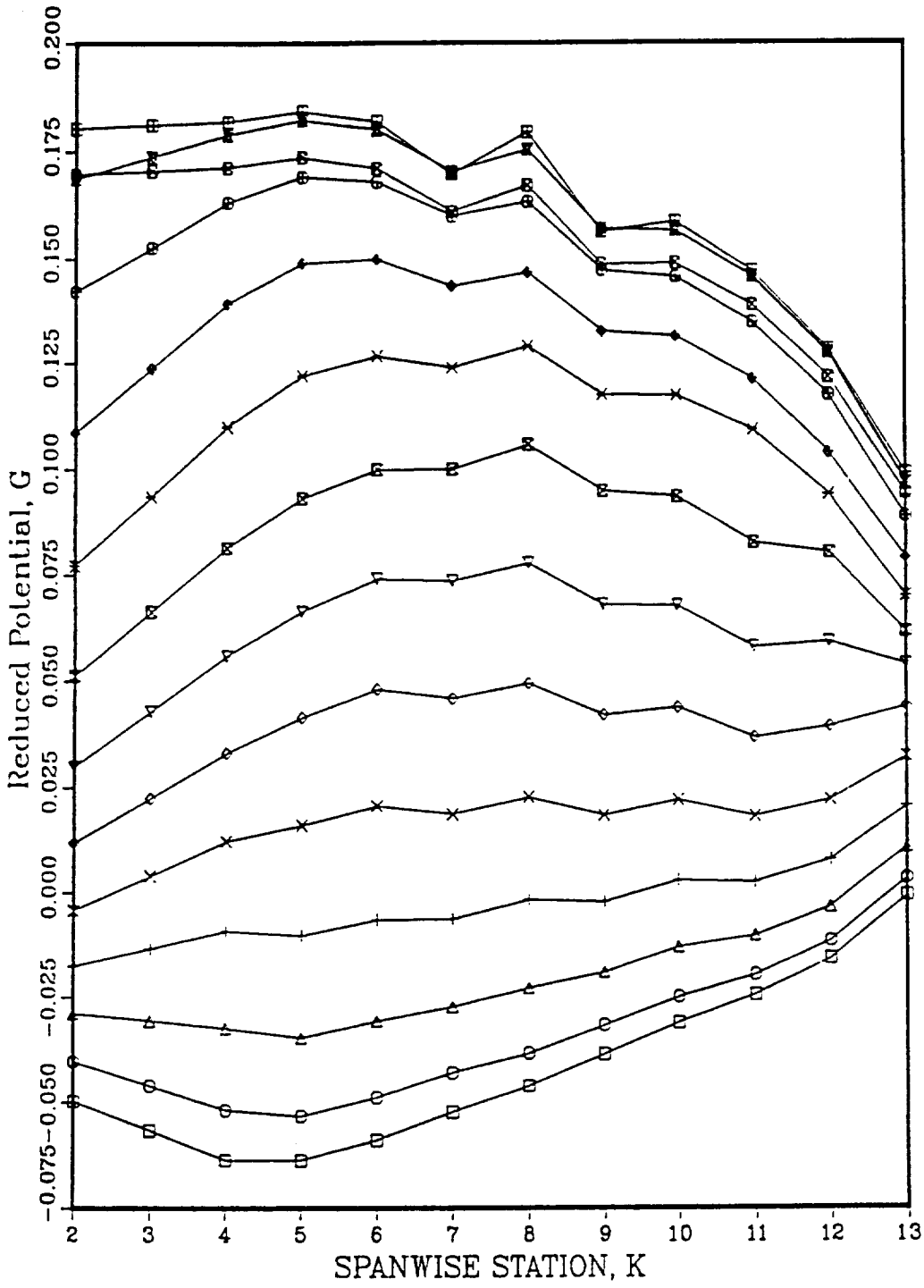

Fig. 19 The potential field on the wing's surface for a diverging design solution

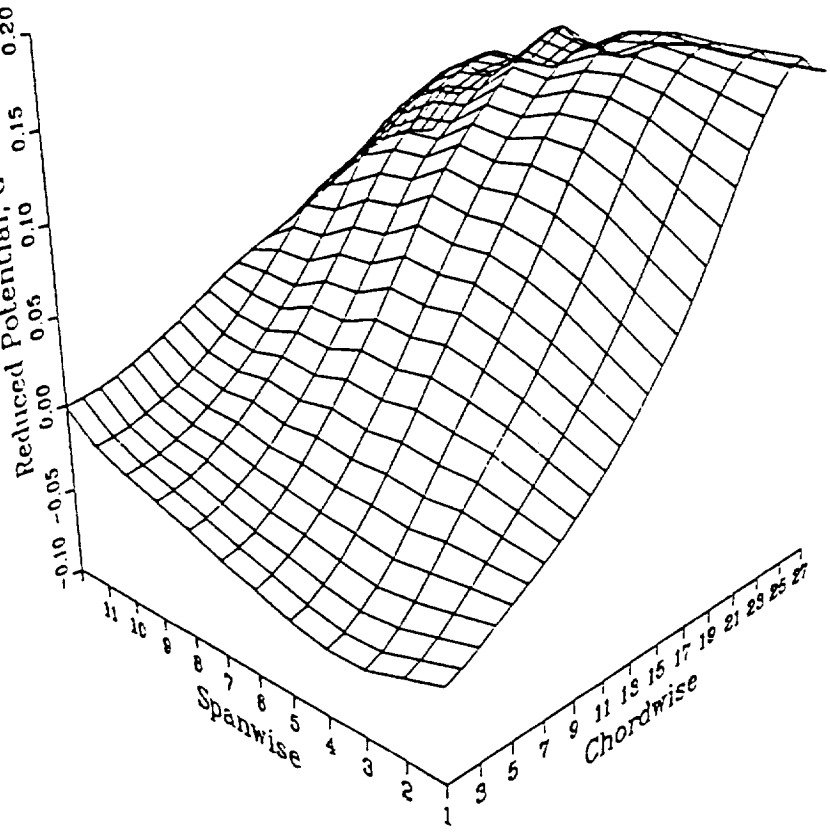

Fig. 19 Continued

the wing. This first difference is important, since the actual thickness of the wing may have less of an impact on the flowfield computed by the ZEBRA scheme due to the fact that the point of application of the boundary condition is not changing with time. Secondly, its full potential, fully conservative numerical scheme uses a mid-segment type of finite difference approach rather than a finite-volume scheme with fourth derivative type compensation terms[16] that seem to be amplifying the errors in the design solution.

Nevertheless, after exploring many alternatives to counter this oscillation problem, four methods based on the previous observations have been devised to damp out the spanwise oscillation:

A) Specify the inverse boundary condition at at least every other spanwise station and linearly interpolate the inverse displacements to the stations lying in between. This has been named the Type II-2 method.

B) Specify the inverse boundary condition at every station, but again only calculate inverse changes at every other station and linearly interpolate the inverse changes to the stations in between. This will be referred to as the Type II method.

C) Immediately prior to every surface update, calculate all spanwise derivatives of the potential in the residual based upon a potential function smoothed in the spanwise direction. This smoothing is accomplished by first defining the operator σ_ζ as

$$\sigma_\zeta f = \frac{\varepsilon}{4} f_{k-1} + \left(1 - \frac{\varepsilon}{2}\right) f_k + \frac{\varepsilon}{4} f_{k+1}, \qquad 0 \leq \epsilon \leq 1 \qquad (4-2)$$

where ε determines the amount of smoothing. Then using σ in the spanwise differentiation of ϕ with the maximum amount of smoothing (i.e., $\varepsilon = 1$)

$$\left(\frac{\partial \phi}{\partial \zeta}\right)_{i,j,k+\frac{1}{2}} = \sigma_\zeta \delta_\zeta \phi \qquad (4-3)$$

the smoothed spanwise derivative of ϕ becomes

$$(\phi_\zeta)_{i,j,k+\frac{1}{2}} = \frac{(\phi_{i,j,k+2} - \phi_{i,j,k} + \phi_{i,j,k+1} - \phi_{i,j,k-1})}{4.0} \qquad (4-4)$$

D) Smooth the slopes, $\frac{\rho h \Gamma}{\rho h U}$, in the spanwise direction in the design region in the same manner as with method C. It should be noted that, as stated earlier, smoothing the integrated slopes, i.e the inverse corrections. did not suppress the oscillation but only slowed the rate of divergence.

Three different cases were studied in order to test the effectiveness of each method at suppressing the oscillation and in reproducing the known target section. All three cases used Lockheed Wing-A at a Mach number of .8 and at an angle of attack of 2^o. The first case utilized a NACA 0012 airfoil as the initial section and the original supercritical wing sections accompanying Wing-A as the target section. The design region stretched from 30-70% semispan of the wing and began 5% aft of the leading edge and extended to the trailing edge. Since a medium grid (80x12x16) was employed, there was a constant ζ grid station at every 10% semispan. Results are

shown in Fig. 20 for the four different approaches.

Although all four approaches worked well for this case, by using the RMS of the errors between the target section and the section designed as a measure of accuracy, methods A and C produced the best results for this case in the interior as well as at the edges of the design region. For the same number of flowfield iterations, the technique D produced the most unsatisfactory results when compared to the target sections.

The effect of each approach on the residual at the trailing edge after 10 surface updates can be seen in Fig. 21. The discontinuities in the residual for method A is due to the fact that the inverse boundary condition is applied only at the 30, 50 and 70% semispan locations. All four approaches have a characteristic jump in the residual at the first spanwise design station at 30% semispan. This jump is probably due to the previously discussed spanwise mismatch problem with the potentials at the direct-inverse interface, which manifests itself in the compensation terms. The Type II method had the largest jump at this interface, while the Type II-2 method had the smallest jump. Notice that the spanwise distributions of the residual for the two smoothing approaches are quite similar in the design region.

Since only small differences existed between the methods for the previous test case, a more severe test was conducted by designing an entire wing using NACA 0006 sections as the initial airfoils and NACA 0012 sections as the targets. These sections were chosen due to the fact that most of the problems in the past were amplified by beginning with a thin section and targeting a thicker section. Furthermore, a

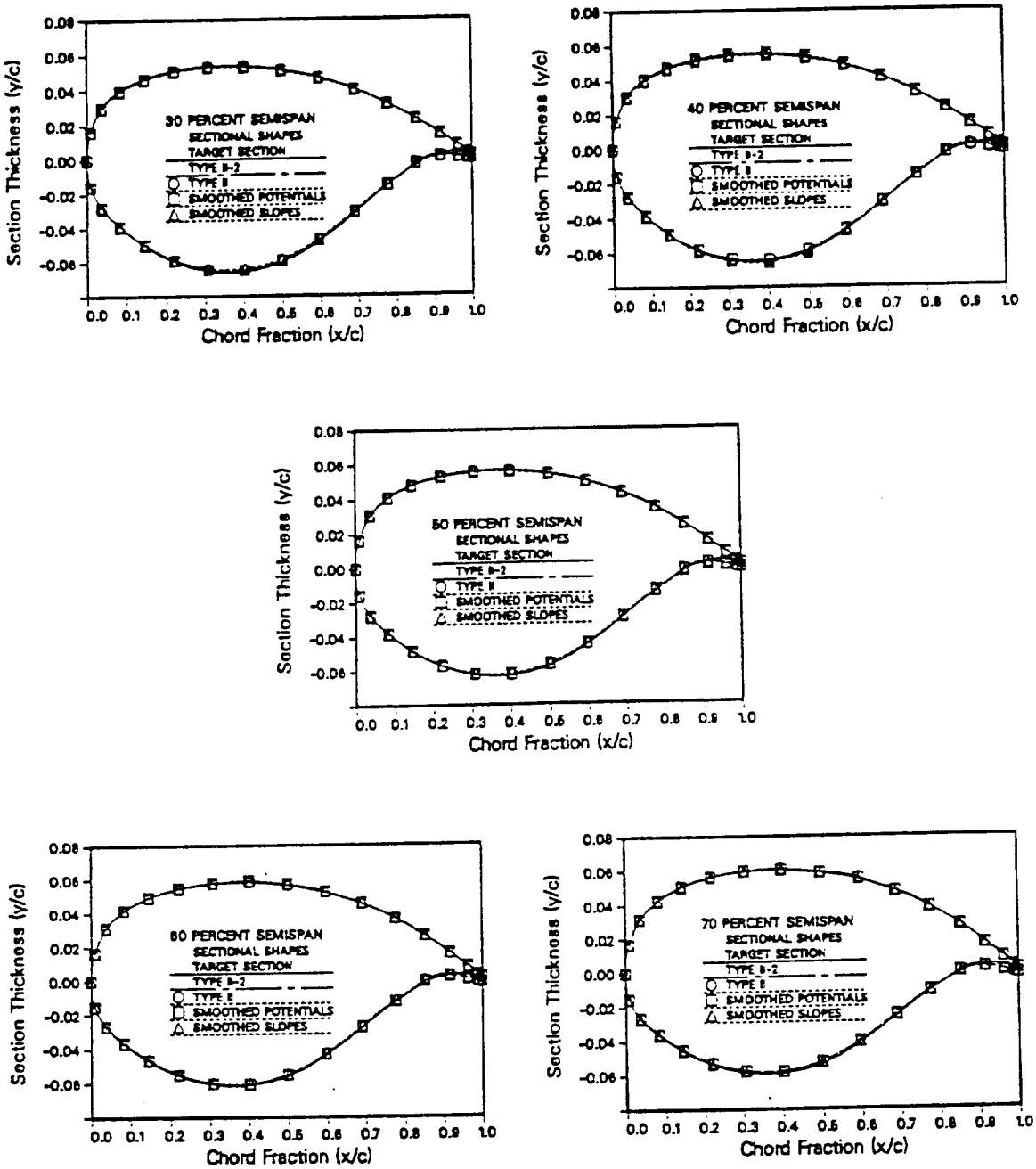

Fig. 20 Comparison of airfoil sections designed using the four spanwise oscillation remedies on a medium grid from 30% to 70% semispan.

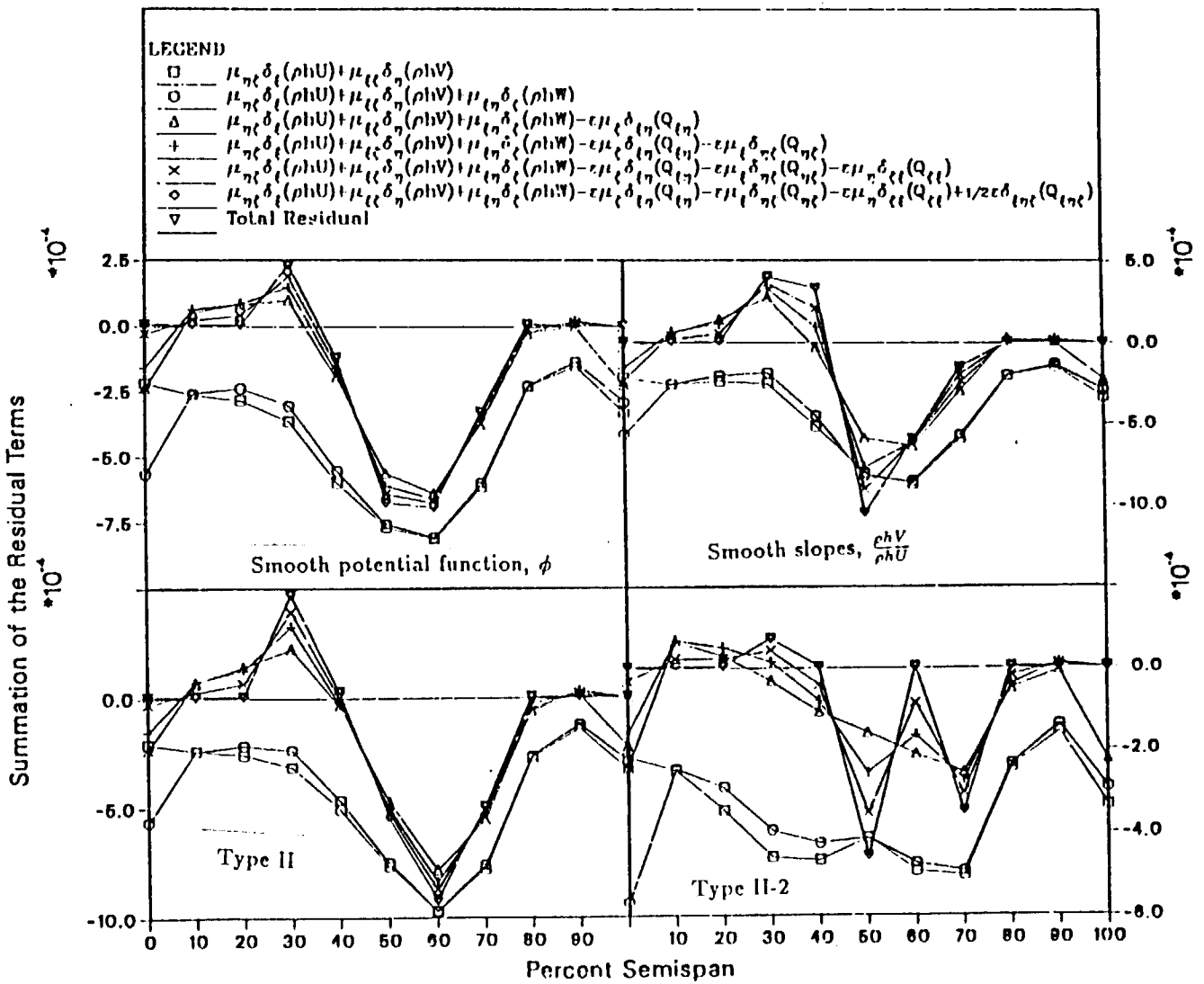

Fig. 21 Breakdown of the Residual at the trailing edge on the upper surface for the four spanwise oscillation remedies after 10 global iterations

full wing design would reveal whether the accuracy of each method depended on the spanwise location of the wing.

When an attempt was made to compute these cases, it was discovered that when using the smoothing two smoothing techniques, (methods C and D), it was necessary to use zero order extrapolation of the displacements from the adjacent grid station to the root section. The root section tended to lag in the convergence process in comparison to the rest of the grid stations. This behavior is possibly due to a slowly converging flowfield at the the wing-fuselage juncture. Since all of the sections started out too thin, this lagging of the root section forced the adjacent grid station to quickly become too thick, which led to divergence at the root in both cases. Zero order extrapolation of the nondimensionalized displacements forced the root section to converge at a rate which was more in compliance with the rest of the grid stations at the expense of degrading the accuracy of the root section. Since the root section has been successfully designed independently, presumably, this problem might be circumvented by simply allowing the flowfield solution to converge further before each relofting, although such a procedure would probably be a less efficient approach.

Also, no smoothing of the potentials or the residuals was used at the tip. Since both the residual and the potentials are quickly varying in the spanwise direction in the tip region, smoothing leads to large errors in the residuals and hence the section shapes. In fact, better results can be obtained for the smoothed potential approach by using a zero order extrapolation of the normalized displacements from the grid station inboard of the tip to the tip. Overall though, the inboard sections of the wing

slowly became thicker, while those outboard responded more quickly, initially causing these outboard sections to actually become too thick.

The resulting sectional shapes for the four different methods are compared in Fig. 22. As can be seen in the figure, method C works well when designing in the interior of the wing, but did not give satisfactory results at the tip of the wing where smoothing the quickly varying potential led to large errors in the section shapes. Since the residuals also varied quickly at the tip, the slopes at the tip were not smoothed with method D. Since there were not any slopes defined at the fuselage ghost point location, (i, ky, 2), the slopes were not smoothed at the root either. This method produced the most accurate results while still managing to suppress the oscillation problem. In contrast, the Type II and Type II-2 methods worked well on the entire wing surface, and nothing special needed to be done at the root or tip.

The same case was executed on the fine grid (160x24x32) to study any effect of grid size on the accuracy and effectiveness of the methods. This grid allowed 21 design stations which were located a distance of 5% semispans from each other. When using the Type II and Type II-2 methods, the lagging of the root section actually forced the section located at 10% semispan, two grid stations outboard, to become too thick, which led again to a divergent solution. Thus, for this fine grid case, it was necessary to use zero order extrapolation of the the normalized displacements from the adjacent station to the root when using all four remedies. Cases which do not require such large changes in thickness at the root have not required this procedure using the Type II and Type II-2 methods. In addition, because of the aforementioned

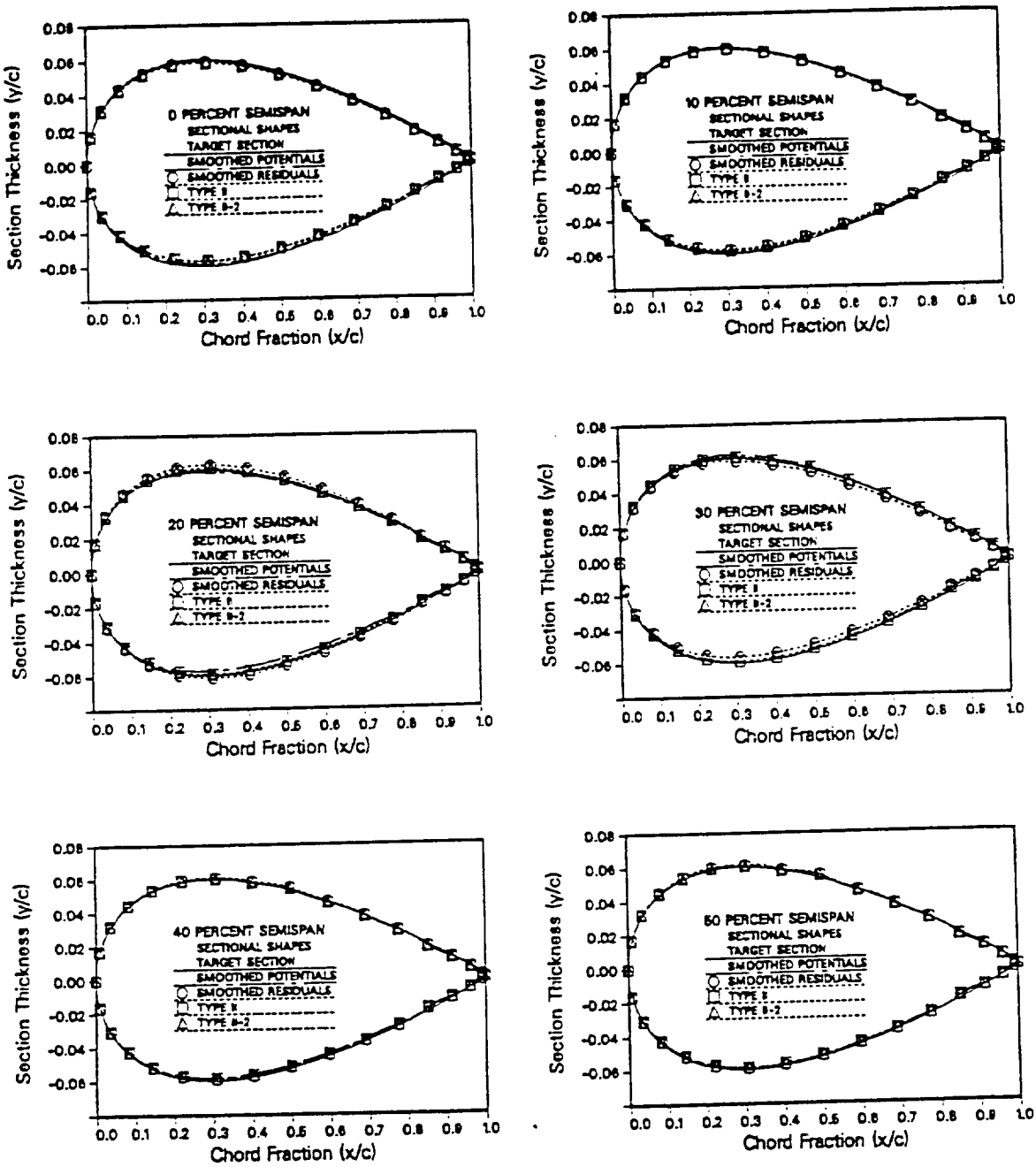

Fig. 22 Comparison of airfoil sections designed using the four spanwise oscillation remedies on a medium grid from 0% to 100% semispan.

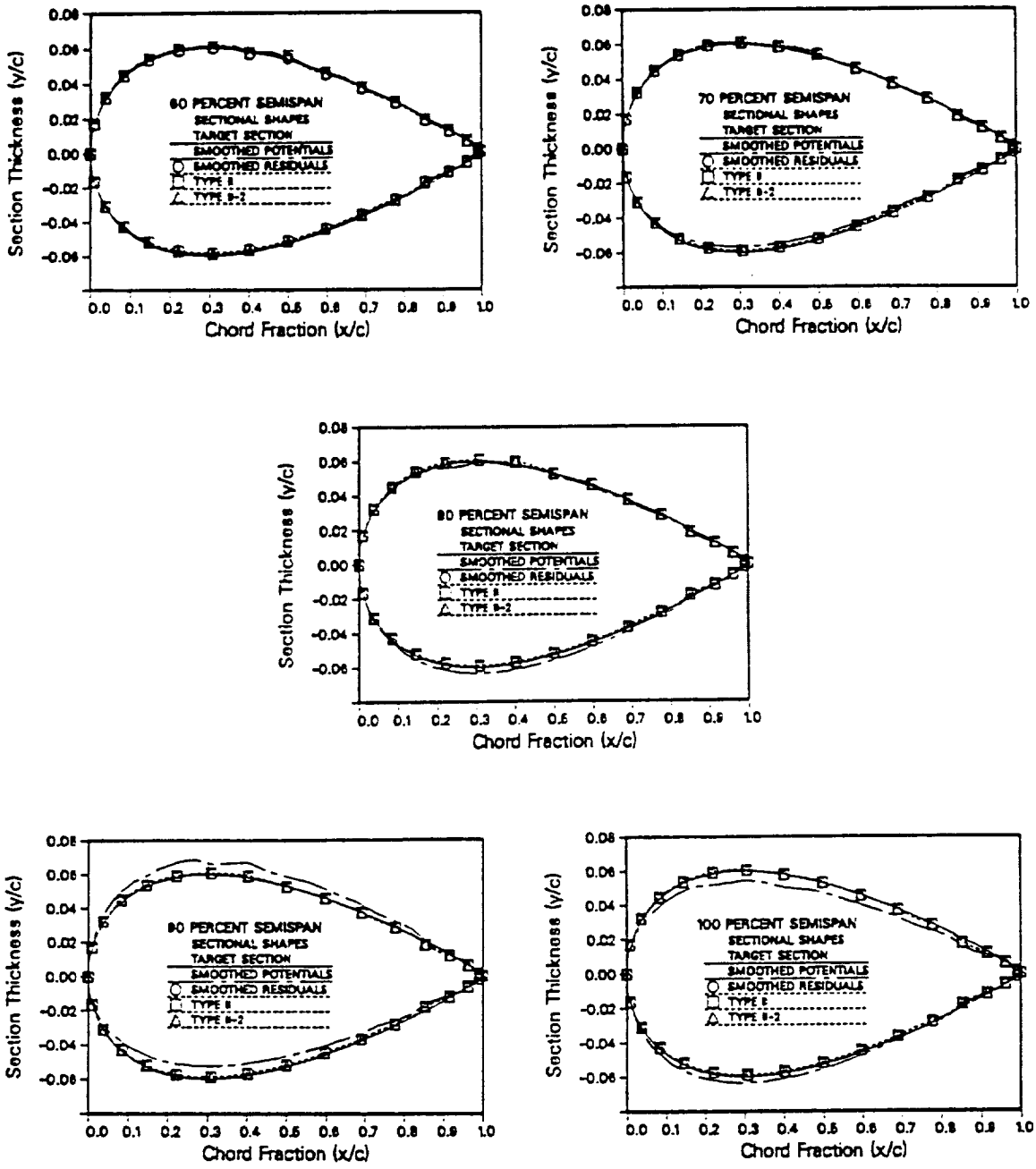

Fig. 22 Continued

problems with the smoothing approaches at the tip, no smoothing was used at the tip section.

The results for this case are shown in Fig. 23. For this case, the smoothing approaches yielded satisfactory sections on the region of the wing spanning from about 30% to 85%. Elsewhere, the sectional shapes vary significantly from the target section. Thus, the smoothing approaches work well when designing in the interior of the wing, but they do not give satisfactory results near the root and tip of the wing.

An objective measurement of the accuracy of the sections in relation to the target can be obtained using a coefficient of determination, r, defined as[42] :

$$r = \sqrt{1 - \frac{\sigma_{y,x}^2}{\sigma_y^2}} \qquad (4-5)$$

where σ_y is the standard deviation of the ordinates of the target section defined as

$$\sigma_y = \left[\frac{\sum_{i=1}^{n} (y_i - y_{mean})^2}{n-1}\right] \qquad (4-6)$$

and

$$\sigma_{y,x} = \left[\frac{\sum_{i=1}^{n} (y_i - y_{design})^2}{n-2}\right] \qquad (4-7)$$

is the deviation of the design from the target for the same x values. This quantity varies from 0 to 1, one being perfect.

Moreover, to further clarify which method produced the least amount of oscillation, the average error variation in the spanwise direction for each method should be compared. The spanwise variation of the coefficient of determination and average percent error are shown in Figs. 24-29. The Type II and Type II-2 methods

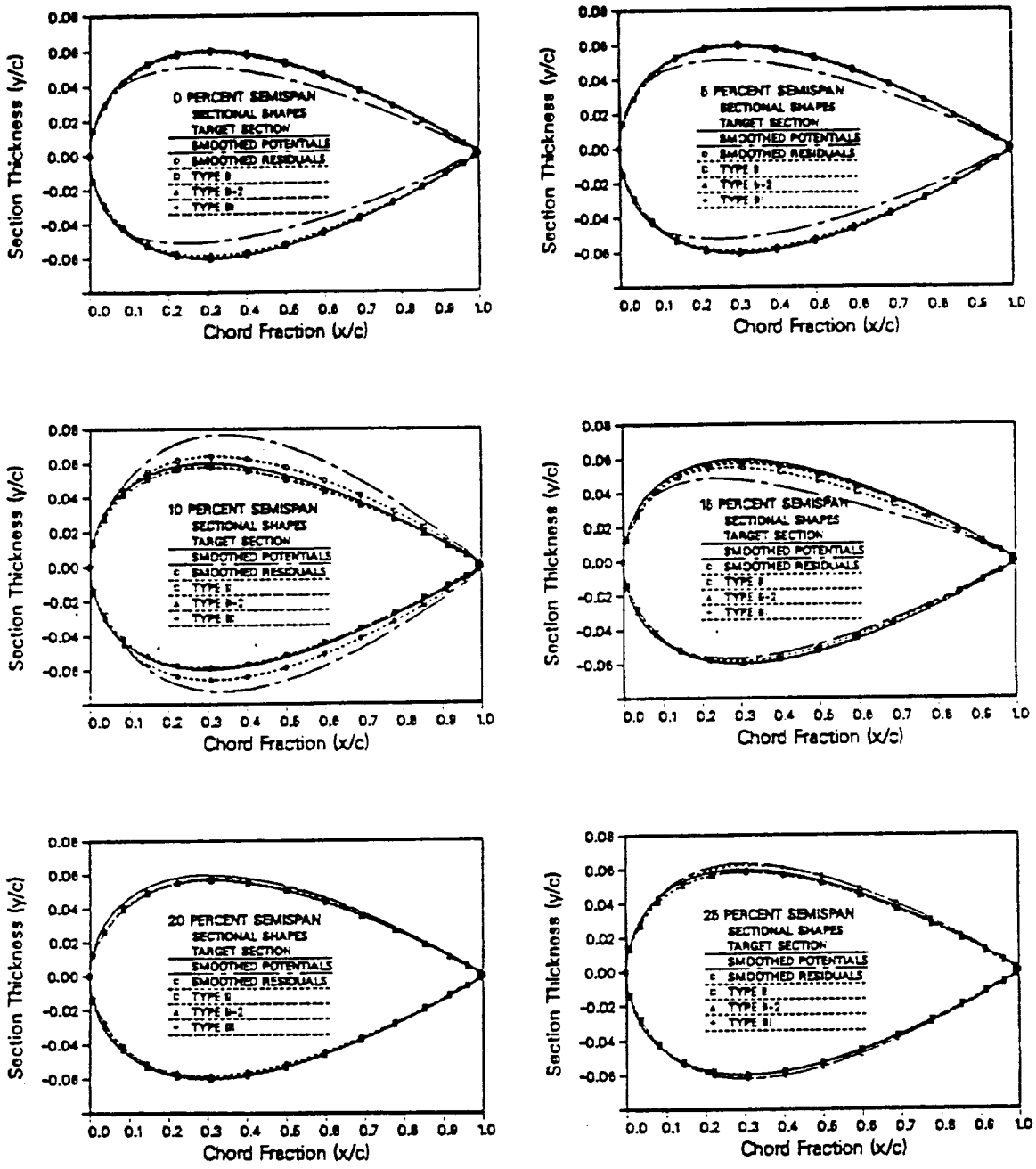

Fig. 23 Comparison of airfoil sections designed using the four spanwise oscillation remedies on a fine grid from 0% to 100% semispan.

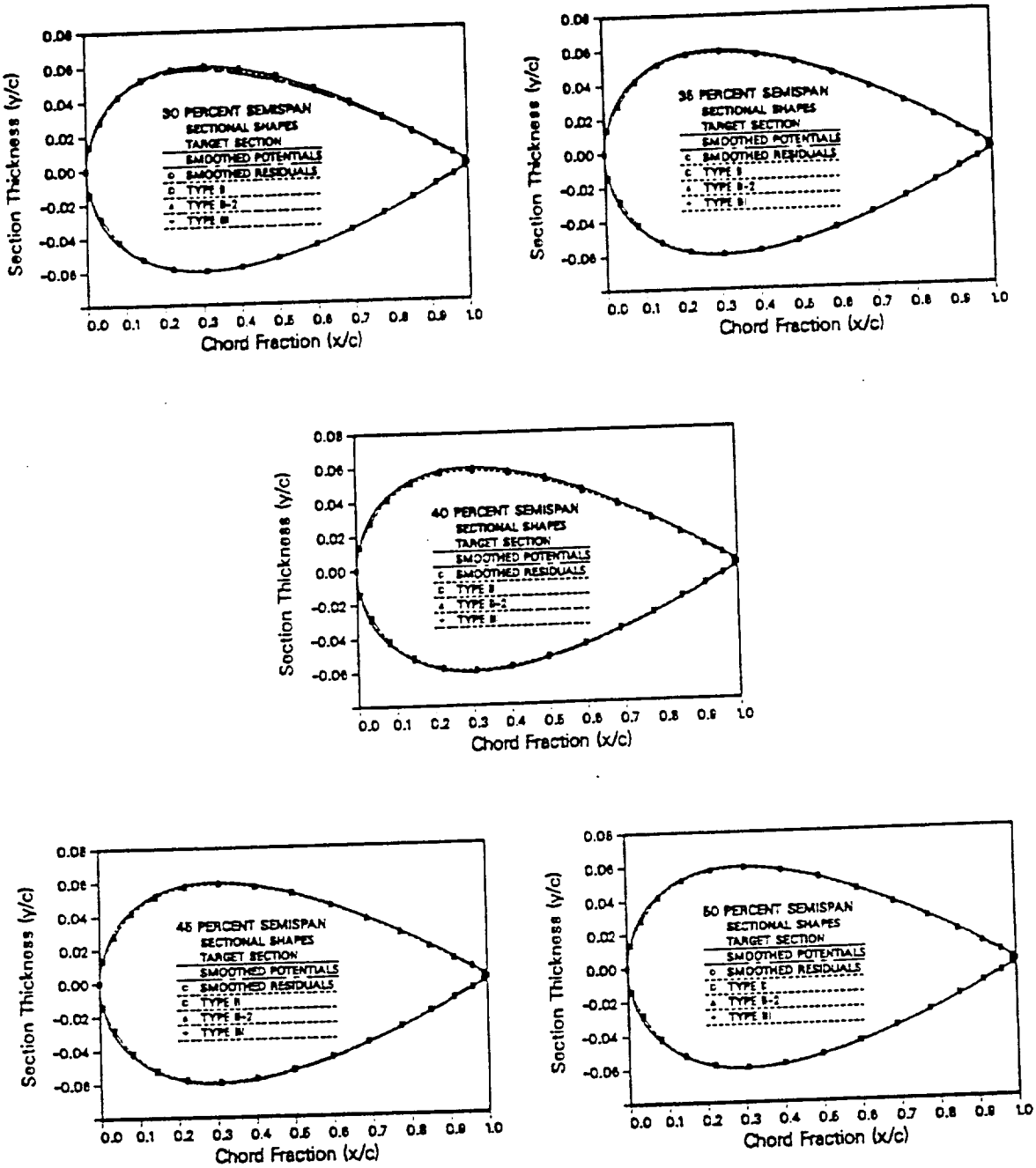

Fig. 23 Continued

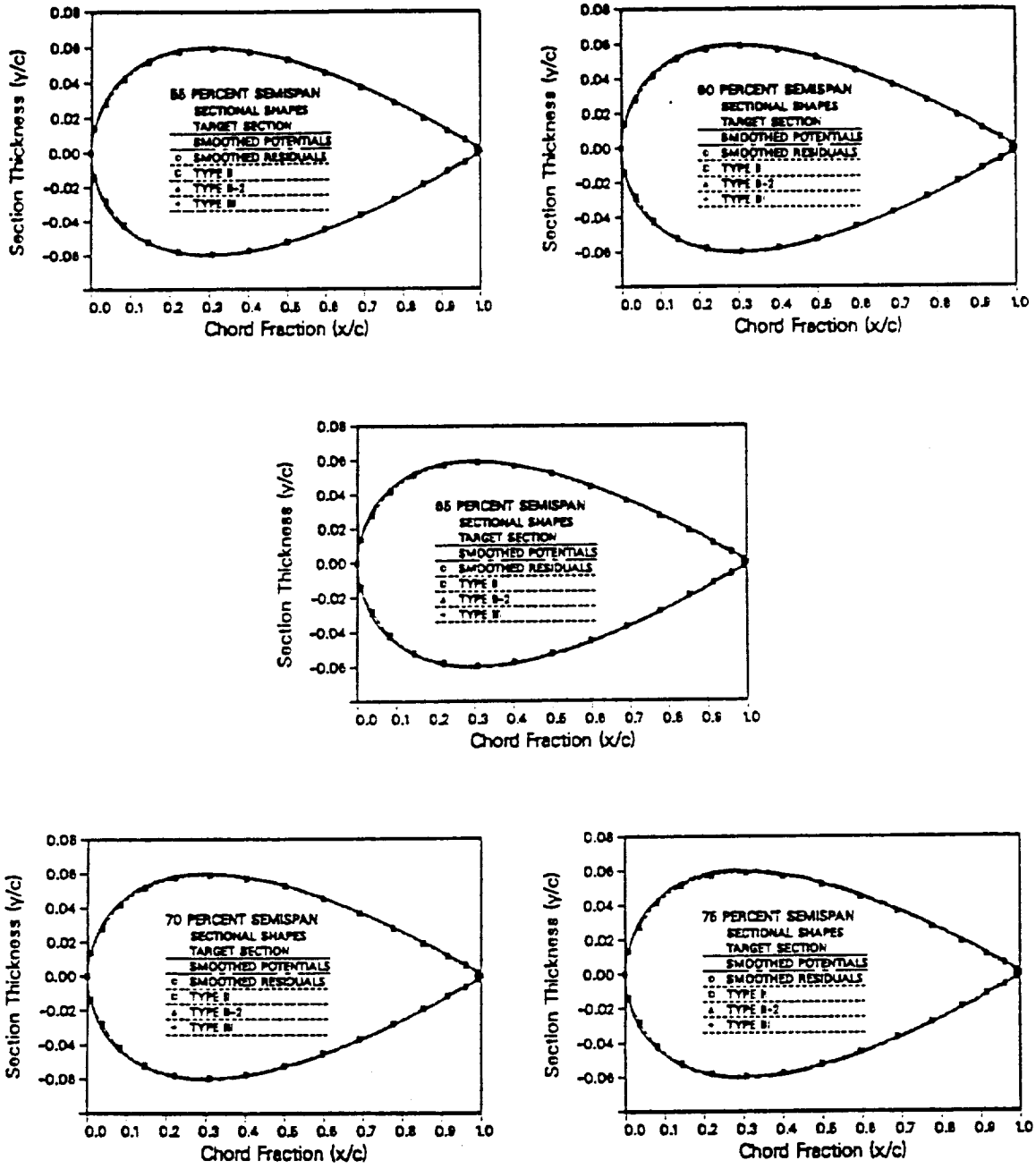

Fig. 23 Continued

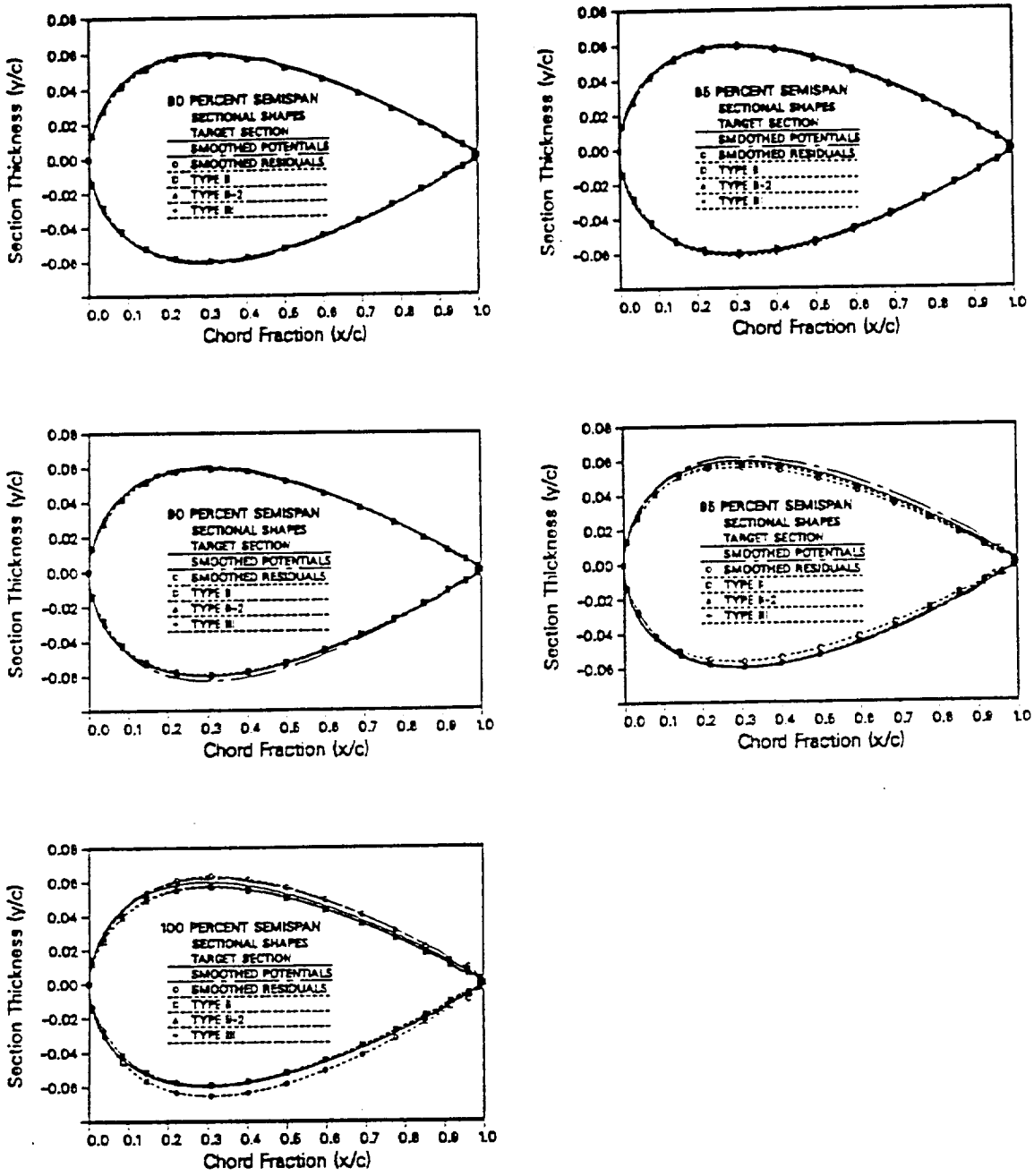

Fig. 23 Continued

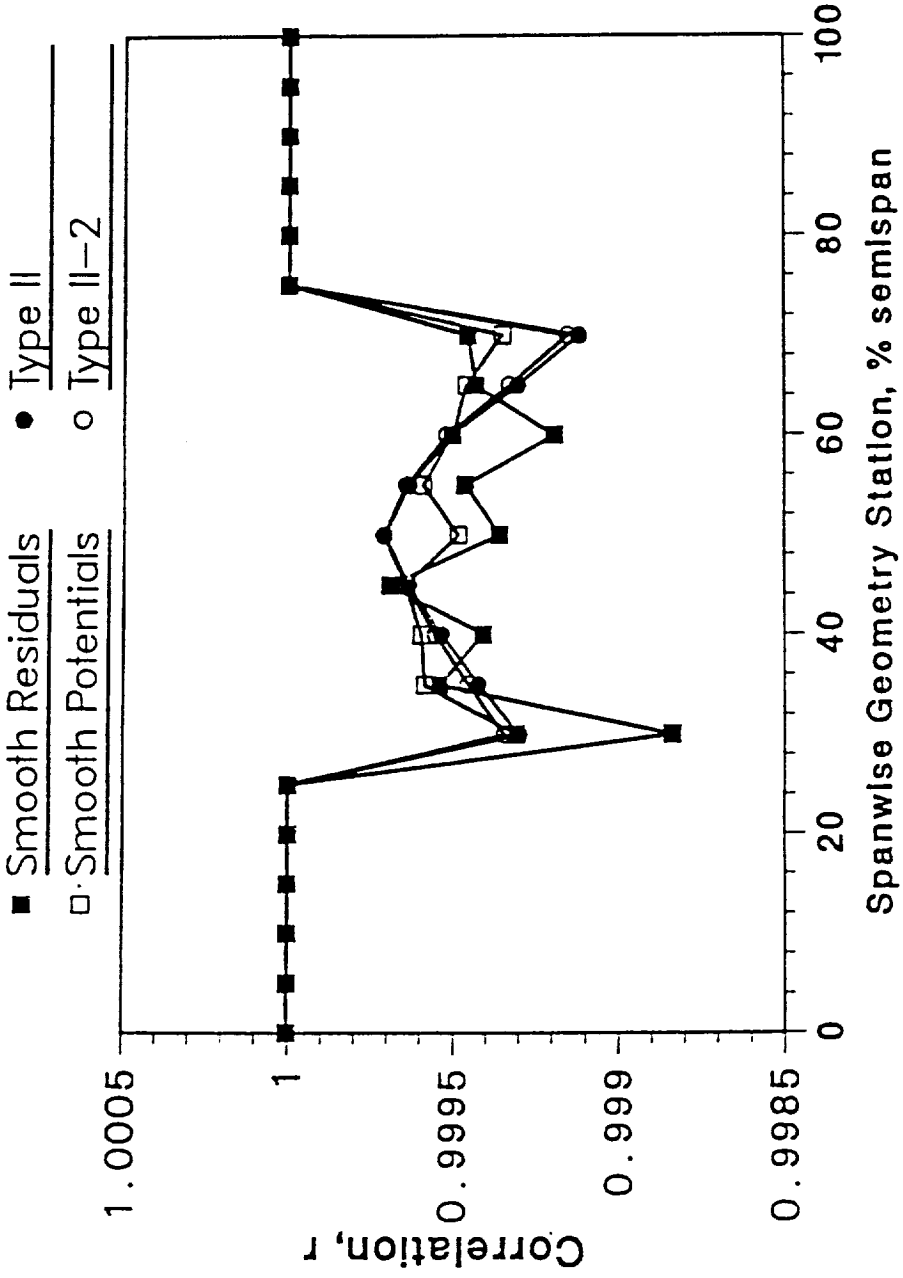

Fig. 24 The effect of the four spanwise oscillation remedies on the coefficient of determination for the medium-grid, partial-wing design

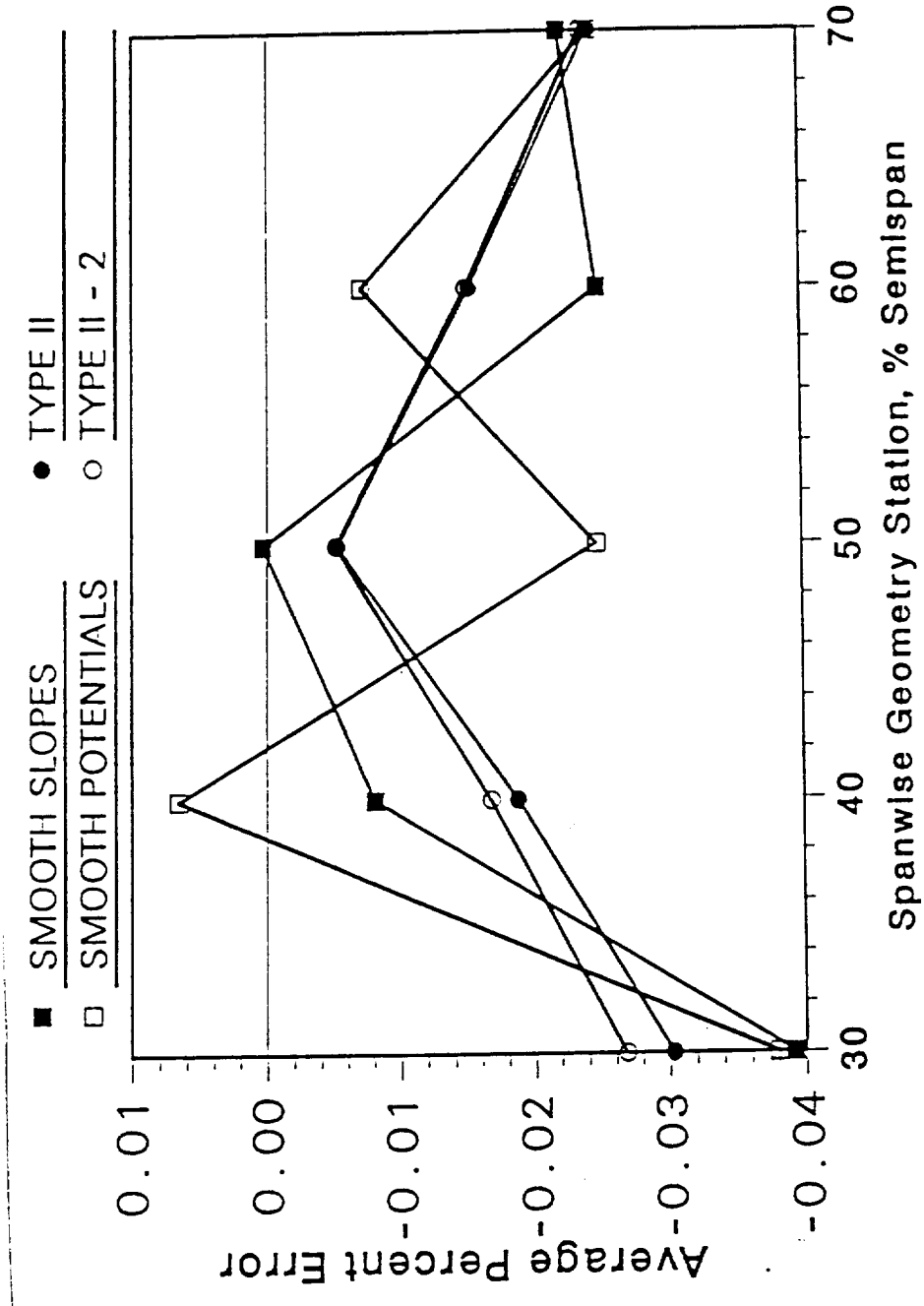

Fig. 25 The effect of the four spanwise oscillation remedies on the average percent error between the target and the design sections for the medium-grid, partial-wing design

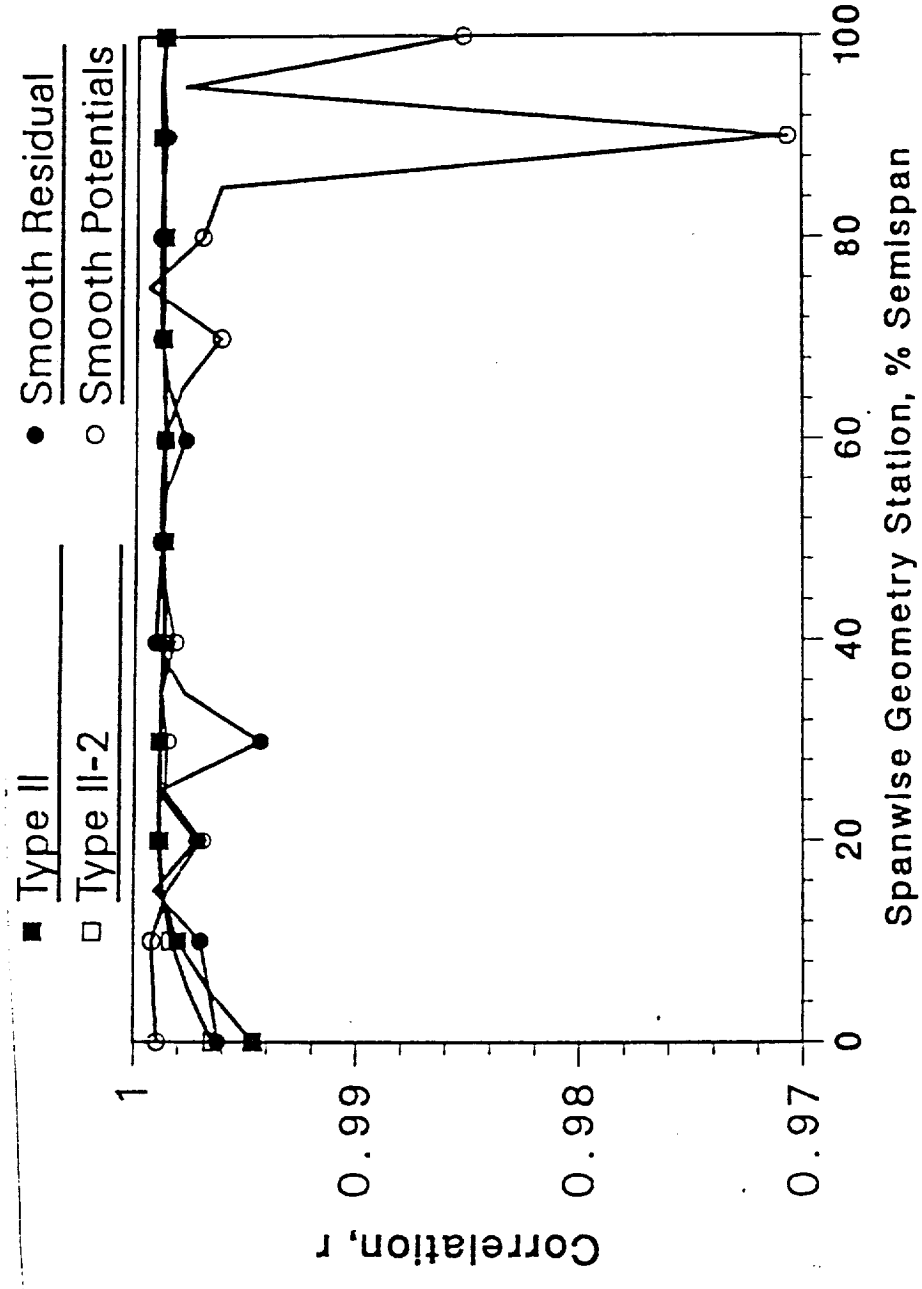

Fig. 26 The effect of the four spanwise oscillation remedies on the coefficient of determination for the medium-grid, full-wing design

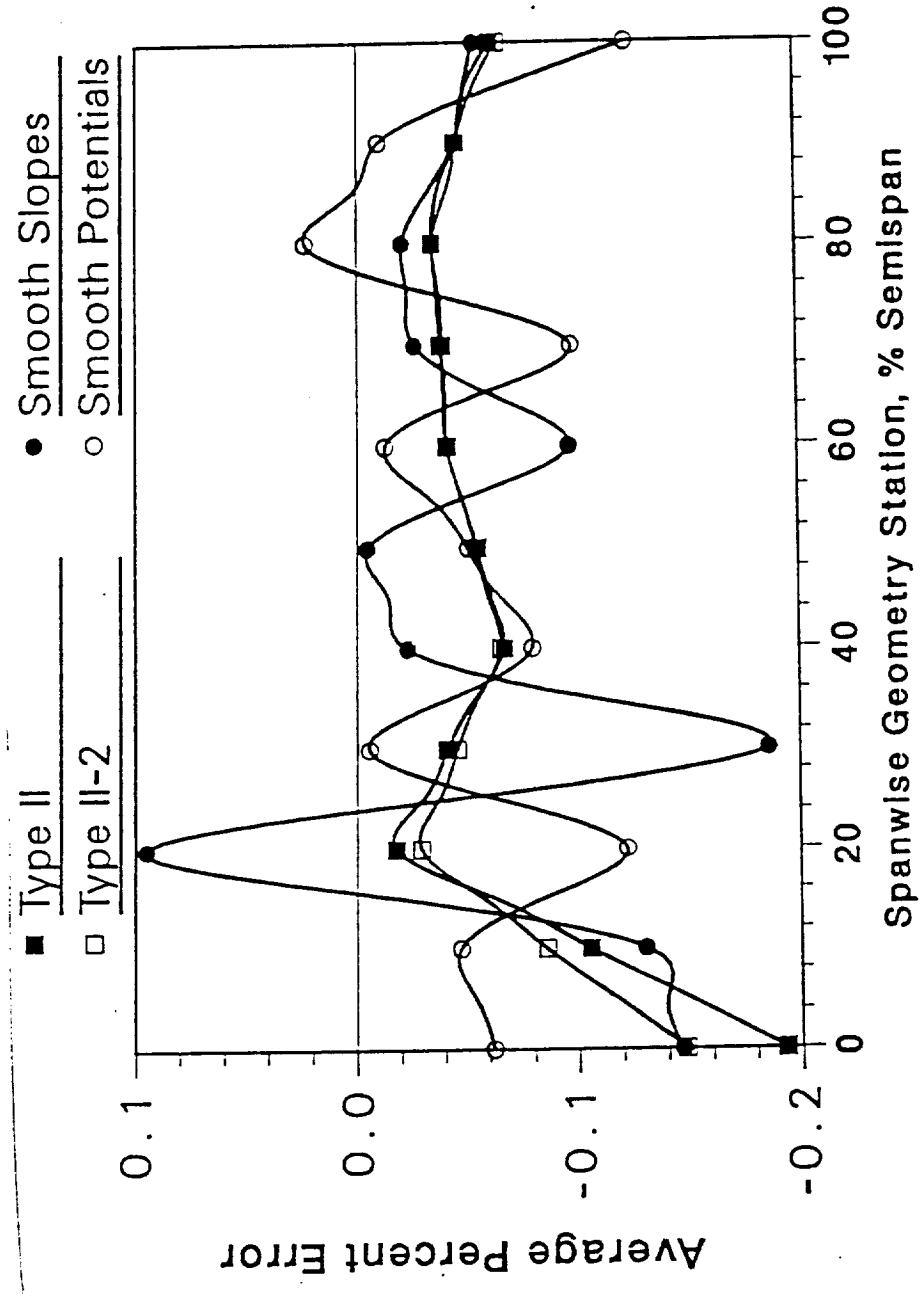

Fig. 27 The effect of the four spanwise oscillation remedies on the average percent error between the target and the design sections for the medium-grid, full-wing design

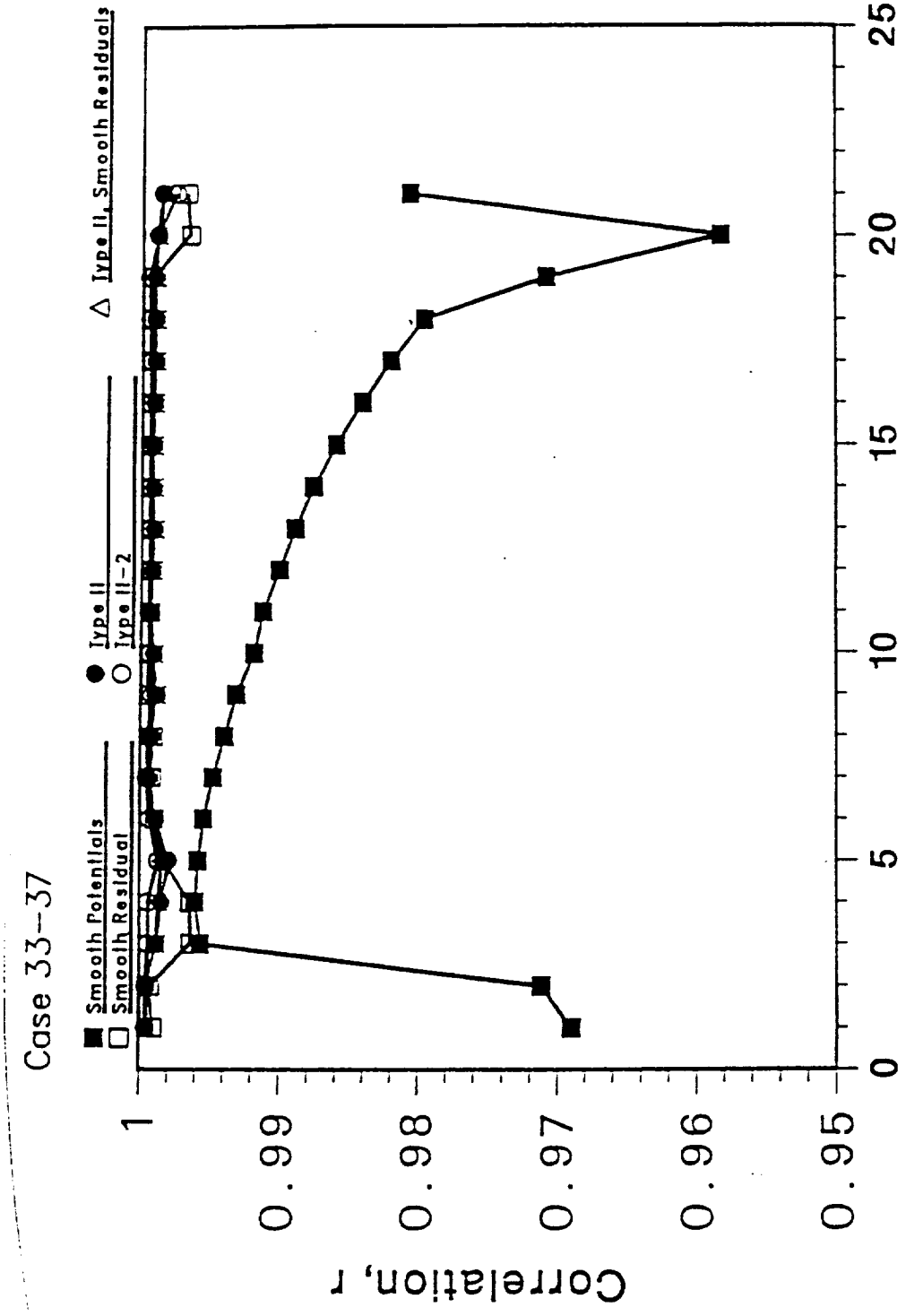

Fig. 28 The effect of the four spanwise oscillation remedies on the coefficient of determination for the fine grid, full wing design

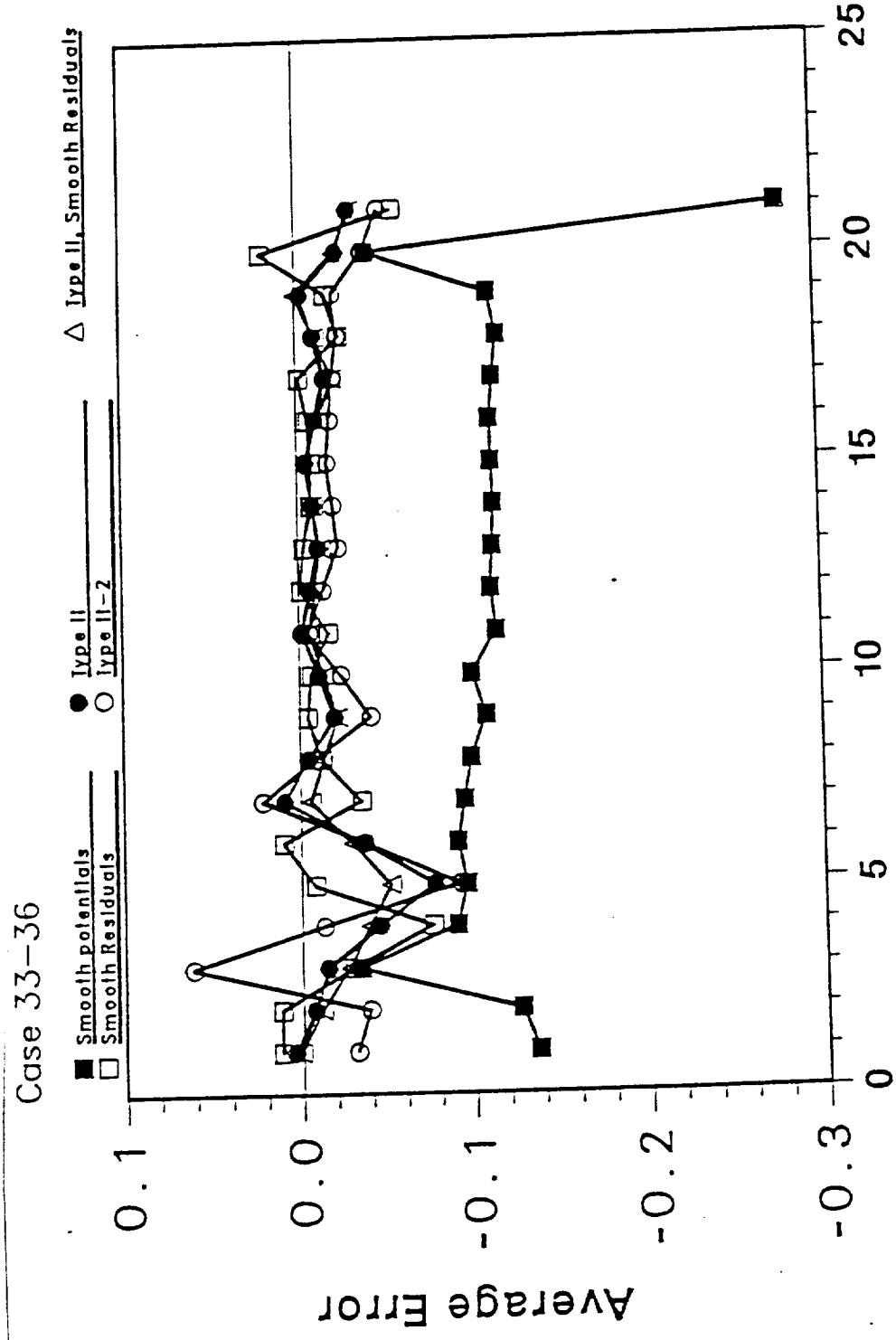

Fig. 29 The effect of the four spanwise oscillation remedies on the average percent error between the target and the design sections for the fine-grid, full-wing design

produced the least amount of oscillation, while smoothing the potentials produced the most amount of oscillation in the error.

There is still some doubt by this investigator whether only secondary aberrations have been observed and not the true, fundamental cause of the oscillation. In light of this, another effect that should be investigated is that of the addition of mass into the flowfield by the inverse boundary condition. Some other investigators[23,43] have included a source correction in the far field and in the near field[43]. In this research, this source correction was neglected since this addition of mass would be driven to zero at convergence. But, its effect on the unconverged solution is not clear. In order to see if this had a significant effect on the solution, a quick, numerical experiment was performed in which the distance to the outer boundary was doubled. (See Fig. 30) Presumably, if the addition of mass was adversely affecting the boundary condition in that region for a given distance, it would have less of an effect if the distance were increased since the additional mass flux arriving at the boundary would be less and the outer boundary boundary condition would be better satisfied. When this computation was completed, however, the solution seemed to be completely unaffected, diverging at the same point in the iteration history. This was only a simple attempt at proving that the sources on the wing were not the fundamental motivation for the oscillation. A thorough analysis must consider the effect of this mass addition on the downstream boundary and the near field. The downstream boundary could be stretched further downstream, and appropriate source correction terms, using the flux ejected from the inverse regions of the wing as the source strength, could be added to the reduced potential in the entire flowfield.

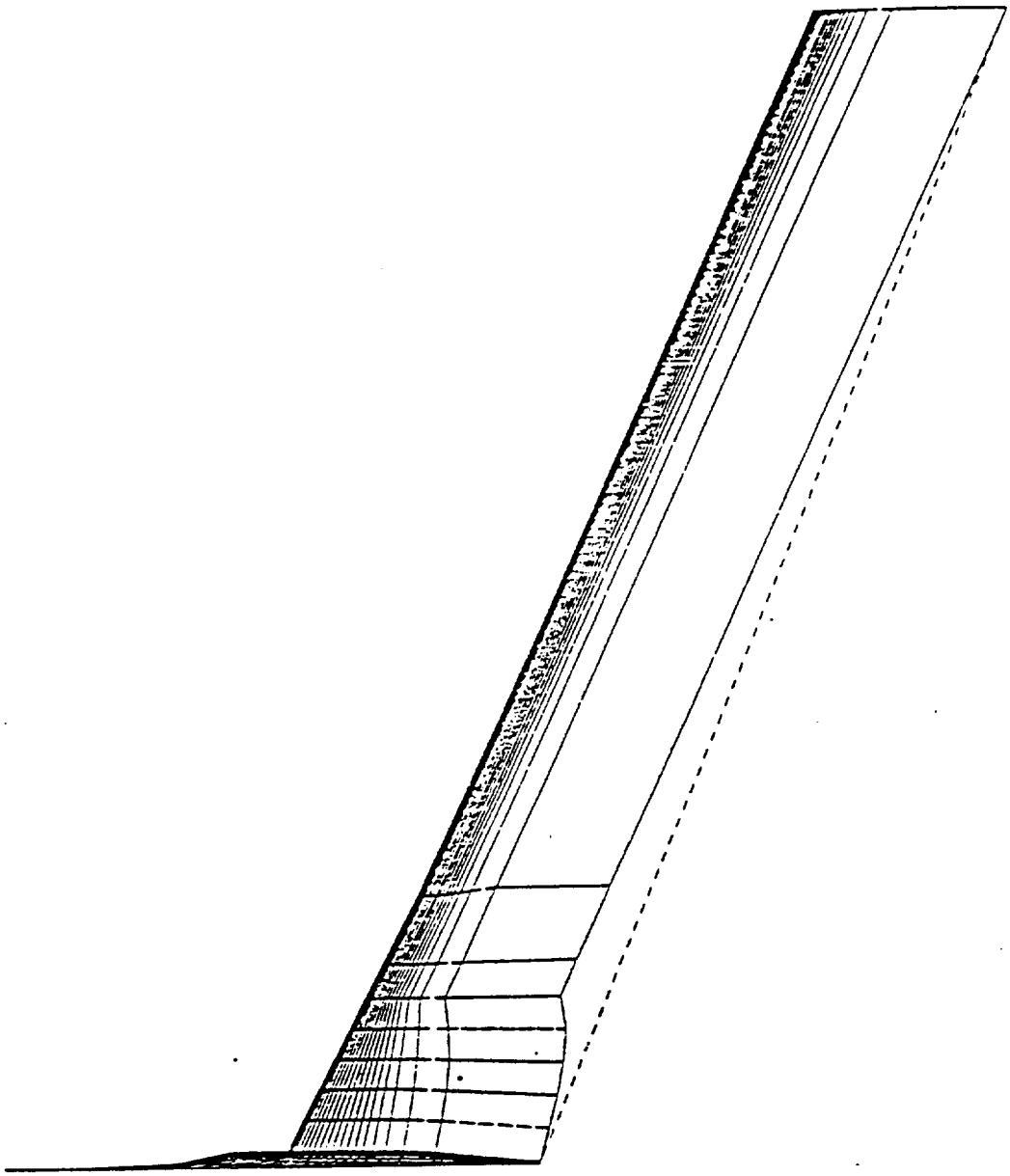

Fig. 30 Grid System at the wing-body's surface with a radial boundary stretched twice as far as the original grid system

Another possible cause could be the assumption of flow tangency used in the residual expression in the integration of the flow tangency equation. When this assumption is made, not only are the fluxes reflected about the current wing boundary, but so are the compensation terms. This procedure in effect doubles the amplitude of the $\delta_{\eta\zeta}$ and the $\delta_{\xi\eta}$ type compensation terms. Since the flow is not generally tangent to the current shape when designing a new airfoil section, reflecting the compensation terms may be initially incorrect. An alternative formulation may be needed.

In retrospect, a few comments about the advantages of each method in different design situations are warranted. For instance, methods C and D give the designer the most flexibility; the desired pressure distributions can be imposed at every spanwise grid station, and the section shapes corresponding to each grid station can be calculated relatively independently of the adjacent stations. On the other hand, because of the interpolation required in the first two methods, the section shapes at 'odd' stations are directly dependent upon the shapes at 'even' stations; so although the designer loses a little flexibility, he gains a smoother spanwise distribution of section thicknesses in the spanwise direction. From a designer's standpoint of course, method A is the most restrictive of the four, but it yields the smoothest designs in the spanwise direction, and converges the quickest. Therefore, method A (i.e., the Type II-2 method) would most probably be the best to use with wings of moderate to high aspect ratios. But, Method B (i.e., the Type II method) would most probably be necessary for wings with aspect ratios of the same order as Lockheed Wing-B.

CHAPTER V

RESULTS AND DISCUSSION

Since the versatility of the method in designing multiple, overlapping regions of the wing has already been well demonstrated by Gally[44,13], most of the test cases presented, herein, were chosen instead to exhibit some of the constraints and limitations of the current inverse design procedure. The cases were chosen to reveal the approximate limits imposed on the aspect ratio and sweep of the wing; and the significance of grid skewness, viscous interaction, grid refinement, and the initial airfoil on the final airfoil section design. Some questions about the compatibility of Mach number and pressure distribution will be answered by designing a wing at one Mach number using pressures obtained from a wing analysis at a different Mach number. Finally, preliminary results will be presented for a partial wing design beginning aft of the leading edge and terminating forward of the trailing edge.

V.1 Boundary Layer and Wake Effects

One of the objectives of this study was to determine the significance of various viscous effect in the design of transonic wings[9]. The wing chosen for this study was a typical transport type wing, Lockheed Wing-A. This wing has an aspect ratio of 8.0, a leading edge sweep of 27°, a taper ratio of .41, a twist of 2.28° at the root and -2.04° at the tip, and 1.5° of dihedral.

An input pressure distribution was obtained by analyzing Lockheed Wing-A using full viscous effects ; these included boundary layer displacement thickness, wake thickness, and wake curvature. The flight Mach number of .8, angle of attack of two degrees, and Reynolds number, Re, of 25 million used in the analysis were thought to represent flight conditions for a typical, average-sized transport; and the distribution was considered to be typical of that which would be available to and desired by a designer. All computations were performed on a fine (160x24x32) grid. The resulting pressure distributions obtained from the analysis were used in two separate design cases, each composed of five and three subcases, respectively. The first series of cases was a full wing design using the target section as the initial section. By using the target section, any effect of the initial section on the final outcome would presumably be eliminated. The type II design method was used and the inverse boundary condition was enforced from 5% aft of the leading edge to the trailing edge. Furthermore, relofting was not initially done at all. The results for the partially converged cases were plotted and then further converged allowing relofting to take place. In this way, the effect of relofting on the final design could be determined. The iteration history of each case was kept the same, even though by doing this the absolute level of convergence could very well be different since changes of various magnitudes were associated with each case. The large amount of computational time required for these cases dictated this type procedure and for comparison purposes this approach is acceptable. Fortunately, it turned out that the sectional shapes in every case were varying quite slowly by the end of the design run, indicating that the sections were near convergence.

In each case, viscous options were 'turned off' one at a time to assess their effect. In the first case, the wing was designed with all viscous effects. In the second, the lag entrainment was turned off. The third case did not use wake curvature, while the fourth neglected both wake curvature and wake thickness. Finally, in the fifth case the wing was designed inviscidly. The resulting unrelofted designs for each case are compared in Fig. 31. As expected, the inviscidly designed sections are slightly thicker at the root where the normalized boundary layer displacements are thinnest (see Fig. 32) and become increasingly thicker towards the tip in accordance with the thickening boundary layer.

Neglecting lag entrainment, wake curvature and thickness had very little effect on the designed sectional shapes overall. But, if the trailing edge region is examined closely for cases with the wake effects neglected, the trailing edges sometimes cross.

Upon converging these shapes further and enforcing a trailing edge ordinate requirement with relofting, significantly different results were obtained. As shown in Fig. 33, the inviscidly designed shapes are now thinner on the upper surface and slightly thicker on the lower surface, especially in the cove region where viscous effects are large. Also, because of the relofting involved, the leading edge radius has become smaller. The rest of the cases produced sections which did not deviate much from the target, except near the tip. However, neglecting both wake effects produced sections that were actually thicker than the target. This change was due to the relofting that was necessary to uncross the trailing edges, which produced larger leading edge radii and hence thicker sections.

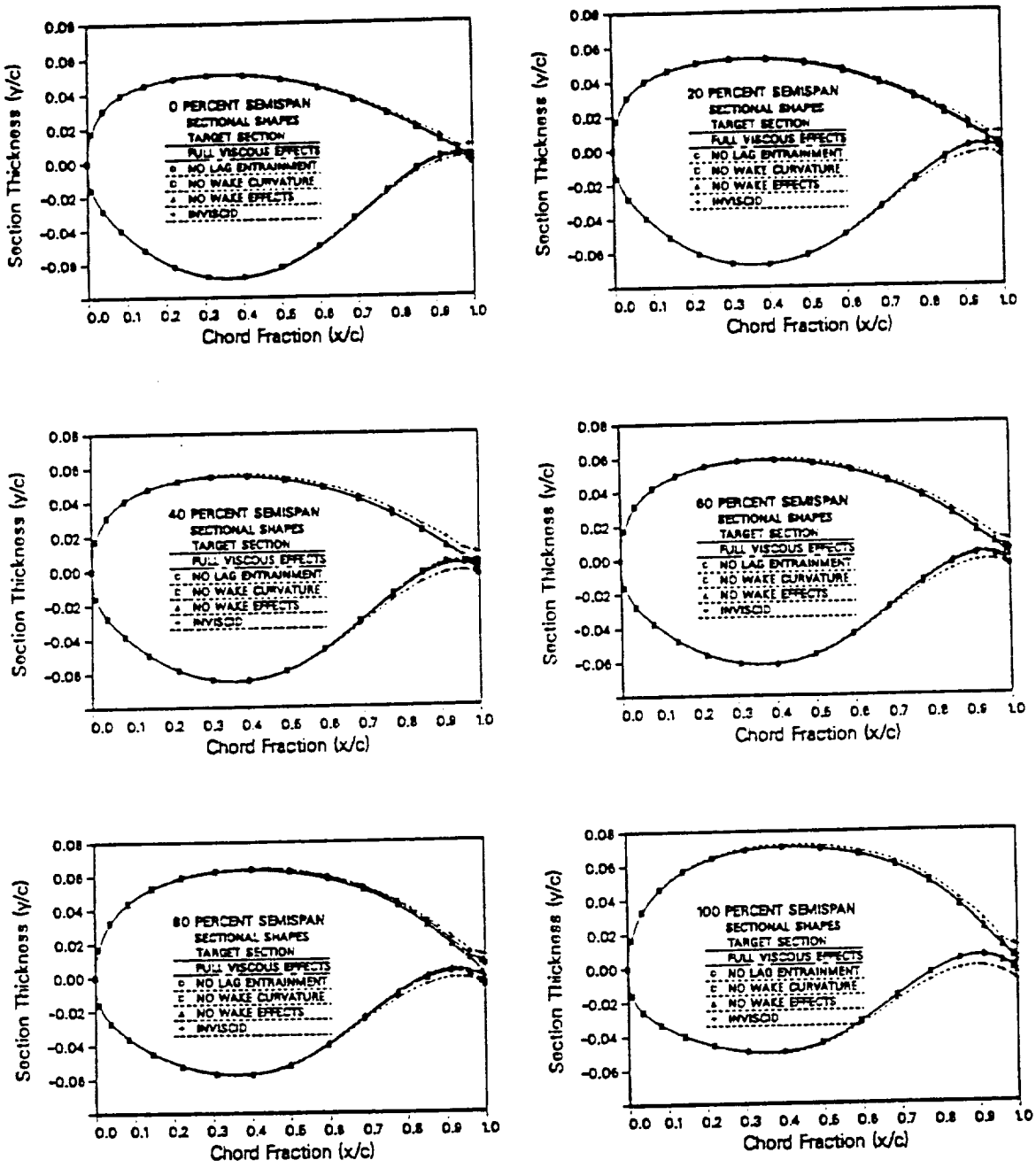

Fig. 31 Comparison of the unrelofted sectional shapes designed using different viscous interaction assumptions with a pressure distribution obtained from a fully viscous analysis of Lockheed Wing-A at a $Re = 24 \times 10^6, M = .8$, and an $\alpha = 2^o$

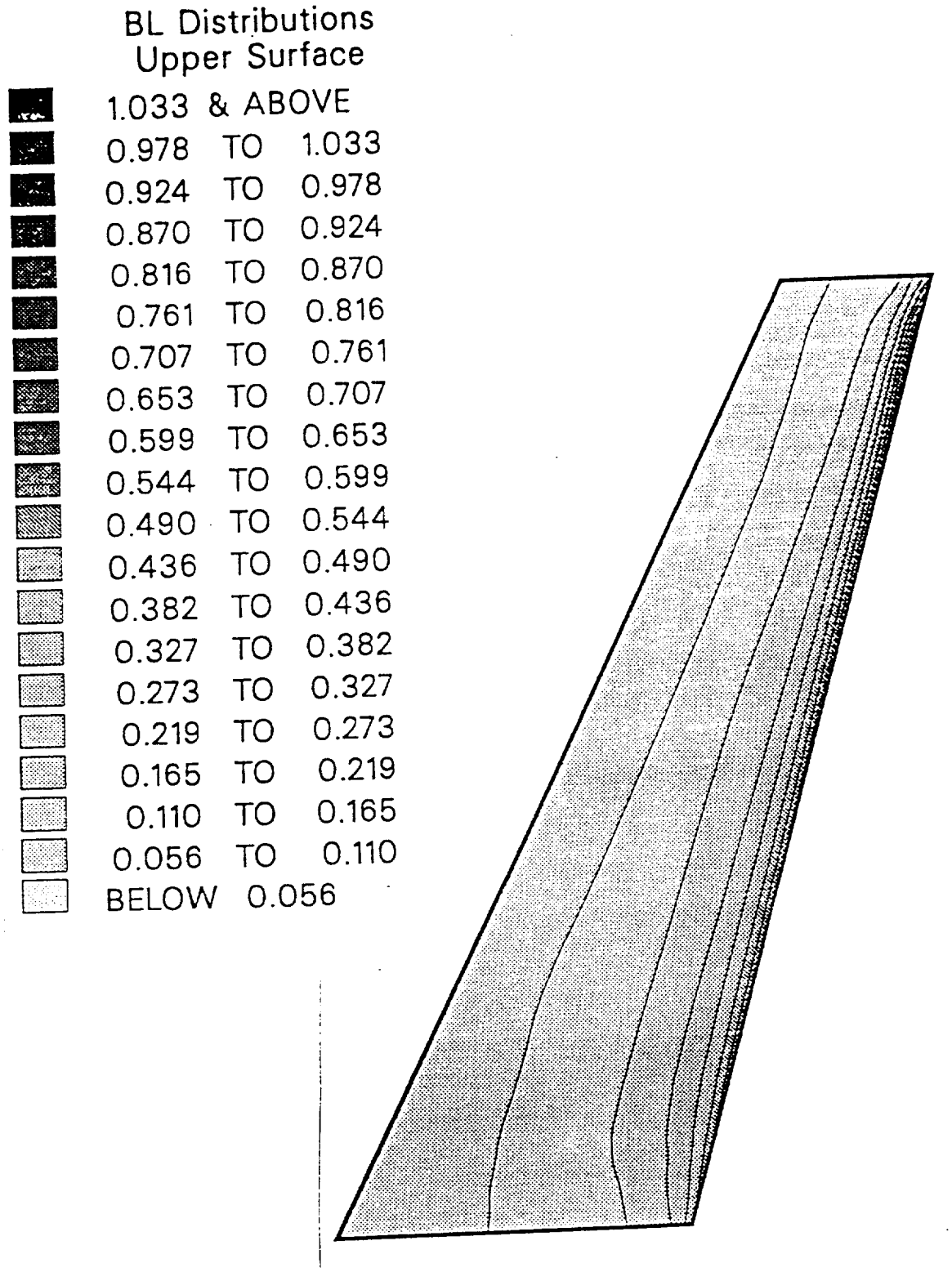

Fig. 32 Distribution of normalized boundary layer displacement thicknesses on the upper and lower surfaces of Wing-A

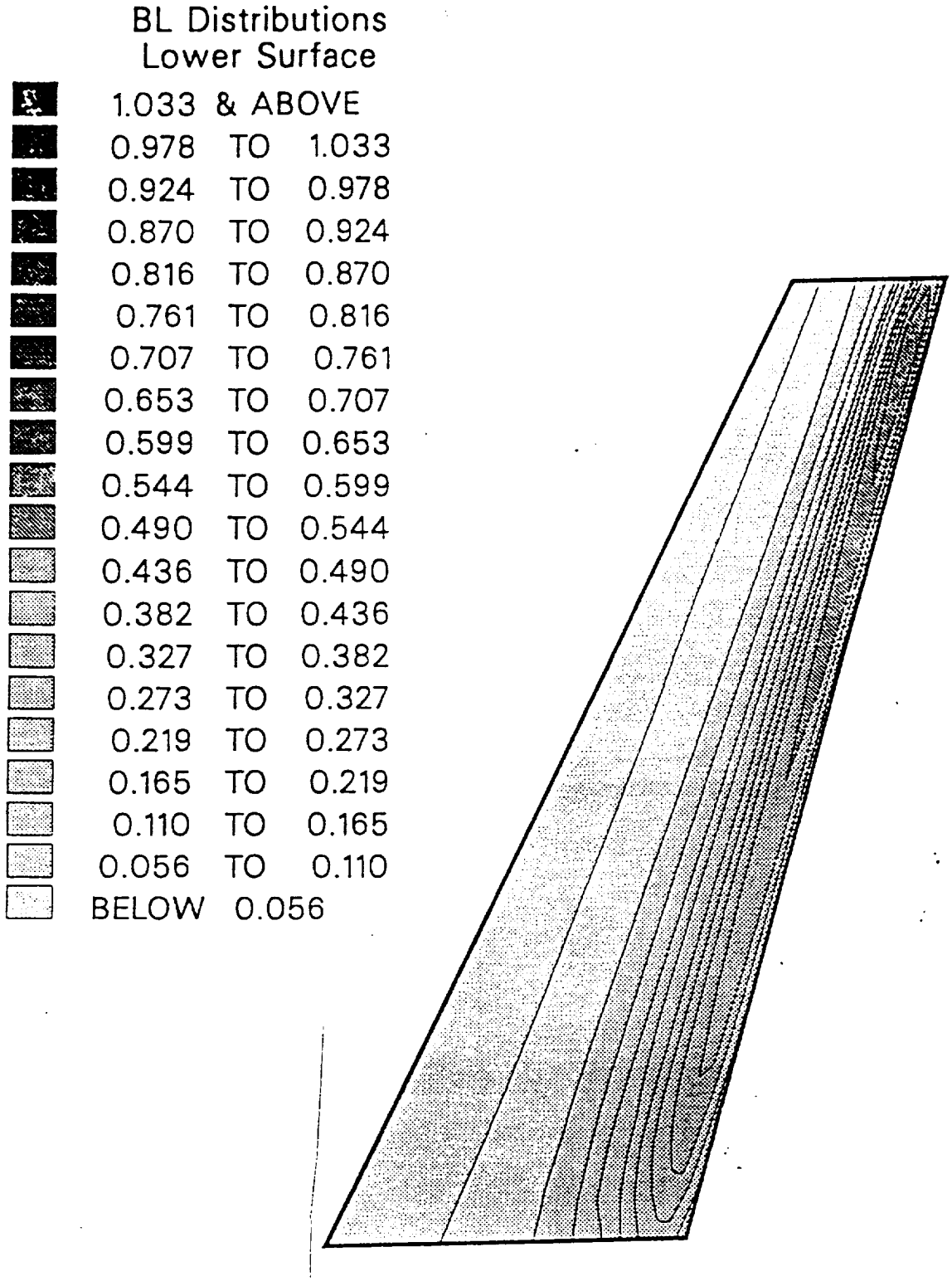

Fig. 32 Continued

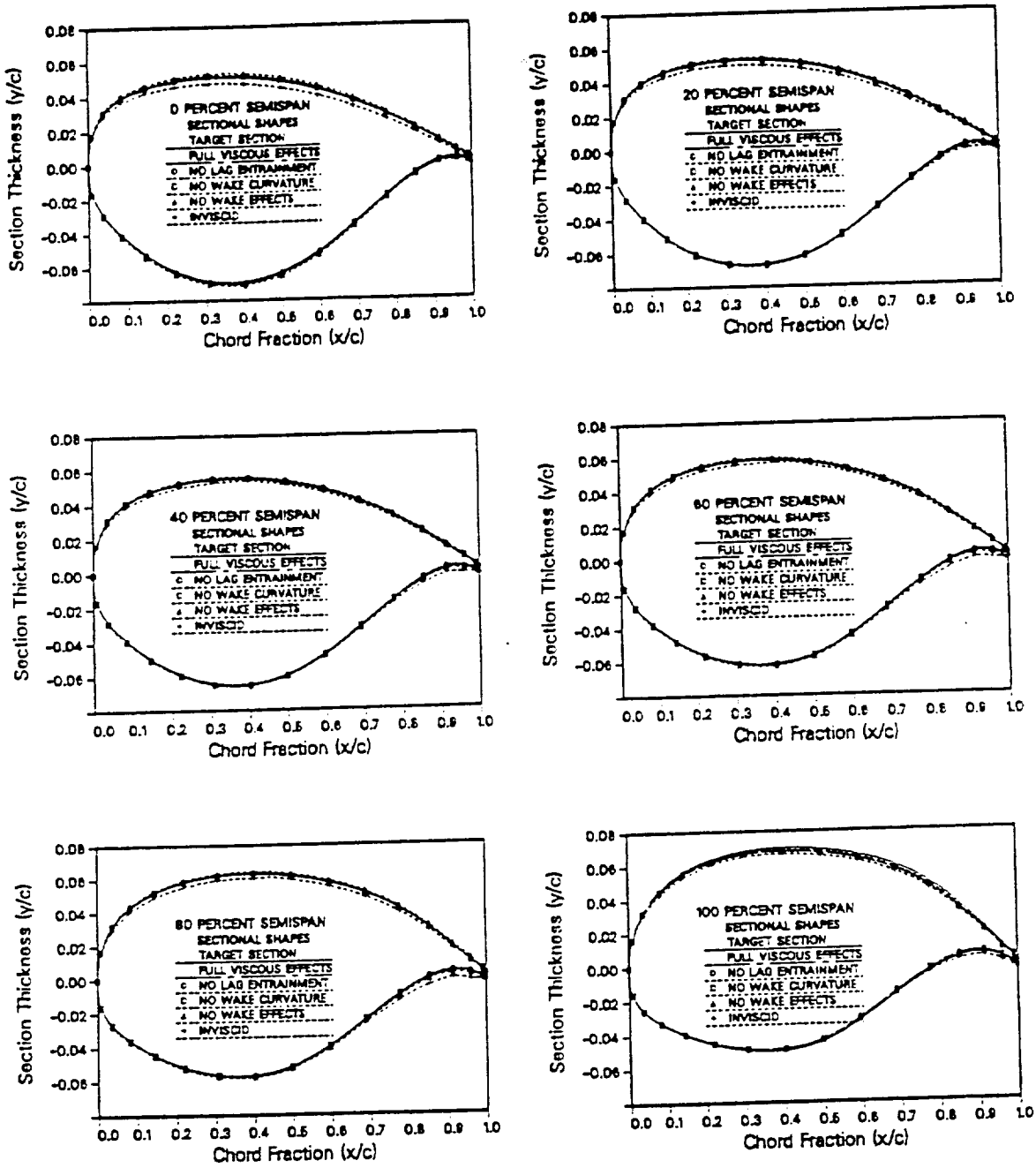

Fig. 33 Comparison of the relofted sectional shapes designed using different viscous interaction assumptions with a pressure distribution obtained from a fully viscous analysis of Lockheed Wing-A at a Re = 24x10^6, M = .8, and an $\alpha = 2^\circ$

Table 1. Results from the analysis of the wings designed with different viscous interaction assumptions at a M = .8 and a Re = 24×10^6

Case	Wing C_L	Wing +Fuselage C_L	C_D
Target	.4745	.5347	.0197
Full Viscous	.4636	.5226	.0195
No Lag Entrainment	.4719	.5316	.0197
No Wake Curvature	.4636	.5226	.0195
No Wake Effects	.4605	.5194	.0193
Inviscid	.4060	.4598	.0169

The resulting wing for each case was analyzed using full viscous effects and the same iteration history. Table 1 gives a comparison of the lift and drag coefficients resulting from the analyses of these designed wings.

As can be seen from the pressure distributions shown in Fig. 34 and Table 1, the inviscidly designed wing produced 15% less lift than did the target wing. The lift usually obtained in the cove region was diminished, in this case, by the decambering of the aft portion of the wing. The thinning of the top in conjunction with the thickening of the bottom of the inviscidly designed airfoils also caused a decambering of each section, which explains the large decrement in lift produced. As shown in Fig. 35, the reason the top was thinner is because the boundary layer displacement thicknesses which are 'built' into the imposed pressure distribution were not subtracted from the inverse displacements in the inviscid design. In order to meet the trailing edge

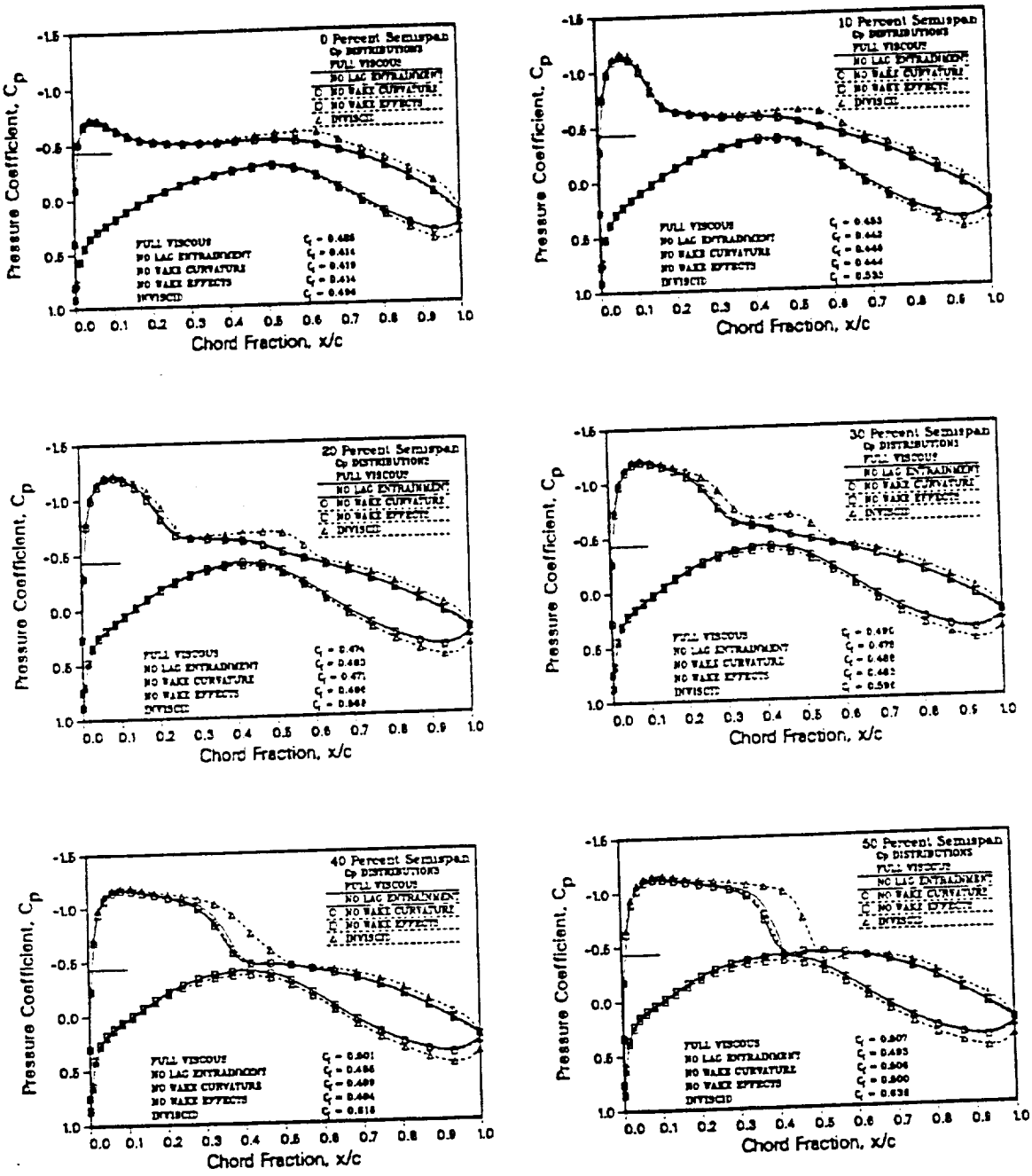

Fig. 34 Comparison of pressure distributions obtained from a viscous analysis of the Lockheed Wing-A using three different viscous interaction assumptions with a M = .8, $\alpha = 2°$, Re = $24x10^6$

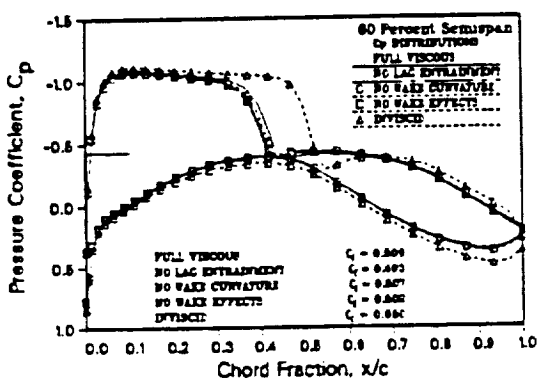

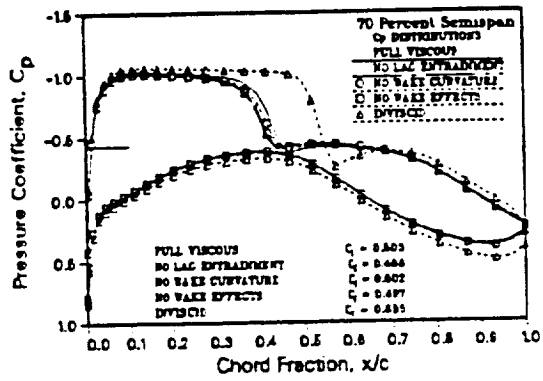

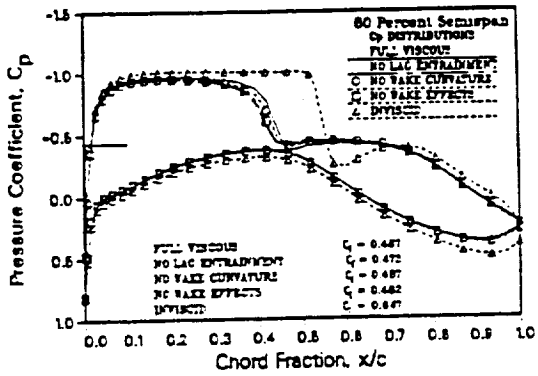

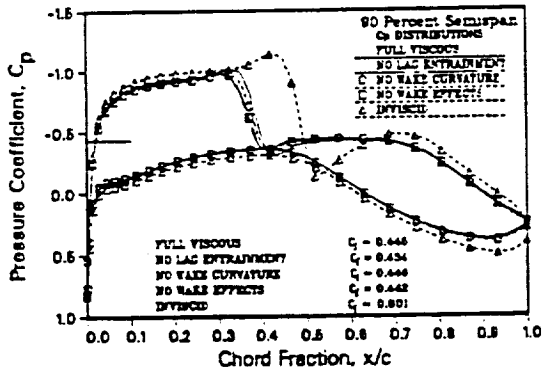

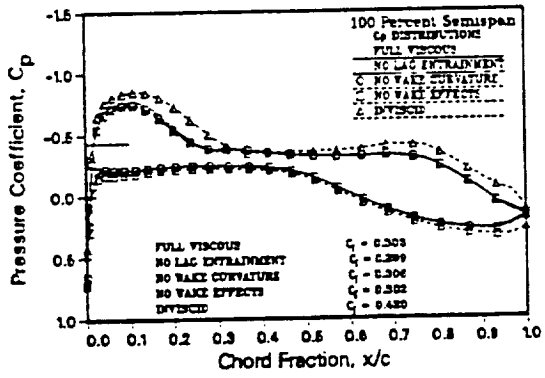

Fig. 34 Continued

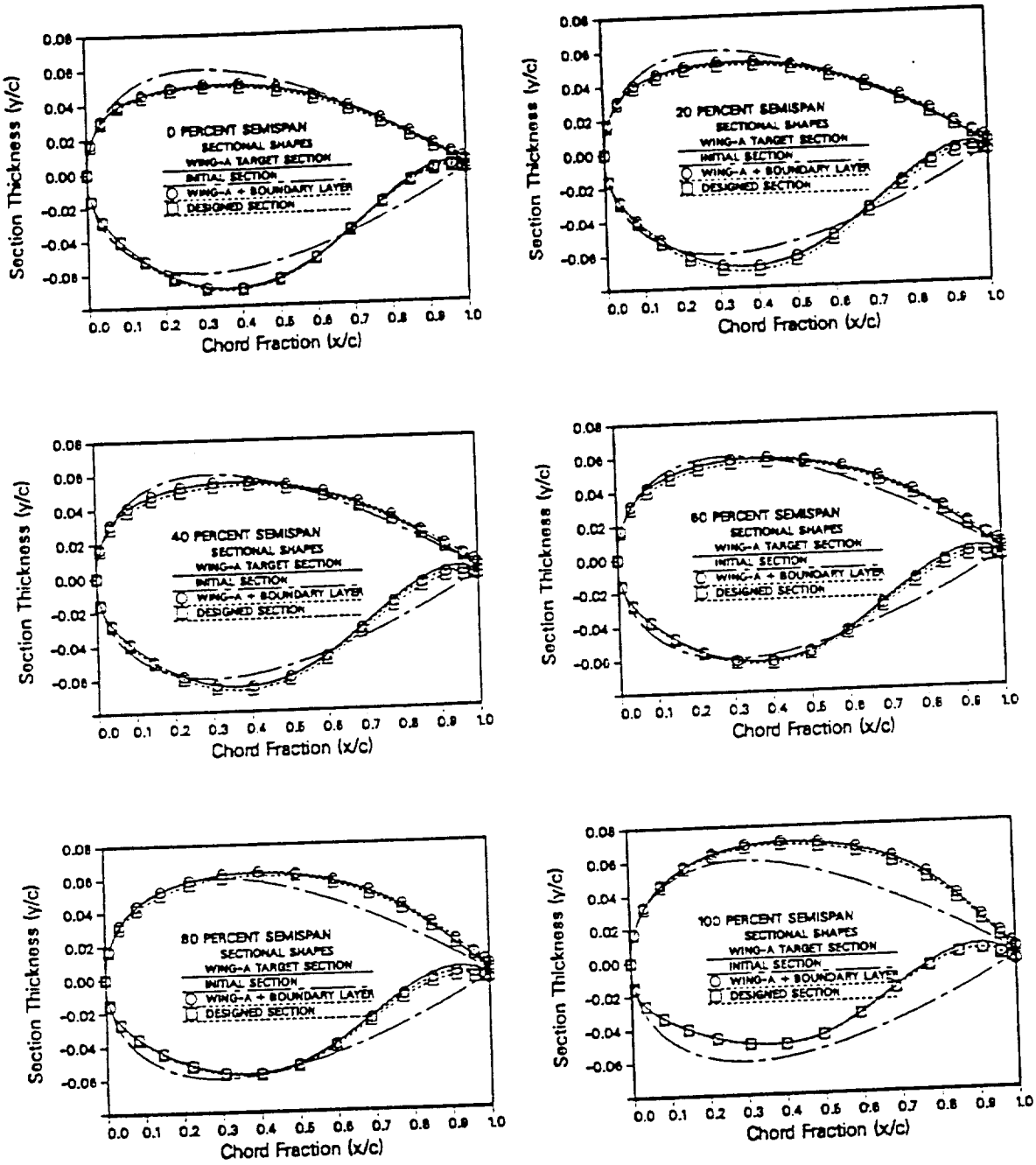

Fig. 35 Comparison of an inviscidly designed section using viscous pressures with the target and the target plus the associated boundary layer displacement thicknesses

ordinate requirement, the resulting section had to be relofted more to compensate, thus leading to a thinner section on top.

The wing lift coefficients obtained from the analyses indicate that by not using lag entrainment, a design correlating closely with the target can be better accomplished for the given sequence and number of flowfield iterations. It is suspected displacements and hence the inverse displacements may take longer to converge to the correct value as compared to excluding lag entrainment. By ignoring wake curvature and using all the other available viscous options, wings with identically slightly lower lift coefficients as compared to the targets were produced. Furthermore, wake thickness influenced the design in a slightly more profound way than did wake curvature by producing a wing with 3% less lift than the target.

As an after thought, the original wing was analyzed with each viscous option to assess its effect. The analysis results of the designed wings, shown in Fig. 36, reveal that wake curvature effects were practically negligible. This result may be due to the relatively high freestream Reynolds number of 25 million used in the comparisons. Since this Re would lead to low values of δ^* and θ, the curvature effects would also be expected to be low; Streett's case[20] used a much lower Reynolds number of 6 million. On the other hand, neglecting wake thickness and lag entrainment effects both had a decremental effect on the wing's lift, which was probably due to the forward shifting of the shock location.

The second set of design cases involved a partial wing design which extended from 30-70% semispan and began 10% aft of the leading edge of the airfoil, but the

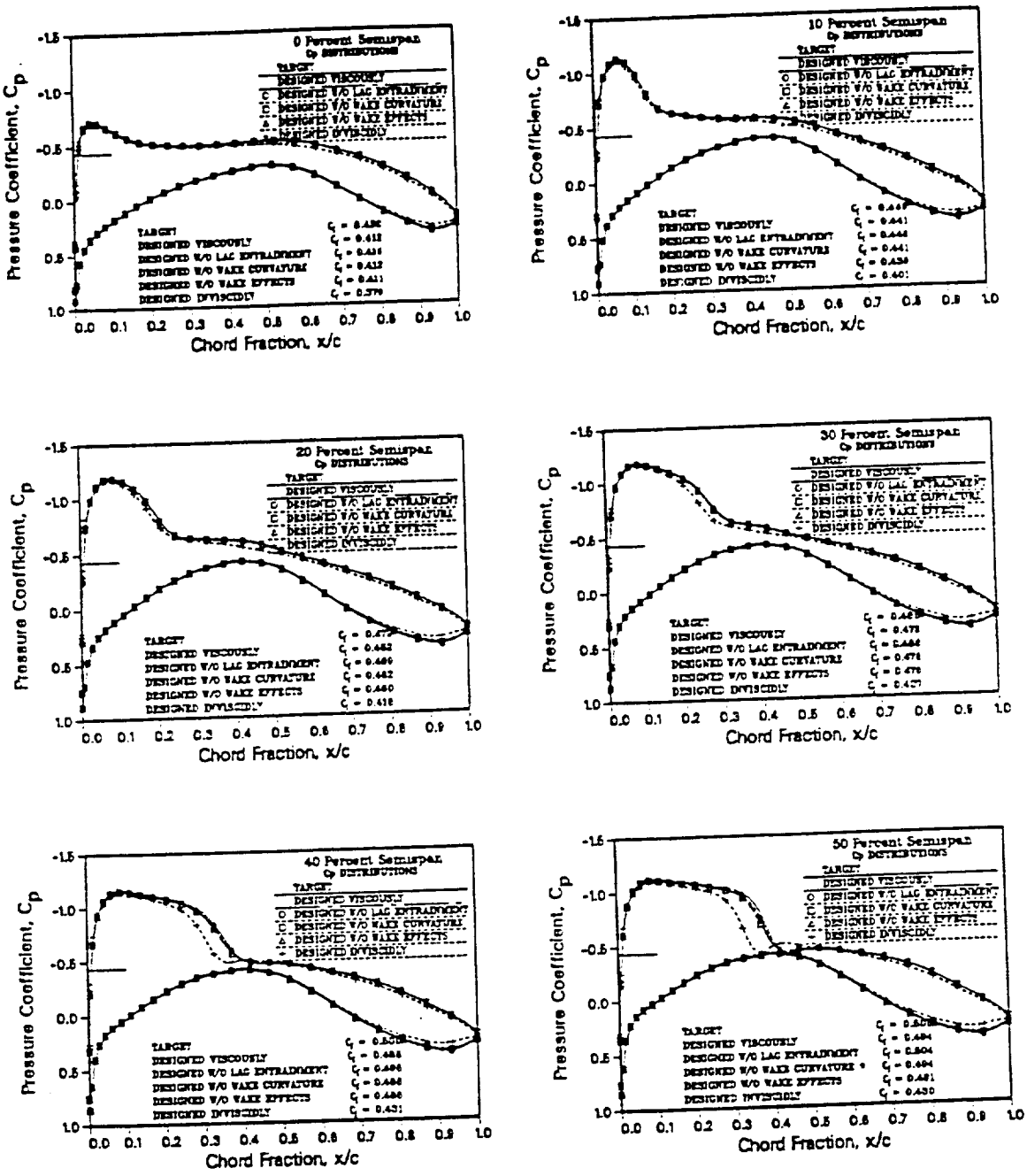

Fig. 36 Comparison of pressure distributions obtained by fully viscous analyses of the wings designed using different viscous interaction assumptions for a M = .8, $\alpha = 2°$, Re = $24x10^6$

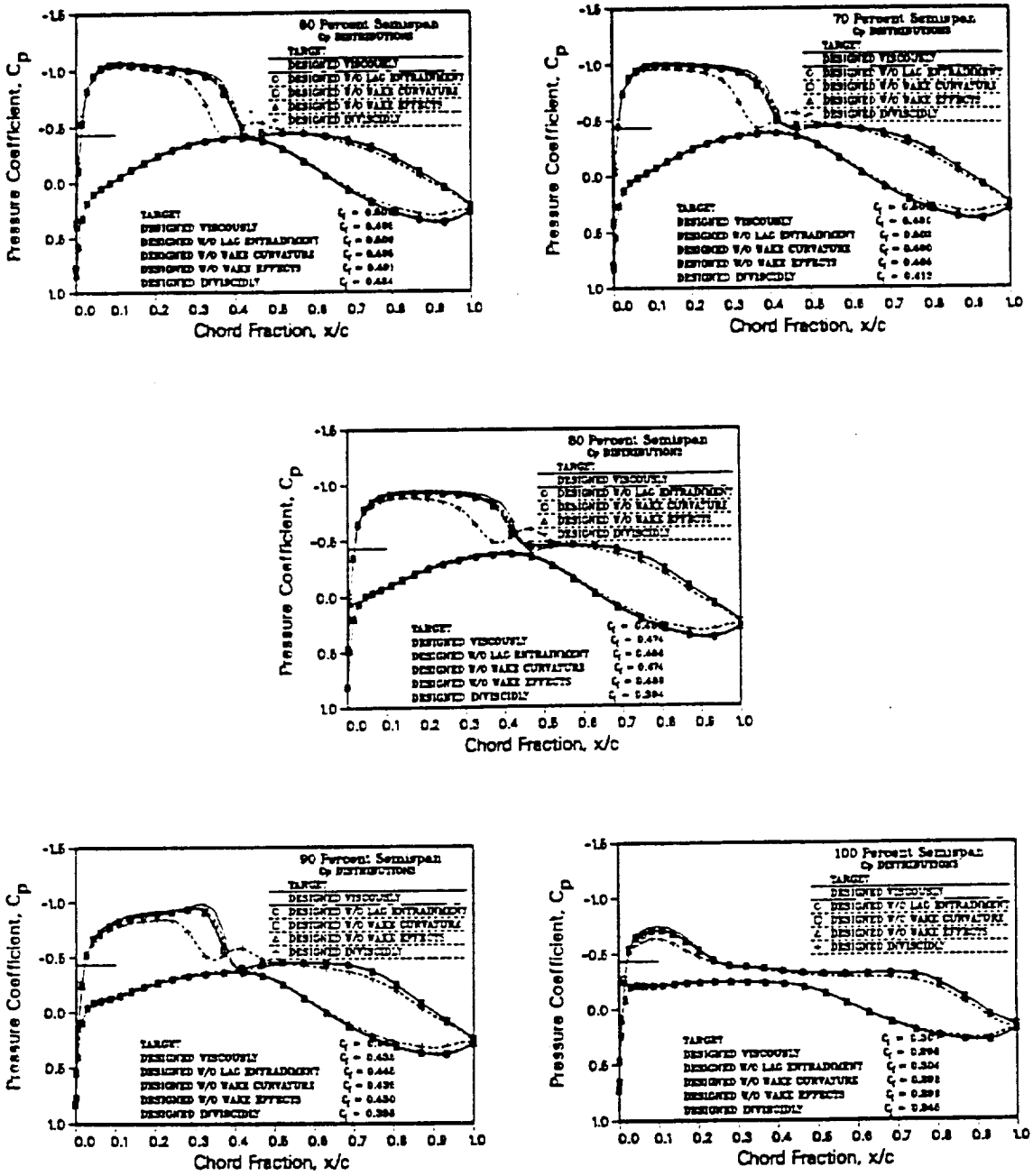

Fig. 36 Continued

inverse boundary condition was only enforced at the 30, 50 and 70% semispan station and the displacements were linearly interpolated to the stations in between. The initial airfoil section at 50% semispan was formed by thinning the supercritical target section by 6% and removing the cove region. The initial sections at the edges of the design region were the same as the target sections, while the remaining sections were obtained through linear interpolation. The results for these cases are presented in Fig. 37. For the Reynold's number chosen, neglecting wake effects seems to have had a small effect on the resulting design. The sections are a little thicker than the sections designed with full viscous effects. As noted earlier, the wake effects had relatively little effect on the pressure distributions obtained from the analysis of the target wing; but, when the boundary layer displacement thicknesses obtained were investigated, it was discovered that neglecting wake effects in the analysis produced boundary layer displacement thicknesses that were on the average 3.5% thicker at the trailing edge than those obtained from a full viscous analysis. Since the boundary layer displacement thicknesses are subtracted from the initial inverse changes to yield the hard airfoil, these larger displacement thicknesses would produce a section that was initially thinner than the target; but, after relofting the airfoil section, it would actually be thicker than the target.

The wing sections designed inviscidly are profoundly different at 30 and 70% semispan, but only slightly different at 50% semispan. The thinning of the top surface in complement with the thickening of the lower surface significantly decambered these sections. The large differences at the inboard and outboard design stations are due to

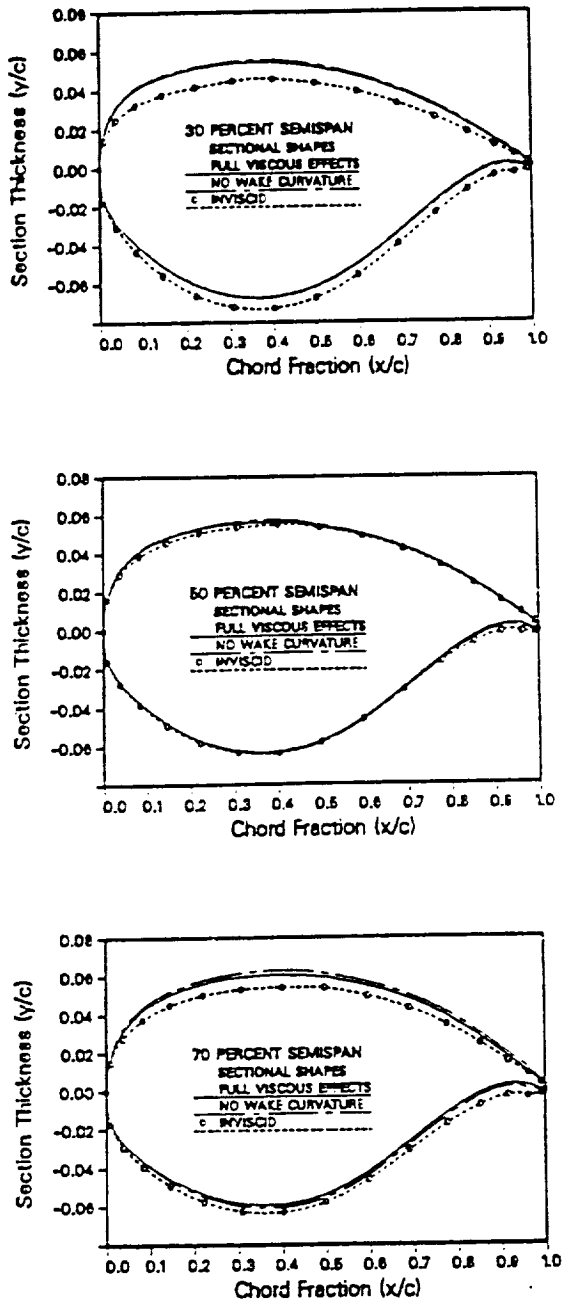

Fig. 37 Comparison of the relofted sectional shapes designed using different viscous interaction assumptions with a pressure distribution obtained from a fully viscous analysis of Lockheed Wing-A at a Re = 24×10^6, M = .8, and an $\alpha = 2^o$. The design region extended from 30%-70% semispan.

the influence of the inviscid pressures outside the design region; and, the remarkable agreement in the middle of the design region, except in the cove region where the boundary layer is thick, is due to the influence of the viscous boundary condition at the edges of the design region. This observation can be verified by reviewing the previous case and noticing that the airfoils sections varied smoothly in the spanwise direction at all spanwise stations.

After the wings were designed, all three were then analyzed with full viscous effects to assess the significance of the changes made to the wing on the pressure distributions and to see how well these pressures matched the target pressures. Knowing that the wing designed with full viscous effects is correct, it is quite obvious from Fig. 38 and Table 2 that the wing designed inviscidly is quite unsatisfactory. The shock is not far enough aft and the lift produced is sometimes 20% smaller than that desired.

Based on the results of this study, it can be concluded that for the Reynold's number and Mach number chosen, wake curvature and wake thickness and lag entrainment have a very small effect on the designed airfoil sections. However, the boundary layer displacement effect has a profound effect on the section shapes and hence must be included in the design process to yield a wing which will produce the desired lift in a viscous environment.

V.2 Spanwise Grid Skewness

In the course of the present research, it was discovered that the skewness of the constant ξ grid lines leaving the tip of the wing (Fig. 39) can have a dramatic effect on

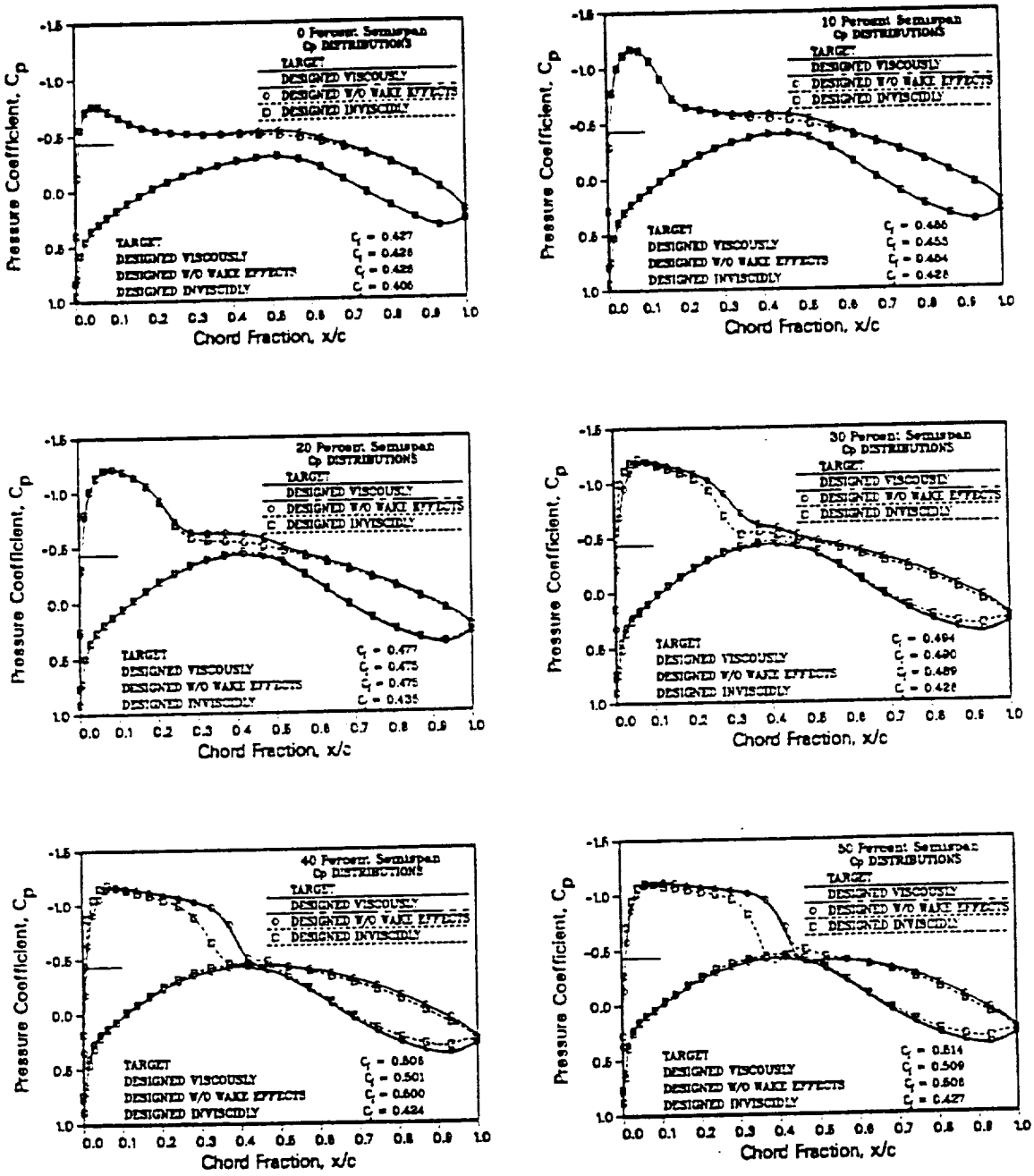

Fig. 38 Comparison of pressure distributions obtained from a viscous analysis of the Lockheed Wing-A using three different viscous interaction assumptions with a M = .8, $\alpha = 2°$, Re = 24×10^6

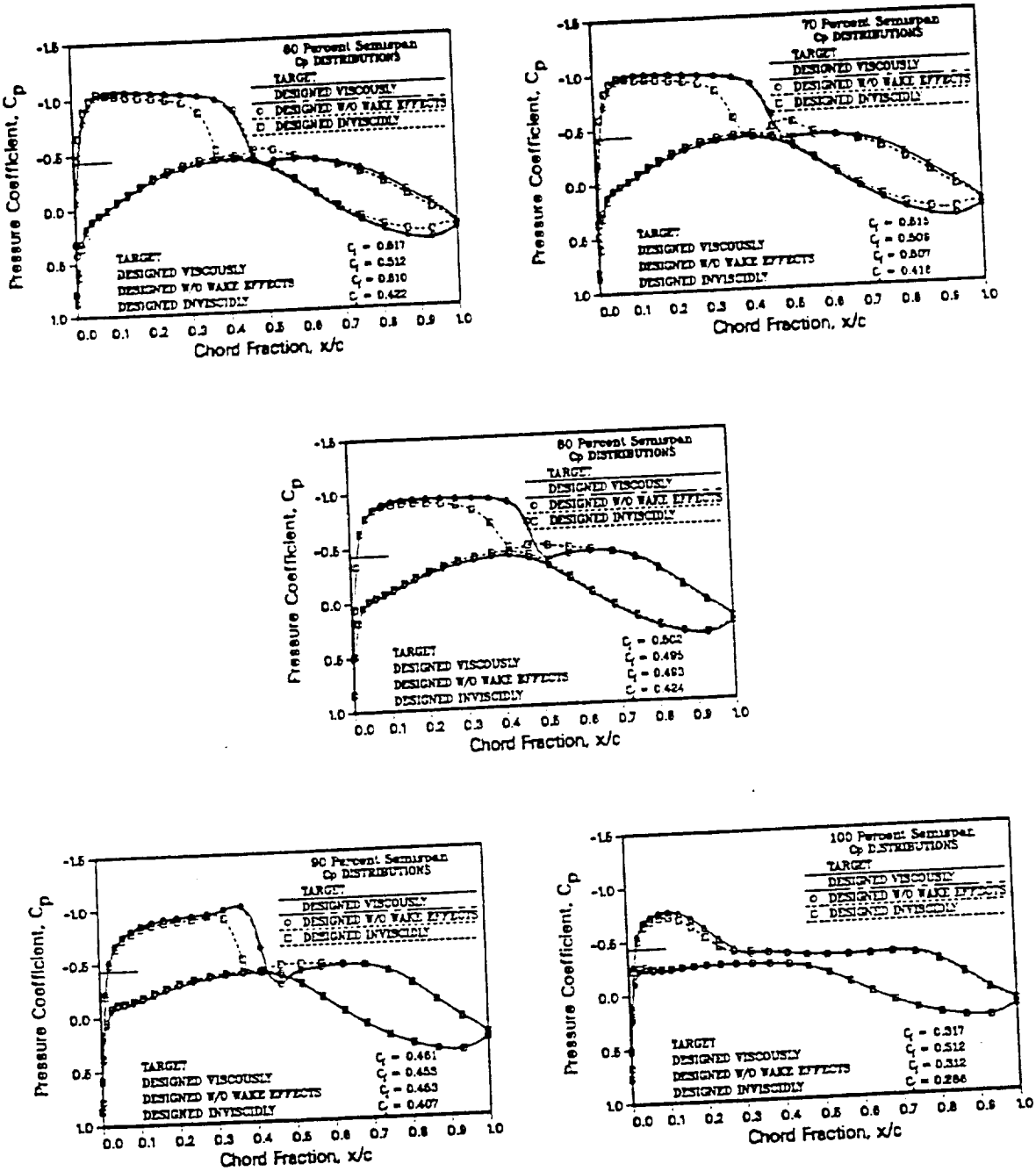

Fig. 38 Continued

Table 2. Comparison of the total and wing lift coefficient obtained from a fully viscous analysis of the wings designed using different viscous interaction assumptions at a M = .8 and a Re = 24×10^6

Lift Coefficient	Target	Full Viscous	No Wake Design	Inviscid Design
C_L	.514	.509	.506	.427
Wing C_L	.483	.478	.477	.419

the design of the sections near the wing tip. As can be seen in Fig. 40, if the grid was significantly skewed and the input pressures were calculated on an nonskewed grid, it was impossible to obtain the correct airfoil shapes in the tip region. This difficulty is due to the large differences in pressures between the skewed and nonskewed grid. These pressure profile differences are shown in Fig. 41. As shown in the figure, the grid skewness has caused the shock location to move further aft. Although the skewness of the grid was quite extreme in this case, these results affirm the need for smoothly varying grids in wing design, at least in the spanwise direction. It should be noted though, that if the input pressures were obtained on a skewed grid and used in the design process with a skewed grid then the tip sections were well resolved. In summary then, if the pressures calculated on an nonskewed grid are correct or closer to real pressures encountered in flight, then it would be wise to ensure that the grid is smoothly varying.

V.3 Wing Planform Effects

Three cases were attempted to roughly delimit the applicable range of aspect ratios and leading edge sweep angles for which good results could be obtained with

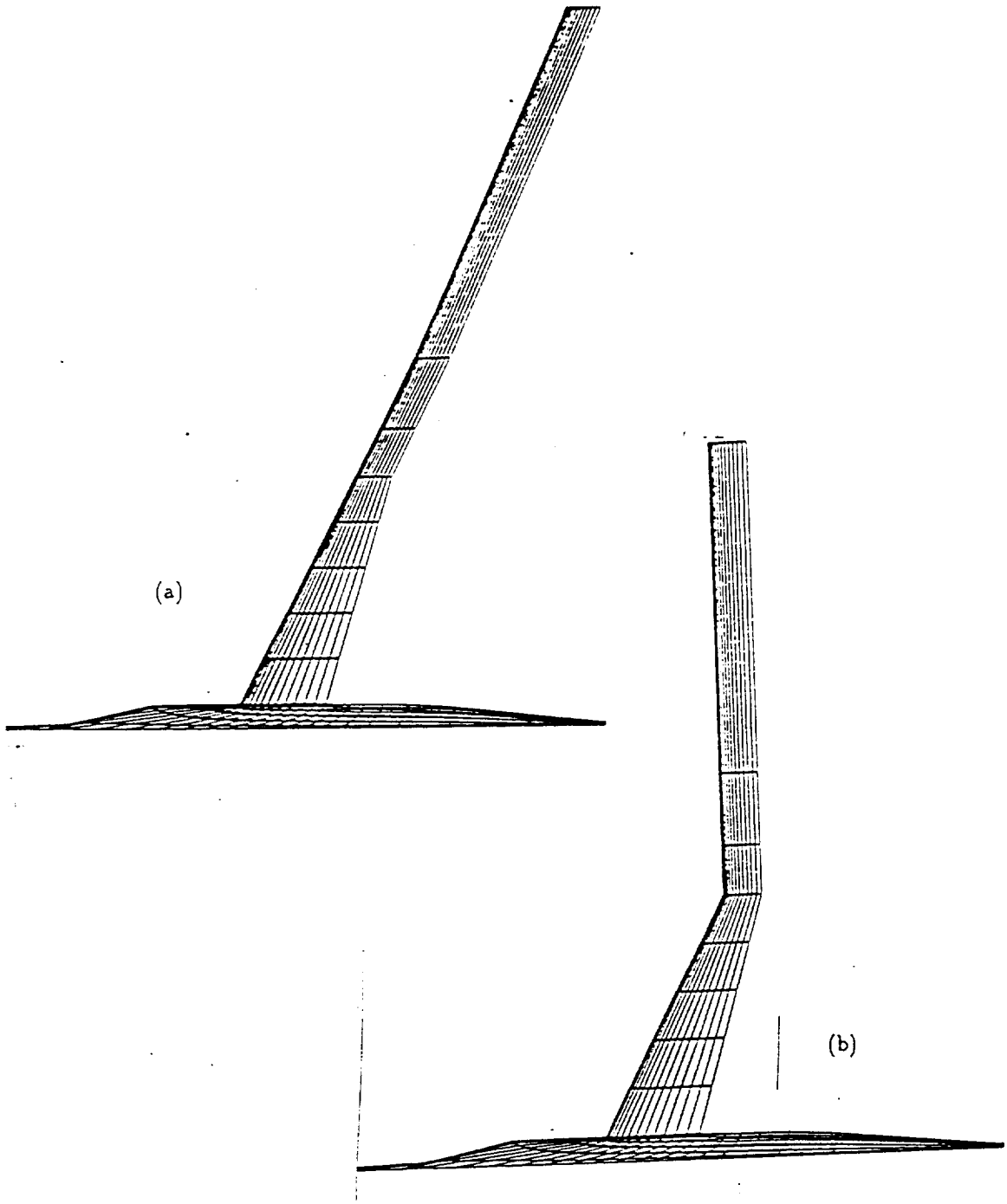

Fig. 39 Comparison between a fairly nonskewed (a) and skewed grid (b)

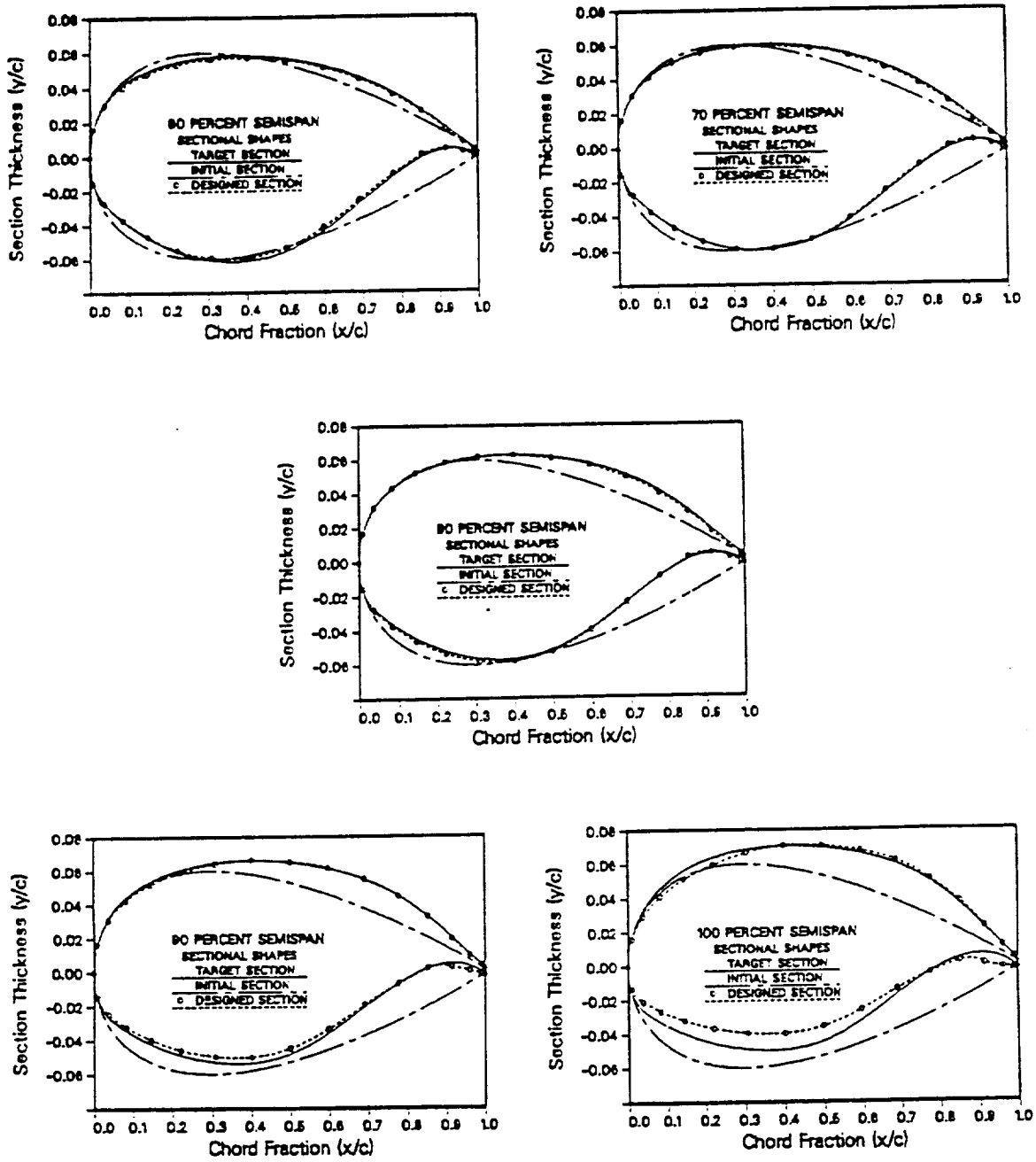

Fig. 40 Sections designed with a skewed grid using pressures obtained from an analysis on a nonskewed grid

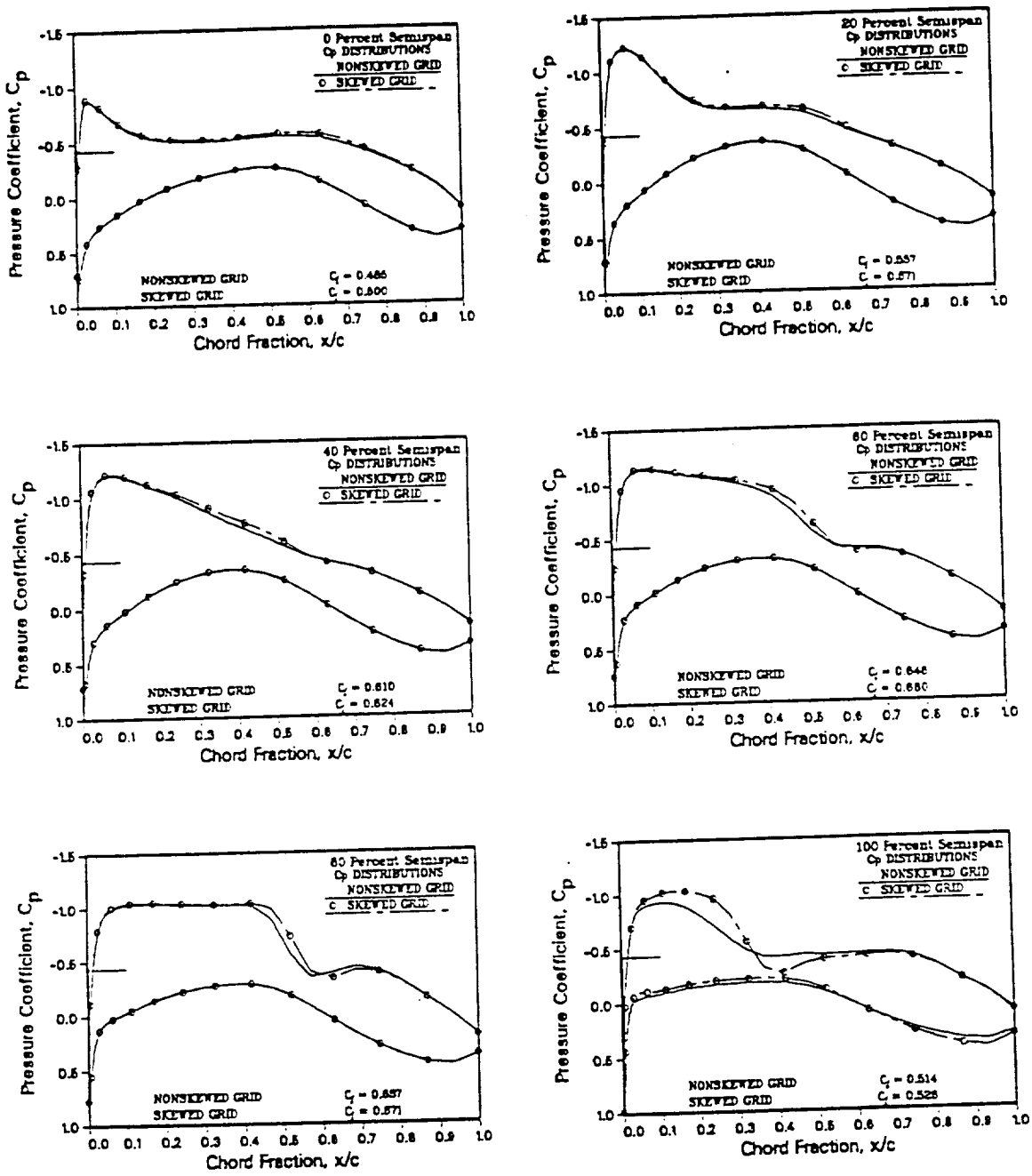

Fig. 41 Comparison of a pressure distribution obtained from an analysis of a skewed grid with one obtained from an analysis of a nonskewed grid

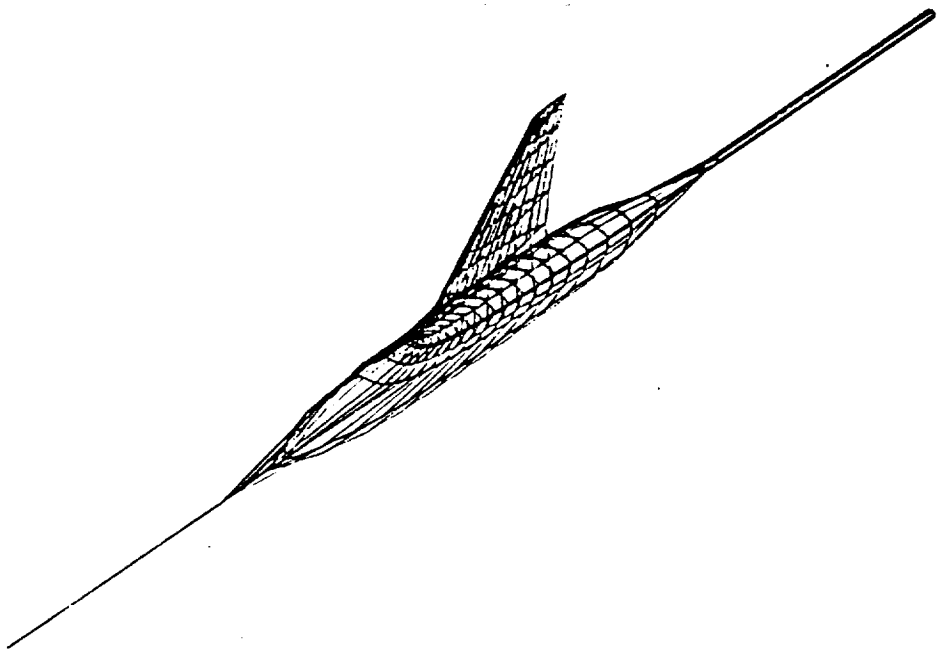

Fig. 42 Grid generated about Wing-C with an incompatible root section and fuselage cross section

the present design method. These included Lockheed Wings A, B and C. These wings have aspect ratios of 8, 3.8, and 2.6, leading edge sweep angles of 27, 35, and 45 degrees and taper ratios of .4, .4, and .3 respectively. The target pressure distributions were obtained by a direct analysis of the target wings in an inviscid environment. The initial section for Wing-A was a NACA 0012, while a NACA 0006 was used for Wing-B. The original section was used with Wing-C due to the difficulty of the case. Also for Wing-C, as opposed to the circular cross-section, an elliptical cross section of the fuselage was used to provide a flatter surface for the grid generation package. The circular cross-section combined with the large relative thickness of the root section compared with the width of the fuselage played havoc on the grid at the root, as can be seen in Fig. 42

In order to better understand the flow about each wing, the corresponding velocity vectors on the surface of each wing were plotted, as shown in Figs. 43–45. As should be expected, the spanwise component of the flow increases as the aspect ratio decreases and sweep increases. It is also interesting that there seems to be an inboard component of the flow for all three cases on the upper surfaces aft of the leading edge. This inboard flow may be attributed to the effect of the fuselage and the wing tip vortex. These effects can be seen most readily by viewing a cross section of the flow just aft of the wing tip shown in Fig. 46. The vortex near the tip of the wing is quite evident, and flow tangency at the fuselage also contributes to the spanwise component of the flow. The momentum of the air over the tip must dominate the flow, since, as seen in Figs. 47–49,the spanwise pressure gradients appear to encourage the air to move outboard. However, in order to determine whether the flow actually traveled in the inboard direction, it would be necessary to plot the actual streamlines of the flow over the surface of the wing.

The design region for Wing-A and Wing-B extended from 10-100% semispan and began 5% and 2.5% aft of the leading edge, respectively. Computations were performed on a fine grid. Results for Wing-A are shown in Fig. 50, while results for Wing-B are shown in Fig. 51. As can be seen the designed and target sections for both wings are in excellent agreement in the interior of the design region and closely match at the edges of the design region.

In the case of Wing-C, the section shapes should not have changed with the application of the inverse boundary condition. But, because of the large amount

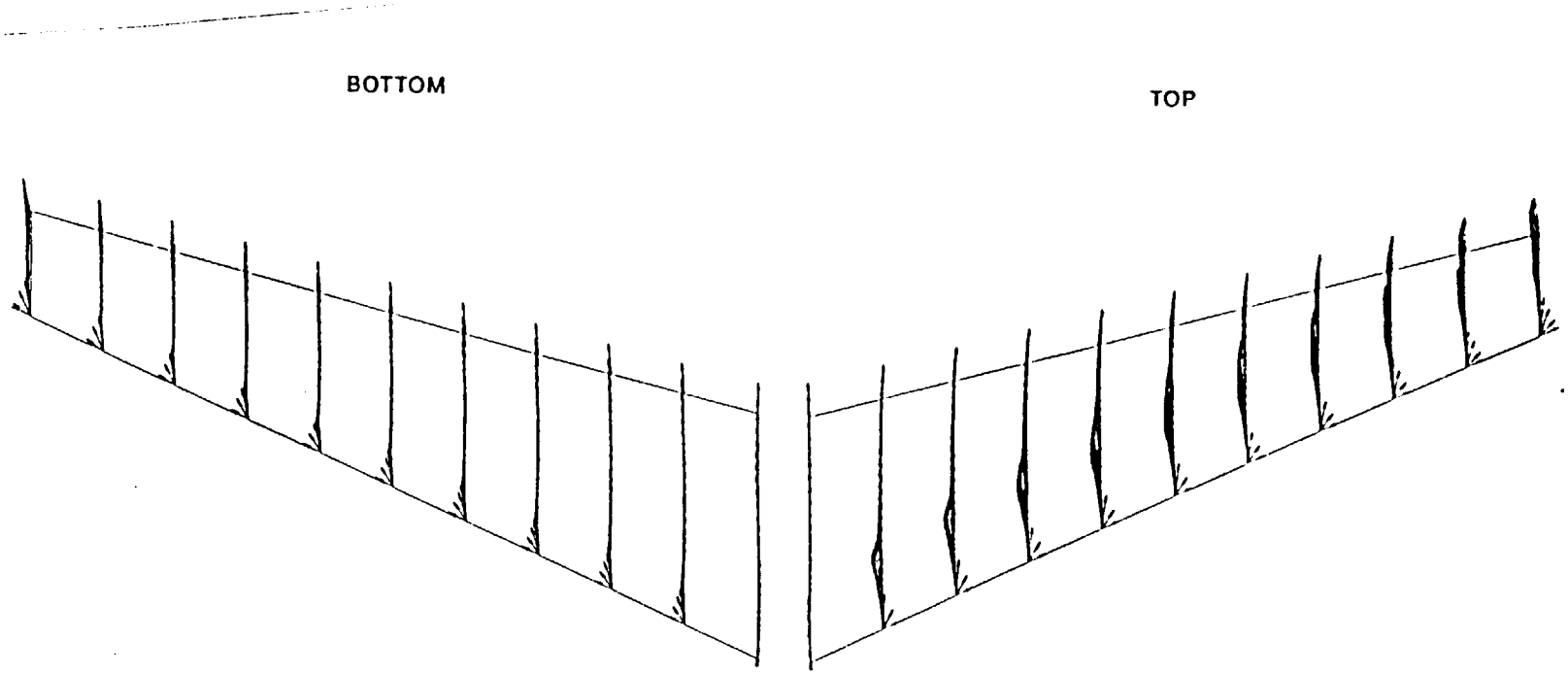

Fig. 43 Surface velocity vectors for Lockheed Wing-A on the upper and lower surface

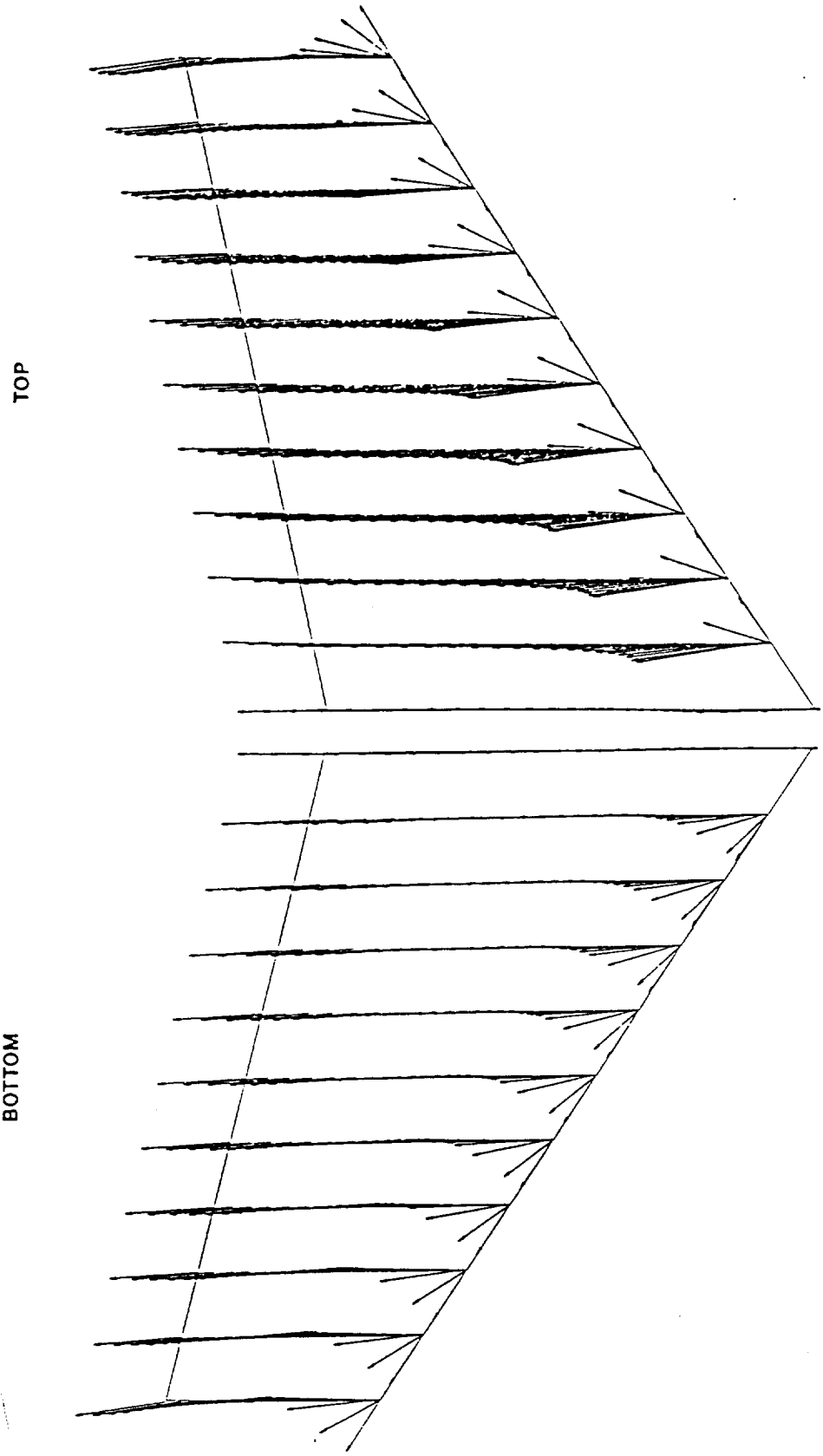

Fig. 44 Surface velocity vectors for Lockheed Wing-B on the upper and lower surface

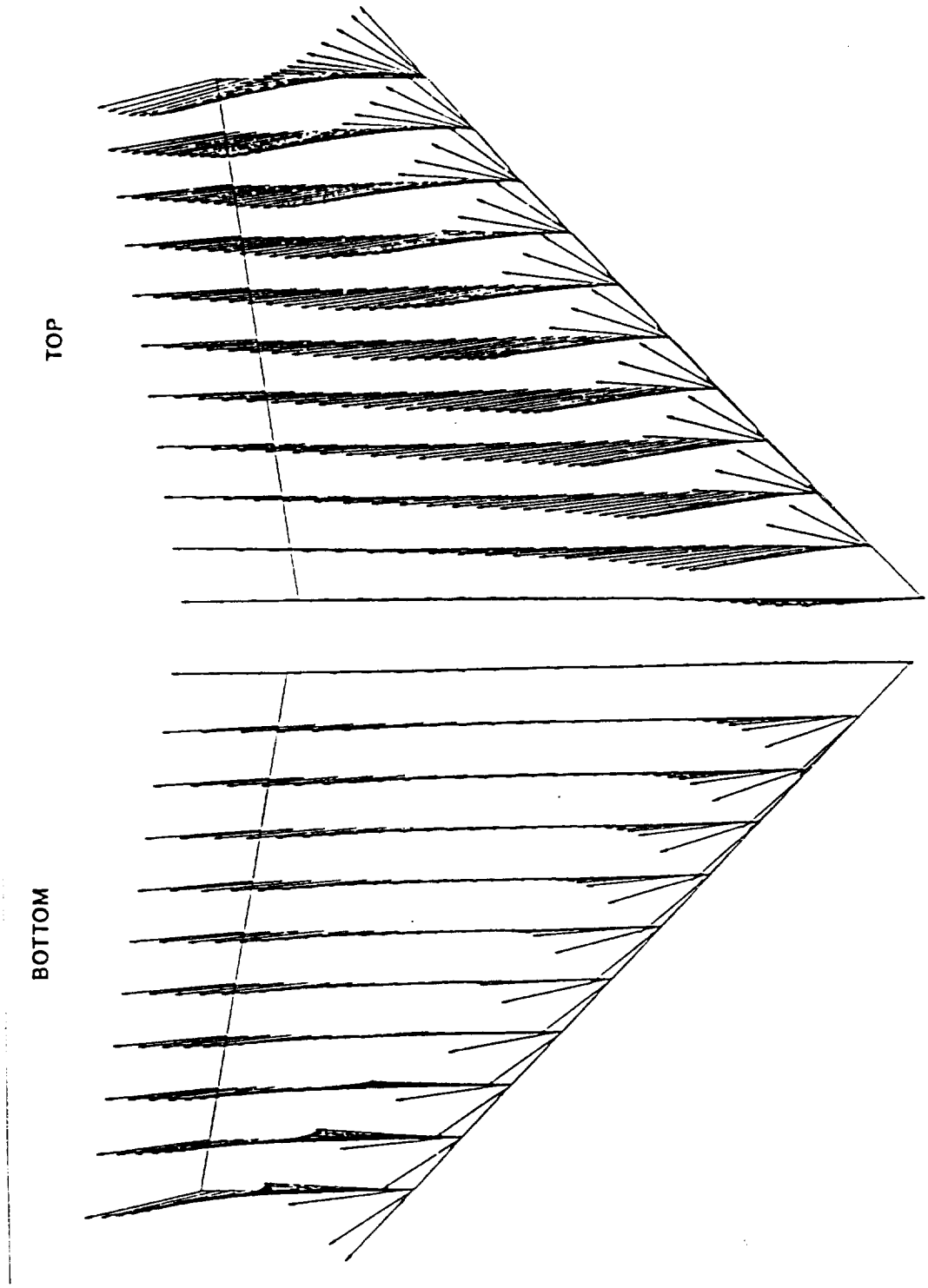

Fig. 45 Surface velocity vectors for Lockheed Wing-C on the upper and lower surface

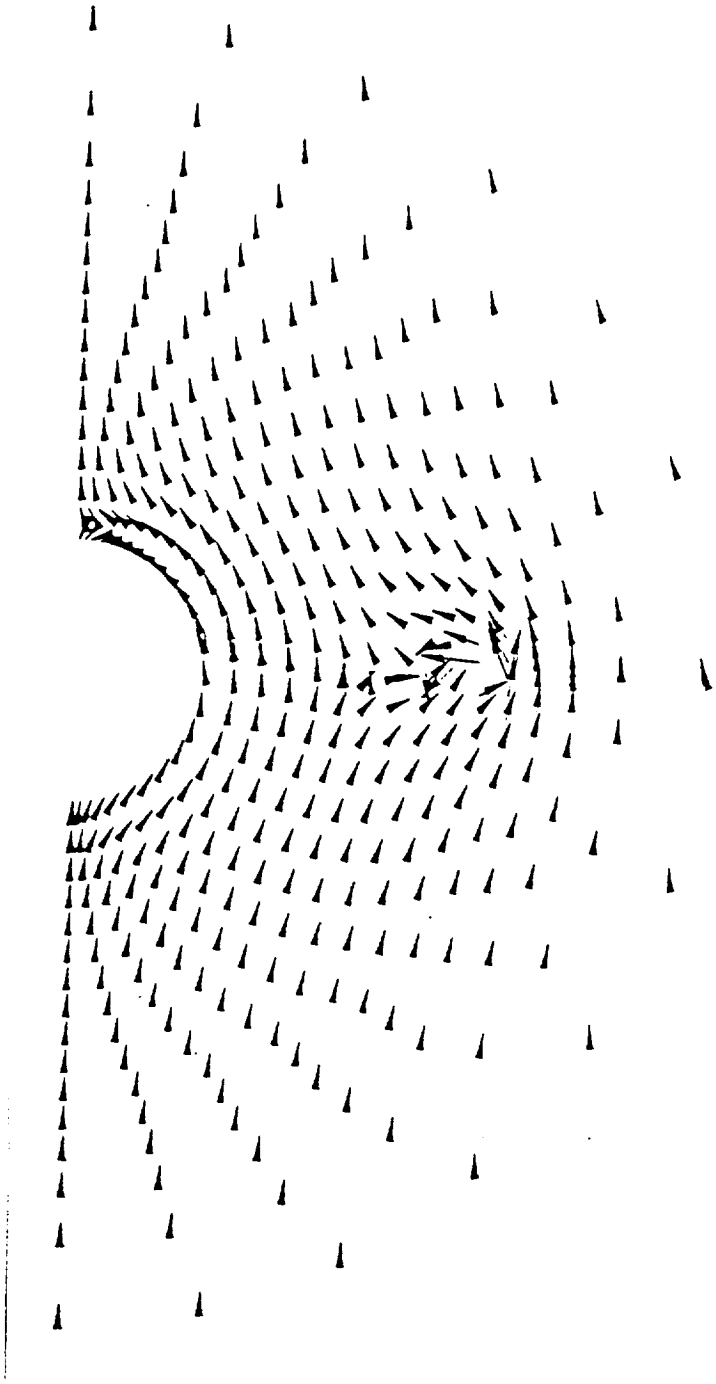

Fig. 46 Cross-section of the flow in the x-y plane for Lockheed Wing-C

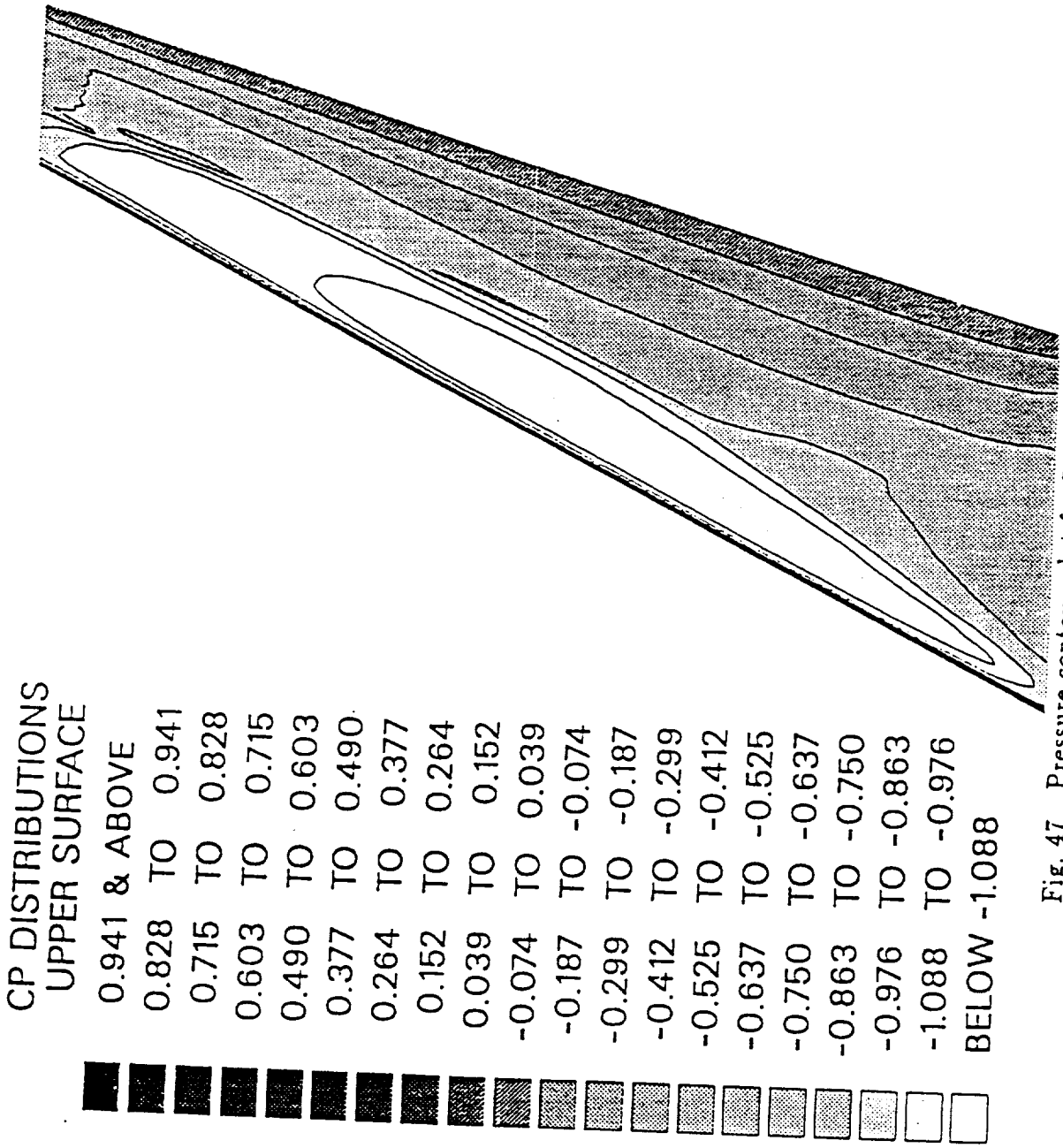

Fig. 47 Pressure contour plot for Lockheed Wing-A M = .8, $\alpha = 2°$

This page is blank

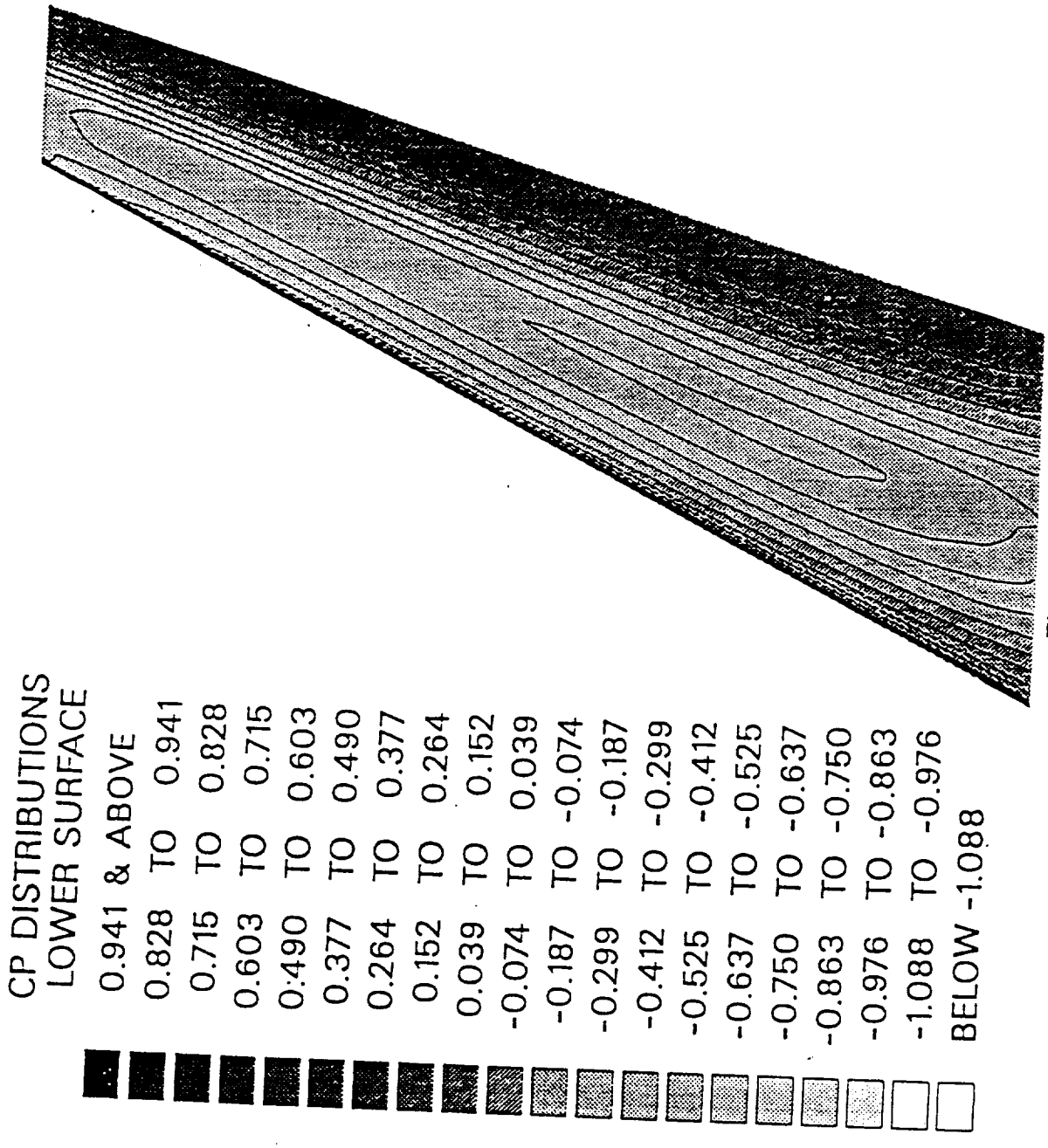

Fig. 47 Continued

This page is blank

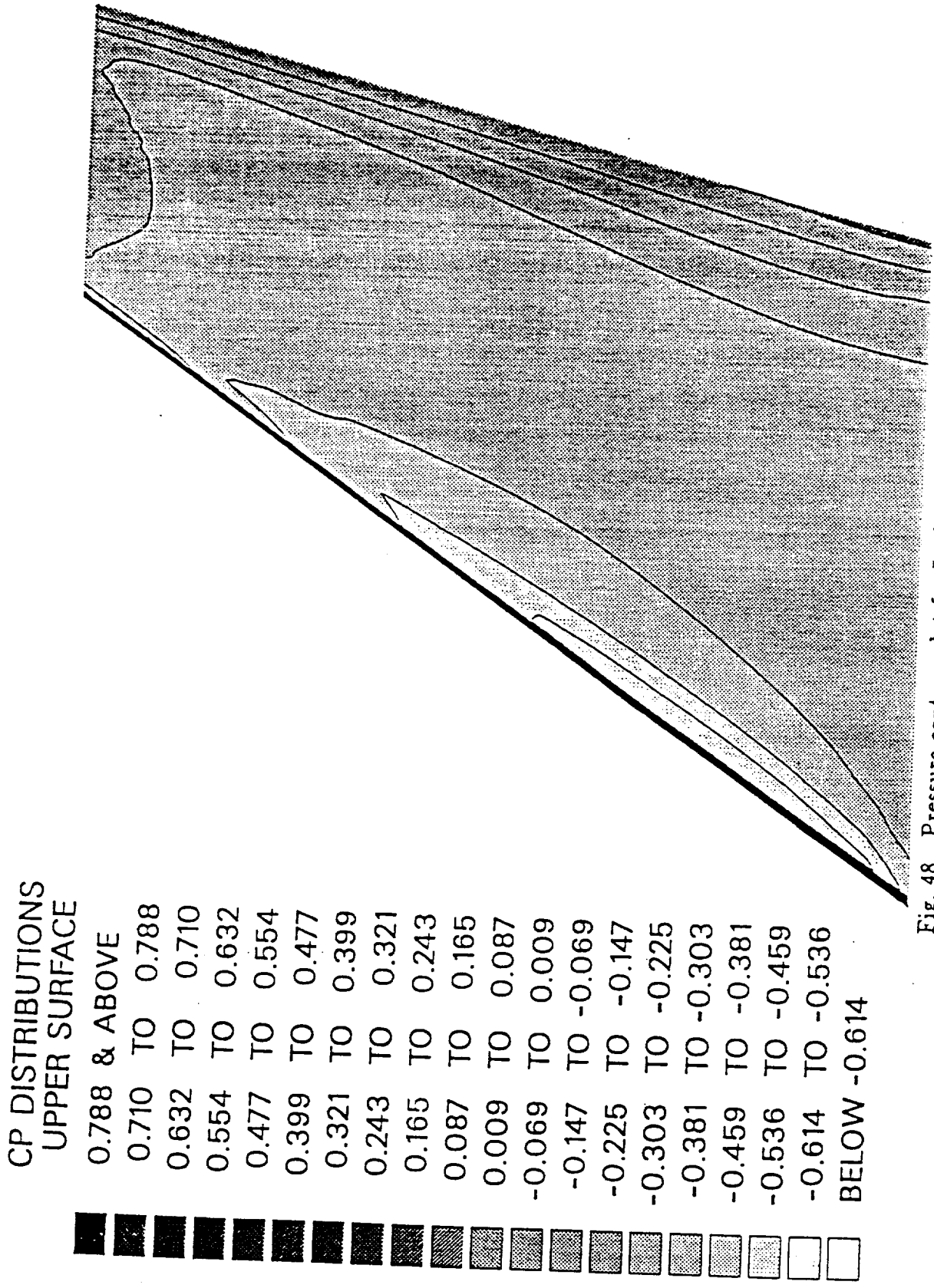

Fig. 48 Pressure contour plot for Lockheed Wing-B M = .8, $\alpha = 2°$

This page is blank

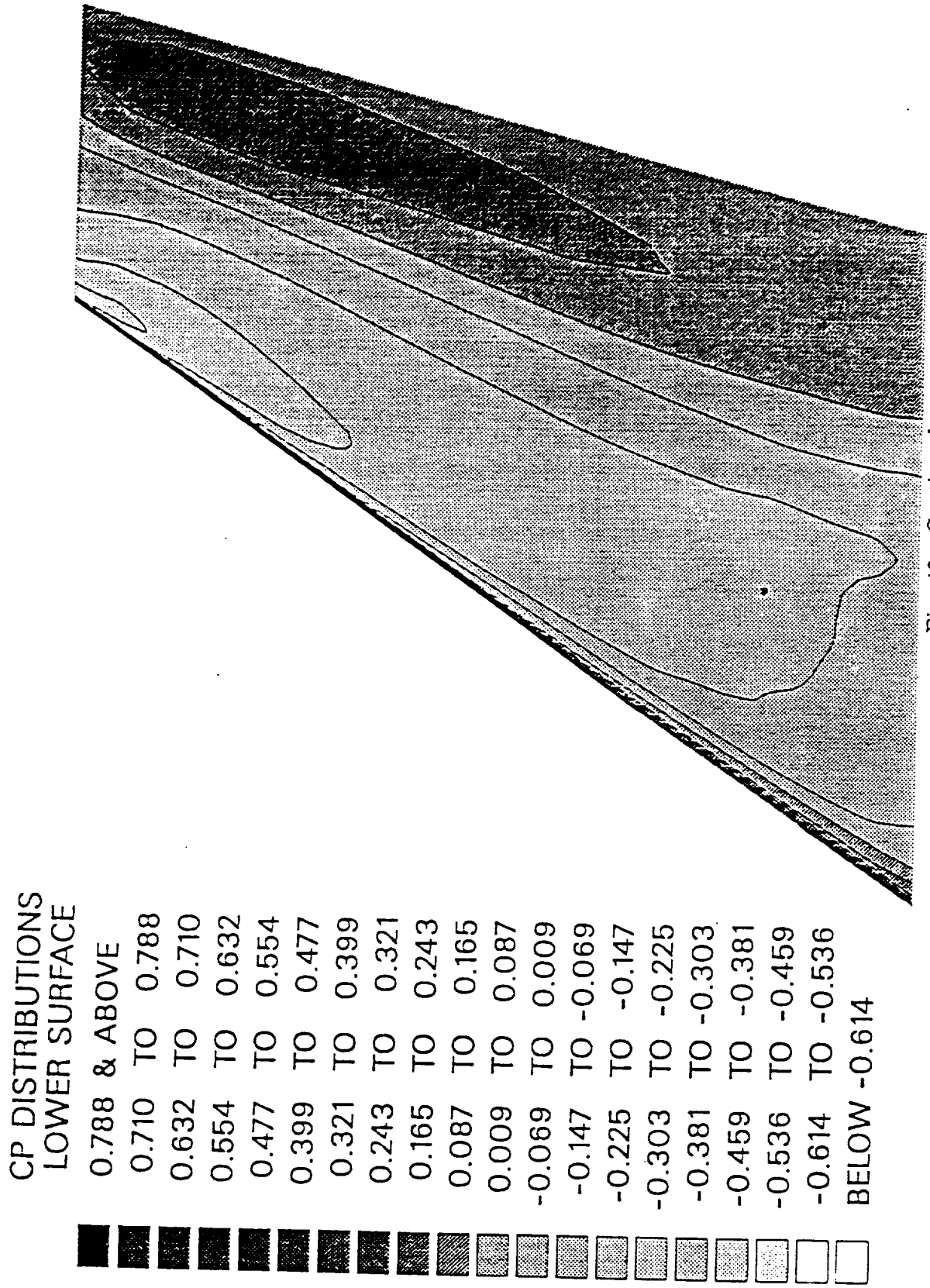

Fig. 48 Continued

This page is blank

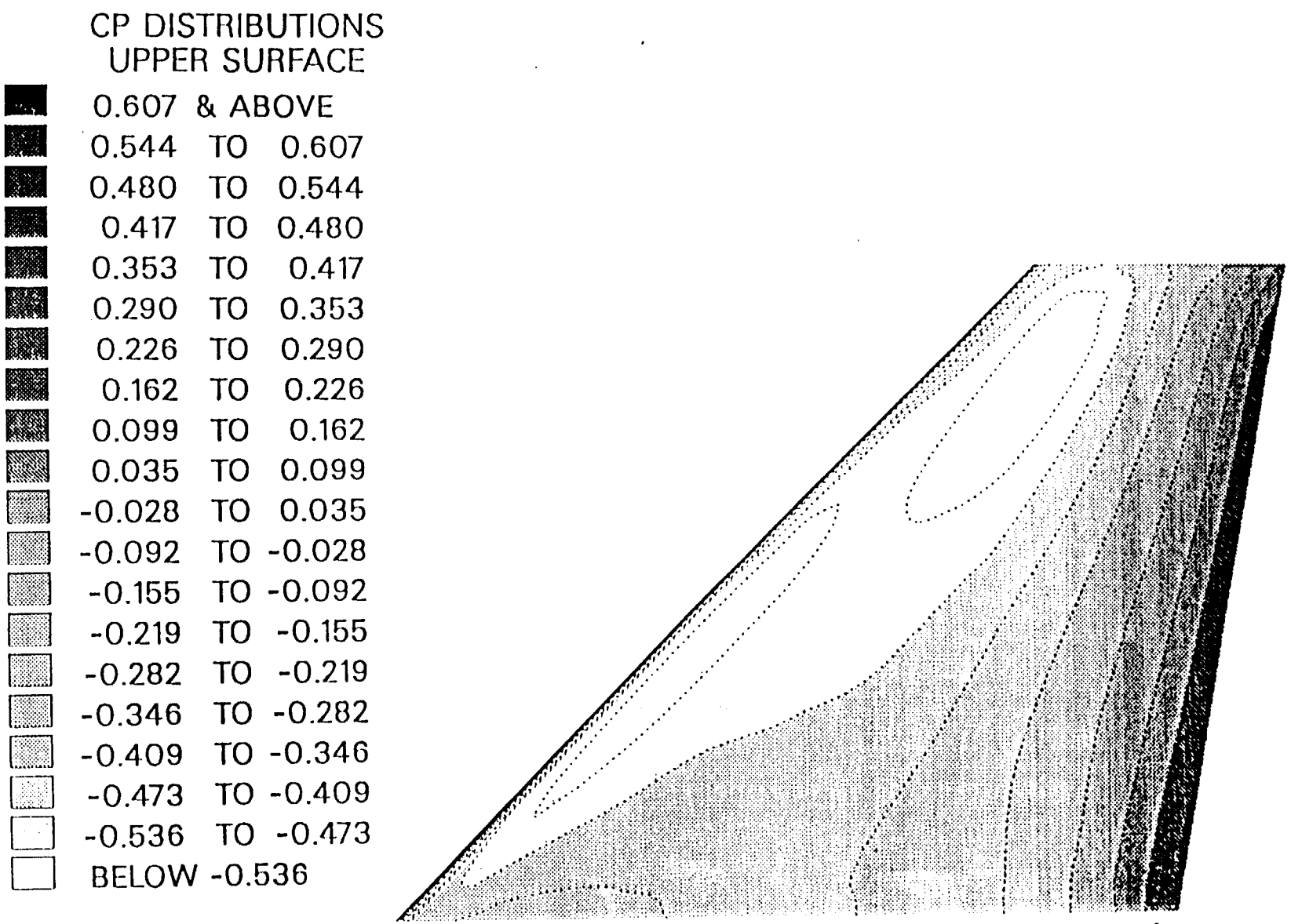

Fig. 49 Pressure contour plot for Lockheed Wing-C M = .796, $\alpha = 4°$

This page is blank

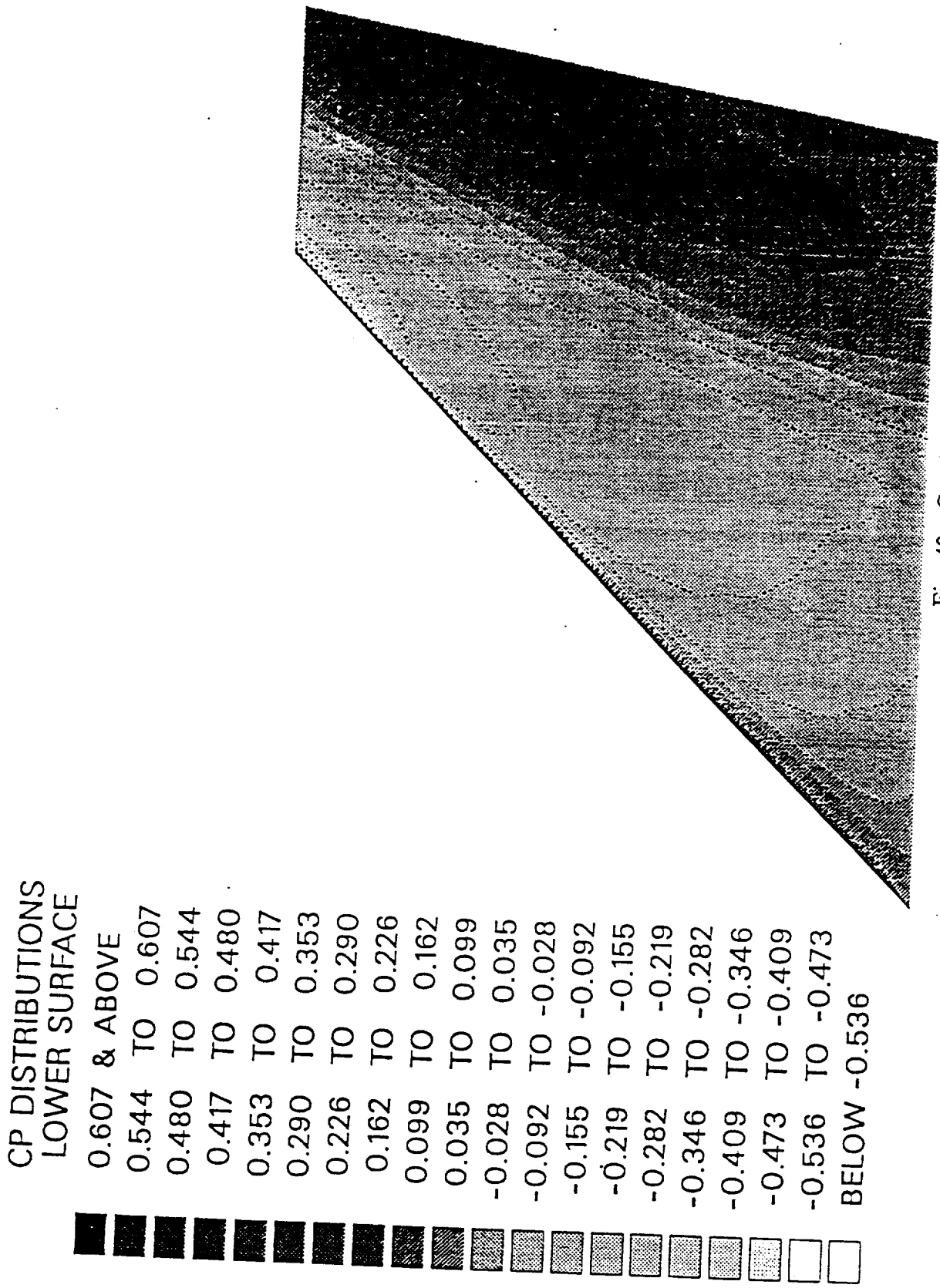

Fig. 49 Continued

This page is blank

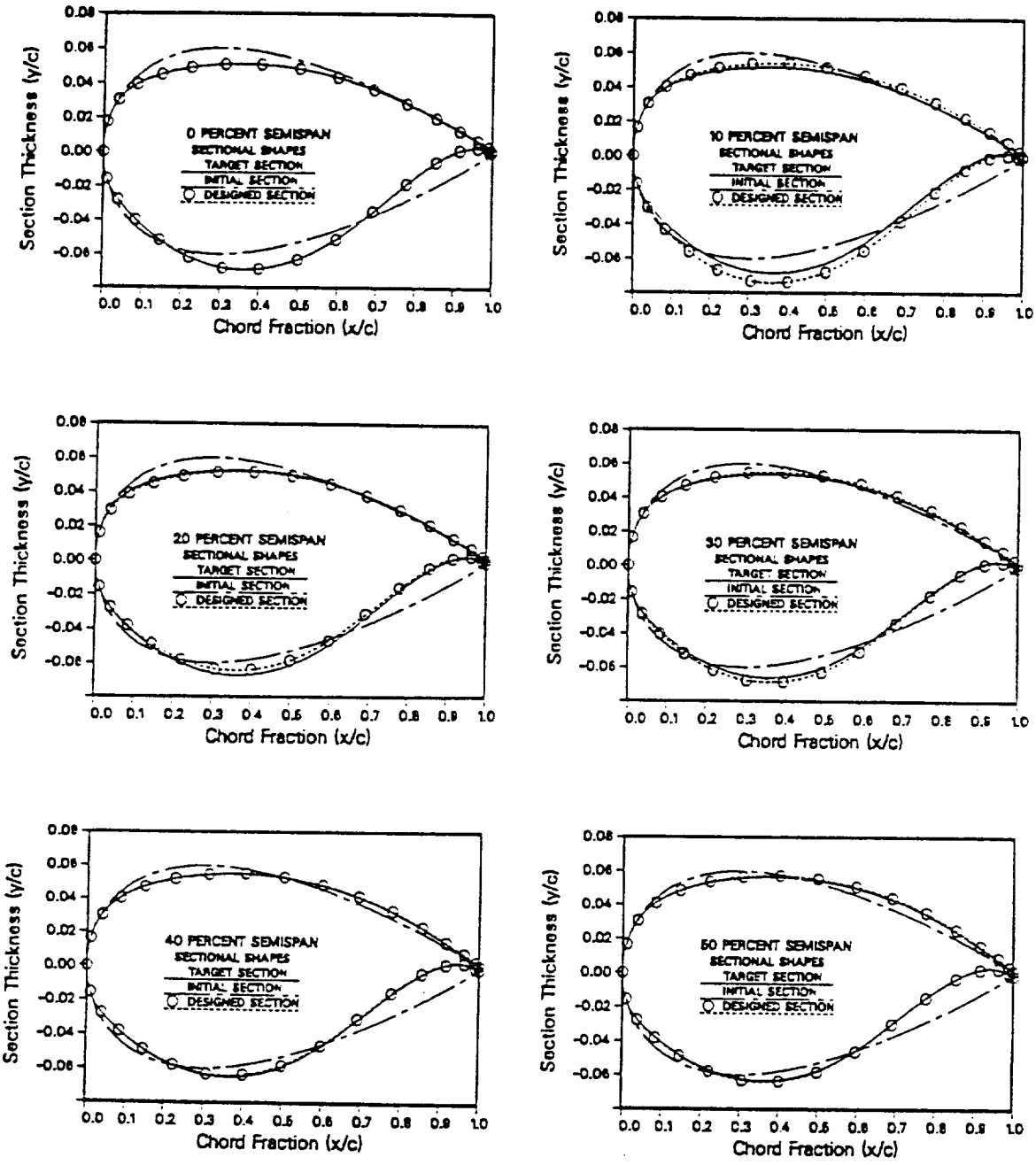

Fig. 50 Comparison of the designed sections with the targets and the initial sections for a fine grid case using Lockheed Wing-A

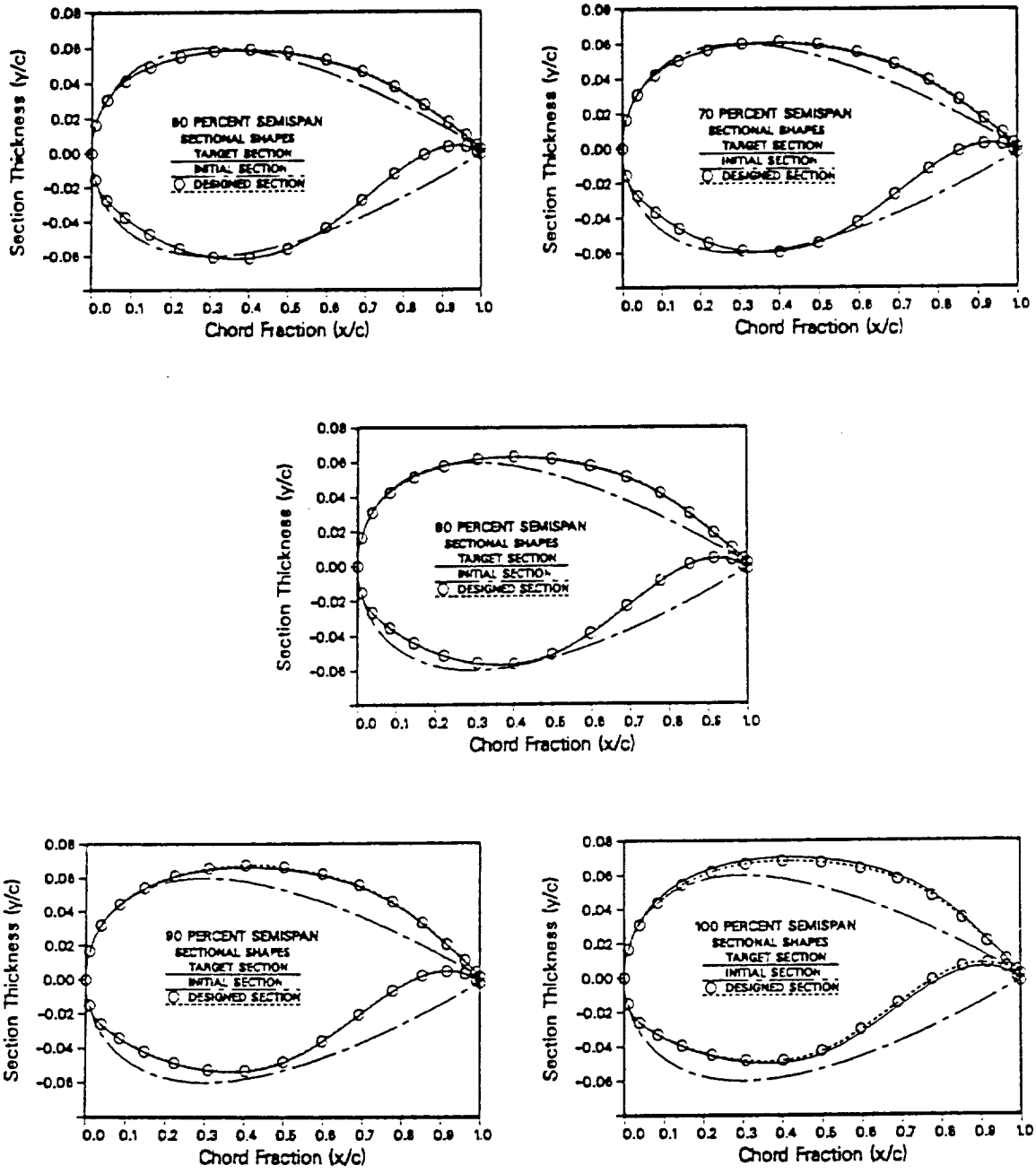

Fig. 50 Continued

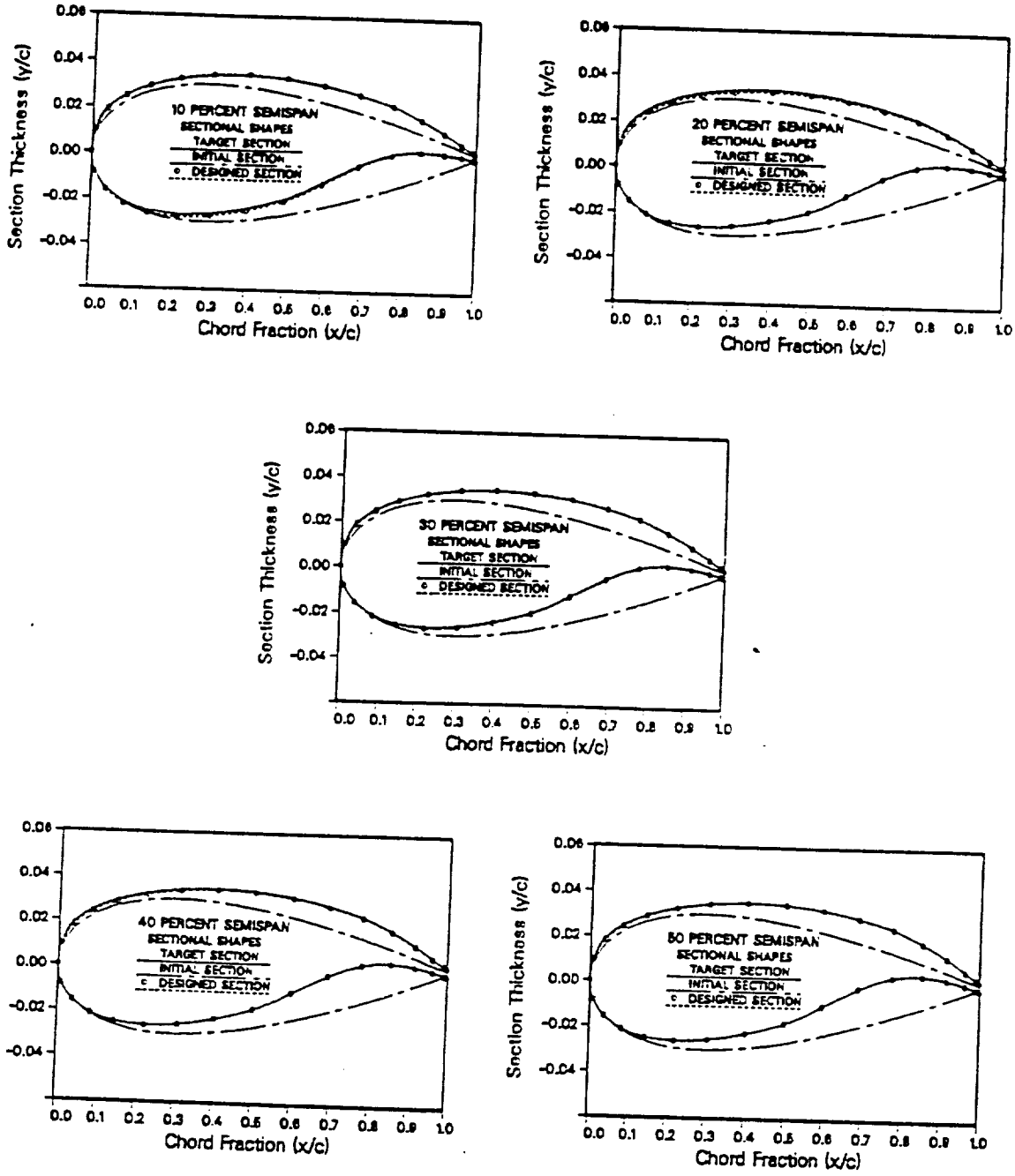

Fig. 51 Comparison of the designed sections with the targets and the initial sections for a fine grid case using Lockheed Wing-B and a design region beginning at 2.5% aft of the leading edge

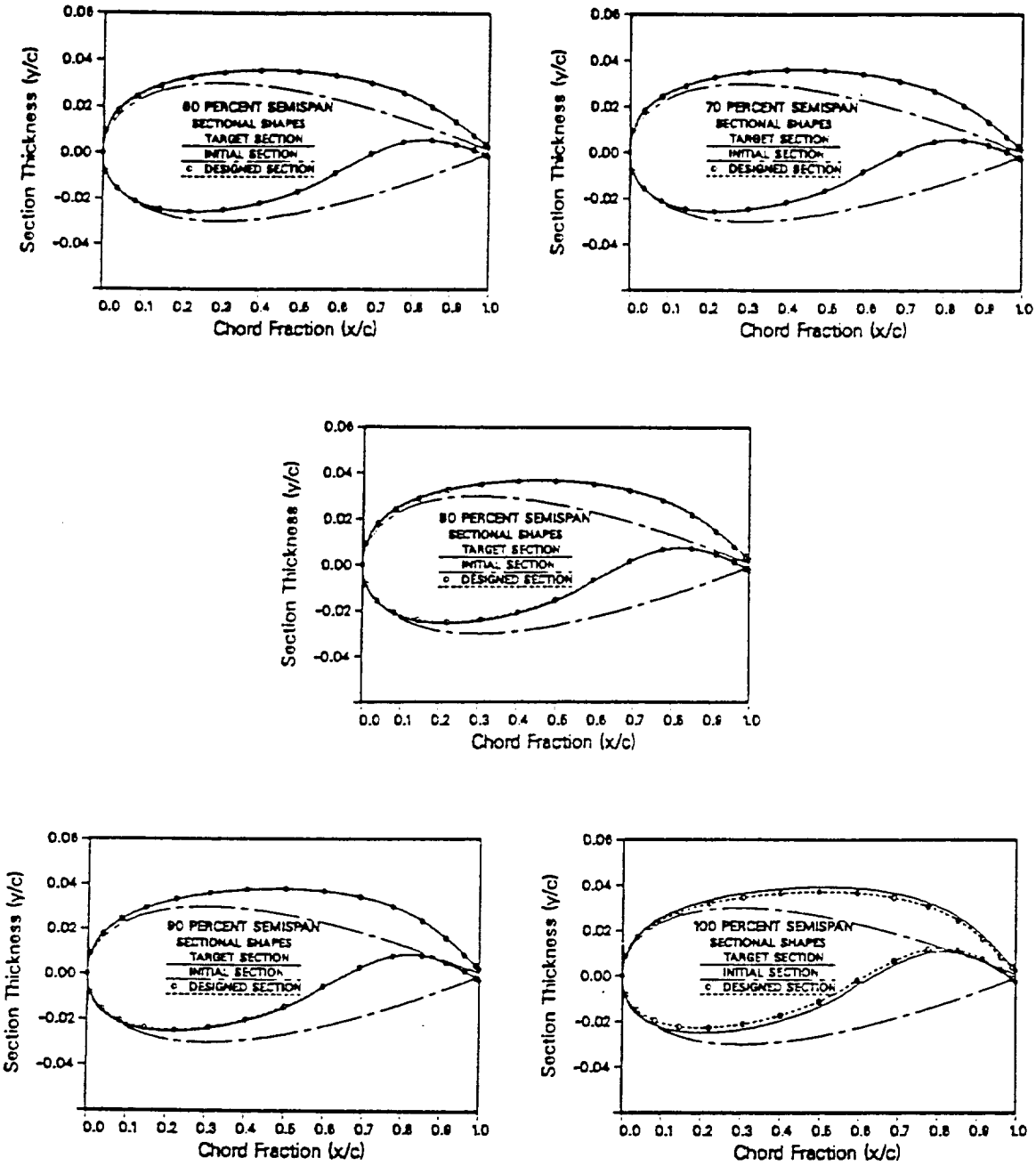

Fig. 51 Continued

of spanwise flow and the associated spanwise gradients for Wing-C, the spanwise oscillation effect could not be overcome with any of the present remedies. Further information about this case was obtained by using the Type II method and not relofting the section shapes. The results for such a converging fine grid case are shown in Fig. 52. The first design station at 18% semispan is too thick on the upper surface as compared to the target. This discrepancy is again due to the over prediction of the residual at the first station due to the initial mismatch in the potentials in the spanwise direction, and, hence, to large spanwise gradients of the potential. The errors diminish as the tip is approached, but are always relatively large in the trailing edge region due to the difficulty in accurately imposing the inverse boundary condition near the trailing edge for this case. If an attempt were made to converge this case further by continuously relofting the shapes to meet the trailing edge ordinate, the same spanwise oscillation problem would again occur. However, non-relofted results such as in Fig. 52 would be very useful for preliminary design studies.

V.4 Initial Profile Effects

One of the disadvantages of the direct-inverse method is that *a priori* knowledge about the correct shape of the leading edge must be known to achieve suitable airfoil shapes and desired trailing edge thickness. Relofting does alleviate this disadvantage to a large degree; but it will not, in general, produce a leading edge that will yield the desired pressure distribution at the leading edge if the inverse boundary condition is by necessity applied too far aft. It was thought that because FLO-30's grid package

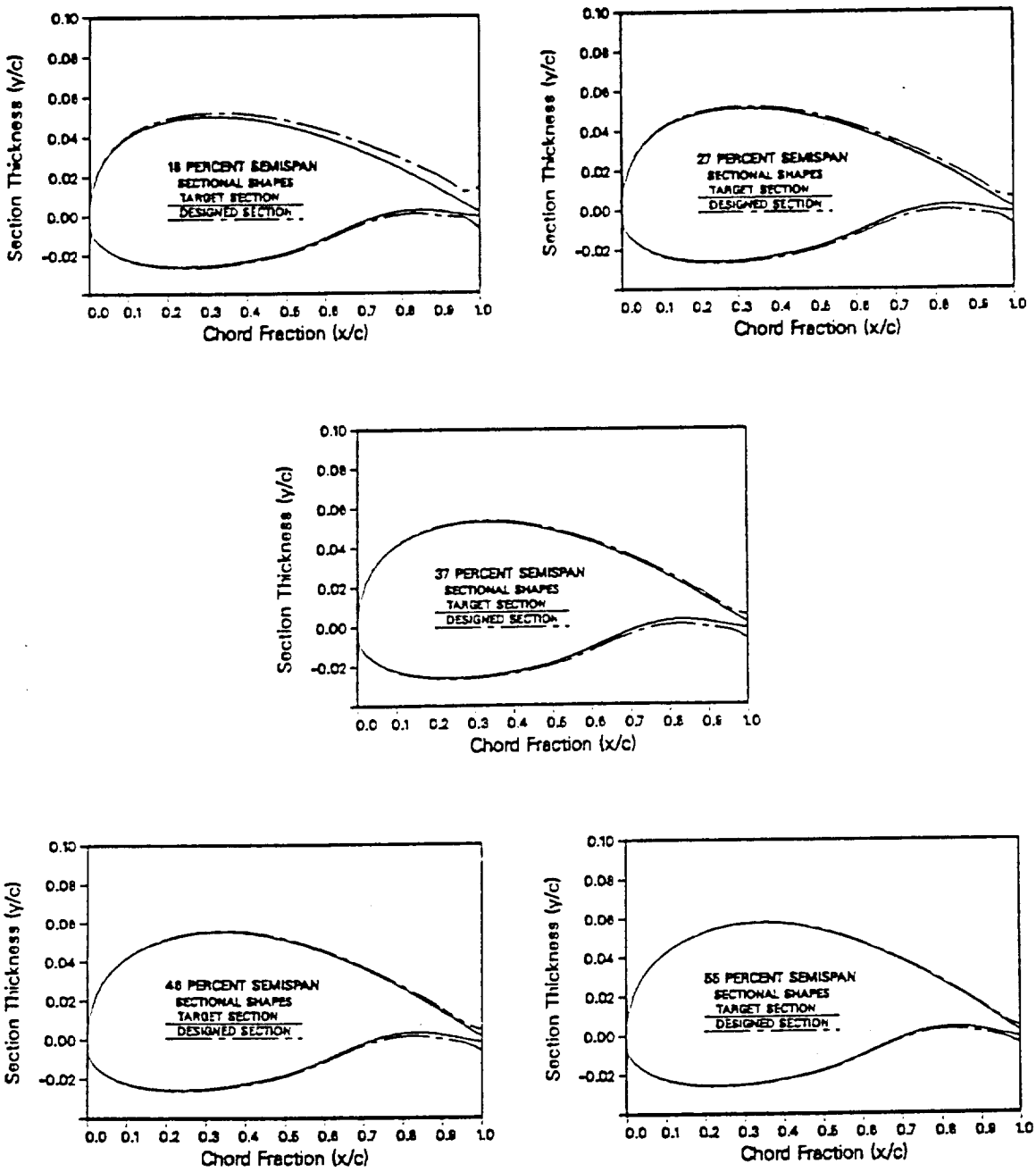

Fig. 52 Comparison of the designed section with the target for an unrelofted fine grid case using Lockheed Wing-C

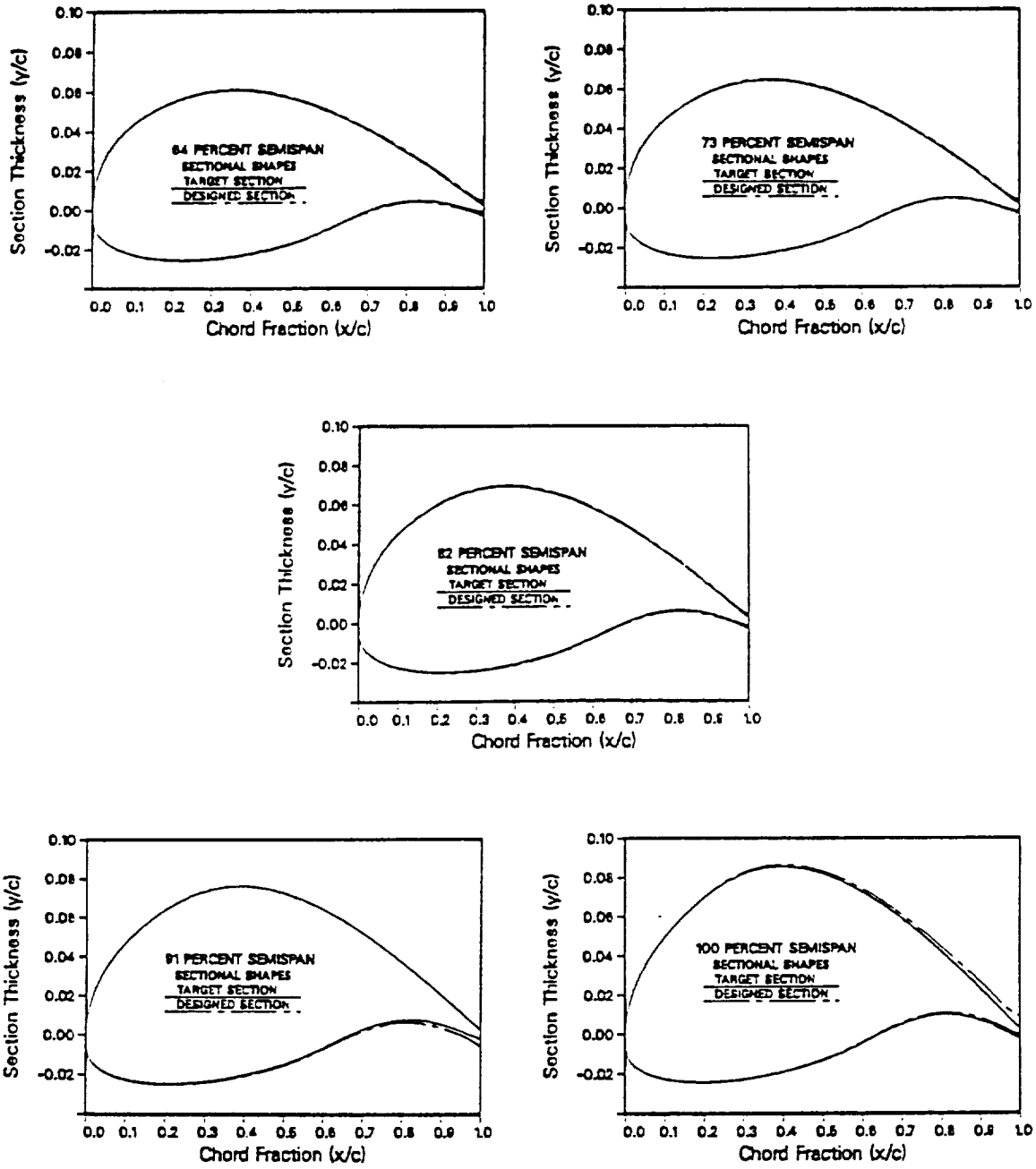

Fig. 52 Continued

clusters grid lines close to the leading edge of the airfoil, that the design could be started quite close to the leading edge, thus relieving the designer of the difficulty of choosing a correct nose shape. Two test cases were conducted to investigate the dependence of the final design on the initial airfoil section. Both used Lockheed Wing-A at the same conditions mentioned earlier for the viscous study. For the first case, the initial airfoils were the same as those in the viscous study. These airfoils all had leading edges which were in the same family as the target section. The design began 10% aft of the leading edge. In the second case, NACA 0012 sections were used at all the design stations; here, the leading edge of these sections were not in the same family as the target airfoil sections. For this case, the pressure boundary condition began 4% aft of the leading edge. Referring to Fig. 53, it can be seen that although slightly better results were obtained near the leading edge for the first case, that the airfoils designed were fairly insensitive to the initial section.

V.4.1 Direct-inverse interface proximity to leading edge

Since experience with the method has shown that the closer the inverse boundary condition is applied to the leading edge, the longer it takes for the solution to converge, it was of interest to determine how the location of the direct-inverse interface affected the final design and the resulting pressure distributions. This study was accomplished with the aid of the previously discussed Wing-B case, whose design region began at 2.5% chord, and an inviscid design of Wing-B also with NACA 0006 sections as the initial geometry. With the second case, the design was started at 5% chord from the leading edge; and, the input pressures were obtained from an inviscid

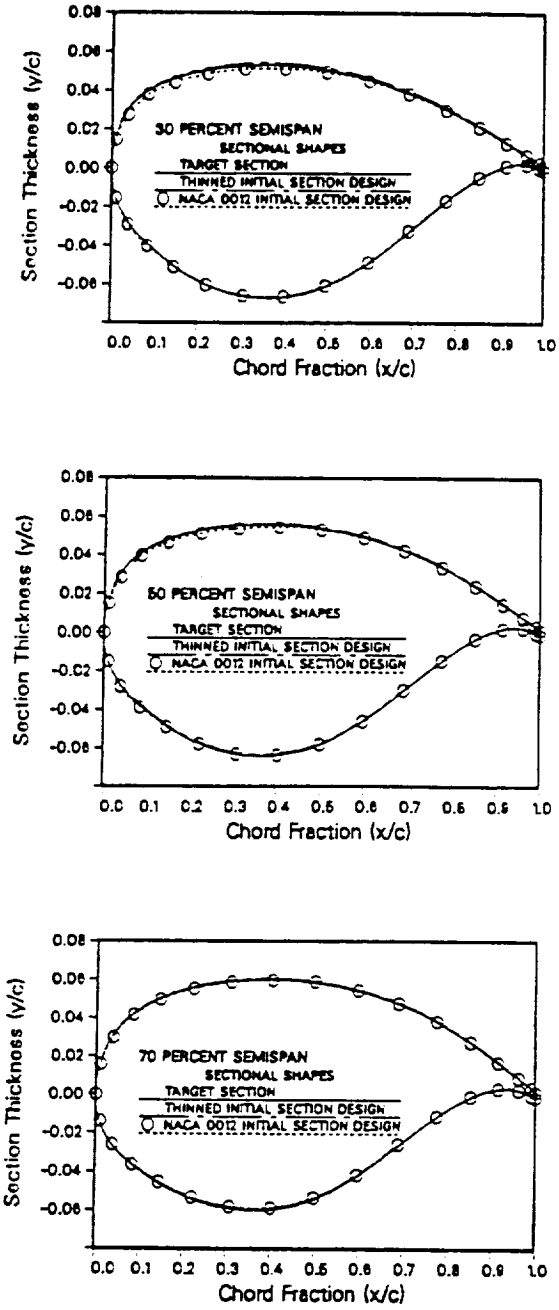

Fig. 53 Comparison of sections designed using two different initial sections

analysis of Wing-B. Since the design pressure distributions were consistent in both of these cases, the fact that one was a viscous design and the other an inviscid design is not important here.

Some representative samples of the resulting section shapes for the second case are shown in Fig. 54. The resulting wings were analyzed under the same conditions that the original input pressure distributions were obtained. Representative samples of the resulting pressure distributions are compared to their respective target distributions in Figs. 55,56. As can be seen, the wing whose design began 2.5% aft captured the suction peek at the leading edge, while the other case, which began at 5% aft of the leading edge, did not.

When designing near (less than 5%) the leading edge, the solution sometimes began to slightly diverge or ceased converging. Usually the design could be converged to the point where there was only a maximum change in the surface of .1-.2% chord. This was more a problem on the fine grid than on the medium. If it was necessary to converge it further, the beginning of the design region was moved aft. This observation is important because if it is necessary to begin the design close to the leading edge to properly determine the shape of the nose, a successful design may be accomplished by beginning the design as close to the leading edge as desired or is possible, then moving the beginning of the design region aft as the solution approaches the last stages of convergence. This method not only frees the designer from the task of choosing the correct leading edge shape, but it should also accelerate the convergence of the design considerably.

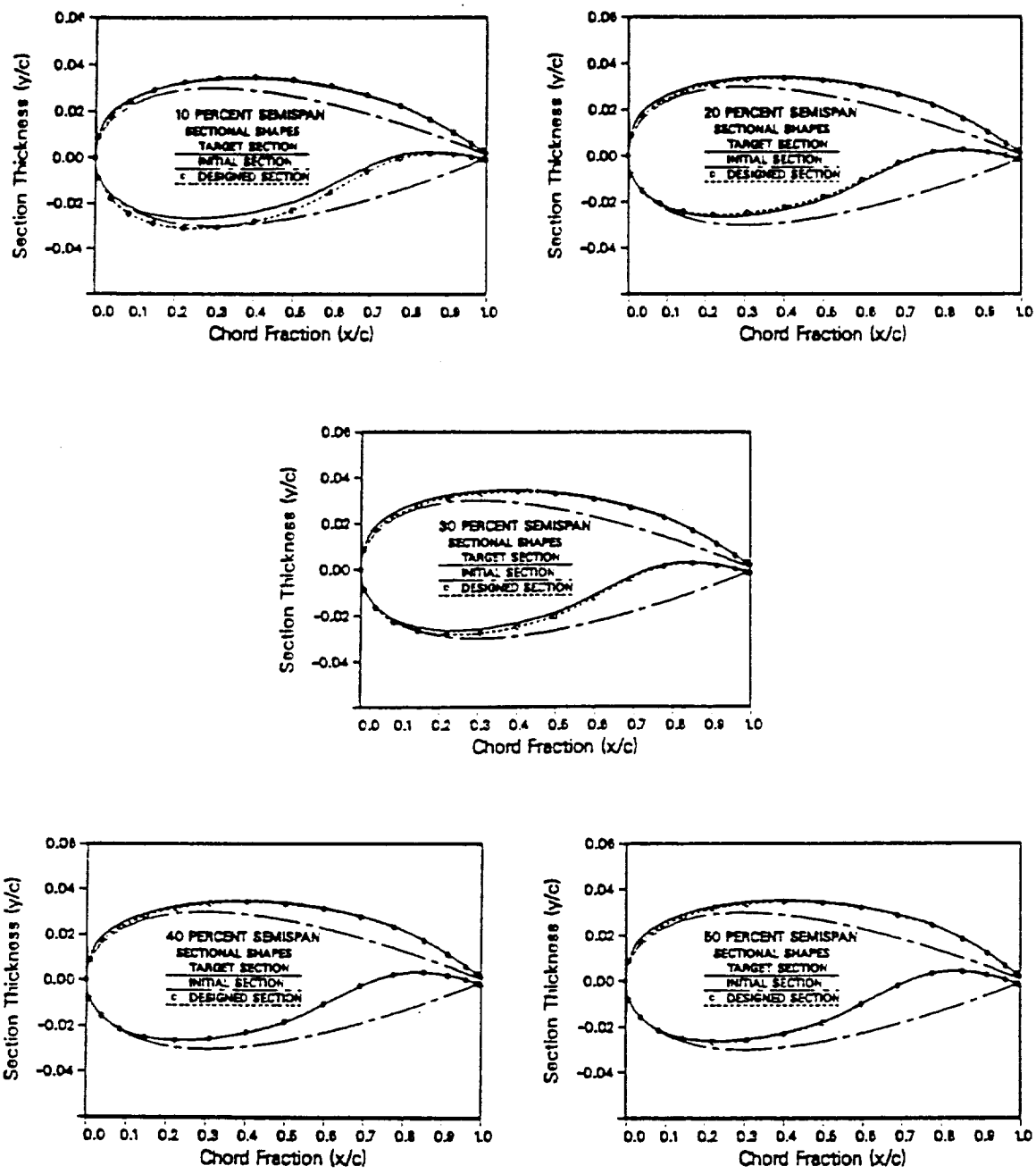

Fig. 54 Comparison of the designed sections with the targets and the initial sections for a fine grid case using Lockheed Wing-B and a design region beginning at 5.0% aft of the leading edge.

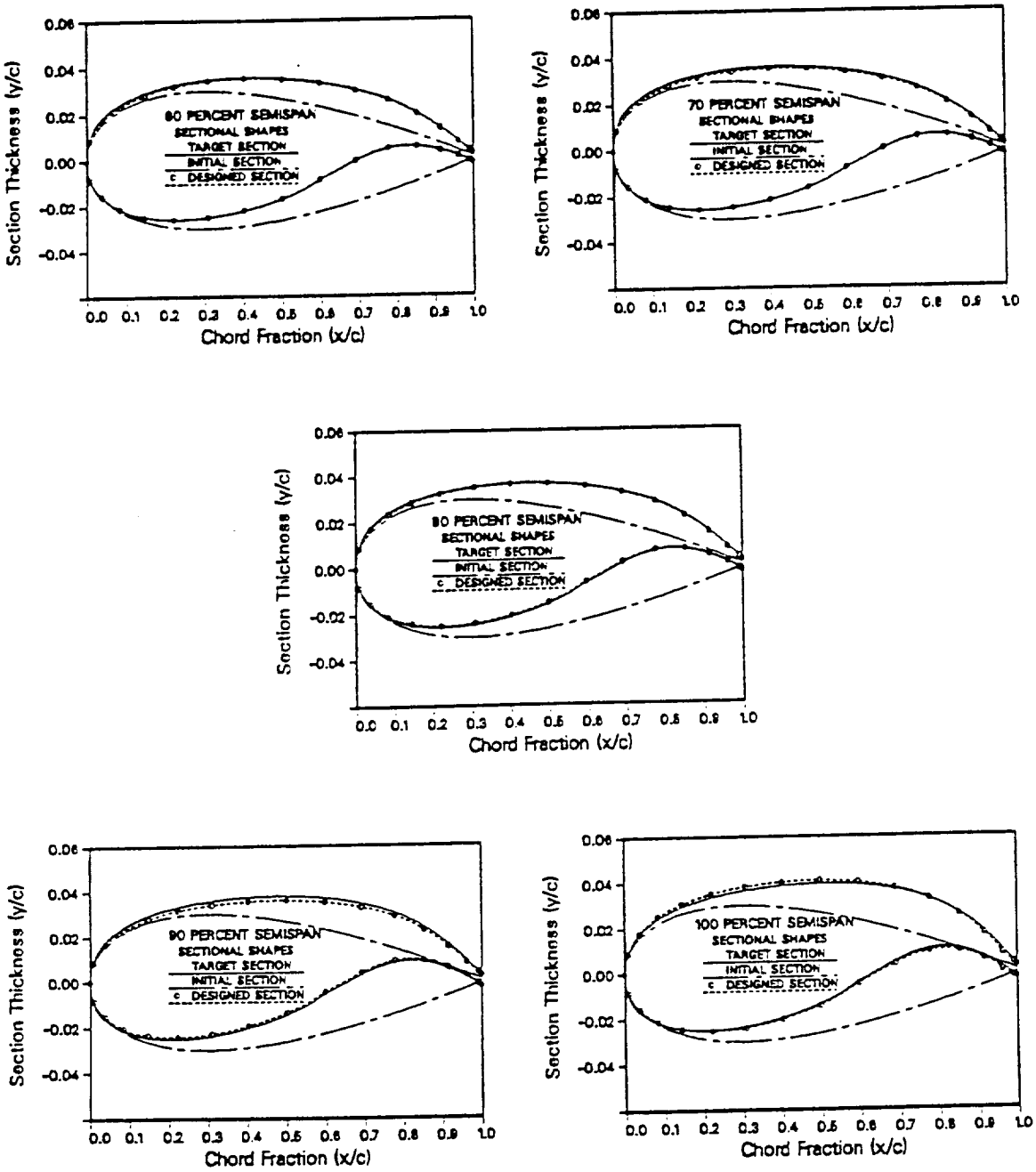

Fig. 54 Continued

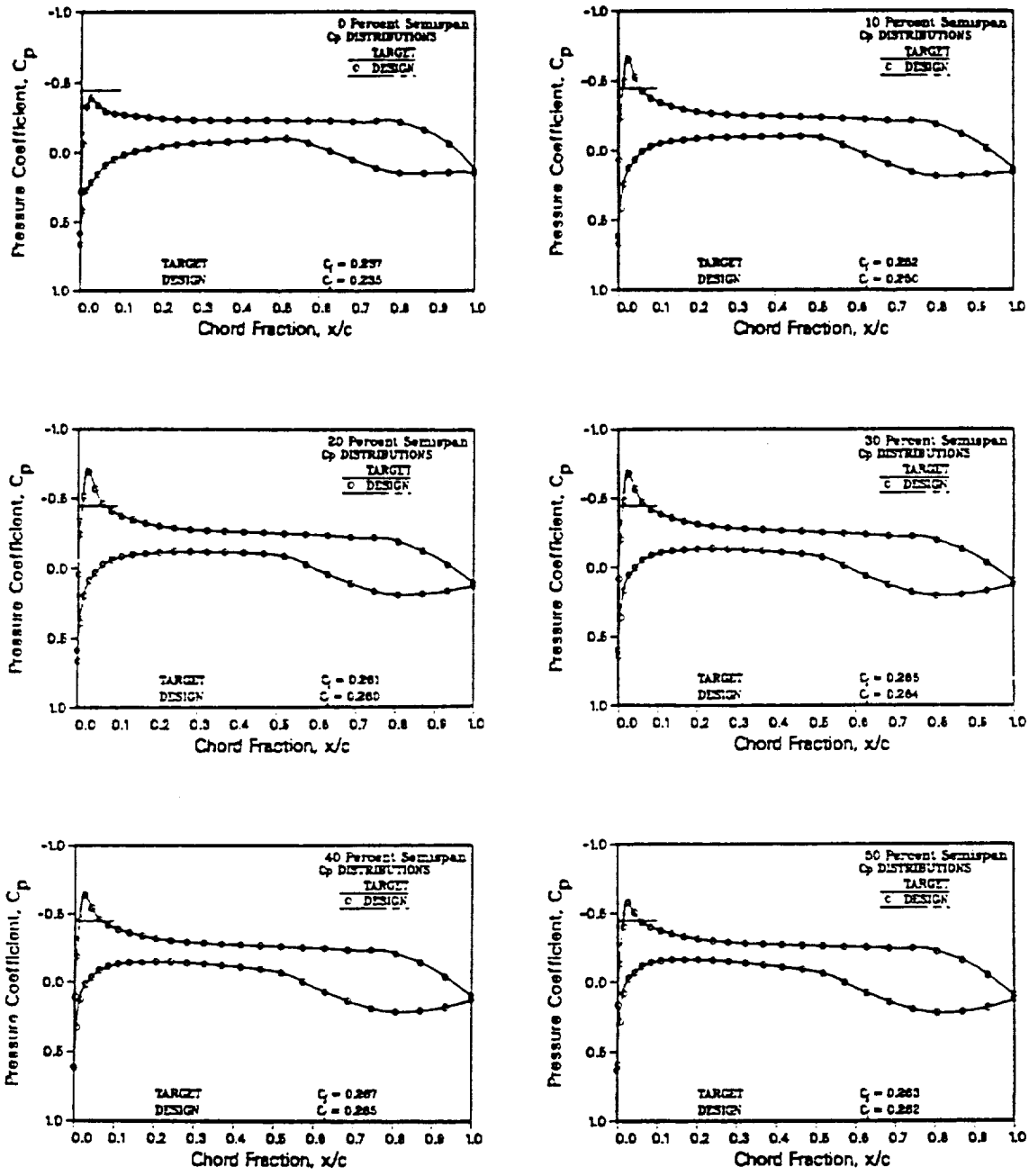

Fig. 55 Comparison of the pressure distributions obtained from an analysis of the Wing-B design, which had a design region that began 2.5% aft of the leading edge, with the target pressure distributions

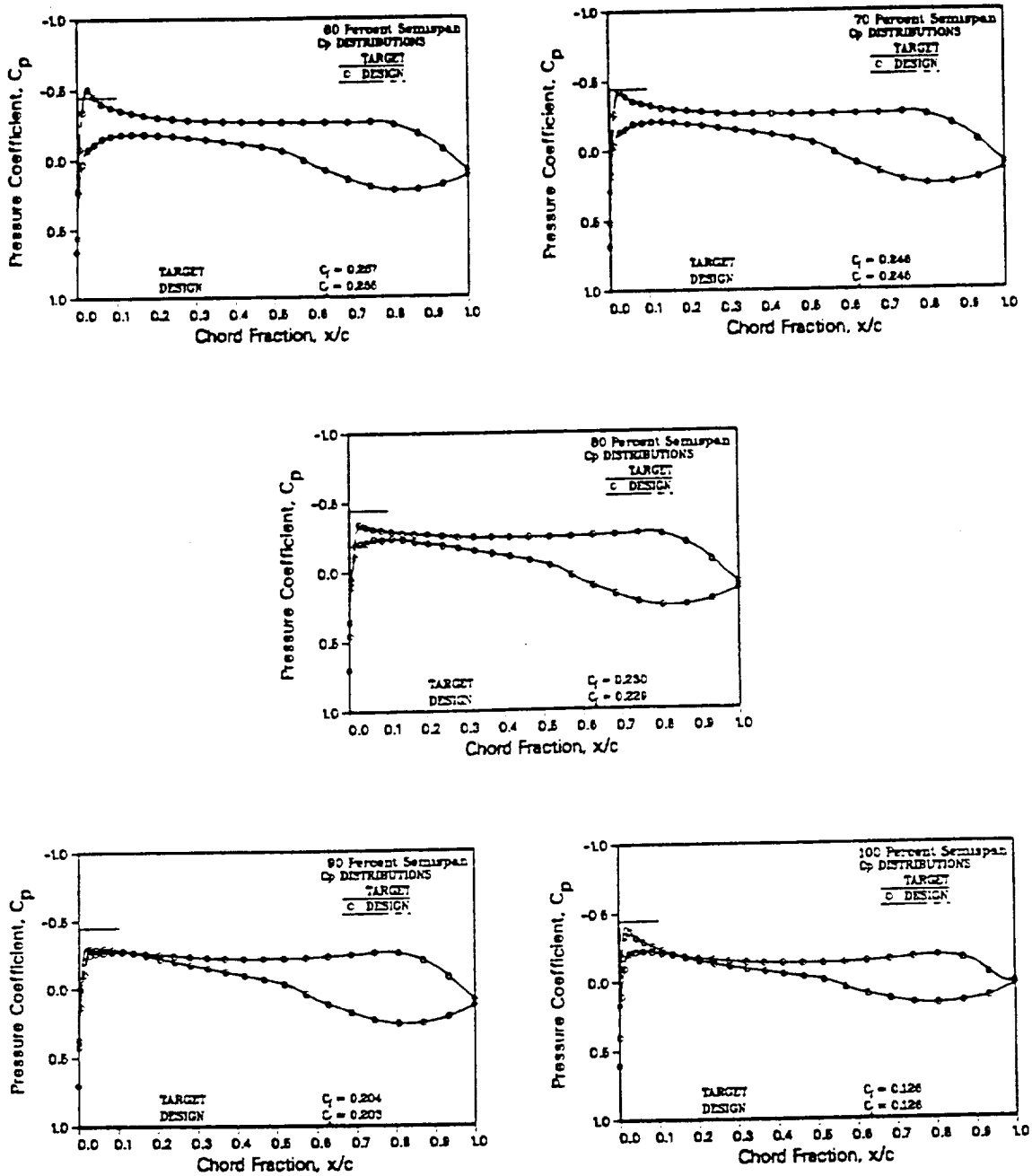

Fig. 55 Continued

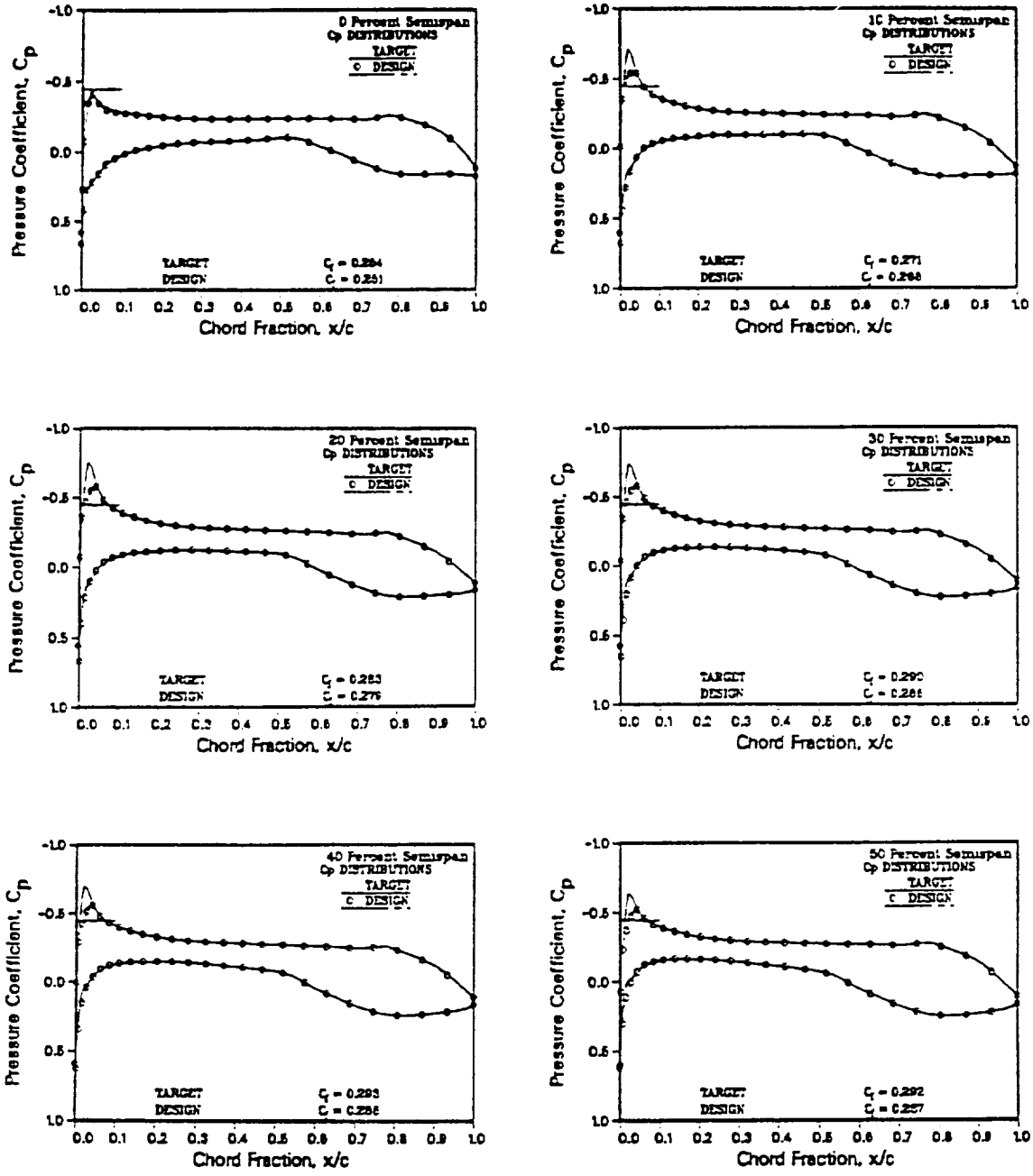

Fig. 56 Comparison of the pressure distributions obtained from an analysis of the Wing-B design, which had a design region that began 5.0% aft of the leading edge, with the target pressure distributions

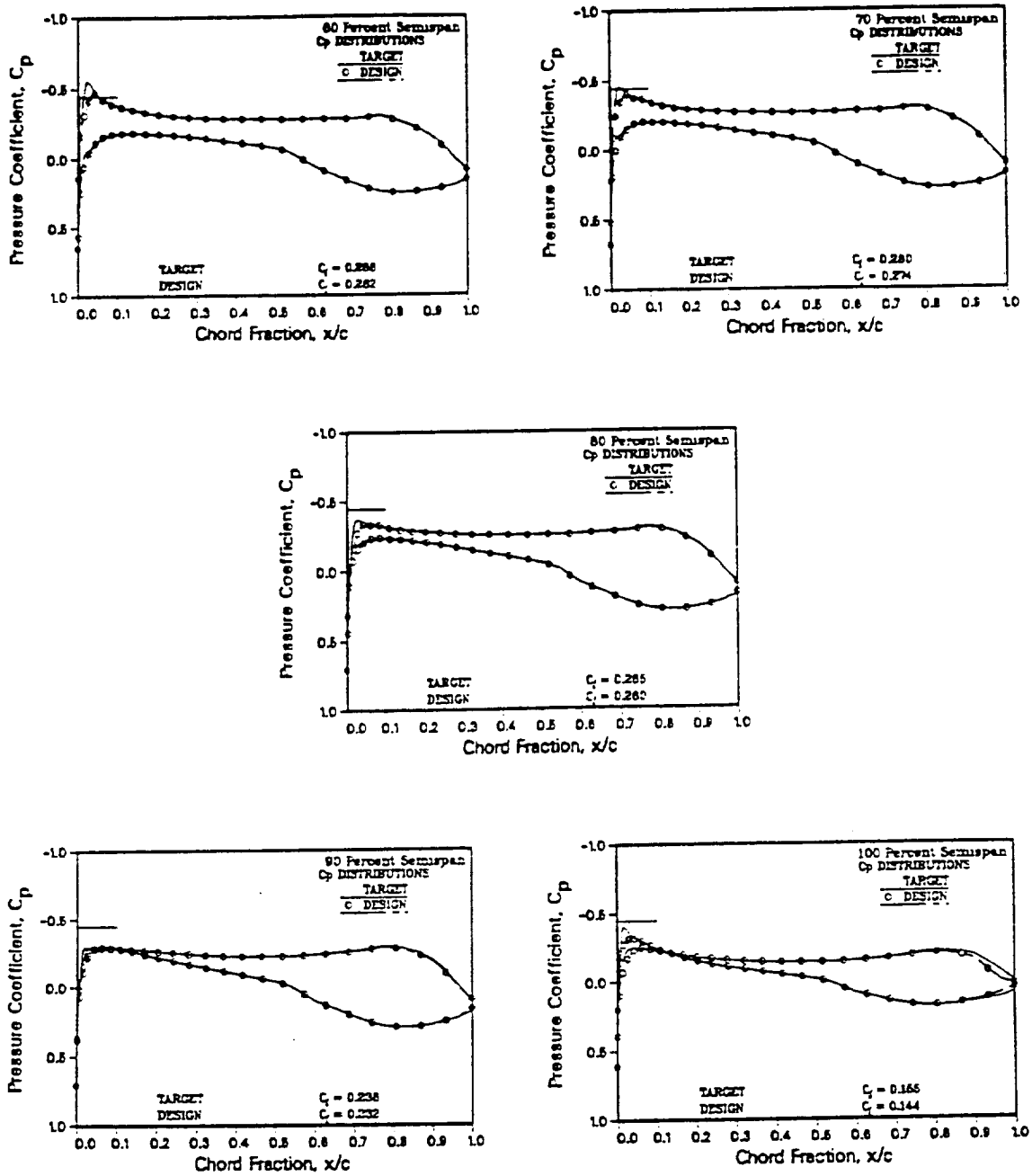

Fig. 56 Continued

Because of the leading edge clustering of grid points in TAW5D, successful designs have been accomplished on the medium grid with the chordwise direct-inverse junction beginning just aft of the stagnation point on the lower surface. If the pressure boundary condition is applied upstream of the stagnation point, major difficulties arise when an attempt is made to integrate past this point of singularity, since the slope, $\frac{V}{U}$, is indeterminate there.

For the case shown in Fig. 57 , the design was begun 1% aft of the leading edge, but in retrospect, it could have begun close to .3% aft of the leading edge since the converged stagnation point was located about .2% aft. Notice how precisely the designed surfaces can be computed when compared to the targets outboard of the first design station. This case effectively demonstrates that since the design region can be extended extremely close to the leading edge with TAW5D, the fact that the pressure boundary condition can only be applied aft of the leading edge is a very small shortcoming of this direct-inverse method.

V.5 Pressure Distribution Compatibility

Since a designer might not readily have available an input pressure distribution compatible with the design freestream Mach number, the effect of designing a wing at one Mach number using a pressure distribution obtained from an analysis of the wing at a different Mach number was investigated. The Wing-A planform was used throughout this portion of the study. NACA 0012 sections were used as the targets and NACA 0006 sections were used as the initial sections in the design. The entire

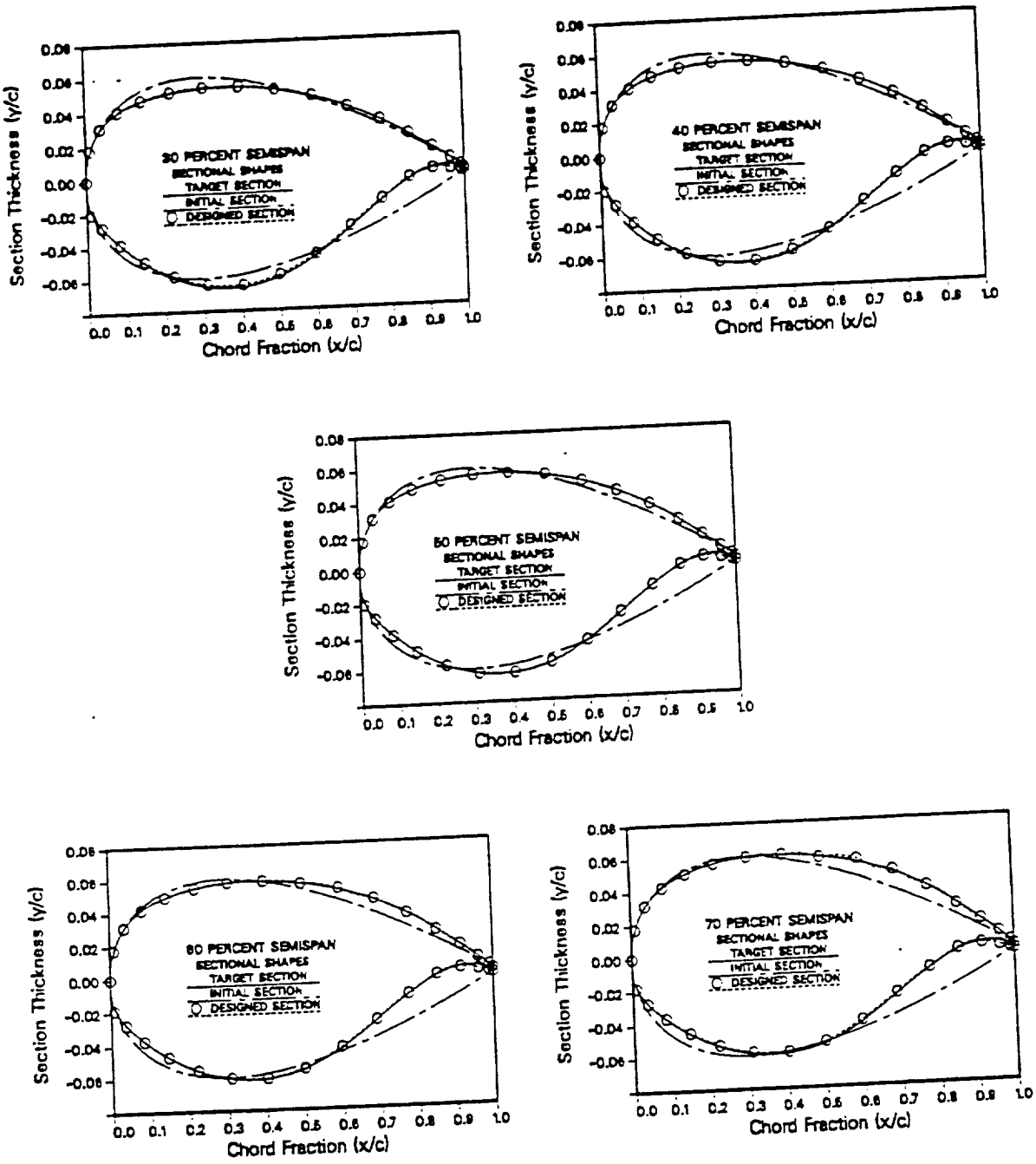

Fig. 57 Comparison of the designed sections with the targets for a case whose design region began 1% aft of the leading edge

wing was designed on from root to tip, and the design region started 10% aft of the leading edge of the wing.

Two separate tests were performed. The first involved a fine design at a nearly incompressible Mach number of .2 using a pressure distribution obtained from an analysis of the target at a Mach number of .1. As can be seen from Fig. 58. thinner section shapes were obtained at the higher Mach number. This thinning is in agreement with the 2-D Prandtl-Glauert similarity rule[45]

$$\frac{\tau_1}{\tau_2} = \frac{\sqrt{1 - M_1^2}}{\sqrt{1 - M_2^2}} \qquad (5-1)$$

which states that the C_p will be invariant with Mach number if the thickness, τ, is reduced as the Mach number is increased for linearized flow. For this case, Eq. (5-1) would predict that a 1.54% decrease in thickness would be necessary to have the same pressure distribution at the higher Mach number. The design code for this 3-D case produced a section which was on the average 1.6% thinner than the NACA 0012 section.

The second case involved a medium grid design at a Mach number of .85 using a pressure distribution obtained at a Mach number of .80. Referring to Fig. 59, the section shapes produced are again thinner than the initial section. The top surface, though, required a sudden thinning of the surface at the shock location. Surprisingly, upon analyzing this wing, the pressure distributions shown in Fig. 60 match quite well with the target everywhere except in the tip region of the wing. So, given the constraints of the problems, it appears that the only way the boundary conditions could be met was to have these dips in the airfoil surface. Since these dips might

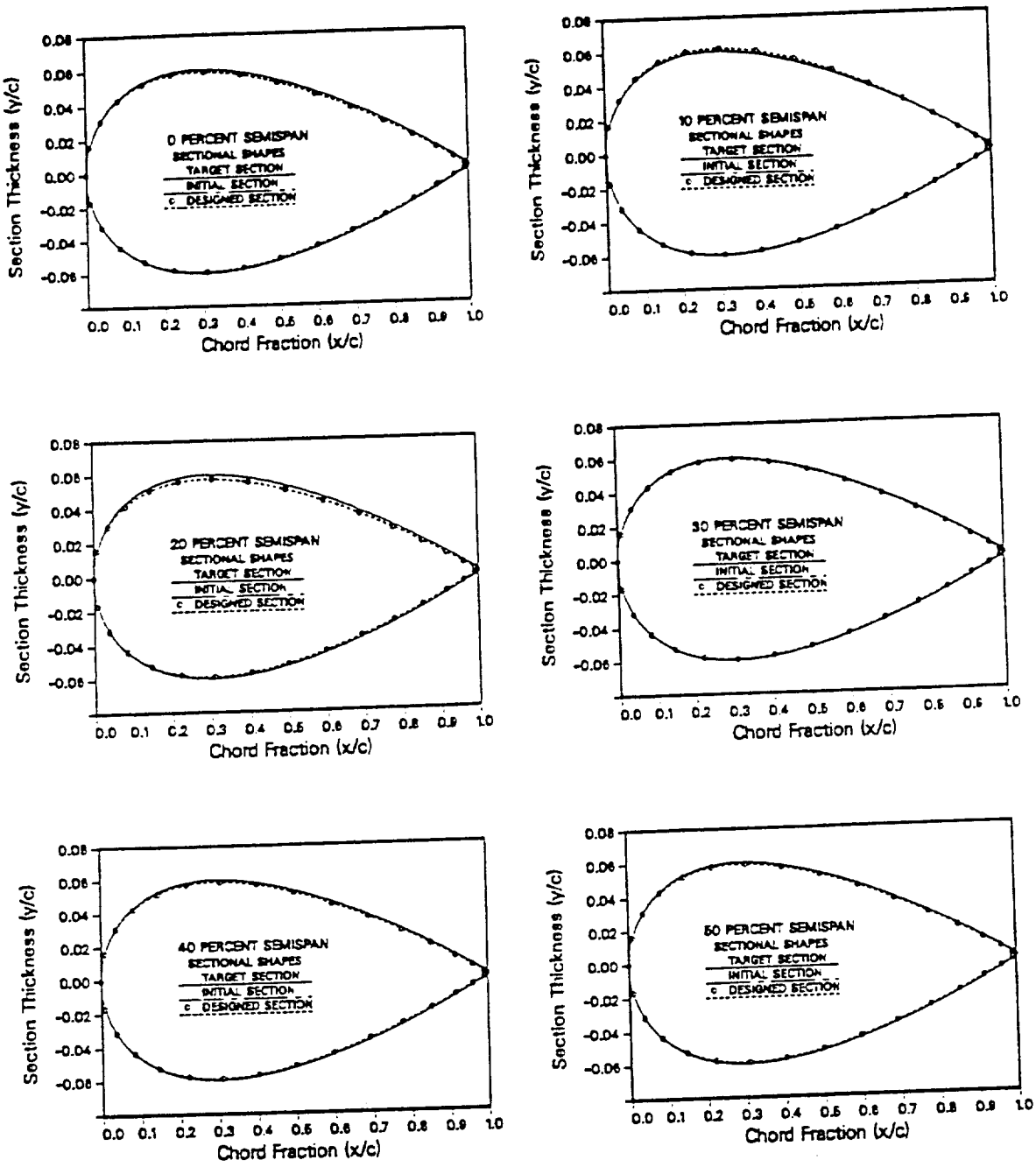

Fig. 58 Comparison of the section designed at a M = .2, using input pressure distributions obtained from an analysis at a M = .1, with the original NACA 0012 sections

ORIGINAL PAGE IS
OF POOR QUALITY

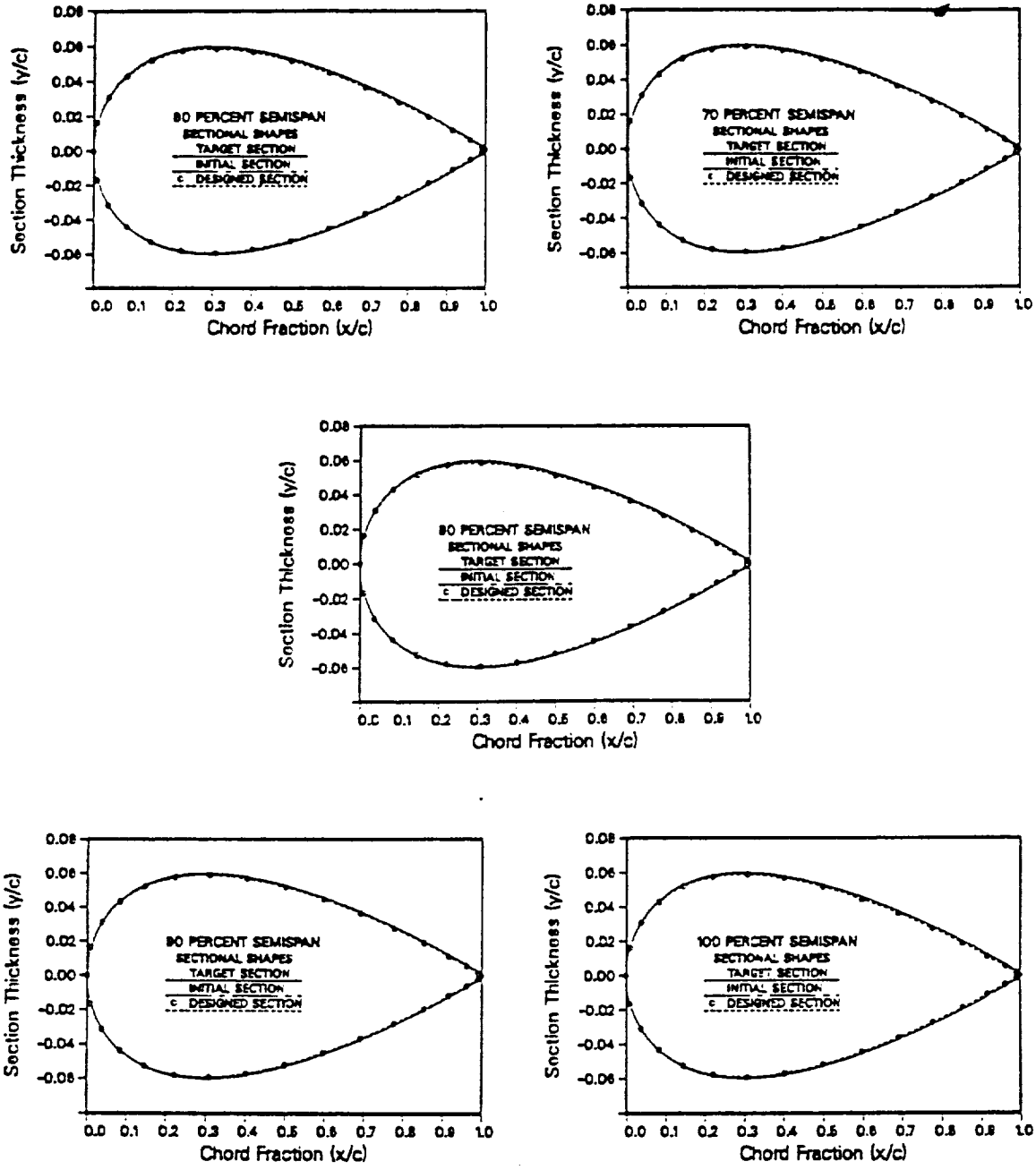

Fig. 58 Continued

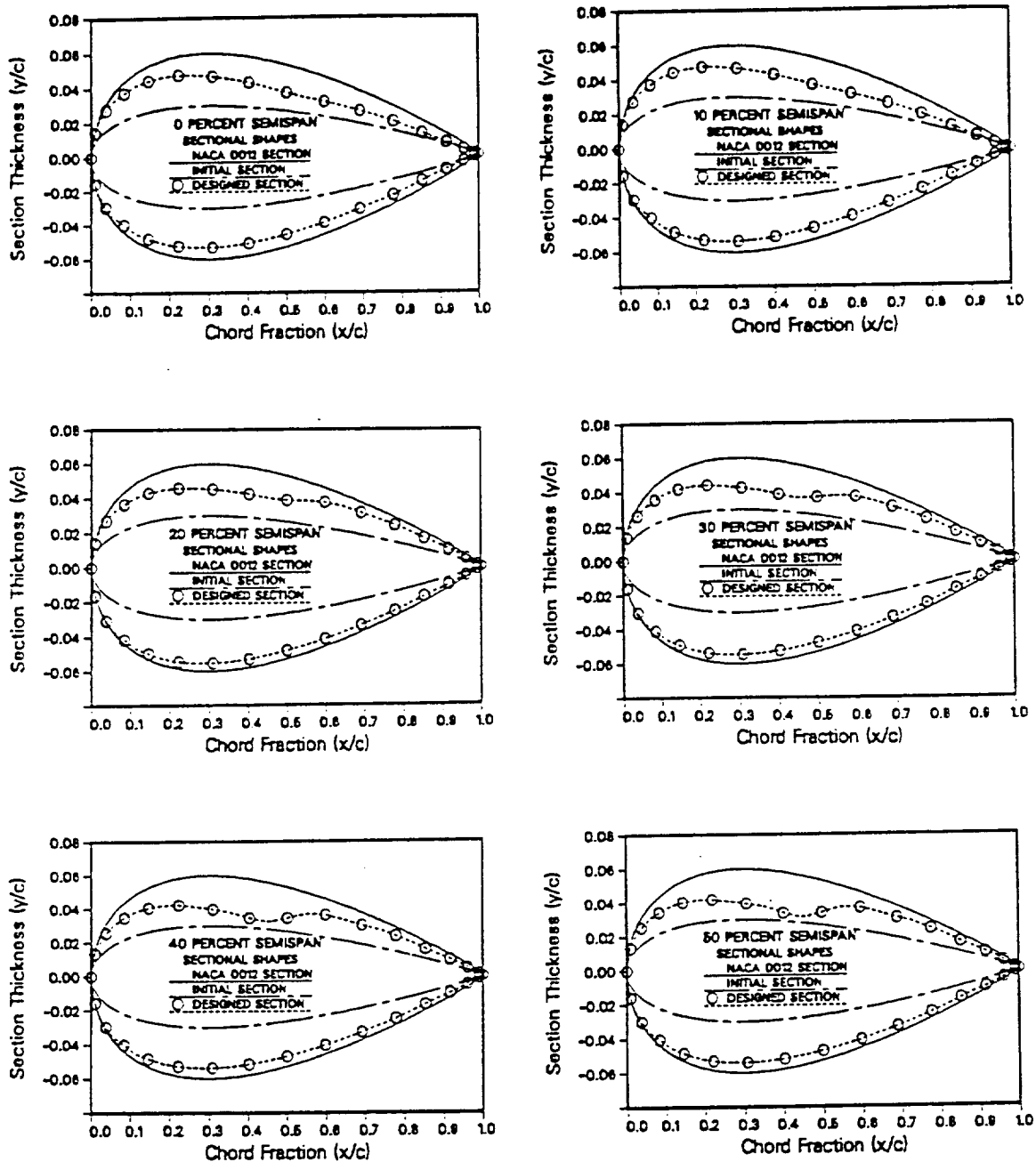

Fig. 59 Comparison of the sections designed at a M = .85, using input pressure distributions obtained from an analysis of Lockheed Wing-A with NACA 0012 airfoils at a M = .8, with the original NACA 0012 sections and initial NACA 0006 sections

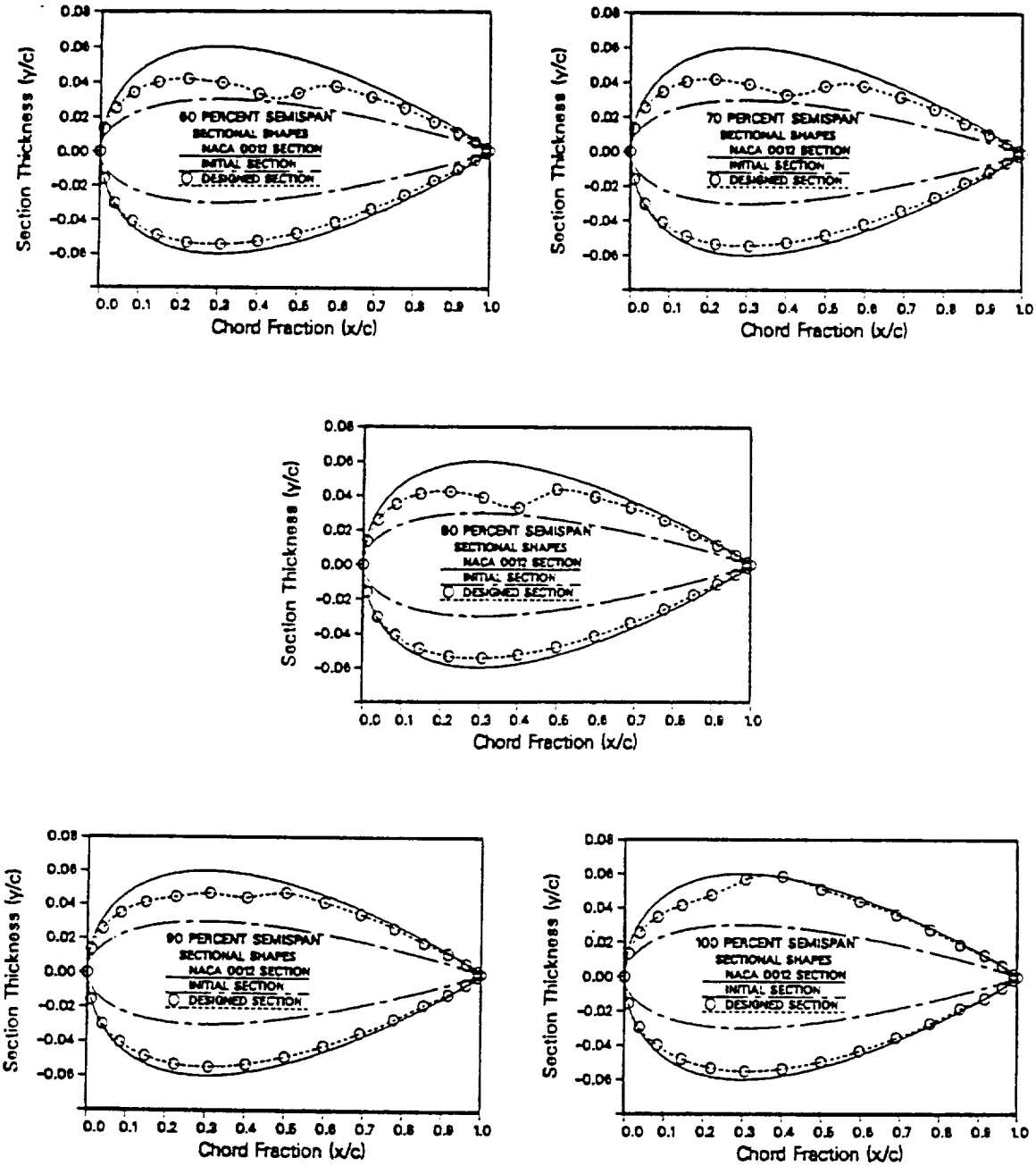

Fig. 59 Continued

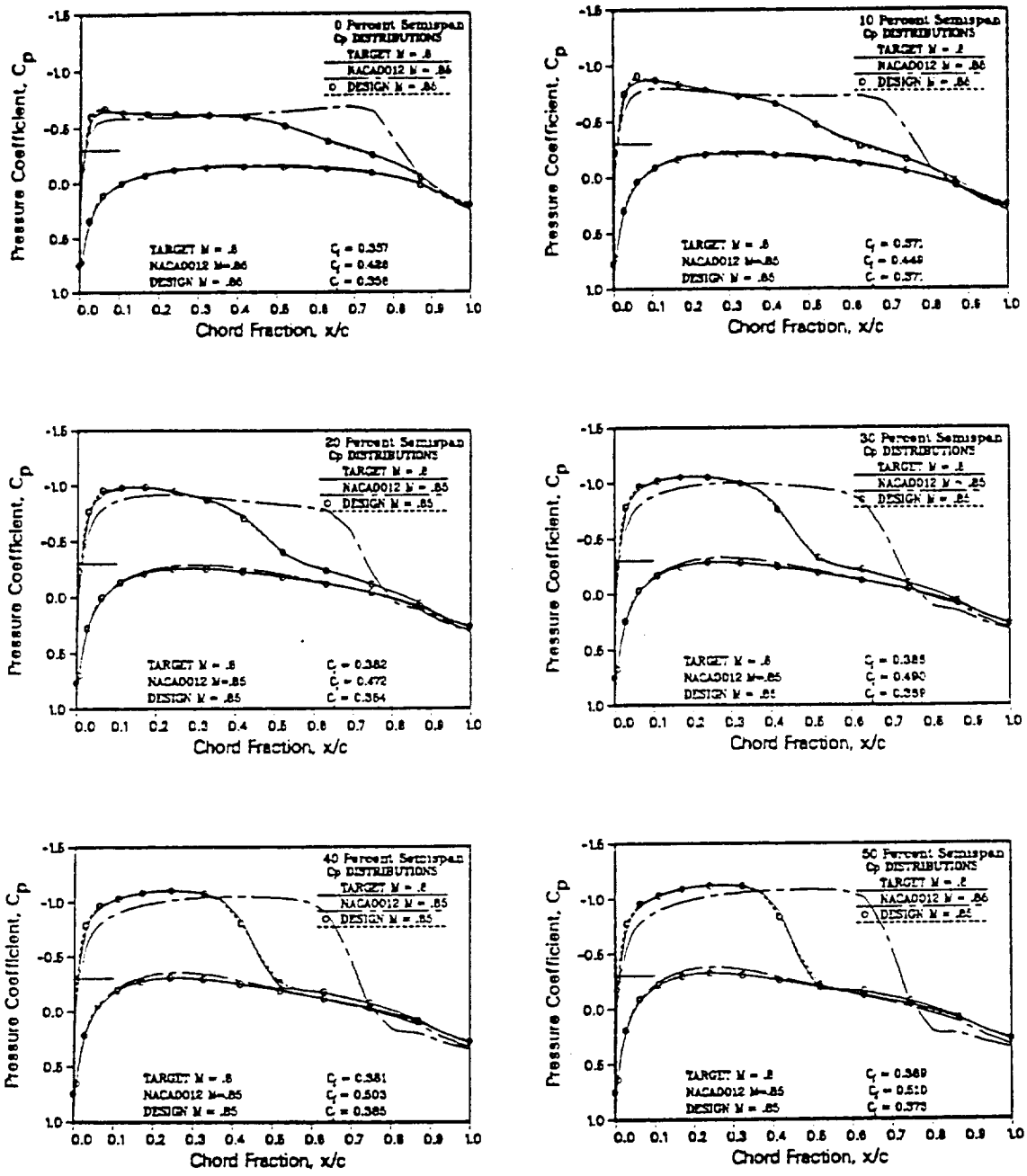

Fig. 60 Comparison of the pressure distributions obtained from an analysis at a M = .85 of the Lockheed Wing-A which was designed at a M = .85 using input pressure distributions obtained from an analysis at a M = .8, with the input pressure distributions

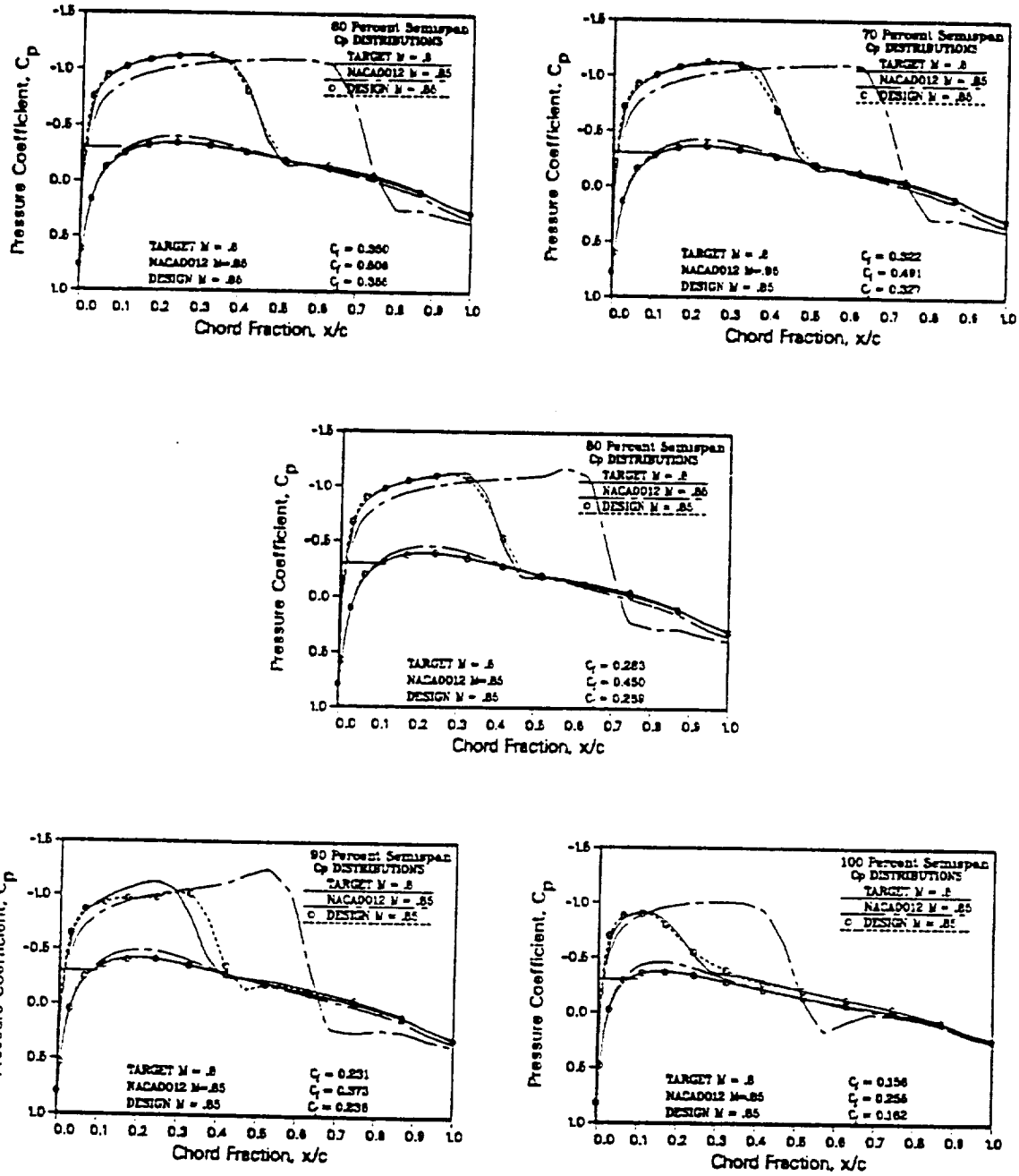

Fig. 60 Continued

lead to boundary layer difficulties, it would probably behoove the designer to vary the Mach number or alter the pressure distribution to eliminate the necessity of these dips.

V.6 Grid Refinement Effects

Since the computational time required for a design on the medium grid is about an eighth of that required on a fine grid, it may be tempting to try to design on the medium grid using fine grid or real pressures. In order to assess the practicality of this approach, a transonic design on a medium grid using fine grid pressures was carried out. The case was performed at a Mach number of .8 and an angle of attack of two degrees. The original supercritical sections for Wing-A were used as the initial, as well as, the target sections. The results are shown in Fig. 61. The only place where the designs came close to the target was near the middle of the wing. A slight wave appears in the upper surfaces of the designed sections near the shock location. This pertubation is due to the smearing of the shock on the medium grid. The section designed at the wing tip deviated considerably from the target. The fact that at the wing tip the fine grid C_l is lower than the medium grid C_l most probably led to the decambering of the sections at the wing tip.

No attempt was made to match the C_L's of the fine grid and medium grid analyses by varying the Mach number or angle of attack, but a comparison of the medium grid pressures at various Mach numbers and angles of attack with the target fine grid pressures for the supercritical wing shown in Fig. 62 reveal that it would probably be necessary to alter the twist of the wing to closely match the C_l's at all

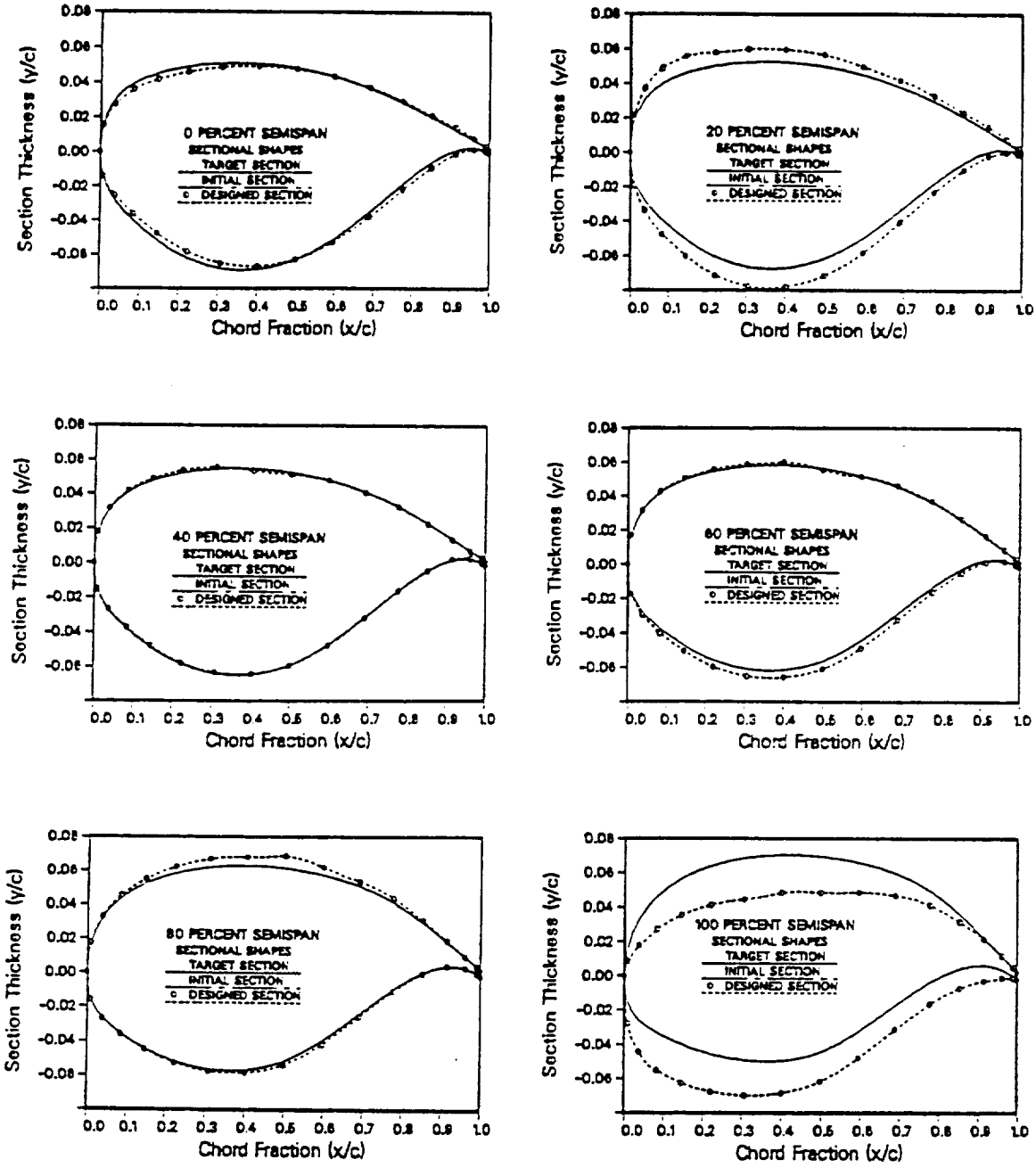

Fig. 61 Comparison of the sections obtained from a medium grid design at M = .8 using input pressure distributions obtained from a fine grid analysis of Lockheed Wing-A with the target sections

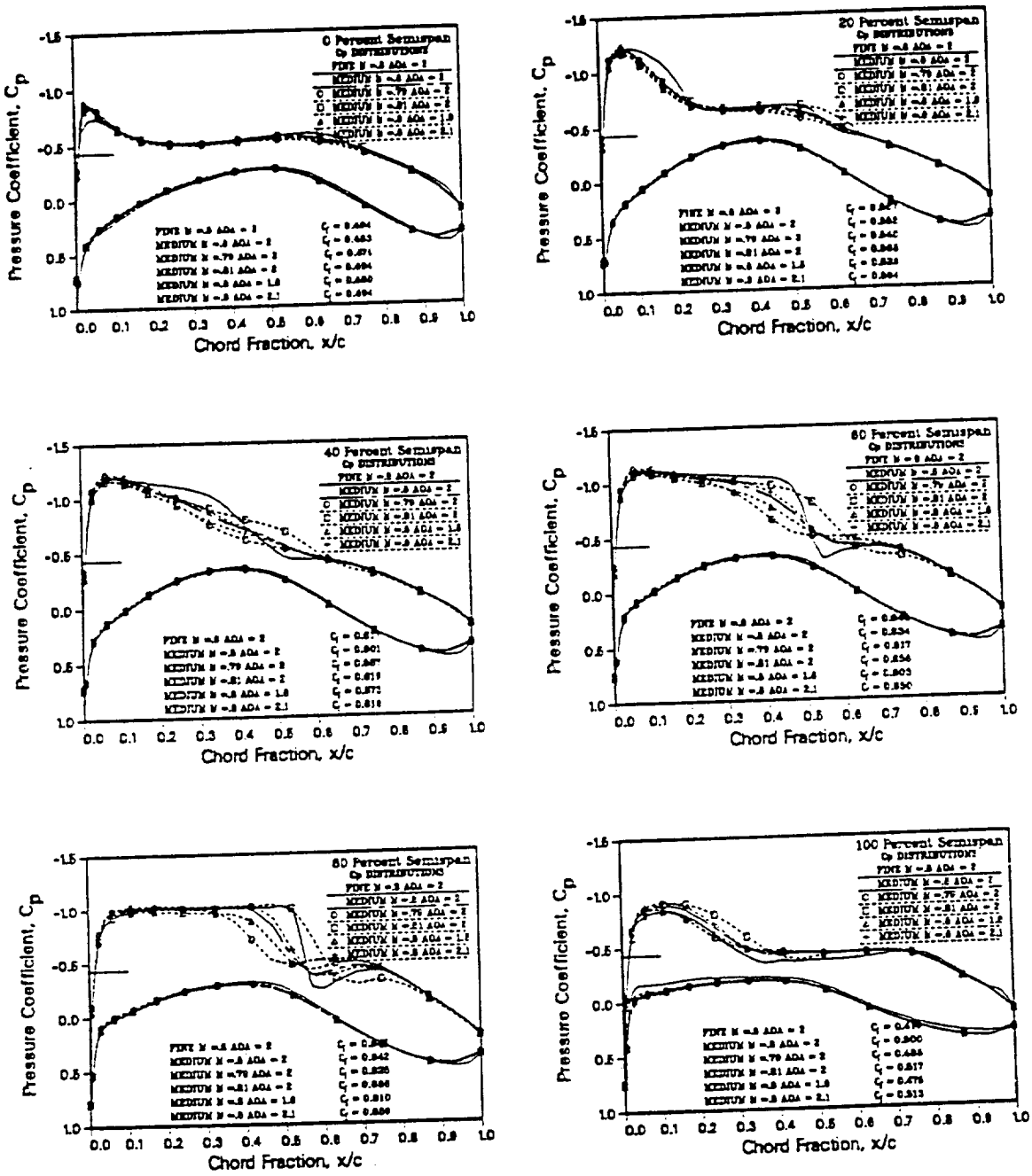

Fig. 62 Comparison of fine grid pressure distributions with medium grid pressure distributions obtained from an analysis of Lockheed Wing-A at various angles of attack and Mach numbers

of the design stations. It also shows that increasing the angle of attack to 2.1° would have produced closer matching C_l's and hence perhaps better designs. In retrospect, though, given that the fine grid pressures are correct or more realistic, it would be necessary, unless appropriate corrections can be found, to use the fine grid to properly design the correct airfoil sections.

V.7 Fixed Trailing Edge Design

This case was investigated to verify that a fixed trailing edge design could be accomplished with the present version of the code. The case chosen utilized Lockheed Wing-A at a Mach number of .8 and an angle of attack of 2°. A NACA 0012 section was used as the initial geometry from 30% to 70% semispan, while the remaining part of the wing used the original supercritical sections. The inverse boundary condition was enforced from 5% to 80% chord. The airfoil aft of 80% chord was fixed so that it maintained the NACA 0012 trailing edge shape. The input pressures were obtained through a medium grid inviscid analysis of the wing with the original supercritical sections used throughout. Furthermore, to provide for a smooth transition at the aft direct-inverse junction, the displacements were smoothed in the chordwise direction. The type II-2 design method was used in this case.

The resulting section shapes are shown in Fig. 63. The target airfoil section would actually be the first 80% of the supercritical section and the last 20% of the NACA 0012 section. Surprisingly, even with the aft portion of the wing fixed, the designed sections came quite close to matching the original Wing-A profiles at the 30% and 50% semispan locations. At the 70% semispan location, the designed section

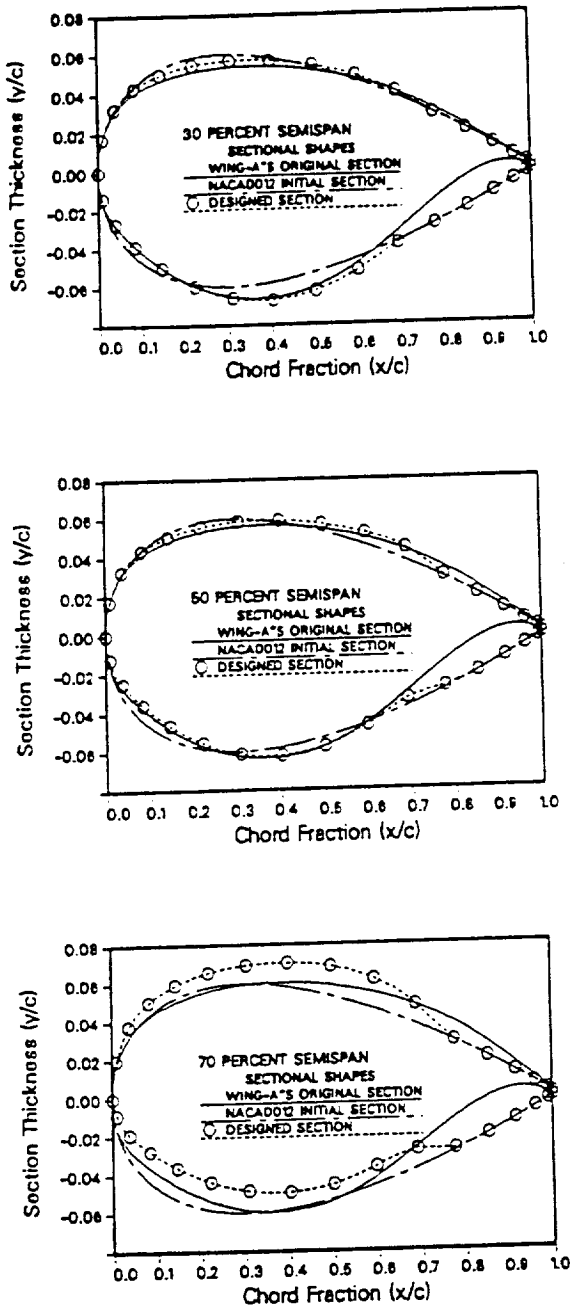

Fig. 63 Comparison of the sectional shapes designed with a fixed trailing edge region with a NACA 0012 and the original Lockheed Wing-A section

as compared to the original Wing-A section is much thicker on top and thinner on the bottom leading to a more cambered profile. This shape is probably due to the interaction of the geometric constraints and the required design pressures. The shock strength of the input C_p distribution does become quite large at this location and it appears that the section may have become more cambered to account for this increase. Or, the increased camber may have been needed to provide the necessary lift required by the inverse boundary condition. The pressure distributions obtained from an inviscid analysis of the resulting shapes are compared with those produced by the original Wing-A sections and the NACA 0012 sections in Fig. 64 The figure reveals that the design pressure distributions are a combination of the Wing-A and NACA 0012 pressure distributions. It is also interesting that it seems a secondary shock near the aft limit of the design region was necessary to meet the constraints of this problem. This very impractical case, of course, was only meant to demonstrate that it is feasible to fix the aft region of the wing. If a more realistic trailing edge were used, better results would surely follow.

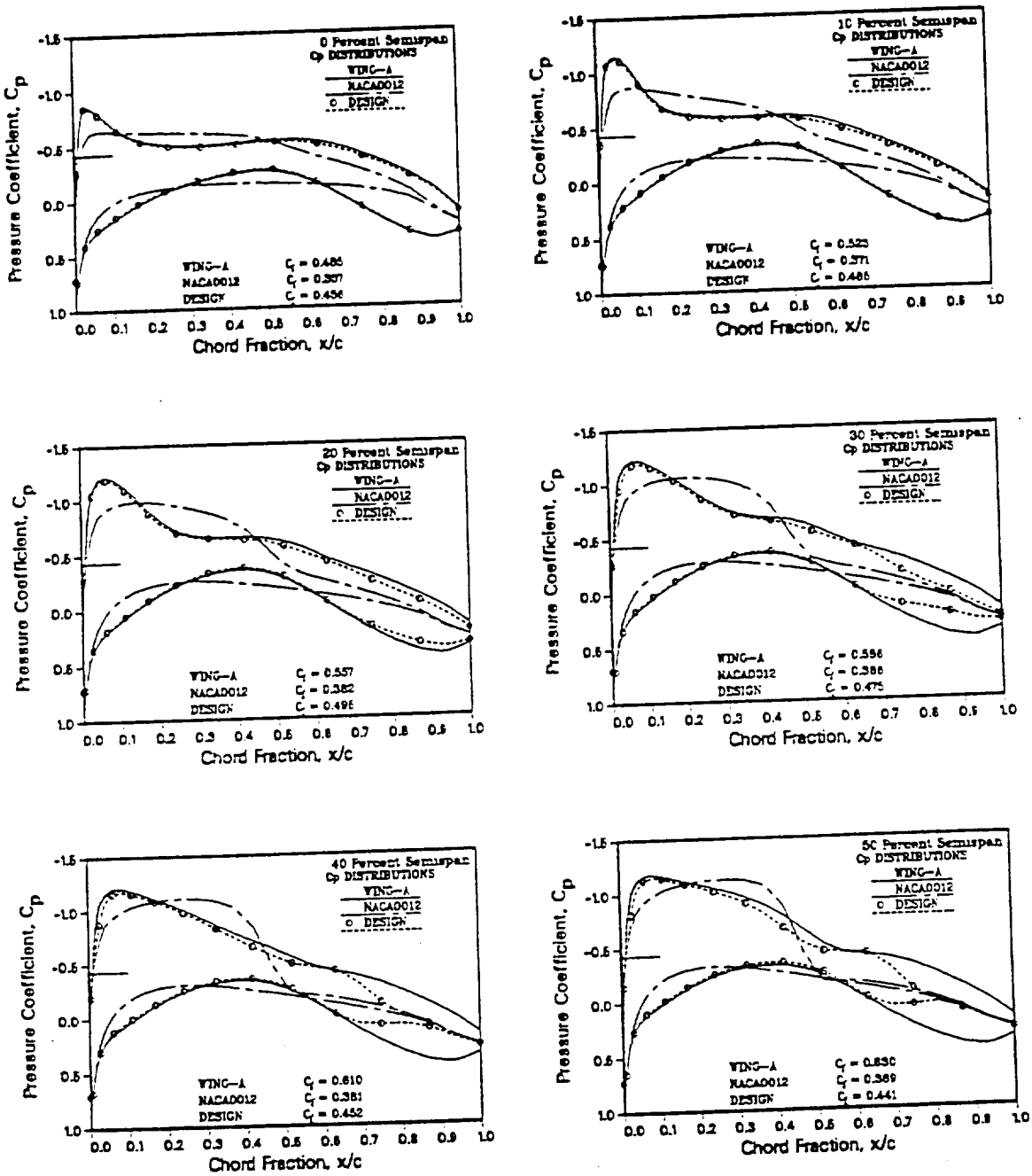

Fig. 64 Comparison of the pressure distributions obtained by an inviscid analysis of the sectional shapes designed with a fixed trailing edge region with those for a NACA 0012 and the original Lockheed Wing-A section. (M = .8, $\alpha = 2^{\circ}$)

ORIGINAL PAGE IS
OF POOR QUALITY

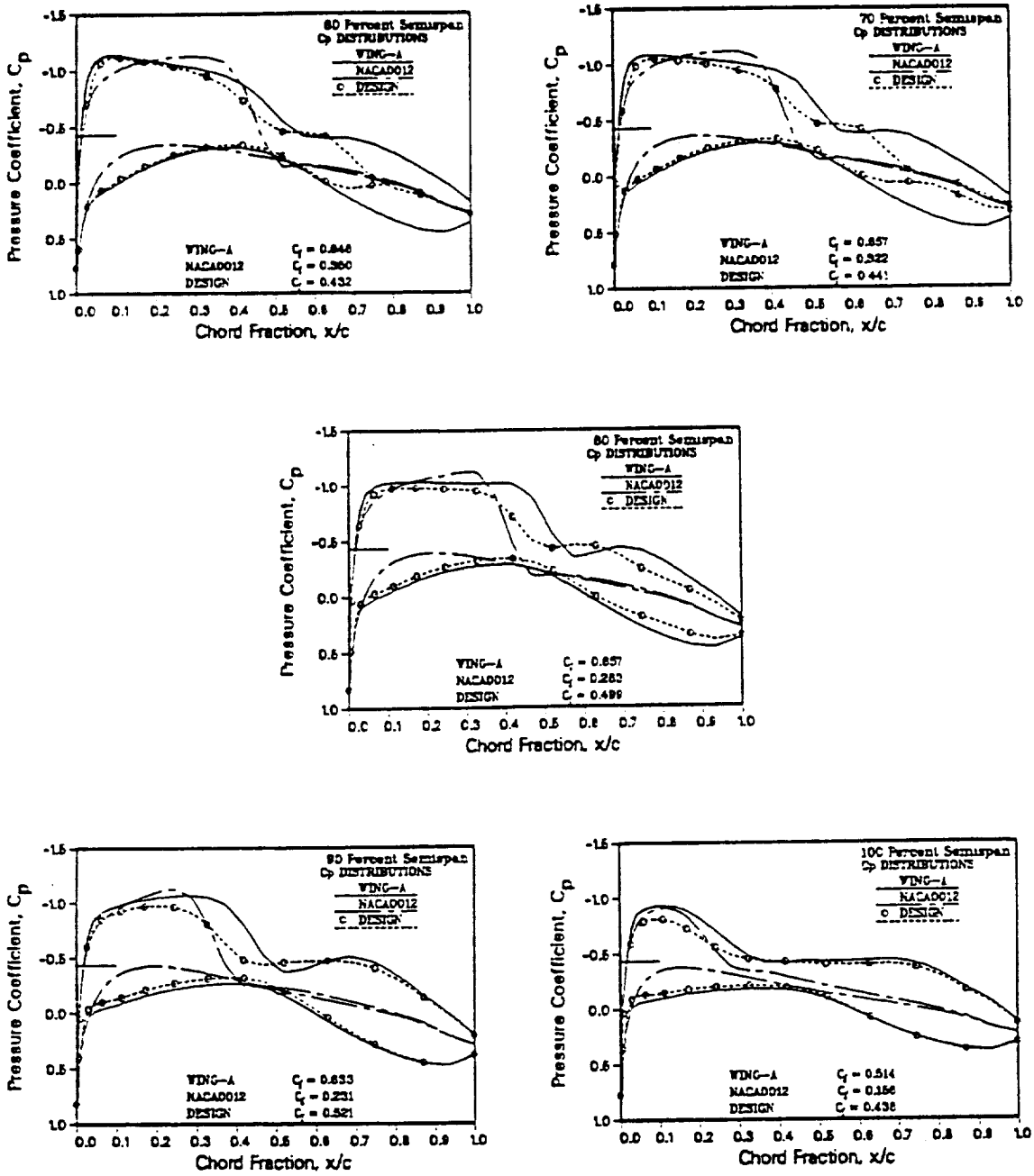

Fig. 64 Continued

CHAPTER VI

CONCLUSIONS AND RECOMMENDATIONS

Progress in the direct-inverse wing design method in curvilinear coordinates has been made, which included the remedying of a spanwise oscillation problem and the assessment of grid skewness, viscous interaction, grid refinement and the initial airfoil section on the final design. Some of the important conclusions were:

(1) In response to the spanwise oscillation problem, designing at every other spanwise station produced the smoothest results for the cases presented.

(2) A smoothly varying grid is especially needed for the accurate design at the wing tip.

(3) The final designed airfoil section is independent of the initial section if the chordwise direct-inverse junction is moved close to the leading edge.

(4) Boundary layer displacement thicknesses must be included in the successful design of a wing in a viscous environment.

(5) Presently the design of only high and medium aspect ratio wings is possible with this code.

(6) A partial wing design beginning aft of the leading edge and terminating prior to the trailing edge is possible with the present method

(7) Designs must be performed on a fine grid.

It is recommended that more work be done to fully understand the fundamental motivation behind the spanwise decoupling problem in order to eliminate all spanwise

oscillations in sectional thickness from the solution. This work should also include the development of a better way to handle the formulation of the residual at the spanwise direct-inverse junction to eliminate the initial spanwise jump in the residual located there. Furthermore, the design scheme at the wing root and tip should be refined to provide more accurate airfoil sections in those regions.

In addition, the necessary logic should be added to begin the integration of the flow tangency boundary condition on either side of the section's stagnation point at the present iteration level. This addition should allow the entire airfoil section to be designed with the pressure boundary condition specified everywhere on the wing's surface except at the stagnation point.

Prelimenary results have indicated that by allowing the trailing edge ordinate to float an untwisted wing can be twisted. If this is a well-posed problem, methods should be devised to accurately calculate the twist given the inverse displacements at the present time level and to include this in the iterative process such that the twist angle converges without undue oscillation. It would also be interesting to investigate the possibility of also allowing the leading edge ordinate to vary in a constrained fashion so that the local dihedral angle could change.

And finally, since the potential solution and, hence, the design, converge rather slowly due to the SLOR numerical scheme, the design scheme should be incorporated into the multi-grid version of FLO-30 to hasten convergence.

REFERENCES

1 Agrawal, S., Vermeland, R.E, and Lowrie, R.B., "Euler Transonic Solutions Over Finite Wings," presented at the AIAA 26^{th} Aerospace Sciences Meeting, Reno, Nevada, January 11-14, 1988, AIAA paper 88-0009.

2 Vatsa, V.N., "Navier-Stokes Solutions for Transonic Flow Over a Wing Mounted in a Tunnel," presented at the AIAA 26^{th} Aerospace Sciences Meeting, Reno, Nevada, January 11-14, 1988, AIAA paper 88-0102.

3 Pulliam, T.H., "Euler and Thin Layer Navier-Stokes Codes: ARC2d, ARC3d," Master's Thesis, NASA Ames Research Center, Moffett Field, California, 1987.

4 Campbell, R.C., and Smith, L.A., "A Hybrid Algorith for Transonic Airfoil and Wing Design," presented at the AIAA 5th Applied Aerodynamics Conference, Monterey, California, August 17-19, AIAA paper 88-0009.

5 Carlson, L. A., "Transonic Airfoil Flowfield Analysis Using Cartesian Coordinates," NASA CR-2577, August 1975.

6 Carlson, L. A., "Transonic Airfoil Design Using Cartesian Coordinates," NASA CR-2578, April 1976.

7 Carlson, L. A., "Inverse Transonic Airfoil Design Including Viscous Interaction," NASA CP-2001, November, 1976.

8 Carlson, L. A., "TRANDES: A Fortran Program for Transonic Airfoil Analysis or Design," NASA CR-2821, June 1977.

9 Carlson, L.A., Ratcliff, R.R., Gally, T. A. , "Inverse Wing Design In Transonic Flow Including Viscous Interaction," *Transonic Symposium*, NASA Langley Research Center, Hampton, Virginia, April 19-21, 1988, NASA CP-3020, Vol. I, Part 2, pp. 497.

10 Carlson, L.A. and Weed, R.A, "A Direct-Inverse Transonic Wing-Design Analysis With Viscous Interaction," *AIAA Proceedings*, Colorado Springs, Colorado, October 14-16, pp. 1-11. 1985

11 Carlson, L.A. and Weed, R.A, "A Direct-Inverse Transonic Wing Analysis-Design Method with Viscous Interaction," *Journal of Aircraft*, vol. 23, September, 1986, pp. 711-718.

12 Carlson, L. A., Rocholl, B. M., "Application of Direct-Inverse Techniques to Airfoil Analysis and Design," *Advanced Technology Airfoil Research*, Langley Research Center, Hampton, Virginia, NASA CP-2045, Part 1, June 1977.

13 Gally, T. A., "Inverse Transonic Wing Design Using Finite-Volume Methods in Curvilinear Coordinates," Master's Thesis, Texas A&M University, May 1987.

14 Gally, T. A. and Carlson, L. A., "Inverse Transonic Wing Design Using Inverse Methods in Curvilinear Coordinates," *5th Applied Aerodynamics Conference*, Monterey, California, August 17-19, 1987, pp. 516-526.

15 Gally, T.A. and Carlson, L.A., "Transonic Wing Design Using Inverse Methods in Curvilinear Coordinates," *Journal of Aircraft*, vol. 25, November, 1988, pp. 1009-1017.

16 Weed, R. A., Anderson, W. K., and Carlson, L. A., "A Direct-Inverse Three-Dimensional Transonic Wing Design Method for Vector Computers," AIAA Paper 84-2156, August 1984.

17 Weed, R.A, Carlson, L.A., "A Direct-Inverse Three-Dimensional Transonic Wing Design Method for Vector Computers," *AIAA 2nd Applied Aerodynamics Conference*, Seattle, Washington, AIAA paper 84-2156, pp. 1, August, 21-23, 1984.

18 Anderson, W. K., and Carlson, L. A., "Inverse Transonic Wing Design on a Vector Processor," Texas A&M Research Foundation Report TAMRF-4535-8212, December 1982.

19 Schlicting, Herman, *Boundary Layer Theory*, 7th Edition, McGraw-Hill Book Co., New York, New York, 1979.

20 Streett, C.L, "Viscous-Inviscid Interaction For Transonic Wing-Body Configurations Including Wake Effects," *AIAA Journal*, vol. 20, July,1982, pp. 915.

21 Smith, P.D., "An Integral Prediction Method For Three-Dimensional Turbulent Boundary Layers," *Royal Aeronautical Establishment R&M* , vol. 3739, 1972, pp. 1-54.

22 Stock, H.W., "Integral Method for the Calculation of Three-Dimensional, Laminar and Turbulent Boundary Layers," NASA TM-75320, N78-27365, July, 1978.

23 Shankar, V., Malmuth, N.D, "Computational Transonic Design Procedure for Three-Dimensional Wings and Wing-Body Combinations," presented at the

17th Aerospace Sciences Meeting, New Orleans, Louisiana, January 15-17, 1979, AIAA paper 79-0344.

24 Shankar, V. and Malmuth, N.D.,, "Computational Transonic Inverse Procedure for Wing Design," AIAA Paper 80-1390R, 1980.

25 Melson, N. D. and Streett, C. L., "TAWFIVE: A User's Guide," NASA TM84619, September 1983.

26 Green, J.E., "The Prediction of Turbulent Boundary Layer Development in Compressible Flow," *Fluid Mechanics*, vol. 31, part 4, 1968, pp. 753–778.

27 Green, J.E., Weeks, D.J., Brooman, J.W.F, "Prediction of Turbulent Boundary Layers and Wakes in Compressible Flow by a Lag-Entrainment Method," RAE TR - 72231, January, 1973.

28 Green, J.E., "Application of Head's Entrainment Method to the Prediction of Turbulent Boundary Layers and Wakes in Compressible Flow," RAE TR - 72079, June, 1972.

29 Jameson, Anthony, "Iterative Solution of Transonic Flows over Airfoils and Wings, Including Flows at Mach 1," *Comm. Pure Appl. Math.*, vol. 27, 1974, pp. 283-309.

30 Jameson, Anthony, "Transonic Potential Flow Calculations Using Conservative Form," *Proceedings of AIAA 2nd Computational Fluid Dynamics Conference*, Hartfort, Connecticut, June 1975, pp. 148-161.

31 Jameson, Anthony and Caughey, D. A., "A Finite Volume Method for Transonic Potential Flow Calculations," *Proceedings of AIAA 3rd Computational Fluid Dynamics Conference*, Albuquerque, New Mexico, June 1977, pp. 35-54.

32 Caughey, D.A., and Jameson, Anthony, "Numerical Calculation of Transonic Potential Flow about Wing-body Combinations," *AIAA Journal*, vol. 77-677, 1977, pp. 175-181.

33 Caughey, D.A., "A Systematic Procedure for Generating Useful Conformal Mappings," *International Journal for Numerical Methods in Engineering*, vol. 12, 1978, pp. 1651-1657.

34 Caughey, D. A. and Jameson, Anthony, "Progress in Finite-Volume Calculation for Wing-Fuselage Combinations," AIAA Paper 79-1513R, 1979.

35 Caughey, D.A., "Multi-Grid Calculation of Three-Dimensional Transonic Potential Flows," *AIAA 21st Aerospace Sciences Meeting*, Reno, Nevada, AIAA paper 83-0374, pp. 1-9, January 10-13, 1983.

36 Anderson, D.A., Tannehill, J.C., and Pletcher, R.H., *Computational Fluid Mechanics and Heat Transfer*, First Edition, Hemisphere Publishing Co., Washington, New York, London, 1984, pp. 50–53,63–66.

37 Melnik, R.E., Chow, R., and Mead, H.R., "Theory of Viscous Transonic Flow Over Airfoils at High Reynolds Number," presented at the AIAA Plasma Dynamics Conference, , 1977, no. 77, pp. 651-700.

38 Cumpsty, N.A. and Head, M.R., "The Calculation of Three-Dimensional Turbulent boundary Layers, Part II: Attachment-Line flow on an Infinite Swept Wing," Aeronautical Quarterly, vol. XVIII, pp. 150, July 1966.

39 Lock, R.C, "A Review of Methods for Predicting Viscous Effects on Aerofoils and Wings at Transonic Speeds," Royal Aircraft Establishment, London, England, pp. 2-9.

40 Bristow, D. R., and Hawk, J.D., "Subsonic Panel Method for Designing Wing Surfaces From Pressure Distribution," NASA CR-3713, 1983.

41 Davis, W., "TRO-2D: A Code for Rational Transonic Aero Optimization," AIAA Paper 85-0425, January 1985.

42 Holman, Jack P., *Experimental Methods for Engineers*, 4^{th} Edition, McGraw-Hill Book Co., New York, New York, 1984.

43 Volpe, G., and Melnik, R.E,, "The Role of Constraints in the Inverse Design Problem for Transonic Airfoils," presented at the AIAA 14^{th} Fluid and Plasma Dynamics Conference, Palo Alto, California, June 23-25, 1981, AIAA paper 81-1233.

44 Flores, J., Holst, T.L., Kwak, D., and Batiste, D., "A New Consistent Spatial Differncing Scheme for the Transonic Full Potential Equation," presented at the AIAA 21^{th} Aerospace Sciences Meeting, Reno, Nevada, January 10-13, 1983, AIAA paper 83-0373.

45 Liepmann, H.W., and Roshko, A., *Elements of Gasdynamics*, 1^{st} Edition, John Wiley & Sons, Inc., New York, New York, 1957.

Supplementary Sources Consulted

1 Bauer, F., Garabedian, P., and McFadden, G., "The NYU Inverse Swept Wing Code," NASA CR-3662, January 1983.

2 Boppe, C. W., "Transonic Flow Field Analysis for Wing-Fuselage Configurations," NASA CR-3243, 1980.

3 Bristow, D.R. and Hawk, J.D., "A Mixed Analysis and Design Surface Panel Method for Two-Dimensional Flows," *AIAA 2nd Applied Aerodynamics Conference*, Orlando, Florida, AIAA paper 82-0022, pp. January 11-14, 1982.

4 Cosentino, G. B. and Holst, T. L., "Numerical Optimization Design of Advanced Transonic Wing Configurations," AIAA Paper 85-0424, January 1985.

5 Daripa, P.K., and Sirovich, Lawrence, "Exact and Approximate Gas Dynamics Using the Tangent Gas," *Journal of Computational Physics*, vol. 62 no. 2, February, 1986, pp. 400-413.

6 Daripa, P.K., and Sirovich, Lawrence, "An Inverse Method for Subcritical Flows," *Journal of Computational Physics*, vol. 63 no. 2, April, 1986, pp. 311-328.

7 Daripa, P.K., "A Fast Approach to Designing Airfoils from Given Pressure Distribution in Compressible Flows," presented at the AIAA/AHS/ASEE Aircraft Design, Systems and Operations Meeting, St. Louis, Missouri, September 14-16, 1987, AIAA paper 87-2862.

8 Daripa, P.K, "On Inverse Airfoil Design," presented at the AIAA 6th Applied Aerodynamics Conference, Williamsburg, Virginia, June 6-8, 1988, AIAA paper 88-2573.

9 Daripa, P.K., "An Exact Inverse Method for Subsonic Flows," *Quarterly of Applied Mathematics*, vol. XLVI, Number 3, September, 1988, pp. 505-526.

10 Hassan, A., Sobieczky, H., Seebass, A.R., "Subsonic Airfoils with a Given Pressure Distribution," *AIAA Journal*, vol. 22, No. 9, September 1984, pp. 1185-1191.

11 Hess, J.L., "Calculation of Potential Flow About Arbitrary Three -Dimensional Lifting Bodies," Aerodynamics Division, Douglas Aircraft Company, Longbeach, California, MDC J5679-01, October, 1972.

12 Hicks. R., "Wing Design by Numerical Optimization," presented at the AIAA Aircraft Systems & Technology Meeting, Seattle, Washington, August 22-24, 1977, AIAA Paper 77-1247.

13 Holst, Terry L. and Ballhaus, William F., "Fast, Conservative Schemes for the Full Potential Equation Applied to Transonic Flow," *AIAA Journal*, vol. 17 no. 2, Febuary 1979, pp. 145-152.

14 Holst, T. and Thomas, S., "Numerical Solution of Transonic Wing Flow Fields," presented at the AIAA 20^{th} Aerospace Sciences Meeting, Orlando, Florida, January 11-14, 1982, AIAA paper 82-0105.

15 Holst, Terry L., "Numerical Solution of Transonic Potential Flows," Handout #4, AA 292S, .Stanford University, July, 1982

16 Kaplan, W., *Advanced Calculus*, Third Edition, Addison-Wesley Publishing, Reading, Massachusetts, August, 1984, pp. 44,101,94–99,110–117,122–125.

17 Klopfer, G.H. and Nixon, D., "Non-Isentropic Potential Formulation for Transonic Flows," *AIAA 21^{st} Aerospace Sciences Meeting*, Reno, Nevada, AIAA paper 83-0375, pp. January 10-13, 1983.

18 Ludford, G. S. S., "the Behavior at Infinity of the Potential Function of a Two Dimensional Subsonic Compressible Flow," *Journal of Mathematics and Physics*, vol. XXX, Number 3, October, 1951, pp. 117-130.

19 Malone, J. B., "An Optimal Surface Transpiration Subsonic Panel Method for Iterative Design of Complex Aircraft Configurations," *Fourteenth Fluid and Plasma Dynamics Conference*, Palo Alto, California, AIAA paper 81-1254, pp. 1-9, June 23-25, 1981.

20 Miranda, L.R., "A Perspective of Computational Aerodynamics from the Viewpoint of Airplane Design Applications," *AIAA 20^{th} Aerospace Sciences Meeting*, Orlando, Florida, AIAA paper 82-0018, pp. January 11-14, 1982.

21 Smith, C.W., Braymen, W.W., Bhateley, I.C., and Londenberg, W.K, "The Application of CFD to Military Aircraft Design at Transonic Speeds," presented at the Transonic Symposium, NASA Langley Research Center, Hampton, Virginia, April 19-21, 1988.

22 Strand, T., "Exact Method of Designing Airfoils With Given Velocity Distributions in Incompressible Flow," *Journal of Aircraft*, vol. Vol. 10, No 11, November 1973, pp. 651-659.

23 Tatsumi, S. and Takanashi, S., "Experimental Verification of Three-Dimensional Transonic Inverse Method," AIAA Paper 85-4077, October 1985.

24 Woodrow, W., Jr., "Application of a Nonisentropic Full Potential Method to Agard Standard Airfoils," AIAA paper 88-0710, 1988.

25 Woods, L. C., "The Design of Two-Dimesional Aerofoils With Mixed Boundary Conditions," *Quarterly of Applied Mathematics*, vol. 13, 1955, pp. 139-146.

APPENDIX A

DERIVATION OF THE FULL POTENTIAL EQUATION IN CURVILINEAR COORDINATES

The full potential equation transformed from cartesian to curvilinear coordinates is derived here as a courtesy to the reader.

The full potential or the continuity equation written in cartesian coordinates is

$$(\rho u)_x + (\rho v)_y + (\rho w)_z = 0 \qquad (A-1)$$

where

$$\rho = \left(1 - \frac{\gamma - 1}{\gamma + 1}\left(u^2 + v^2 + w^2\right)\right)^{\frac{1}{\gamma - 1}} \qquad (A-2)$$

It is desired to transform this equation to a curvilinear coordinate system of ξ, η, and ζ where

$$\xi = \xi(x, y, z) \qquad \eta = \eta(x, y, z) \qquad \zeta = \zeta(x, y, z) \qquad (A-3)$$

By using the standard chain rule, the following operators can be defined

$$\begin{aligned} \frac{\partial}{x} &= \xi_x \frac{\partial}{\xi} + \eta_x \frac{\partial}{\eta} + \zeta_x \frac{\partial}{\zeta} \\ \frac{\partial}{y} &= \xi_y \frac{\partial}{\xi} + \eta_y \frac{\partial}{\eta} + \zeta_y \frac{\partial}{\zeta} \\ \frac{\partial}{z} &= \xi_z \frac{\partial}{\xi} + \eta_z \frac{\partial}{\eta} + \zeta_z \frac{\partial}{\zeta} \end{aligned} \qquad (A-4)$$

Using these operators in Eq. (A-1) yields

$$\begin{aligned} &\xi_x (\rho u)_\xi + \eta_x (\rho u)_\eta + \zeta_x (\rho u)_\zeta \\ &+ \xi_y (\rho v)_\xi + \eta_y (\rho v)_\eta + \zeta_y (\rho v)_\zeta \\ &+ \xi_z (\rho w)_\xi + \eta_z (\rho w)_\eta + \zeta_z (\rho w)_\zeta = 0 \end{aligned} \qquad (A-5)$$

Defining the Jacobian, J, as

$$J = \frac{\partial(\xi,\eta,\zeta)}{\partial(x,y,z)} = \begin{vmatrix} \xi_x & \xi_y & \xi_z \\ \eta_x & \eta_y & \eta_z \\ \zeta_x & \zeta_y & \zeta_z \end{vmatrix} \qquad (A-6)$$

Then after Holst, multiplying the Eq. (A-5) by J^{-1}, and rearranging to conservative form plus remainder gives

$$\begin{aligned} &\left[\left((\rho u)\,\xi_x J^{-1}\right) + \left((\rho v)\,\xi_y J^{-1}\right) + \left((\rho w)\,\xi_z J^{-1}\right)\right]_\xi \\ &+ \left[\left((\rho u)\,\eta_x J^{-1}\right) + \left((\rho v)\,\eta_y J^{-1}\right) + \left((\rho w)\,\eta_z J^{-1}\right)\right]_\eta \\ &+ \left[\left((\rho u)\,\zeta_x J^{-1}\right) + \left((\rho v)\,\zeta_y J^{-1}\right) + \left((\rho w)\,\zeta_z J^{-1}\right)\right]_\zeta \\ &- (\rho u)\left[\left(\xi_x J^{-1}\right)_\xi + \left(\eta_x J^{-1}\right)_\eta + \left(\zeta_x J^{-1}\right)_\zeta\right] \\ &- (\rho v)\left[\left(\xi_y J^{-1}\right)_\xi + \left(\eta_y J^{-1}\right)_\eta + \left(\zeta_y J^{-1}\right)_\zeta\right] \\ &- (\rho w)\left[\left(\xi_z J^{-1}\right)_\xi + \left(\eta_z J^{-1}\right)_\eta + \left(\zeta_z J^{-1}\right)_\zeta\right] = 0 \end{aligned} \qquad (A-7)$$

Now using the fact that

$$\frac{\partial J^{-1}}{\partial s} = -J^{-2}\frac{\partial J}{\partial s} \qquad (A-8)$$

the last three terms in brackets can be shown to be zero. For example, equating the first of these terms to zero

$$(\rho u)\left[\left(\xi_x J^{-1}\right)_\xi + \left(\eta_x J^{-1}\right)_\eta + \left(\zeta_x J^{-1}\right)_\zeta\right] = 0 \qquad (A-9)$$

and expanding the derivatives and collecting like terms gives

$$\begin{aligned} &J^{-1}\left[(\xi_x)_\xi + (\eta_x)_\eta + (\zeta_x)_\zeta\right] \\ &- J^{-2}\left[\xi_x J_\xi + \eta_x J_\eta + \zeta_x J_\zeta\right] = 0 \end{aligned} \qquad (A-10)$$

Rewriting Eq. (A-4) in matrix notation

$$\begin{pmatrix} \frac{\partial}{\partial x} \\ \frac{\partial}{\partial y} \\ \frac{\partial}{\partial z} \end{pmatrix} = \begin{pmatrix} \xi_x & \eta_x & \zeta_x \\ \xi_y & \eta_y & \zeta_y \\ \xi_z & \eta_z & \zeta_z \end{pmatrix} \begin{pmatrix} \frac{\partial}{\partial \xi} \\ \frac{\partial}{\partial \eta} \\ \frac{\partial}{\partial \zeta} \end{pmatrix} \qquad (A-11)$$

After solving for $\frac{\partial}{\partial \xi}, \frac{\partial}{\partial \eta}, \frac{\partial}{\partial \zeta}$, this becomes

$$\begin{pmatrix} \frac{\partial}{\partial \xi} \\ \frac{\partial}{\partial \eta} \\ \frac{\partial}{\partial \zeta} \end{pmatrix} = \begin{pmatrix} A_{11} & -A_{12} & A_{13} \\ -A_{21} & A_{22} & -A_{23} \\ A_{31} & -A_{32} & A_{33} \end{pmatrix} \begin{pmatrix} \frac{\partial}{\partial x} \\ \frac{\partial}{\partial y} \\ \frac{\partial}{\partial z} \end{pmatrix} [J^{-1}] \qquad (A-12)$$

where :

$$A_{11} = \eta_y \zeta_z - \zeta_y \eta_z \quad A_{12} = \xi_y \zeta_z - \xi_z \zeta_y \quad A_{13} = \xi_y \eta_z - \eta_y \xi_z$$

$$A_{21} = \eta_z \zeta_z - \eta_z \zeta_z \quad A_{22} = \xi_z \zeta_z - \xi_z \zeta_z \quad A_{23} = \xi_z \eta_z - \xi_z \eta_z \qquad (A-13)$$

$$A_{31} = \eta_z \zeta_y - \eta_y \zeta_z \quad A_{32} = \xi_z \zeta_y - \xi_y \zeta_z \quad A_{33} = \xi_z \eta_y - \eta_z \xi_y$$

These operators can be used to expand the derivatives of ξ_z, η_z, and ζ_z so that

$$(\xi_z)_\xi = [A_{11}\xi_{zz} - A_{21}\xi_{zy} + A_{31}\xi_{zz}]\, J^{-1}$$

$$(\eta_z)_\eta = [A_{12}\eta_{zz} - A_{22}\eta_{zy} + A_{32}\eta_{zz}]\, J^{-1} \qquad (A-14)$$

$$(\zeta_z)_\zeta = [A_{13}\zeta_{zz} - A_{23}\zeta_{zy} + A_{33}\zeta_{zz}]\, J^{-1}$$

Substituting these into Eq. (A-10) and collecting terms yields

$$\begin{aligned} & J^{-2}[A_{11}\xi_{zz} - A_{21}\xi_{zy} + A_{31}\xi_{zz} \\ & -A_{12}\xi_{zz} - A_{22}\xi_{zy} + A_{32}\xi_{zz} \\ & +A_{13}\xi_{zz} - A_{23}\xi_{zy} + A_{33}\xi_{zz}] \\ & -J^{-3}[A_{11}J_x\xi_z - A_{21}J_y\xi_z + A_{31}J_z\xi_z \\ & -A_{12}J_x\eta_z - A_{22}J_y\eta_z + A_{32}J_z\eta_z \\ & +A_{13}J_x\zeta_z - A_{23}J_y\zeta_z + A_{33}J_z\zeta_z] = 0 \end{aligned} \qquad (A-15)$$

$$\text{with} \quad J = \xi_z A_{11} - \eta_z A_{12} + \zeta_z A_{13}$$

Expanding the second term in brackets in the previous equation to

$$\begin{aligned} & -J^{-3}[J_x J + J_y(\xi_x\eta_x\zeta_x - \xi_x\eta_x\zeta_x \\ & +\xi_x\eta_x\zeta_x - \xi_x\eta_x\zeta_x + \xi_x\eta_x\zeta_x - \xi_x\eta_x\zeta_x) \\ & +J_z(\xi_x\eta_x\zeta_y - \xi_x\eta_y\zeta_x - \xi_x\eta_x\zeta_y \\ & +\xi_y\eta_x\zeta_x + \xi_x\eta_y\zeta_x - \xi_y\eta_x\zeta_x)] \end{aligned} \qquad (A-16)$$

and cancelling like terms, this reduces simply to

$$\text{Second term } = J^{-2} J_z \qquad (A-17)$$

$$\begin{aligned} \text{where : } J_z =& \xi_z (A_{11})_z - \eta_z (A_{12})_z + \zeta_z (A_{13})_z \\ &+ \xi_{zz} A_{11} - \eta_{zz} A_{12} + \zeta_{zz} A_{13} \end{aligned} \qquad (A-18)$$

Partially expanding J_z to

$$\begin{aligned} J_z =& \xi_{zz} A_{11} - \eta_{zz} A_{12} + \zeta_{zz} A_{13} \\ &+ \xi_z (\eta_{zy}\zeta_z + \eta_y \zeta_{zz} - \eta_z \zeta_{zy} - \zeta_y \eta_{zz}) \\ &- \eta_z (\xi_{zy}\zeta_z + \xi_y \zeta_{zz} - \xi_{zz}\zeta_y - \xi_z \zeta_{zy}) \\ &+ \zeta_z (\xi_{zy}\eta_z + \xi_y \eta_{zz} - \eta_{zy}\xi_z - \eta_y \xi_{zz}) \end{aligned} \qquad (A-19)$$

Upon collection of like terms, this becomes identical to the first term in brackets in Eq. (A-15), thus satisfying the equality. This can be shown to be true of the other remainder type terms in Eq. (A-7).

Now, reducing the conservative part of Eq. (A-7) to

$$\begin{aligned} &\left[J^{-1}\left((\rho u)\xi_z + (\rho v)\xi_y + (\rho w)\xi_z\right)\right]_\xi \\ &+ \left[J^{-1}\left((\rho u)\eta_z + (\rho v)\eta_y + (\rho w)\eta_z\right)\right]_\eta \\ &+ \left[J^{-1}\left((\rho u)\zeta_z + (\rho v)\zeta_y + (\rho w)\zeta_z\right)\right]_\zeta = 0 \end{aligned} \qquad (A-20)$$

and defining the contravariant velocities, U, V, W, as

$$\begin{pmatrix} U \\ V \\ W \end{pmatrix} = \begin{pmatrix} \xi_z & \xi_y & \xi_z \\ \eta_z & \eta_y & \eta_z \\ \zeta_z & \zeta_y & \zeta_z \end{pmatrix} \begin{pmatrix} u \\ v \\ w \end{pmatrix} \qquad (A-21)$$

with

$$\mathrm{h} = J^{-1} = \begin{vmatrix} x_\xi & x_\eta & x_\zeta \\ y_\xi & y_\eta & y_\zeta \\ z_\xi & z_\eta & z_\zeta \end{vmatrix} \qquad (A-22)$$

Eq. (A-20) reduces to the desired conservative form of

$$(\rho \mathrm{h} U)_\xi + (\rho \mathrm{h} V)_\eta + (\rho \mathrm{h} W)_\zeta = 0 \qquad (A-23)$$

APPENDIX B

DERIVATION OF THE C_P EQUATION

Although this derivation probably appears in most good books on aerodynamics, it is included here as a courtesy to the reader.

C_p is defined as

$$C_p = \frac{p - p_\infty}{\frac{1}{2}\rho_\infty {q^2}_\infty} \qquad (B-1)$$

Using the definition of the speed of sound and isentropic relations, this can be rewritten as

$$C_p = \frac{2}{\gamma {M^2}_\infty}\left(\frac{p}{p_\infty} - 1\right) \qquad (B-2)$$

It is desired to obtain a relation for the pressure coefficient, C_p, in terms of soley the freestream Mach number and the local q_∞. This can be easily accomplished by beginning with Eq. (2-14),

$$\rho = (aM_\infty)^{\frac{2}{\gamma-1}} \qquad (B-3)$$

and using the isentropic relation in Eq. (2-10), pressure can be written as

$$\frac{p}{p_\infty} = (aM_\infty)^{\frac{2\gamma}{\gamma-1}} \qquad (B-4)$$

Upon substituting this into Eq. (B-2), equation, C_p becomes

$$C_p = \frac{2}{\gamma {M^2}_\infty}\left((aM_\infty)^{\frac{2}{\gamma-1}} - 1\right) \qquad (B-5)$$

And finally, making use of Eqs. (2-8) and (2-9), the previous equation can be reduced to the desired relation :

$$C_p = \frac{2}{\gamma {M^2}_\infty}\left[\left[1 + \frac{\gamma-1}{2}{M_\infty}^2\left(1 - \frac{q^2}{q_\infty^2}\right)\right]^{\frac{\gamma}{\gamma-1}} - 1\right] \qquad (B-6)$$

where $q^2 = \left(u^2 + v^2 + w^2\right){q^2}_\infty$.

VITA

Robert R. Ratcliff was born [redacted] on [redacted] He grew up in the west Texas town of El Paso and graduated from Irvin high school in 1981. He received a B.S in Mechanical and Aerospace engineering from Texas A&M in the spring of 1986 and a M.S. in Aerospace engineering in August, 1989.

Any correspondance may be addressed to him in care of his mother, Jane E. Ratcliff, at 8706 Magnetic, El Paso, Texas 79904.

Appendix IV

User's Manual for TAW5D

Originally, it was planned to include the user's manual in this final report. However, due difficulties in the preparation of figures, it will not be available until mid-November. Thus, it will be provided to NASA Langley under separate cover.